NASA/CR-97-206248

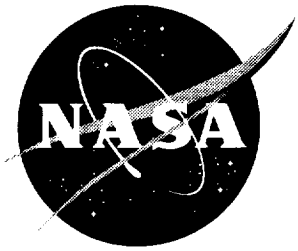

NASA-UVa Light Aerospace Alloy and Structure Technology Program Supplement: Aluminum-Based Materials for High Speed Aircraft

Final Report

E. A. Starke, Jr.
University of Virginia, Charlottesville, Virginia

National Aeronautics and
Space Administration

Langley Research Center
Hampton, Virginia 23681-2199

Prepared for Langley Research Center
under Grant NAG1-745

December 1997

Available from the following:

NASA Center for AeroSpace Information (CASI)
800 Elkridge Landing Road
Linthicum Heights, MD 21090-2934
(301) 621-0390

National Technical Information Service (NTIS)
5285 Port Royal Road
Springfield, VA 22161-2171
(703) 487-4650

Table of Contents

UNIVERSITY OF VIRGINIA (R.P. Gangloff)

Elevated Temperature Fracture Toughness of Advanced RS/PM and I/M Aluminum Alloys

EXECUTIVE SUMMARY

Market projections indicate that a substantial potential demand exists for a high-speed civil transport (HSCT) to operate in the long-range international market. Preliminary design and technology development efforts are underway to better understand all requirements including the technical and economic feasibility of the HSCT. Ongoing studies show airplanes designed to fly between Mach 2.0 and 2.4, with a capacity of 250 to 300 passengers and a range of at least 5000 nautical miles, have the best opportunity of meeting the economic objectives. The key critical development issue for an economically viable HSCT airframe will be the development of materials and processes which allow a complex, highly-stressed, extremely weight-efficient airframe to be fabricated and assembled for a dollar-per-pound not greatly different than today's mature airframes.

This document is the final report of the study "Aluminum-Based Materials for High Speed Aircraft" which had the objectives: (1) to identify the most promising aluminum-based materials with respect to major structural use on the HSCT and to further develop those materials, and (2) to assess the materials through detailed trade and evaluation studies with respect to their structural efficiency on the HSCT. The research team consisted of ALCOA, Allied-Signal, Boeing, McDonnell Douglas, Reynolds Metals, and the University of Virginia. Four classes of aluminum alloys were investigated; (1) I/M 2XXX containing Li (Reynolds) and I/M 2XXX without Li (ALCOA), (2) I/M 6XXX (ALCOA), (3) two P/M 2XXX alloys (ALCOA and Allied-Signal) and (4) two different Aluminum-base metal matrix composites (MMC) (ALCOA and UVa). The I/M alloys were targeted for a Mach 2.0 aircraft and the P/M and MMC alloys were targeted for a Mach 2.4 aircraft.

Boeing and McDonald Douglas conducted design studies using several different concepts including skin/stiffener (baseline), honeycomb sandwich, integrally stiffened (including extruded stringers, orthogrid and isogrid concepts) and hybrid adaptations (conventionally stiffened thin-sandwich skins). The design concepts were exercised with respect to the wing box (upper), wing box (lower), wing strake, and the crown, window belt and keel areas of the fuselage. The results of these studies indicated that the preferred concept depended greatly upon the part of the aircraft being considered, but that many had advantages over the baseline skin-stringer design.

All team members were involved in the materials studies. Early in the program it was determined that the strengths of the I/M 6XXX alloys were too low for the target application and research on that class of alloys was discontinued. Although the microstructures of the P/M alloys were very stable at the temperatures of interest for a Mach 2.4 aircraft, both ductility and fracture

toughness decreased as the temperature increased from ambient temperature and research on the P/M materials was also discontinued. A fundamental analysis of this fracture problem is included in this report. Research on the ALCOA MMC was also discontinued due to poor high temperature properties, although some basic research on MMC's was continued at the University of Virginia to the end of this Grant.

Two lithium-free 2XXX alloys (ALCOA) based on 2519, and two 2XXX alloys containing lithium (Reynolds) based on the Weldalite family, were identified as having attractive mechanical properties and thermal stability. The lithium-free alloys, designated C415 and C416, are considered prime candidates for the high toughness goals. Their chemical compositions in weight percent are:

Alloy	Cu	Mg	Mn	Ag	Zr	Fe	Si
C415	5.0	0.8	0.6	0.5	0.13	0.06	0.04
C416	5.4	0.5	0.3	0.5	0.13	0.06	0.04

Alloy C415 exhibited higher room temperature and elevated temperature strengths than alloy C416, while alloy C416 appeared to be more thermally stable and more creep resistant than alloy C415. C415 contained undissolved constituents and three lower solute variants will be evaluated on a follow-on program.

The two lithium-containing alloys, designated RX818 and ML377, are considered prime candidates for the high strength goals for a Mach 2.0 aircraft. Their chemical compositions in weight percent are:

Alloy	Li	Cu	Mg	Mn	Ag	Zr
RX818	0.96	3.7	0.37	0	0.34	0.14
ML377	0.97	3.6	0.35	0.37	0.39	0.14

RX818-T8 had the higher strength, but both RX818 and ML377 exhibited good strength and elongation combinations. RX818 sheet was highly anisotropic, (20% lower strength) at 45° to the rolling direction. Both alloys show promising thermal stability based on relatively short-time data.

Fundamental studies of coarsening behavior, the effect of stress on nucleation and growth of precipitates, and fracture toughness as a function of temperature were an integral part of this program. The details of all phases of the research on the aluminum-based alloys are described in this final report.

ALCOA

Aluminum-Based Materials for High Speed Aircraft - Final Report

L. M. Karabin
Alcoa Technical Center

Abstract

In the first phase of the program, four classes of aluminum alloys were investigated as candidates for the lower wing and fuselage of a high speed aircraft. Three of these classes, e.g., I/M 2XXX, I/M 6XXX and P/M 2XXX alloys, were targeted at a Mach 2.0 aircraft while the fourth type, e.g., P/M Al-Fe-Ce-Mg, was targeted at a Mach 2.4 aircraft. All were produced as 0.125" thick sheet. Of the Mach 2.0 candidates, the best strength/plane stress toughness combination was achieved in a P/M alloy having the composition Al-5.72 Cu-0.54 Mg-0.31 Mn-0.51 Ag-0.57 Zr-0.1V. That alloy achieved a tensile yield strength of 74 ksi at a K_c of 126 ksi $\sqrt{in}$. The best I/M 2XXX alloy, Al-5.75 Cu-0.52 Mg-0.30 Mn-0.49 Ag-0.16 Zr-0.09V achieved a tensile yield strength of 70 ksi at a K_c of 110 ksi $\sqrt{in}$. Since the alloys are similar in composition except for the higher Zr content of the P/M alloy, the difference in strength/plane stress fracture toughness combination may be due to grain structure differences, i.e., the P/M sheet was predominantly unrecrystallized while the I/M sheet was recrystallized. The hardnesses and strengths of all the I/M 6XXX alloys were too low to warrant further study. The best I/M 2XXX alloys were chosen for further investigation in subsequent phases.

Although Mg additions to the P/M Al-8 Fe-4 Ce alloy resulted in greater work hardenability, the plane stress fracture toughness was reduced. For the Al-8 Fe-4 Ce-0.5 Mg alloy, the best strength/plane stress fracture toughness combination was achieved in product forms receiving the highest degree of thermomechanical processing. Furthermore, the greatest crack growth resistance and the most stable crack growth was measured in specimens that were tested at low crosshead speeds.

Some characterization of 0.125" thick sheet of discontinuously reinforced metal matrix composites was also carried out in Phase I of the current program since those materials were considered as candidates for the upper wing of a high speed aircraft. Variations in rolling practice did not produce significant differences in strength/plane stress fracture toughness combinations. In the composites having a 2XXX-T6 matrix and 20% SiC, tensile yield strengths varied from 70 to 76 ksi, while all K_c values were less than 30 ksi Higher

toughnesses and lower strengths were obtained for composites having a 6113-T6 matrix.

Preliminary studies of the effects of stressed and unstressed elevated temperature exposure on residual strengths were also conducted during Phase I for three materials: 2519-T87, 2080/SiC/20p and 6013-T6. All materials were degraded as a result of exposures at 300°F, however, stresses of 18 ksi did not enhance degradation in any of the materials.

The focus of Phases II and III was on the development of the I/M 2XXX alloys for the lower wing and fuselage. Work on the I/M 6XXX alloys, P/M alloys, P/M Al-Fe-Ce alloy and the discontinuously reinforced composites was discontinued. Studies of the effects of stressed and unstressed elevated temperature exposures were also discontinued.

During Phase II, four I/M 2XXX alloys were studied; e.g., the two best candidates from Phase I and two additional alloys studied in a companion program at Alcoa. The objective of that phase was to determine the effect of aging practice on strength, toughness and thermal stability. The highest longitudinal tensile yield strengths of 77 to 78 ksi were obtained in an alloy whose composition was close to the composition which eventually became alloy C415. It obtained invalid L-T fracture toughness values of 107 to 120 ksi $\sqrt{\text{in}}$.

Peak aged tensile yield strengths and fracture toughness values were relatively independent of aging practice. Tensile properties of all four alloys were unaffected or slightly enhanced as a result of exposures of 1000 h at 225°F, but were degraded considerably after exposures of 1000 h at 275°F. For all four alloys, fracture toughness was degraded as a result of either elevated temperature exposure, although the effect was smallest in an alloy whose composition was close to the composition which eventually became alloy C416. That alloy achieved lower longitudinal tensile yield strengths; e.g., 71 to 72 ksi, than the alloy with the composition close to C415.

The compositions of the two most promising alloys from Phase II were modified slightly to minimize undissolved constituent and were named C415 and C416.

	Composition, wt%						
Alloy	Cu	Mg	Mn	Ag	Zr	Fe	Si
C415	5.0	0.8	0.6	0.5	0.13	0.06	0.04
C416	5.4	0.5	0.3	0.5	0.13	0.06	0.04

During Phase III, the focus was on studying the effects of stretch level and grain structure on strength/toughness combinations, retention of strength/toughness combinations after exposure and creep in both C415 and C416.

Alloy C415 exhibited higher room temperature and elevated temperature strengths than alloy C416, while alloy C416 appeared to be more thermally stable and more creep resistant than alloy C415. It was recommended that property targets for high speed civil transport applications be reviewed in order to choose a single alloy. Furthermore, it was recognized that C415 still contained undissolved constituent and three lower solute variants were recommended for further study. Also, the needs for valid wide panel fracture toughness data and more reliable creep data were emphasized.

During the final Phase IV, three lower solute variants of C415 were cast and fabricated to sheet. The sheet was provided to a follow-on NASA program, NAS1-20220 HSRII/BOEI, for characterization.

1.0 I/M 2XXX Alloy Development

Objective

The primary objective of this task was to develop a damage tolerant aluminum-based material for the lower wing and fuselage of a Mach 2.0 aircraft. This material must first meet preliminary strength and toughness targets at room temperature and then several criteria associated with elevated temperature service, (e.g. retention of room temperature properties after exposure, performance at the operating temperature and resistance to creep deformation). Corrosion resistance will also be important.

The ingot metallurgy (I/M) 2XXX alloys were under consideration here because existing Al-Cu-Mg alloys combined relatively high strengths with good thermal stability.

Introduction

Phase I. Period 1992 January 01 through 1992 December 31

The most up-to-date Alcoa data on 2XXX exploratory alloys, archival Alcoa data on 2XXX alloys and external literature were reviewed in order to arrive at a set of 2XXX alloys and a detailed experimental plan for the current program. These alloy compositions were discussed with Professor E. A. Starke of UVA and Barry Lisagor and Tom Bales of NASA-Langley.

Four alloys were selected. Their nominal compositions in weight percent were:

S.No	Alloy Composition
689245	Al-5.85 Cu-0.20 Mg-0.30 Mn-0.15 Zr-0.10 V
689246	Al-5.85 Cu-0.20 Mg-0.30 Mn-0.15 Zr-0.10 V-0.25 Si
689247	Al-5.85 Cu-0.50 Mg-0.30 Mn-0.15 Zr-0.10 V
689248	Al-5.85 Cu-0.50 Mg-0.30 Mn-0.15 Zr-0.10 V-0.50 Ag

The alloys designed to study the effects of Mg, Si and Ag on precipitation in 2519-type alloys. Note that S. No. 689245 is the 2519 control, S. No. 689246 contains excess Si, S. No. 689247 contains excess Mg and S. No. 689248 contains combined additions of Mg and Ag. Alloy 2519 was chosen as the baseline since recent data suggested that it had a promising strength/plane stress toughness combination when compared to 2024-T3 and 6013-T6.

The interest in these additions relied heavily on prior Alcoa investigations. Firstly, there are many studies which would support the use of higher Mg levels than those in 2519. During the late 1940's and early 1950's, Alcoa carried out extensive alloy development work surrounding the compositions which eventually became 2219 and 2618. One alloy, called M237, contained 0.5% Mg and exhibited significantly higher strengths than 2219. This higher strength alloy was not pursued at the time, and later, when 2519 was developed, Mg levels were kept low in order to maintain weldability.

The effects of Si level were also explored in the early days, however, those results were very difficult to interpret without the benefit of original raw data. An investigation carried out much later in conjunction with Alcoa's forging plant in Cleveland, however, was more conclusive. Si additions served as nucleation aids for the θ' precipitates, thereby increasing the peak aged yield strengths which could be achieved in T6-type tempers. This discovery, which was particularly useful for product forms like forgings which cannot be stretched prior to artificial aging, led to the development of the forging alloy C197. It may also have potential for HSCT materials. If high strengths can be achieved without the use of cold work, the thermal stability may be improved.

Recent Alcoa research on small ingots had shown that combined additions of Ag and Mg to 2519 can lead to a 10% increase in the peak aged tensile yield strength of the T8-type temper.

This strength advantage, which had been attributed to the replacement of θ' by the more potent plate-like Ω phase, was maintained after short exposures at temperatures up to 400°F. S. No. 689248 was selected so that this promising alloy could be explored further.

Phase II. Period 1993 January 01 through 1994 January 31

In addition to the four I/M 2XXX alloys studied in Phase I, six alloys were carried through a companion program at Alcoa. Of the ten alloys, for which microstructures and room temperature tensile and fracture toughness were characterized, four were considered most promising. Their nominal compositions in weight percent were:

S. No.	Alloy Composition
689247	Al-5.85 Cu-0.5 Mg-0.3 Mn-0.1V-0.15 Zr
689248	Al-5.85 Cu-0.5 Mg-0.3 Mn-0.5 Ag-0.1V-0.15 Zr
689250	Al-5.2 Cu-0.8 Mg-0.5 Ag-0.15 Zr
689251	Al-5.2 Cu-0.8 Mg-0.6 Mn-0.5 Ag-0.1V-0.15 Zr

The nominal compositions of all four of the promising alloys contained more solute than could be put into an aluminum solid solution. That excess solute could not be used for strengthening. Instead, it was present in coarse deleterious constituent. Therefore, all compositions would need to be adjusted eventually if they were to be commercialized. However, available ingot sections, having somewhat suboptimal compositions, were selected for use in the second phase of this program.

In Phase II, various T8-type aging practices were to be studied for the four alloys. Room temperature strength/toughness combinations were to be measured before and after elevated temperature exposures. Once two alloys were judged to be superior to the rest, the composition(s) were to be adjusted and new ingot(s) were to be cast.

Phase III. Period 1994 February 01 through 1995 October 31

Two Al-Cu-Mg-Mn-Ag alloys, S. Nos. 689248 and 689251 from Phase II, were identified as having promising strength-plane stress fracture toughness relationships (based on room temperature properties of T8-type tempers) and were selected for evaluation in Phase III. The Cu and Mg levels were reduced slightly from their original values so that undissolved

constituent would be minimized. The nominal compositions of the alloys are given below:

	Composition (wt.%)						
Alloy	Cu	Mg	Mn	Ag	Zr	Fe	Si
C415	5.0	0.8	0.6	0.5	0.13	0.06	0.04
C416	5.4	0.5	0.3	0.5	0.13	0.06	0.04

These alloys were studied along with other Al-Cu-Mg-Mn-(Ag) alloys during the last several reporting periods (References 1-5) and several general observations had been made:

- Both of the alloys of interest contain Ag and sufficient levels of Mg to promote the formation of Ω phase, a precipitate which forms on the {111} planes in Al-Cu-Mg-Ag alloys. This phase is a more potent strengthener than Θ', the precipitate which forms on {100} planes in Al-Cu alloys and in Al-Cu-Mg alloys if Mg levels are low.

- Both alloys contain Mn in the form of submicron $Al_{20}Cu_2Mn_3$ particles and Zr in an unidentified form for grain structure control. Despite microstructural characterization by optical metallography, Laue x-ray diffraction and orientation distribution function measurements, definitive conclusions concerning the extent of recrystallization could not be made.

- Variations in aging practice did not have a significant effect on strength or thermal stability. Isothermal practices at 275°F and 325°F and a two-step practice involving time at 275°F followed by time at 325°F were investigated. The tensile yield strengths for the peak aged conditions and thermally exposed conditions varied by less than 2 ksi for the different aging practices. There may have been a small toughness advantage associated with isothermal aging of these alloys at 325°F.

- Tensile yield strengths and ultimate tensile strengths were unaffected or slightly enhanced as a result of exposures of 1000 h at 225°F. Both were degraded considerably after exposures of 1000 h at 275°F. Fracture toughness values were degraded as a result of elevated temperature exposure. Exposure tended to promote intergranular fracture.

- Undissolved constituent were present in both alloys. Differential scanning calorimetry data were used to estimate the amounts to which solubility had been exceeded, so that the modified compositions could be recommended for further phases of the study.

- The K_c fracture toughness values measured in this program were almost always invalid because of the narrow width; i.e. 6", of the center cracked panels tested. This continues to be a concern for proper ranking of the alloys.

There were two main objectives for Phase III of the current investigation:

- To study the effect of level of stretch on strength/toughness combinations, retention of strength/toughness combinations after exposure, and creep.

- To study grain structure effects on strength/toughness combinations, retention of strength/toughness combinations after exposure, and creep.

In addition, studies were conducted to examine the following:

- elevated temperature tensile properties of C415 and C416 sheet
- room temperature strength and toughness of C415 and C416 plate
- the effect of overaging on toughness in C415 and C416 sheet

Phase IV. Period 1995 May through 1995 October 31

During Phase III, it was recognized that C415 had higher strength, yet lower toughness than C416. The low toughness of C415 was attributed to its high Mn level (e.g. 0.6 wt% as compared to the 0.3 wt% in C416) and to the presence of undissolved Cu-bearing constituent. It was felt that the toughness could be improved without a significant loss in strength if alloys lower in Cu, Mg and Mn were explored. Three new compositions were proposed:

729126	Al-4.5 Cu-0.75 Mg-0.3 Mn-0.5 Ag-0.13 Zr
729125	Al-4.1 Cu-0.70 Mg-0.3 Mn-0.5 Ag-0.13 Zr
729127	Al-4.3 Cu-0.70 Mg-0.6 Mn-0.5 Ag-0.13 Zr

These compositions maintain the same effective Cu/Mg ratio as in C415, taking into account the loss of Cu to the Al_{20} Cu, Mn_3 dispersoids.

Procedure

Phase I. Period 1992 January 01 through 1992 December 31

Four alloys were cast as 6" thick x 16" wide x 60" long ingots and stress relieved in an 850°F furnace. Nominal and actual compositions are presented in Table I. Rolling sections were machined and preheated at 985°F.

The four I/M 2XXX variants were rolled to sheet, using a combination of cross rolling and straight rolling. Preheated rolling sections were initially heated to 825°F and reheated whenever surface temperatures reached about 750°F. Twelve passes and two reheats were used to produce sheet having a width of 17" and a thickness of 0.125".

A set of sheet samples were heat treated, stretched 8% and artificially aged at 350°F to produce T8-type tempers. Aging times of 1, 3, 8 and 24 hr were selected for all alloys. In addition, a set of sheet samples were heat treated, stretched less than 1% in order to straighten the sheet, and artificially aged at 350°F to produce T6-type tempers. Aging times of 2, 8, 16 and 48 hr were selected for all alloys.

The solution heat treatment temperatures varied for the four alloys. These temperatures were chosen based on differential scanning calorimetry on preheated ingot samples.

S. No.	Alloy Description	Solution Heat Temperature (°F)
689245	2519 control	995
689246	High Si 2519	990
689247	High Mg 2519	985
689248	High Mg 2519 + Ag	985

Rockwell B hardness and electrical conductivity measurements were taken for each of the four aging times. Optical metallography and Guinier X-ray diffraction were done on samples aged to peak hardness. Additional preheating studies using optical metallography and thermal analysis were carried out on S. Nos. 689247 and 689248, in order to determine whether maximum solid solubilities for Cu and Mg had been exceeded in these alloys.

Two longitudinal tensile samples were prepared for each alloy and aging condition. One tensile sample was used to generate complete stress-strain curves, the other to obtain precise values for tensile yield strength and ultimate tensile strength. A single L-T 6.3" x 20" center crack panel and two L-T Kahn tear samples were prepared for each alloy and condition.

Once the aging time required to reach peak strength was determined, peak aged T8-type samples were subjected to a Mach 2.0 simulation of 600 hr at 300°F. Two longitudinal tensile samples and a single L-T 6.3" x 20" center crack fracture toughness panel were tested from these samples.

Phase II. Period 1993 February 01 through 1994 January 31

Two ingot sections, about 5.5" x 14" x 14", from each of four compositions were preheated and rolled to 0.125" thick sheet, at least 22" wide. Nominal and actual compositions are presented in Table II. Sheets from each composition was solution heat treated, cold water quenched and stretched. Sheets from S. Nos. 689247, 689250 and 689251 were stretched 8%. The original batch of sheet from S. No. 689248 was stretched only 2%, as greater amounts of stretching caused failure of the sheet. An additional batch of sheet from S. No. 689248 was solution heat treated at 990°F to avoid eutectic melting, i.e. 5°F lower than the original batch, cold water quenched and stretched 8%. Processing parameters for the alloys are summarized in Table III.

Sheet from each of the four alloys was aged using three practices:

- isothermal aging at 275°F
- isothermal aging at 325°F
- two step aging, using 24 hr at 275°F or 120 hr at 275°F + various times at 325°F

Longitudinal and transverse tensile tests were done to determine the peak aging times for each aging practice and alloy. Plane stress fracture toughness was measured for the peak aged conditions in the L-T and T-L orientations using duplicate 6.3" x 20" center cracked panels.

Additional sheet was aged to peak strength and exposed for either 1000 hr at 225°F or 1000 hr at 275°F. Single tensile tests were conducted in L and T directions; single plane stress fracture toughness measurements were made in the L-T and T-L orientations using the 6.3" x 20" center cracked panels.

Phase III. Period 1994 February 01 through 1995 October 31

(a) Fabrication of Sheet and Plate

Nominal and actual compositions of the two alloys under investigation in Phase III, measured at the mid-width and mid-depth, are compared in Table IV.

Six rolling sections of C415 and four rolling sections of C416 were available. Each section was 5.5" thick by 14" wide by 14" long. Tables V and VI provide summaries of the thermomechanical processing routes used to produce various grain structures in C415 and C416, respectively. The tables describe the preheat practices, the pre-aging practices (where applicable), and the rolling practices.

The preheat practices were varied to affect both the $Al_{20}Cu_2Mn_3$ dispersoid size and the soluble constituent volume fraction. By eliminating the preheat practice, one ensures that the dispersoids form either during ingot stress relieval operations or during time spent at the rolling temperature. Since these processes are done at temperatures below typical preheating temperatures, the dispersoids are expected to be finer than those in material preheated at more typical temperatures, and as a result, they are expected to be more potent in inhibiting recrystallization. Unfortunately, material which is not preheated will contain significant quantities of constituent which tend to promote recrystallization through the formation of intensely deformed regions near constituent/matrix interfaces.

An extended preheat will ensure that the constituent is minimized, however, considerable coarsening of the $Al_{20}Cu_2Mn_3$ dispersoids will have occurred. A minimal preheat is a compromise; i.e., trying to dissolve as much constituent as possible without coarsening the dispersoids too much.

Three different preheat practices were used for each alloy: no preheat, a minimal preheat, and an extended preheat. The preheat practices involve minimum (4 hr) or extended (24 hr) holds at 970°F or 990°F for alloys C415 or C416, respectively. For alloy C415, the sections were heated in 16 hr to 905°F and ramped to 970°F in 2 hr. For alloy C416, the sections were heated in 16 hr to 950°F and ramped to 990°F in 2 hr. Differential scanning calorimetry data were used to determine that the 4 hr holds were sufficient to eliminate most of the soluble constituent but that some additional dissolution continued through 24 hr.

Pre-aging practices were used in two instances. For alloy C415, a pre-aging practice of 24 hr at 500°F was used in one section to grow Ω or Θ precipitates which would work in combination with the dispersoids to inhibit recrystallization. For alloy C416, a pre-aging practice of 24 h at 800°F was used in one section to produce large particles which would increase the number of heavily deformed sites and stimulate the nucleation of recrystallized grains, thereby providing the conditions needed for a fine, recrystallized grain structure.

Sections were heated to either 825°F or 550°F prior to rolling, depending on the section. The first four passes were cross rolled. Reheats to the original rolling temperature were done

every other pass to a gage of 3.6" and then every pass. A total of 17 hot rolling passes were taken to produce 0.160" thick sheet. Three additional cold rolling passes were taken to produce 0.090" sheet.

A 4" length of 0.75" thick plate was taken from three of the C415 and three of the C416 sections for characterization of room temperature tensile properties and fracture toughness. These were sections 1, 2 and 4 from C415 and sections 2, 7 and 8 from C416 (see Tables V and VI); i.e., thereby including one section from each alloy which had been given no preheat, one which had been given a minimal preheat and one which had been given an extended preheat. All were rolled from 825°F.

(b) Heat Treating and Aging

The thermomechanical processing variations were designed to produce as many varied grain structures as possible, so that several could be selected for subsequent characterization. In all instances, further variations in grain structure were achieved by using fast, moderate and slow heat up rates to the solution heat treatment temperature. A fast heat up rate was achieved by putting the sheet (or plate) into a furnace set at the solution heat treatment temperature, a moderate rate was achieved by ramping from 500°F to the heat treatment temperature in 4 hr and a slow rate was achieved by ramping from 500°F to the heat treatment temperature in 16 hr. Solution heat treatment temperatures were 970°F and 985°F for alloys C415 and C416, respectively. All sheet (and plate) were heat treated for 20 minutes and cold water quenched.

Polarized light viewing of Barker's etched specimens was conducted on sections containing the longitudinal and short transverse directions to determine how much variation in grain structure had been produced. Once the variation in grain structure which could be produced was determined, a single grain structure was selected from each of C415 and C416 for use in the stretch level studies. These grain structures were identified as Grain Structure A. Three additional grain structures from C415; i.e., Grain Structures B, C and D, and two additional grain structures from C416; i.e., Grain Structures B and C, were selected for use in the grain structure studies.

For the stretch level studies, pieces of sheet were solution heat treated, cold water quenched, stretched 0.5%, 2% or 8% and then aged to the near peak strength condition at 325°F. Hardness measurements on samples aged for times of either 8, 16, 24, 36, 48 or 72 hours were used to establish: (a) that the time to develop peak hardness was relatively independent of stretch level, and (b) that it took approximately 24 hr and 36 hr to achieve peak hardnesses in C415 and

C416, respectively. Therefore, all C415 samples were aged for 24 hr and all C416 samples were aged for 36 hr.

For the grain structure studies, all sheet was solution heat treated, cold water quenched, stretched 2% and then aged to near peak strength at 325°F. As before, C415 and C416 were aged for 24 hr and 36 hr, respectively.

Pieces of C415 and C416 sheet from the stretch level and grain structure studies were given elevated temperature exposures of either 1000 hr or 3000 hr at 225°F.

All C415 and C416 plate samples were heat treated using a fast heat up rate, cold water quenched and aged at 325°F for 24 hr or 36 hr, respectively.

A single variant of each of C415 and C416 sheet was selected to examine the effect of overaging on toughness recovery in sheet. For C415, sheet having Grain Structure D was available; for C416, sheet having Grain Structure B was available. Pieces of sheet were solution heat treated for 20 min. at either 970°F (C415) or 985°F (C416), cold water quenched, stretched 2% and aged at 325°F. Times of 8, 16, 24, 48, 72 and 108 hr were studied.

(c) Characterization

Optical metallography was performed on all sheet and plate samples. Polarized light viewing of Barker's etched specimens was conducted on sections containing the longitudinal and short transverse directions to examine grain structures. Laue x-ray diffraction and orientation distribution function (ODF) data were also collected for the t/2 locations of the sheet samples designed to contain varied grain structures.

Transmission electron microscopy was performed on selected samples of C415 and C416, i.e. those which had been stretched 0.5%, 2% or 8% and peak aged and those which had been stretched 0.5%, 2% or 8%, peak aged and then exposed for 3000 hr at 225°F. These samples were chosen so that the effects of stretch level and exposure on precipitate size could be qualitatively studied.

Duplicate longitudinal and transverse tensile specimens were tested for all sheet materials from the stretch level and grain structure studies. Duplicate tensile specimens in the longitudinal direction only were tested from the plates and from the sheet materials for the overaging study.

Two different sizes of center cracked fracture toughness panels were tested: 6.3" wide by 20" long and 16" wide by 44" long. In most cases, duplicate 6.3" wide L-T and T-L panels were tested. Where additional material was available, a single 16" wide L-T panel was also tested. All panels were fatigue precracked. Compact tension fracture toughness specimens from the C415 and C416 plate were also tested.

Single, longitudinal creep tests were run under two conditions for most sheet materials: 275°F, 30 ksi and 225°F, 40 ksi. Specimens were 4" long, flat specimens with holes. The extensometer was not mounted directly onto the specimen, but rather onto the grips.

Phase IV. Period 1995 May 01 through 1995 October 31

Three alloys were cast as 6" thick x 16" wide x 60" long ingots and stress relieved. Nominal and actual compositions are presented in Table VII. Rolling sections were machined, preheated at 970°F, and rolled from 825°F. Initially, two rolling passes were taken before reheating, but as the plate became thinner, reheats were taken every pass. Sheet was hot rolled to 0.160" and then cold rolled in three additional passes to 0.090".

Pieces of sheet were solution heat treated for 20 minutes at 970°F, cold water quenched and stretched 2%. Isothermal aging at 325°F was done to establish that approximately 28 hr was needed to achieve peak strength in all three variants. All sheet was aged to peak strength and portions were given elevated temperature exposures of either 1000 hr or 3000 hr at 225°F. This material was set aside for characterization within the follow-on NASA program NAS1-20220.

Results

Phase I. Period 1992 January 01 through 1992 December 31

Differential scanning calorimetry (DSC) data, e.g., onset temperatures, maximum temperatures and areas of reactions, from preheated ingot and T8-type sheet were presented in Reference 2. A single eutectic melting reaction occurred in all of the preheated ingot and T8 sheet samples. The reaction of interest, Al (ss) + $Al_2Cu \rightarrow L$, begins at temperatures of 989°F or higher in the preheated samples. Since the maximum temperature seen during preheating by all four variants was 985°F, there should have been no eutectic melting in any of the samples and this was confirmed by optical metallography. However, there was undissolved θ phase in all, suggesting that the actual compositions are beyond maximum solubility or that the preheating temperatures used were not high enough. Similarly, the eutectic melting reaction persists in DSC data from the solution heat treated and aged samples and undissolved θ phase was seen in optical metallography.

Additional DSC data from further investigation of solution heat treatment practices for S. Nos. 689247 and 689248 were also presented in Reference 2. By increasing solution heat treatment temperature in increments of 5°F, eutectic melting reactions and solvi were approximated. For S. No. 689247, the eutectic melting reaction could not be eliminated entirely, indicating that maximum solid solubility for Cu and Mg had been exceeded. Solution heat treatments for this

alloy must be limited to 990°F in order to avoid the melting reaction. For S. No. 689248, the reaction Al (ss) + $Al_2Cu \rightarrow L$ was eliminated if a solution heat treatment temperature of 995°F or higher was used, suggesting that the solvus is between 990°F and 995°F and that solid solubilities had not been exceeded for this composition.

The grain structures of sheet from the 2519 variants were recrystallized. Guinier X-ray diffraction and transmission electron microscopy results provided information on the dispersoids and precipitates in the 2519 variants. All of the 2519 variants contained $Al_{20}Cu_2Mn_3$ dispersoids and Al_7Cu_2Fe constituent. The only sample for which any Zr-bearing phase was detected by this method was the high Si variant. In that sample, reflections consistent with a tetragonal Al-Si-Zr phase (Reference 6) were observed. That phase is probably related to Al_3Zr. The $L1_2$ or DO_{23} forms of Al_3Zr were not detected in any of the other samples, however, this does not necessarily mean neither are present. Both forms are difficult to detect by this method unless present in relatively large quantities.

Transmission electron microscopy revealed Al-Cu-Mn and Al-Cu-Zr dispersoids in all of the variants. The composition of the Al-Cu-Mn phase is described by $Al_{20}Cu_2Mn_3$ as suggested by X-ray diffraction but the composition of the Al-Cu-Zr phase is unknown. No structural characterization by TEM was done, although it could be hypothesized that it is a Cu modified form of Al_3Zr, e.g., $(Al, Cu)_3Zr$, since there is a precedence for the substitution of Cu onto the Al sublattice to stabilize the $L1_2$ phase. This is probably the same phase that has been called Al_5CuZr_2 by Pearson. It has the $L1_2$ structure and a lattice parameter of 0.404 nm (Reference 7).

Guinier X-ray diffraction data revealed the θ' and θ phases in the T8 tempers of all four variants, but the technique does not distinguish between θ phase and Ω phase. In the Ag-bearing alloy, S. No. 689248, diffuse background intensity was present at the θ phase reflections, suggesting that these reflections were due to fine Ω precipitates. Transmission electron microscopy confirmed the presence of Ω in the T8 temper of the Ag-bearing alloy, S. No. 689248.

The results of tensile and toughness testing of sheet of 2519 variants in the T8 and T6 type tempers are presented in Tables VIII and IX, respectively. None of the plane stress toughness tests produced valid K_c numbers. All failed the criterion requiring that the net section stress/tensile yield strength is < 0.8.

In T8 type tempers, additions of Mg and combined additions of Mg and Ag were equally effective in increasing the strength of alloy 2519. The high Si variant developed a tensile yield strength equivalent to the 2519 control, while the other two variants developed 10% higher tensile yield strengths. The rate of overaging in all of the variants was similar.

In T6 type tempers, combined additions of Mg and Ag were most effective in increasing the strength of alloy 2519, but additions of Mg or Si alone also had a strengthening effect.

The most promising strength/toughness combinations were obtained in the T8 tempers of the high Mg variant and the high Mg variant with Ag. Both alloys exhibited a significant performance improvement over the 2519 control. When combined with the optical metallography results which suggested that constituent volume fraction could be further reduced to improve toughness, these strength/toughness combinations were particularly promising. The T8 and T6 strength/toughness combinations were very similar for the Ag-bearing alloy, while the T8 strength/toughness combinations were superior to the T6 combinations for all of the other variants.

Losses in strength and toughness occurred in the 2519 variants after a Mach 2.0 simulation of 600 hr at 300°F. Tensile and toughness data from T8 sheet tested before and after simulation of Mach 2.0 service are presented in Table X. The greatest losses in strength (about 8%) and toughness (about 15%) occurred in the highest strength alloys, e.g., the high Mg variant and the high Mg variant with Ag, however, both still had a strength/toughness advantage over the 2519 control and the high Si variant.

Values for unit propagation energies (UPE) from the Kahn tear test were not a good indication of the plane stress fracture toughness (see Table VIII). For a given variant, the highest values for UPE were measured in samples given a different aging time than the samples which produced the highest values for K_c. In some instances, very different values for UPE were measured in two samples in which similar values for K_c were measured. Finally, the alloy that had the highest values for K_c (S. No. 689248), had some of the lowest values for UPE.

Phase II. Period 1993 February 01 through 1994 January 31

As expected from the results of Phase I, optical microscopy revealed undissolved constituent in sheet from S. Nos. 689247-T8, 689250-T8 and 689251-T8. Rosettes, which are characteristic of eutectic melting, were observed in the sheet from S. No. 689248, which had been solution heat treated at 995°F. The presence of undissolved constituent was consistent with the fact that the compositions contained more solute than the maximum solubility in aluminum.

The inability to obtain 8% stretch in sheet from S. No. 689248, which had been solution heat treated at 995°F without failure, is consistent with the evidence of melting.

Optical metallography observations, Laue X-ray diffraction results and orientation distribution function data were presented in Reference 4, however, no conclusive statements could be made concerning grain structures. Transmission electron microscopy showed the Mn to be present in rod-like $Al_{20}Cu_2Mn_3$ dispersoids, with a length of 0.5 microns or less. The Ag-bearing alloys, S. Nos. 689248-T8, 689250-T8 and 689251-T8 were shown to be strengthened predominantly by Ω phase while S. No. 689247-T8 was shown to be strengthened predominantly by θ'.

All room temperature tensile data were presented in Reference 4. All four alloys reached peak tensile yield strength after 16 to 24 hr at 325°F. The two step practices involving time at 275°F followed by time at 325°F produced the same peak tensile yield strengths that were produced by isothermal aging at 325°F. Isothermal aging at 275°F provided 0 to 2 ksi of additional tensile yield strength when compared to isothermal aging at 325°F. This advantage may not be large enough to justify the long aging times which are required to reach peak strength at this temperature.

The highest tensile yield strengths were obtained in the two alloys with 5.2 Cu and 0.8 Mg, S. Nos. 689250 and 689251. Tensile yield strengths of 75 and 77 ksi were achieved in S. Nos. 689250 and 689251, while tensile yield strengths less than 71 ksi were obtained in the other two alloys. The highest strength alloys had the lowest amounts of work hardening. The highest ultimate tensile strength, 80 ksi, was obtained in S. No. 689251.

Tensile and fracture toughness data for the I/M 2XXX sheet in peak aged conditions and after elevated temperature exposure are presented in Table XI. Tensile data are provided for longitudinal and transverse orientations. Where available, three measures of toughness are provided for the L-T and T-L panels, K_c, K_{app} and K_R at $\Delta a_{eff} = 0.3$". In most instances, the criterion requiring that the ratio of the net section stress divided by the yield strength be less than or equal to 0.8 was not met and, as a result, K_c values were invalid. In fact, most L-T values would still be invalid if a less conservative ratio of 1.0 is used.

Since so many K_c values are invalid, a useful comparison of materials required included examination of the entire R-curve or alternatively, a comparison of the crack extension resistance, K_R, at an equivalent crack extension. A crack extension of 0.3" was chosen since most R-curves of the present investigation extend beyond this value and normally, at this crack extension, the

K_R value is valid if the requirement for the ratio of net section stress to yield strength is relaxed to a value of 1.0. In some instances, the specimen either failed or experienced unstable crack growth at an extension less than 0.3". In these cases, the K_R value should be taken to be equal to the K_c value.

Use of a lower solution heat treatment temperature for S. No. 689248 and a higher level of stretch improved strength/toughness combinations for all aging practices examined. The specimens which were solution heat treated at 990°F, quenched and stretched 8% prior to artificial aging developed a better strength/toughness combination than those which were heat treated at 995°F, quenched and stretched 2% prior to artificial aging. Values for K_R at Δa_{eff} = 0.3" showed the same behavior. Since earlier studies (Reference 2) showed no effect of stretch on the strength/toughness combination in S. No. 689248, the difference here is attributed to the difference in solution heat treatment temperature. Rosettes, which are characteristic of eutectic melting and which were observed in the sheet which was heat treated at 995°F, had negative impact on the fracture toughness.

Measures of L-T and T-L fracture toughness in the peak aged conditions did not vary in a systematic way with aging practice. Large variations in toughness were observed for the sheet from S. No. 689248 which had been stretched 2%; however, data from that lot of sheet is suspect because of the eutectic melting problem. Most other data suggest that fracture toughness is optimized if sheet is isothermally aged at 325°F to peak strength. Examination of all data in Table XI, however, does not reveal several K_c and/or K_R values which do not show that tendency.

Longitudinal and transverse tensile yield strengths were either unaffected or slightly enhanced by exposures of 1000 hr at 225°F and noticeably degraded by exposures of 1000 hr at 275°F. L-T and T-L fracture toughness, as given by K_c values, were degraded as a result of exposure for either 1000 hr at 225°F or 1000 hr at 275°F (Table XI). The effect was most severe for sheet exposed at 275°F. (Data from the sheet of S. No. 689248 which had been stretched 2% should be disregarded because of the eutectic melting problem. All other data sets show degradation in toughness with elevated temperature exposure.)

Scanning electron microscopy of fracture surfaces showed a greater tendency for intergranular fracture in exposed samples than in peak aged samples. For example, the near plane strain regions, e.g. just ahead of the machined notches at the center of the sheet, were examined for the peak aged and exposed L-T samples of sheet from S. No. 689250 which had

been isothermally aged at 325°F. While the peak aged samples exhibited a predominantly dimpled structure characteristic of transgranular failure, the samples exposed for 1000 hr at 225°F showed some flat, intergranular facets and the samples exposed for 1000 hr at 275°F showed even more flat, intergranular facets. There also appeared to be an increased tendency for cracking within the plane of the sheet in the exposed samples. The same behavior was observed in plane stress regions of the same L-T sample, in plane stress regions of T-L samples from the same material and in plane stress regions from L-T samples of another material, e.g., S. No. 689251, although the effect may be less pronounced.

Aging practice variations did not affect thermal stability of strength or fracture toughness.

All four experimental alloys were shown in Reference 4 to compare favorably with the fuselage material 2024-T3 and two compositions were recommended for further study:

C415	Al-5.0 Cu-0.8 Mg-0.6 Mn-0.5 Ag-0.13 Zr
C416	Al-5.4 Cu-0.5 Mg-0.3 Mn-0.5 Ag-0.13 Zr

C415 and C416 are modifications to the compositions of S. Nos. 689251 and 689248, respectively. Cu levels were lowered somewhat to minimize constituent.

Phase III. Period 1994 February 01 through 1995 October 31

(a) Microstructures

A wide variation in recrystallized grain sizes was produced in the heat treated C415 and C416 0.090" thick sheet. The grains in C415 sheet are elongated in the rolling direction and vary significantly in size. The grains in C416 sheet were much more equiaxed than those in C415 sheet.

The four grain structures selected for characterization of C415 were produced using the following practices. (More details can be found in the Procedures section of this report.)

- Grain Structure A (S. No. 727443-2, 727443-6 or 727443-7): extended preheat, rolled from 825°F, rapid heat-up rate to the solution heat treatment temperature

- Grain Structure B (S. No. 727443-1): no preheat, rolled from 825°F, moderate heat-up rate to the solution heat treatment temperature

- Grain Structure C (S. No. 727443-4): minimal preheat, rolled from 825°F, moderate heat-up rate to the solution heat treatment temperature

- Grain Structure D (S. No. 727443-5): minimal preheat, pre-aged 24 hr at 500°F, rolled from 550°F, moderate heat-up rate to the solution heat treatment temperature

C415 having Grain Structure A was used for the stretch level study. C415 having Grain Structures A, B, C and D were used for the grain structure study. Polarized light micrographs of these structures are presented in Figure 1. The finest structures were Grain Structures A and D; the coarsest structures were Grain Structures B and C.

The three grain structures selected for characterization of C415 were produced using the following practices.

- Grain Structure A (S. No. 727442-7): extended preheat, rolled from 825°F, rapid heat-up rate to the solution heat treatment temperature

- Grain Structure B (S. No. 727442-2): minimal preheat, rolled from 825°F, moderate heat-up rate to the solution heat treatment

- Grain Structure C (S. No. 727442-8): no preheat, rolled from 825°F, moderate heat-up rate to the solution heat treatment temperature

C416 having Grain Structure A was used for the stretch level study. C416 having Grain Structures A, B and C were used for the grain structure study. Polarized light micrographs of these structures are presented in Figure 2. The finest structures were Grain Structures A and C; the coarsest structures were Grain Structure B.

None of the structures produced using very slow heat-up rates to the solution heat treatment were selected, since they were not significantly different than those produced with moderate rates and since very slow rates would present processing difficulties later in production.

Laue results and Orientation Distribution Function (ODF) results are summarized in Table XII.

Laue x-ray diffraction patterns are presented in Figures 3 and 4 for C415 and C416 sheet, respectively. By this technique, all grain structures were judged to be completely or nearly

completely recrystallized. ASTM grain sizes varied from 5.5 to 7.5, and were in qualitative agreement with the polarized light micrograph observations.

Constant φ_2 ODF sections containing the most important information have been presented for the various grain structures in C415 and C416 sheet in Figures 5 and 6, respectively. These figures are best interpreted using the key in Figure 6, where the locations of the ideal FCC texture components are shown for the same φ_2 sections.

With the exception of Grain Structure D, the C415 grain structures show small amounts of the cube recrystallization texture and essentially no deformation texture, indicating that the orientation distribution is mostly random. C415's Grain Structure D shows significant intensities for both cube and goss recrystallization components and for both S and Copper deformation components.

The orientation distributions in C416 are mostly random. Figure 6 shows only a hint of the cube recrystallization component for Grain Structure A and no significant intensity for any of the deformation components in any of Grain Structures A, B or C.

Grain structures which appeared at least partially unrecrystallized were obtained in several variants of heat treated samples from 0.75" thick C415 plate (Figure 7). Recrystallized grain structures, having varied grain sizes, were achieved in several variants of heat treated samples from 0.75" thick C416 plate (Figure 8). For each alloy, the variable was preheat: one section had seen no preheat, another saw a minimal preheat and another saw an extended preheat. All were rolled from 825°F and given a rapid heat-up rate to the solution heat treatment. In the case of C415 plate (Figure 7), the extent of recrystallization appeared to increase with increasing preheat time. In the case of C416 plate (Figure 8), the recrystallized grain size appeared to increase with increasing preheat time.

Dark field transmission electron micrographs for samples stretched 0.5%, 2% and 8% before peak aging are presented in Figures 9 and 10 for C415 and C416 sheet, respectively. For both alloys, the dominant precipitate is Ω phase, as expected. The size of the Ω plates appears to be independent of the level of stretch prior to aging, although there does appear to be a difference between the two alloys. The Ω plates in C415 appear somewhat finer than those in C416, an observation which is consistent with the fact that the strengths of C415 are always higher than those of C416 (see next section).

The Ω plates do not grow noticeably during exposures of 3000 h at 225°F. This can be seen in Figure 11, where dark field transmission electron micrographs of two pieces of the C415 sheet

having Grain Structure A are presented, i.e. one which had been stretched 8% and peak aged and another which had been stretched 8%, peak aged and exposed for 3000 h at 225°F. The same observation was made for the C415 sheet stretched 0.5% and 2% and for all of the C416 sheet samples.

(b) Room Temperature Tensile and Fracture Toughness Data

The room temperature tensile and fracture toughness data for C415 and C416 sheet from the stretch level and grain structure studies are presented in Tables XIII and XIV, respectively. The tensile data are averages from duplicate specimens while the toughness data are values from individual tests. Included in these tables are notes for each toughness panel, indicating whether the test was valid and whether the fracture surfaces exhibited single shear, double shear, or partially double shear character.

Typically, the longitudinal tensile yield strengths were 2 to 5 ksi higher than transverse tensile yield strengths and longitudinal ultimate tensile strengths were 0 to 3 ksi higher than the transverse ultimate tensile strengths. Elongations were similar for both orientations.

The tensile yield strengths of C415 are higher and more sensitive to stretch level than those of C416. Figure 12 presents longitudinal tensile yield strength as a function of % stretch prior to artificial aging. The C415 tensile yield strength is increased by more than 4 ksi if stretch level is increased from 0.5% to 8%, while the C416 tensile yield strength is increased by only 1 ksi for the same increase in stretch level. Examination of the data in Table XIII reveals the same trend for transverse tensile yield strengths. Also, ultimate tensile strengths show the same effect, although the magnitude of the effect is somewhat smaller.

Grain structure did affect the strength levels obtained in the C415 and C416 sheet. For example, the peak aged tensile yield strengths for C415 samples stretched 2% prior to artificial aging varied from 71 to 75 ksi, depending on grain structure. Peak aged tensile yield strengths of 70 to 72 ksi were obtained in the grain structure variants of C416.

Despite the fact that the 6.3" wide center cracked toughness panels produced mostly invalid K_c data, reproducibility between duplicate specimens was quite good. Figure 13 shows K_R crack growth resistance as a function of Δa_{eff}, the R-curve, for two 6.3" wide and one 16" wide center cracked fracture toughness panels from C415 sheet having Grain Structure A and having been stretched 2% prior to artificial aging. Both R-curves for the 6.3" wide specimens lie almost directly on top of one another. The R-curve for the 16" wide specimen lies directly on top of those from the 6.3" wide specimens at low values of Δa_{eff} but begins to deviate at the point

where data become invalid. At high values of Δa_{eff}, the R-curve for the 16" wide specimen is lower than those from the 6.3" wide specimens. The value for K_c, however, is higher for the 16" wide specimen than for the 6.3" wide specimens. It is also valid, at least in this case and in many other cases where 16" wide specimens were tested.

No good correlation was found between the value for K_c and the character of the fracture surface, i.e. whether there were single or double shear lips on the fracture surfaces. Examination of the data in Tables XIII and XIV show that there are a number of instances where two samples were tested for a given condition and one exhibited single shear while the other exhibited double shear. In some cases, the K_c values associated with the double shear were higher than those associated with single shear, however, there were also cases where the reverse was observed.

The variation in values for K_c from duplicate specimens and the overall invalidity for most of the data from 6.3" wide specimens and for some of the data from 16" wide specimens makes it difficult to draw conclusions about the effect of stretch and grain structure on toughness and about the relative performance of C415 and C416. Some very qualitative observations, however, can be made. Usually, but not always, the K_c values were slightly lower in the T-L orientations than in the L-T orientations. Typically, values for C415 were higher than for C416, although they were mostly invalid for both alloys.

The effect of % stretch on strength/toughness combination is presented in Figures 14 and 15 for C415 and in Figure 16 for C416. Although the values for K_c are different for 6.3" wide (Figure 14) and 16" wide (Figure 15) specimens, the trend is the same. The C415 materials stretched 2% and 8% had better strength/toughness combinations than the C415 materials stretched 0.5%, with the material stretched 8% having higher strength at the expense of toughness.

The various grain structures had similar overall strength/toughness combinations.

Some caution is required when drawing conclusions from data for 6.3" wide specimens. For 6.3" wide specimens from both C415 (Figure 14) and C416 (Figure 16), K_c values did not vary over a wide range despite variations in tensile yield strength of 4 or 5 ksi. One might argue that the K_c values would be more discriminating if they were valid.

Sheet from C415 and C416 are compared directly in the plots of K_c fracture toughness versus tensile yield strength in Figure 17. Regardless of stretch level, C415 has an overall better strength/toughness combination than C416.

The strength/toughness advantage of C415 over C416 is further illustrated in the results of the overaging study which are presented in Table XV and the K_c fracture toughness versus tensile yield strength plot of Figure 18. Here, data spanning conditions from underaged, through peak aged to overaged are presented for both C415 and C416. Both alloys behaved as expected: for a given strength level, the toughness of the underaged material is better than the toughness of the overaged material. In the case of C415, the toughness did improve somewhat as the sheet was overaged while in C416, no improvement in toughness was observed. Furthermore, the overall strength/toughness combination for C415 is better than that of C416.

As 0.75" thick plate, C415 was stronger than C416 and C416 was tougher than C415 (Table XVI, Figure 19). The best strength/toughness combination obtained in C415 was measured for the material which was given a minimal preheat while the best strength/toughness combination obtained in C416 was measured for the material which was given an extended preheat. This may be due to that fact that in the case of C416, all plate samples appeared recrystallized so that the best strength/toughness combination was achieved when as much as possible of the soluble phase was dissolved. In the case of C415, the plate produced after a minimal preheat may have maintained a higher volume fraction of unrecrystallized grains than the plate given the extended preheat. Perhaps the benefit of having more unrecrystallized grains with a minimal preheat outweighed the benefit of dissolving more soluble constituent with the extended preheat.

(c) Tensile and Fracture Toughness Data After Elevated Temperature Exposure

Regardless of stretch level, exposures of 1000 hr or 3000 hr at 225°F did not have a notable effect on the tensile yield strength of C415 (Figure 20) or C416 (Figure 21). Also, the tensile yield strengths of C415 and C416 sheet having different grain structures did not respond any differently to thermal exposure (Figures 22 and 23). The data in Tables XIII and XIV show that ultimate tensile strengths and elongations are not affected by the thermal exposures either.

For all three levels of stretch examined for Grain Structure A, there did appear to be a noticeable loss in fracture toughness in C415 as a result of exposures of 3000 hr at 225°F (Figure 24). A similar loss was not consistently observed for C416 (Figure 25). Data were unavailable for the sheet stretched 0.5% and exposed for 3000 hr, however, data for the sheet stretched 2% suggest that fracture toughness actually improved as a result of 3000 hr at 225°F.

The C415 sheet having other grain structures behaved more promisingly. With the exception of Grain Structure A, there was no significant loss in toughness as a result of either

1000 hr or 3000 hr at 225°F (Figure 26). The C416 sheet with any of Grain Structures A, B or C was also relatively stable with respect to toughness (Figure 27).

The effects of 3000 hr at 225°F on the strength/toughness combinations are presented for C415 and C416 in Figures 28 and 29, respectively. Data from peak aged sheet are shown as open symbols, while data from exposed sheet are shown as closed symbols. Regardless of stretch, all C415 sheet samples lose toughness without much of a change in strength (Figure 28). The net result is a decrease in the overall strength/toughness combination. For C415, the best combination is obtained in the sheet which was stretched either 2% or 8%. In C416, the strength/toughness combinations are not changed much as a result of the same exposure (Figure 29). The best combination of strength and toughness is maintained in the sheet stretched 2%.

The strength/toughness combinations of peak aged sheet and sheet exposed 3000 hr at 225°F from C415 and C416 are compared directly in Figure 30. Data from peak aged sheet are shown as open symbols while data from exposed sheet are shown as closed symbols. While the higher strengths are obtained in C415, the best after-exposure strength/toughness combinations are obtained in C416.

(d) Elevated Temperature Tensile Data

Elevated temperature tensile data for C415 and C416 sheet are presented in Table XVII and tensile yield strength is plotted as a function of test temperature in Figure 31. The C415 and C416 samples were held 300 hr prior to testing. Included in Figure 31 also are data for 2519-T87 plate, 2618-T61 plate and 6013-T6 sheet, all being held 100 hr prior to testing. The best elevated temperature strengths are obtained in C415, with C416 falling closely behind. Both of the new alloys have significantly higher strengths than 2618-T61 and 6013-T6.

(e) Creep Data

Creep testing was initiated with the expectation that samples stretched the least prior to artificial aging would be the most creep resistant. Furthermore, it was expected that differences in grain size would lead to differences in creep resistance, with the coarsest grain structures being the most resistant. Some of the data collected here support those expectations while some did not.

Table XVIII presents a summary of creep test results for C415 and C416. Included are test identification numbers, test conditions, the length of each test and the total strain measured during the test. Included also are data from loading and from measurements made after the test. The loading data and measurements made after the tests were collected because of concerns about

the accuracy of the creep data. The concern is that the strain measuring device was not mounted directly onto the specimen gage length, but rather onto the upper grip connecting the specimen to the load frame. As a result, strain occurring anywhere along the specimen or along the loading train of the machine is included in the measurement. While it may be reasonable to assume there is no strain in the loading train of the machine, it may not be reasonable to assume that the only strain occurring in the specimen is occurring in the gage length. Some tested specimens exhibited noticeable deformation in the holes. Any of this deformation which happened during loading would have been subtracted out, but if deformation occurred during loading, it is expected that it would continue to occur during the test. Any hole deformation which occurred during the test would be included in the strain versus time creep curves.

These concerns were first introduced when it was noted that plots of load versus extension which were collected during loading were not consistent with the elastic modulus of aluminum. Values for "modulus" calculated from the curves were typically much less than the expected > 9 Msi (see Table XVIII). A value for "excess strain" could also be calculated, it being the difference between the observed strain at maximum load and the strain expected for a material with a modulus of 9 Msi. The values for "excess strain" are often much greater than the total % creep strain measured in the test.

Creep strain is plotted as a function of time for C415 and C416 having Grain Structure A in Figures 32 and 33, respectively. Two sets of curves are presented in each figure: one for tests run at 275°F, 30 ksi and one for tests run at 225°F, 40 ksi. For both sets of tests of C415 with Grain Structure A, the data behave as expected. The most creep resistant sheet was that which had been stretched 0.5% and the least resistant sheet was that which had been stretched higher amounts (Figure 32). For both sets of tests of C416 with Grain Structure A, the reverse is observed: the sheet which had been stretched 2% or 8% was the most creep resistant (Figure 33).

The effect of grain structure on creep resistance was not clear. Creep strain is plotted as a function of time in Figure 34 for C415 having various grain structures and having been stretched 2% prior to artificial aging for the two test conditions: 275°F, 30 ksi and 225°F, 40 ksi. In the tests at 275°F and 30 ksi, the coarser Grain Structures B and C were more creep resistant than the finer Grain Structures A and D. In the tests at 225°F, 40 ksi, however, Grain Structure A is the most creep resistant. For C416, similar results are presented in Figure 35. Grain Structure A appears to be the most creep resistant in the higher temperature tests, while Grain Structures A and B are indistinguishable in the lower temperature test.

Alloys C415 and C416 are compared directly in the plots of strain versus time in Figures 36 to 38 for stretch levels of 0.5%, 2% and 8%. Once again, some data are consistent with

expectations, some are not. For sheet stretched 0.5%, C415 appears most creep resistant. For sheet stretched 2% or 8%, C416 appears most resistant.

Discussion

(a) Effect of Stretch Level

The tensile yield strengths and ultimate tensile strengths of C415 were more sensitive to stretch level than the tensile yield strengths and ultimate tensile strengths of C416. Higher strengths were achieved when higher levels of stretch are applied prior to artificial aging. Although tensile elongations are not affected by stretch level in either alloy, other measures of formability or fabricability are expected to decrease as the level of stretch is increased. Therefore, unless high stretch levels are needed to develop properties like strength or toughness, high levels are not recommended.

As with strength, the effect of stretch level on strength/toughness combination was larger for C415 than for C416. This is mostly due to the fact that toughness measurements made in this study were not very discriminating.

The thermal stability was not affected by stretch level, at least under the conditions of the current study. Strengths were unaffected by exposure, regardless of stretch level. In cases where exposures degraded toughness, i.e. alloy C415, the level of stretch did not affect the degree of degradation. In the other case, i.e. alloy C416, toughness was not degraded.

Although there are some concerns about the accuracy of the creep data, the data obtained in this study was roughly consistent with expectations regarding stretch level, i.e. the higher the level of stretch, the lower the creep resistance. In the case of C415, tests at 275°F and 30 ksi showed that material stretched 0.5% was more creep resistant than material stretched 2 or 8%. The lower temperature tests (225°F, 40 ksi) did not behave the same way, however, those data are considered somewhat less reliable than the data from the higher temperature tests, due to the smaller strains being measured.

Both sets of creep tests on C416 did not follow the expected behavior either. In fact, data for all three stretch levels examined were very similar. Since the stretch level did not have a large effect on the strength of C416, it is not surprising that it did not have a large effect on creep resistance either.

Use of 2% stretch prior to artificial aging is recommended. At this level, the best after exposure strength/toughness combinations were obtained, while still maintaining adequate overall strength and creep resistance. Fabricability is also expected to be good.

(b) Grain Structure Effect

The various grain structures produced small changes in the strengths obtained in C415 and even smaller changes in the strengths obtained in C416. The highest strengths were obtained in Grain Structures A of both alloys, the only grain structure variants made from sections which had seen extended preheats. The slightly lower strengths of all other variants can be attributed to an incomplete preheat, which presumably does not allow for effective use of all of the solute.

Despite differences in grain structure, values for toughness were similar within each alloy. This may be due to the fact that the invalid data from 6.3" wide specimens is not discriminating enough.

No effect of grain structure on thermal stability was noted, either.

The effect of grain structure on creep resistance was reasonably consistent in this study. A coarse grain structure is expected to be more creep resistant than a fine grain structure. The 275°F tests on C415 were consistent with this expectation: the coarser Grain Structures B and C were more resistant than the finer Grain Structures A and D. The 275°F tests on C416, however, showed little differences in creep resistance despite differences in grain size.

Based on the data in this study, Grain Structure A appears the most promising for both alloys.

(c) C415 versus C416

The differences between C415 and C416 were quite clear after this study:

- C415 exhibits higher room temperature and elevated temperature strengths than C416.
- In T8-type tempers, C415 has a better room temperature strength/toughness combination than C416.
- C416 appears to be more thermally stable than C415. The effects of elevated temperature exposures of 3000 hr at 225°F were more deleterious to the fracture toughness of C415 than to the fracture toughness of C416.
- C416 appears to be more creep resistant than C415, at least in materials stretched 2 or 8%. Also, the creep resistance of C416 seemed to vary less with stretch level or grain structure than the creep resistance of C415.

Summary and Recommendations

In order to choose between C415 and C416, it is important to review the property targets for high speed civil transport applications. If high strength is critical, C415 is clearly superior to C416. Tensile yield strengths as high as 78 ksi have been obtained in C415 while tensile yield strengths of 74 ksi or less have been obtained in C416 (Reference 4). One can expect minimum values for tensile yield strength to be at least 3 ksi lower once either material is made in production.

If tensile yield strengths of 70 ksi are attractive, however, then C416 is recommended for further evaluation. C416 exhibited greater thermal stability with respect to fracture toughness and better creep resistance, at least in material stretched 2 or 8% prior to peak aging. In any case, the C415 variants having low Cu, Mg and Mn which were fabricated in Phase IV, should also be characterized and considered.

As a plant trial is initiated, compositional and processing limits need to be explored. The effects of variations in the major alloying additions of Cu and Mg on properties need to be explored. In additional, a process study must be conducted on the nominal composition to examine the effects of normal variations in processing parameters on properties. The processing variables of greatest importance are preheat temperature, rolling temperature, solution heat treating practice and natural aging interval between quenching and stretching. These temperatures and times should be varied to the extent that they may vary in normal production. Certain variables can be held constant, like stretch level (2%) and isothermal aging temperature (325°F), since these have already been studied in some detail in the current program.

As plant-produced material becomes available, valid wide panel fracture toughness data must be collected.

2.0 I/M 6XXX Alloy Development

Phase I. Period 1992 January 01 through 1992 December 31

Objective

The primary objective of this task was to develop a damage tolerant aluminum based material for the lower wing and fuselage of a Mach 2.0 aircraft. This material must first meet preliminary strength and toughness targets at room temperature and then several criteria associated with elevated temperature service (e.g., retention of room temperature properties after exposure, performance at the operating temperature and resistance to creep deformation).

The I/M 6XXX alloys, or Al-Mg-Si-Cu alloys, were under consideration here because alloy 6013-T6 exhibits a strength/toughness combination equivalent to 2024-T3, but with significantly greater thermal stability.

Background

A set of alloys representing modifications to 6013 was selected. Thermodynamic modeling by Joanne L. Murray (Reference 8) was used to select compositions which would utilize the maximum amount of Mg, Si and Cu which can be put into solution during heat treatment. The actual compositions are shown below. S. Nos. 715670 through 715674 represent total weight percents of solute of 2.7, 3.5, 4.4, 5.1 and 5.8, respectively. With respect to Cu, Mg and Si levels, S. Nos. 715670 and 715674 may be thought of as approximate 6013 and 2519 controls, respectively while the other compositions explore the Cu, Mg and Si levels of compositions intermediate to 2519 and 6013 (e.g., if these commercial compositions are corrected for their losses of Cu, Mg and Si to form constituent and dispersoid). During aging, these compositions were expected to produce Mg_2Si, Q and θ' phases in various proportions. Zr was chosen as the dispersoid forming element in all of the alloys.

715670: Al-0.8 Cu-1.01 Mg-0.84 Si-0.14 Zr
715671: Al-1.81 Cu-0.86 Mg-0.69 Si-0.15 Zr
715672: Al-3.16 Cu-0.75 Mg-0.60 Si-0.15 Zr
715673: Al-3.93 Cu-0.66 Mg-0.55 Si-0.15 Zr
715674: Al-5.17 Cu-0.21 Mg-0.25 Si-0.16 Zr

Several compositions exploring the effects of certain elevated temperature dispersoid-forming elements and Ag effects on the θ' precipitates were also selected. Actual compositions of those ingots are shown below.

715675: Al-1.18 Cu-1.02 Mg-0.83 Si-0.18 Zr-0.50 Mn-0.09 V
715676: Al-0.81 Cu-1.03 Mg-0.85 Si-0.14 Zr-0.51 Ag
715677: Al-3.13 Cu-0.78 Mg-0.60 Si-0.17 Zr-0.55 Ag

S. No. 715675 was designed to contain the same strengthening phases as S. No. 715670 but with additional high temperature dispersoids. In this alloy, Cu levels were increased from 0.85 wt% in alloy 715670 to 1.2 wt% to account for the loss of Cu expected as a result of formation of $Al_{20}Cu_2Mn_3$ in S. No. 715675. S. Nos. 715676 and 715677 were selected to determine whether

there is any advantage to having Ω phase, rather than θ', in these alloys. By analogy to the work done on Ag additions to 2519, it was expected that any θ' would be replaced by Ω in these alloys. During aging, these compositions were expected to produce Mg_2Si, Q and Ω.

Procedure

Book mold ingots approximately 6" x 2.75" x 1.25" in size were cast. Nominal and actual compositions are presented in Table XIX. Differential scanning calorimetry was done on as-cast samples and preheated samples in order to first establish the practices and then determine their effectiveness.

Book mold ingots were then preheated, rolled to 0.125" thick sheet and heat treated. Severe blistering occurred on the surfaces of all of the alloys. This was most likely due to hydrogen and, therefore, is not expected to be a problem in larger lab scale ingots where hydrogen levels can be controlled.

After heat treatment, samples of each alloy were cold water quenched. Half of the samples were artificially aged immediately at 350°F, the other samples were naturally aged 10 days before artificial aging. Rockwell B hardness measurements were taken as a function of artificial aging time for both sets of samples.

Optical metallography and transmission electron microscopy were carried out on selected samples. Tensile testing was carried out on peak aged conditions of the samples which developed the highest hardnesses.

Results and Discussion

Results of the differential scanning calorimetry studies on as-cast and preheated samples are summarized in Table XX. All of the as-cast samples exhibited a eutectic melting reaction with an onset at a relatively low temperature, e.g. 952°F to 961°F. This reaction was the reason to give each alloy an initial preheat at 950°F before attempting to preheat above the highest solvus. The data in Table XX shows that the 950°F preheat was effective in eliminating this reaction completely in all alloys.

Five of the alloys, S. Nos. 715670 through 715674, were also given a stepped preheat involving a hold at 950°F, followed by a hold at a higher temperature (990°F to 1080°F, depending on composition). In S. Nos. 715672, 715673 and 715674, samples given the stepped preheat were free of eutectic melting reactions. Samples from S. Nos. 715670 and 715671, on the other hand, experienced minor amounts of melting during the stepped preheat. This can be seen in the

data of Table XX, where low temperature melting reactions re-appear in the analyses from samples given the stepped preheats. The extents of melting, however, were small.

Rockwell B hardness and electrical conductivity data are summarized in Table XXI. A great deal of scatter was present in all hardness data, some of which was likely due to the blistering problem described earlier. Three of the exploratory compositions, S. No. 715672, 715673 and 715677, achieved Rockwell B hardnesses higher than achieved by the approximate 6013 control composition but none achieved higher hardnesses than the approximate 2519 control. Ag had very little effect on the hardnesses of the Al-Cu-Mg-Si alloys. Any small hardness advantage Ag may have in the approximate 6013 control is far outweighed by the still higher hardnesses of the approximate 2519. Similarly, there is no effect of Ag on the hardness which can be achieved in the alloy with intermediate Cu, Mg, and Si levels, e.g., compare hardness of S. Nos. 715672 and 715677. Finally, Mn had little or no effect on the peak hardness of the approximate 6013 control. This is not unexpected, though, since it was added for its effect on grain structure, ductility and toughness, not strength.

The 10-day natural aging interval had no beneficial effect on peak hardness for any of the compositions examined here. The peak hardnesses of the samples that had the natural aging interval were equal or less than the peak hardnesses of the samples aged immediately after quenching.

Preliminary transmission electron microscopy studies suggested that a rod-like phase along <100> directions was the dominant strengthening phase in both 715672 and 715677. The Ag did not appear to have a significant impact on precipitation. No Al_3Zr precipitation was observed.

Tensile data, like the hardness data, were not encouraging for the I/M 6XXX alloys (see Table XXII). Here, the tensile yield strengths and ultimate tensile strengths for three of these Al-Cu-Mg-Si alloys, e.g., S. Nos. 715672, 715674, and 715677 and two of the Phase I 2519 variants, S. Nos. 689246 and 689248 are compared. Several points are worth noting. Firstly, both yield and ultimate strengths are similar for S. No. 715674 and S. No. 689246, the high Si 2519 variant. This is expected since both are similar in composition. Secondly, the alloys having intermediate Cu, Mg and Si levels, e.g., S. Nos. 715672 and 715677, have lower strengths than the other alloys.

Summary

- Minimal undissolved soluble constituents were present in sheet produced from these Al-Cu-Mg-Si alloys, suggesting that the appropriate compositions were selected.

- The highest peak hardnesses were achieved in the approximate 2519 control and lowest peak hardnesses were achieved in the approximate 6013 control. Alloys having intermediate Cu, Mg and Si levels developed intermediate peak hardnesses.

- Ag had little or no effect on hardnesses which developed during T6 aging, although there was some indication that it may confer a stability advantage.

- A 10-day natural aging period preceding artificial aging provided no hardening benefit.

- While thermodynamic modeling would have predicted that the alloys with intermediate Cu, Mg and Si levels would be strengthened by Mg_2Si, Q and θ', transmission electron microscopy indicated that a single rod-like precipitate along <100> was dominant. Ag did not appear to alter the structure or morphology of the precipitate.

3.0 P/M 2XXX Alloy Development.

Phase I. Period 1992 January 01 through 1992 December 31

Objective

The primary objective of this task was to develop a damage tolerant aluminum based material for the lower wing and fuselage of a Mach 2.0 aircraft. This material must first meet preliminary strength and toughness targets at room temperature and then several criteria associated with elevated temperature service (e.g., retention of room temperature properties after exposure, performance at the operating temperature and resistance to creep deformation).

The P/M 2XXX alloys were under consideration here for several reasons. Firstly, P/M processing provides rapid solidification rates, enabling one to introduce greater amounts of dispersoid forming elements into the aluminum solid solution than can be introduced using conventional ingot metallurgy methods. As a result, the wrought P/M products may be more resistant to recrystallization than I/M alloys with lower levels of these additions. Generally, unrecrystallized structures possess better strength/toughness combinations than recrystallized structures. Furthermore, if these additions are added in great enough amounts, modest dispersion strengthening may result. Finally, the refinement of constituent which is expected to accompany the rapid solidification will also have beneficial effects on toughness.

Background

Because of the anticipated promising strength/toughness relationships, the P/M 2XXX alloys were pursued in the present investigation. Three alloys having high levels of dispersoid forming elements were selected and atomized.

S. No. 710820: Al-4.34 Cu-1.46 Mg-0.57 Mn-0.55 Zr-0.1 V
S. No. 710821: Al-5.72 Cu-0.54 Mg-0.31 Mn-0.51 Ag-0.57 Zr-0.1 V
S. No. 710822: Al-6.68 Cu-0.52 Mg-1.70 Mn-0.52 Ag-0.20 Zr-0.1 V

S. No. 710820 is essentially a high Zr version of 2124. Its composition is nearly identical to the alloy studied in the NASA program where excellent strength/toughness relationships were achieved (References 9 through 12).

S. Nos. 710821 and 710822 represent high Zr and Mn versions of the Ω phase alloy being considered in the ingot metallurgy portion of this program. Since the Ω phase alloy was expected to be the highest strength 2519 variant, it was chosen as a baseline into which excess Zr and Mn could be added. The Cu level in S. No. 710822 was increased to account for the loss of Cu to formation of the $Al_{20}Cu_2Mn_3$ phase.

The addition of 0.1% V to all three alloys was made since all contain some Mn and Alcoa internal research has shown that V additions may refine the $Al_{20}Cu_2Mn_3$ phase which forms.

Procedure

The three lots of atomized powder were cold isostatically pressed, hot pressed and extruded to produce extrusions having a 2" by 4" cross-section. Nominal and actual compositions are presented in Table XXIII. Extrusions were heated to 800°F prior to rolling. They were then rolled by a combination of cross rolling and straight rolling to produce sheet 8" wide by 0.125" thick. A total of seven passes and two reheats were used.

Differential scanning calorimetry was used to select solution heat treat temperatures:

S. No.	Solution Heat Treatment Temperature (°F)
710820	930
710821	980
710822	980

Sheet was solution heat treated for 1 hr, cold water quenched, stretched 8% and aged at 350°F for times between 1 and 16 hr.

Optical metallography, microprobe, Guinier X-ray diffraction and TEM were used to characterize microstructures. Duplicate longitudinal tensile samples and single L-T center crack fracture toughness samples 6.3" wide by 20" were tested.

Results and Discussion

Optical metallography revealed unrecrystallized structures in sheet from all three alloys. Coarse clusters of particles, which were identified my microprobe analyses to be rich in Fe, Cu and Ce and depleted in Mg and Zr, were present as defects in all. Such defects were probably related to prior lot contamination at the atomization facility.

Information regarding dispersoids and strengthening precipitates was derived from Guinier X-ray diffraction and TEM. The results of Guinier X-ray diffraction and transmission electron microscopy were presented in Reference 2. All three P/M 2XXX alloys contained the $Al_{20}Cu_2Mn_3$ and Al_7Cu_2Fe phases and the two with high Zr levels, e.g., S. Nos. 710820 and 710821, also contain the DO_{23} tetragonal form of Al_3Zr. No $L1_2$ Al_3Zr was detected in any of the alloys. Sheet from S. No. 710820 contained S' precipitates while sheet from S. Nos. 710821 and 710822 contained Ω precipitates.

Tensile and toughness data for the three P/M 2XXX alloys are summarized in Table XXIV. The highest tensile yield strength, 79 ksi, was obtained in the high Mn Ω phase alloy, S. No. 710822, although overaging of this alloy was rapid at 350°F. The high Zr 2024 type alloy and the high Zr Ω phase alloy achieved peak tensile yield strengths of 75.9 and 74.5 ksi, respectively.

The best strength/toughness combination was achieved in the high Zr Ω phase alloy, S. No. 710821, e.g. a K_c value of 125.5 ksi $\sqrt{in}$ was achieved at a tensile yield strength of 74.5 ksi. The lowest strength/toughness combination was measured for the high Mn Ω phase alloy, S. No. 710822.

Summary

- Unrecrystallized grain structures were present in 0.125" thick sheet produced from the P/M 2XXX alloys. Defects, likely due to prior lot contamination, were present in the three products.

- S' precipitates are the dominant strengthening phase in S. No. 710820; Ω phase is the dominant strengthening phase in S. Nos. 710821 and 710822.

- At least two types of dispersoids were present in these alloys. The Mn was present in large rod-like or globular particles which probably have a composition close to $Al_{20}Cu_2Mn_3$. The Zr was present in Al-Cu-Zr cuboids which are finer than the $Al_{20}Cu_2Mn_3$ particles but coarser than expected for the coherent $L1_2$ phase. These particles may have the DO_{23} crystal structure since that structure was detected by Guinier X-ray diffraction.

- The highest yield strengths, 79 ksi, were achieved in the high Mn Ω phase alloy. The best strength/toughness combinations were achieved in the high Zr Ω phase alloy.

4.0 Toughness & Ductility Minima in Al-Fe-Ce.

Phase I. Period 1992 January 01 through 1992 December 31

Objective

The objective of this task was to gain a greater understanding of the ductility and fracture toughness reductions that occur in the dispersion strengthened alloys as temperature is increased into the range of interest for HSCT. If the phenomena were understood, it might be possible to propose methods for reducing or eliminating the effect.

Background

Rapidly solidified Al-Fe-X alloys and mechanically alloyed materials exhibit a "ductility minima" at intermediate temperatures which have been attributed to dynamic strain aging by some researchers (References 13-15). Dynamic strain aging models assume that solute diffuses to

tangles of immobile dislocations. When mobile dislocations encounter these obstacles, they are impeded to a greater extent than if the solute had not been there. The effect only occurs during deformation at intermediate temperatures. At lower temperatures, solute diffusion rates are too low to allow solute to diffuse to the tangles. At the higher temperatures, diffusion rates are high enough that the mobile dislocations can carry the solute along with them, i.e., the immobile dislocation tangles are no greater obstacles to mobile dislocations when solute atmospheres are present than when they are not. At these intermediate temperatures, the flow stress does not decrease as rapidly as expected and the strain rate sensitivity in decreased.

Not all researchers agree that the ductility minima are due to dynamic strain aging. Even though strain rate change tests performed on Al-Cr-Zr and Al-Fe-V-Si support the occurrence of dynamic strain aging, i.e., combinations of strain rate and temperature which produce low ductilities are consistent with diffusion rates for the alloying additions, other experimental observations do not support it. No evidence of serrated yielding, which is generally accepted as a characteristic of dynamic strain aging, has been observed in stress strain curves for these materials. Furthermore, products of mechanically alloyed aluminum alloys, which should not contain excess solute, exhibit ductility minima.

W. C. Porr, Jr. (Reference 15) had done work on 8009 and proposed a model that does not involve dynamic strain aging. He suggested that dislocations climb around dispersoids during intermediate temperature deformation. When dislocations climb to avoid particle looping the result is intensified dislocation flow, plastic damage accumulation and void nucleation at oxides and dispersoid clusters. According to his model, reducing the amount of oxide in 8009 and/or improving the distributions of silicide dispersoids would eliminate void nucleation sites.

Much attention has been paid to the minima that occurs at elevated temperatures, however, very little work has been done to explore what effect the elevated temperature exposures have on microstructures and room temperature properties. There are some indications that there may also be a reduction in room temperature ductility (and possibly fracture toughness) after exposures of these materials to intermediate temperatures (Reference 1). Furthermore, there have been many questions raised about toughness data that are available. Alcoa data on F-temper material shows that the plane stress toughness of the Al-Fe-Ce alloy X8019 is excellent when compared to ingot metallurgy alloys although plane strain fracture toughness data show X8019 to be inferior. Unfortunately, little plane stress or plane strain toughness data are available for material exposed to elevated temperatures. Furthermore, any plane stress toughness data that are available are from Kahn tear tests, and therefore, are not considered to be as reliable as wide panel data.

Therefore, the primary goal of this portion of the investigation was to generate ductility and toughness data at room temperature before and after elevated temperature exposures and determine possible mechanisms for the observed behavior. A P/M Al-Fe-Ce alloy with Mg additions was selected for this task. The Mg bearing alloys were selected for two reasons. Since Mg in solid solution affects dislocation/particle interactions and increases the work hardening behavior of aluminum, Al-Fe-Ce-Mg was considered a good system to examine the tensile and toughness behavior. Furthermore, Al-Fe-Ce powder with Mg additions was already available for use by the program. This allowed the timetable established for the program to be followed.

Procedure

An experimental test plan was developed. Three different microstructures were to be produced in products using varying amounts of thermomechanical processing. Room temperature tensile and fracture toughness testing was to be conducted on all three products using the same sample geometries. In this way, the true effects of different amounts of thermomechanical processing could be studied and some of the questions regarding plane stress and plane strain behavior could be answered. One of the thicker product forms would also be tested using additional tensile and toughness sample geometries. Also, the effects of elevated temperature exposure would also be examined in one of the product forms.

All tensile and fracture toughness tests were to be performed at different strain rates. Since all tests would be carried out at room temperature, the effect of strain rate can be studied without the additional variable of solute diffusion being introduced, as is done when test temperatures are elevated.

Al-8 Fe-4 Ce-0.4 Mg powders were cold isostatically pressed, hot pressed, and extruded to 2" x 4" bars. Some of the extruded material was rolled to 1" plate (8" wide) and some was rolled to 0.125" sheet (8" wide).

The experimental details are summarized below: Three microstructures were produced: 2" extrusion, 1" plate, and 0.125" sheet. From each microstructure 0.125" thick compact tension fracture toughness samples (3.125" in width and 3" in height) were evaluated as well as sheet tensile samples. From the 1" plate, 0.6" compact tension fracture toughness samples (1.25" in width and 1.2" in height) and 1/4" round tensile samples were also taken. Tension tests and toughness tests were run at different crosshead speeds as indicated.

Microstructures	Sample Geometry	
	Tensile	Toughness
Extrusion, 2" thick	flat, 0.125" thick	0.125" thick compact tension
Plate, 1" thick	flat, 0.125" thick round, 0.250" diameter	0.125" thick compact tension 0.60" thick compact tension
Sheet, 0.125" thick	flat, 0.125" thick	0.125" thick compact tension

Cross Head Speeds (in./min)

Tension	Toughness
0.375	0.59
0.0375	0.059
0.00375	0.0059

Room temperature tensile and fracture toughness tests were performed on the three product forms in the as-fabricated conditions. In addition, the extrusion was exposed for 1000 hr at 300°F and tested at room temperature.

Results and Discussion

The results of tensile and fracture toughness testing are summarized in Table XXV. Tensile data include tensile yield strength, tensile ultimate strength, and % elongation. Toughness data include K_{R25} values and/or K at maximum load. K_{R25} is a value for K on the R-curve based upon the 25% secant intercept of the load-displacement test record and the effective crack length at that point. K_{R25} is determined in general compliance with ASTM method E561 using a compact specimen. K_{R25} indicates a true property of the material.

The effects of thermomechanical processing, crosshead speed, specimen orientation, specimen geometry and location within the thickness were examined.

For a given crosshead speed, the tensile yield strength of the P/M Al-Fe-Ce-Mg alloy increased as the amount of thermomechanical processing increased. As a result, sheet has the highest yield strength, followed by plate and extrusion. This is not unexpected since the same behavior has been observed in the P/M Al-Fe-Ce alloy with no Mg.

Mg increased the work hardening of the Al-Fe-Ce alloy. The tensile yield strengths of the A1-8 Fe-4 Ce-0.4 Mg alloy and Al-8Fe 4Ce (X8019) were similar for all product forms, however, the ultimate tensile strengths of the alloy with Mg were much higher than those of the alloy having no Mg.

For all product forms and conditions, ultimate tensile strengths increased as crosshead speed increased. In general no significant changes in elongation were noted as a function of crosshead speed for the different product forms, with one exception. In the case of the 1/8" sheet samples taken from 1" plate (t/4 plane), elongation increased as crosshead speed decreased.

For most of the conditions examined, tensile yield strength was relatively insensitive to crosshead speed. Here, the exception was the 0.125" thick sheet, where the longitudinal tensile yield strength increased with decreasing strain rate and the transverse tensile yield strength was constant for fast and intermediate crosshead speeds but decreased at the slowest speed.

The effects of specimen location within the thickness and specimen geometry were examined in the 0.6" thick plate. For any given crosshead speed, tensile yield strength values were 1 to 2 ksi higher at t/2 than at t/4. The effects of specimen geometry are illustrated by comparing the data from 0.250" round specimens to data from 0.125" thick sheet specimens from the t/2 location. Differences in tensile yield and ultimate tensile strengths were insignificant at the slow and intermediate crosshead speeds. The difference in tensile yield strength of nearly 2 ksi which was observed between the two specimens tested at the fastest crosshead speed may be significant.

The effects of elevated temperature exposure, e.g., 1000 hr at 300°F, were studied in the 2" thick extrusion. While the tensile properties of the as-fabricated material were insensitive to crosshead speed, the tensile yield strengths of the exposed material exhibited a minima at the intermediate crosshead speed. For the high and low crosshead speeds, the tensile yield strengths of the exposed material were about 2 ksi higher than the tensile yield strengths of the as-fabricated material. Elongations were not affected by the elevated temperature exposure.

The best strength/fracture toughness combinations are achieved in product forms that saw the highest degree of thermomechanical processing. Data in Table XXV for 0.125" thick specimens from as-fabricated sheet, plate and extrusions show that tensile yield strengths and K_{R25} values for the as fabricated sheet are higher than those of plate and the tensile yield

strengths and K_{R25} values for plate are higher than those of extrusions for all crosshead speeds studied.

Crack growth resistance curves were examined for 0.125" thick specimens from as-fabricated sheet, plate and extrusions. For the as-fabricated sheet and plate, the slowest crosshead speed produces the greatest crack growth resistance and the most stable crack extension. In the extrusion, the greatest crack resistance and the most stable crack extension are obtained in the specimens tested at the slowest and fastest crosshead speeds. Regardless of crosshead speed, all of the 0.125" thick specimens from the sheet, plate and extrusion had fracture surfaces with a combination of slanted and flat regions.

Crack growth resistance curves for the 0.6" thick compact tension specimens taken from 1" plate were also examined. Duplicate samples were tested at each crosshead speed. For all crosshead speeds, values for toughness were low and very little stable crack growth was obtained. Failed test samples had flat fracture surfaces, indicative of plane strain conditions. The differences in the crack growth resistance curves of duplicate samples suggest that these data are not reproducible.

In general, the effect of the elevated temperature exposure was to increase crack growth resistance. For example, specimens from the exposed extrusion exhibited the greatest crack growth resistance and the most stable crack extension when tested at the slowest crosshead speed. Specimens tested at the fastest crosshead speed exhibited the least crack growth resistance and the least stable crack growth. This behavior is somewhat different than the behavior of the as-fabricated extrusion, where specimens tested at the slowest and fastest crosshead speeds were similar in terms of crack growth resistance and the extent of stable crack growth.

Many of the 0.125" thick fracture toughness specimens had fracture surfaces suggesting a mixed mode of failure, e.g. some plane stress and some plane strain character. In theory, brittle fracture is usually associated with a flat featureless surface without any shear lips whereas a slanted fracture surface has shear lips and is typically associated with an increase in the energy necessary for fracture and a more ductile type of fracture. A flat fracture is representative of plane strain conditions while a slanted fracture is representative of plane stress conditions. As-fabricated samples which were tested at intermediate crosshead speeds have a flat fracture surface while those samples tested at the slowest and fastest speeds have a combination of slanted and flat (mixed mode) fracture. Samples of the extrusion exposed to elevated temperatures exhibited slanted and flat (mixed mode) fracture surfaces when tested at the intermediate and slowest speeds and flat fracture when tested at the fastest speed. Values for K

at maximum load correlate with the observed fracture morphology, i.e. mixed mode fractures produce higher values for K than flat fractures. Regardless of crosshead speed, failed samples from the as-fabricated extrusion and the exposed extrusion had markings on the fracture surfaces that were correlated with rapid load drops on the load-displacement curves. The rapid load drops are due to regions of unstable crack propagation. These regions on the load-displacement curves were avoided when drawing secant intercepts.

Strength/toughness data generated for the P/M Al-Fe-Ce-Mg alloy were compared with data on X8019 (Reference 16). The Al-Fe-Ce-Mg alloy has lower strengths and lower toughness values than X8019.

Summary

- Mg increases the work hardenability of P/M Al-Fe-Ce. Tensile yield strengths for X8019 and Al-8 Fe-4 Ce-0.4 Mg are similar but ultimate tensile strengths are greater for Al-8 Fe-4 Ce-0.4 Mg.

- The highest tensile yield strengths are achieved in product forms receiving the most hot working during thermomechanical processing. Tensile yield strength increases in the following order: extrusion, plate and sheet. Similarly, the best strength/plane stress fracture toughness combinations are achieved in product forms receiving the most hot working.

- Except in sheet, crosshead speed had no significant effect on tensile yield strength or elongation to failure. In sheet, the tensile yield strength decreased slightly when crosshead speed was increased.

- The effects of specimen geometry and location were small. When tested at the highest crosshead speed, the tensile yield strength measured in a round specimen was about 2 ksi higher than the tensile yield strength measured in the flat specimen. Also at the highest crosshead speed, the tensile yield strength measured in a flat specimen located at t/2 was 3 ksi higher than the tensile yield strength measured in a flat specimen located at t/4.

- After exposure of the extrusion for 1000 hr at 300°F, tensile yield strengths measured at the slowest and fastest crosshead speeds were increased slightly while the tensile yield strength measured at the intermediate crosshead speed was decreased. Elongations to failure were not

affected by the exposure. For all crosshead speeds, the exposure resulted in greater crack growth resistance and more stable crack growth.

- In general, the greatest crack growth resistance and most stable crack growth was measured in specimens tested at the slowest crosshead speed. The effects at the fastest and intermediate crosshead speed varied for the different products, specimen geometries and locations.

- For some toughness tests, transients of unstable crack growth resulted in discontinuities in the load-displacements curves.

- When compared to X8019, Al-8 F-4 Ce-0.4 Mg alloy has a reduced strength/toughness relationship.

5.0 Strength/Toughness Combination in DMMCs.

Phase I. Period 1992 January 01 through 1992 December 31

Objective

The objective of this task was to characterize sheet produced from discontinuously reinforced metal matrix composites. Room temperature tensile and plane stress fracture toughness tests were to be conducted on materials aged to peak strengths and on materials given Mach 2.0 simulations.

Background

Three materials were identified for evaluation: 2080/SiC/20_p, MB85/SiC/20_p, and 6113/SiC/20_p. The notation indicates that these materials contain 20 vol% SiC. 2080/SiC/20_p and MB85/SiC/20_p are similar in composition, i.e. 3.8% Cu-1.8% Mg except 2080/SiC/20_p has 0.25% Zr and MB85/SiC/20_p has 0.35% Zr. By examining different rolling practices and two levels of Zr, it was intended that significantly different grain structures would be produced. As a result, different strength/toughness combinations might be expected.

The 2080/SiC/20_p and MB85/SiC/20_p were fabricated using two different rolling practices. The different rolling practices were used in an attempt to produce material with two different

grain structures: a large grain size material, i.e., ASTM grain size of 2, and a fine grain size material, i.e., ASTM grain size of 8.

Procedure

Atomized powders of 2080, MB85, and 6113 and SiC reinforcement powders were donated to the University of Virginia Subcontract No. 5.28406 so that fabrication, consolidation and characterization could proceed without delay.

The aluminum powders were blended with SiC reinforcement, cold isostatically pressed, hot pressed, extruded and rolled. Two 2" x 4" extruded bars at least 30" in length were fabricated for 6113/SiC/20_p and four 2" x 4" extruded bars at least 30" in length were fabricated for 2080/SiC/20_p and MB85/SiC/20_p. For 2080/SiC/20_p and MB85/SiC/20_p, the rolling practice intended to produce fine grain material (Process A) required a reheat every other pass whereas the rolling practice intended to produce the coarse grain material (Process B) required a reheat every pass. In theory, a fine grain size can be produced by increasing the amount of deformation during processing. Ideally, cold rolling would be the most feasible way to produce the fine grain size but since edge cracking becomes a problem when cold rolling, hot rolling is required. 2080/SiC/20_p and MB85/SiC/20_p samples were heated to 850°F prior to rolling.

6113/SiC/20_p was heated to 900°F prior to rolling and reheated when the temperature dropped between 800°F and 700°F .

Each composite was rolled to 1/8" thickness and to 6 1/2" to 7" in width.

MB85/SiC/20_p and 2080/SiC/20_p were both solution heat treated at 930°F for 4 hr followed by a cold water quench and then aged at 350°F for 24 hr to produce the T6 temper. 6113/SiC/20p was solution heat treated at 1047°F for 1 hr followed by a room temperature water quench and 24 hr of artificial aging at 325°F to produce the T6 temper.

Tensile and toughness data were generated for each DMMC. Tensile tests in L and LT directions were performed on 1/8" thick and 4" long sheet type tensile specimens with a 1/4" reduced section width. Toughness tests were performed on 1/8" thick, 6.3" x 20" center cracked panels.

Results and Discussion

Micrographs taken of the material produced from the two rolling practices, Process A and Process B, were presented in Reference 2, although it was difficult to determine the grain sizes for both 2080/SiC/20_p and MB85/SiC/20_p due to the large volume of SiC (20%) present.

Table XXVI presents the strength and toughness data generated for MB85/SiC/20$_p$ and 2080/SiC/20$_p$ as a function of grain size and amount of Zr. No significant strength differences are observed between 2080/SiC/20$_p$ and MB85/SiC/20$_p$ coarse grain materials. The MB85/SiC/20$_p$ fine grain material however has higher strengths than the 2080/SiC/20$_p$ for L and T orientations. MB85/SiC/20$_p$ is believed to have more unrecrystallized grains due to the higher Zr level.

Figure 39 is a plot of fracture toughness as a function of tensile yield strength for MB85/SiC/20$_p$ (Process A and Process B), 2080/SiC/20$_p$ (Process A and Process B) and 6113/SiC/20$_p$. The 6013/SiC/20$_p$ exhibits greater toughness but at a yield strength lower than either MB85 or 2080 composites. The 2080/SiC/20$_p$ and MB85/SiC/20$_p$ materials show comparable toughness levels. Data from a 2080/SiC/20$_p$ composite tested at a thinner gage, i.e., 0.063", using a wider panel, i.e., 16" wide, is included for comparison in Figure 39. In addition, data for the Phase I I/M 2XXX alloy, S. No. 689248-T8, is also included. The toughness values for the composites are seen to be very low in comparison to the monolithic alloy.

Summary

- MB85/SiC/20$_p$ and 2080/SiC/20$_p$ made by process A and process B show comparable toughness values.

- MB85/SiC/20$_p$ made by process A had higher tensile yield and ultimate strengths in both L and T directions than 2080/SiC/20$_p$.

- 6113/SiC/20$_p$ exhibited higher toughness values than MB85/SiC.20$_p$ or 2080/SiC/20$_p$ but at lower yield strengths.

6.0 Accelerated Exposure Study.

Phase I. Period 1992 January 01 through 1992 December 31

Objective

There were two objectives to this task. The first objective required development of fixtures for simultaneously exposing samples to constant stress and elevated temperature. Once the fixtures were developed and shown to function properly, representative samples from three classes of HSCT candidate materials were to be exposed and tested for residual tensile properties.

Background

A spring fixture was developed for creep aging materials for the HSCT program and initial tests to verify the suitability were performed. A spring, loaded in compression, imparts a tensile load to the specimen located in the center of the spring. This fixture has been designed to load 1/8" diameter tensile specimens. After aging the specimen under load, the specimen can be removed from the fixture and tested to determine the residual tensile strength of the material.

The current fixture can be used at temperatures up to 400°F and will load specimens to stresses of up to 20 ksi. Stiffer springs can be obtained which will permit loading specimens to 60 ksi. The major difference between this fixture and the fixture used in alternate immersion testing is that the former provides a constant stress while the latter provides a constant displacement. This difference is important when exposure temperatures are high enough and times are long enough that significant creep deformation occurs. The fixture is quite compact, e.g. 2" in diameter and approximately 7" long, permitting a large number of specimens to be aged in a single oven.

Three materials were identified for accelerated exposures in the constant-stress aging fixtures: 2080/SiC/20_p, 2519-T87 and 6013-T6. These materials were chosen since they represent three different candidates for a Mach 2.0 aircraft: a discontinuously reinforced metal matrix composite for use on the upper wing and two different precipitation strengthened monolithic alloys for use in the fuselage and lower wing. Exposure temperatures of 300°F and 215°F were to be used. The temperature of 300°F was considered a reasonable temperature for accelerated tests intended to simulate Mach 2.0 service. To simulate 120,000 hr at 215°F, exposures of 600 to 1000 hr at 300°F were to be considered. Tensile specimens were to be taken

out at various time intervals and tested at room temperature for residual strength and elongation. Both stressed (18 ksi) and unstressed samples were placed in aging ovens.

Results and Discussion

Table XXVII summarizes residual tensile data at room temperature for specimens exposed at both 215°F and 300°F. After exposure at 215°F, no significant differences were observed between the stressed and unstressed samples. After exposure at 300°F, no effect of stress is observed for the 2519-T87 and 2080/SiC/20_p. Degradation in tensile yield strength after 2000 hr at 300°F is roughly 12% for 2519-T87, 22% for 2080/SiC/20_p and 6% for 6013-T6. Stressed samples exhibit greater stability and higher strengths for 6013-T6.

Summary

- The tensile yield strength for 2519-T87 decreased by 12%, by 22% for 2080/SiC/20_p and by 6% for 6013-T6 after 2000 hr at 300°F.
- No significant effect of stress was observed for 2519-T87 and 2080/SiC/20_p exposures.
- A significant effect of stress was observed for 6013-T6 after 1,000 hr and 2,000 hr at 300°F.

7.0 Characterization of Alloy 1143

Phase II-III. Period 1993 February 01 through 1995 October 31

Objective

The objective of this task was to evaluate the Russian alloy 1143 as a damage tolerant aluminum based material for the lower wing and fuselage of a Mach 2.0 aircraft. The material must meet preliminary strength and toughness targets at room temperature and then several criteria associated with elevated temperature service, (e.g. retention of room temperature properties after exposure, performance at the operating temperature and resistance to creep deformation).

Background

A purchase order requesting sheet and plate of 1143 to the Aviation Industry in Moscow was initiated. Ten pieces of alloy 1143 sheet (0.12 in x 15.75 in x 51.2 in) and two pieces of alloy 1143 plate (2 in x 15.75 in x 35.4 in) were ordered. Five of the ten pieces of sheet and one of the two pieces of plate were to be provided in the T651 temper. The remaining material was to be provided in the F-temper.

Results and Discussion

Material was provided to NASA-Langley, but no material was allocated for Alcoa Technical Center studies. This task was canceled.

References

1. E. A. Starke, "NASA-UVA Light Aerospace Alloy and Structure Technology Program Supplement: Aluminum-Based Materials for High Speed Aircraft", NASA Contractor Report 4517, June 1993. (Biannual Report No. 1)

2. E. A. Starke, "NASA-UVA Light Aerospace Alloy and Structure Technology Program Supplement: Aluminum-Based Materials for High Speed Aircraft", NASA Contractor Report 4645, (Biannual Report No. 2)

3. E. A. Starke, "NASA-UVA Light Aerospace Alloy and Structure Technology Program Supplement: Aluminum-Based Materials for High Speed Aircraft", (Biannual Report No. 3), in press.

4. E. A. Starke, "NASA-UVA Light Aerospace Alloy and Structure Technology Program Supplement: Aluminum-Based Materials for High Speed Aircraft", (Biannual Report No. 4), in press.

5. E. A. Starke, "NASA-UVA Light Aerospace Alloy and Structure Technology Program Supplement: Aluminum-Based Materials for High Speed Aircraft", (Biannual Report No. 5), in press.

6. JCPDS - International Center for Diffraction Data, "Powder Diffraction File, Inorganic Phases," Swarthmore, PA, 1992.

7. P. Villars and L. D. Calvert, "Pearson's Handbook of Crystallographic Data for Intermetallic Phases," Vol. 2, American Society for Metals, Metals Park, OH, 1985.

8. J. L. Murray, unpublished research, Alcoa Technical Center, 1992.

9. D. J. Chellman, "Development of Powder Metallurgy Al Alloys for High Temperature Aircraft Structural Applications - Phase II," NASA Contractor Report 172408, 1984 November.

10. D. J. Chellman, "Development of Powder Metallurgy 2XXX Series Al Alloys for High Temperature Aircraft Structural Applications," NASA Contractor Report 1721408, 1984 November.

11. D. J. Chellman, "Development of Powder Metallurgy 2XXX Series Al Alloy Plate and Sheet Materials for High Temperature Aircraft Structural Applications," NASA Contractor Report 172521, 1985 April.

12. D. J. Chellman, T. B. Gurganus and J. A. Walker, "Development and Characterization of Powder Metallurgy (PM) 2XXX Series Al Alloy Products and Metal Matrix Composite (MMC) 2XXX Al/SiC Materials for High Temperature Aircraft Structural Application," NASA Contractor Report 187631, 1992 February.

13. E. Bouchard, L. Kubin and H. Octor, "Ductility and Dynamic Strain Aging in Rapidly Solidified Aluminum Alloys", Met. Trans. A, 22A, p. 1021-1028 (1990).

14. D. J. Skinner, M. S. Zedalis, and P. Gilman, "Effect of Strain Rate on Tensile Ductility for a Series of Dispersion-Strengthened Al-based Alloys", Mat. Sci. and Eng., A119, p. 81-86, (1989).

15. W. C. Porr, "Elevated Temperature Fracture of Advanced Powder Metallurgy Aluminum Alloy 8009," Ph.D. Dissertation, University of Virginia, 1992.

16. D. K. Denzer, unpublished research, Alcoa Technical Center, 1988.

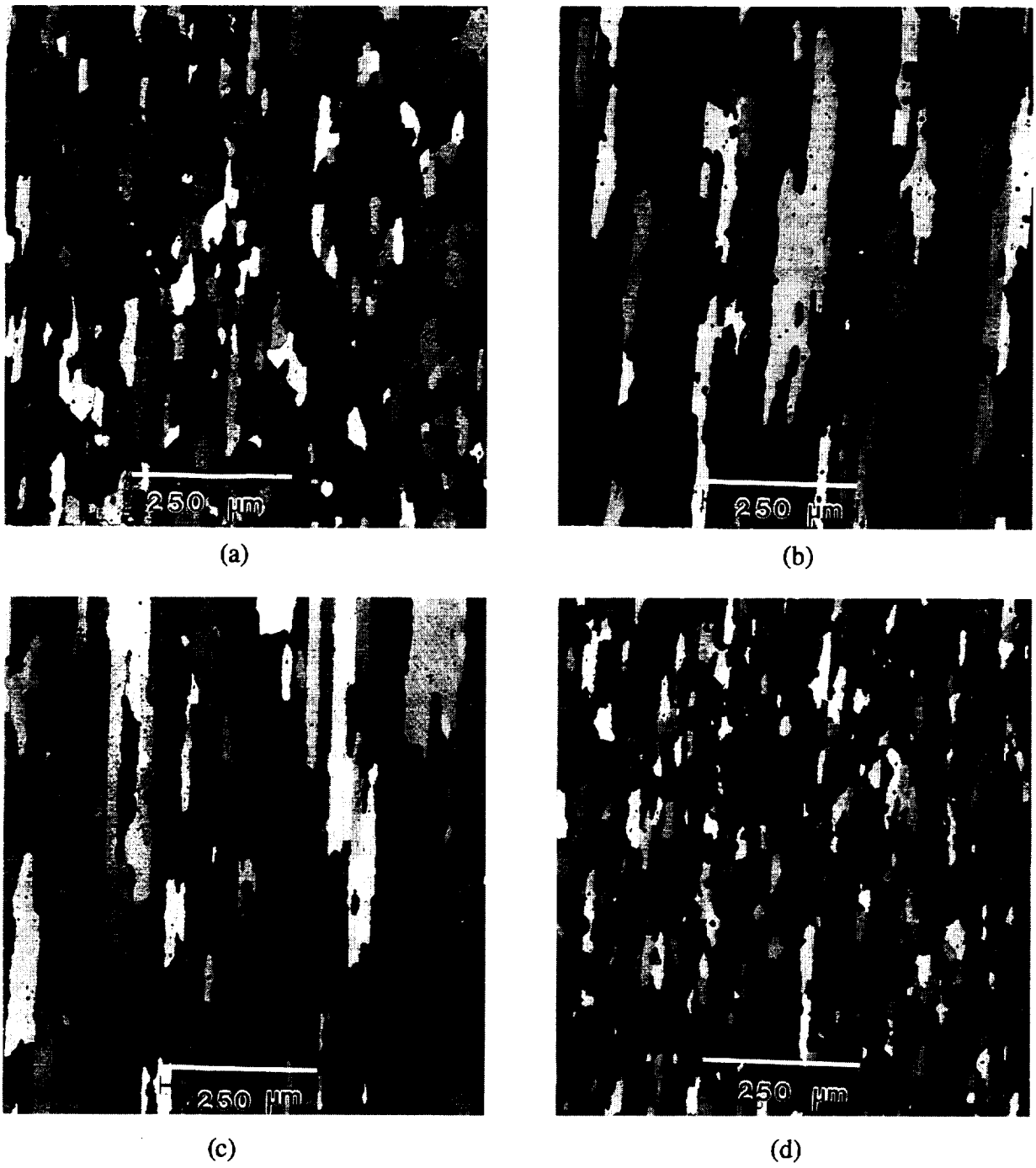

Figure 1 Polarized light micrographs from Barker's etched samples of heat treated C415 0.090" thick sheet. Sections shown are those containing the longitudinal and short transverse directions. Samples were processed using thermomechanical processing variations: (a) Grain Structure A: extended preheat, rolled from 825°F, rapid heat-up rate to the solution heat treatment temperature, (b) Grain Structure B: no preheat, rolled from 825°F, moderate heat-up rate to solution heat treatment temperature, (c) Grain Structure C: minimal preheat, rolled from 825°F, moderate heat-up rate to solution heat treatment temperature, and (d) Grain Structure D: minimal preheat, preage, rolled from 500°F, moderate heat-up rate to solution heat treatment temperature.

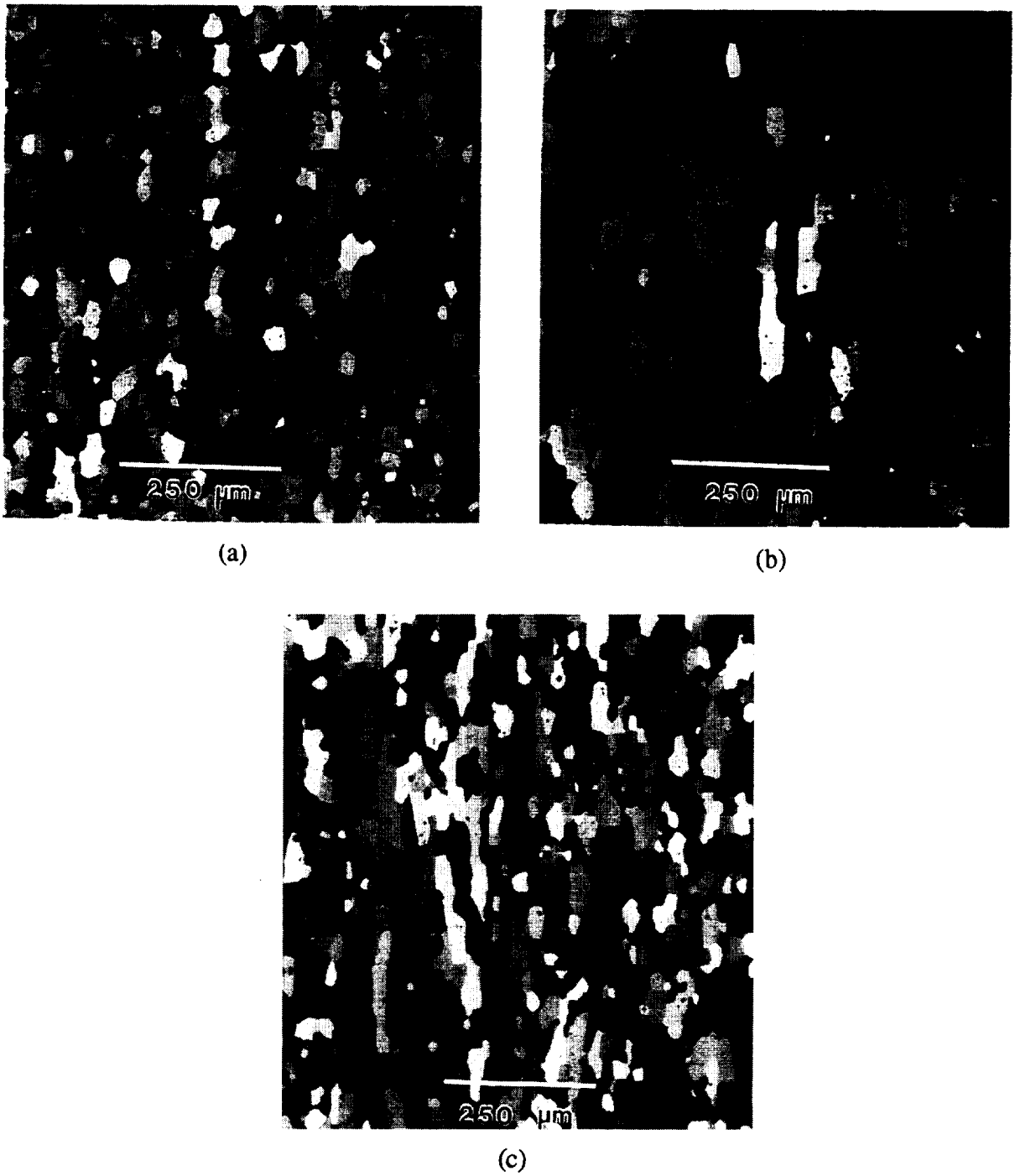

(a) (b)

(c)

Figure 2 Polarized light micrographs from Barker's etched samples of heat treated C415 0.090" thick sheet. Sections shown are those containing the longitudinal and short transverse directions. Samples were processed using thermomechanical processing variations: (a) Grain Structure A: extended preheat, rolled from 825°F, rapid heat-up rate to the solution heat treatment temperature, (b) Grain Structure B: minimal preheat, rolled from 825°F, moderate heat-up rate to solution heat treatment temperature, and (c) Grain Structure C: no preheat, rolled from 825°F, moderate heat-up rate to solution heat treatment temperature.

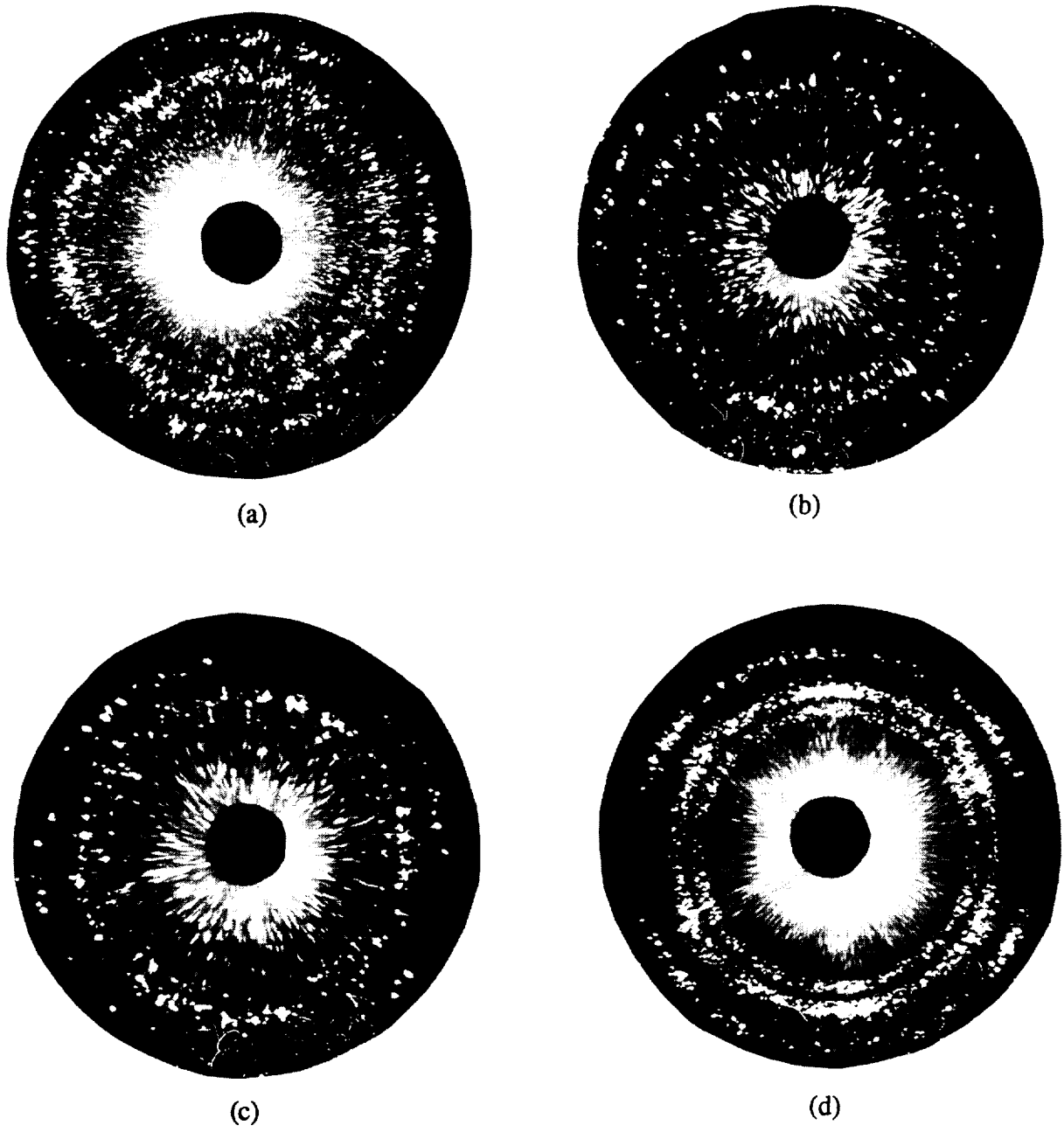

Figure 3 Laue x-ray diffraction patterns from the t/2 planes of C415 0.090" thick sheet. Samples were processed using thermomechanical processing variations: (a) Grain Structure A, (b) Grain Structure B, (c) Grain Structure C, and (d) Grain Structure D.

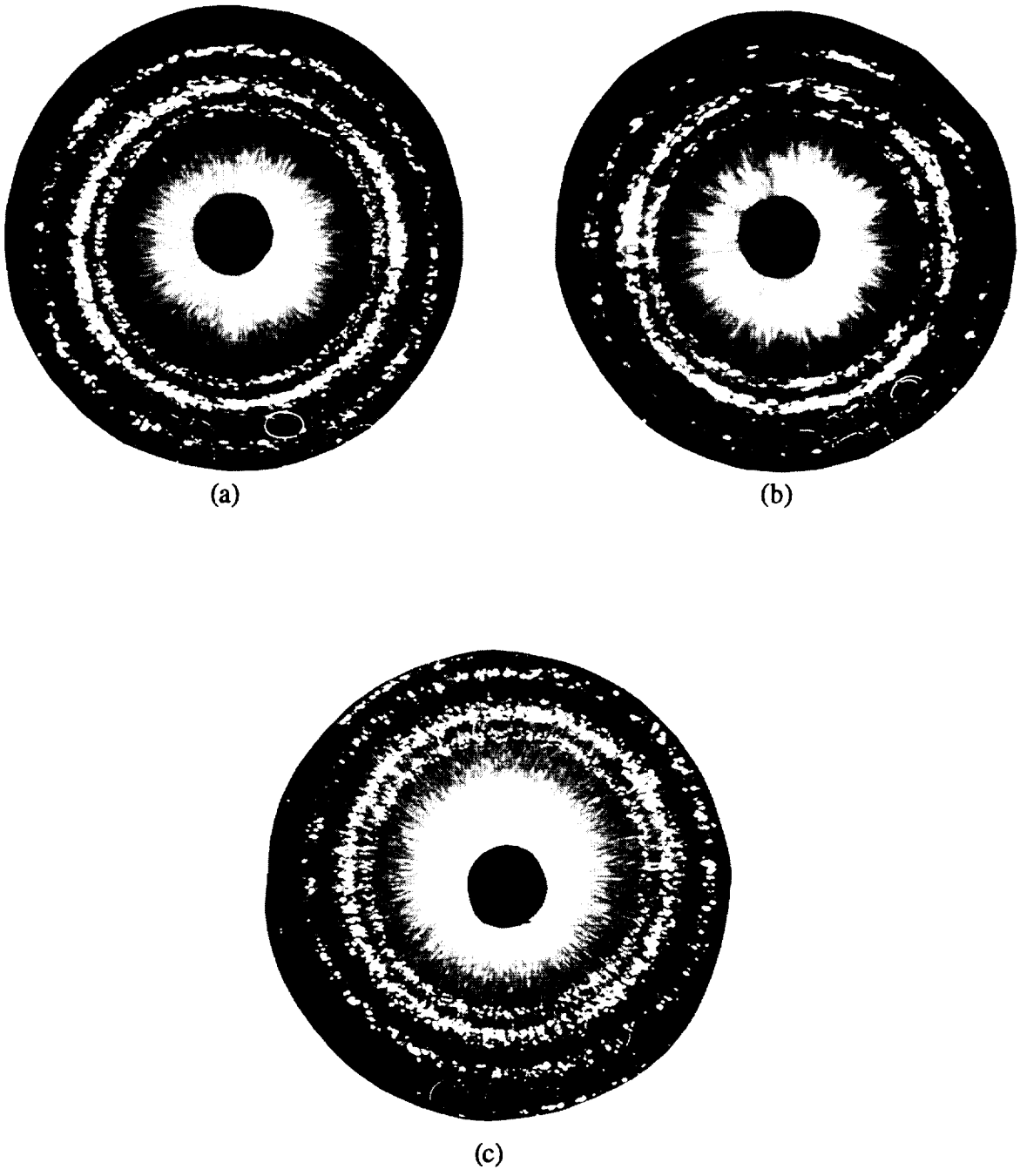

Figure 4 Laue x-ray diffraction patterns from the t/2 planes of C416 0.090" thick sheet. Samples were processed using thermomechanical processing variations: (a) Grain Structure A, (b) Grain Structure B, and (c) Grain Structure C.

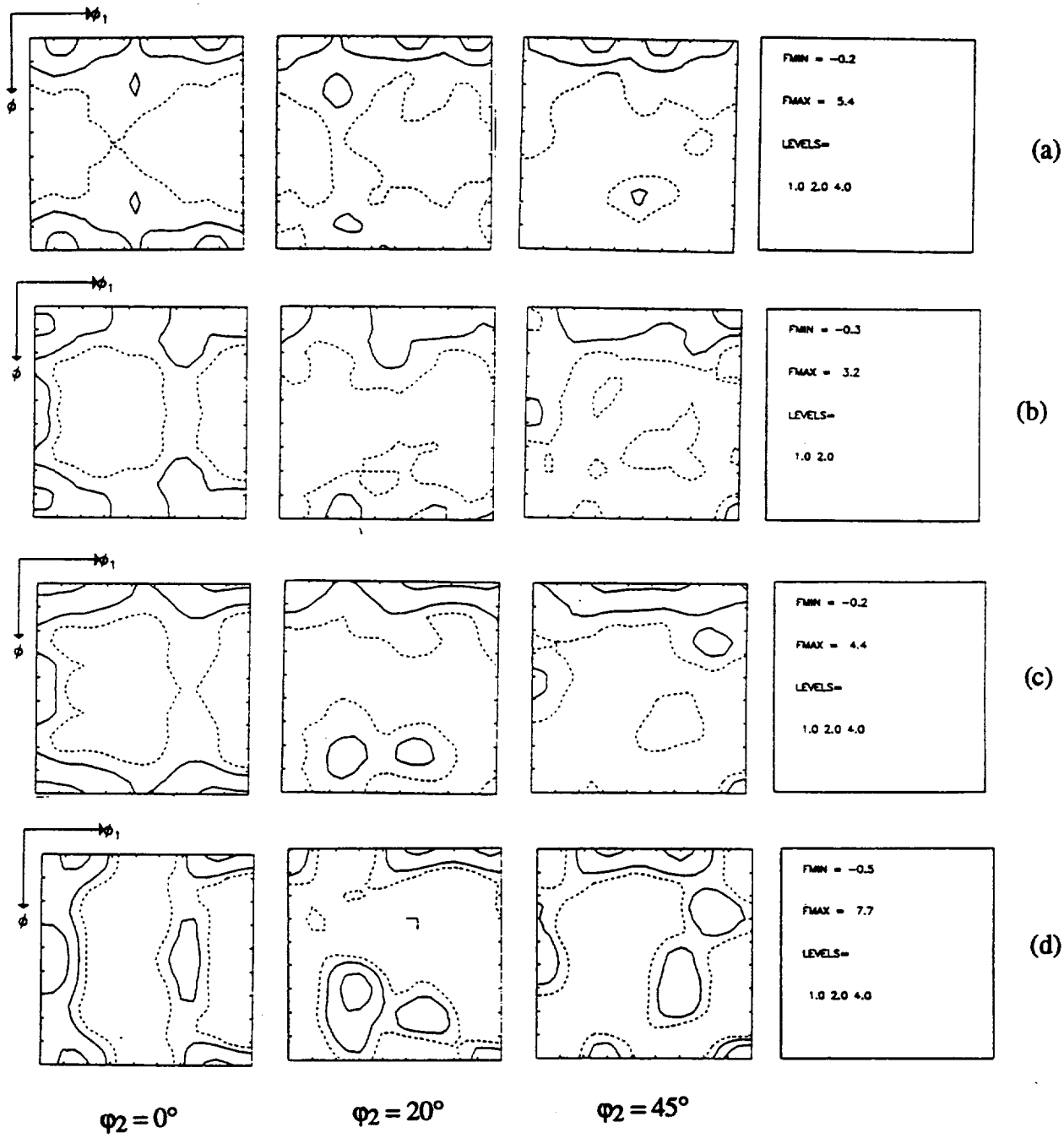

Figure 5 Constant φ_2 ODF sections from the t/2 planes of C415 0.090" thick sheet. Samples were processed using thermomechanical processing variations: (a) Grain Structure A, (b) Grain Structure B, (c) Grain Structure C, and (d) Grain Structure D.

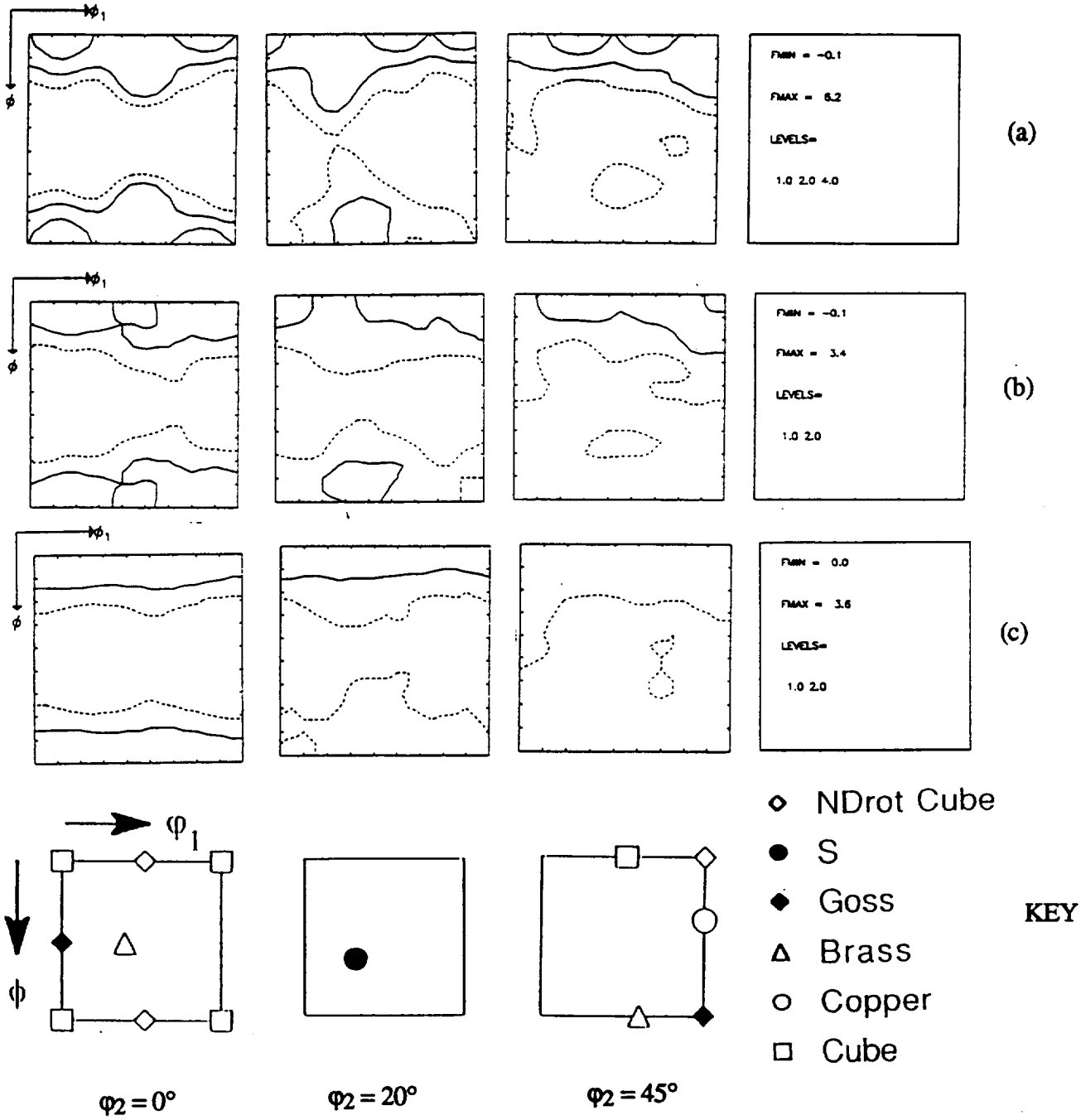

Figure 6 Constant φ_2 ODF sections from the t/2 planes of C416 0.090" thick sheet. Samples were processed using thermomechanical processing variations: (a) Grain Structure A, (b Grain Structure B, and (c) Grain Structure C.

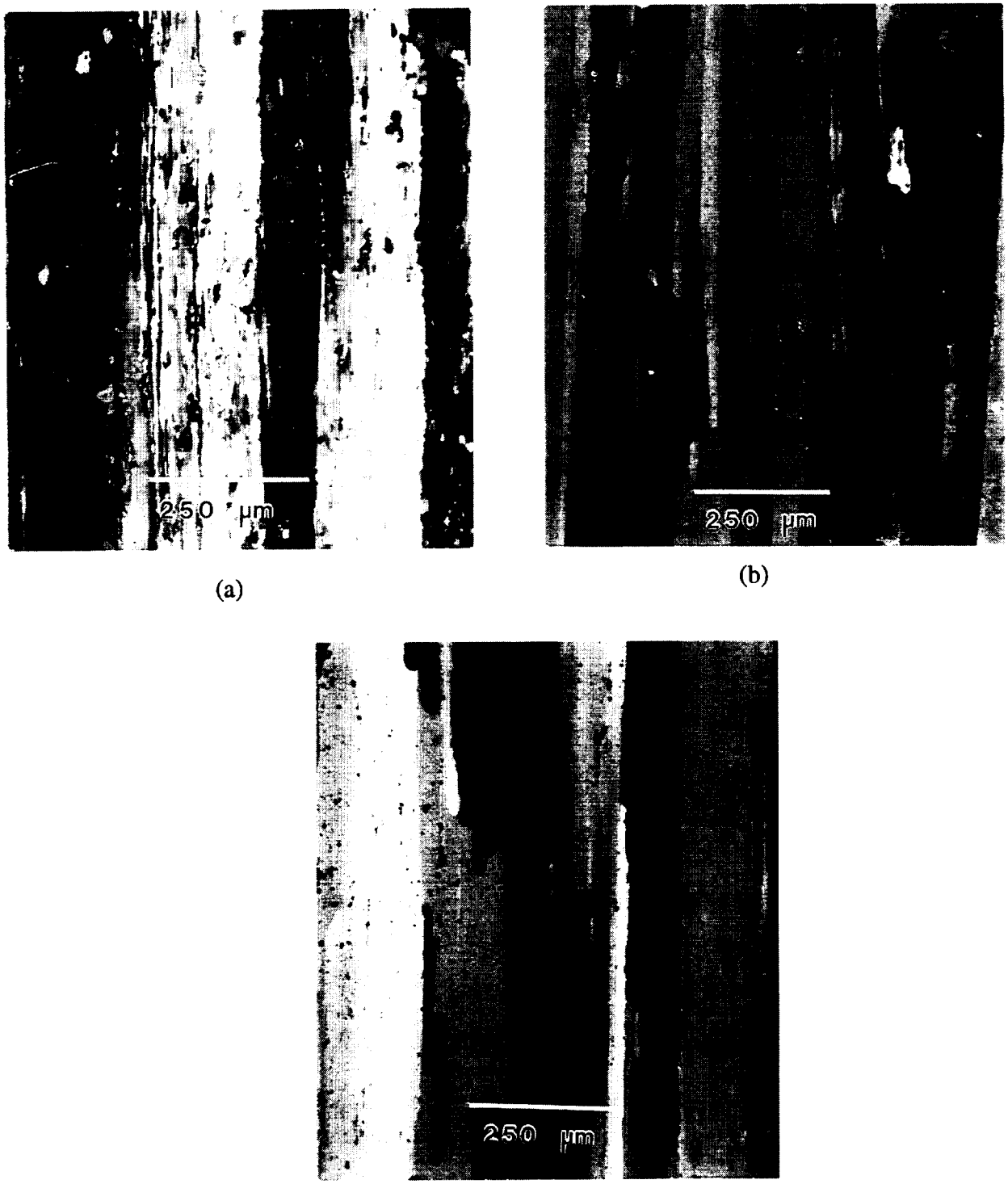

(a) (b)

(c)

Figure 7 Polarized light micrographs from Barker's etched samples of heat treated C415 0.750" thick plate. Sections shown are those containing the longitudinal and short transverse directions. Samples were fabricated using preheat variations: (a) no preheat, (b) minimal preheat, and (c) extended preheat. All three variants were rolled from 825°F and given a rapid heat-up rate to the solution heat treatment temperature.

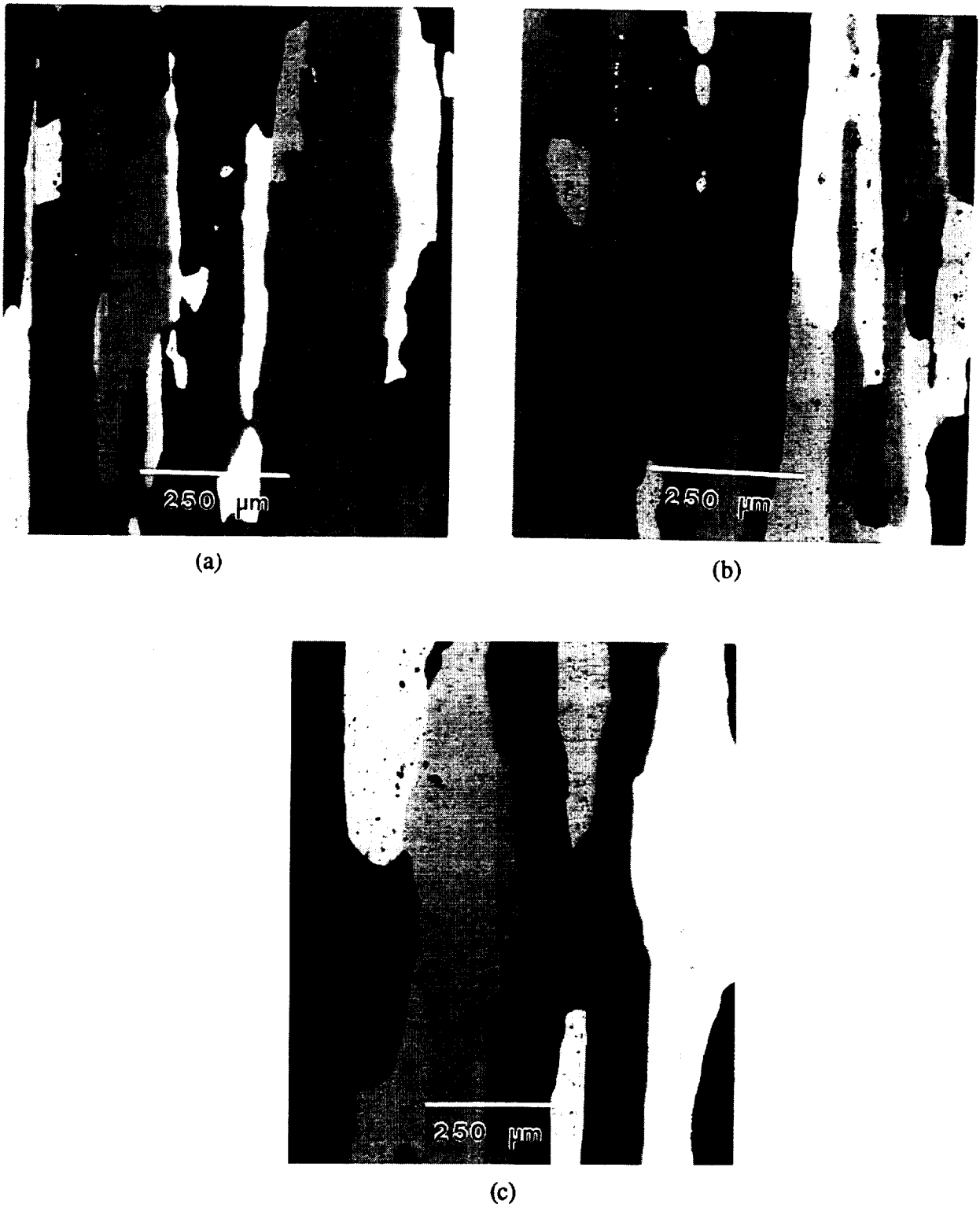

(a) (b)

(c)

Figure 8 Polarized light micrographs from Barker's etched samples of heat treated C416 0.750" thick plate. Sections shown are those containing the longitudinal and short transverse directions. Samples were fabricated using preheat variations: (a) no preheat, (b) minimal preheat, and (c) extended preheat. All three variants were rolled from 825°F and given a rapid heat-up rate to the solution heat treatment temperature.

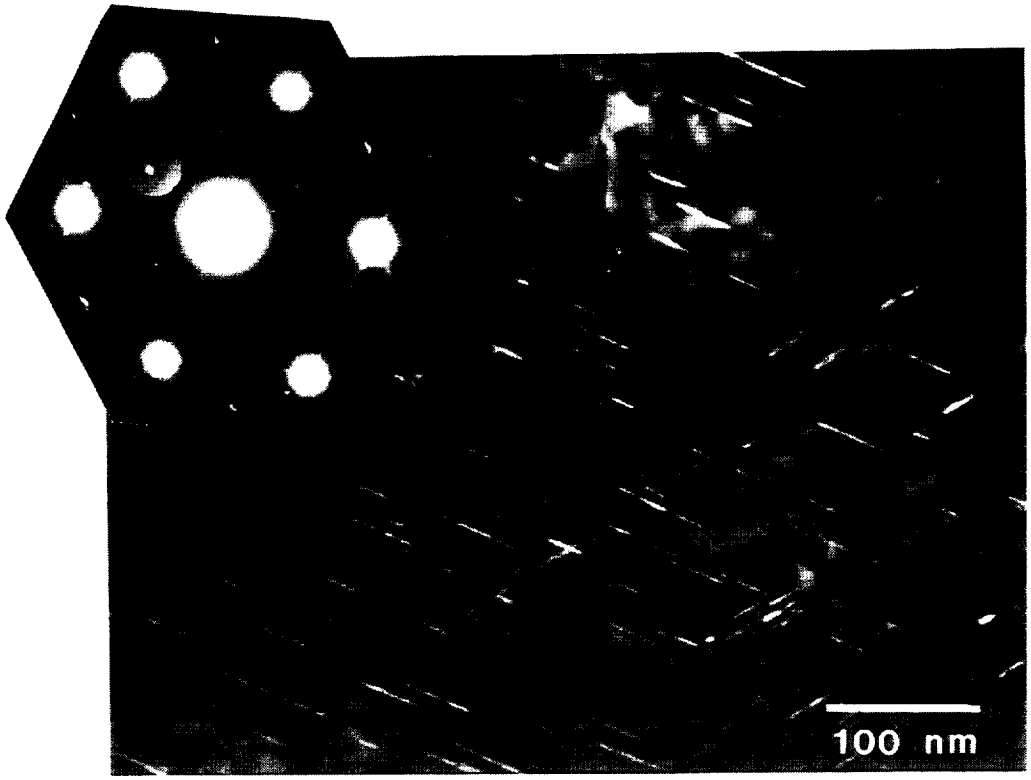

(a)

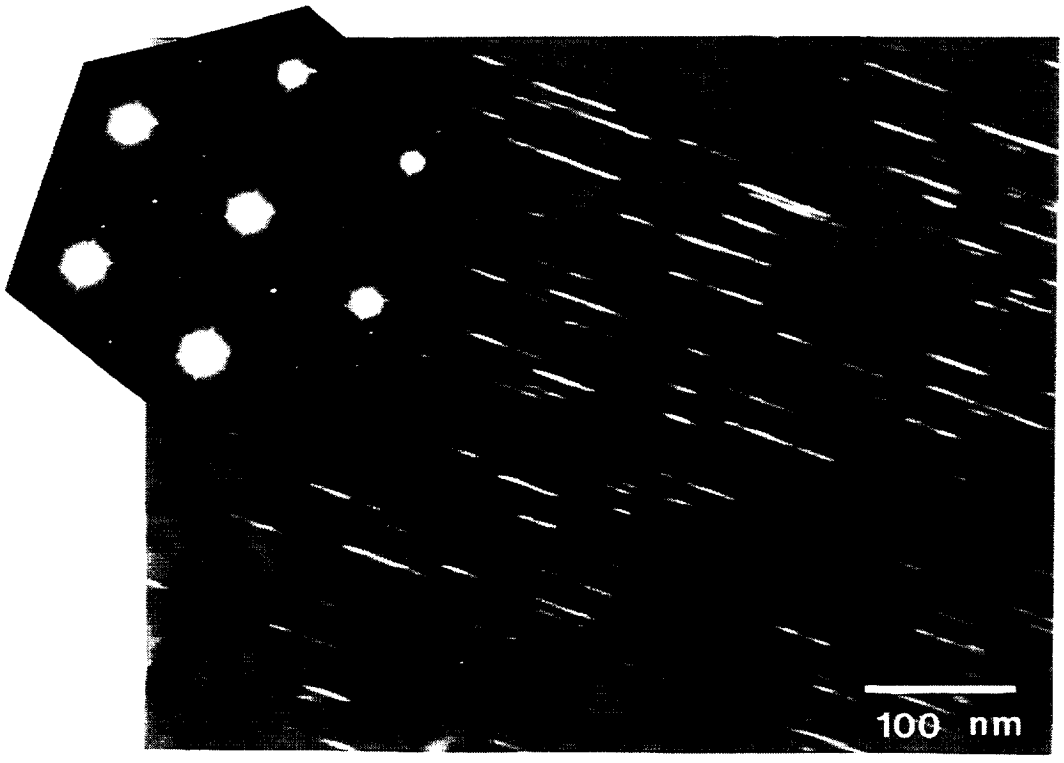

(b)

Figure 9 Dark field transmission electron micrographs of C415 sheet having Grain Structure A and having been stretched (a) 0.5%, (b) 2% and (c) 8% prior to artificial aging.

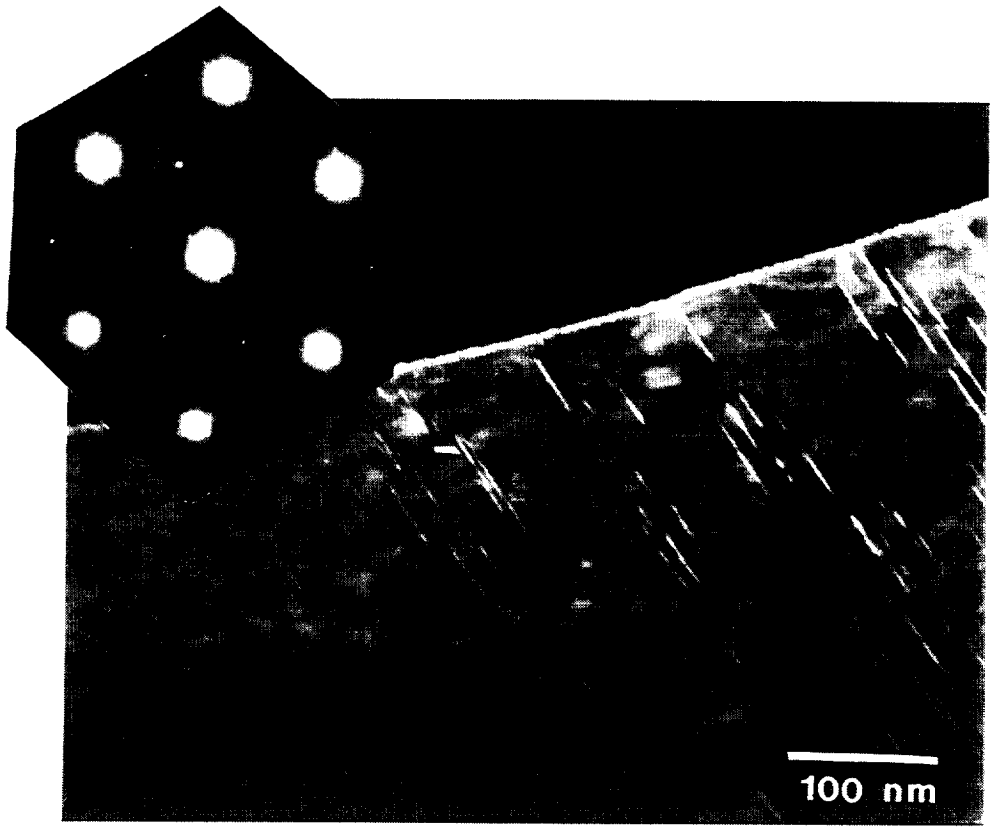

(c)

Figure 9 (continued)

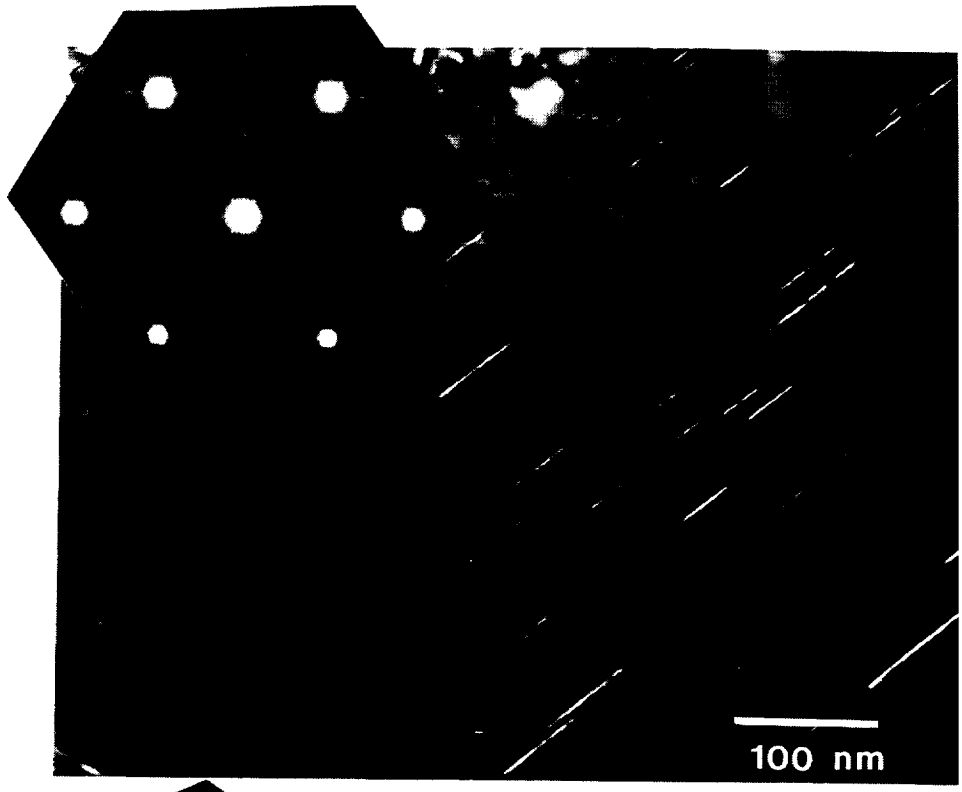

(a)

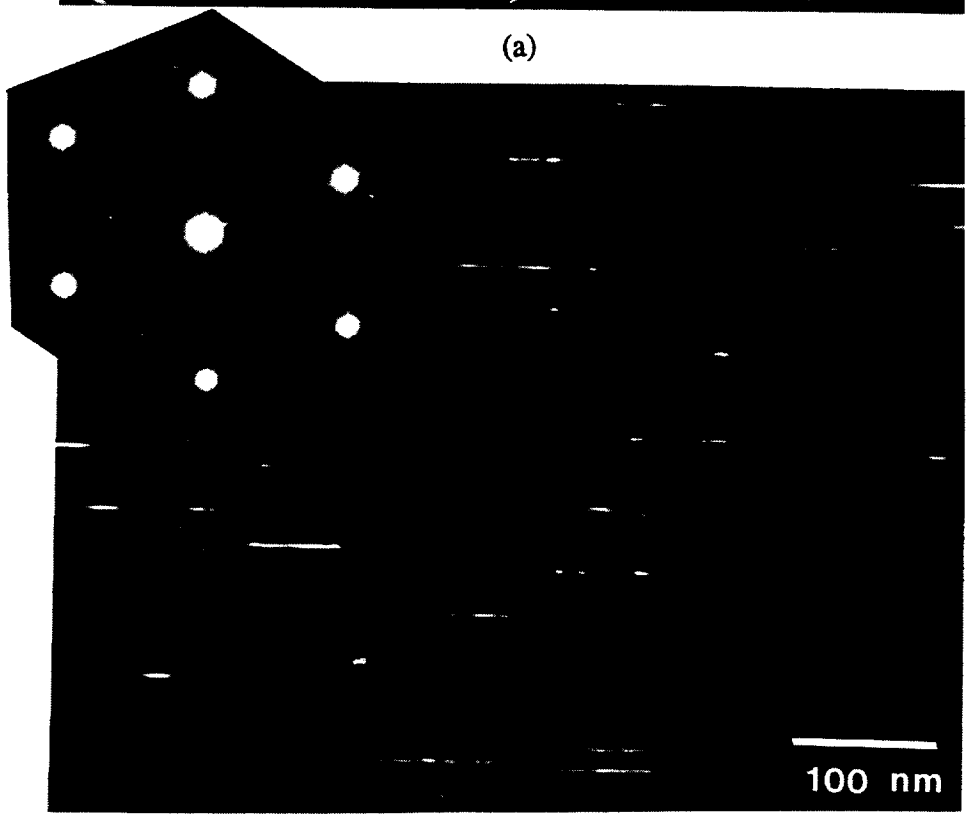

(b)

Figure 10 Dark field transmission electron micrographs of C416 sheet having Grain Structure A and having been stretched (a) 0.5%, (b) 2% and (c) 8% prior to artificial aging.

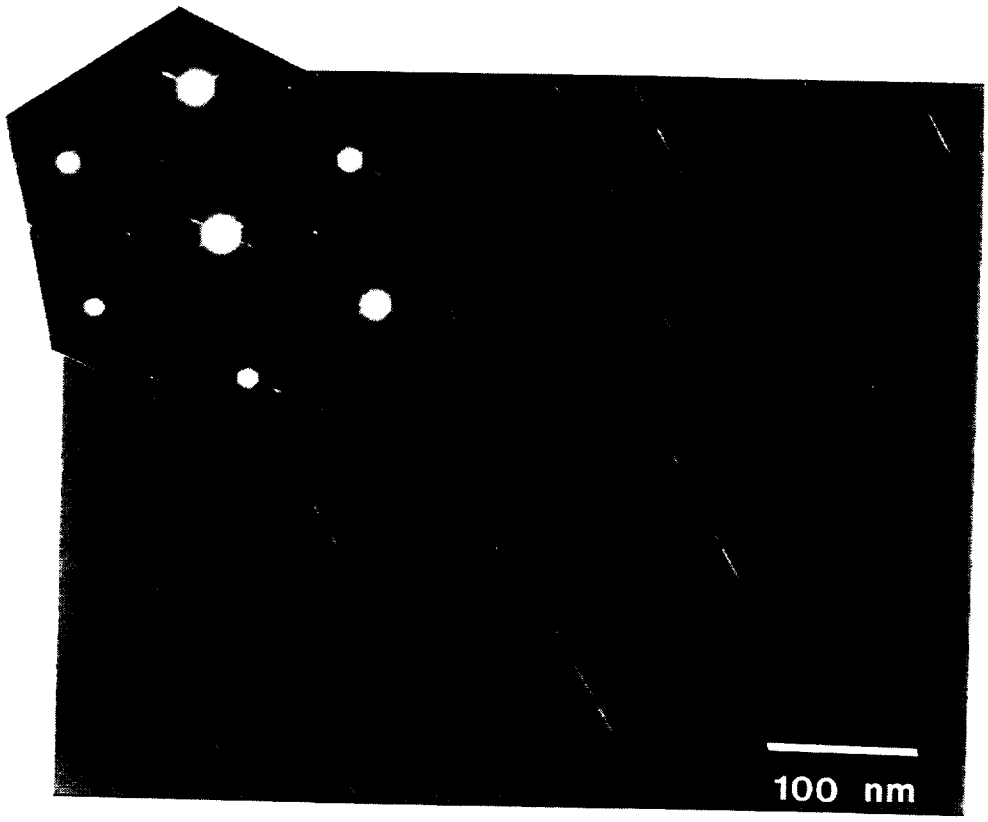

(c)

Figure 10 (continued)

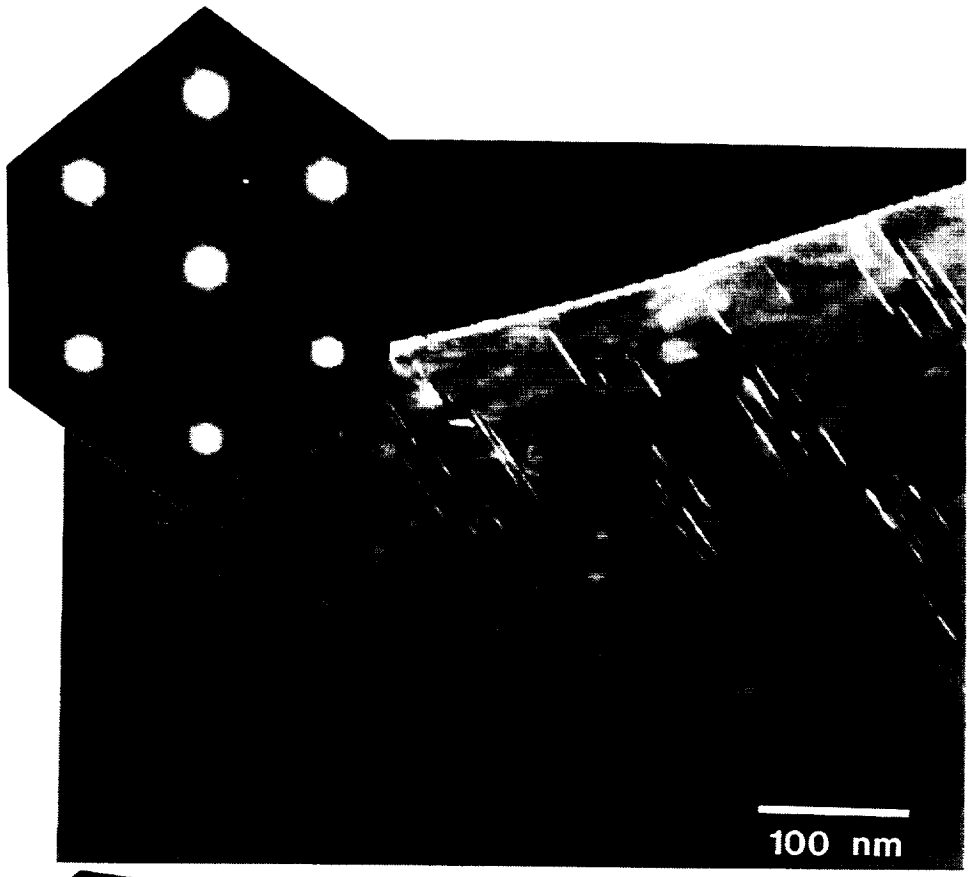

(a)

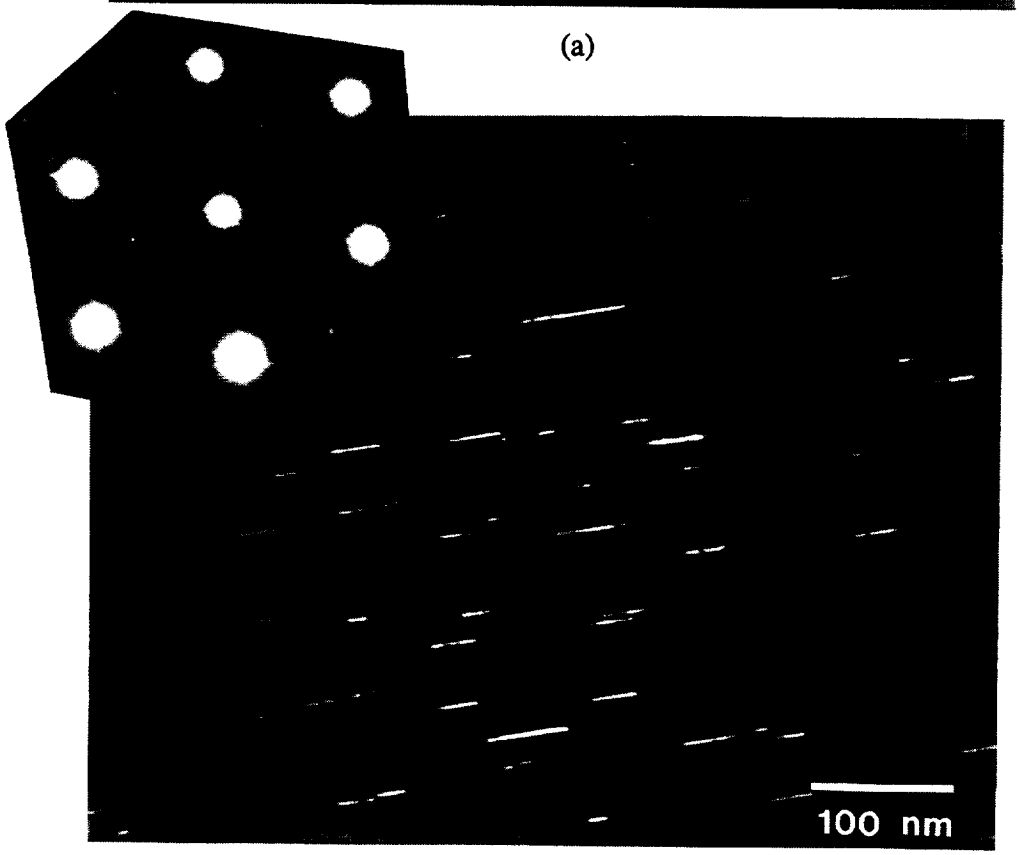

(b)

Figure 11 Dark field transmission electron micrographs of C415 sheet having Grain Structure A and having been stretched 8% prior to artificial aging: (a) aged to the near peak aged condition, and (b) aged to the near peak aged condition and then exposed for 3000 hr at 225°F.

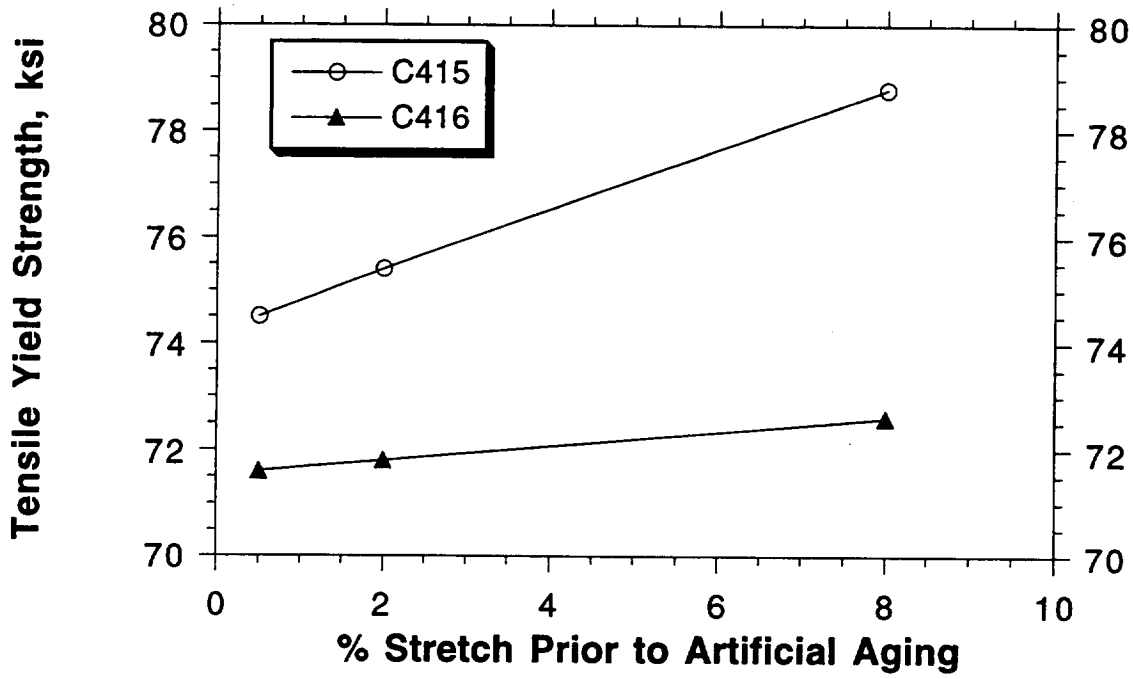

Figure 12 Longitudinal tensile yield strength as a function of % stretch prior to artificial aging, for C415 and C416 sheet having Grain Structure A.

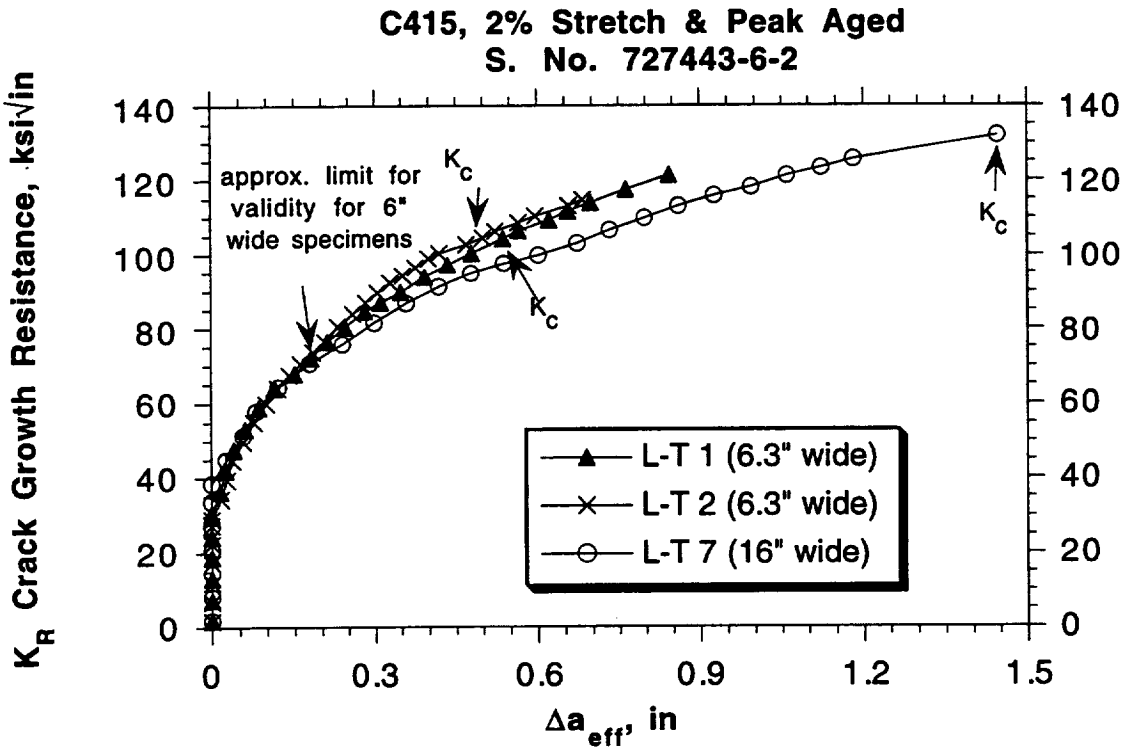

Figure 13 L-T K_R crack growth resistance as a function of Δa_{eff} for two 6.3" wide and one 16" wide center cracked fracture toughness panels from C415 sheet having Grain Structure A and having been stretched 2% prior to artificial aging.

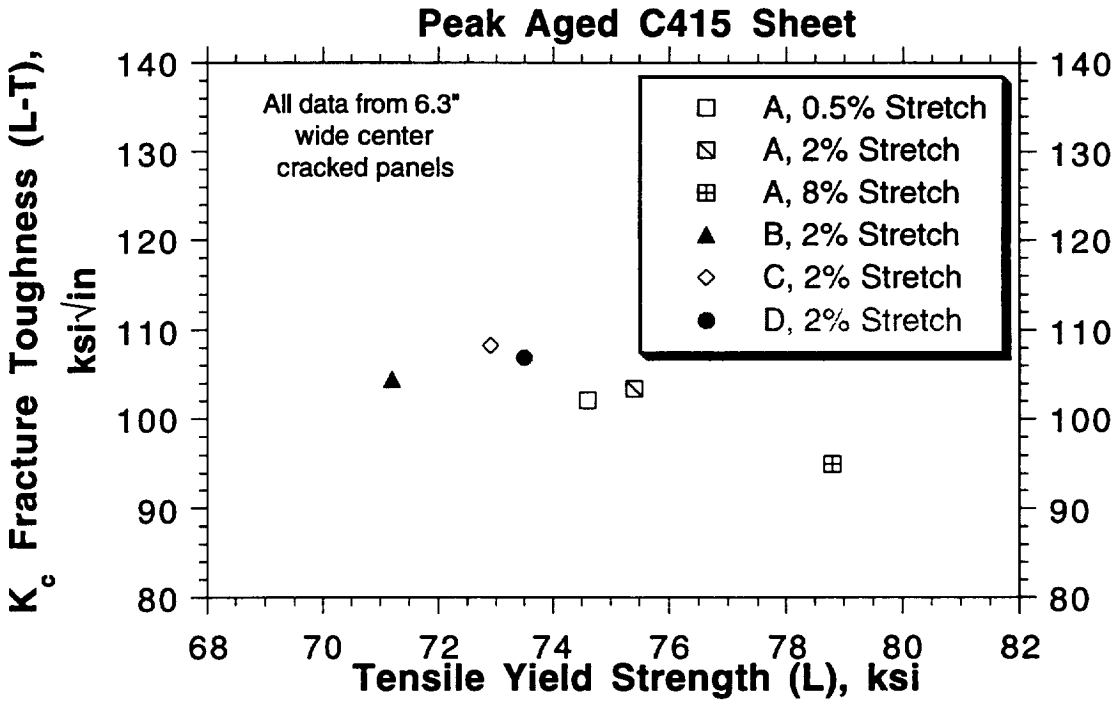

Figure 14 L-T K_c fracture toughness as a function of L tensile yield strength for C415 sheet, having various grain structures (A, B, C and D) and having been stretched 0.5%, 2% or 8% prior to artificial aging. All tensile yield strength values and K_c values are averages of duplicate specimens. All K_c data were from 6.3" wide center cracked panels and were invalid.

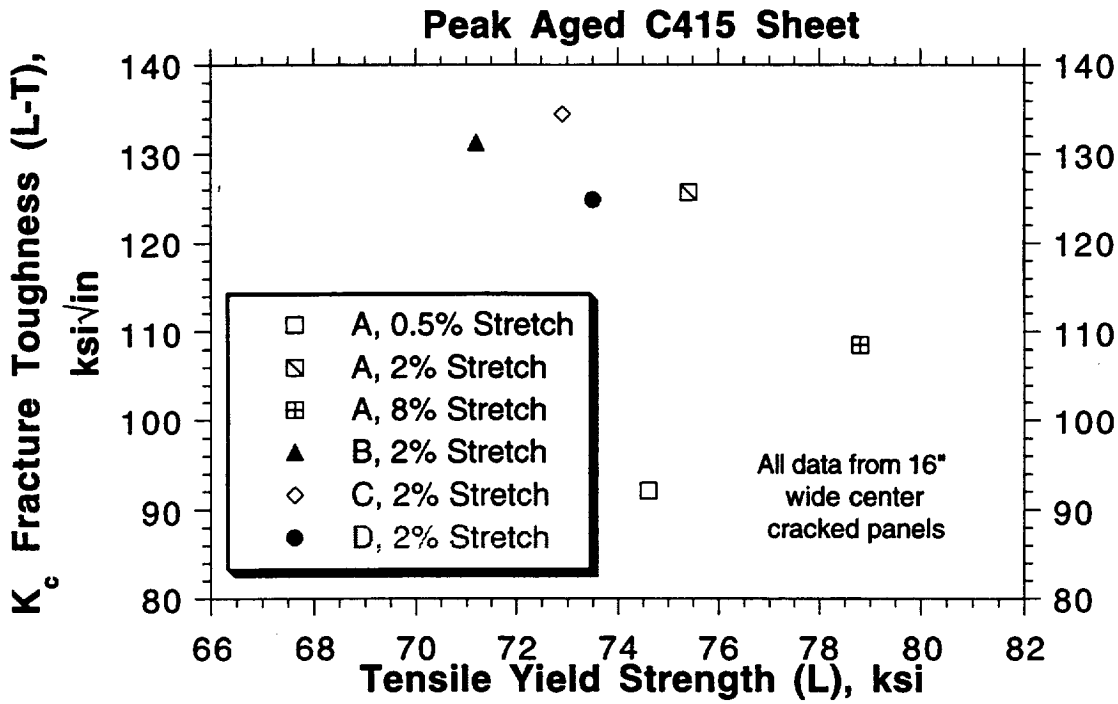

Figure 15 L-T K_c fracture toughness as a function of L tensile yield strength for C415 sheet, having various grain structures (A, B, C and D) and having been stretched 0.5%, 2% or 8% prior to artificial aging. All tensile yield strength values are averages from duplicate specimens and K_c values are from single specimens. All K_c data were from 16" wide center cracked panels.

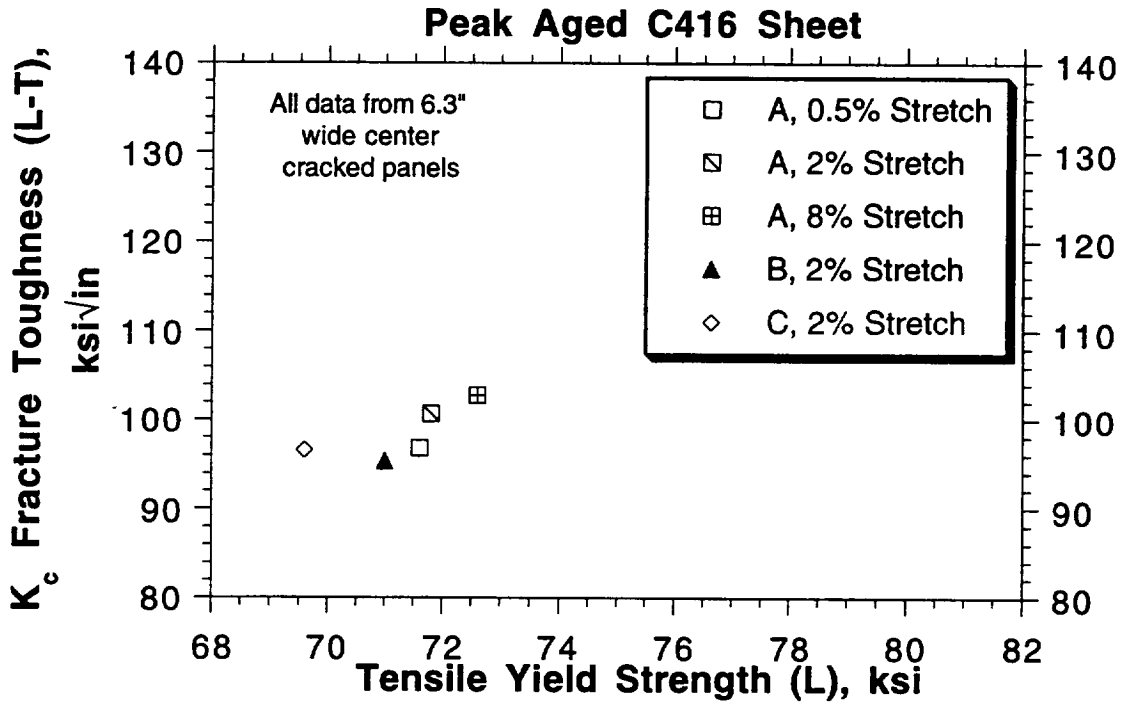

Figure 16 L-T K_c fracture toughness as a function of L tensile yield strength for C416 sheet, having various grain structures (A, B, and C) and having been stretched 0.5%, 2% or 8% prior to artificial aging. All tensile yield strength values and K_c values are averages of duplicate specimens. All K_c data were from 6.3" wide center cracked panels and were invalid.

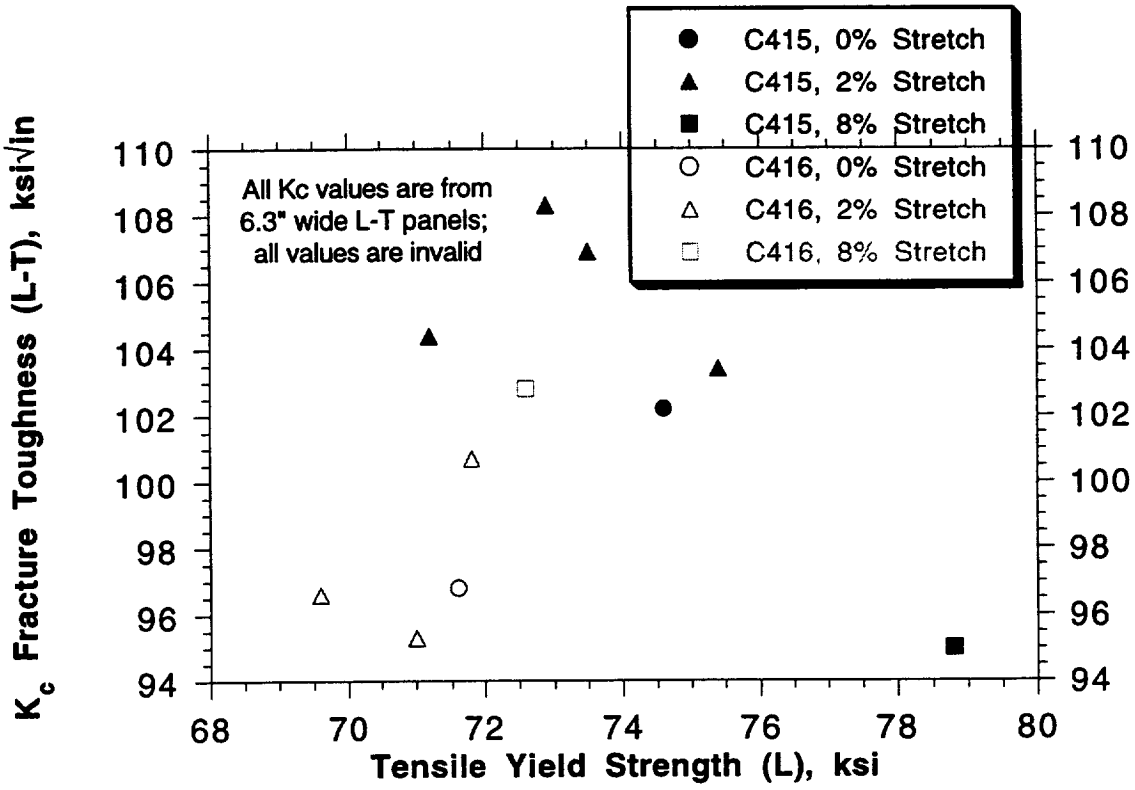

Figure 17 L-T K_c fracture toughness as a function of L tensile yield strength for C415 and C416 sheet, having Grain Structure A and having been stretched 0.5%, 2% or 8% prior to artificial aging. All tensile yield strength values and K_c values are averages of duplicate specimens. All K_c data were from 6.3" wide center cracked panels and were invalid.

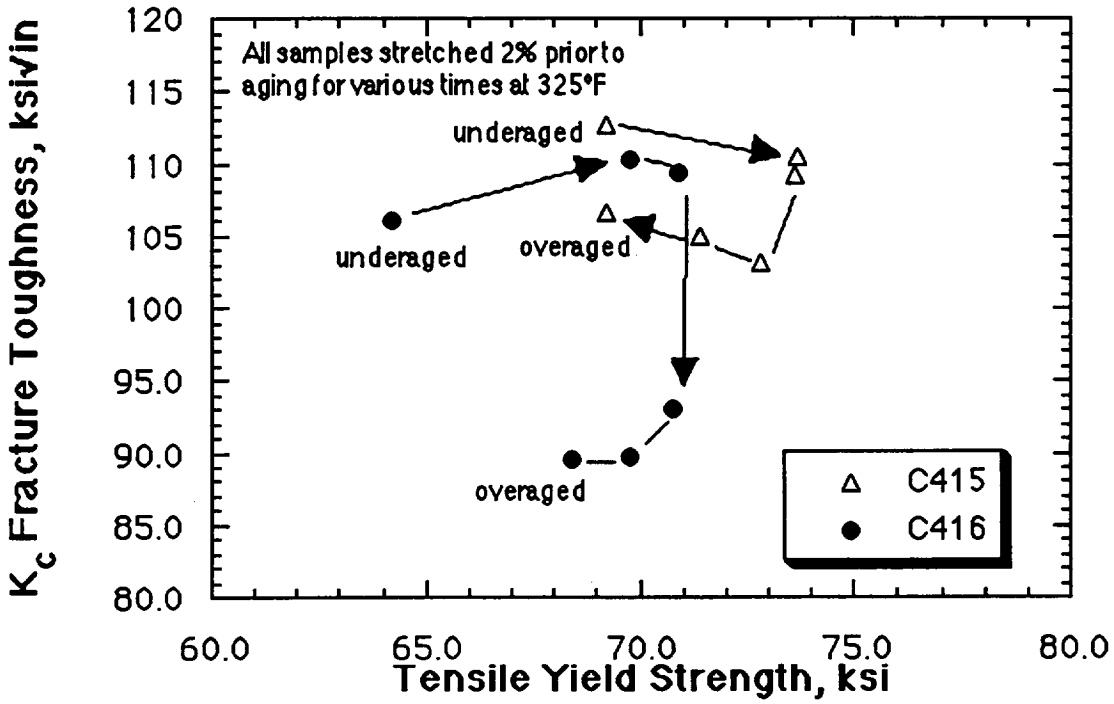

Figure 18 L-T K_c fracture toughness as a function of tensile yield strength for C415 and C416 sheet which had been stretched 2% and artificially aged at 325°F for various times. All tensile yield strength value and K_c values are averages of duplicate specimens. All K_c data were from 6.3" wide center cracked panels and were invalid.

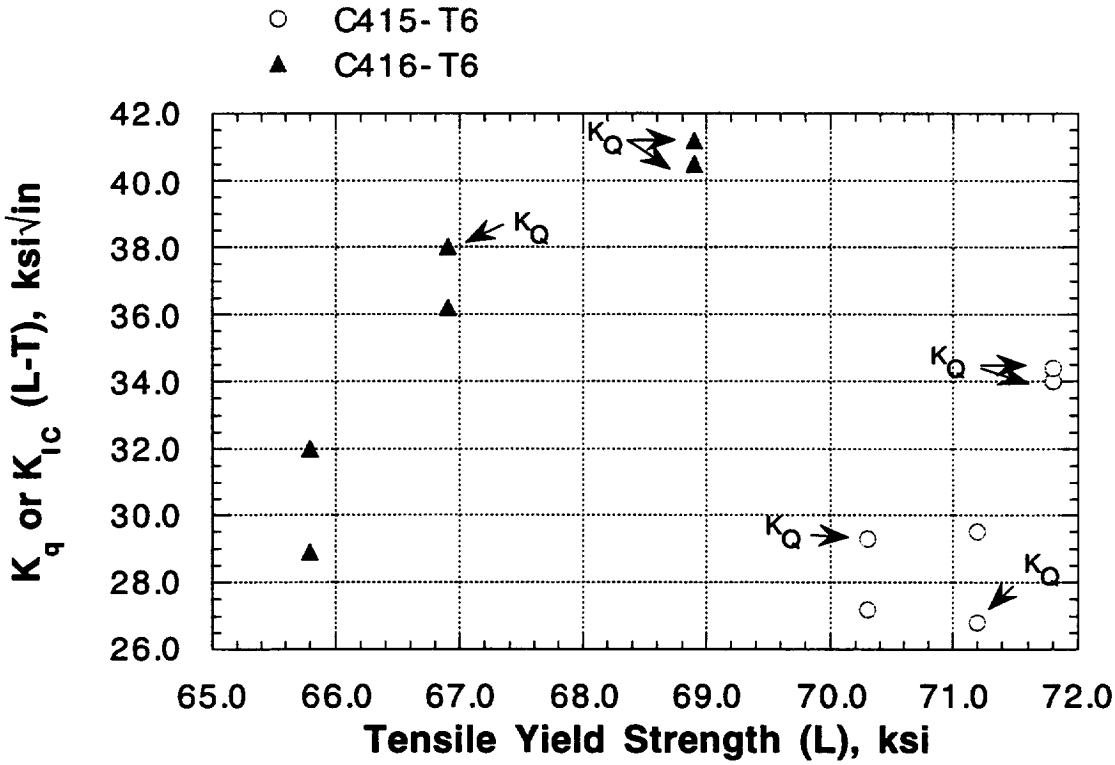

Figure 19 L-T K_q or K_{IC} fracture toughness versus L tensile yield strength for 0.750" thick C415 and C416 plate.

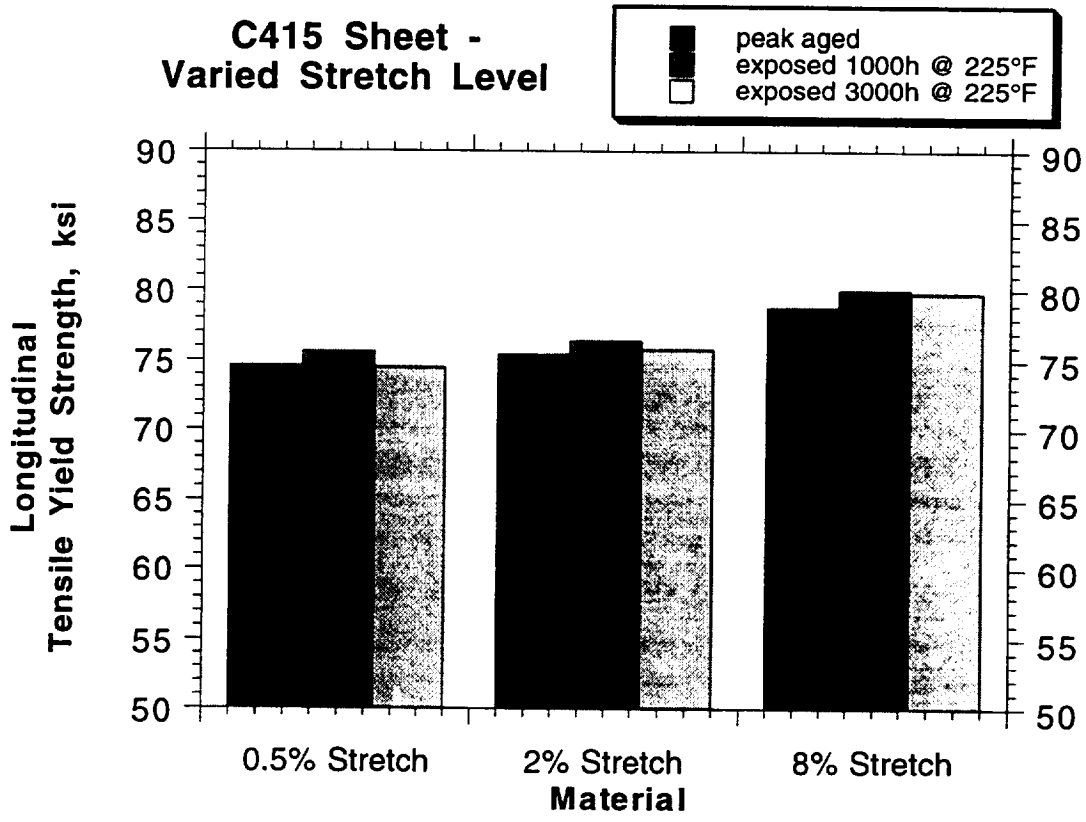

Figure 20 Longitudinal tensile yield strength for C415 sheet given various levels of stretch prior to peak aging, and then tested in the peak aged condition and after exposures of either 1000 hr or 3000 hr at 225°F.

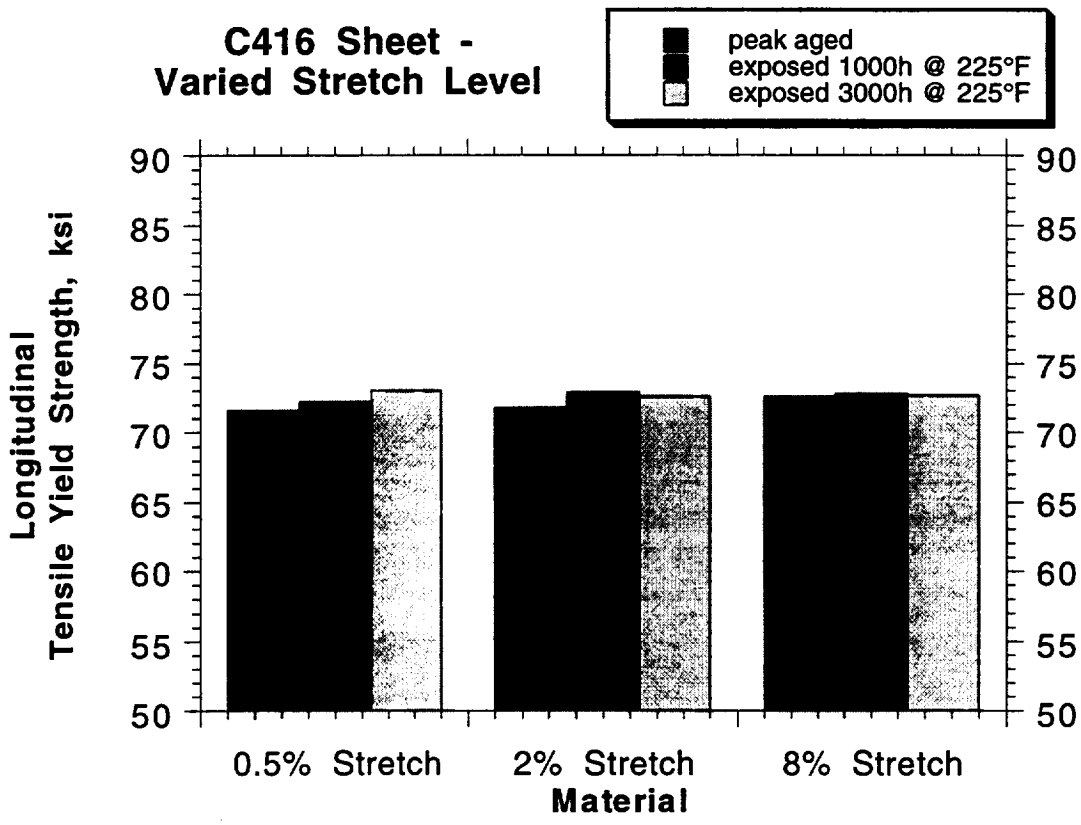

Figure 21 Longitudinal tensile yield strength for C416 sheet given various levels of stretch prior to peak aging, and then tested in the peak aged condition and after exposures of either 1000 hr or 3000 hr at 225°F.

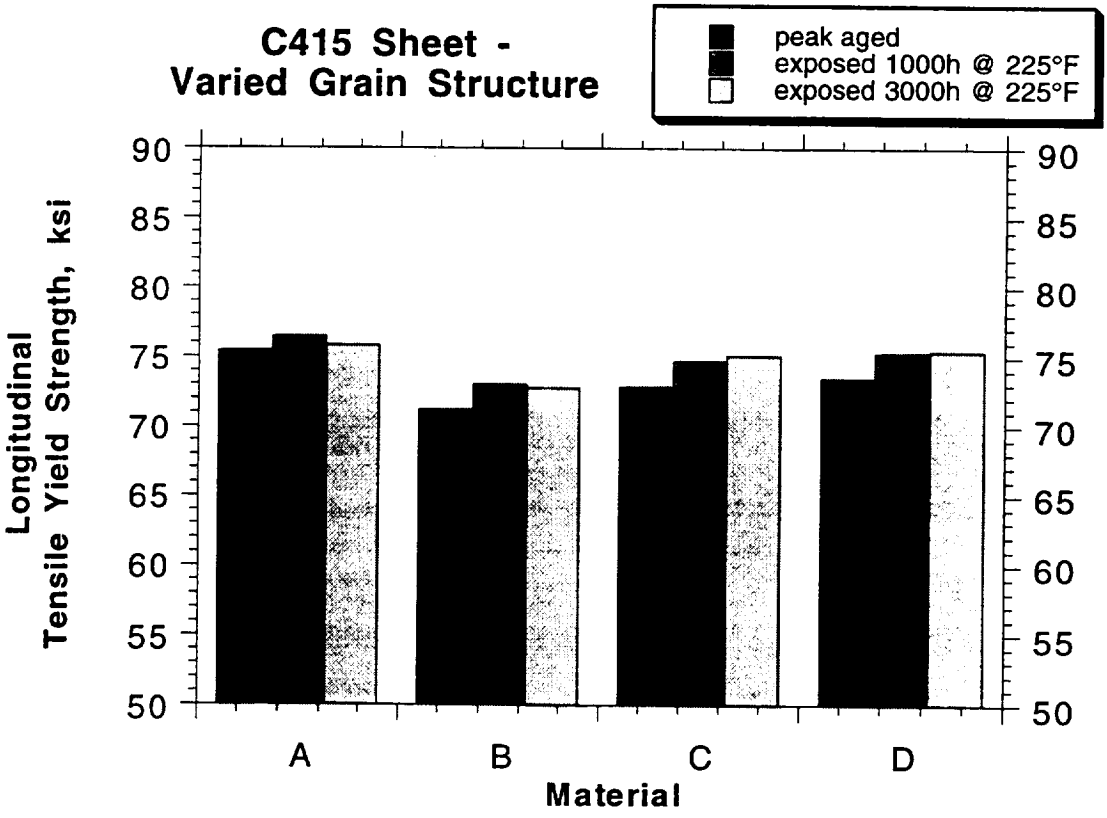

Figure 22 Longitudinal tensile yield strength for C415 sheet having various grain structures and having been given 2% stretch prior to peak aging, and having been tested in the peak aged condition and after exposures of either 1000 hr or 3000 hr at 225°F.

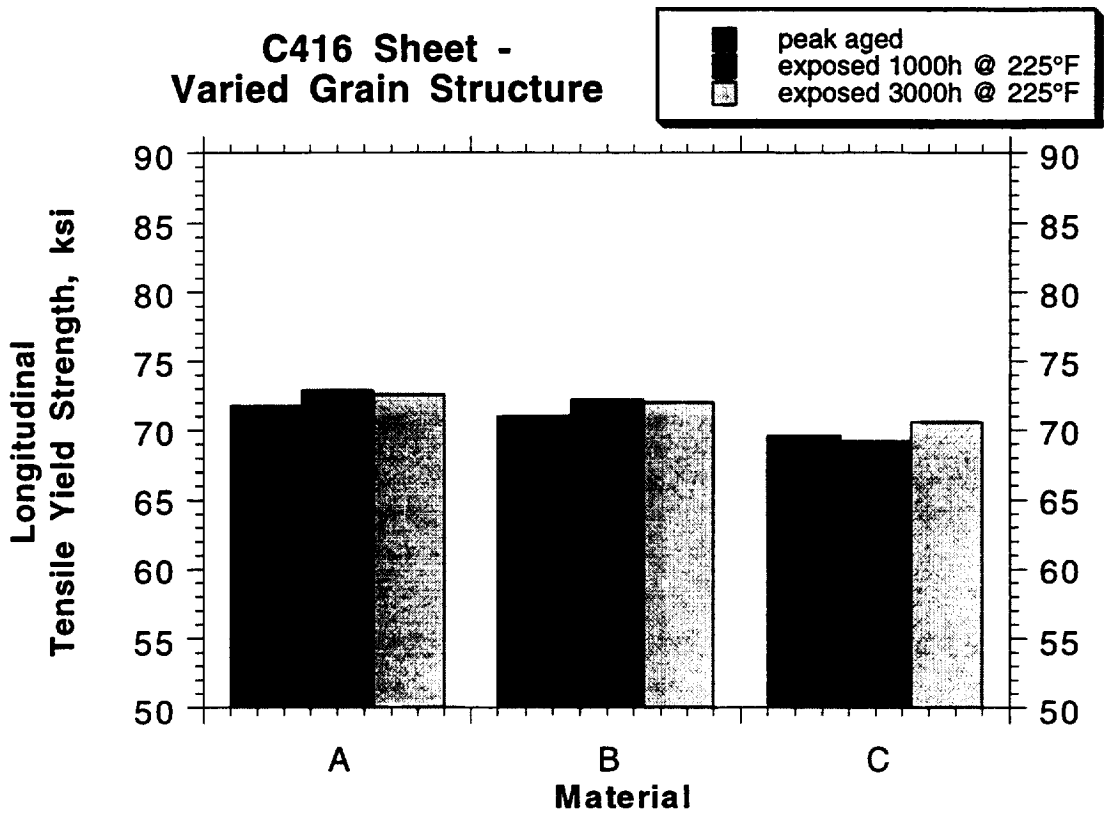

Figure 23 Longitudinal tensile yield strength for C416 sheet having various grain structures and having been given 2% stretch prior to peak aging, and having been tested in the peak aged condition and after exposures of either 1000 hr or 3000 hr at 225°F.

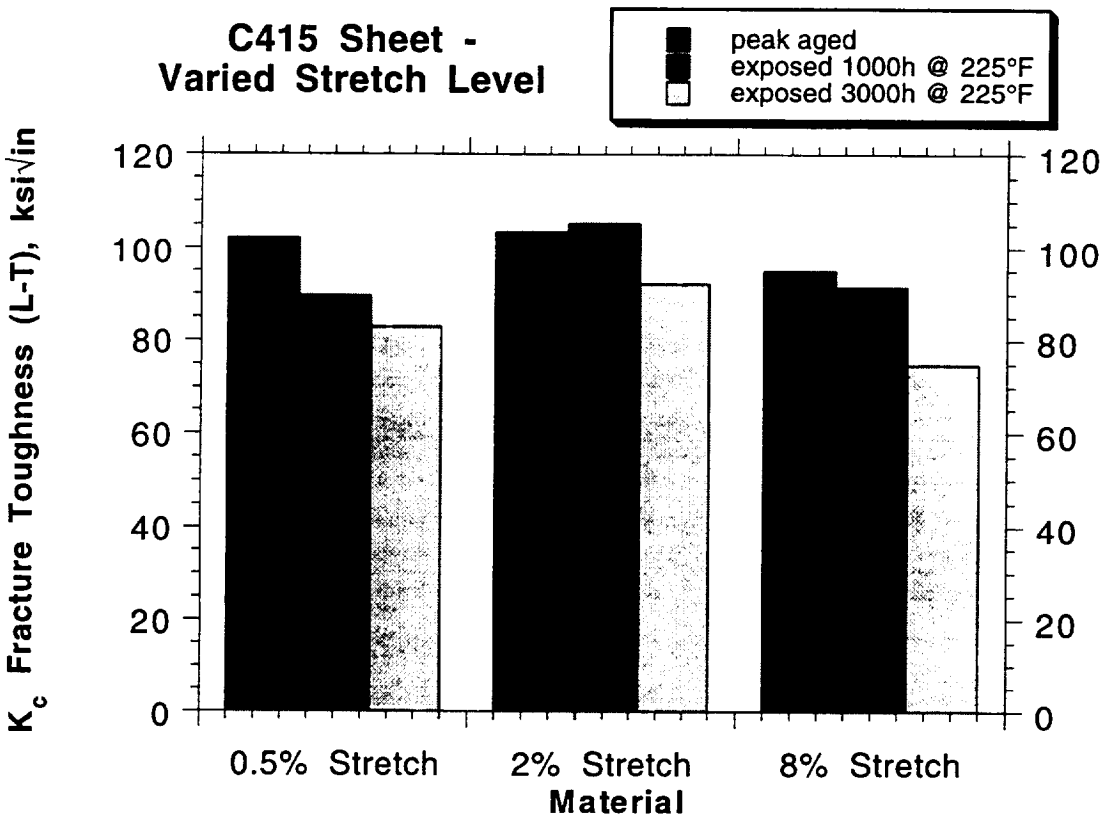

Figure 24 L-T K_c fracture toughness for C415 sheet given various levels of stretch prior to peak aging, and then tested in the peak aged condition and after exposures of either 1000 hr or 3000 hr at 225°F.

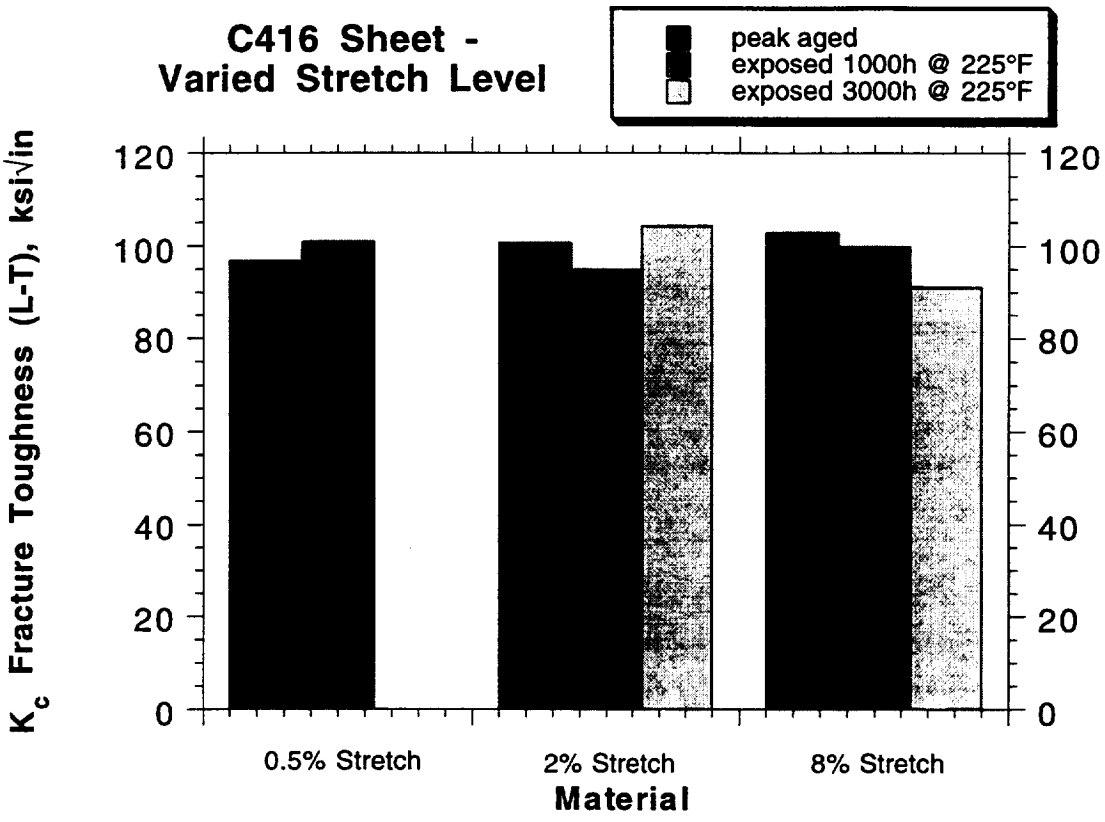

Figure 25 L-T K_c fracture toughness for C416 sheet given various levels of stretch prior to peak aging, and then tested in the peak aged condition and after exposures of either 1000 hr or 3000 hr at 225°F.

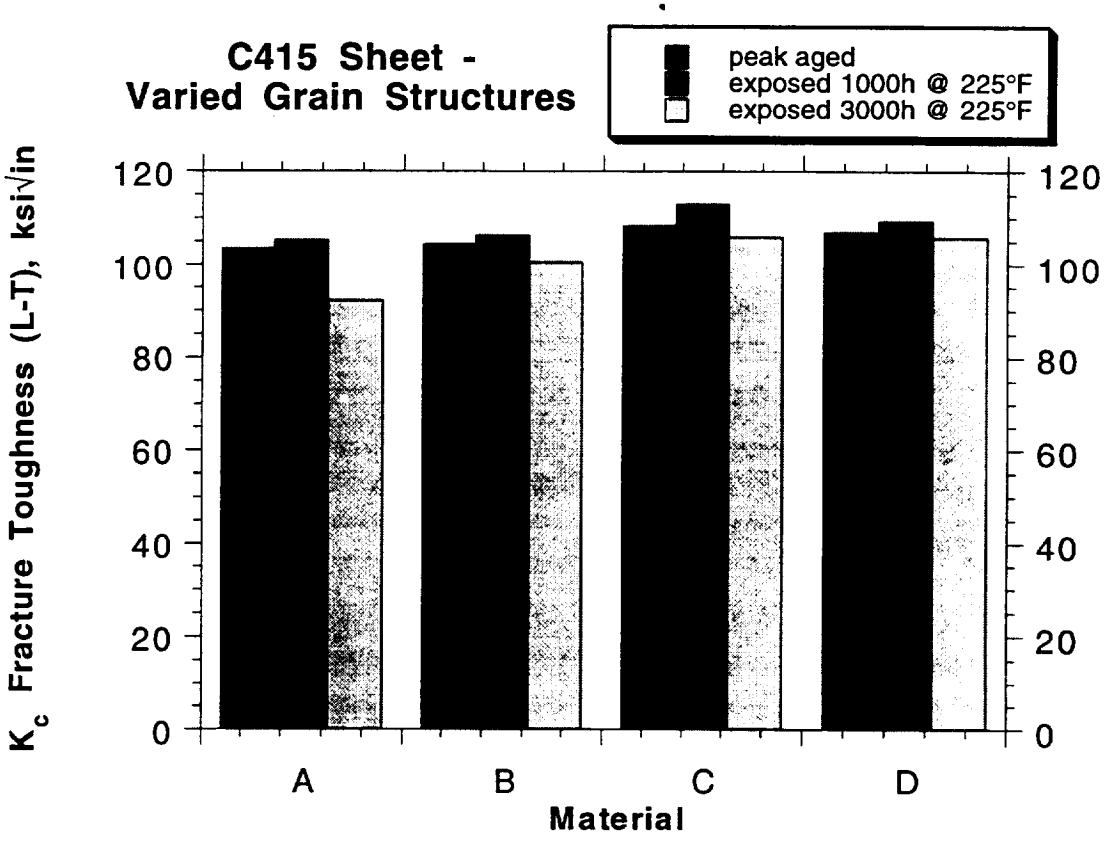

Figure 26 L-T K_c fracture toughness for C415 sheet having various grain structures and having been given 2% stretch prior to peak aging, and having been tested in the peak aged condition and after exposures of either 1000 hr or 3000 hr at 225°F.

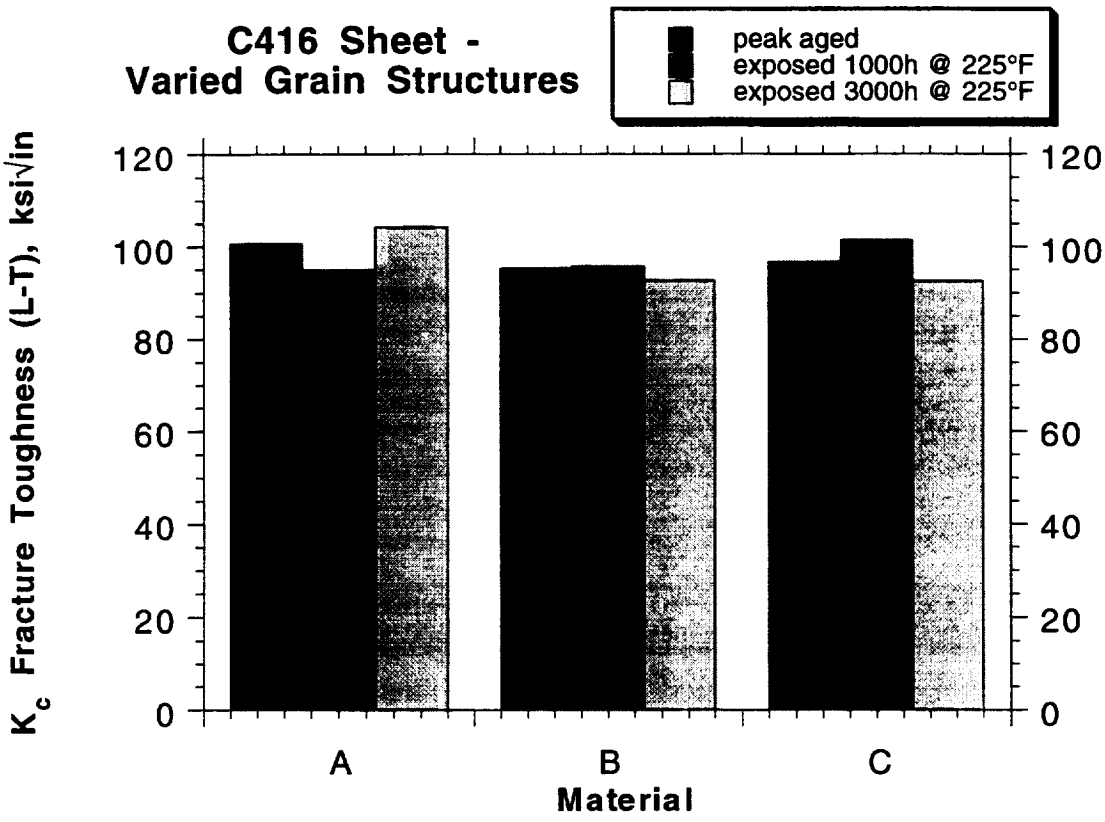

Figure 27 L-T K_c fracture toughness for C416 sheet having various grain structures and having been given 2% stretch prior to peak aging, and having been tested in the peak aged condition and after exposures of either 1000 hr or 3000 hr at 225°F.

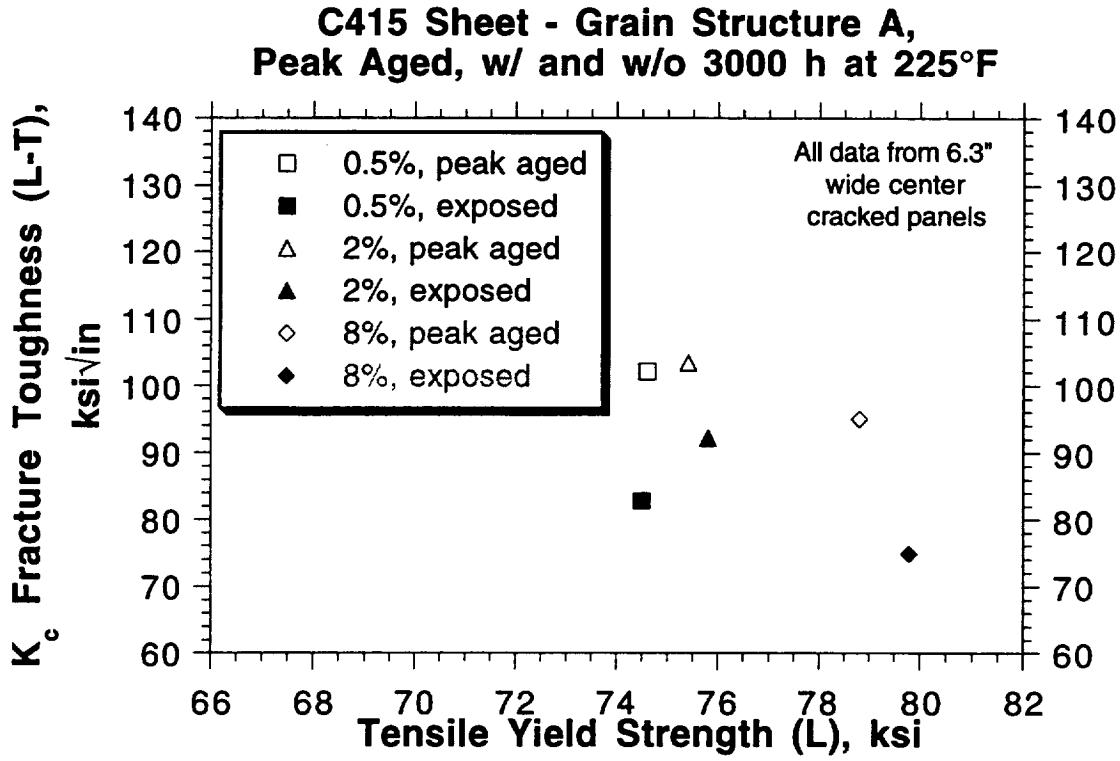

Figure 28 L-T K_c fracture toughness versus L tensile yield strength for C415 sheet, having Grain Structure A and having been given various levels of stretch prior to peak aging, and having been tested in the peak aged condition and after an exposure of 3000 hr at 225°F. All tensile yield strength and fracture toughness values are averages of duplicate specimens.

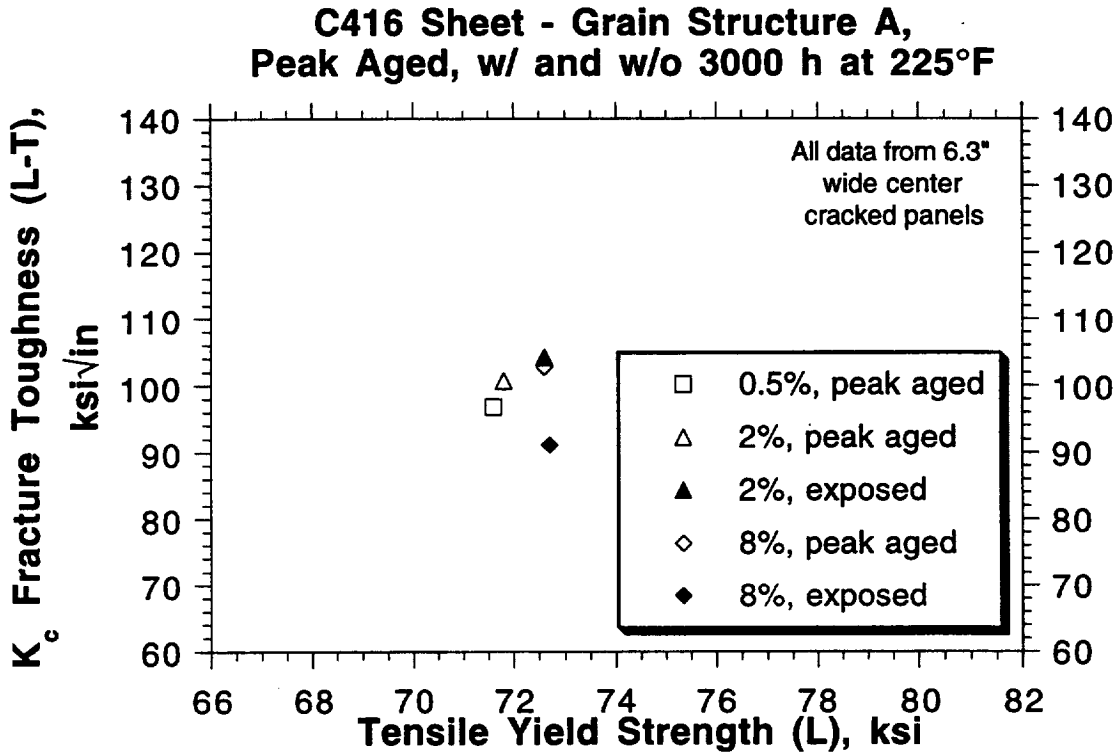

Figure 29 L-T K_c fracture toughness versus L tensile yield strength for C416 sheet, having Grain Structure A and having been given various levels of stretch prior to peak aging, and having been tested in the peak aged condition and after an exposure of 3000 hr at 225°F. All tensile yield strength and fracture toughness values are averages of duplicate specimens.

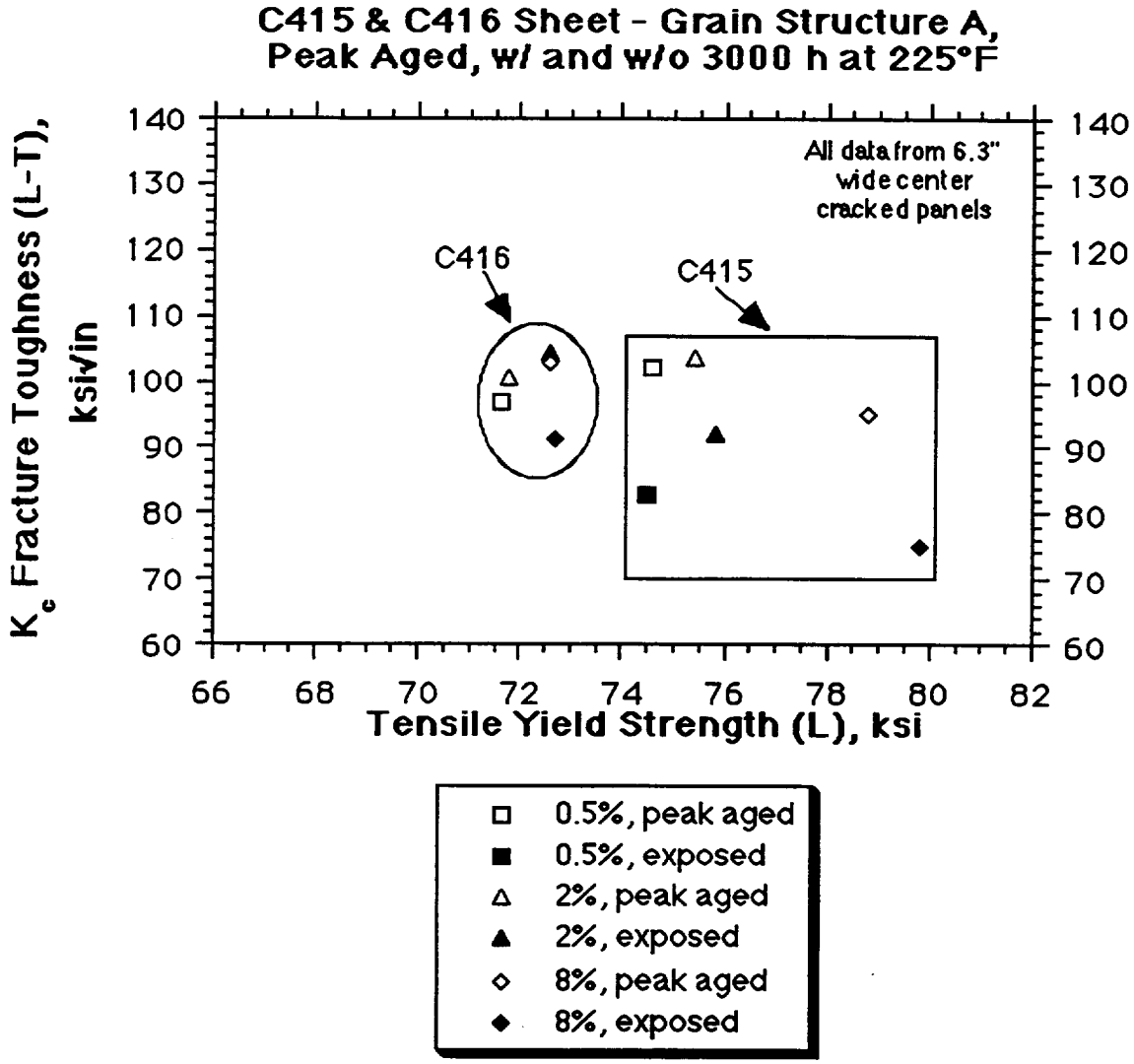

Figure 30 L-T K_c fracture toughness versus L tensile yield strength for C415 and C416 sheet, having Grain Structure A and having been given various levels of stretch prior to peak aging, and having been tested in the peak aged condition and after an exposure of 3000 hr at 225°F. All tensile yield strength and fracture toughness values are averages of duplicate specimens.

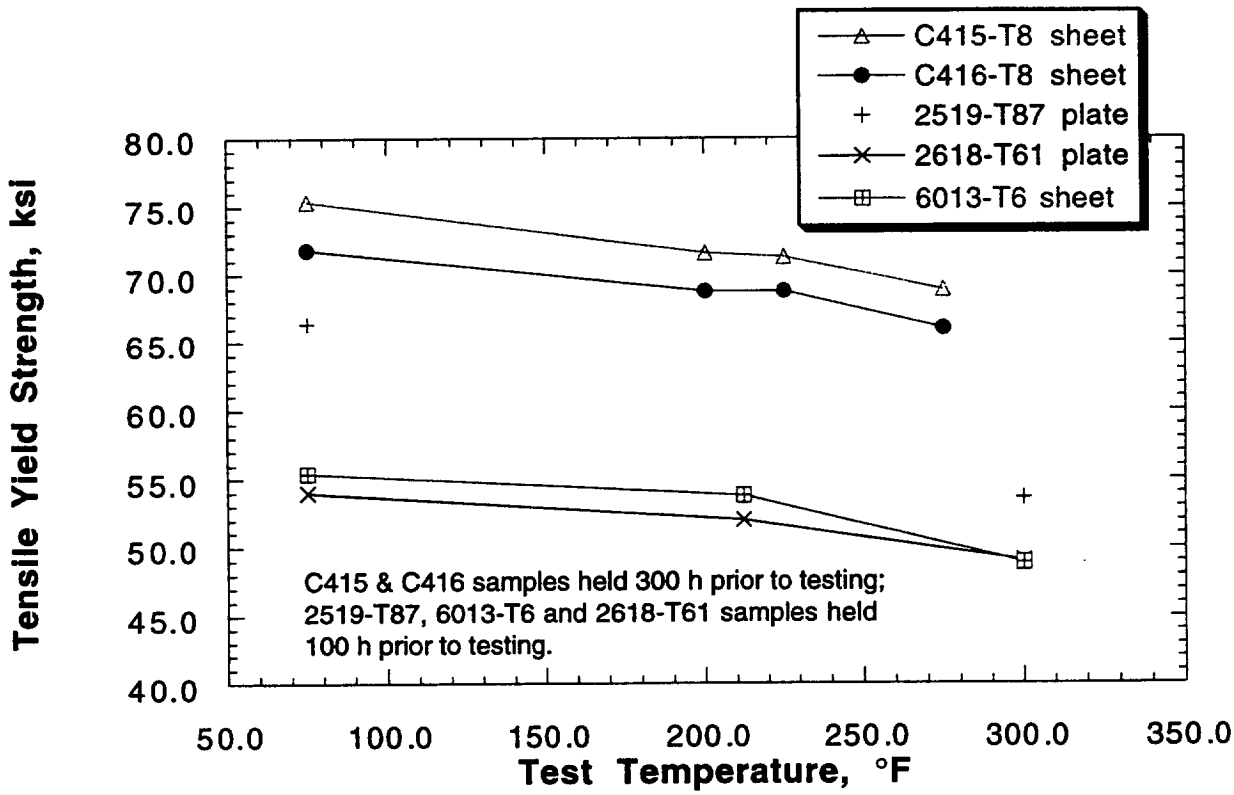

Figure 31 Elevated temperature L tensile yield strength versus test temperature for C415 and C416 sheet, having Grain Structure A and having been stretched 2% prior to artificial aging. The C415 and C416 samples were held 300 hr prior to testing. Included also are data for 2519-T87 plate, 2618-T61 plate and 6013-T6 sheet which had been held 100 hr prior to testing.

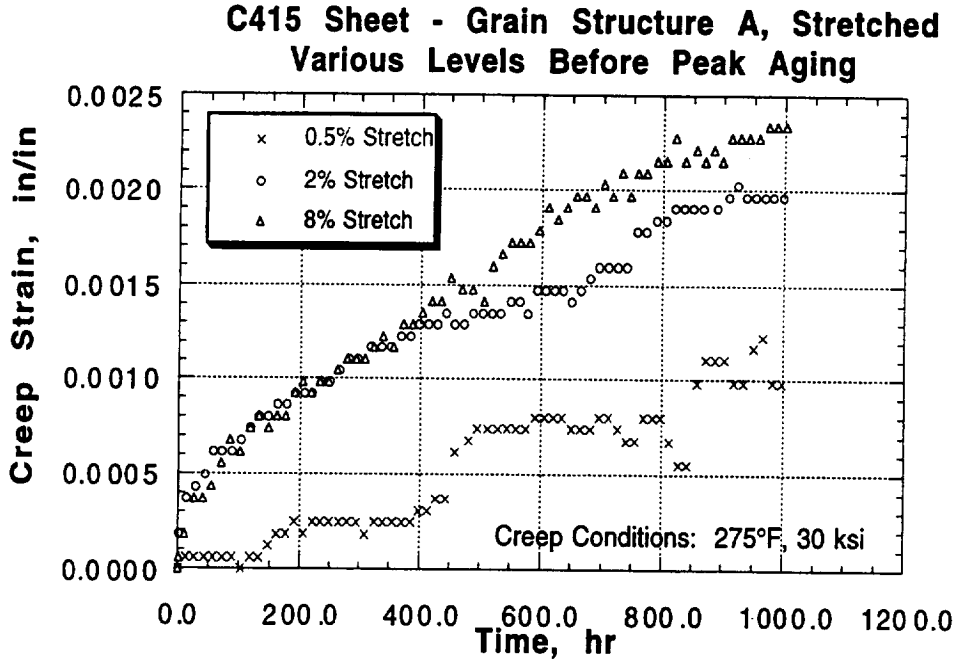

(a)

Figure 32 Creep strain as a function of time for C415 sheet having Grain Structure A, and having been stretched 0.5%, 2% or 8% prior to artificial aging. Creep conditions were:(a) 275°F, 30 ksi and (b) 225°F, 40 ksi.

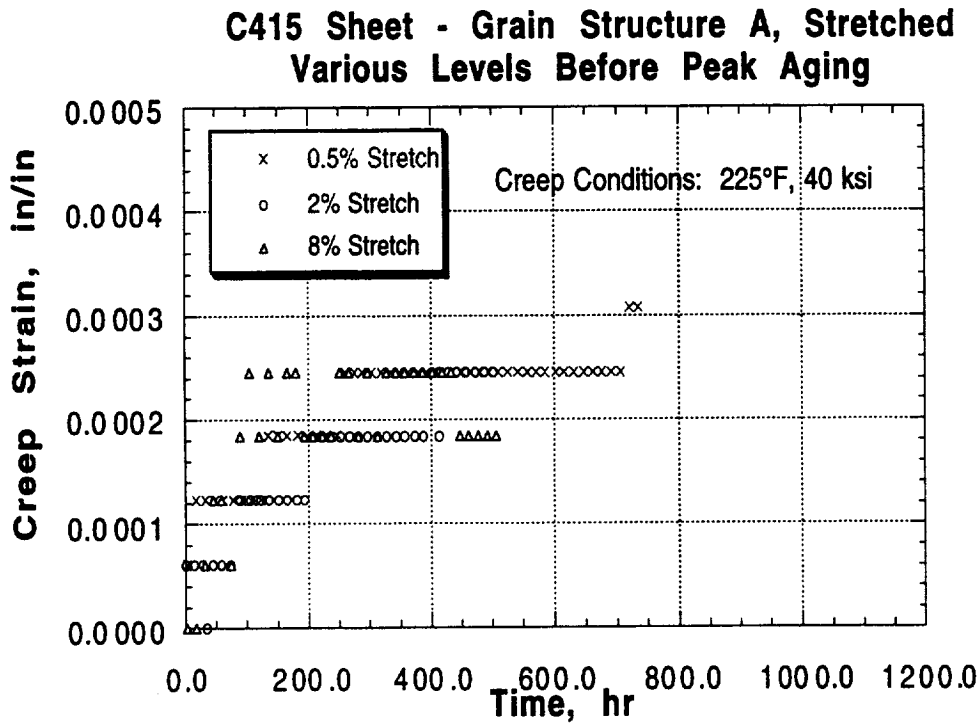

(b)

Figure 32 (Continued)

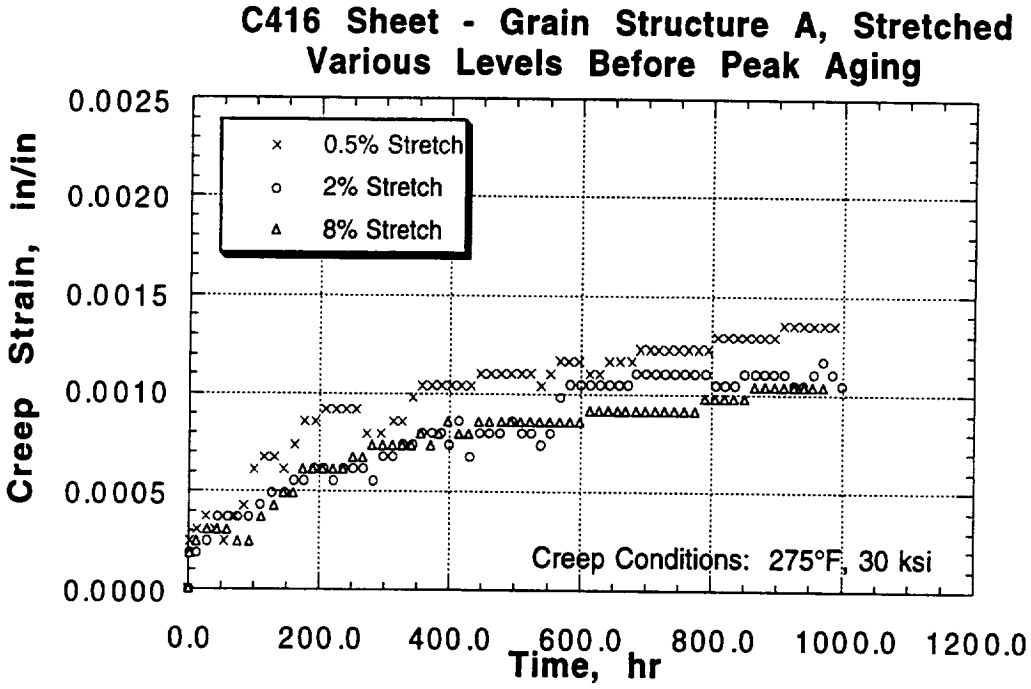

(a)

Figure 33 Creep strain as a function of time for C416 sheet having Grain Structure A, and having been stretched 0.5%, 2% or 8% prior to artificial aging. Creep conditions were: (a) 275°F, 30 ksi and (b) 225°F, 40 ksi.

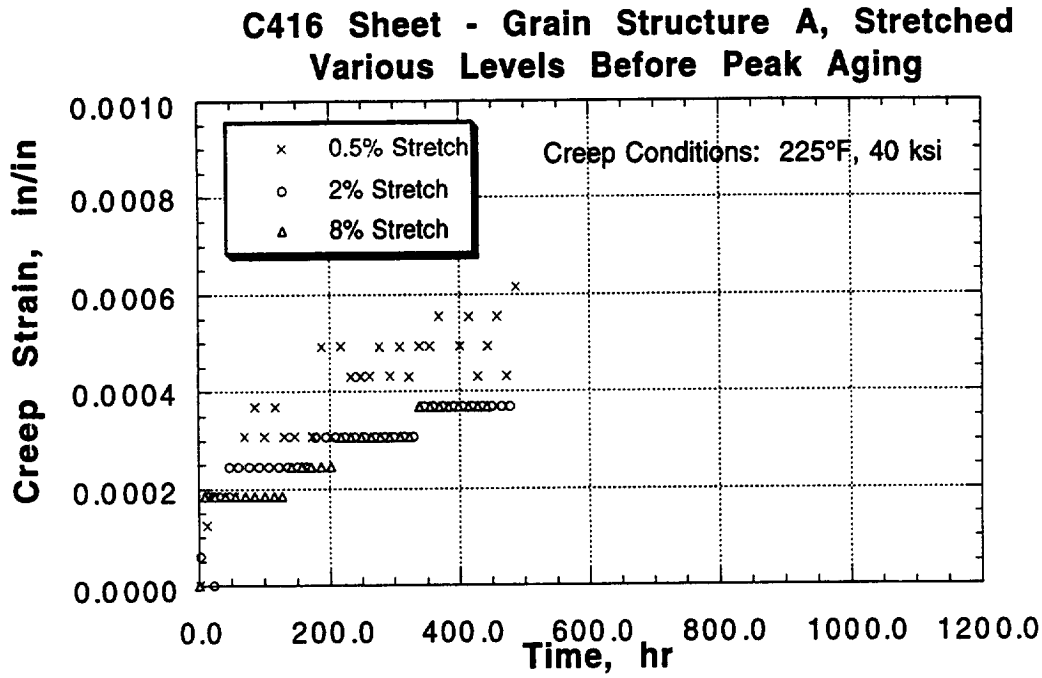

(b)

Figure 33 (Continued)

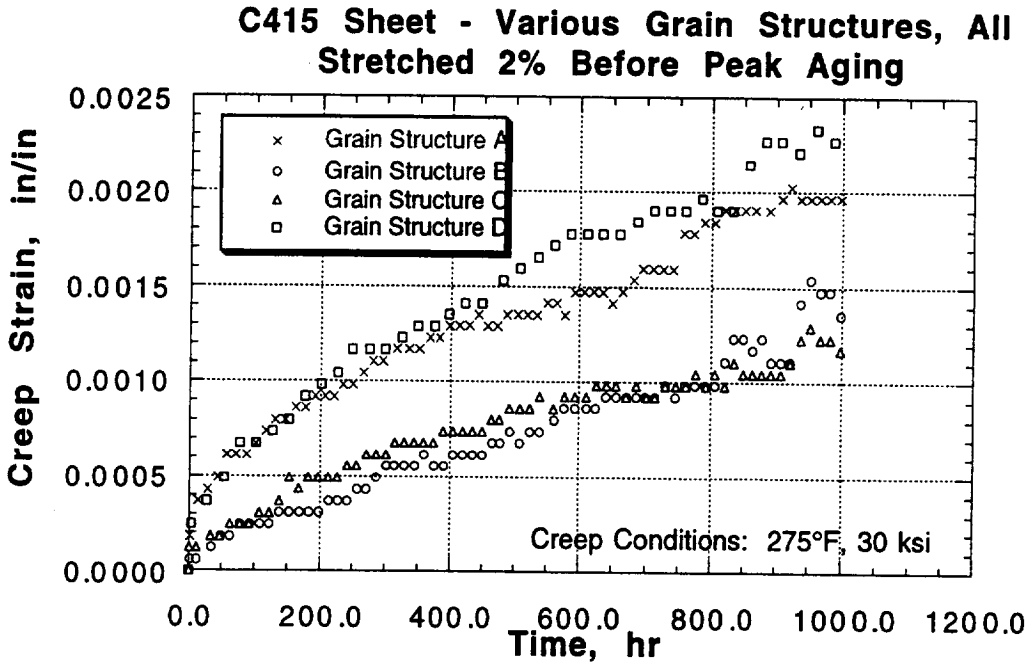

(a)

Figure 34 Creep strain as a function of time for C415 sheet having various grain structures and having been stretched 2% prior to artificial aging. Creep conditions were: (a) 275°F, 30 ksi and (b) 225°F, 40 ksi.

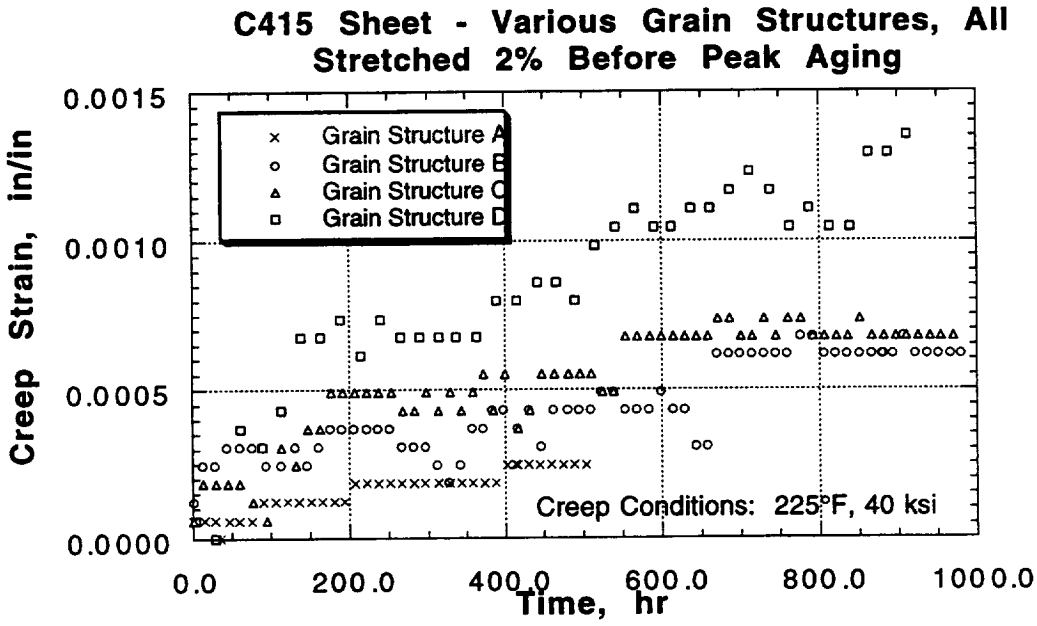

(b)

Figure 34 (Continued)

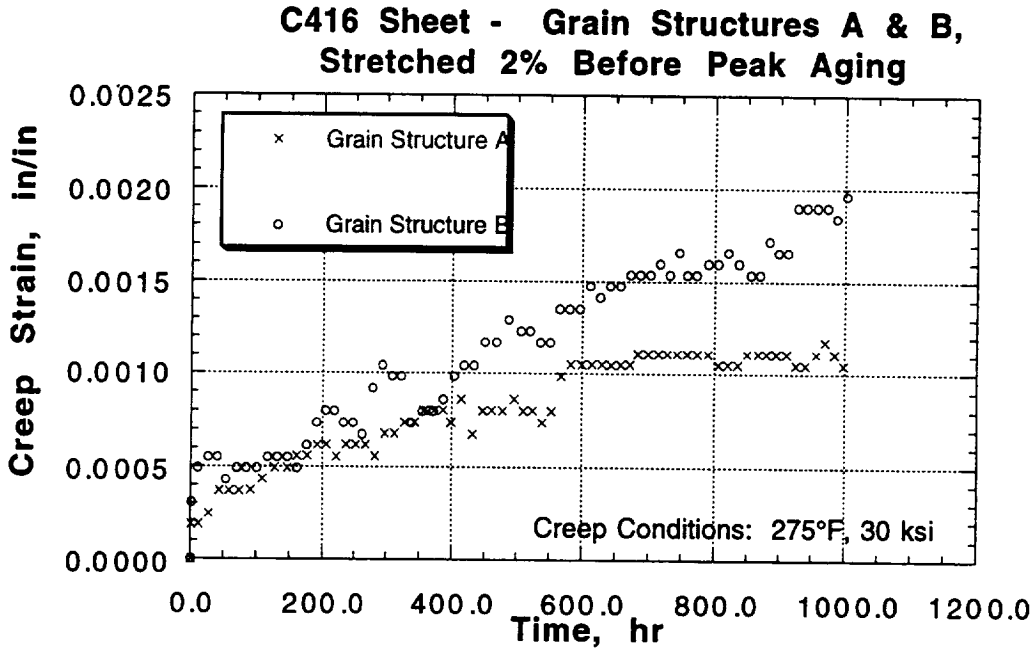

(a)

Figure 35 Creep strain as a function of time for C416 sheet having various grain structures and having been stretched 2% prior to artificial aging. Creep conditions were: (a) 275°F, 30 ksi and (b) 225°F, 40 ksi.

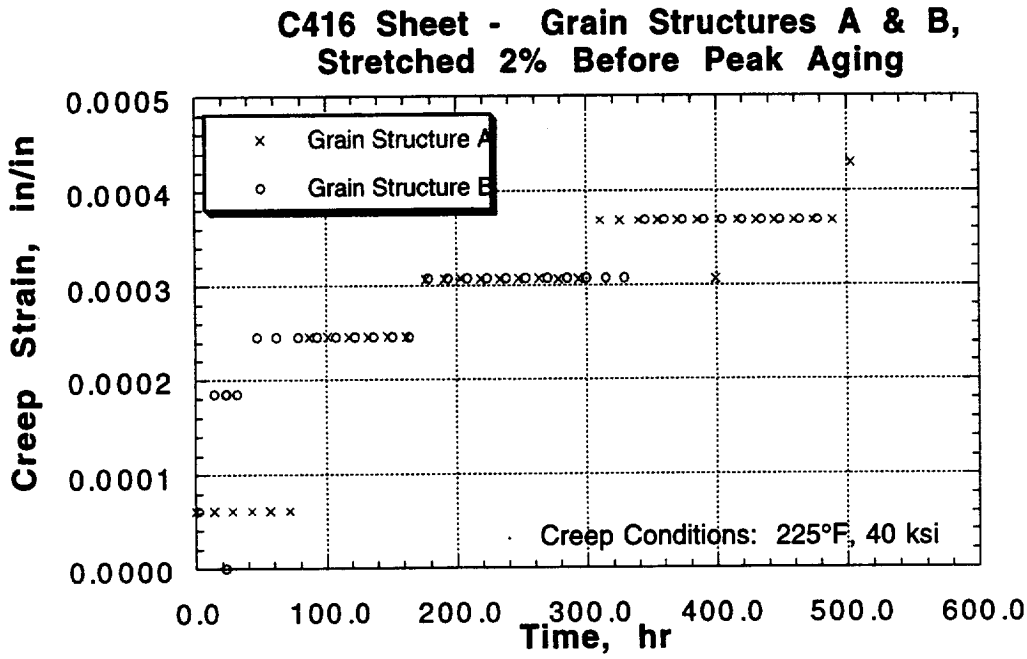

(b)

Figure 35 (Continued)

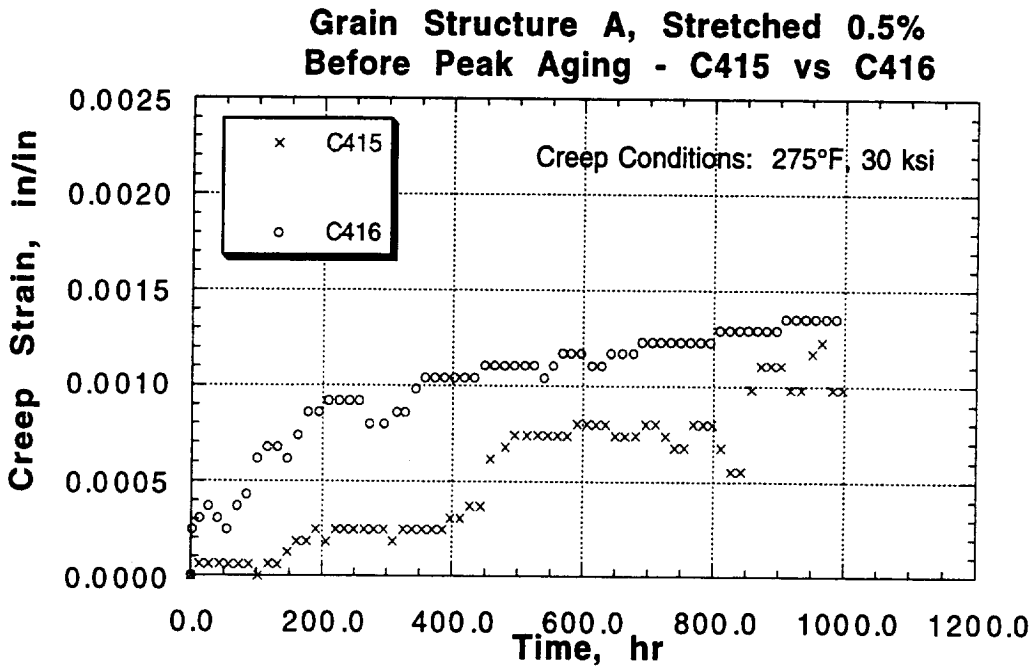

(a)

Figure 36 Creep strain as a function of time for C415 and C416 sheet having Grain Structure A and having been stretched 0.5% prior to artificial aging. Creep conditions were: (a) 275°F, 30 ksi and (b) 225°F, 40 ksi.

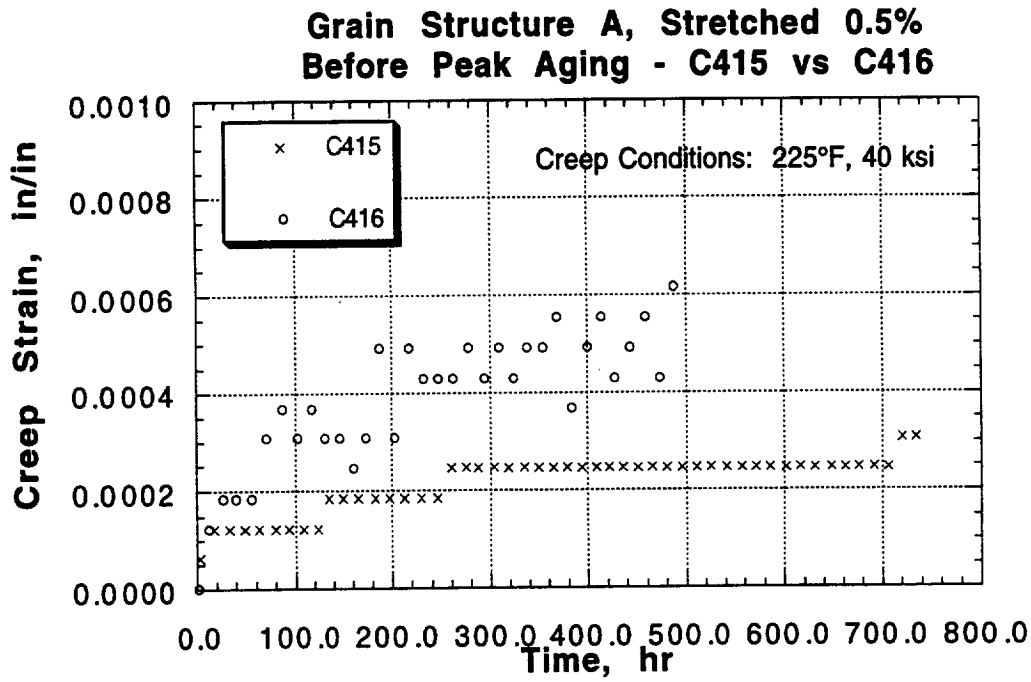

(b)

Figure 36 (Continued)

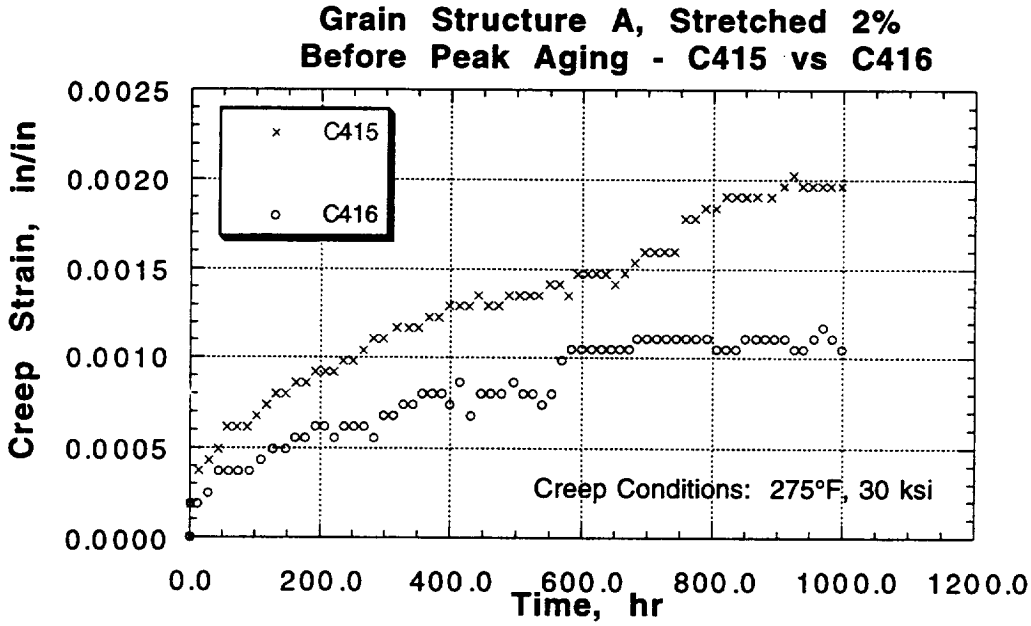

(a)

Figure 37 Creep strain as a function of time for C415 and C416 sheet having Grain Structure A and having been stretched 2% prior to artificial aging. Creep conditions were: (a) 275°F, 30 ksi and (b) 225°F, 40 ksi.

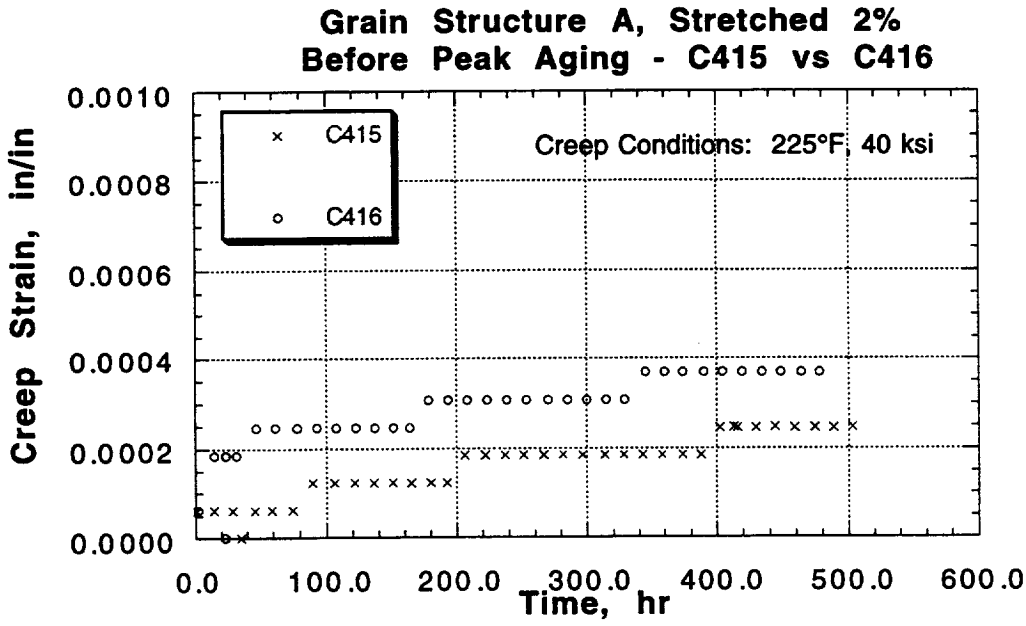

(b)

Figure 37 (Continued)

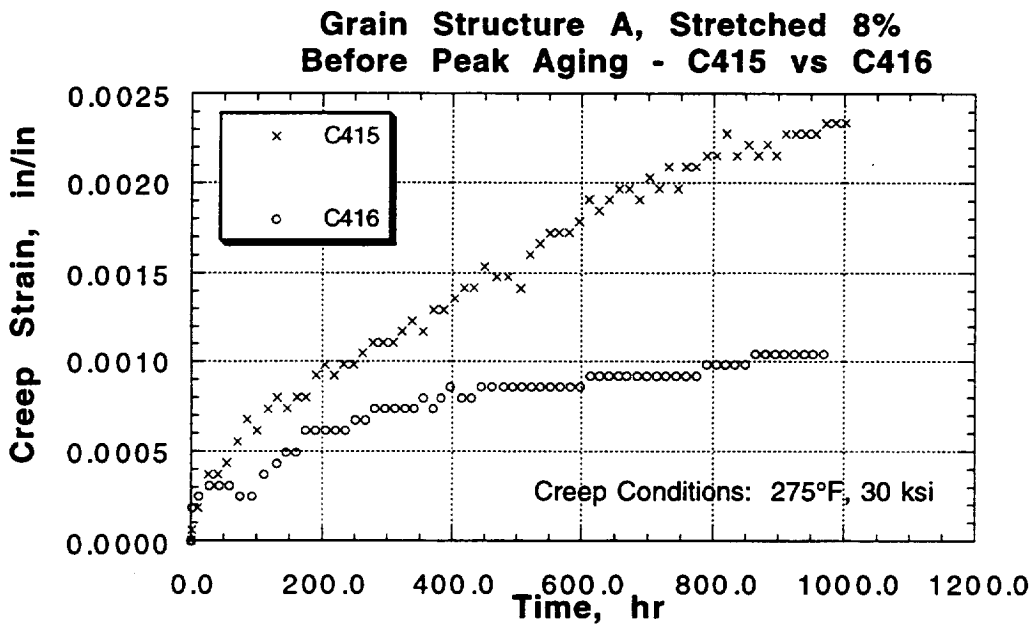

(a)

Figure 38 Creep strain as a function of time for C415 and C416 sheet having Grain Structure A and having been stretched 8% prior to artificial aging. Creep conditions were: (a) 275°F, 30 ksi and (b) 225°F, 40 ksi.

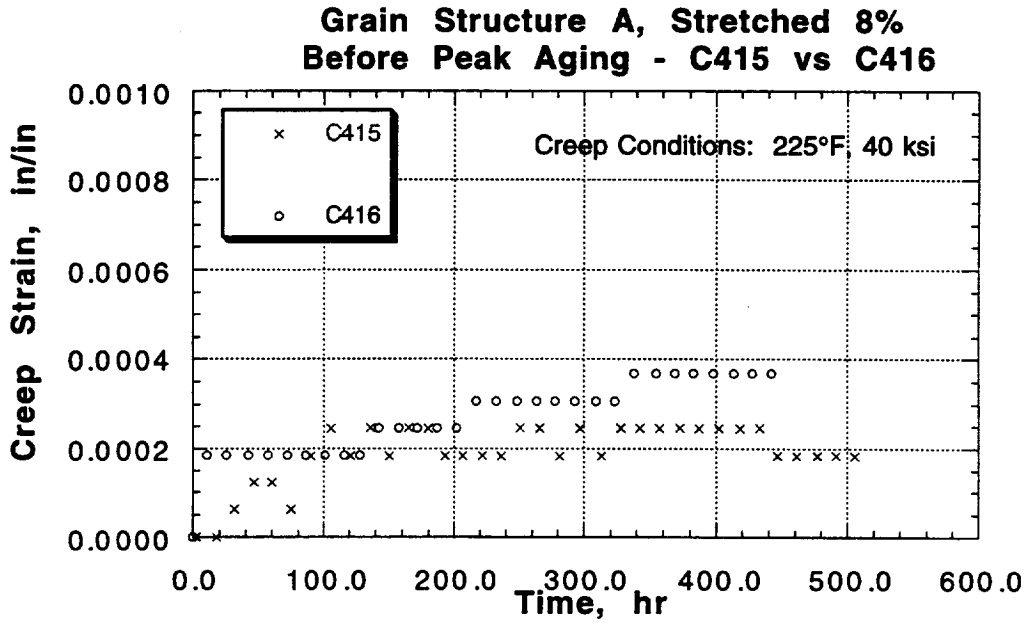

(b)

Figure 38 (Continued)

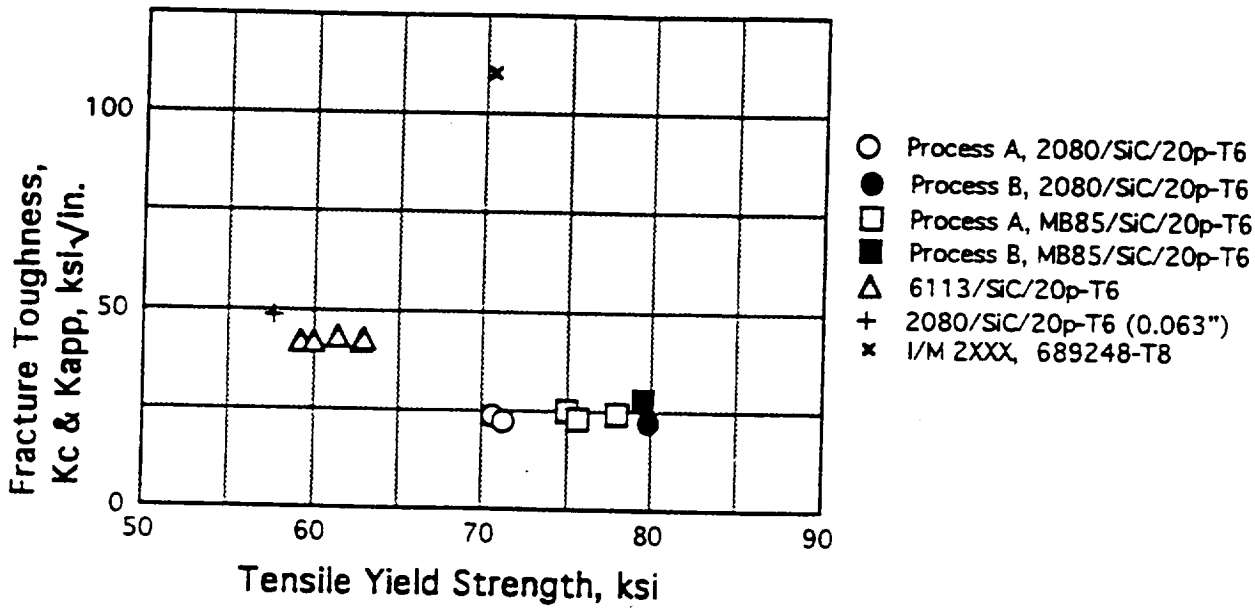

Figure 39 Fracture toughness, K_c and K_{app}, as a function of tensile yield strength for the DMMC sheet. Included for comparison is a datum for an I/M 2XXX alloy: 689248-T8.

ALLIEDSIGNAL, INC.

Processing Based Improvements in the Mechanical Isotropy and Intermediate Temperature Damage Tolerance in Al-Fe-V-Si Alloy 8009

M.S. Zedalis, Ph.D.
Metals Laboratory, Research & Technology

Abstract

Two potential areas of concern identified by aircraft and engine designers when contemplating the use of rapidly solidified, high temperature aluminum (HTA) alloy 8009 were examined in the present study, namely

(i) mechanical anisotropy as a function of product form; and,

(ii) reduced plasticity in the 450-550K temperature range.

To further examine these unique characteristics for HTA 8009, modification to practice and processing parameters were performed to:

(i) improve the metallurgical bonding between prior powder particles by reducing the oxide layer thickness at the particles interface, and,

(ii) improve intermediate temperature embrittlement in plate and sheet products by employing thermomechanical processing (TMP) treatments to reduce the concentration of solute Fe, V and Si in the Al-solid solution matrix.

The primary results of the research found that the oxide layer thickness on planar flow cast HTA 8009 ribbon could be successfully reduced by casting under a dry inert gas shroud. However, these reductions were noted to have little if any effect on the tensile properties of extrusions, plate or sheet samples. Mechanical isotropy in rolled sheet or plate was increased by employing cross-rolling (i.e., rolling normal to the extrusion direction). This behavior was attributed to improved dispersion and fracture of the oxide layer present at the prior particle boundaries.

Irrespective of sheet gauge or rolling direction, increasing the strain rate by a factor of ten typically adds approximately 15-25 MPa (2-3 ksi) to the ultimate tensile strength as well as typically increases the % plastic elongation by as much as 50% in some cases. Strain rate sensitivity values for the plate and sheet samples tested in the present program indicates an "m" value ranging from about 0.015 to 0.030, irrespective of the rolling practice employed (e.g., temperature, direction TMP).

Tensile data for 0.10 cm (0.040") cold rolled sheet which received intermittent annealing treatments (as part of the TMP) indicate little change in comparison to sheet samples which received

cold-rolling only. Tensile strengths for this material were generally lower than measured for the cold rolled sheet over the test temperatures. Values of tensile ductility and its variation with test temperature were very nearly equivalent to levels measured for sheet samples which received only cold rolling.

Cold rolling, with and without intermittent annealing treatments, did result in an overall improvement in the measured tensile ductility over the range of test temperatures in comparison to values measured for hot rolled sheet.

While tensile ductility for all of the HTA 8009 plate and sheet rolled in the present program displays the characteristic ductility "dip" over the temperature range of 422-505K (300-450°F), measured values of % reduction in area drops from about 40-50% at 298K (77°F) to about 25-30% at 422K (300°F) and higher.

Energy dispersive X-ray spectroscopy (EDX), performed to assess the effect of TMP on the solute content present in the Al-solid solution matrix of hot and cold rolled plate and sheet samples, indicate that V and Fe levels measured in the Al-solid solution of cold rolled/annealed 0.10 cm (0.040") gauge sheet are comparable to levels measured in the matrix of extruded and hot rolled 0.64 cm (0.25") plate.

EDX data supports the hypothesis that the true "equilibrium" level of solute Si, V or Fe in rapidly solidified HTA 8009 is in actuality, multiple orders of magnitude greater than the equilibrium solute levels reported in the literature for these elements in Al.

Objective

The objectives of this research are to improve the mechanical isotropy and elevated temperature damage tolerance of high temperature aluminum (HTA) alloy 8009 plate and sheet by modifying the current processing parameters and practice. Specifically, these objectives will be accomplished by:

(i) improving the metallurgical bonding between prior powder particles by reducing the oxide layer thickness at the particle interfaces; and,

(ii) reducing the concentration of solute Fe, V and Si in the Al matrix as well as modifying the alloy's grain/sub-grain structure by thermo-mechanical processing. I n practice, the oxide layer present at the prior powder particle boundaries will be reduced by casting and comminuting the planar flow cast 8009 ribbon in a protective atmosphere. Moreover, supersaturated solute atoms as well as grain/sub-grain structure in 8009 plate and sheet will be affected by employing a thermo-mechanical process which involves modifications to current hot / cold rolling practices. Each of these process modifications will be performed on commercial scale

quantities of material, and hence, may be directly implemented into current manufacturing specifications.

Introduction

Commercially available high temperature Al-Fe-V-Si (HTA) alloy 8009 has emerged as a leading candidate Al-base material for aerospace applications with service temperatures approaching 600K. [1-4] HTA 8009 (formerly designated FVS0812) is processed utilizing rapid solidification / powder metallurgy technologies and combines the room temperature strength, ductility and fracture toughness of conventional 2000 and 7000 series aerospace aluminum alloys with greatly improved elevated temperature strength and stability. HTA 8009 derives its excellent mechanical and physical properties from a uniform dispersion of $Al_{13}(Fe,V)_3Si$ particles dispersed in an aluminum solid solution matrix. The silicide dispersoids typically range from 50-80 nm in diameter after consolidation (e.g., extrusion, forging, and rolling) and are extremely resistant to particle coarsening at elevated temperatures. As a result, no measurable material degradation occurs even after exposure for 1000 hours to temperatures approaching 725K. [5,6] HTA 8009 also exhibits approximately a 25% increase in Young's modulus over conventional Al-base alloy and on a specific stiffness basis, is superior to Ti-6Al-4V and 17-4 PH steel to temperatures approaching 750K. [7] This combination of properties make HTA 8009 extremely attractive for applications which have been previously restricted to heavier titanium or steel alloys, and superior to polymer composites at elevated temperatures. HTA 8009 is presently being evaluated for wing skins, aircraft landing wheels, missile bodies and fins as well as a variety of gas turbine engine components which operate at slight elevated temperatures.

While the benefits of using HTA 8009 over titanium and steel alloys for certain applications are clearly recognized, extensive mechanical characterization of the alloy has identified two (2) potential areas of concern to high speed aircraft and engine designers:

i) mechanical anisotropy as a function of product form; and,

ii) reduced plasticity in the 450-550K temperature range.

Anisotropy in the mechanical behavior of HTA 8009 is most apparent in variation in toughness and ductility for samples tested in directions orthogonal to the rolling/extrusion directions. Porr et al. [8] have recently shown for HTA 8009 flat bar extrusions that values of plane strain fracture toughness, K_{IC}, could vary from as high as about 36.6 $MPa\sqrt{m}$ for samples tested in the L-T orientation to as low as about 16.1 $MPa\sqrt{m}$ for samples tested in the T-L orientation. Fractography performed by Chan [9,10] and later confirmed by Porr et al. [8], indicates that the variation in toughness is related to the extent of delamination occurring along oxide decorated prior

particle boundaries. Based on these observations, Chan [9] concluded that K_{IC} values measured for samples tested in the L-T orientation are enhanced as a result of a loss in through-thickness constraint associated with delamination. The mechanism of "thin sheet toughening" is viewed as contributing substantially to L-T toughness, while leading to lower toughness in orthogonal orientations.

Reduced plasticity in the 450-550K temperature range in HTA 8009, on the other hand, has been attributed to the phenomenon of dynamic strain aging (DSA) occurring in the alloy. [11] DSA is not uncommon to conventional aluminum alloys, but typically occurs below ambient temperatures due to the higher diffusivity of the more traditional alloying constituents, (e.g., Cu, Mg, Si). For HTA 8009, Skinner et al. [11] has observed that DSA occurs at intermediate temperatures due to the more sluggish diffusivity of Fe and V present in the matrix. Solute levels of these two (2) elements in the Al-base matrix have been measured to be greatly in excess of equilibrium levels, and at present, do not appear to be affected by hot working or static thermal exposure. While DSA is known to reduce ductility and toughness in HTA 8009 [6,11], the effect becomes significantly more serious when it is combined with the mechanical anisotropy of the material. for example Porr et al [8] measured that K_{IC} values for samples tested in the L-T orientation decreased to a minimum of about 15 MPa$\sqrt{m}$ over this intermediate temperature range compared to a minimum of about 9.5 MPa$\sqrt{m}$ for samples tested at similar temperatures in the T-L orientation.

Results

Tensile Testing of HTA 8009 Extrusions

Tensile testing of HTA 8009 rolling preforms extruded at Spectrulite Consortium Inc. in Madison, IL was performed to assess the effect of extrusion conditions (e.g., temperature, lubrication, speed. etc.) on mechanical properties. Tensile testing was performed at 25°C (77°F) and 232°C (450°F) on specimens machined from both the nose and tail of HTA extrusions 92A022 and 92A024. Specimens were machined from various locations in the cross-section of the extrusion, Fig. 1. and were oriented in both the longitudinal and transverse directions (i.e., with respect to the extrusion direction).

Tensile testing was performed at AlliedSignal using an Instron 1125 testing machine. Testing was performed using a modified ASTM E21 procedure. Here, tests were initially run at a strain rate corresponding to 0.5% /min as per specification. At this strain rate, tensile yield and an ultimate tensile strength were measured. After the ultimate tensile strength of the sampled was achieved, the imposed strain rate was then increased ten-fold to a rate of 5% /min, Fig. 2. This testing practice in effect provided tensile data for HTA 8009 at two (2) strain rates on a single

sample. Measured total plastic elongation therefore represents the sum of plasticities exhibited for a combination of strain rates.

Tensile data as a function of location and test temperature for specimens machined from the nose and tail of extrusions 92A022 and 92A024 are summarized in Table 1. (Table numbers followed by the leter "a" are in SI units, while Table numbers followed by the letter "b" are in traditional British units.) Variation as a function of position and test temperature are graphically presented in Figs. 3 & 4. In general, there is very little difference in tensile strengths between the two (2) extrusions and variations as a function of sample position (with respect to the cross-section of the extrusion) were comparable. Based on this data, a number of observations and hypotheses may be made:

(i) increasing the strain rate ten-fold from 0.5%/min to 5.0%/min on average increases the tensile strength by approximately 14-21 MPa (2-3 ksi) for tests conducted at 298K (77°F) and 505K (450°F).

(ii) tensile strength, irrespective of strain rate, increases by approximately 14-21 MPA (2-3 ksi) for specimens machined from the mid-planes of the extrusion in comparison to specimens machined from the outer perimeter. This behavior may be attributed to the fact that the outer surface of the preform tends to be much hotter than the bulk due to frictional heating during extrusion. Higher surface temperature promotes a slightly coarser microstructure, and therefore, lower strength. This tendency is present for specimens machined from the nose as well as the tail of the extrusions.

(iii) tensile ductility decreases in the mid-plane of the extrusion and overall is less for specimens oriented transverse to the extrusion direction irrespective of position in the extrusion. Ductility in these extrusions is largely dependent on the interparticle bonding of the HTA powder particles and variations in ductility reflect the extent of shear the particles experience during extrusion (i.e., particles located near the surface of the preform, extruded through a shear-faced die, exhibit greater amounts of shear than particles located at mid-plane in the preform).

(iv) tensile ductility, on average, is comparable for specimens machined from extrusions 92A022 and 92A024. While shrouding of the melt puddle during planar flow casting resulted in a reduction in total oxide content (i.e., related to hydrate layer thickness present on the powder particle surfaces), improved bonding of powder particles apparently was not substantially affected.

Tensile Testing of HTA 8009 Plate and Sheet

Tensile testing of HTA 8009 plate and sheet rolled at Kaiser Aluminum's Center for Technology (CFT) in Pleasanton, CA was conducted to assess the effect of rolling schedule and parameters on mechanical properties. The rolling campaign was designed to evaluate the major objectives of the program, namely:

(i) to evaluate the effects of rolling direction and total reduction in gauge on mechanical isotropy in HTA 8009 plate and sheet; and,

ii) to evaluate the application of thermo-mechanical processing to improve elevated temperature ductility and toughness by modifying the grain / sub-grain structure i n HTA 8009 sheet as well as by reducing the solute content in the Al matrix.

The specific rolling schedules designed to meet the aforementioned objectives are illustrated in Fig. 5. To evaluate the effects of rolling direction and total reduction in gauge on mechanical isotropy in HTA 8009 plate and sheet, one-half of the preforms from each casting modification received only cross-rolling (i.e., rolled normal to the extrusion direction), while the balance received only straight-rolling (i.e., rolled parallel to the extrusion direction). An identical pass schedule (i.e., reduction per pass and the number of passes per rolling heat) was practiced for all lots of material. Plate and sheet having respective gauges of 0.64 cm (0.25"), 0.22 cm (0.090") and 0.10 cm (0.040") were produced during this phase of the program.

To evaluate the application of thermo-mechanical processing (TMP) to improve elevated temperature ductility and toughness, HTA 8009 sheet was initially hot rolled to approximately 0.22 cm (0.090") gauge. Three (3) different rolling practices were then employed to fabricate 0.10 cm (0.040") gauge sheet. The first rolling practice involved only hot rolling to the final gauge. Here the sheet was soaked at approximately 673K (750°F) prior to being rolled to gauge. Sheet temperature was monitored during rolling to verify that the sheet temperature never fell below about 500K (450°F).

The second rolling practice involved only cold rolling from 0.22 cm (0.090") to a final gauge of about 0.10 cm (0.040" gauge). Here the sheet was allowed to cool to approximately 298K (77°F) prior to being cold rolled to its final gauge. Some work induced adiabatic heating of the sheet during cold rolling; however, the sheet temperature never exceeded about 340K (150°F).

The third rolling practice also involved only cold rolling [298K (77°F)] to the final gauge; however, here the sheet was subjected to an annealing treatment of approximately 673K (750°F) for 0.5 hrs., after every 30% reduction in gauge. The premise behind this TMP was to further

reduce the concentration of Fe, V and Si in the HTA 8009 matrix via heterogeneous nucleation of dispersoids as well as through the "sweeping" action of glissile dislocations.

In total, approximately 150 kg of sheet were rolled at Kaiser Aluminum - CFT for the program, Tables 2 & 3. Prior to being shipped back to AlliedSignal, all of the sheet was trimmed to remove minor edge cracks and sectioned into approximately 250 cm (100") lengths. Approximately two-thirds of the HTA 8009 plate and sheet were supplied to the University of Virginia for testing.

Tensile data for the plate and sheet samples identified in Tables 2 & 3 are summarized in the following sections for HTA sheet rolled from extrusions 92A022 and 92A024. Tensile testing was performed on an Instron 1125 testing machine at temperatures of 298, 422, 505 & 589K (77, 300, 450 & 600°F). Testing was also performed on selected samples after exposure for 100 hrs. to 644K (700°F). Testing at all temperatures was performed using a modified ASTM E21 procedure. Here, tests were initially performed at a strain rate corresponding to 0.5% /min as per specification. At this strain rate, a 0.2% tensile yield and an ultimate tensile strength were measured. After an ultimate tensile strength was achieved, the imposed strain rate was then increased ten-fold to a rate of 5% /min, Fig. 2, and the test was run until failure. This testing practice, in effect, provided tensile strength data for HTA 8009 at two (2) strain rates using a single sample. Measured total plastic elongation, therefore represents the sum of ductilities for a combination of strain rates. To further assess the strain rate sensitivity of HTA 8009 plate and sheet, samples were also tensile tested at a single strain rate of 50% /min. Here, 0.2% yield strength, ultimate tensile strength and total plastic elongation were measured for a single strain rate.

Tensile data for plate and sheet samples rolled from extrusions 92A022 and 92A024 are summarized in Tables 4-6 a&b and Tables 7-12 a&b, respectively. (Tables numbers followed by the letter "a" are in SI units, while Table numbers followed by the letter "b" are in traditional British units.)

Effect of Rolling Direction & Reduction in Gauge on Mechanical Isotropy

To evaluate the effect of rolling direction and reduction in gauge on mechanical isotropy in HTA 8009 plate and sheet, one-half of the preforms from each casting modification received only cross-rolling (i.e., rolled normal to the extrusion direction), while the balance received only straight-rolling (i.e., rolled parallel to the extrusion direction). An identical pass schedule (i.e., reduction per pass and number of passes per rolling heat) was practiced for all lots of material. Tensile testing was performed on plate and sheet have respective gauges of approximately 0.64 cm (0.25"), 0.22 cm (0.090") and 0.10 cm (0.040").

Mechanical anisotropy in HTA 8009 plate and sheet is most clearly reflected in values for total plastic elongation measured during tensile testing. Tensile strength is observed to be fairly similar for samples oriented longitudinally or transverse to the preform rolling direction at all of the strain rates evaluated. As may be seen in Figs. 6-20 and Figs. 21-35 for plate and sheet rolled from extrusions 92A022 and 92A024, respectively, cross-rolled 0.64 cm (0.25") gauge plate exhibits mechanical isotropy within the scatter band for the material tested. Total plastic elongation measured over all temperatures is basically equivalent at this gauge and remains equivalent for sheet cross-rolled to thinner gauges. Straight-rolled sheet, on the other hand, indicates similar isotropy only for the sheet rolled to approximately 0.10 cm (0.040").

This response clearly indicates that rolling direction has a greater impact on improving mechanical isotropy in HTA 8009 plate and sheet than does the total reduction in gauge achieved during rolling. From a microstructural point of view, this response may be attributed to the fact that cross-rolling more effectively breaks-up and disperses the oxide / hydrate layer present at the prior particle boundaries than straight-rolling alone. While comparable levels of shear are achieved in sheet that has been cross- and straight- rolled to a similar gauge, the oxide / hydrate layer in straight-rolled sheet remains in contiguous bands oriented to the extrusion and rolling directions. As a result, tensile specimens oriented transverse to the rolling direction fail at lower plastic strains along the original prior particle boundaries.

The reduction in the oxide / hydrate layer thickness for plate and sheet rolled from extrusion 92A024, comprised of planar flow cast ribbon which was shrouded in a dry inert gas environment during casting, in comparison to plate and sheet rolled from conventionally processed extrusion 92A022 did not result in any measurable improvement in transverse tensile ductility. While shrouding the melt puddle and the down-stream planar flow cast ribbon with a dry inert gas did reduce the hydrate layer thickness from approximately 3.25 nm to 2.9 nm and the total oxygen content from 0.087% to 0.079%, a consistent improvement in transverse tensile ductility was not observed for the plate and sheet samples examined in the study.

Effect(s) of Thermomechanical Processing

Hot rolled 0.22 cm (0.090") gauge HTA 8009 sheet from both lots of material (i.e., 92A022 and 92A024) was rolled to a final gauge of approximately 0.10 cm (0.040") following three (3) different rolling practices to evaluate the effect of thermomechanical processing (TMP) on ambient and elevated temperature tensile properties. The first rolling practice involved only hot (cross- and straight-) rolling to the final gauge. A second rolling practice involved only cold

(cross- and straight-) rolling to the final gauge. And the third rolling practice involved cold (cross- and straight-) rolling to gauge; wherein, an intermittent annealing treatment of 673K (750°F) for approximately 0.5 hrs. was performed after every 30% reduction in total gauge. Here, the hope was to reduce the Fe, V & Si solute content in the (rapidly solidified) matrix by inducing heterogenous nucleation of dispersoids and/or through the scavenging of solute atoms by glissile dislocations.

Tensile data for sheet rolled following these three (3) schedules from extrusions 92A022 and 92A024 clearly indicate a sizable variation in properties. Hot cross- and straight- rolled sheet exhibits the highest tensile strengths over the range of test temperatures for any of the plate and sheet rolled in the present program. Room temperature tensile strength is typically in the 430-450 MPa (63-65 ksi) range for tests run at a strain rate of 0.5% /min. Overall, this material also exhibits the lowest levels of ductility for all TMP batches over the range of test temperatures. Tensile ductility is observed to decrease from approximately 7-10% at room temperature to approximately 2.1-2.7% at a test temperature of 422K (300°F). As the test temperature is increased, tensile ductility is observed to increase to as high as 26%.

Cold rolled 0.10 cm (0.040") gauge HTA 8009 sheet exhibits a sizable increase in tensile ductility in comparison to the hot rolled sheet, with only a small decrease in tensile strength. Tensile strengths (at 0.5% /min strain rate) for cold rolled sheet range from about 400-425 MPa (58.5-61.6 ksi) at 298K (77°F) and a very attractive level of about 150-193 MPa (22.4-28.0 ksi) at 589K (600°F). Tensile ductility for this material is also observed to exhibit a drop in ductility at intermediate test temperatures. Here, ductility values of about 15-19% at room temperature decrease to levels of only about 6-9% at 422K (300°F). As the test temperature is further increased, tensile ductility in this sample is observed to increase to values often in excess of 25%.

Tensile data for 0.10 cm (0.040") sheet cold rolled which received intermediate annealing treatments indicate a response fairly comparable to the sheet samples which received cold-rolling only. Tensile strengths for this material were generally approximately 20-30 MPa (3-4 ksi) lower than measured for the cold rolled sheet over the test temperatures. Values of tensile ductility and its variation with test temperature was very nearly equivalent to levels measured for sheet samples which received only cold rolling.

While these data clearly indicate that TMP had an effect on the tensile properties of 0.10 cm (0.040") gauge HTA 8009 sheet, the TMP's practiced did not substantially improve the intermediate temperature plasticity (e.g., ductility) as originally hoped and intended. Cold rolling, with and without intermittent annealing treatments did, however, result in an overall improvement in the measured tensile ductility over the range of test temperatures in comparison to values

measured for hot rolled sheet. Further discussion on the effects of TMP on the microstructure of HTA 8009 sheet is presented in the subsequent section on Transmission Electron Microscopy.

% Reduction in Area as a Function of Test Temperature for HTA 8009 Plate and Sheet

Values of % reduction in cross-sectional area as a function of test temperature for plate and sheet samples cross-rolled from extrusions 92A022 and 92A024 are summarized in Tables 4-6 & 7-9 and shown graphically in Figs. 36-37 and 38-39, respectively. While tensile ductility for all of the HTA 8009 plate and sheet rolled in the present program displays the characteristic ductility "dip" over the temperature range of 422-505K (300-450°F), measured values of % reduction in cross-sectional area are found to primarily decrease with increasing test temperature. This response is similar to toughness data measured by S.S. Kim and R.P. Gangloff at the UVa for sheet having similar pedigree provided for testing in their phase of the present program. Irrespective of rolling temperature or TMP practice, % reduction in area drops from about 40-50% at 298K (77°F) to about 25-30% at 422K (300°F) and higher.

Effect of Strain Rate on Ambient Temperature Tensile Strength & Ductility

The effect of strain rate on HTA 8009 has been examined by D.J. Skinner et al. [19], but only for extrusions or hot rolled sheet. In the present program, the effect of strain rate on ambient temperature tensile strength and ductility was evaluated over two (2) decades of imposed strain rates for all variants of 92A024 cross- and straight- rolled plate and sheet, Figs. 40-44. Irrespective of sheet gauge or rolling direction, increasing the strain rate by a factor of ten (10) typically adds approximately 15-25 MPa (2-3 ksi) to the ultimate tensile strength as well as typically increases the % plastic elongation by as much as 50% in some cases, Tables 10-12. Strain rate sensitivity values for the plate and sheet samples tested in the present program indicates an "m" value ranging from about 0.015 to 0.030, irrespective of the rolling practice employed, (e.g., temperature, direction, TMP). Here, "m" may be calculated using the following equation:

$$m = [\ln (\sigma_2/\sigma_1)] / [\ln (\varepsilon_2/\varepsilon_1)],$$

where σ_1 is the original stress level and σ_2 is the new stress value obtained after increasing the strain rate from ε_1 to ε_2. The values for "m" measured in the present study overlap the ambient temperature "m" value of approximately 0.025 previously measured by Skinner et. al. [19].

It has been suggested that the high strain rate sensitivity measured for HTA 8009 reflects the strong interplay between glissile dislocations and solute atoms in the Al-solid solution matrix. At intermediate temperatures, 422-505K (300-450°F), the strain rate sensitivity for HTA 8009,

likes its ductility, has been shown to exhibit a minimum (i.e., nearly equal to zero).[19] This drop in both ductility and the strain rate sensitivity has been attributed to a dynamic strain aging phenomenon in HTA 8009, wherein the movement of dislocations through the matrix is strongly impeded by solute atoms (e.g., Fe, V, Si). Attempts to improve the intermediate temperature ductility in HTA 8009 in the present program by employing various TMP practices to further reduce the amount of solute present in the Al-solid solution, was unsuccessful. This response indicates that more exotic TMP processes might be necessary to improve the intermediate temperature ductility, or alternatively, that the level of solute present in the Al-solid solution matrix represents a near "equilibrium" concentration for rapidly solidified Al-Fe-base alloys.

Effect of Exposure on Ambient Temperature Tensile Properties

The family of high temperature Al-Fe-V-Si alloys is recognized as the most thermally stable of all Al-Fe -base alloys. HTA 8009 has been found to resist degradation of tensile properties even after exposure for 1000 hrs. at 723K (842°F). [20] In the present program, a somewhat modest exposure for 100 hrs. at 644K (700°F) was applied to assess any effects of TMP practice on the thermal stability of HTA 8009. Tensile data for plate and sheet rolled in the present study after 100 hrs. / 644K exposure are summarized in Tables 4-9.

Irrespective of extrusion number or rolling direction, 100 hrs. exposure at 644K (700°F) was found to have no effect on the tensile properties of hot rolled 0.64 cm (0.25") or 0.25 cm (0.090") gauge plate and sheet, Tables 4 & 7. In fact, a slight increase in tensile strength is observed after exposure for these samples. Hot rolled 0.10 cm (0.040") gauge sheet after 100 hrs. / 644K (700°F) exposure also indicates no apparent degradation in tensile strength; however, a slight decrease (10-30%) in total plastic elongation was noted for many of the samples.

Cold rolled 0.10 cm (0.040") gauge sheet, which did not receive intermittent annealing treatments, indicates the largest response to 100 hrs. / 644K (700°F) exposure, Tables 5 & 8. Measured values of tensile yield and ultimate strength are observed to increase by as much as 70 MPa (approximately 10 ksi) after exposure. More significant, however, is the very sizable decrease in total plastic elongation measured for this material after exposure. Ductility levels as high as approximately 18% measured for as-rolled samples were observed to decrease to levels in the 3.0 - 6.6% range.

The response of exposed, cold rolled 0.10 cm (0.040") gauge sheet, which did receive intermittent annealing treatments, is fairly similar to the aforementioned cold rolled variant, Tables 6 & 9. Tensile strength after 100 hrs. / 644K (700°F) exposure was observed to increase by as much as approximately 90 MPa (13 ksi); however, the decrease in ductility for sheet rolled from

extrusion 92A022 does not appear to be as severely affected after exposure. For this material, total plastic elongation decreases from about 16-17.5% to about 4.8-8.8% after exposure. Sheet rolled from extrusion 92A024, on the other hand, does exhibit a severe decrease in ductility after exposure to values ranging from 2-3%. Possible reasons for the larger decrease in the total plastic elongation for this particular extrusion is discussed in a subsequent section detailing the results of microstructural analyses.

Microstructural Analyses of HTA 8009 Extrusion, Plate & Sheet Samples

Transmission electron microscopy (TEM) was performed on all variants of HTA 8009 extrusion, plate and sheet samples. TEM was performed using a Philips EM400T electron microscope equipped with STEM and EDS capabilities. TEM foils were mechanically thinned and electropolished in a 20% HNO_3 - 80% CH_3OH solution at 223K. As anticipated, the microstructure of the as-extruded rolling preform 92A022 is comprised of very fine, 50-80 nm $Al_{13}(Fe,V)_3Si$ dispersoids present in an Al-solid solution matrix, Fig. 45. Grain (or sub-grain) size for this material was measured to be about 0.5μm.

Extrusion 92A024 indicates a fairly comparable microstructure to that of extrusion 92A022; however, large regions of carbon (i.e., graphite) contamination were observed to be scattered throughout the material, Fig. 46. The possibility of carbon contamination in this material had been identified early in the program by X-ray photoelectron spectroscopy (XPS) performed on planar flow cast ribbon manufactured specifically for this batch of material (i.e., Process Modification B which involved shrouding the melt puddle and downstream ribbon surface with a dry inert gas). Since this contamination was not observed on the planar flow cast ribbon or 92A022 extrusions, etc., its source may be directly attributed to the graphite device added to the casting machine to shroud the melt puddle and ribbon surface with a dry, protective atmosphere. Carbon flakes were also observed to be present in plate and sheet samples rolled from extrusion 92A024 and it is suggested that their presence may be a source for anomalously low tensile ductilities and % reduction in cross-sectional area measured for this material. Because of the presence of contamination in 92A024 plate and sheet samples, detailed TEM was only performed on material rolled from extrusion 92A022. The results of these analyses are summarized below.

TEM performed on hot rolled 0.64 cm (0.25") gauge 92A022 plate indicates a microstructure very comparable to that of the parent extrusion, Fig. 47. As reflected by comparable tensile strengths for both product forms, the silicide particle size and the grain / sub-grain size do not appear to have been affected by hot rolling. Similarly, little change in microstructure is observed for hot rolled 0.22 cm (0.090") gauge 92A022 sheet, Fig 48. As

indicated, silicide particles that are associated with grain / sub-grain boundaries are slightly coarser than particles present within the grains. Obviously, pipe diffusion along grain / sub-grain boundaries is assisting this coarsening and one can further assume that diffusion is fed by solute atoms dumped at these boundaries by scavenging glissile dislocations during hot rolling.
The tendency to find coarser silicide particles present at grain / sub-grain boundaries in the thinner gauge, hot rolled 92A022 sheet is clearly evident in Fig. 49, which is a photomicrograph of the hot rolled 0.10 cm (0.040") gauge sheet. Very coarse silicide particles (> 300 nm in diameter) may be observed associated with sub-grain boundaries in the material. Moreover, dislocation tangles decorating these boundaries are clearly apparent in the micrograph. It is suggested that the lower ductilities measured for the hot rolled 0.10 cm (0.040") gauge sheet are the result of these coarser particles present along the grain / sub-grain boundaries.

The microstructure of 0.10 cm (0.040") gauge sheet cold rolled from 0.22 cm (0.090") gauge hot rolled sheet does not exhibit the same extent of coarsen silicide particles present at the boundaries as the hot rolled 0.10 cm (0.040") gauge sheet. In general, a fairly uniform distribution of dispersoid were observed to be present in this material, Fig. 50. The major differences noted for the cold rolled sheet in comparison to any of the hot rolled variants examined in the present study are the high-lighted grain / sub-grain and particle boundaries in the cold rolled material. In many areas, the grain /sub-grain boundaries appear wider in size than typically observed for hot rolled variants. Weak beam, dark field electron microscopy performed on these high-lighted areas in cold rolled sheet, Figs. 51 (brightfield) & 52 (weak-beam darkfield), clearly indicate dislocations associated with these boundaries. Moreover, dislocation tangles are notably absent from within the grains which is fairly typical for this material. A possible reason for the lack of tangles may simply be due to the fact that this material does not exhibit a large volume fraction of silicide particles present within the grains; hence, their are fewer obstacles to impede dislocation motion through the grains during cold deformation.

TEM performed on cold rolled 0.10 cm (0.040") gauge sheet which experienced intermittent annealing treatments during the rolling campaign tends to indicate a microstructure representative of both the hot and cold rolled 0.10 cm (0.040") gauge sheets presented above, Fig. 53. At lower magnifications, the presence of coarsened silicide particles at the grain / sub-grain boundaries may be observed, (i.e., typical of the hot rolled variant). Moreover, bands of silicide particles were also apparent in this material (indicated by the arrows in Fig. 53) which might reflect the effect of the intermittent annealing treatments applied to this material during rolling. Decorated grain / sub-grain and particle boundaries, typical of cold rolled sheet, are also apparent in this sheet variant, Fig. 54.

Energy Dispersive X-ray Spectroscopy of the Al-Solid Solution Matrix

Energy dispersive X-ray spectroscopy (EDX) was performed to assess the effect of TMP on the solute content present in the Al-solid solution matrix of hot and cold rolled plate and sheet samples. Data was acquired on a JEOL 2010 TEM equipped with a Noran 5500 analyzer and an ultrathin window EDX detector. The spot size used was approximately 30 nm and data was acquired at a count rate was around 1000 counts per second for a total of 150 seconds. Spectra were measured for five different locations in the samples; in all cases being as near the edge of the TEM foil as possible. Computed k-factors (supplied by the manufacturer) were used in the analysis (i.e., internal standards were employed) and standard pure element spectra were used for the curve fitting of the experimental spectra.

The results of EDX performed on extrusion 92A022, hot rolled 0.64 cm (0.25") plate and cold rolled 0.10 cm (0.040") gauge sheet, which experienced intermittent annealing treatments, are presented in Table 13. In all cases, the count rates for Si, V and Fe in the Al-solid solution matrix were very low. Error values noted in the table represent only one standard deviation. In comparison to V and Fe levels measured in the Al-solid solution matrix of extruded and hot rolled 0.64 cm (0.25") plate, the cold rolled / annealed 0.10 cm (0.040") gauge sheet does not indicate any reduction in solute content. Si levels of about 0.4 wt. % are also noted for this variant which was found to be completely absent from the spectra for the extrusion and plate samples. These data support the results of mechanical testing, and specifically, the fact that cold rolling with intermittent annealing treatments does not result in any sizable increase in intermediate temperature plasticity due to a lessened dynamic strain aging response resulting from lower, solute present in the Al-solid solution matrix. These data also support the aforementioned hypothesis that the true "equilibrium" level of solute Si, V or Fe in rapidly solidified HTA 8009 is in actuality, multiple orders of magnitude greater than the equilibrium solute levels reported in the literature for these elements in Al.

Summary

Two (2) potential areas of concern identified by aircraft and engine designers when contemplating the use of rapidly solidified, high temperature aluminum (HTA) alloy 8009 were examined in the present study, namely

i) mechanical anisotropy as a function of product form; and,

ii) reduced plasticity in the 450-550K temperature range.

To further examine these unique characteristics for HTA 8009, modifications to practice and processing parameters were performed to:

(i) improve the metallurgical bonding between prior powder particles by reducing t h e oxide layer thickness at the particle interface; and,

(ii) improve intermediate temperature embrittlement in plate and sheet products b y employing thermomechanical processing (TMP) treatments to reduce the concentration of solute Fe, V and Si in the Al-solid solution matrix.

During the first half of this program (Jan. - July 1992), the oxide layer thickness on planar flow cast HTA 8009 ribbon was successfully reduced by casting under a dry inert gas shroud. Moreover, extrusions, plate and sheet samples were fabricated during this period following modified rolling practices that were specifically designed to alter the solute concentration in the Al-solid solution. The processes employed and detailed results of this effort are summarized in the 1992 mid-year report to the University of Virginia and NASA.

This report details the results of tensile and microstructural testing performed on the extruded and rolled HTA 8009 plate and sheet samples. The major conclusions that may be drawn from this effort are summarized below:

(i) Employing casting modifications to reduce the oxide /hydrate layer thickness on HTA 8009 planar flow cast ribbon, while successful, had little, if any, effect on the tensile properties of extrusions, plate or sheet samples fabricated from these two (2) casting variants.

(ii) Tensile strength, irrespective of strain rate, increases by approximately 14-21 MPa (2-3 ksi) for specimens machined from the mid-planes of the extrusion in comparison to specimens machined from the outer perimeter. This behavior may be attributed to the fact that the outer surface of the preform tends to be much hotter than the bulk due to frictional heating during extrusion. Higher surface temperature promotes a slightly coarser microstructure, and therefore, lower strength. This tendency is present for specimens machined from the nose as well as the tail of the extrusions.

(iii) Tensile ductility decreases in the mid-plane of the extrusion and overall is less for specimens oriented transverse to the extrusion direction irrespective of position in the extrusion. Ductility in these extrusions is largely dependent on the interparticle bonding of the HTA powder particles and variations in ductility reflect the extent of

shear the particles experience during extrusion (i.e., particles located near the surface of the preform, extruded through a shear-faced die, exhibit greater amounts of shear than particles located at mid-plane in the preform).

(iv) Increasing the strain rate ten-fold from 0.5%/min to 5.0%/min on average increases the tensile strength by approximately 14-21 MPa (2-3 ksi) for tests conducted on extrusions at 298K (77°F) and 505K (450°F).

(v) Rolling direction has a greater impact on improving mechanical isotropy in HTA 8009 plate and sheet than does the total reduction in gauge achieved during rolling. This response may be attributed to the fact that cross-rolling more effectively breaks-up and disperses the oxide / hydrate layer present at the prior particle boundaries than straight-rolling alone.

(vi) The reduction in the oxide / hydrate layer thickness for plate and sheet rolled from extrusion 92A024, comprised of planar flow cast ribbon which was shrouded in a dry inert gas environment during casting, in comparison to plate and sheet rolled from conventionally processed extrusion 92A022 did not result in any measurable improvement in transverse tensile ductility.

(vii) Tensile properties for hot rolled 0.64 cm (0.25") gauge plate and hot rolled 0.22 cm (0.090") gauge sheet are fairly comparable over all of the temperatures tested. Tensile ductility for these materials is observed to exhibit a drop in ductility at intermediate test temperatures.

(viii) TMP clearly had an effect on the tensile properties of 0.10 cm (0.040") gauge HTA 8009 sheet; however, TMP did not substantially improve the intermediate temperature plasticity (e.g., ductility) as originally hoped and intended.

(ix) Hot cross- and straight- rolled 0.10 cm (0.040") gauge sheet exhibits the highest tensile strengths over the range of test temperatures for any of the plate and sheet rolled in the program. Overall, this material also exhibits the lowest levels of ductility for all TMP variants over the range of test temperatures. At intermediate temperatures, ductility values ranging from 3-5% were not uncommon.

(x) Cold rolled 0.10 cm (0.040") gauge HTA 8009 sheet exhibits a sizable increase in tensile ductility in comparison to the hot rolled sheet, with only a small decrease in tensile strength. Tensile ductility for this material is also observed to exhibit a drop in ductility at intermediate test temperatures.

(xi) Tensile data for 0.10 cm (0.040") cold rolled sheet which received intermittent annealing treatments indicate a response fairly comparable to the sheet samples

which received cold-rolling only. Tensile strengths for this material were generally lower than measured for the cold rolled sheet over the test temperatures. Values of tensile ductility and its variation with test temperature was very nearly equivalent to levels measured for sheet samples which received only cold rolling.

(xii) Cold rolling, with and without intermittent annealing treatments did result in an overall improvement in the measured tensile ductility over the range of test temperatures in comparison to values measured for hot rolled sheet.

(xiii) While tensile ductility for all of the HTA 8009 plate and sheet rolled in the present program displays the characteristic ductility "dip" over the temperature range of 422-505K (300-450°F), measured values of % reduction in cross-sectional area are found to primarily decrease with increasing test temperature. Irrespective of rolling temperature or TMP practice, % reduction in area drops from about 40-50% at 298K (77°F) to about 25-30% at 422K (300°F) and higher.

(xiv) Irrespective of sheet gauge or rolling direction, increasing the strain rate by a factor of ten (10) typically adds approximately 15-25 MPa (2-3 ksi) to the ultimate tensile strength as well as typically increases the % plastic elongation by as much as 50% in some cases. Strain rate sensitivity values for the plate and sheet samples tested in the present program indicates an "m" value ranging from about 0.015 to 0.030, irrespective of the rolling practice employed, (e.g., temperature, direction, TMP).

(xv) Irrespective of extrusion number or rolling direction, 100 hrs. exposure at 644K (700°F) was found to have no effect on the tensile properties of hot rolled 0.64 cm (0.25") or 0.25 cm (0.090") gauge plate and sheet. In fact, a slight increase in tensile strength is observed after exposure for these samples.

(xvi) Hot rolled 0.10 cm (0.040") gauge sheet after 100 hrs. / 644K (700°F) exposure also indicates no apparent degradation in tensile strength; however, a slight decrease (10-30%) in total plastic elongation was noted for many of the samples.

(xvii) Cold rolled 0.10 cm (0.040") gauge sheet, which did <u>not</u> receive intermittent annealing treatments, indicated the largest response to 100 hrs. / 644K (700°F) exposure. Measured values of tensile yield and ultimate strength are observed to increase by as much as 70 MPa (approximately 10 ksi) after exposure. More significant, however, is the very sizable decrease in total plastic elongation measured for this material after exposure.

(xviii) The response of exposed, cold rolled 0.10 cm (0.040") gauge sheet, which did receive intermittent annealing treatments, is fairly similar to the aforementioned cold

rolled variant. Tensile strength after 100 hrs. / 644K (700°F) exposure was observed to increase by as much as approximately 90 MPa (13 ksi); however, the decrease in ductility for sheet rolled from extrusion 92A022 does not appear to be as severely affected after exposure.

(xix) the microstructure of the as-extruded rolling preform 92A022 is comprised of very fine, 50-80 nm $Al_{13}(Fe,V)_3Si$ dispersoids present in an Al-solid solution matrix. Grain (or sub-grain) size for this material is approximately 0.5μm.

(xx) Extrusion 92A024 exhibits a fairly comparable microstructure to that of extrusion 92A022; however, large regions of carbon (i.e., graphite) contamination were observed to be scattered throughout the material. The source of carbon contamination may be directly attributed to the graphite device added to the casting machine to shroud the melt puddle and ribbon surface with a dry, protective atmosphere during casting. Carbon flakes were also observed to be present in plate and sheet samples rolled from extrusion 92A024 and it is suggested that their presence may be a source for anomalously low tensile ductilities and % reduction in cross-sectional area measured for this material.

(xxi) TEM performed on hot rolled 0.64 cm (0.25") gauge 92A022 plate and 0.22 cm (0.090") gauge sheet indicates a microstructure very comparable to that of the parent extrusion. Silicide particles in the hot rolled 0.22 cm (0.090") gauge sheet that are associated with grain / sub-grain boundaries are slightly coarser than particles present within the grains.

(xxii) Lower tensile ductilities measured for 0.10 cm (0.040") gauge hot rolled sheet may be attributed to a greater tendency to find coarser silicide particles present at grain / sub-grain boundaries as well as dislocation tangles associated with these boundaries. Coarsened silicide particles at boundaries were not observed for cold rolled 0.10 cm (0.040") gauge sheet.

(xxiii) Weak beam, dark field electron microscopy performed on cold rolled 0.10 cm (0.040") gauge sheet clearly indicates dislocations associated with grain / sub-grain and particle boundaries. Moreover, dislocation tangles are notably absent from within the grains which is fairly typical for this material. A possible reason for the lack of tangles may simply be due to the fact that this material does not exhibit a large volume fraction of silicide particles present within the grains; hence, their are fewer obstacles to impede dislocation motion through the grains during cold deformation.

(xxiv) TEM performed on cold rolled 0.10 cm (0.040") gauge sheet which experienced intermittent annealing treatments during the rolling campaign tends to indicate the presence of coarsen silicide particles at the grain / sub-grain boundaries.

(xxv) Energy dispersive X-ray spectroscopy (EDX), performed to assess the effect of TMP on the solute content present in the Al-solid solution matrix of hot and cold rolled plate and sheet samples, indicate that V and Fe levels measured in the Al-solid solution of cold rolled / annealed 0.10 cm (0.040") gauge sheet are comparable to levels measured in the matrix of extruded and hot rolled 0.64 cm (0.25") plate. And,

(xxvi) EDX data support the hypothesis that the true "equilibrium" level of solute Si, V or Fe in rapidly solidified HTA 8009 is in actuality, multiple orders of magnitude greater than the equilibrium solute levels reported in the literature for these elements in Al.

References

1. U.S. Air Force Contract F33615-85-R-5160, "900°F Aluminum-Base Materials Research", Awarded to the University of Virginia, 1985.
2. U.S. Air Force Contract F33615-87-R-3206, "Elevated Temperature Aluminum Program", Awarded to Lockheed - California Company, 1987.
3. Naval Air Development Center Contract N62269-88-C-0255, "Elevated Temperature Aluminum Base Alloys for Applications in Advanced Turbofan Jet Engines", Awarded to Allied-Signal Inc., January 1989.
4. E.Y. Ting and J.R. Kennedy, NASA Contractor Report 181849, "Superplastic Forming and Diffusion Bonding of Rapidly Solidified, Dispersion Strengthened Aluminum Alloys for Elevated Temperature Structural Applications", 181-198 (1989).
5. D.J. Skinner, "The Physical Metallurgy of Dispersion Strengthened Al-Fe-V-Si Alloys", in Dispersion Strengthened Aluminum Alloys, Y.W. Kim and W.M. Griffith, eds., TMS, (1988).
6. P.S. Gilman, M.S. Zedalis, J.M. Peltier and S.K. Das, "Rapidly Solidified Aluminum-Transition Metal Alloys for Aerospace Applications", AIAA/AHS/ASEE Aircraft Design, Systems and Operations Conference, Atlanta, GA, Sept. 1988.

7. M.S. Zedalis and D.J. Skinner, "Young's Moduli of Al-Fe-X-Si Alloys and Al-Fe-V-Si -Base Metal Matrix Composites", in Lightweight Alloys for Aerospace Applications, eds., E.W. Lee, E.H. Chia and N.J. Kim, TMS, 335-344 (1989).
8. W.C. Porr, Y. Leng and R.P. Gangloff, "Elevated Temperature Fracture Toughness of P/M Al-Fe-V-Si", in Low Density, High Temperature P/M Alloys, TMS-AIME, Warrendale, PA, submitted (1990).
9. K.S. Chan, "Evidence of Thin Sheet Toughening Mechanism in Al-Fe-X Alloys", Met. Trans., **20A**, 155-164 (1989).
10. K.S. Chan, "Confirmation of Thin Sheet Toughening Mechanism adn Anisotropic Fracture in Al-Fe-X Alloys", Met. Trans., **20A**, 2337-2344 (1989).
11. D.J. Skinner, M.S. Zedalis and J.M. Peltier, "Anomalous Ductility Variation at Intermediate Temperatures in Rapidly Solidified Al-Base Alloys", in Lightweight Alloys for Aerospace Applications, eds., E.W. Lee, E.H. Chia and N.J. Kim, TMS, 71-78 (1989).
12. A.I. Litvintsev and L.A. Arbuzova, Sov. P/M Met. Cer., **1**, 1 (1967).
13. W.M. Mullins and B.L. Averback, "The Electronic Structure of Anodized and Etched Aluminum Alloy Surfaces", Surf. Sci., **206**, 52 (1988).
14. B.R. Strohmeier, Surf. and Interface Anal., "An ESCA Method for Determining the Oxide Thickness on Aluminum Alloys", **15**, 51 (1990).
15. D.J. Skinner, K. Okazaki and C.M. Adam, "Physical Metallurgy and Mechanical Properties of Aluminum Alloys Containing Eight to Twelve Percent Iron", in Rapidly Solidified Powder Al Alloys, eds., M.E. Fine and E.A. Starke, ASTM, 211-236 (1986).
16. C.M. Adam, V.R.V. Ramanan and D.J. Skinner, in Undercooled Alloy Phases, eds., E.W. Collings and C.C. Koch, TMS, 59 (1987).
17. D.J. Skinner, V.R.V. Ramanan, M.S. Zedalis and N.J. Kim, "Stability of Quasicrystalline Phases in Al-Fe-V Alloys", Mat. Sci. Eng., **99**, 407-411 (1988).
18. M.S. Zedalis, V.R.V. Ramanan and D.J. Skinner, "Thermal Analysis of Rapidly Solidified Al-Fe-V Alloys, and SiCp Reinforced Al-Li-Cu-Mg-Zr Composites" in Thermal Analysis in Metallurgy, eds., R.D. Shull and A. Joshi, TMS, 279-295 (1992).
19. D.J. Skinner, M.S. Zedalis and P.S. Gilman, "Effect of Strain Rate on Tensile Ductility for a Series of Dispersion Strengthened Aluminum-Based Alloys", Mat. Sci. & Eng., **A119**, 81-86 (1990).
20. M. Zedalis, presented at 1987 Fall TMS-AIME Meeting, Cincinatti, OH, October.

Table 1a

EXTRUSION: 91A022 NOSE Temperature - 298K

Nos.	Spec. ID	Orient.	.2% Y.S. 0.5% min (MPa)	U.T.S. 0.5%/min (MPa)	U.T.S. 5%/min (MPa)	% Elong.
1	T1	L	340.4	396.9	415.5	16.2
2	T2	L	343.8	396.2	413.5	17.8
3	T3	L	345.9	396.2	414.8	18.9
4	T4	L	345.9	392.7	409.3	15.0
5	M1	L	343.8	402.4	421.0	10.7
6	M2	L	347.9	401.7	418.9	8.7
7	M3	L	342.4	401.0	420.3	10.0
8	M1	T	350.7	414.8	433.4	7.8
9	M2	T	347.5	408.6	428.6	8.5
10	B1	T	343.1	410.6	427.2	8.3
11	B2	T	348.6	408.6	426.5	8.4
12	B3	T	346.6	408.6	427.9	9.8
13	B4	T	345.2	408.6	427.9	7.4

EXTRUSION: 92A022 TAIL Temperature - 298K

Nos.	Spec. ID	Orient.	.2% Y.S. 0.5% min (MPa)	U.T.S. 0.5%/min (MPa)	U.T.S. 5%/min (MPa)	% Elong.
1	T1	L	306.6	354.1	372.5	15.1
2	T2	L	323.8	376.2	395.5	15.4
3	T3	L	322.4	375.5	395.5	16.6
4	T4	L	325.2	376.9	395.5	16.3
5	M1	L	332.8	383.8	402.4	18.1
6	M2	L	341.7	391.4	410.6	17.3
7	M3	L	359.0	392.6	418.2	17.2
8	M1	T	350.0	401.0	425.1	9.0
9	M2	T	351.4	406.5	427.2	9.6
10	B1	T	355.5	397.6	417.5	8.0
11	B2	T	359.0	397.6	418.2	8.2
12	B3	T	336.9	396.9	418.2	8.4
13	B4	T	338.3	398.2	419.6	9.7

Table 1b

EXTRUSION: 91A022 NOSE Temperature - 77°F

Nos.	Spec. ID	Orient.	.2% Y.S. 0.5% min (ksi)	U.T.S. 0.5%/min (ksi)	U.T.S. 5%/min (ksi)	% Elong.
1	T1	L	49.4	57.6	60.3	16.2
2	T2	L	49.9	57.5	60.0	17.8
3	T3	L	50.2	57.5	60.2	18.9
4	T4	L	50.2	57.0	59.4	15.0
5	M1	L	49.9	58.4	61.1	10.7
6	M2	L	50.5	58.3	60.8	8.7
7	M3	L	49.7	58.2	61.0	10.0
8	M1	T	50.9	60.2	62.9	7.8
9	M2	T	50.4	59.3	62.2	8.5
10	B1	T	49.8	59.6	62.0	8.3
11	B2	T	50.6	59.3	61.9	8.4
12	B3	T	50.3	59.3	62.4	9.8
13	B4	T	50.1	59.3	62.1	7.4

EXTRUSION: 92A022 TAIL Temperature - 77°F

Nos.	Spec. ID	Orient.	.2% Y.S. 0.5% min (ksi)	U.T.S. 0.5%/min (ksi)	U.T.S. 5%/min (ksi)	% Elong.
1	T1	L	44.5	51.4	54.1	15.1
2	T2	L	47.0	54.6	57.4	15.4
3	T3	L	46.8	54.5	57.4	16.6
4	T4	L	47.2	54.7	57.4	16.3
5	M1	L	48.3	55.7	58.4	18.1
6	M2	L	49.6	56.8	59.6	17.3
7	M3	L	52.1	57.7	60.7	17.2
8	M1	T	50.8	58.2	61.7	9.0
9	M2	T	51.0	59.0	62.0	9.6
10	B1	T	48.7	57.7	60.6	8.0
11	B2	T	49.2	57.7	60.7	8.2
12	B3	T	48.9	57.6	60.7	8.4
13	B4	T	49.1	57.8	60.9	9.7

Table 1a (cont.)

EXTRUSION: 91A022 NOSE Temperature - 505K

Nos.	Spec. ID	Orient.	.2% Y.S. 0.5 %/min (MPa)	U.T.S. 0.5%/min (MPa)	U.T.S. 5%/min (MPa)	% Elong.
1	T5	L	249.4	262.5	283.9	13.5
2	T6	L	252.2	266.6	285.2	12.1
3	T7	L	256.3	270.1	291.4	10.3
4	T8	L	253.6	270.1	292.1	10.4
5	M4	L	251.5	268.7	290.8	13.6
6	M5	L	257.7	279.0	300.4	7.4
7	M6	L	257.0	274.2	295.0	7.2
8	M3	T	250.8	270.8	292.1	3.3
9	M4	T	251.5	270.8	292.1	4.0
10	B5	T	254.2	273.5	296.3	4.8
11	B6	T	250.1	271.5	293.5	6.1
12	B7	T	250.8	270.8	293.5	5.2
13	B8	T	250.8	274.2	296.3	5.8

EXTRUSION: 92A022 TAIL Temperature - 505K

Nos.	Spec. ID	Orient.	.2% Y.S. 0.5 %/min (MPa)	U.T.S. 0.5%/min (MPa)	U.T.S. 5%/min (MPa)	% Elong.
1	T5	L	233.0	246.0	266.6	11.3
2	T6	L	236.3	248.7	268.7	14.0
3	T7	L	232.2	245.3	266.0	14.6
4	T8	L	237.0	250.8	271.5	16.1
5	M4	L	261.8	272.2	293.5	9.0
6	M5	L	255.6	265.3	283.9	10.8
7	M6	L	256.13	268.7	289.4	14.0
8	M3	T	260.4	280.4	302.5	6.3
9	M4	T	NM	NM	NM	NM
10	B5	T	234.9	259.1	281.8	8.0
11	B6	T	242.5	262.5	284.6	6.9
12	B7	T	237.7	259.1	279.7	7.1
13	B8	T	241.8	261.1	283.2	9.3

Table 1b (cont.)

EXTRUSION: 91A022 NOSE Temperature - 450°F

Nos.	Spec. ID	Orient.	.2% Y.S. 0.5 %/min (ksi)	U.T.S. 0.5%/min (ksi)	U.T.S. 5%/min (ksi)	% Elong.
1	T5	L	36.2	38.1	41.2	13.5
2	T6	L	36.6	38.7	41.4	12.1
3	T7	L	37.2	39.2	42.3	10.3
4	T8	L	36.8	39.2	42.4	10.4
5	M4	L	36.5	39.0	42.2	13.6
6	M5	L	37.4	40.5	43.6	7.4
7	M6	L	37.3	39.8	42.9	7.2
8	M3	T	36.4	39.3	42.4	3.3
9	M4	T	36.5	39.3	42.4	4.0
10	B5	T	36.9	39.7	43.0	4.8
11	B6	T	36.3	39.4	42.6	6.1
12	B7	T	36.4	39.3	42.6	5.2
13	B8	T	36.4	39.8	43.0	5.8

EXTRUSION: 92A022 TAIL Temperature - 450°F

Nos.	Spec. ID	Orient.	.2% Y.S. 0.5 %/min (ksi)	U.T.S. 0.5%/min (ksi)	U.T.S. 5%/min (ksi)	% Elong.
1	T5	L	33.9	35.7	38.7	11.3
2	T6	L	34.3	36.1	39.0	14.0
3	T7	L	33.7	35.6	38.6	14.6
4	T8	L	34.4	36.4	39.4	16.1
5	M4	L	38.0	39.5	42.6	9.0
6	M5	L	37.1	38.5	41.2	10.8
7	M6	L	37.2	39.0	42.0	14.0
8	M3	T	37.8	40.7	43.9	6.3
9	M4	T	NM	NM	NM	NM
10	B5	T	34.1	37.6	40.9	8.0
11	B6	T	35.2	38.1	41.3	6.9
12	B7	T	34.5	37.6	40.6	7.1
13	B8	T	35.1	37.9	41.1	9.3

NM - Not Measured

Table 1a (cont.)

EXTRUSION: 92A024 NOSE Temperature - 298K

Nos.	Spec. ID	Orient.	.2% Y.S. 0.5%/min (MPa)	U.T.S. 0.5%/min (MPa)	U.T.S. 5%/min (MPa)	% Elong.
1	T1	L	336.9	385.8	403.8	13.7
2	T2	L	334.2	383.1	403.1	13.8
3	T3	L	331.4	382.4	402.4	14.3
4	T4	L	328.7	378.3	398.2	14.3
5	M1	L	335.5	388.6	407.9	14.7
6	M2	L	334.2	386.5	406.5	15.0
7	M3	L	331.4	381.0	401.0	14.4
8	M1	T	354.8	408.6	428.6	8.7
9	M2	T	352.1	405.8	427.2	7.1
10	B1	T	361.7	413.4	435.4	10.8
11	B2	T	367.2	416.2	434.8	14.5
12	B3	T	357.6	413.4	434.8	13.3
13	B4	T	362.4	413.4	434.8	12.2

EXTRUSION: 92A024 TAIL Temperature - 298K

Nos.	Spec. ID	Orient.	.2% Y.S. 5%/min (MPa)	U.T.S. 5%/min (MPa)	U.T.S. 5%/min (MPa)	% Elong.
1	T1	L	334.9	383.8	403.1	12.8
2	T2	L	332.1	382.1	403.8	21.2
3	T3	L	339.0	383.8	402.4	18.6
4	T4	L	332.1	380.3	399.6	20.7
5	M1	L	334.9	381.7	401.0	19.5
6	M2	L	339.7	392.7	411.3	16.8
7	M3	L	355.5	394.8	414.8	14.8
8	M1	T	350.0	406.5	427.9	9.0
9	M2	T	352.8	410.0	427.9	6.7
10	B1	T	332.8	395.5	414.1	8.2
11	B2	T	337.6	396.2	418.2	7.6
12	B3	T	332.8	392.7	414.1	8.0
13	B4	T	356.9	395.5	413.4	7.0

Table 1b (cont.)

EXTRUSION: 92A024 NOSE Temperature- 77°F

Nos.	Spec. ID	Orient.	.2% Y.S. 0.5%/min (ksi)	U.T.S. 0.5%/min (ksi)	U.T.S. 5%/min (ksi)	% Elong.
1	T1	L	48.9	56.0	58.6	13.7
2	T2	L	48.5	55.6	58.5	13.8
3	T3	L	48.1	55.5	58.4	14.3
4	T4	L	47.7	54.9	57.8	14.3
5	M1	L	48.7	56.4	59.2	14.7
6	M2	L	48.5	56.1	59.0	15.0
7	M3	L	48.1	55.3	58.2	14.4
8	M1	T	51.5	59.3	62.2	8.7
9	M2	T	51.1	58.9	62.0	7.1
10	B1	T	52.5	60.0	63.2	10.8
11	B2	T	53.3	60.4	63.1	14.5
12	B3	T	51.9	60.0	63.1	13.3
13	B4	T	52.6	60.0	63.1	12.2

EXTRUSION: 92A024 TAIL Temperature - 77°F

Nos.	Spec. ID	Orient.	.2% Y.S. 5%/min (ksi)	U.T.S. 5%/min (ksi)	U.T.S. 5%/min (ksi)	% Elong.
1	T1	L	48.6	55.7	58.5	12.8
2	T2	L	48.2	55.6	58.6	21.2
3	T3	L	49.2	55.7	58.4	18.6
4	T4	L	48.2	55.2	58.0	20.7
5	M1	L	48.6	55.4	58.2	19.5
6	M2	L	49.3	57.0	59.7	16.8
7	M3	L	51.6	57.3	60.2	14.8
8	M1	T	50.8	59.0	62.1	9.0
9	M2	T	51.2	59.5	62.1	6.7
10	B1	T	48.3	57.4	60.1	8.2
11	B2	T	49.0	57.5	60.7	7.6
12	B3	T	48.3	57.0	60.1	8.0
13	B4	T	48.9	57.4	60.0	7.0

Table 1a (cont.)

EXTRUSION: 92A024 NOSE Temperature - 505K

Nos.	Spec. ID	Orient.	.2% Y.S. 0.5 %/min (MPa)	U.T.S. 0.5%/min (MPa)	U.T.S. 5%/min (MPa)	% Elong.
1	T5	L	234.9	246.7	267.3	10.1
2	T6	L	233.6	245.3	266.6	14.2
3	T7	L	232.9	246.7	267.3	15.2
4	T8	L	234.3	249.4	270.8	13.9
5	M4	L	230.1	263.2	263.2	10.4
6	M5	L	236.3	250.1	267.3	7.7
7	M6	L	237.7	272.8	272.8	10.1
8	M3	T	249.4	266.6	288.0	4.0
9	M4	T	248.7	266.6	288.0	3.7
10	B5	T	252.9	267.3	289.4	9.1
11	B6	T	252.9	268.0	288.7	9.1
12	B7	T	253.6	268.0	290.2	6.0
13	B8	T	272.8	273.5	296.3	7.0

EXTRUSION: 92A024 TAIL Temperature - 505K

Nos.	Spec. ID	Orient.	.2% Y.S. 0.5%/min (MPa)	U.T.S. 0.5%/min (MPa)	U.T.S. 5%/min (MPa)	% Elong.
1	T5	L	237.0	252.2	272.8	14.5
2	T6	L	235.6	251.5	272.8	13.2
3	T7	L	237.7	250.8	271.5	14.2
4	T8	L	238.4	250.8	271.5	13.3
5	M4	L	261.1	271.5	293.5	10.4
6	M5	L	247.4	259.8	279.0	11.3
7	M6	L	239.8	252.9	272.8	14.2
8	M3	T	250.1	274.2	294.9	5.1
9	M4	T	254.2	275.6	298.3	6.5
10	B5	T	249.3	294.2	294.2	5.9
11	B6	T	245.3	267.3	286.6	8.1
12	B7	T	248.7	291.4	291.4	7.0
13	B7	T	246.7	266.0	289.4	9.0

Table 1b (cont.)

EXTRUSION: 92A024 NOSE Temperature - 450°F

Nos.	Spec. ID	Orient.	.2% Y.S. 0.5 %/min (ksi)	U.T.S. 0.5%/min (ksi)	U.T.S. 5%/min (ksi)	% Elong.
1	T5	L	34.1	35.8	38.8	10.1
2	T6	L	33.9	35.6	38.7	14.2
3	T7	L	33.8	35.8	38.8	15.2
4	T8	L	34.0	36.2	39.3	13.9
5	M4	L	33.4	38.2	38.2	10.4
6	M5	L	34.3	36.3	38.8	7.7
7	M6	L	34.5	39.6	39.6	10.1
8	M3	T	36.2	38.7	41.8	4.0
9	M4	T	36.1	38.7	41.8	3.7
10	B5	T	36.7	38.8	42.0	9.1
11	B6	T	36.7	38.9	41.9	9.1
12	B7	T	36.8	38.9	42.1	6.0
13	B8	T	39.6	39.7	43.0	7.0

EXTRUSION: 92A024 TAIL Temperature - 450°F

Nos.	Spec. ID	Orient.	.2% Y.S. 0.5%/min (ksi)	U.T.S. 0.5%/min (ksi)	U.T.S. 5%/min (ksi)	% Elong.
1	T5	L	34.4	36.6	39.6	14.5
2	T6	L	34.2	36.5	39.6	13.2
3	T7	L	34.5	36.4	39.4	14.2
4	T8	L	34.6	36.4	39.4	13.3
5	M4	L	37.9	39.4	42.6	10.4
6	M5	L	35.9	37.7	40.5	11.3
7	M6	L	34.8	36.7	39.6	14.2
8	M3	T	36.3	39.8	42.8	5.1
9	M4	T	36.9	40.0	43.3	6.5
10	B5	T	36.2	42.7	42.7	5.9
11	B6	T	35.6	38.8	41.6	8.1
12	B7	T	36.1	42.3	42.3	7.0
12	B7	T	35.8	38.6	42.0	9.0

Table 2

MATERIAL SUPPLIED TO THE UVA FOR TESTING

Casting Modification A

ID	Dimensions (cm)	Comments
92A022-1C	0.63 x 36.80 x 88.90	Hot, Cross Rolled
92A022-1A	0.63 x 22.90 x 139.70	Hot, Straight Rolled
92A022-2A	0.26 x 35.60 x 114.30	Hot, Cross Rolled
92A022-2A	0.25 x 35.60 x 162.60	Hot, Cross Rolled
92A022-2B	0.26 x 22.90 x 167.60	Hot, Straight Rolled
92A022-2B	0.26 x 21.60 x 241.30	Hot, Straight Rolled
92A022-2C1	0.07 x 21.60 x 198.10	Hot, Straight Rolled
92A022-2C1	0.07 x 21.60 x 223.50	Hot, Straight Rolled
92A022-1B1	0.10 x 35.60 x 203.20	Hot, Cross Rolled
92A022-2C2	0.10 x 10.20 x 245.10	Cold, Straight Rolled
92A022-1B2	0.10 x 34.30 x 207.00	Cold Cross Rolled
92A022-2C3	0.10 x 17.10 x 124.50	Cold/Anneal, Straight Roll
92A022-2C3	0.10 x 15.90 x 124.50	Cold/Anneal, Straight Roll
92A022-1B3	0.10 x 35.60 x 204.50	Cold/Anneal, Cross Roll

Table 3

MATERIAL SUPPLIED TO THE UVA FOR TESTING

Casting Modification B

ID	Dimensions (cm)	Comments
92A024-1C	0.64 x 29.20 x 78.70	Hot, Cross Rolled
92A024-1A	0.64 x 23.50 x 83.80	Hot, Straight Rolled
92A024-1B	0.27 x 23.50 x 108.00	Hot, Straight Rolled
92A024-1B	0.27 x 23.50 x 185.40	Hot, Straight Rolled
92A024-1D	0.22 x 27.90 x 121.30	Hot, Cross Rolled
92A024-1D	0.22 x 27.90 x 182.90	Hot, Cross Rolled
92A024-2A1	0.08 x 24.10 x 125.70	Hot, Straight Rolled
92A024-2A1	0.08 x 25.40 x 73.70	Hot, Straight Rolled
92A024-2B1	0.10 x 29.80 x 175.30	Hot, Cross Rolled
92A024-2A2	0.10 x 10.10 x 160.00	Cold, Straight Rolled
92A024-2A2	0.09 x 10.80 x 80.00	Cold, Straight Rolled
92A024-2B2	0.10 x 26.70 x 171.50	Cold, Cross Rolled
92A024-2A3	0.09 x 15.20 x 63.90	Cold/Anneal, Straight Rolled
92A024-2B3	0.10 x 27.30 x 40.60	Cold/Anneal, Cross Rolled
92A024-2B3	0.11 x 27.30 x 177.80	Cold/Anneal, Cross Rolled

Table 4a

Sample ID#	Temp. (K)	Orient.	0.2% Y.S. (MPa)	U.T.S. 0.5% /min. (Mpa)	U.T.S. 5% /min. (MPa)	Elong. (%)	% R.A.
92A022-1C HOT CROSS ROLLED							
0.64 cm	298	L	381.0	413.9	427.5	18.4	48.4
	298	T	376.9	407.5	426.1	19.6	**
	422	L	295.6	342.8	359.0	8.6	32.8
	422	T	271.1	335.2	352.1	7.8	**
	505	L	246.7	266.2	293.6	16.2	27.6
	505	T	241.1	280.4	292.9	11.6	**
	589	L	155.2	171.4	197.9	25.8	25.1
	589	T	129.8	167.8	193.8	25.2	**
	298E*	L	403.8	427.9	447.9	14.0	48.1
	298E*	T	380.3	412.0	432.0	14.1	**
92A022-1A HOT STRAIGHT ROLLED							
0.64 cm	298	L	421.0	431.7	445.8	13.0	**
	298	T	396.2	421.0	433.0	11.6	**
	422	L	347.9	350.7	362.1	7.8	**
	422	T	319.0	347.9	361.7	6.5	**
	505	L	163.2	292.0	305.4	14.3	**
	505	T	241.2	267.0	294.8	10.7	**
	589	L	162.6	174.4	201.9	28.7	**
	589	T	155.4	190.0	203.5	18.3	**
	298E*	L	411.3	449.9	460.9	11.5	**
	298E*	T	401.0	429.9	441.0	9.7	**
92A022-2A HOT CROSS ROLLED							
0.25 cm	298	L	378.3	431.3	448.5	9.7	38.0
	298	T	372.1	408.2	427.5	13.5	**
	422	L	289.7	346.9	366.5	6.9	31.3
	422	T	291.4	338.6	357.9	8.3	**
	505	L	208.8	274.4	302.9	13.2	34.3
	505	T	130.1	255.0	284.1	14.6	**
	589	L	157.6	172.3	201.2	25.8	26.7
	589	T	156.5	175.1	203.9	21.3	**
	298E*	L	396.9	436.1	457.5	11.3	53.5
	298E*	T	392.7	443.0	453.4	7.6	**
92A022-2B HOT STRAIGHT ROLLED							
0.25 cm	298	L	34.4	438.7	457.3	10.1	**
	298	T	81.9	425.3	435.2	9.6	**
	422	L	325.6	347.9	364.5	6.4	**
	422	T	330.0	346.9	363.8	5.3	**
	505	L	243.9	256.7	285.5	16.7	**
	505	T	206.4	275.4	289.5	9.6	**
	589	L	162.1	173.9	202.0	26.3	**
	589	T	157.5	174.5	203.5	16.0	**
	298E*	L	394.1	434.8	450.6	9.3	**
	298E*	T	382.4	428.6	449.2	7.7	**

* Samples tested at 298K after 644K for 100 hrs. exposure

** Not Measured

Table 4b

Sample ID#	Temp (°F)	Orient.	0.2% Y.S. (ksi)	U.T.S. 0.5% /min. (ksi)	U.T.S. 5% /min. (ksi)	Elong. (%)	% R.A.
92A022-1C HOT CROSS ROLLED							
0.25" Gauge	77	L	55.3	60.1	62.1	18.4	48.4
		T	54.7	59.2	61.9	19.6	**
	300	L	42.9	49.8	52.1	8.6	32.8
		T	39.4	48.7	51.1	7.8	**
	450	L	35.8	38.6	42.6	16.2	27.6
		T	35.0	40.7	42.5	11.6	**
	600	L	22.5	24.9	28.7	25.8	25.1
		T	18.8	24.4	28.1	25.2	**
	77E*	L	58.6	62.1	65.0	14.0	48.1
	77E*	T	55.2	59.8	62.7	14.1	**
92A022-1A HOT STRAIGHT ROLLED							
0.25" Gauge		L	61.1	62.7	64.7	13.0	**
	77	T	57.5	61.1	62.9	11.6	**
		L	50.5	50.9	52.6	7.8	**
	300	T	46.3	50.5	52.5	6.5	**
		L	23.7	42.4	44.3	14.3	**
	450	T	35.0	38.8	42.8	10.7	**
		L	23.6	25.3	29.3	28.7	**
	600	T	22.6	27.6	29.5	18.3	**
	77E*	L	59.7	65.3	66.9	11.5	**
	77E*	T	58.2	62.4	64.0	9.7	**
92A022-2A HOT CROSS ROLLED							
0.10" Gauge	77	L	54.9	62.6	65.1	9.7	38.0
	77	T	54.0	59.3	62.1	13.5	**
	300	L	42.1	50.4	53.2	6.9	31.3
	300	T	42.3	49.2	52.0	8.3	**
	450	L	30.3	39.8	44.0	13.2	34.3
	450	T	18.9	37.0	41.2	14.6	**
	600	L	22.9	25.0	29.2	25.8	26.7
	600	T	22.7	25.4	29.6	21.3	**
	77E*	L	57.6	63.3	66.4	11.3	53.5
	77E*	T	57.0	64.3	65.8	7.6	**
92A022-2B HOT STRAIGHT ROLLED							
0.10" Gauge	77	L	59.7	63.7	66.4	10.1	**
	77	T	58.6	61.7	63.2	9.6	**
	300	L	47.3	50.5	52.9	6.4	**
	300	T	47.9	50.4	52.8	5.3	**
	450	L	35.4	37.3	41.4	16.7	**
	450	T	30.0	40.0	42.0	9.6	**
	600	L	23.5	25.2	29.3	26.3	**
	600	T	22.9	25.3	29.5	16.0	**
	77E*	L	57.2	63.1	65.4	9.3	**
	77E*	T	55.5	62.2	65.2	7.7	**

* Samples tested at 77°F after 700°F for 100 hrs. exposure

** Not Measured

Table 5a

Sample ID#	Temp (K)	Orient.	0.2% Y.S. (MPa)	U.T.S. 0.5% /min. (MPa)	U.T.S. 5% /min. (MPa)	Elong. (%)	% R.A.
92A022-1B1 HOT CROSS ROLLED							
0.10 cm	298	L	418.9	436.1	448.2	10.2	44.3
	298	T	397.2	434.8	459.2	7.0	**
	422	L	272.8	359.3	377.6	2.1	37.6
	422	T	306.9	361.7	379.6	2.7	**
	505	L	258.2	267.2	295.4	10.8	30.4
	505	T	259.9	271.1	301.9	9.4	**
	589	L	128.9	156.3	182.5	23.9	27.3
	589	T	129.5	159.2	185.3	13.1	**
	298E*	L	370.0	441.6	453.4	5.7	51.3
	298E*	T	401.0	438.9	461.6	5.6	**
92A022-2C1 HOT STRAIGHT ROLLED							
0.10 cm	298	L	395.1	438.9	460.3	7.3	**
	298	T	384.1	448.5	481.6	6.6	**
	422	L	311.1	354.1	369.6	2.7	**
	422	T	313.8	369.6	390.0	2.2	**
	505	L	143.0	257.1	284.3	12.0	**
	505	T	230.7	250.8	278.6	12.2	**
	589	L	79.2	189.2	205.6	20.6	**
	589	T	128.4	169.1	201.0	16.8	**
	298E*	L	360.3	449.9	460.9	7.9	**
	298E*	T	430.6	456.1	476.8	4.5	**
92A022-1B2 COLD CROSS ROLLED							
0.10 cm	298	L	381.4	408.2	435.4	18.9	28.8
	298	T	345.5	405.1	431.3	17.1	**
	422	L	263.9	345.2	370.3	9.2	26.5
	422	T	256.3	343.8	369.3	10.1	**
	505	L	204.8	253.8	287.3	15.7	21.2
	505	T	186.1	246.7	280.1	15.2	**
	589	L	111.1	189.6	189.6	25.1	22.5
	589	T	126.1	156.1	192.0	25.4	**
	298E*	L	414.8	449.2	476.8	3.0	27.4
	298E*	T	421.0	476.8	491.3	5.7	**
92A022-2C2 COLD STRAIGHT ROLLED							
0.10 cm	298	L	376.2	397.2	423.7	15.5	**
	298	T	354.1	396.5	423.7	15.9	**
	422	L	271.1	338.6	365.2	8.3	**
	422	T	251.1	341.1	365.9	7.3	**
	505	L	210.9	248.0	280.8	15.9	**
	505	T	183.5	251.8	286.3	12.6	**
	589	L	110.2	154.3	188.4	25.9	**
	589	T	108.0	166.9	183.1	19.9	**
	298E*	L	435.4	459.6	487.1	6.6	**
	298E*	T	425.1	483.7	497.5	5.1	**

* Samples tested at 298K after 644K for 100 hrs. exposure

** Not Measured

Table 5b

Sample ID#	Temp (°F)	Orient.	0.2% Y.S. (ksi)	U.T.S. 0.5% min. (ksi)	U.T.S. 5% min. (ksi)	Elong. (%)	% R.A.
92A022-1B1 HOT CROSS ROLLED							
0.040" Gauge	77	L	60.8	63.3	65.1	10.2	44.3
	77	T	57.7	63.1	66.7	7.0	**
	300	L	39.6	52.2	54.8	2.1	37.6
	300	T	44.6	52.5	55.1	2.7	**
	450	L	37.5	38.8	42.9	10.8	30.4
	450	T	37.7	39.4	43.8	9.4	**
	600	L	18.7	22.7	26.5	23.9	27.3
	600	T	18.8	23.1	26.9	13.1	**
	77E*	L	53.7	64.1	65.8	5.7	51.3
	77E*	T	58.2	63.7	67.0	5.6	**
92A022-2C1 HOT STRAIGHT ROLLED							
0.030" Gauge	77	L	57.4	63.7	66.8	7.3	**
	77	T	55.8	65.1	69.9	6.6	**
	300	L	45.2	51.4	53.7	2.7	**
	300	T	45.6	53.7	56.6	2.2	**
	450	L	20.8	37.3	41.3	12.0	**
	450	T	33.5	36.4	40.4	12.2	**
	600	L	11.5	27.5	29.8	20.6	**
	600	T	18.6	24.6	29.2	16.8	**
	77E*	L	52.3	65.3	66.9	7.9	**
	77E*	T	62.5	66.2	69.2	4.5	**
92A022-1B2 COLD CROSS ROLLED							
0.040" Gauge	77	L	55.4	59.3	63.2	18.9	28.8
	77	T	50.2	58.8	62.6	17.1	**
	300	L	38.3	50.1	53.8	9.2	26.5
	300	T	37.2	49.9	53.6	10.1	**
	450	L	29.7	36.8	41.7	15.7	21.2
	450	T	27.0	35.8	40.7	15.2	**
	600	L	16.1	27.5	27.5	25.1	22.5
	600	T	18.3	22.7	27.9	25.4	**
	77E*	L	60.2	65.2	69.2	3.0	27.4
	77E*	T	61.1	69.2	71.3	5.7	**
92A022-2C2 COLD STRAIGHT ROLLED							
0.040" Gauge	77	L	54.6	57.7	61.5	15.5	**
	77	T	51.4	57.6	61.5	15.9	**
	300	L	39.4	49.2	53.0	8.3	**
	300	T	36.5	49.5	53.1	7.3	**
	450	L	30.6	36.0	40.8	15.9	**
	450	T	26.6	36.5	41.6	12.6	**
	600	L	16.0	22.4	27.3	25.9	**
	600	T	15.7	24.2	26.6	19.9	**
	77E*	L	63.2	66.7	70.7	6.6	**
	77E*	T	61.7	70.2	72.2	5.1	**

* Samples tested at 77°F after 700°F for 100 hrs. exposure

** Not Measured

Table 6a

Sample ID#	Temp (K)	Orient.	0.2% Y.S. (MPa)	U.T.S. 0.5% min. (MPa)	U.T.S. 5% min. (MPa)	Elong. (%)	% R.A.
92A022-1B3 COLD CROSS ROLLED/ANNEALED							
0.10 cm	298	L	362.1	393.8	419.6	15.9	48.1
	298	T	346.2	386.5	415.1	15.8	**
	422	L	284.6	325.2	349.3	7.9	31.8
	422	T	244.6	328.3	352.8	8.0	**
	505	L	197.1	226.3	259.1	16.9	26.1
	505	T	201.7	243.2	276.4	14.1	**
	589	L	117.8	171.1	188.6	21.2	26.2
	589	T	111.3	159.2	193.7	24.4	**
	298E*	L	394.8	482.3	501.6	8.2	41.8
	298E*	T	422.4	467.8	481.6	4.9	**
92A022-2C3 COLD STRAIGHT ROLLED/ANNEALED							
0.10 cm	298	L	374.8	387.9	412.0	17.4	**
	298	T	335.5	388.6	415.1	16.6	**
	422	L	298.2	340.1	365.3	5.9	**
	422	T	280.8	348.0	362.1	6.2	**
	505	L	210.8	250.0	281.6	15.3	**
	505	T	205.3	249.4	283.9	13.4	**
	589	L	107.6	149.7	183.8	25.1	**
	589	T	109.6	155.8	189.5	23.2	**
	298E*	L	384.5	459.6	482.3	8.8	**
	298E*	T	413.4	480.2	493.3	4.8	**

* Samples tested at 298K after 644K for 100 hrs. exposure

** Not Measured

Table 6b

Sample ID#	Temp. (°F)	Orient.	0.2% Y.S. (ksi)	U.T.S. 0.5% /min. (ksi)	U.T.S. 5% /min. (ksi)	Elong. (%)	% R.A.
92A022-1B3 COLD CROSS ROLLED/ANNEALED							
0.040" Gauge	77	L	52.6	57.2	60.9	15.9	48.1
	77	T	50.3	56.1	60.3	15.8	**
	300	L	41.3	47.2	50.7	7.9	31.8
	300	T	35.5	47.7	51.2	8.0	**
	450	L	28.6	32.9	37.6	16.9	26.1
	450	T	29.3	35.3	40.1	14.1	**
	600	L	17.1	24.8	27.4	21.2	26.2
	600	T	16.2	23.1	28.1	24.4	**
	77E*	L	57.3	70.0	72.8	8.2	41.8
	77E*	T	61.3	67.9	69.9	4.9	**
92A022-2C3 COLD STRAIGHT ROLLED/ANNEALED							
0.040" Gauge	77	L	54.4	56.3	59.8	17.4	**
	77	T	48.7	56.4	60.3	16.6	**
	300	L	43.3	49.4	53.0	5.9	**
	300	T	40.8	50.5	52.6	6.2	**
	450	L	30.6	36.3	40.9	15.3	**
	450	T	29.8	36.2	41.2	13.4	**
	600	L	15.6	21.7	26.7	25.1	**
	600	T	15.9	22.6	27.5	23.2	**
	77E*	L	55.8	66.7	70.0	8.8	**
	77E*	T	60.0	69.7	71.6	4.8	**

* Samples tested at 77°F after 700°F for 100 hrs. exposure

** Not Measured

Table 7a

Sample ID#	Temp (K)	Orient.	0.2% Y.S. (MPa)	U.T.S. 0.5% /min. (MPa)	U.T.S. 5% /min. (MPa)	Elong. (%)	% R.A.
92A024-1C HOT CROSS ROLLED							
0.64 cm	298	L	411.3	437.2	449.6	13.2	49.5
		T	411.0	423.7	443.0	13.8	**
	422	L	328.9	354.1	372.1	7.4	28.7
		T	330.7	344.5	362.4	6.0	**
	505	L	280.4	301.6	301.6	13.4	30.4
		T	277.9	289.9	303.6	12.5	**
	589	L	178.5	201.3	214.7	22.8	31.0
		T	169.8	184.0	210.1	21.7	**
	298E*	L	404.9	437.5	457.5	16.4	49.6
		T	409.7	438.2	458.9	11.3	**
92A024-1A HOT STRAIGHT ROLLED							
0.64 cm	298	L	407.9	437.9	456.5	16.6	**
		T	396.2	434.1	453.0	11.0	**
	422	L	312.7	360.3	376.9	6.5	**
		T	321.9	350.4	367.9	7.9	**
	505	L	265.9	273.8	301.6	13.2	**
		T	290.1	312.7	312.7	10.1	**
	589	L	113.8	186.2	196.6	23.6	**
		T	162.8	183.6	210.5	20.9	**
	298E*	L	414.2	434.8	454.4	15.1	**
		T	428.8	449.0	469.2	10.3	**
92A024-1D HOT CROSS ROLLED							
0.23 cm	298	L	408.6	429.2	456.8	8.9	44.6
		T	421.0	432.7	461.6	9.4	**
	422	L	335.3	354.8	371.2	7.7	34.3
		T	308.7	351.4	365.2	8.9	**
	505	L	207.5	280.4	308.2	13.0	32.2
		T	189.1	271.3	298.7	8.5	**
	589	L	114.9	188.3	215.5	19.9	36.9
		T	172.5	201.8	215.9	20.9	**
	298E*	L	404.2	443.7	465.1	10.3	35.1
		T	396.9	450.6	473.3	8.3	**
92A024-1B HOT STRAIGHT ROLLED							
0.23 cm	298	L	414.8	437.5	457.2	10.1	**
		T	404.8	442.3	459.2	8.2	**
	422	L	327.3	355.0	369.9	4.9	**
		T	322.2	352.1	367.2	3.3	**
	505	L	240.5	278.0	292.8	16.2	**
		T	242.6	286.3	315.5	9.5	**
	589	L	169.9	204.8	219.9	22.7	**
		T	113.2	209.0	223.9	17.4	**
	298E*	L	442.3	445.8	468.5	11.5	**
		T	435.5	461.6	473.3	13.1	**

* Samples tested at 298K after 644K for 100 hrs. exposure

** Not Measured

Table 7b

Sample ID#	Temp (°F)	Orient.	0.2% Y.S. (ksi)	U.T.S. 0.5% /min. (ksi)	U.T.S. 5% /min. (ksi)	Elong. (%)	%R.A.
92A024-1C HOT CROSS ROLLED							
0.25" Gauge	77	L	59.7	63.5	65.3	13.2	49.5
	77	T	59.7	61.5	64.3	13.8	**
	300	L	47.7	51.4	54.0	7.4	28.7
	300	T	48.0	50.0	52.6	6.0	**
	450	L	40.7	43.8	43.8	13.4	30.4
	450	T	40.3	42.1	44.1	12.5	**
	600	L	25.9	29.2	31.2	22.8	31.0
	600	T	24.6	26.7	30.5	21.7	**
	77E*	L	58.8	63.5	66.4	16.4	49.6
		T	59.5	63.6	66.6	11.3	**
92A024-1A HOT STRAIGHT ROLLED							
0.25" Gauge	77	L	59.2	63.6	66.3	16.6	**
		T	57.5	63.0	65.8	11.0	**
	300	L	45.4	52.3	54.7	6.5	**
		T	46.7	50.9	53.4	7.9	**
	450	L	38.6	39.7	43.8	13.2	**
		T	42.1	45.4	45.4	10.1	**
	600	L	16.5	27.0	28.5	23.6	**
		T	23.6	26.7	30.6	20.9	**
	77E*	L	60.1	63.1	66.0	15.1	**
		T	62.2	65.2	68.1	10.3	**
92A024-1D HOT CROSS ROLLED							
0.09" Gauge	77	L	59.3	62.3	66.3	8.9	44.6
		T	61.1	62.8	67.0	9.4	**
	300	L	48.7	51.5	53.9	7.7	34.3
		T	44.8	51.0	53.0	8.9	**
	450	L	30.1	40.7	44.7	13.0	32.2
		T	27.4	39.4	43.4	8.5	**
	600	L	16.7	27.3	31.3	19.9	36.9
		T	25.0	29.3	31.3	20.9	**
	77E*	L	58.7	64.4	67.5	10.3	35.1
		T	57.6	65.4	68.7	8.3	**
92A024-1B HOT STRAIGHT ROLLED							
0.09" Gauge	77	L	60.2	63.5	66.4	10.1	**
		T	58.8	64.2	66.7	8.2	**
	300	L	47.5	51.5	53.7	4.9	**
		T	46.8	51.1	53.3	3.3	**
	450	L	34.9	40.4	42.5	16.2	**
		T	35.2	41.6	45.8	9.5	**
	600	L	24.7	29.7	31.9	22.7	**
		T	16.4	30.3	32.5	17.4	**
	77E*	L	64.2	64.7	68.0	11.5	**
		T	63.2	67.0	68.7	13.1	**

* Samples tested at 77°F after 700°F for 100 hrs. exposure

** Not Measured

Table 8a

Sample ID#	Temp (K)	Orient	0.2% Y.S. (MPa)	U.T.S. 0.5% /min. (MPa)	U.T.S. 5% /min. (MPa)	Elong (%)	% R.A.
92A024-2B1 HOT CROSS ROLLED							
0.076 cm	298	L	360.7	442.0	463.4	7.7	45.7
		T	381.0	442.0	464.4	7.0	**
	422	L	334.9	370.0	379.6	2.2	26.9
		T	323.1	363.8	381.0	2.7	**
	505	L	158.3	268.5	296.2	8.7	27.9
		T	247.4	264.5	293.9	9.3	**
	589	L	151.1	196.3	227.9	22.2	34.4
		T	141.9	187.4	218.6	17.0	**
	298E*	L	386.5	427.9	449.2	4.6	28.9
		T	387.9	429.9	453.4	5.1	**
92A024-2A1 HOT STRAIGHT ROLLED							
0.10 cm	298	L	323.1	430.6	451.3	4.1	**
		T	376.2	439.2	479.5	3.9	**
	422	L	312.1	350.0	359.0	8.3	**
		T	321.8	362.4	369.3	11.0	**
	505	L	199.3	251.2	266.2	13.7	**
		T	217.0	249.3	280.0	6.2	**
	589	L	145.7	182.8	213.7	21.4	**
		T	147.9	198.8	215.5	26.0	**
	298E*	L	458.2	469.9	479.5	3.2	**
		T	454.1	468.5	479.5	2.8	**
92A024-2B2 COLD CROSS ROLLED							
0.10 cm	298	L	366.5	407.5	434.8	17.9	44.8
		T	357.9	404.8	430.6	12.2	**
	422	L	277.7	344.8	369.2	4.8	31.9
		T	281.1	343.8	369.7	4.6	**
	505	L	240.7	283.0	317.9	17.3	36.0
		T	212.8	261.5	295.4	17.1	**
	589	L	124.6	167.8	203.0	27.2	24.4
		T	143.4	192.6	209.9	24.9	**
	298E*	L	424.4	476.8	489.9	5.1	29.1
		T	434.1	480.2	493.3	4.8	**
2A024-2A2 COLD STRAIGHT ROLLED							
0.10 cm	298	L	354.8	424.4	424.4	16.7	**
		T	331.4	419.9	433.7	16.8	**
	422	L	291.4	353.5	373.4	6.8	**
		T	304.5	352.1	371.4	5.4	**
	505	L	224.6	251.7	287.2	12.8	**
		T	206.7	250.8	286.8	11.7	**
	589	L	132.3	174.2	208.1	22.3	**
		T	141.2	183.1	199.9	20.9	**
	298E*	L	429.9	485.1	500.9	5.2	**
		T	434.1	483.0	496.8	5.0	**

* Samples tested at 298K after 644K for 100 hrs. exposure

** Not Measured

Table 8b

Sample ID#	Temp (°F)	Orient.	0.2% Y.S. (ksi)	U.T.S. 0.5% /min. (ksi)	U.T.S. 5% /min. (ksi)	Elong. (%)	% R.A.
92A024-2B1 HOT CROSS ROLLED							
0.03" Gauge	77	L	52.4	64.2	67.3	7.7	45.7
		T	55.3	64.2	67.4	7.0	**
	300	L	48.6	53.7	55.1	2.2	26.9
		T	46.9	52.8	55.3	2.7	**
	450	L	23.0	39.0	43.0	8.7	27.9
		T	35.9	38.4	42.7	9.3	**
	600	L	21.9	28.5	33.1	22.2	34.4
		T	20.6	27.2	31.7	17.0	**
	77E*	L	56.1	62.1	65.2	4.6	28.9
		T	56.3	62.4	65.8	5.1	**
92A024-2A1 HOT STRAIGHT ROLLED							
0.04" Gauge	77	L	46.9	62.5	65.5	4.1	**
		T	54.6	63.8	69.6	3.9	**
	300	L	45.3	50.8	52.1	8.3	**
		T	46.7	52.6	53.6	11.0	**
	450	L	28.9	36.5	38.6	13.7	**
		T	31.5	36.2	40.6	6.2	**
	600	L	21.2	26.5	31.0	21.4	**
		T	21.5	28.9	31.3	26.0	**
	77E*	L	66.5	68.2	69.6	3.2	**
		T	65.9	68.0	69.6	2.8	**
92A024-2B2 COLD CROSS ROLLED							
0.04" Gauge	77	L	53.2	59.2	63.1	17.9	44.8
		T	52.0	58.8	62.5	12.2	**
	300	L	40.3	50.1	53.6	4.8	31.9
		T	40.8	49.9	53.7	4.6	**
	450	L	34.9	41.1	46.1	17.3	36.0
		T	30.9	38.0	42.9	17.1	**
	600	L	18.1	24.4	29.5	27.2	24.4
		T	20.8	28.0	30.5	24.9	**
	77E*	L	61.6	69.2	71.1	5.1	29.1
		T	63.0	69.7	71.6	4.8	**
2A024-2A2 COLD STRAIGHT ROLLED							
0.04" Gauge	77	L	51.5	61.6	61.6	16.7	**
		T	48.1	61.0	63.0	16.8	**
	300	L	42.3	51.3	54.2	6.8	**
		T	44.2	51.1	53.9	5.4	**
	450	L	32.6	36.5	41.7	12.8	**
		T	30.0	36.4	41.6	11.7	**
	600	L	19.2	25.3	30.2	22.3	**
		T	20.5	26.6	29.0	20.9	**
	77E*	L	62.4	70.4	72.7	5.2	**
		T	63.0	70.1	72.1	5.0	**

* Samples tested at 77°F after 700°F for 100 hrs. exposure

** Not Measured

Table 9a

Sample ID#	Test Temp (K)	Orient.	0.2% Y.S. (MPa)	U.T.S. 0.5% /min. (MPa)	U.T.S. 5% /min. (MPa)	Elong. (%)	% R.A.
92A024-2B3 COLD CROSS ROLLED/ANNEALED							
0.10 cm	298	L	328.0	382.7	406.9	16.3	42.3
		T	321.8	384.1	405.5	13.8	**
	422	L	296.3	338.6	362.9	4.4	32.8
		T	301.8	338.8	364.1	4.4	**
	505	L	199.1	246.2	281.9	17.6	29.9
		T	185.8	246.6	279.4	16.7	**
	589	L	121.3	170.5	206.5	21.9	19.5
		T	119.3	169.6	205.7	20.1	**
	298E*	L	381.7	467.8	480.9	2.0	36.6
		T	411.3	475.4	493.3	2.3	**
92A024-2A3 COLD STRAIGHT ROLLED/ANNEALED							
0.10 cm	298	L	355.5	385.5	411.7	16.8	**
		T	359.0	388.3	407.9	14.0	**
	422	L	283.2	328.2	352.3	5.78	**
		T	293.5	316.8	340.5	5.94	**
	505	L	222.5	257.0	289.0	16.4	**
		T	207.4	243.0	276.7	11.3	**
	589	L	114.4	183.8	200.2	22.8	**
		T	117.8	166.7	200.4	21.2	**
	298E*	L	462.3	479.5	492.6	2.0	**
		T	443.0	486.4	498.1	3.1	**

* Samples tested at 298K after 644K for 100 hrs. exposure

** Not Measured

Table 9b

Sample ID#	Temp (°F)	Orient.	0.2% Y.S. (ksi)	U.T.S. 0.5% /min. (ksi)	U.T.S. 5% /min. (ksi)	Elong. (%)	% R.A.
92A024-2B3 COLD CROSS ROLLED/ANNEALED							
0.040" Gauge	77	L	47.6	55.6	59.1	16.3	42.3
		T	46.7	55.8	58.9	13.8	**
	300	L	43.0	49.2	52.7	4.4	32.8
		T	43.8	49.2	52.9	4.4	**
	450	L	28.9	35.7	40.9	17.6	29.9
		T	27.0	35.8	40.6	16.7	**
	600	L	17.6	24.8	30.0	21.9	19.5
		T	17.3	24.6	29.9	20.1	**
	77E*	L	55.4	67.9	69.8	2.0	36.6
		T	59.7	69.0	71.6	2.3	**
92A024-2A3 COLD STRAIGHT ROLLED/ANNEALED							
0.040" Gauge	77	L	51.6	56.0	59.8	16.8	**
		T	52.1	56.4	59.2	14.0	**
	300	L	41.1	47.6	51.1	5.78	**
		T	42.6	46.0	49.4	5.94	**
	450	L	32.3	37.3	41.9	16.4	**
		T	30.1	35.3	40.2	11.3	**
	600	L	16.6	26.7	29.1	22.8	**
		T	17.1	24.2	29.1	21.2	**
	77E*	L	67.1	69.6	71.5	2.0	**
		T	64.3	70.6	72.3	3.1	**

* Samples tested at 77°F after 700°F for 100 hrs. exposure

** Not Measured

Table 10a

Sample ID#	Temp (K)	Orient.	U.T.S. 0.5% /min. (MPa)	U.T.S. 5% /min. (MPa)	U.T.S. 50% /min. (MPa)	Elong. 5% /min (%)	Elong. 50% /min. (%)
92A024-1C HOT CROSS ROLLED							
0.64 cm	298	L	437.2	449.6	456.8	13.2	17.6
		T	423.7	443.0	465.8	13.8	17.6
	422	L	354.1	372.1	**	7.4	**
		T	344.5	362.4	**	6.0	**
	505	L	301.6	301.6	**	13.4	**
		T	289.9	303.6	**	12.5	**
	589	L	201.3	214.7	**	22.8	**
		T	184.0	210.1	**	21.7	**
	298E*	L	437.5	457.5	**	16.4	**
		T	438.2	458.9	**	11.3	**
92A024-1A HOT STRAIGHT ROLLED							
0.64 cm	298	L	437.9	456.5	456.8	16.6	21.9
		T	434.1	453.0	478.2	11.0	19.0
	422	L	360.3	376.9	**	6.5	**
		T	350.4	367.9	**	7.9	**
	505	L	273.8	301.6	**	13.2	**
		T	312.7	312.7	**	10.1	**
	589	L	186.2	196.6	**	23.6	**
		T	183.6	210.5	**	20.9	**
	298E*	L	434.8	454.4	**	15.1	**
		T	449.0	469.2	**	10.3	**
92A024-1D HOT CROSS ROLLED							
0.23 cm	298	L	429.2	456.8	494.7	8.9	11.7
		T	432.7	461.6	498.8	9.4	8.6
	422	L	354.8	371.2	**	7.7	**
		T	351.4	365.2	**	8.9	**
	505	L	280.4	308.2	**	13.0	**
		T	271.3	298.7	**	8.5	**
	589	L	188.3	215.5	**	19.9	**
		T	201.8	215.9	**	20.9	**
	298E*	L	443.7	465.1	**	10.3	**
		T	450.6	473.3	**	8.3	**
92A024-1B HOT STRAIGHT ROLLED							
0.23 cm	298	L	437.5	457.2	487.1	10.1	11.8
		T	442.3	459.2	482.3	8.2	10.2
	422	L	355.0	369.9	**	4.9	**
		T	352.1	367.2	**	3.3	**
	505	L	278.0	292.8	**	16.2	**
		T	286.3	315.5	**	9.5	**
	589	L	204.8	219.9	**	22.7	**
		T	209.0	223.9	**	17.4	**
	298E*	L	445.8	468.5	**	11.5	**
		T	461.6	473.3	**	13.1	**

* Samples tested at 298K after 644K for 100 hrs. exposure

** Not Measured

Table 10b

Sample ID#	Temp (°F)	Orient.	U.T.S. 0.5% /min. (ksi)	U.T.S. 5% /min. (ksi)	U.T.S. 50% /min (ksi)	Elong. 5% /min (%)	Elong. 50% /min (%)
92A024-1C HOT CROSS ROLLED							
0.25" Gauge	77	L	63.5	65.3	66.3	13.2	17.6
	77	T	61.5	64.3	67.6	13.8	17.6
	300	L	51.4	54.0	**	7.4	**
	300	T	50.0	52.6	**	6.0	**
	450	L	43.8	43.8	**	13.4	**
	450	T	42.1	44.1	**	12.5	**
	600	L	29.2	31.2	**	22.8	**
	600	T	26.7	30.5	**	21.7	**
	77E*	L	63.5	66.4	**	16.4	**
		T	63.6	66.6	**	11.3	**
92A024-1A HOT STRAIGHT ROLLED							
0.25" Gauge	77	L	63.6	66.3	66.3	16.6	21.9
		T	63.0	65.8	69.4	11.0	19.0
	300	L	52.3	54.7	**	6.5	**
		T	50.9	53.4	**	7.9	**
	450	L	39.7	43.8	**	13.2	**
		T	45.4	45.4	**	10.1	**
	600	L	27.0	28.5	**	23.6	**
		T	26.7	30.6	**	20.9	**
	77E*	L	63.1	66.0	**	15.1	**
		T	65.2	68.1	**	10.3	**
92A024-1D HOT CROSS ROLLED							
0.09" Gauge	77	L	62.3	66.3	71.8	8.9	11.7
		T	62.8	67.0	72.4	9.4	8.6
	300	L	51.5	53.9	**	7.7	**
		T	51.0	53.0	**	8.9	**
	450	L	40.7	44.7	**	13.0	**
		T	39.4	43.4	**	8.5	**
	600	L	27.3	31.3	**	19.9	**
		T	29.3	31.3	**	20.9	**
	77E*	L	64.4	67.5	**	10.3	**
		T	65.4	68.7	**	8.3	**
92A024-1B HOT STRAIGHT ROLLED							
0.09" Gauge	77	L	63.5	66.4	70.7	10.1	11.8
		T	64.2	66.7	70.0	8.2	10.2
	300	L	51.5	53.7	**	4.9	**
		T	51.1	53.3	**	3.3	**
	450	L	40.4	42.5	**	16.2	**
		T	41.6	45.8	**	9.5	**
	600	L	29.7	31.9	**	22.7	**
		T	30.3	32.5	**	17.4	**
	77E*	L	64.7	68.0	**	11.5	**
		T	67.0	68.7	**	13.1	**

* Samples tested at 77°F after 700°F for 100 hrs. exposure

** Not Measured

Table 11a

Sample ID#	Temp (K)	Orient.	U.T.S. 0.5% /min. (MPa)	U.T.S. 5% /min. (MPa)	U.T.S. 50% /min. (MPa)	Elong. 5% /min (%)	Elong. 50% /min (%)
92A024-2B1 HOT CROSS ROLLED							
0.076 cm	298	L	442.0	463.4	429.2	7.7	13.0
		T	442.0	464.4	464.4	7.0	9.0
	422	L	370.0	379.6	**	2.2	**
		T	363.8	381.0	**	2.7	**
	505	L	268.5	296.2	**	8.7	**
		T	264.5	293.9	**	9.3	**
	589	L	196.3	227.9	**	22.2	**
		T	187.4	218.6	**	17.0	**
	298E*	L	427.9	449.2	**	4.6	**
		T	429.9	453.4	**	5.1	**
92A024-2A1 HOT STRAIGHT ROLLED							
0.10 cm	298	L	430.6	451.3	456.1	4.1	1.9
		T	439.2	479.5	438.9	3.9	3.9
	422	L	350.0	359.0	**	8.3	**
		T	362.4	369.3	**	11.0	**
	505	L	251.2	266.2	**	13.7	**
		T	249.3	280.0	**	6.2	**
	589	L	182.8	213.7	**	21.4	**
		T	198.8	215.5	**	26.0	**
	298E*	L	469.9	479.5	**	3.2	**
		T	468.5	479.5	**	2.8	**
92A024-2B2 COLD CROSS ROLLED							
0.10 cm	298	L	407.5	434.8	436.1	17.9	16.9
		T	404.8	430.6	467.8	12.2	13.0
	422	L	344.8	369.2	**	4.8	**
		T	343.8	369.7	**	4.6	**
	505	L	283.0	317.9	**	17.3	**
		T	261.5	295.4	**	17.1	**
	589	L	167.8	203.0	**	27.2	**
		T	192.6	209.9	**	24.9	**
	298E*	L	476.8	489.9	**	5.1	**
		T	480.2	493.3	**	4.8	**
2A024-2A2 COLD STRAIGHT ROLLED							
0.10 cm	298	L	424.4	424.4	436.8	16.7	17.0
		T	419.9	433.7	468.5	16.8	17.2
	422	L	353.5	373.4	**	6.8	**
		T	352.1	371.4	**	5.4	**
	505	L	251.7	287.2	**	12.8	**
		T	250.8	286.8	**	11.7	**
	589	L	174.2	208.1	**	22.3	**
		T	183.1	199.9	**	20.9	**
	298E*	L	485.1	500.9	**	5.2	**
		T	483.0	496.8	**	5.0	**

* Samples tested at 298K after 644K for 100 hrs. exposure

** Not Measured

Table 11b

Sample ID#	Temp (°F)	Orient.	U.T.S. 0.5% /min. (ksi)	U.T.S. 5% /min. (ksi)	U.T.S. 50% /min (ksi)	Elong. 5% /min (%)	Elong. 50% /min (%)
92A024-2B1 HOT CROSS ROLLED							
0.03" Gauge	77	L	64.2	67.3	62.3	7.7	13.0
		T	64.2	67.4	67.4	7.0	9.0
	300	L	53.7	55.1	**	2.2	**
		T	52.8	55.3	**	2.7	**
	450	L	39.0	43.0	**	8.7	**
		T	38.4	42.7	**	9.3	**
	600	L	28.5	33.1	**	22.2	**
		T	27.2	31.7	**	17.0	**
	77E*	L	62.1	65.2	**	4.6	**
		T	62.4	65.8	**	5.1	**
92A024-2A1 HOT STRAIGHT ROLLED							
0.04" Gauge	77	L	62.5	65.5	66.2	4.1	1.9
		T	63.8	69.6	63.7	3.9	3.9
	300	L	50.8	52.1	**	8.3	**
		T	52.6	53.6	**	11.0	**
	450	L	36.5	38.6	**	13.7	**
		T	36.2	40.6	**	6.2	**
	600	L	26.5	31.0	**	21.4	**
		T	28.9	31.3	**	26.0	**
	77E*	L	68.2	69.6	**	3.2	**
		T	68.0	69.6	**	2.8	**
92A024-2B2 COLD CROSS ROLLED							
0.04" Gauge	77	L	59.2	63.1	63.3	17.9	16.9
		T	58.8	62.5	67.9	12.2	13.0
	300	L	50.1	53.6	**	4.8	**
		T	49.9	53.7	**	4.6	**
	450	L	41.1	46.1	**	17.3	**
		T	38.0	42.9	**	17.1	**
	600	L	24.4	29.5	**	27.2	**
		T	28.0	30.5	**	24.9	**
	77E*	L	69.2	71.1	**	5.1	**
		T	69.7	71.6	**	4.8	**
2A024-2A2 COLD STRAIGHT ROLLED							
0.04" Gauge	77	L	61.6	61.6	63.4	16.7	17.0
		T	61.0	63.0	68.0	16.8	17.2
	300	L	51.3	54.2	**	6.8	**
		T	51.1	53.9	**	5.4	**
	450	L	36.5	41.7	**	12.8	**
		T	36.4	41.6	**	11.7	**
	600	L	25.3	30.2	**	22.3	**
		T	26.6	29.0	**	20.9	**
	77E*	L	70.4	72.7	**	5.2	**
		T	70.1	72.1	**	5.0	**

* Samples tested at 77°F after 700°F for 100 hrs. exposure

** Not Measured

Table 12a

Sample ID#	Temp (K)	Orient.	U.T.S. 0.5% /min. (MPa)	U.T.S. 5% /min. (MPa)	U.T.S. 50% /min (MPa)	Elong. 5%/min (%)	Elong. 50%/min (%)
92A024-2B3 COLD CROSS ROLLED/ANNEALED							
0.10 cm	298	L	382.7	406.9	405.1	16.3	20.0
		T	384.1	405.5	403.8	13.8	19.1
	422	L	338.6	362.9	**	4.4	**
		T	338.8	364.1	**	4.4	**
	505	L	246.2	281.9	**	17.6	**
		T	246.6	279.4	**	16.7	**
	589	L	170.5	206.5	**	21.9	**
		T	169.6	205.7	**	20.1	**
	298E*	L	467.8	480.9	**	2.0	**
		T	475.4	493.3	**	2.3	**
92A024-2A3 COLD STRAIGHT ROLLED/ANNEALED							
0.10 cm	298	L	385.5	411.7	434.8	16.8	16.4
		T	388.3	407.9	438.9	14.0	17.6
	422	L	328.2	352.3	**	5.78	**
		T	316.8	340.5	**	5.94	**
	505	L	257.0	289.0	**	16.4	**
		T	243.0	276.7	**	11.3	**
	589	L	183.8	200.2	**	22.8	**
		T	166.7	200.4	**	21.2	**
	298E*	L	479.5	492.6	**	2.0	**
		T	486.4	498.1	**	3.1	**

* Samples tested at 298K after 644K for 100 hrs. exposure

** Not Measured

Table 12b

Sample ID#	Temp (°F)	Orient.	U.T.S. 0.5% /min. (ksi)	U.T.S. 5% /min. (ksi)	U.T.S. 50% /min (ksi)	Elong. 5% /min (%)	Elong. 50% /min (%)
92A024-2B3 COLD CROSS ROLLED/ANNEALED							
0.040" Gauge	77	L	55.6	59.1	58.8	16.3	20.0
		T	55.8	58.9	58.6	13.8	19.1
	300	L	49.2	52.7	**	4.4	**
		T	49.2	52.9	**	4.4	**
	450	L	35.7	40.9	**	17.6	**
		T	35.8	40.6	**	16.7	**
	600	L	24.8	30.0	**	21.9	**
		T	24.6	29.9	**	20.1	**
	77E*	L	67.9	69.8	**	2.0	**
		T	69.0	71.6	**	2.3	**
92A024-2A3 COLD STRAIGHT ROLLED/ANNEALED							
0.040" Gauge	77	L	56.0	59.8	63.1	16.8	16.4
		T	56.4	59.2	63.7	14.0	17.6
	300	L	47.6	51.1	**	5.78	**
		T	46.0	49.4	**	5.94	**
	450	L	37.3	41.9	**	16.4	**
		T	35.3	40.2	**	11.3	**
	600	L	26.7	29.1	**	22.8	**
		T	24.2	29.1	**	21.2	**
	77E*	L	69.6	71.5	**	2.0	**
		T	70.6	72.3	**	3.1	**

* Samples tested at 77°F after 700°F for 100 hrs. exposure

** Not Measured

Table 13. Average Concentration of Si, Fe, and V Measured ny Energy Dispersive X-ray Spectroscopy in HTA 8009

Sample ID	Al	Si	V	Fe
Extruded	99.8 + 0.05	ND	0.1 + 0.04	0.1 + 0.02
Hot Rolled 0.64 cm (0.25") Plate	99.7 + 0.05	ND	0.18 + 0.04	0.13 + 0.02
Cold Rolled / Annealed 0.10 cm (0.040") Gauge Sheet	99.3 + 0.2	0.4 + 0.2	0.16 + 0.02	0.12 + 0.02

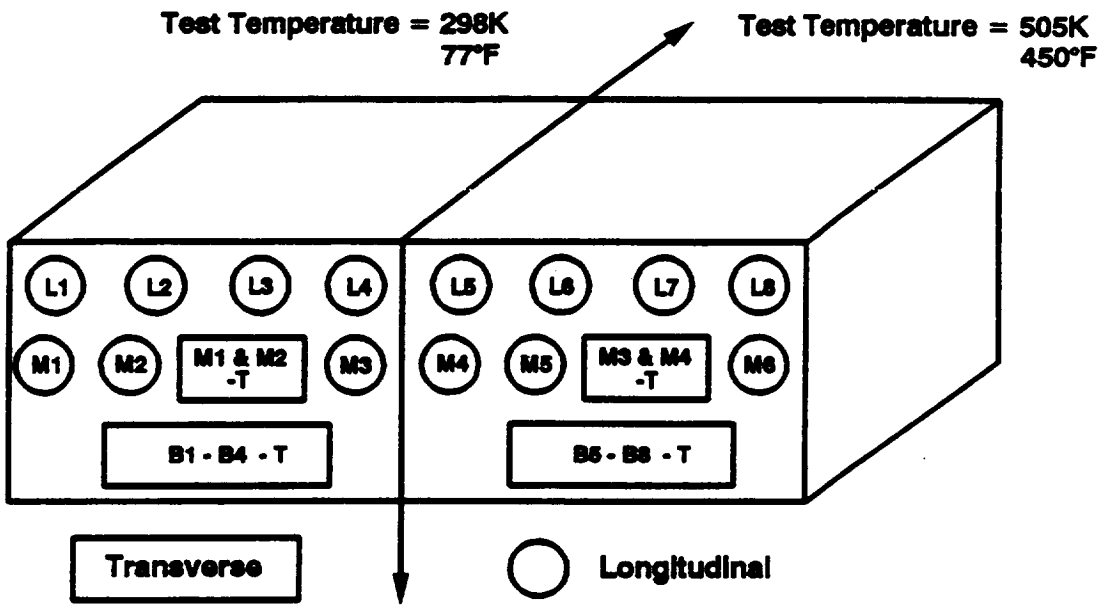

Fig. 1 Cut plan for specimens machined from the nose and tail of HTA 8009 extrusions 92A022 and 92A024.

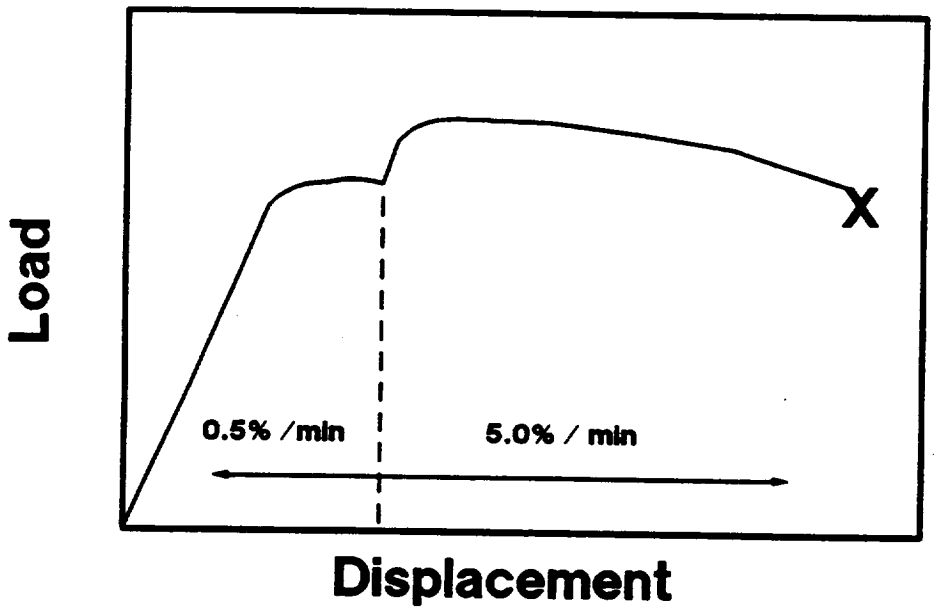

Fig. 2. Typical load-displacement curve for a tensile specimen tested in the present study. After the specimen experienced a maximum tensile stress, the strain rate was increased ten-fold from 0.5%/min to 5.0%/min and tested to failure.

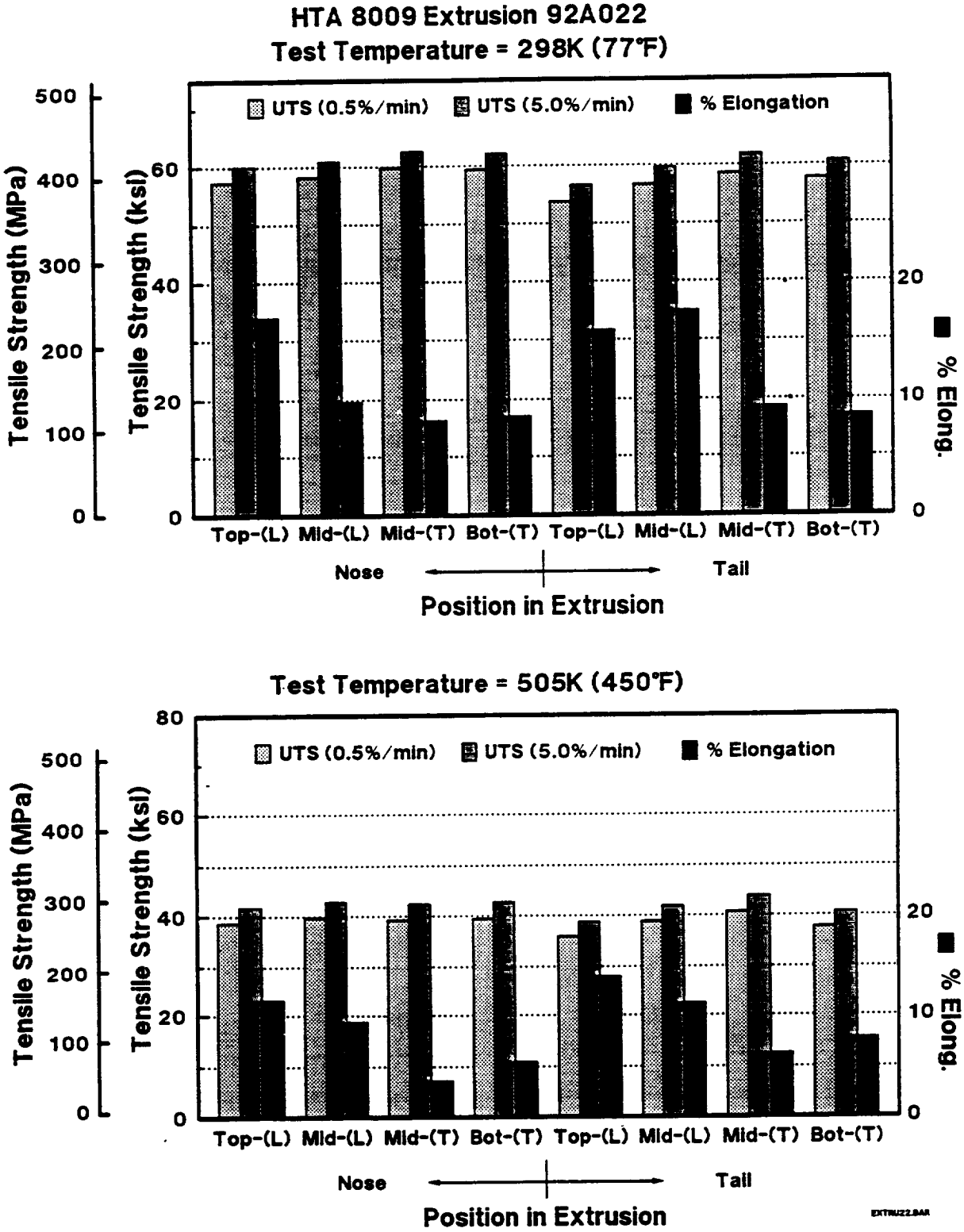

Fig. 3. Tensile strength and ductility as a function of position in HTA 8009 extrusion 92A022 at 298K (77°F) and 505K (450°F) for specimens machined from the nose and tail of the preforms.

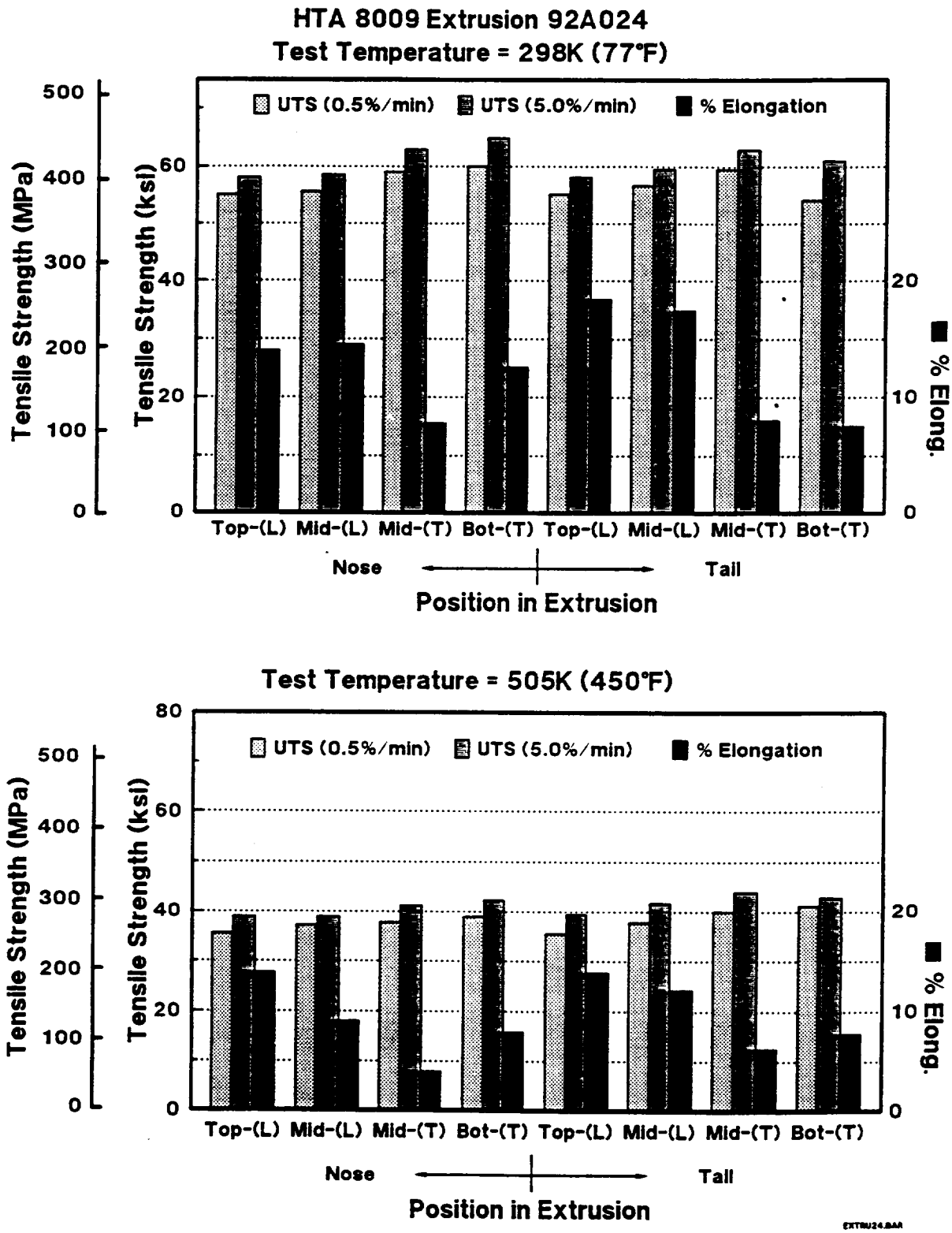

Fig. 4. Tensile strength and ductility as a function of position in HTA 8009 extrusion 92A024 at 298K (77°F) and 505K (450°F) for specimens machined from the nose and tail of the preforms.

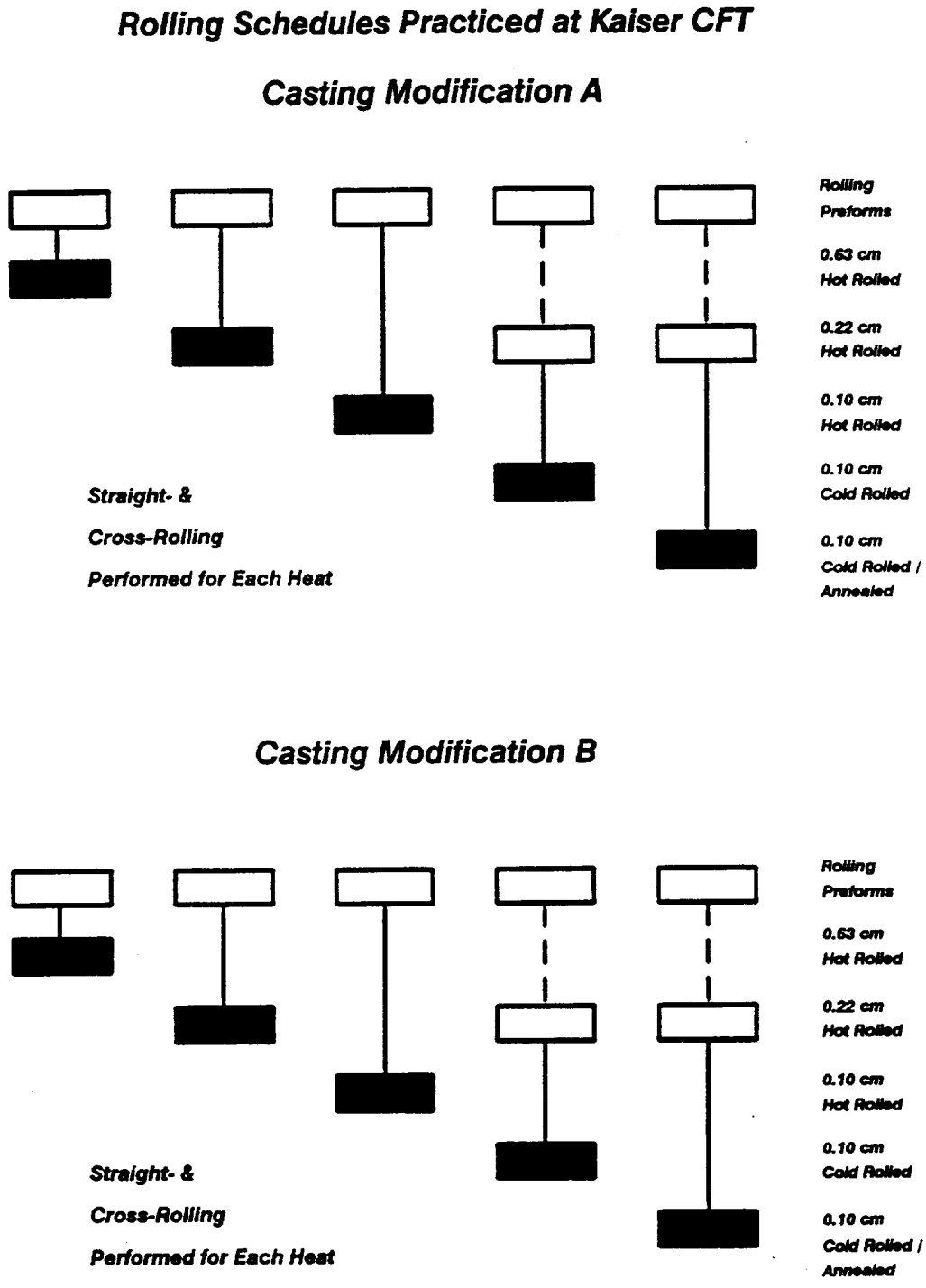

Figure 5. Pass schedules were designed to evaluate the effects of rolling direction and thermo-mechanical processing on ambient and elevated temperature mechanical properties of HTA 8009 plate and sheet.

Fig. 6

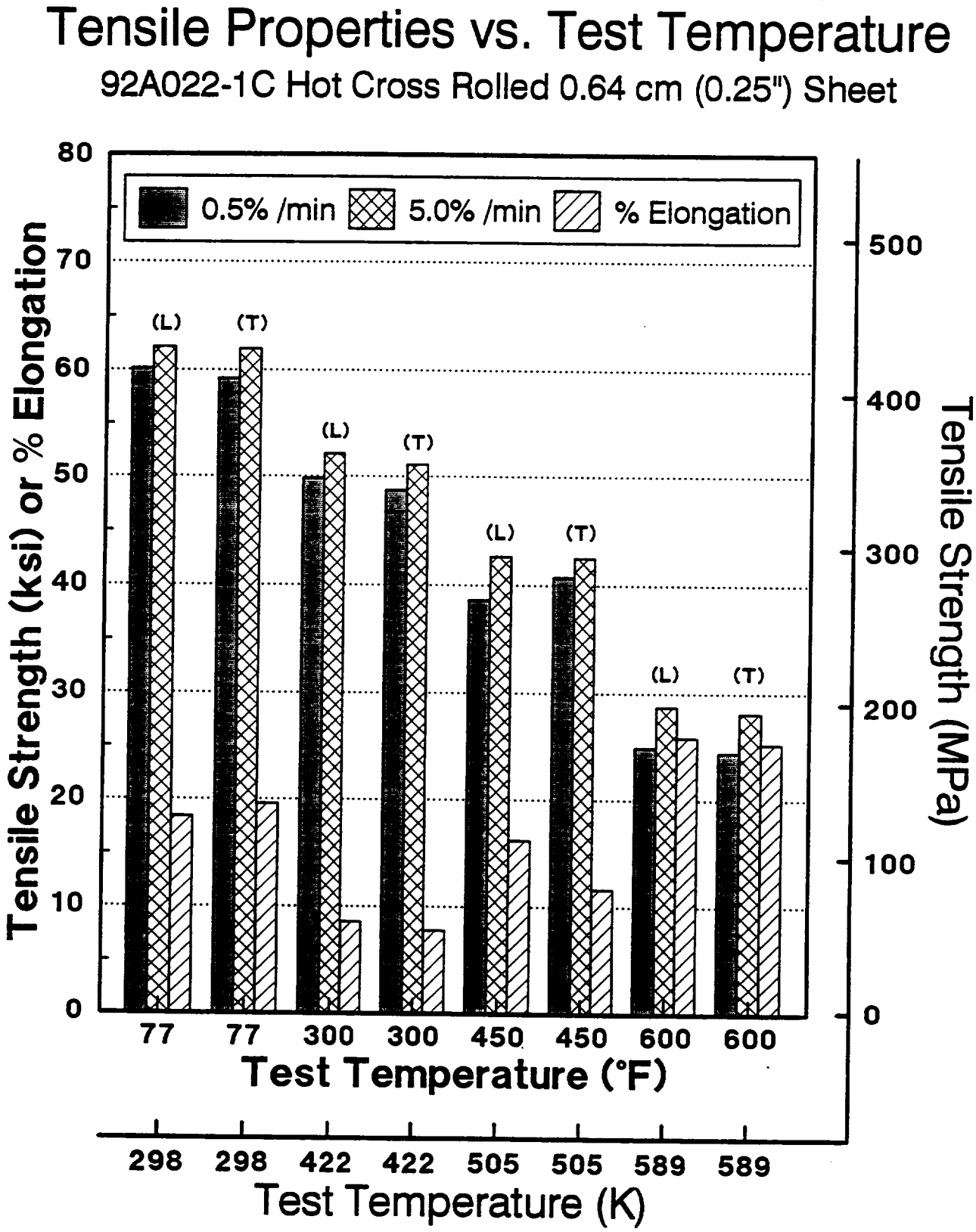
Tensile Properties vs. Test Temperature
92A022-1C Hot Cross Rolled 0.64 cm (0.25") Sheet
0.5% /min
5.0% /min
% Elongation
Tensile Strength (ksi) or % Elongation
Tensile Strength (MPa)
(L)
(T)
77
77
300
300
450
450
600
600
Test Temperature (°F)
298
298
422
422
505
505
589
589
Test Temperature (K)

Fig. 7

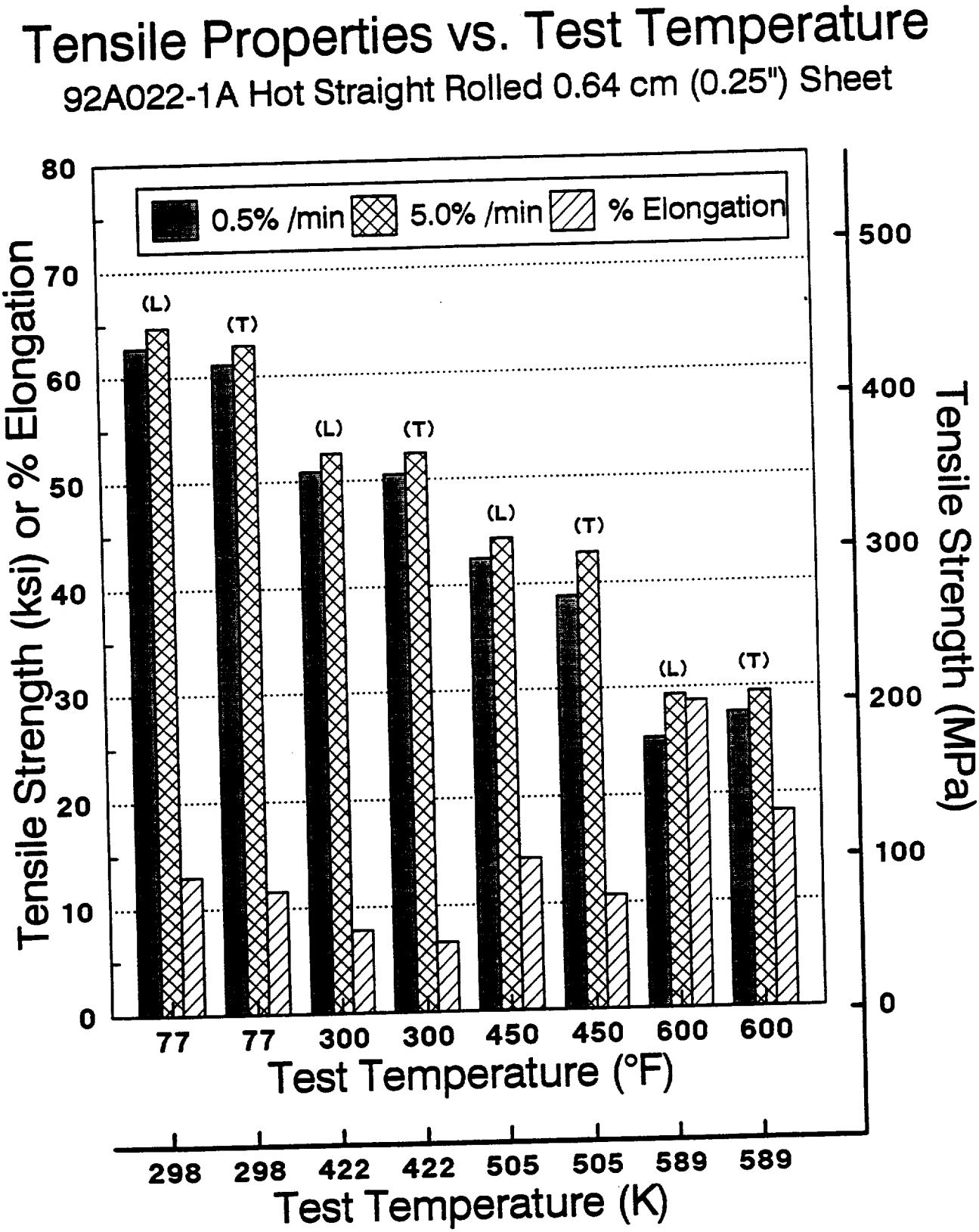
Tensile Properties vs. Test Temperature
92A022-1A Hot Straight Rolled 0.64 cm (0.25") Sheet
0.5% /min
5.0% /min
% Elongation
Tensile Strength (ksi) or % Elongation
Tensile Strength (MPa)
(L)
(T)
77
77
300
300
450
450
600
600
Test Temperature (°F)
298
298
422
422
505
505
589
589
Test Temperature (K)

Fig. 8

Tensile Properties vs. Test Temperature

0.64 cm (0.25") Hot Cross vs. Hot Straight Rolled Sheet

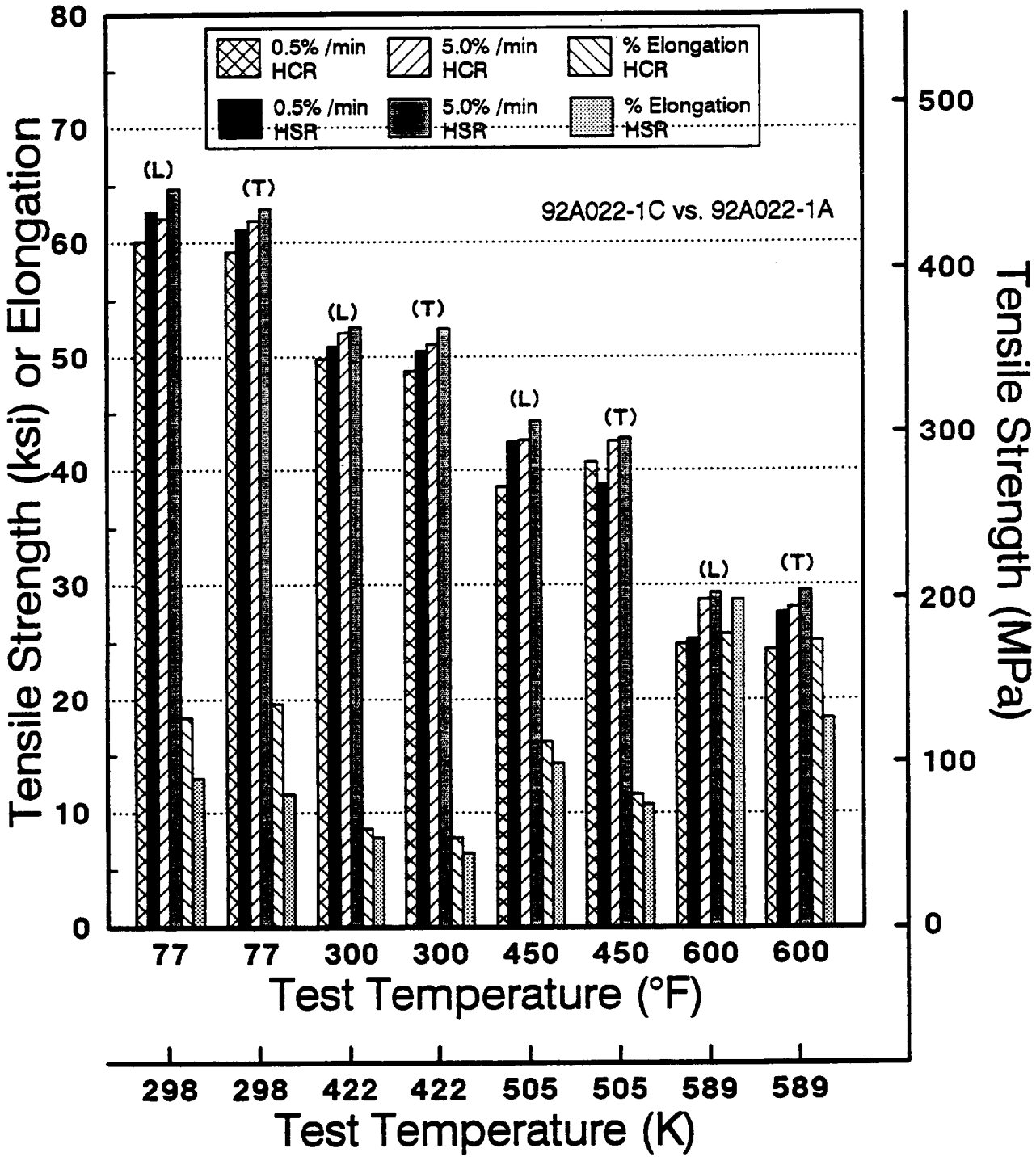

Fig. 9

Tensile Properties vs. Test Temperature

92A022-2A Hot Cross Rolled 0.25 cm (0.10") Sheet

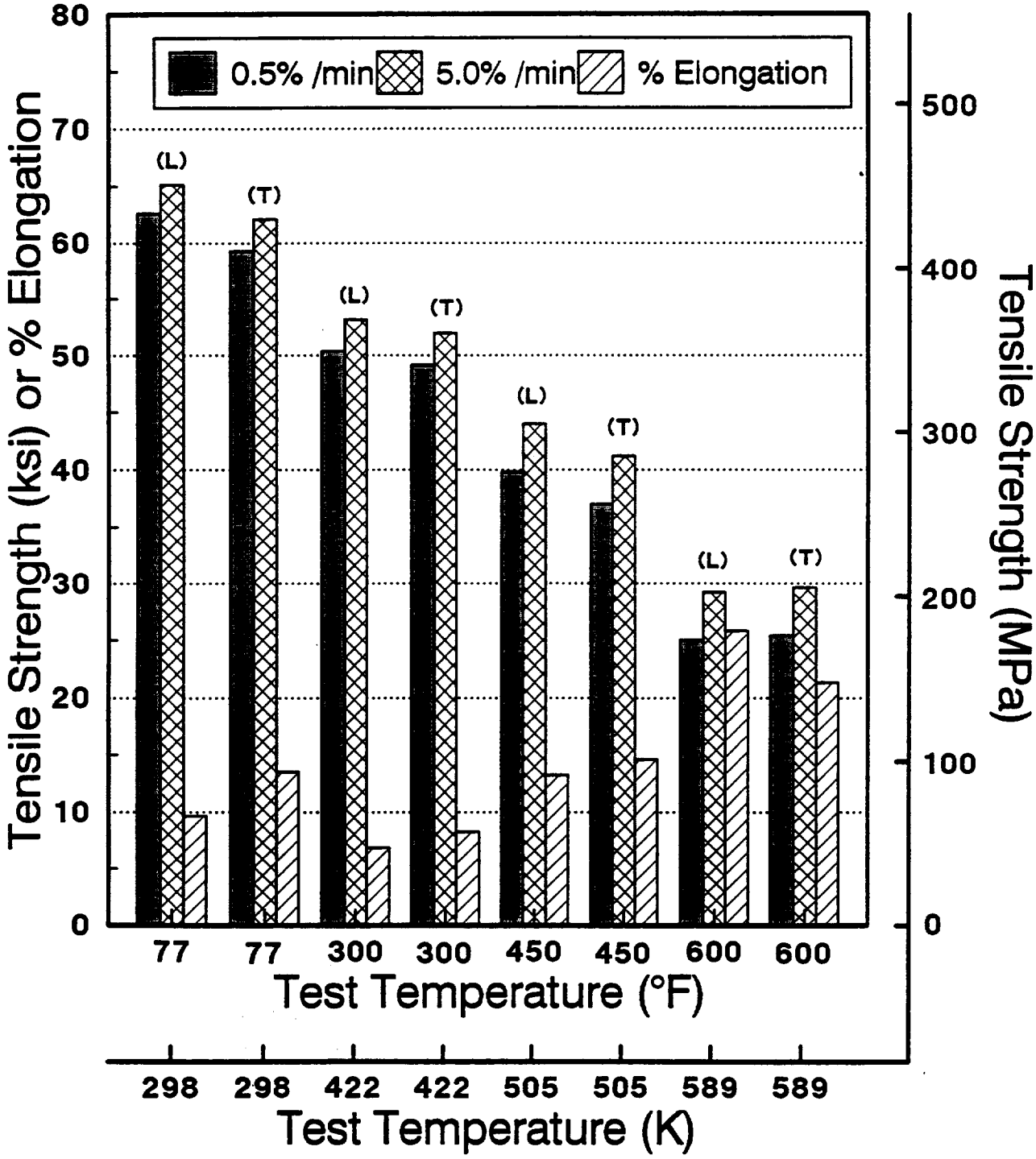

Fig. 10

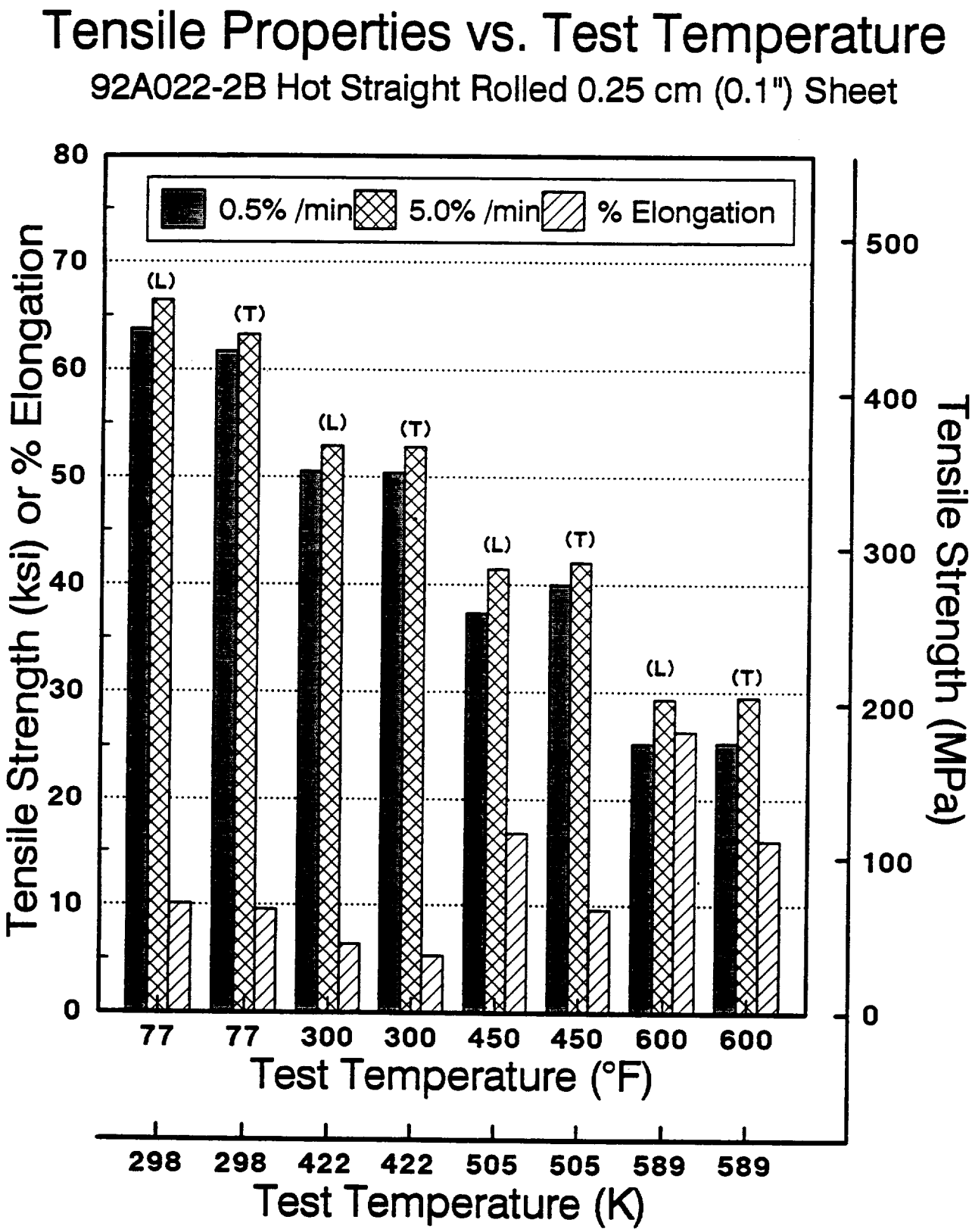
Tensile Properties vs. Test Temperature
92A022-2B Hot Straight Rolled 0.25 cm (0.1") Sheet
0.5% /min
5.0% /min
% Elongation
Tensile Strength (ksi) or % Elongation
Tensile Strength (MPa)
0
10
20
30
40
50
60
70
80
0
100
200
300
400
500
(L)
(T)
(L)
(T)
(L)
(T)
(L)
(T)
77 77 300 300 450 450 600 600
Test Temperature (°F)
298 298 422 422 505 505 589 589
Test Temperature (K)

Fig. 11

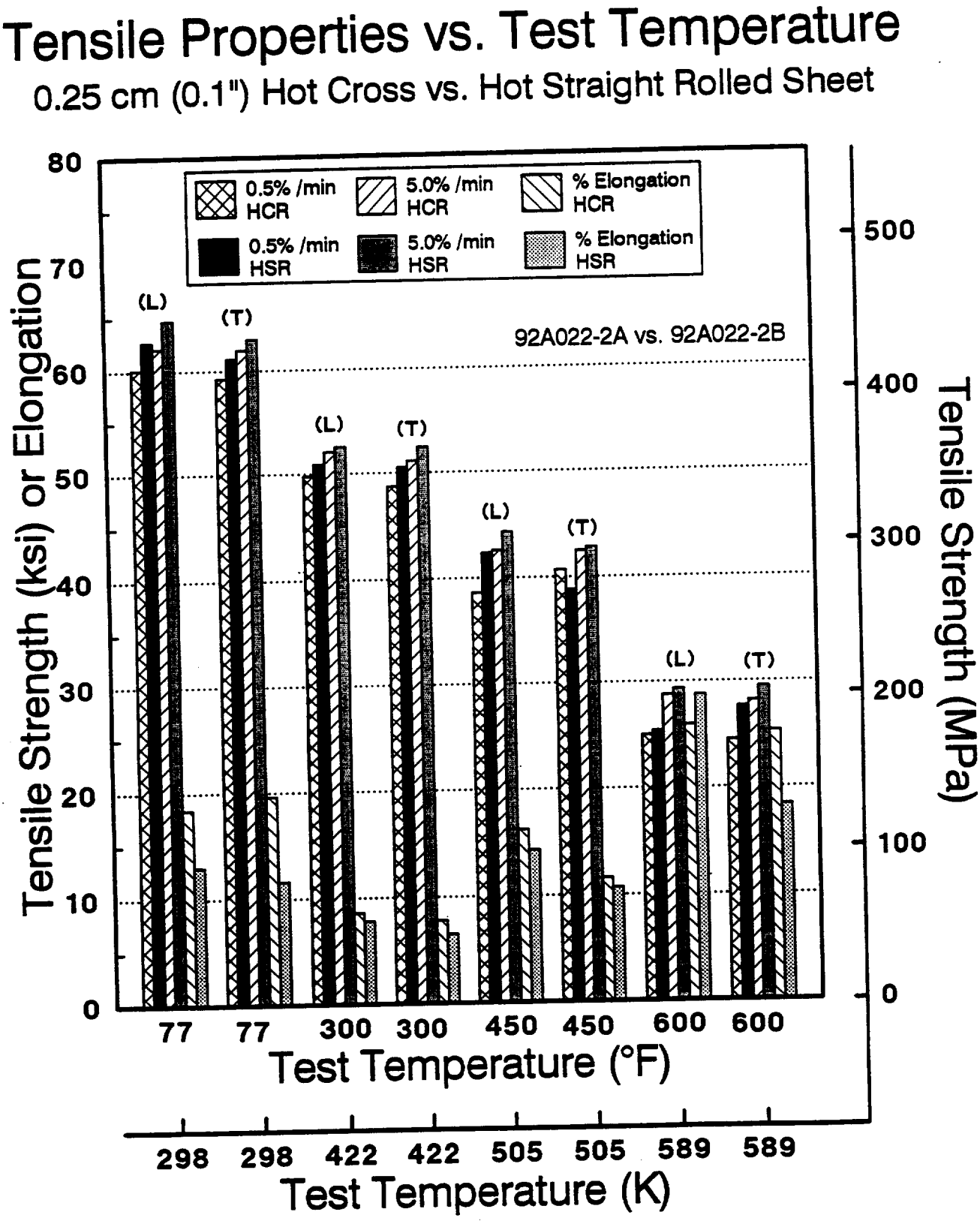
Tensile Properties vs. Test Temperature
0.25 cm (0.1") Hot Cross vs. Hot Straight Rolled Sheet
0.5% /min HCR
5.0% /min HCR
% Elongation HCR
0.5% /min HSR
5.0% /min HSR
% Elongation HSR
92A022-2A vs. 92A022-2B
(L)
(T)
Tensile Strength (ksi) or Elongation
Tensile Strength (MPa)
0
10
20
30
40
50
60
70
80
0
100
200
300
400
500
77 77 300 300 450 450 600 600
Test Temperature (°F)
298 298 422 422 505 505 589 589
Test Temperature (K)

Fig. 12

Tensile Properties vs. Test Temperature

92A022-1B1 Hot Cross Rolled 0.10 cm (0.04") Sheet

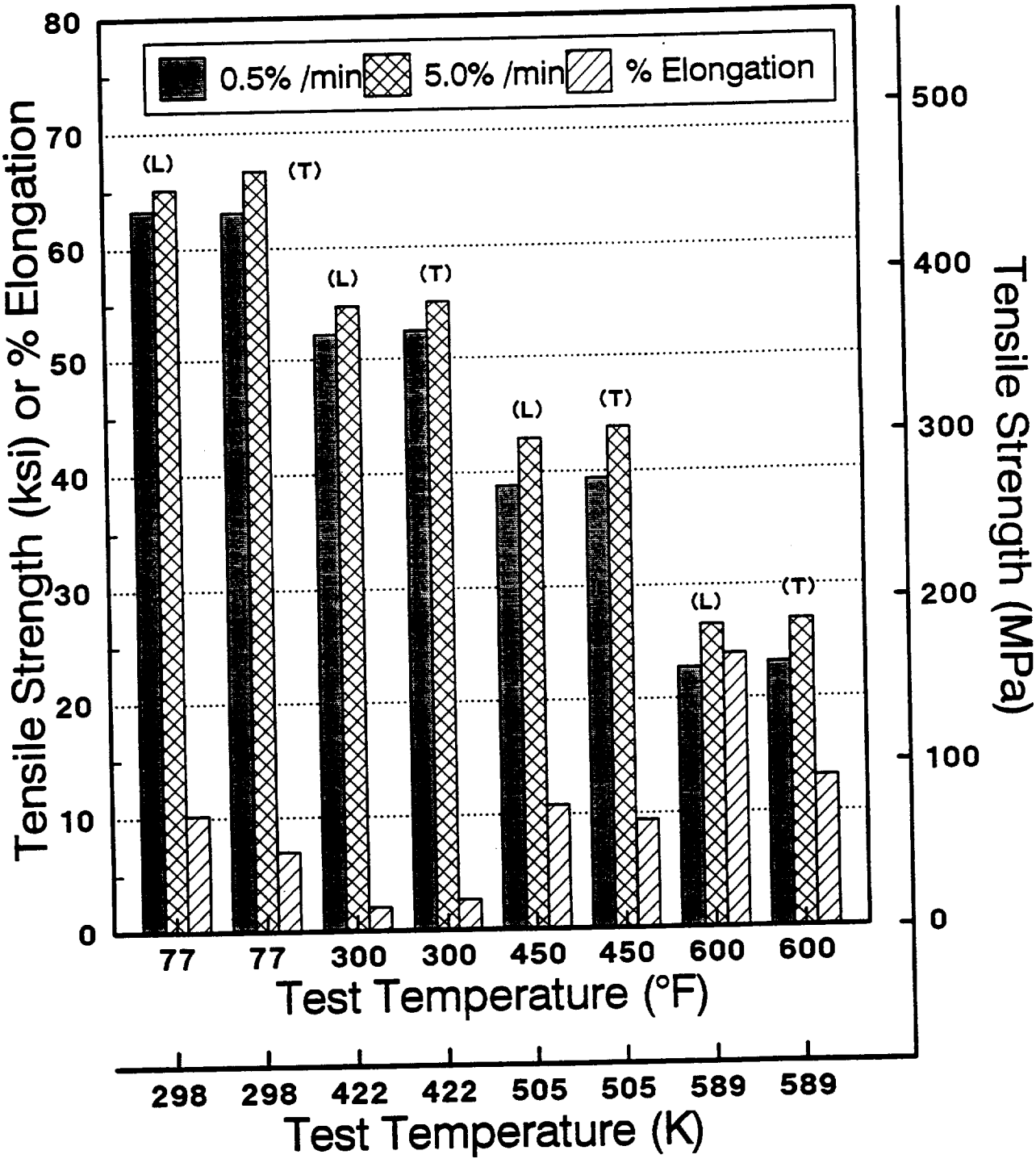

Fig. 13

Tensile Properties vs. Test Temperature

92A022-2C1 Hot Straight Rolled 0.08 cm (0.03") Sheet

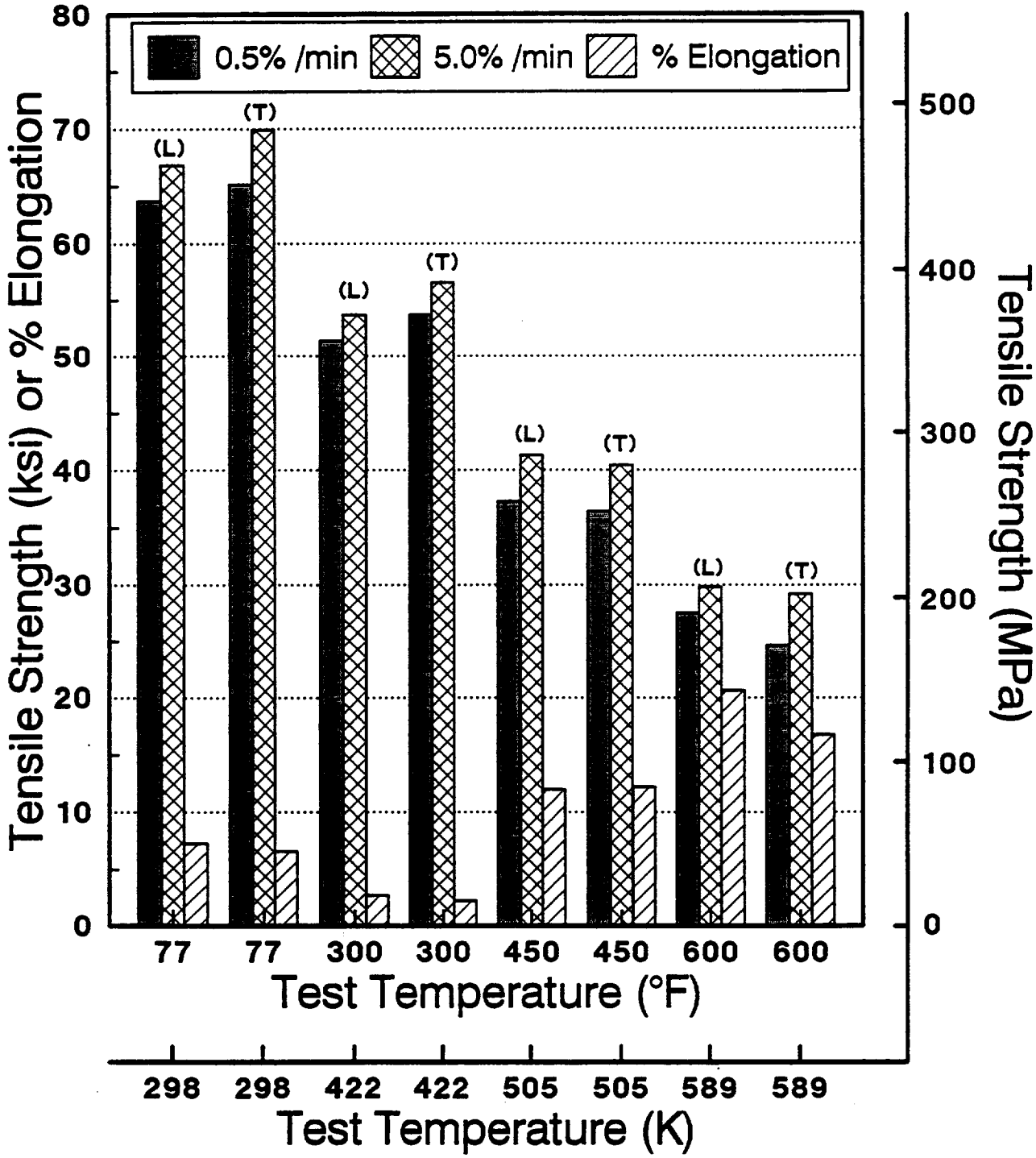

Fig. 14

Tensile Properties vs. Test Temperature

0.1 cm (0.04") Hot Cross vs. Hot Straight Rolled Sheet

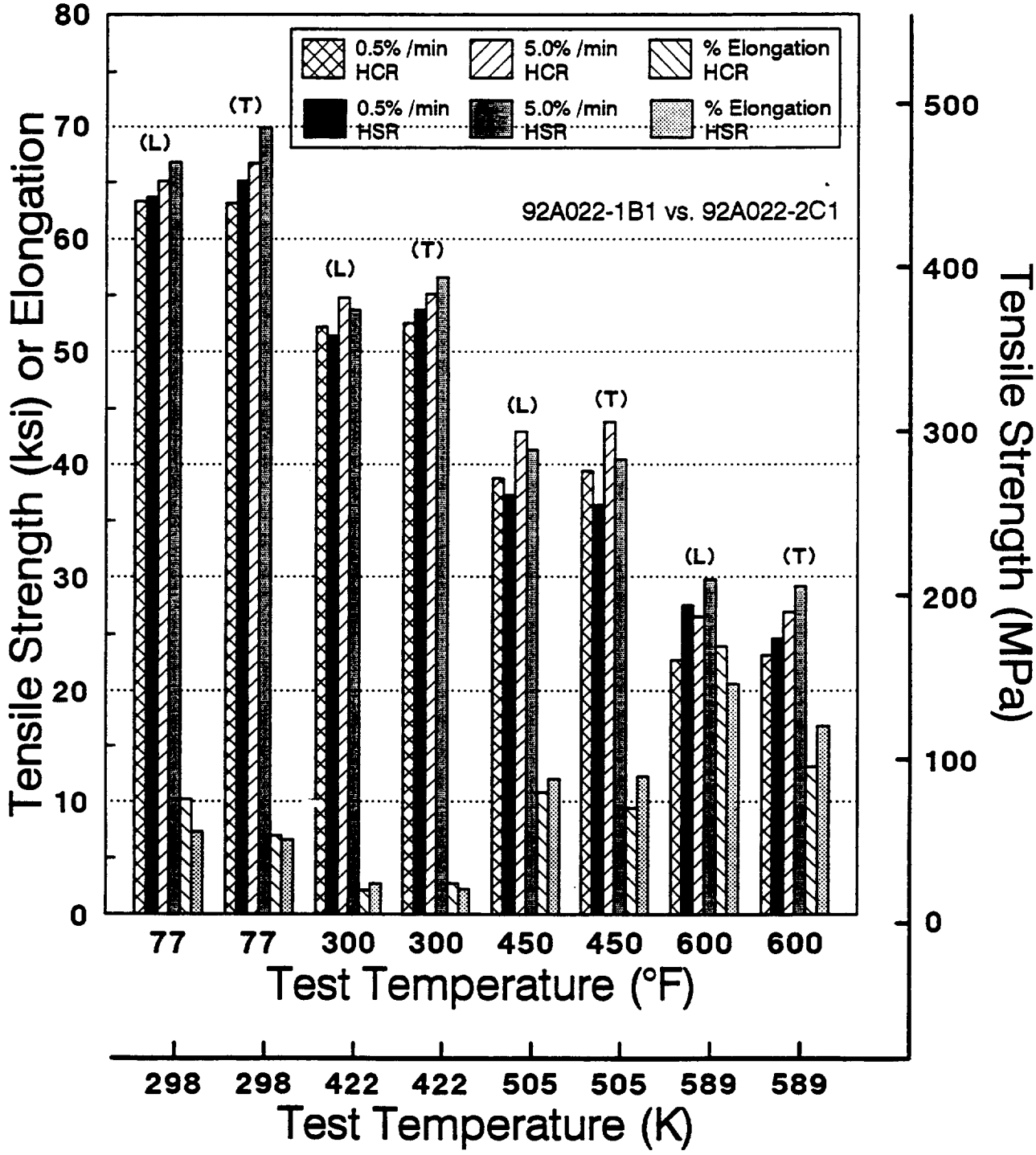

Fig. 15

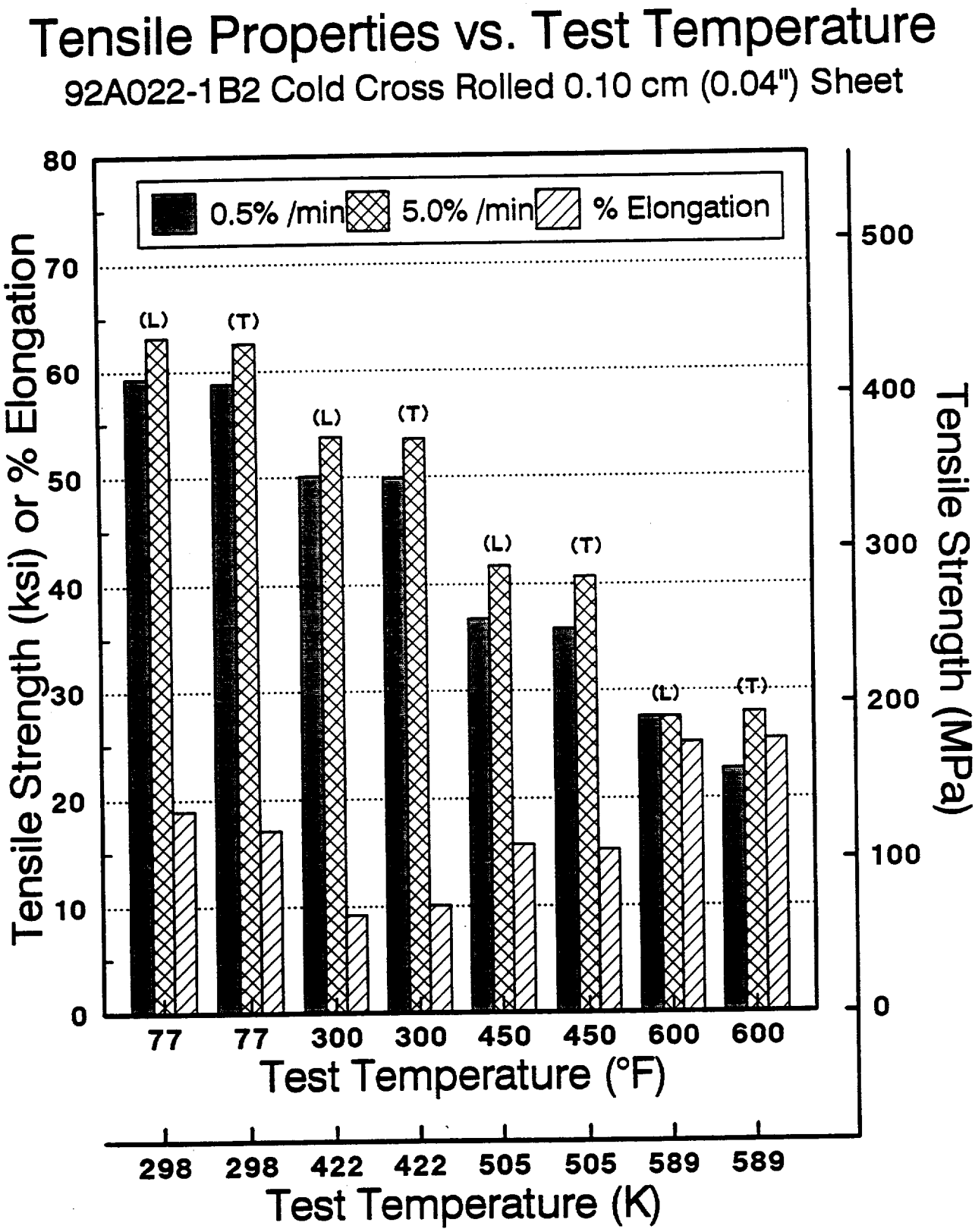
Tensile Properties vs. Test Temperature
92A022-1B2 Cold Cross Rolled 0.10 cm (0.04") Sheet
0.5% /min
5.0% /min
% Elongation
Tensile Strength (ksi) or % Elongation
Tensile Strength (MPa)
0
10
20
30
40
50
60
70
80
0
100
200
300
400
500
(L)
(T)
77
77
300
300
450
450
600
600
Test Temperature (°F)
298
298
422
422
505
505
589
589
Test Temperature (K)

Fig. 16

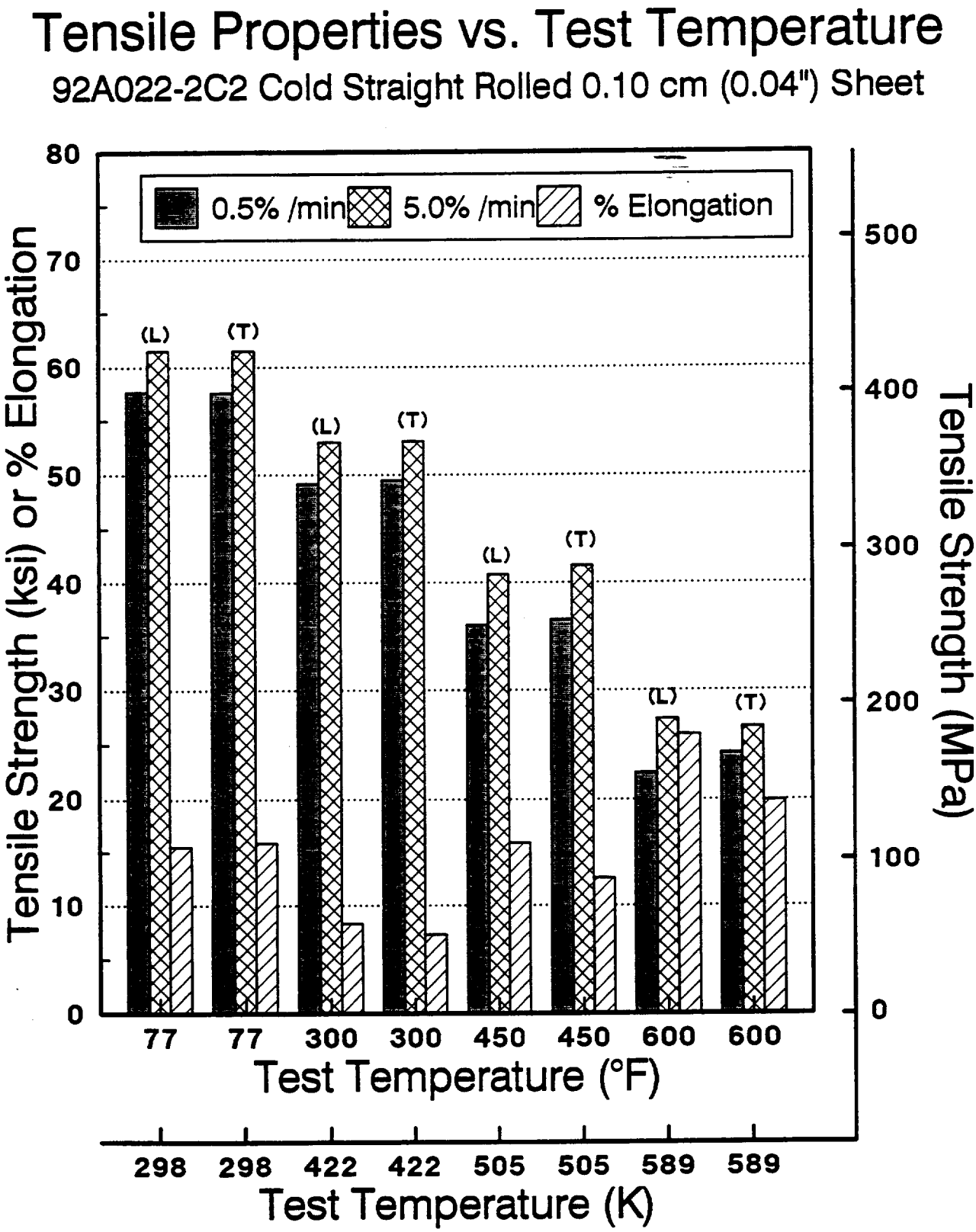
Tensile Properties vs. Test Temperature
92A022-2C2 Cold Straight Rolled 0.10 cm (0.04") Sheet
0.5% /min
5.0% /min
% Elongation
Tensile Strength (ksi) or % Elongation
Tensile Strength (MPa)
0
10
20
30
40
50
60
70
80
0
100
200
300
400
500
(L)
(T)
77
77
300
300
450
450
600
600
Test Temperature (°F)
298
298
422
422
505
505
589
589
Test Temperature (K)

Fig. 17

Tensile Properties vs. Test Temperature

0.1 cm (0.04") Cold Cross vs. Cold Straight Rolled Sheet

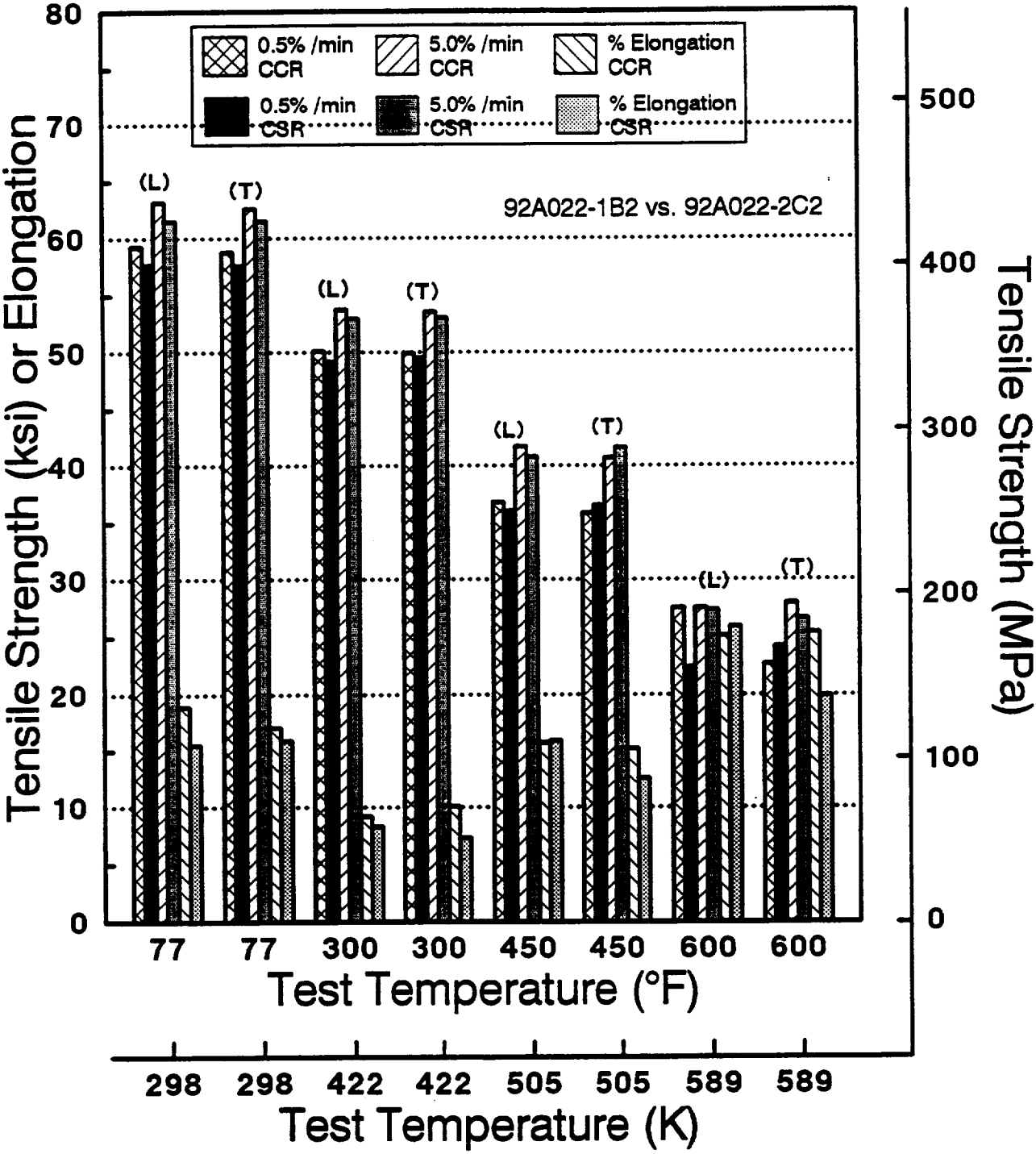

Fig. 18

Tensile Properties vs. Test Temperature

92A022-1B3 Cold Cross Rolled w/ Anneals 0.1 cm (0.04") Sheet

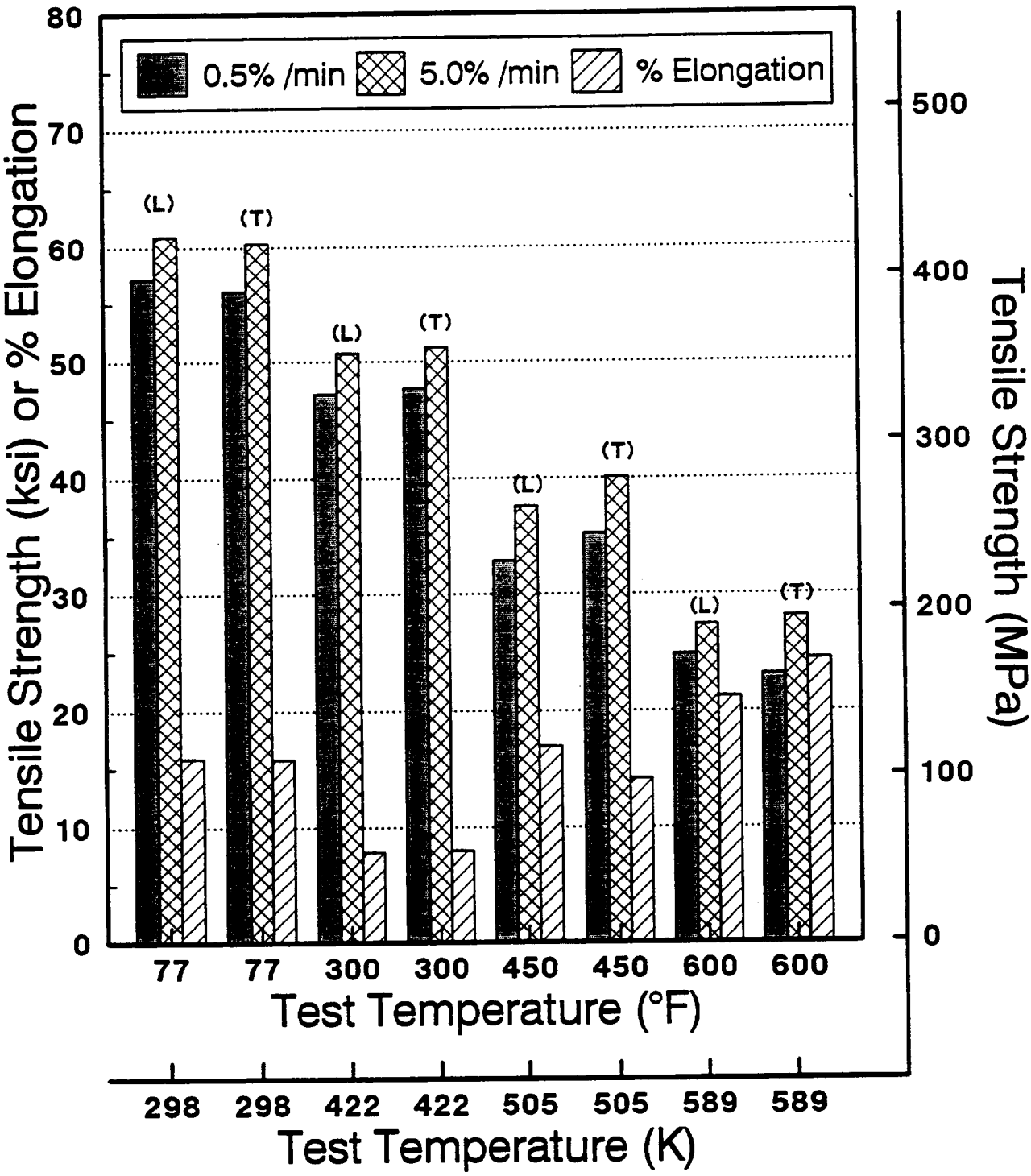

Fig. 19

Tensile Properties vs. Test Temperature

92A022-2C3 Cold Straight Rolled w/ Anneals 0.1 cm (0.04") Sheet

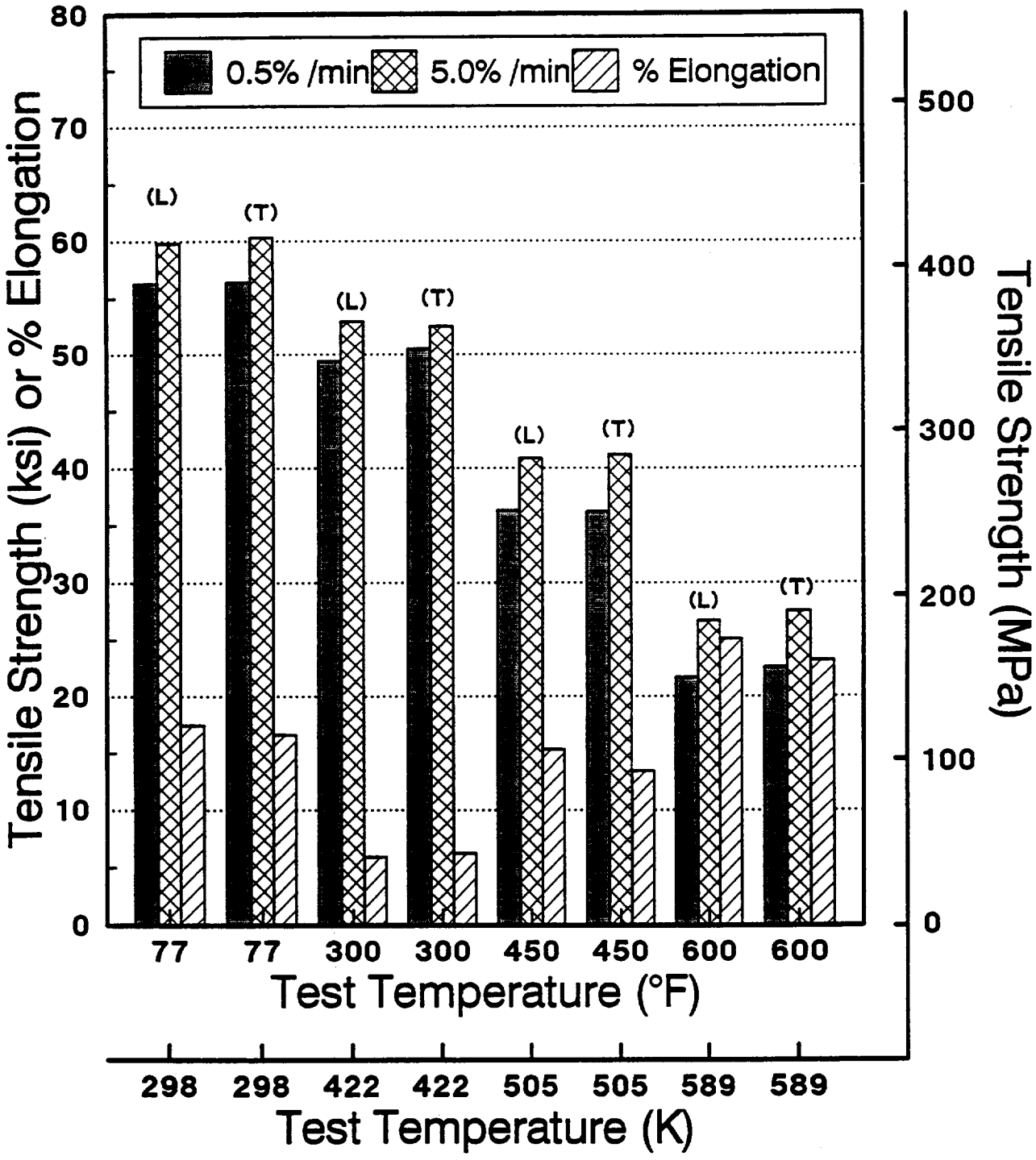

Fig. 20

Tensile Properties vs. Test Temperature

0.1 cm (0.40") Cold Cross vs. Cold Straight Rolled Sheet w/ Anneals

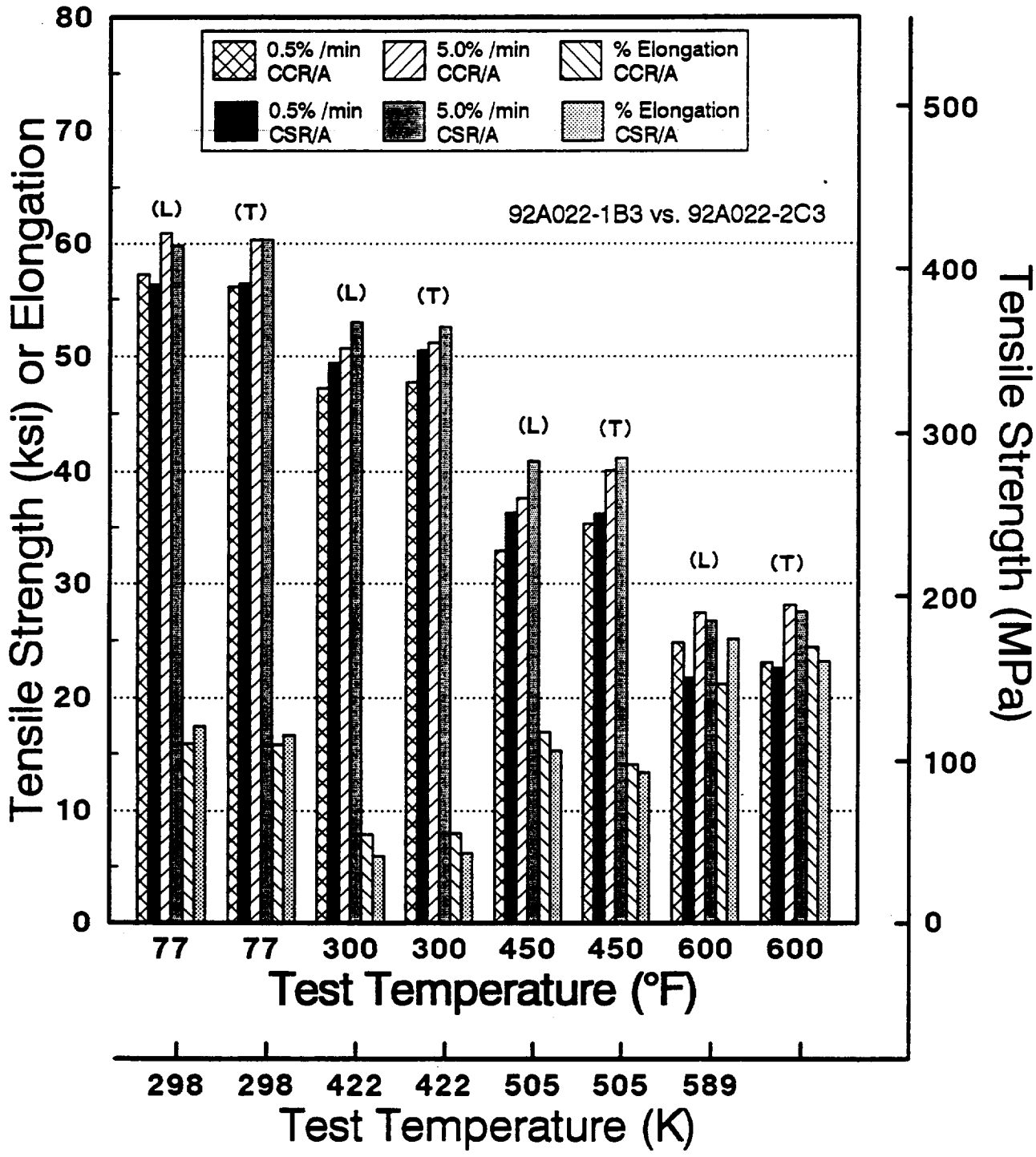

Fig. 21

Tensile Properties vs. Test Temperature

92A024-1C Hot Cross Rolled 0.64 cm (0.25") Sheet

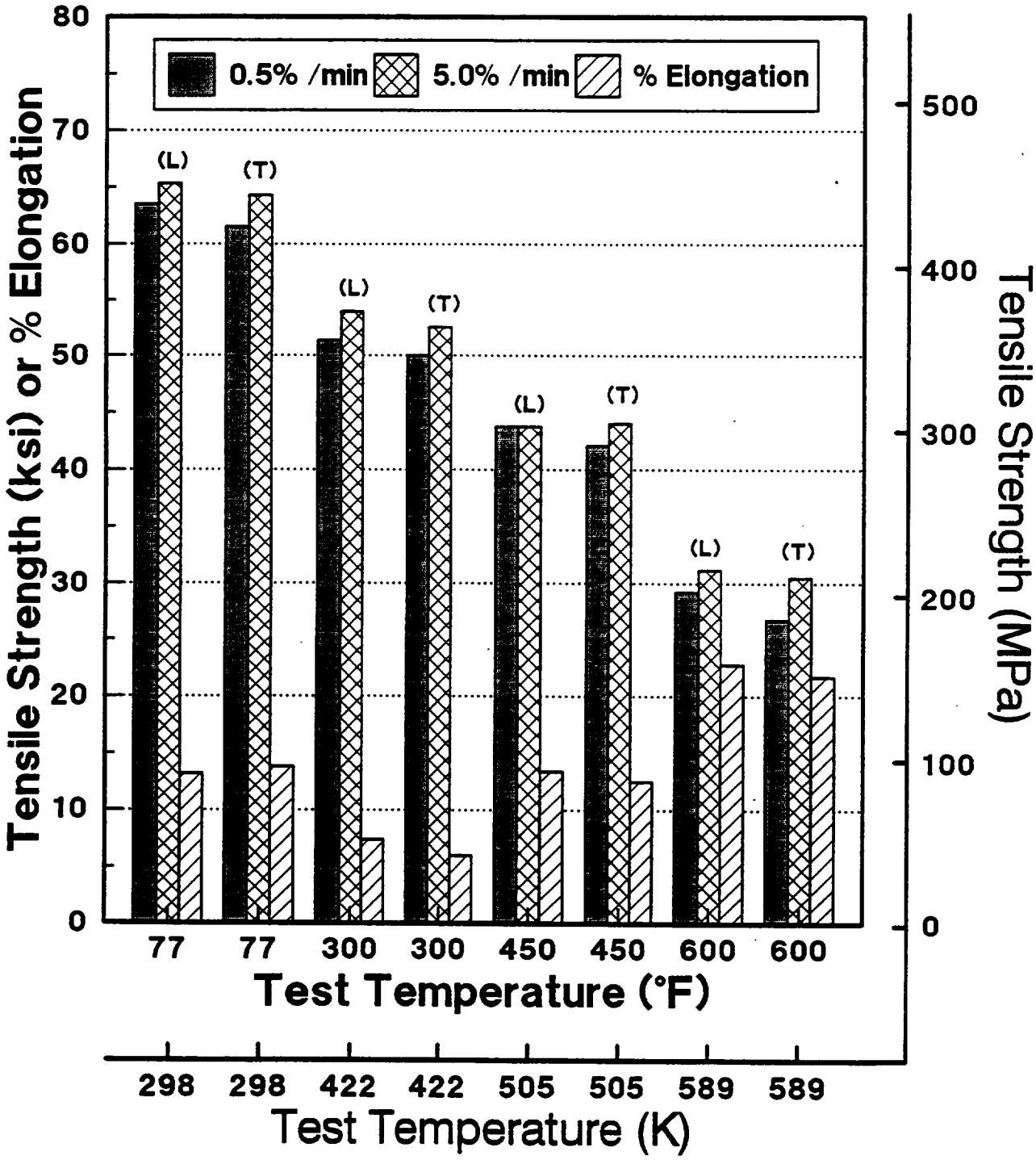

Fig. 22

Tensile Properties vs. Test Temperature

92A024-1A Hot Straight Rolled 0.64 cm (0.25") Sheet

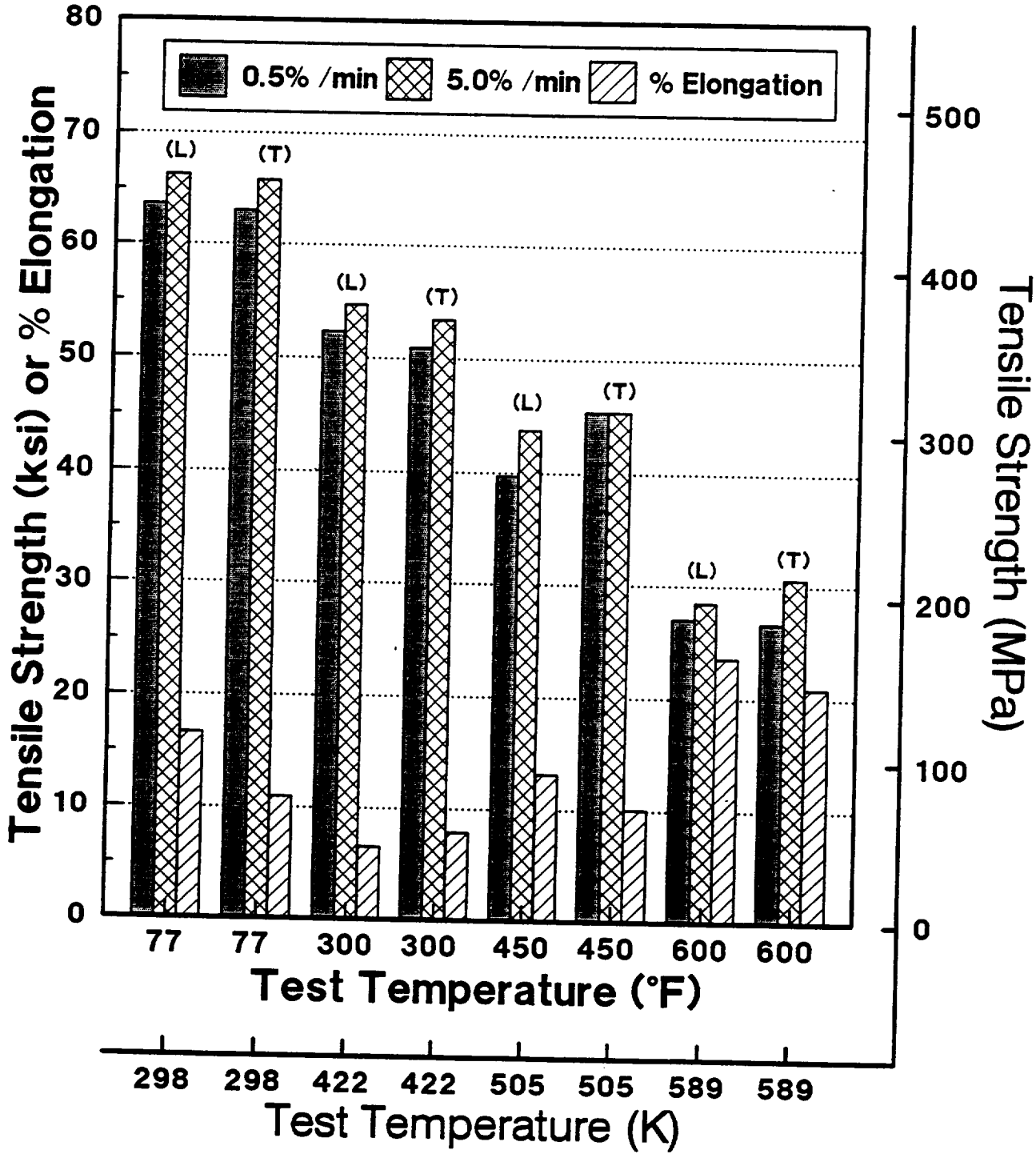

Fig. 23

Tensile Properties vs. Test Temperature

Hot Cross Rolled vs Hot Straight Rolled 0.64 cm (0.25") Sheet

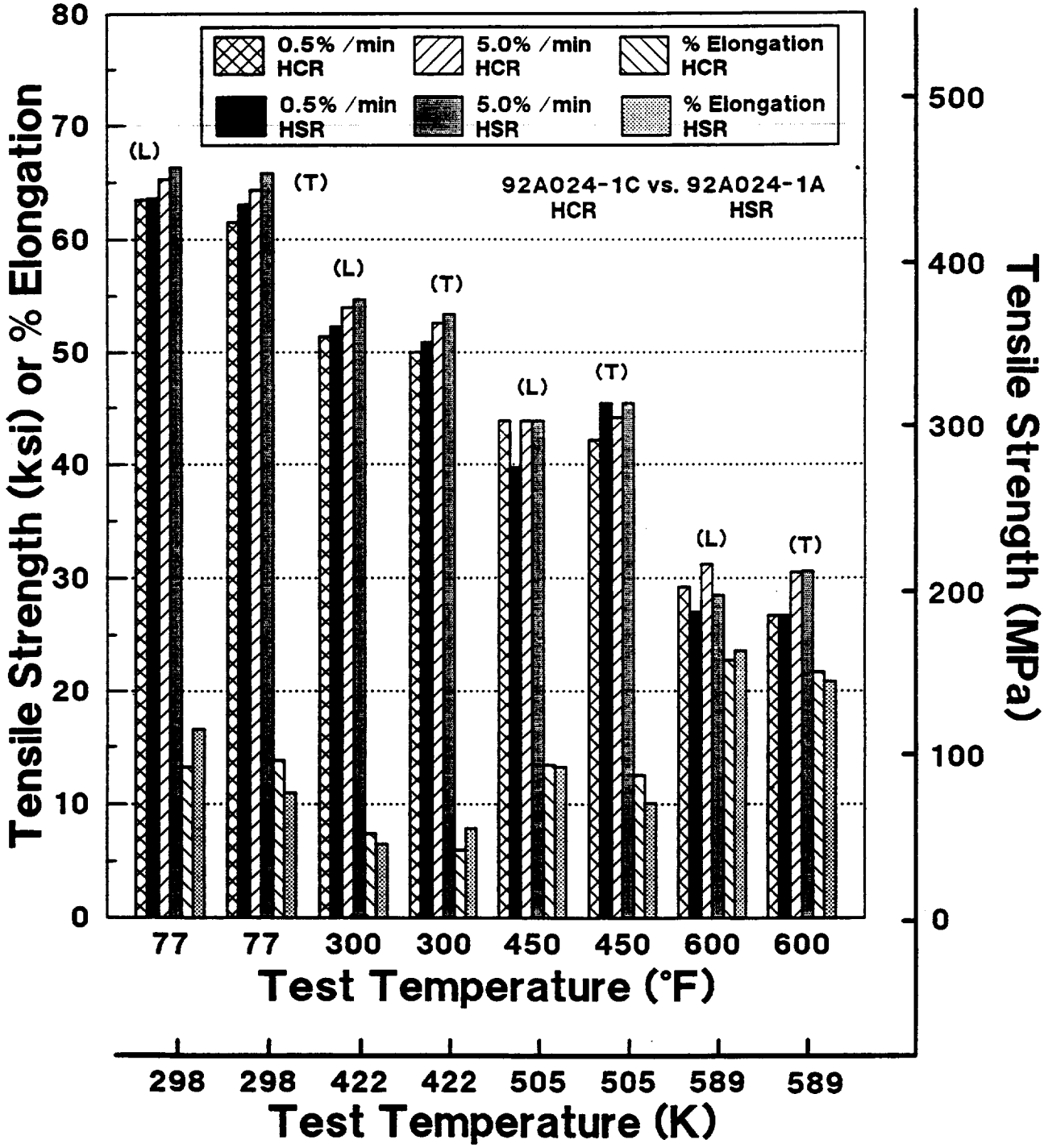

Fig. 24

Tensile Properties vs. Test Temperature

92A024-1D Hot Cross Rolled 0.23 cm (0.09") Sheet

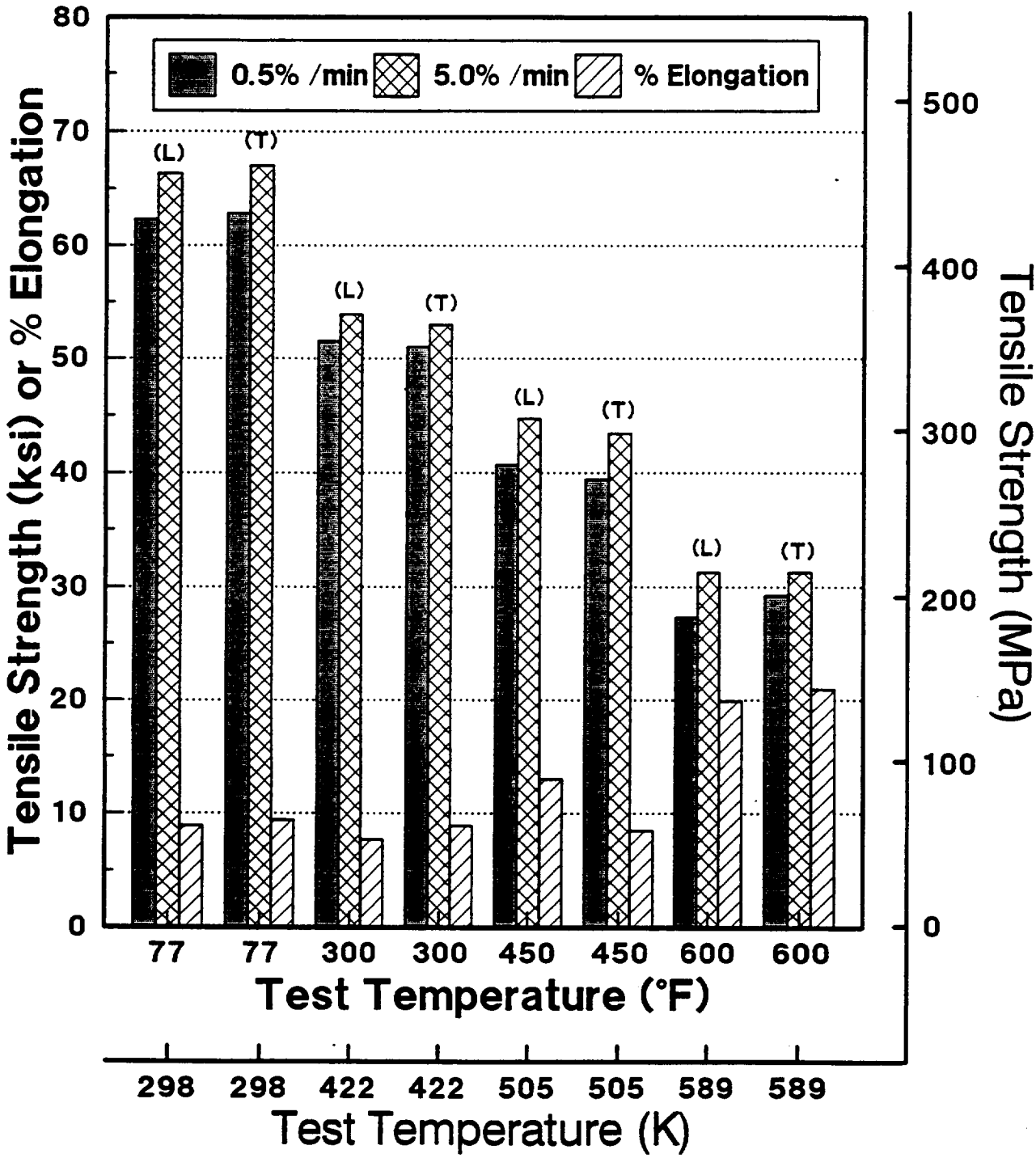

Fig. 25

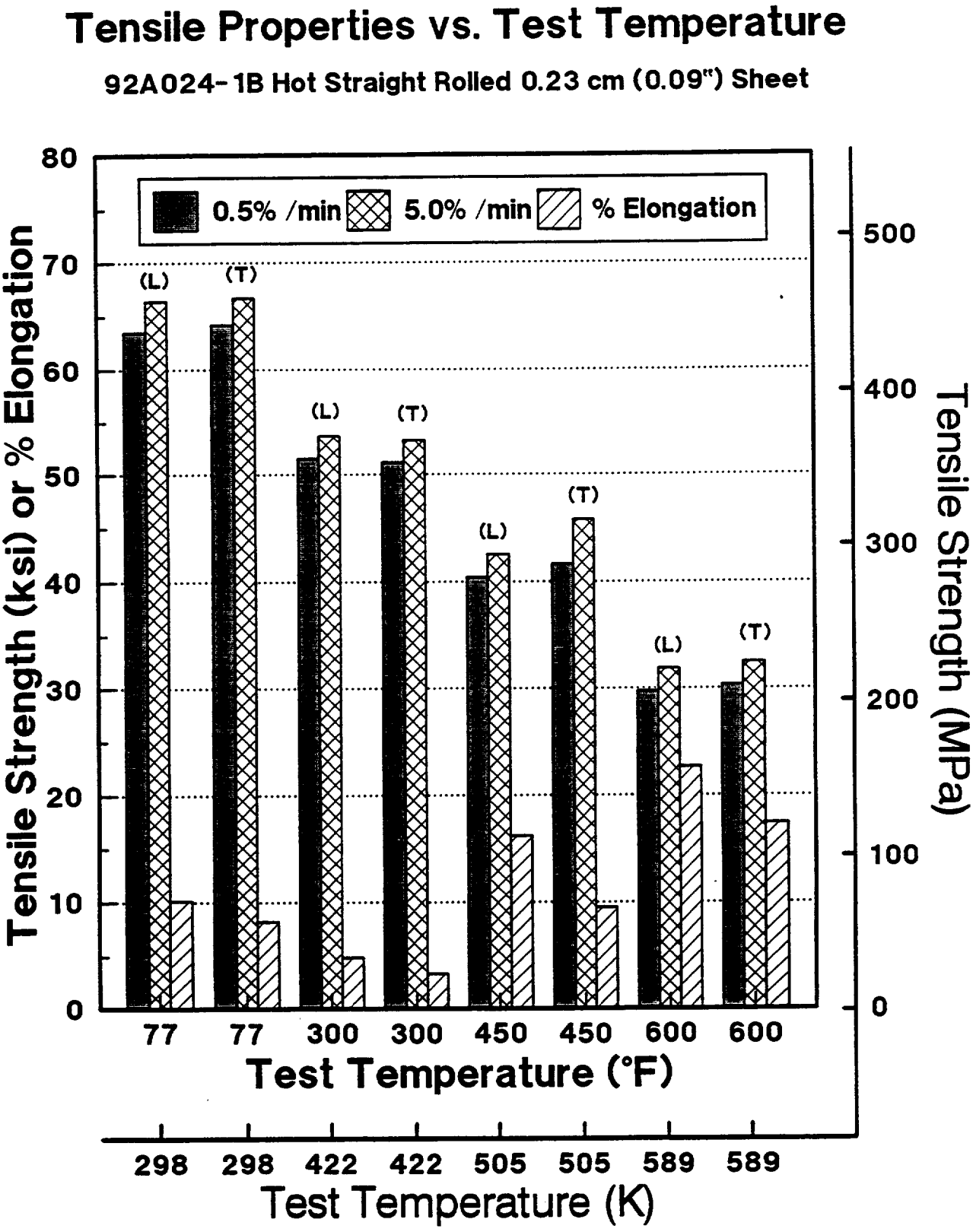
Tensile Properties vs. Test Temperature
92A024-1B Hot Straight Rolled 0.23 cm (0.09") Sheet
0.5% /min
5.0% /min
% Elongation
Tensile Strength (ksi) or % Elongation
Tensile Strength (MPa)
0
10
20
30
40
50
60
70
80
0
100
200
300
400
500
(L)
(T)
77
77
300
300
450
450
600
600
Test Temperature (°F)
298
298
422
422
505
505
589
589
Test Temperature (K)

Fig. 26

Tensile Properties vs. Test Temperature

Hot Cross Rolled vs Hot Straight Rolled 0.26 cm (0.1") Sheet

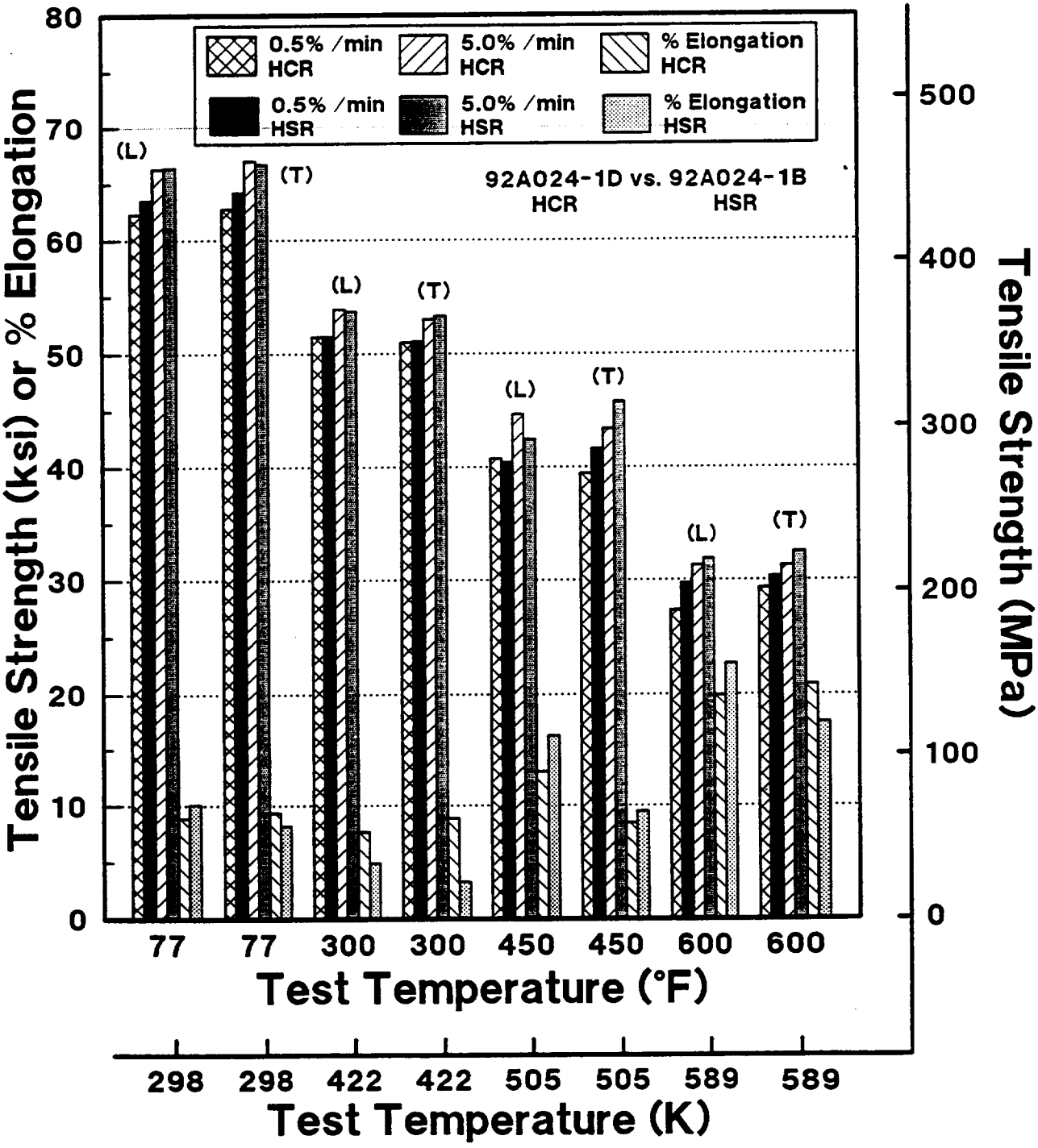

Fig. 27

Tensile Properties vs. Test Temperature

92A024-2B1 Hot Cross Rolled 0.08 cm (0.03") Sheet

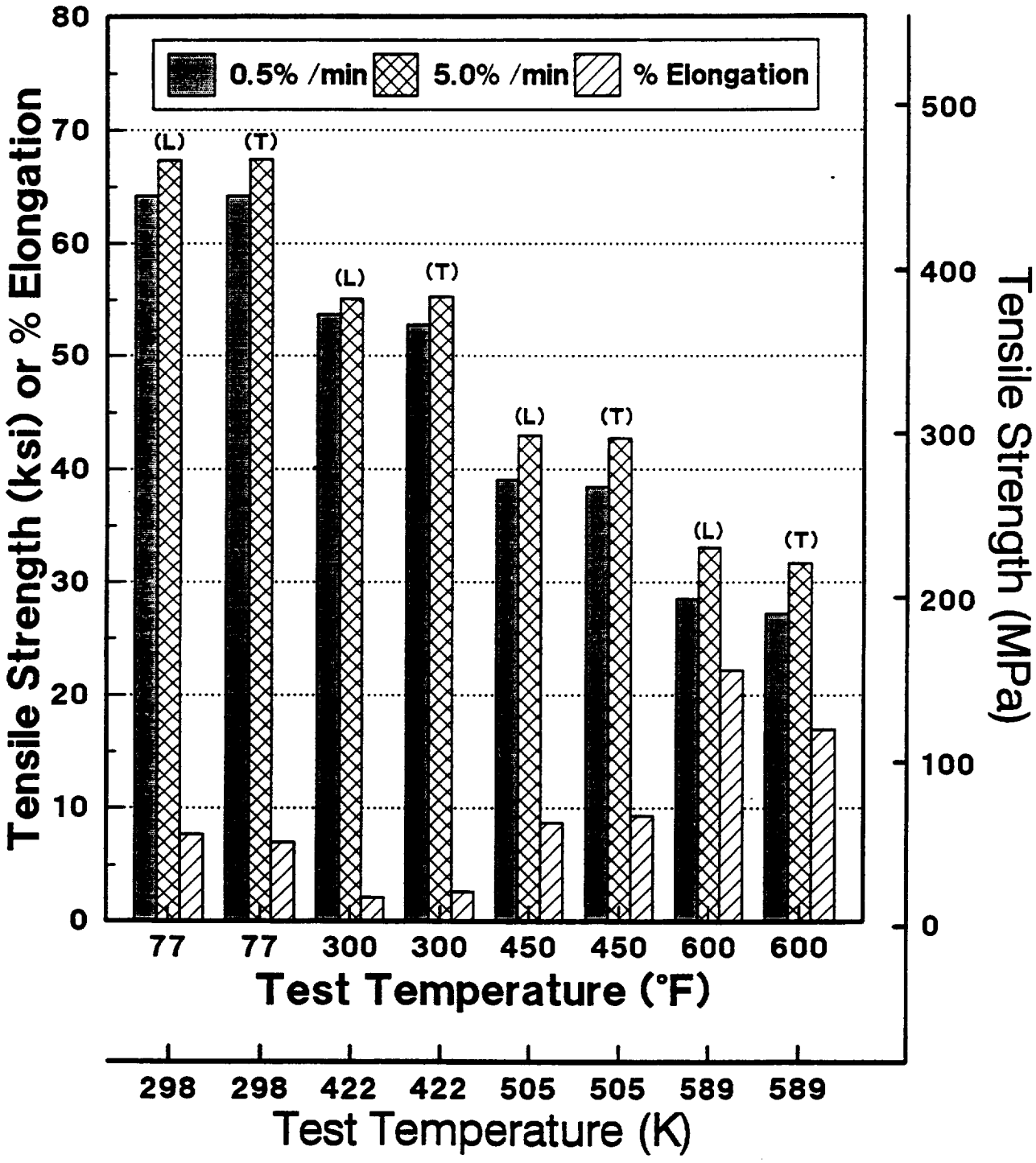

Fig. 28

Tensile Properties vs. Test Temperature

92A024-2A1 Hot Straight Rolled 0.1 cm (0.04") Sheet

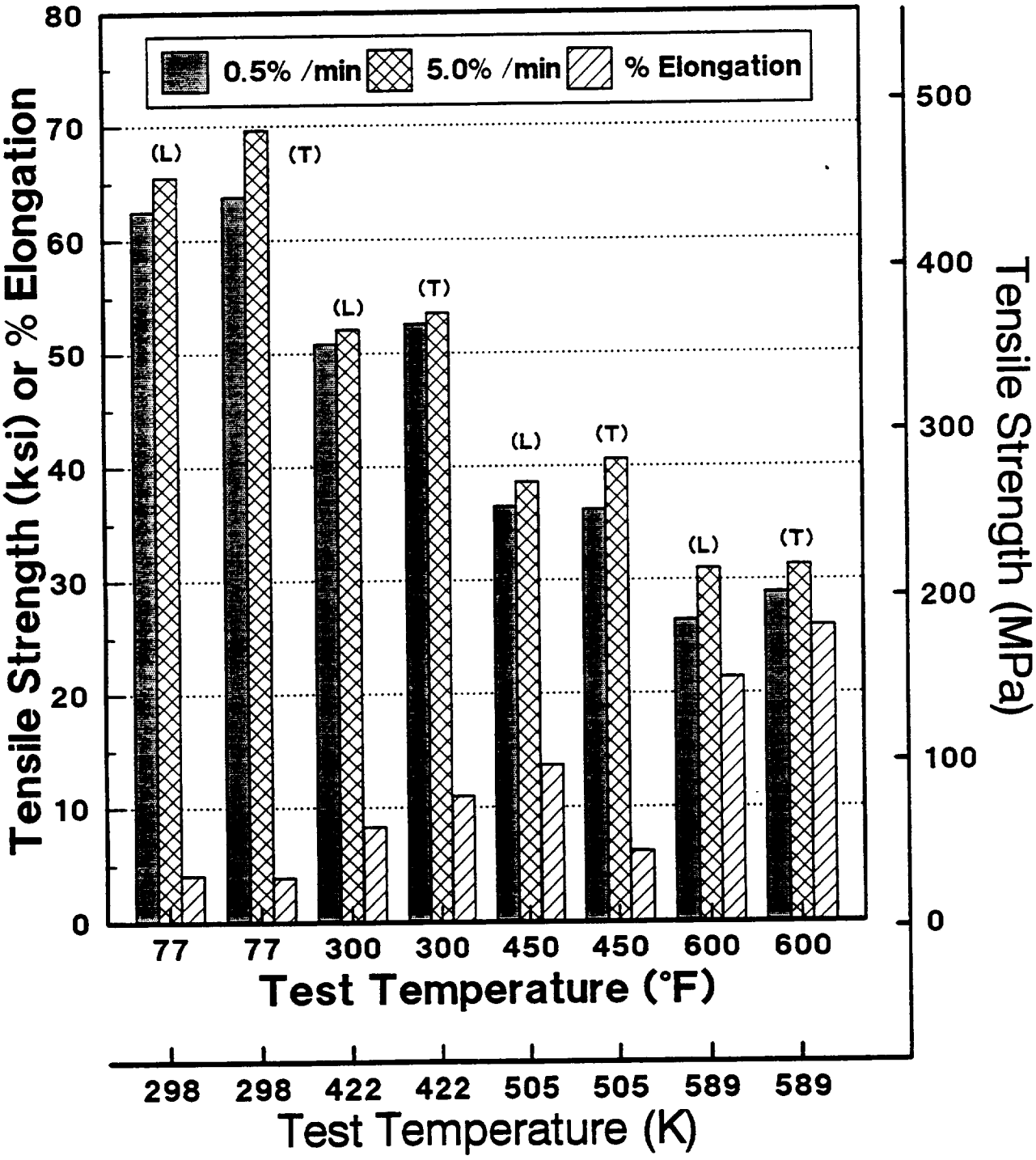

Fig. 29

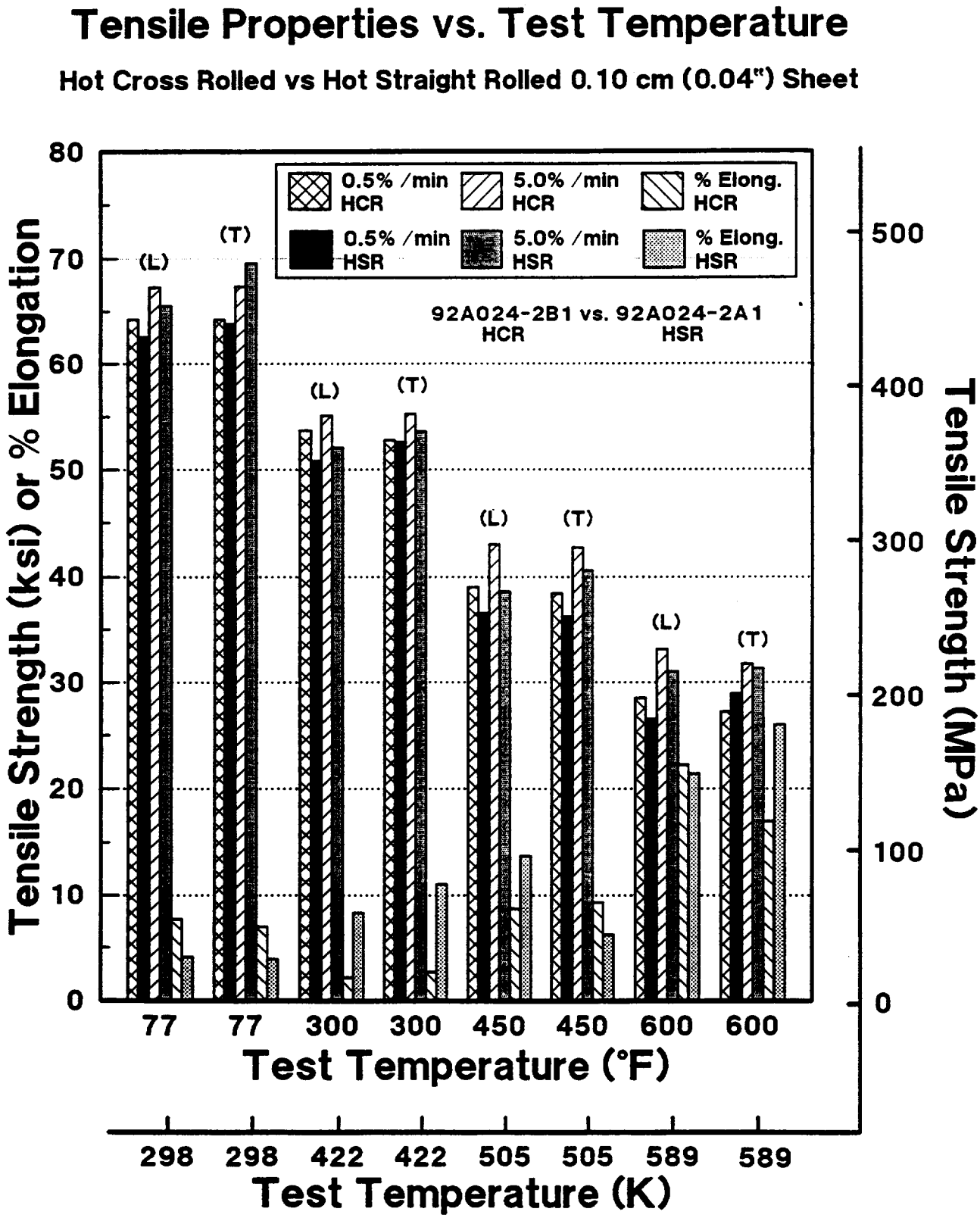
Tensile Properties vs. Test Temperature
Hot Cross Rolled vs Hot Straight Rolled 0.10 cm (0.04") Sheet
0.5% /min HCR
5.0% /min HCR
% Elong. HCR
0.5% /min HSR
5.0% /min HSR
% Elong. HSR
92A024-2B1 vs. 92A024-2A1
HCR HSR
(L)
(T)
Tensile Strength (ksi) or % Elongation
Tensile Strength (MPa)
0
10
20
30
40
50
60
70
80
0
100
200
300
400
500
77 77 300 300 450 450 600 600
Test Temperature (°F)
298 298 422 422 505 505 589 589
Test Temperature (K)

Fig. 30

Tensile Properties vs. Test Temperature

92A024-2B2 Cold Cross Rolled 0.1 cm (0.04") Sheet

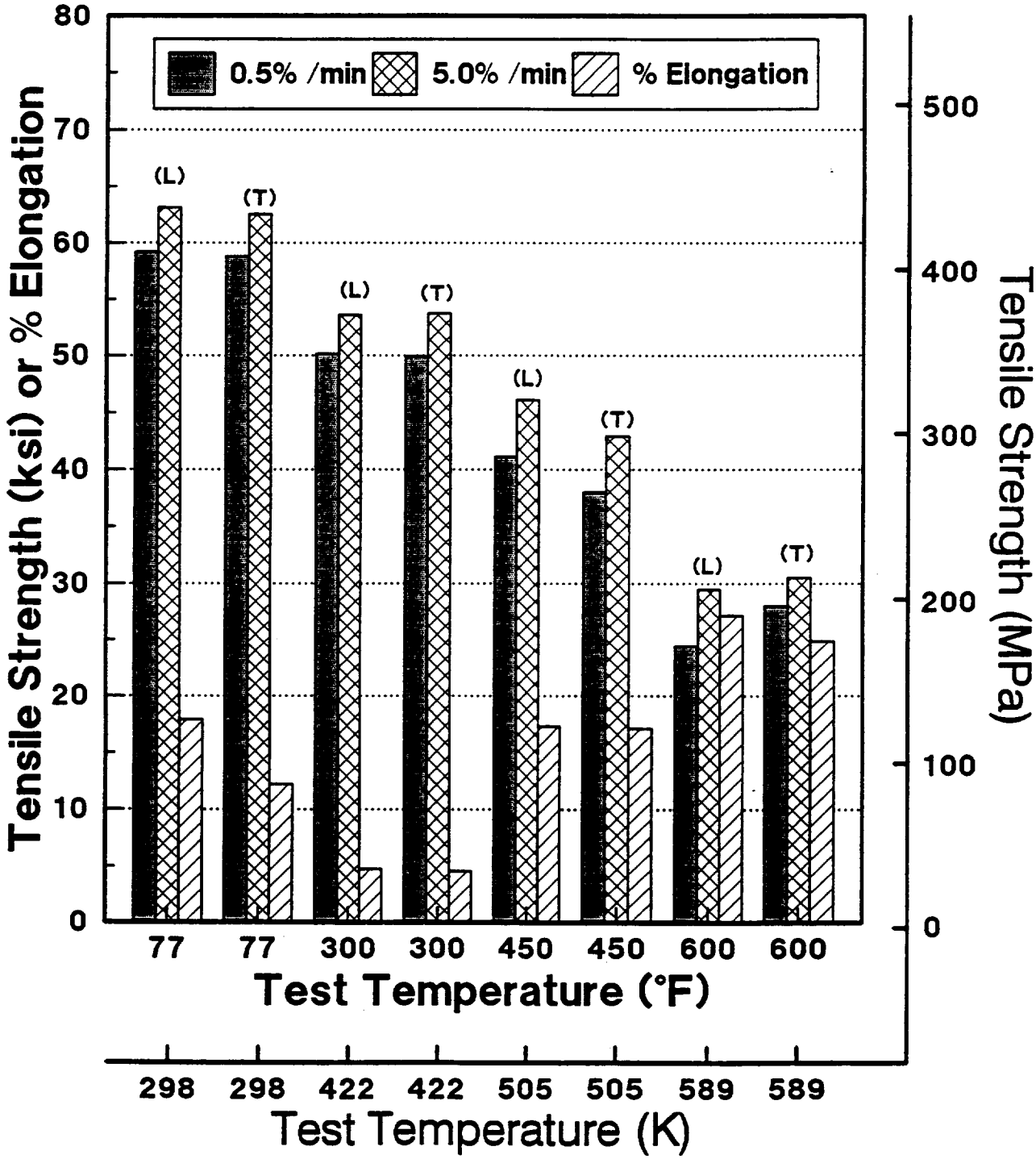

Fig. 31

Tensile Properties vs. Test Temperature

92A024-2A2 Cold Straight Rolled 0.1 cm (0.04") Sheet

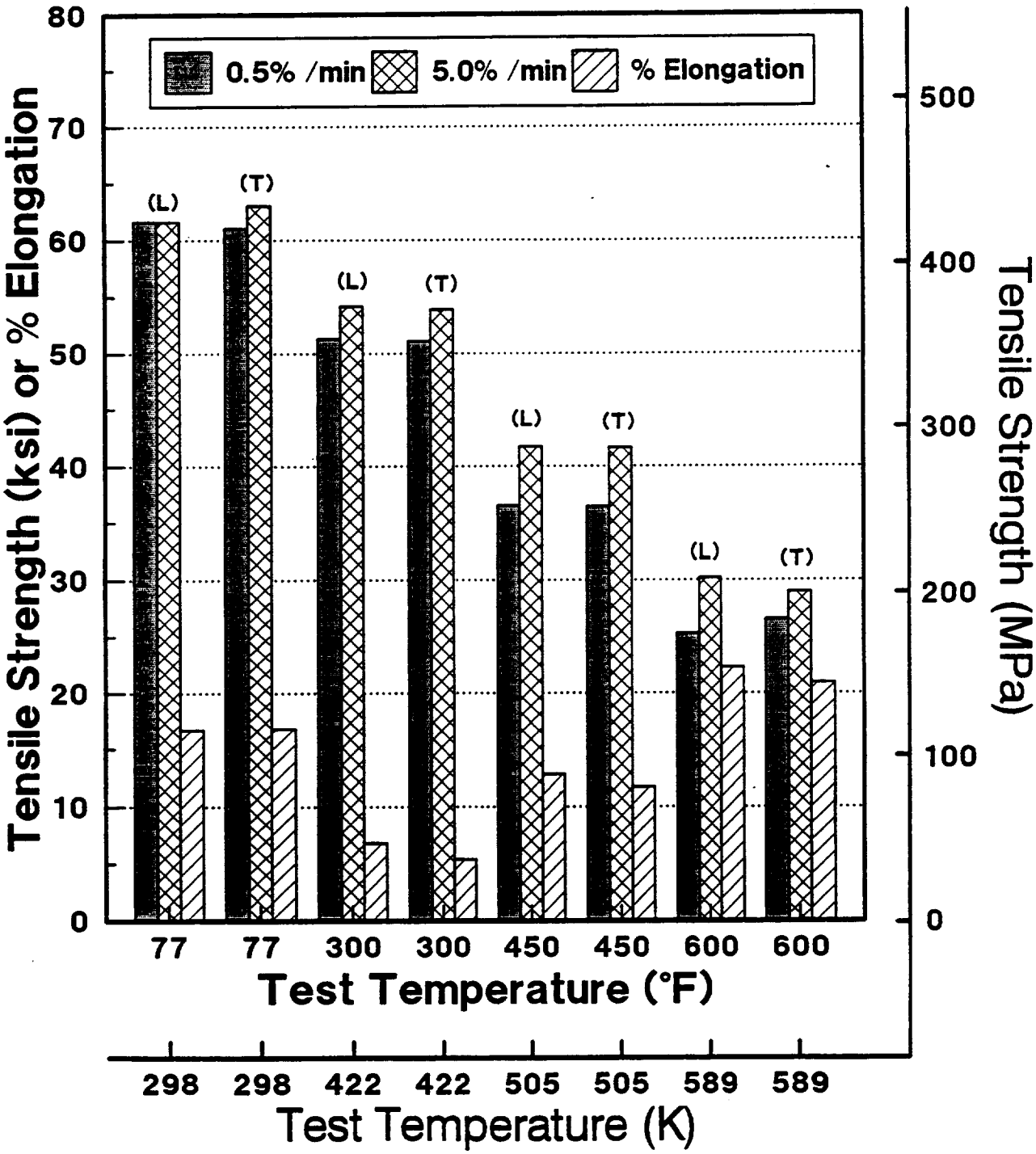

Fig. 32

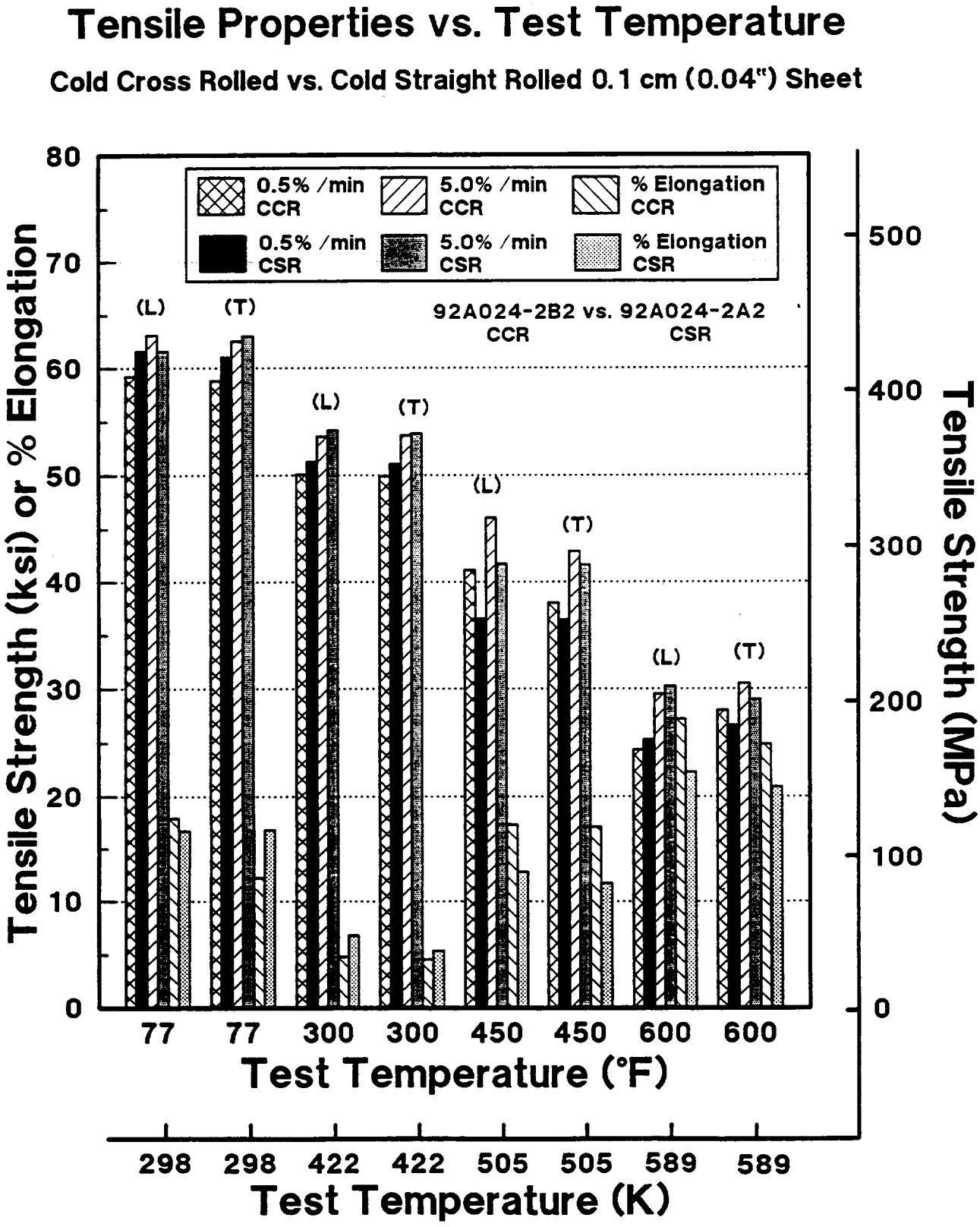
Tensile Properties vs. Test Temperature
Cold Cross Rolled vs. Cold Straight Rolled 0.1 cm (0.04") Sheet
0.5% /min CCR
5.0% /min CCR
% Elongation CCR
0.5% /min CSR
5.0% /min CSR
% Elongation CSR
92A024-2B2 vs. 92A024-2A2
CCR
CSR
(L)
(T)
Tensile Strength (ksi) or % Elongation
Tensile Strength (MPa)
0
10
20
30
40
50
60
70
80
0
100
200
300
400
500
77 77 300 300 450 450 600 600
Test Temperature (°F)
298 298 422 422 505 505 589 589
Test Temperature (K)

Fig. 33

Tensile Properties vs. Test Temperature

92A024-2B3 Cold Cross Rolled w/ Anneals 0.1 cm (0.04") Sheet

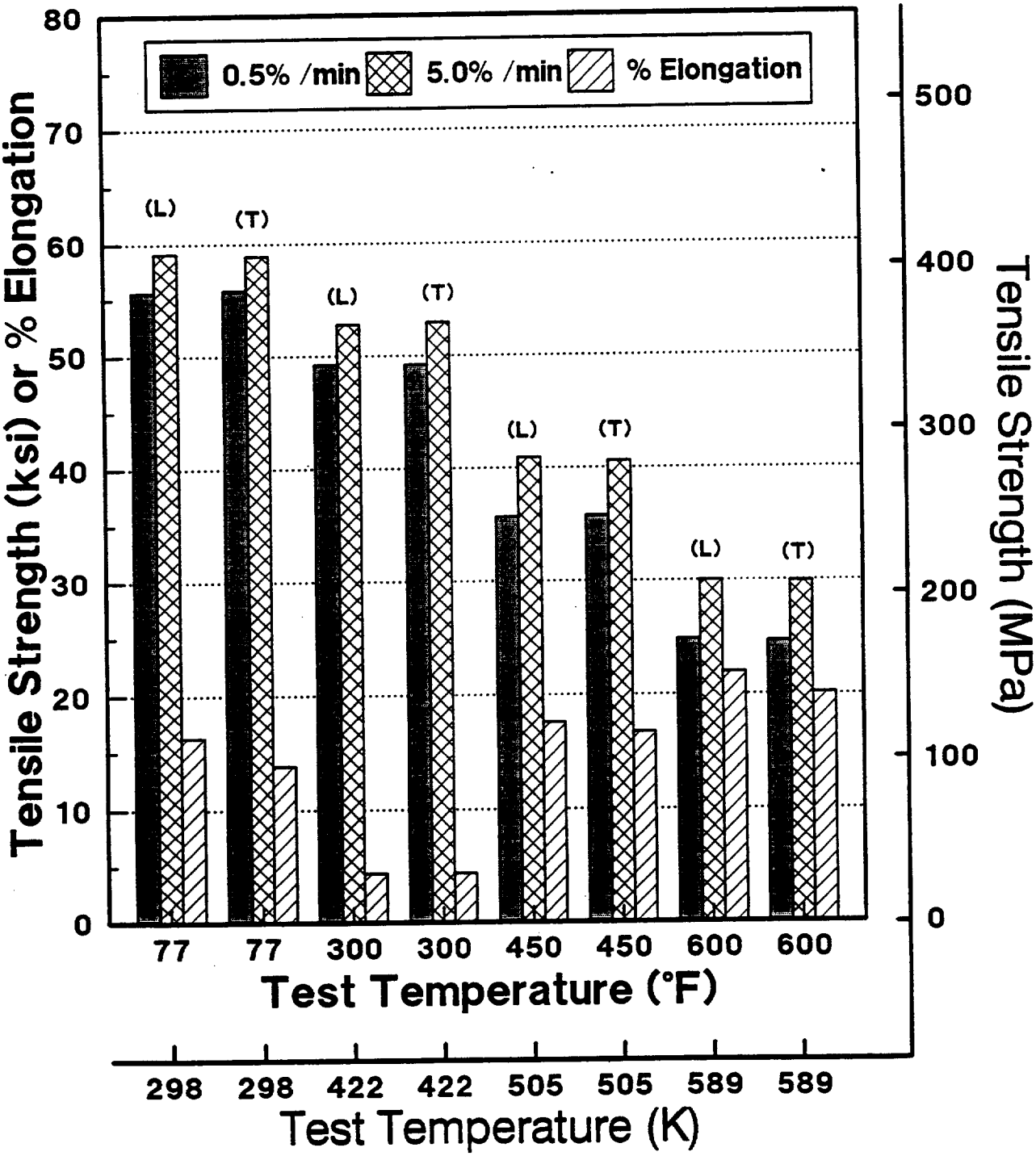

Fig. 34

Tensile Properties vs. Test Temperature

92A024-2A3 Cold Straight Rolled w/ Anneals 0.1 cm (0.04") Sheet

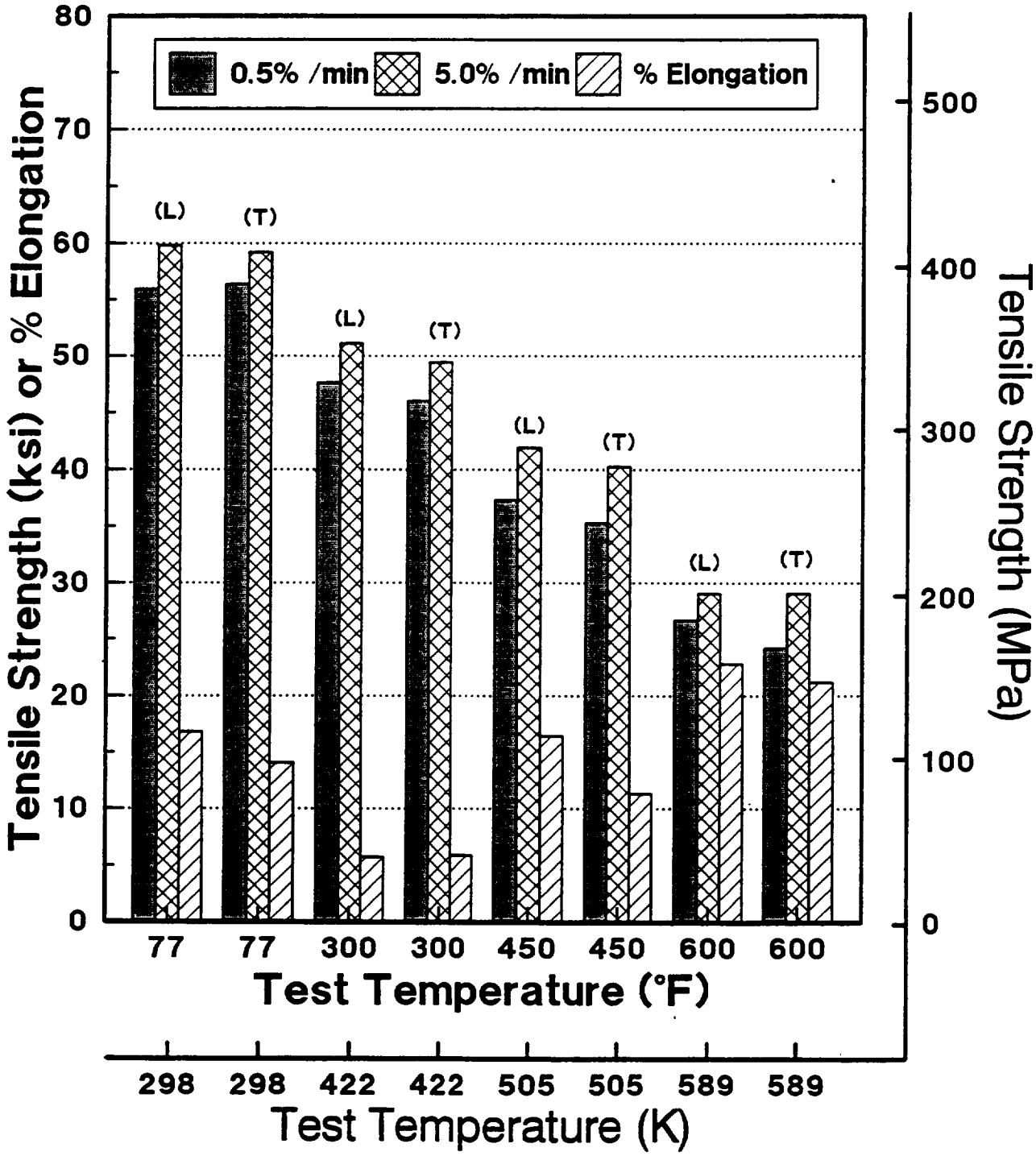

Fig. 35

Tensile Properties vs. Test Temperature

Cold Cross Rolled vs. Cold Straight Rolled 0.1 cm (0.04") Sheet w/ Anneals

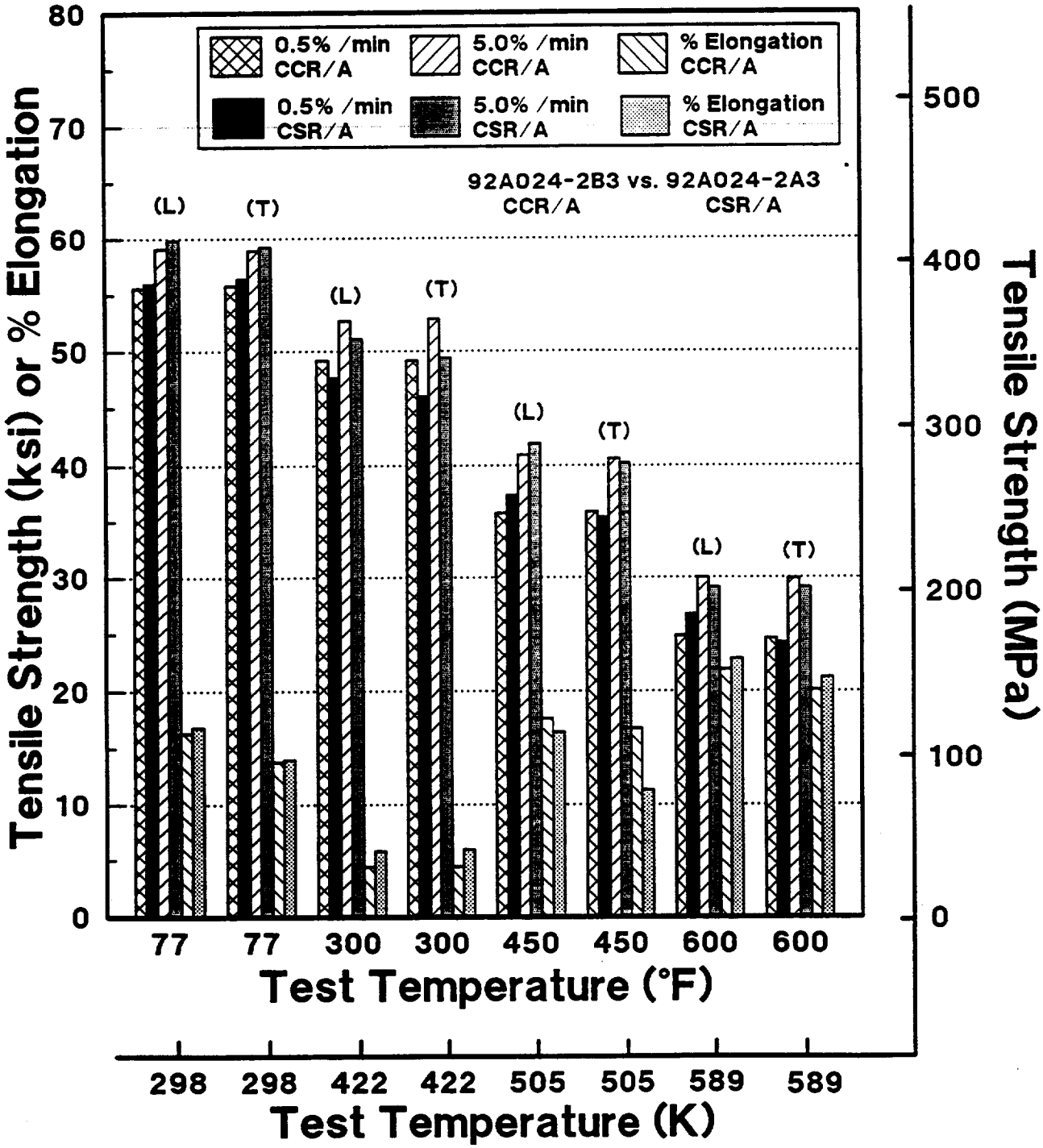

Fig. 36

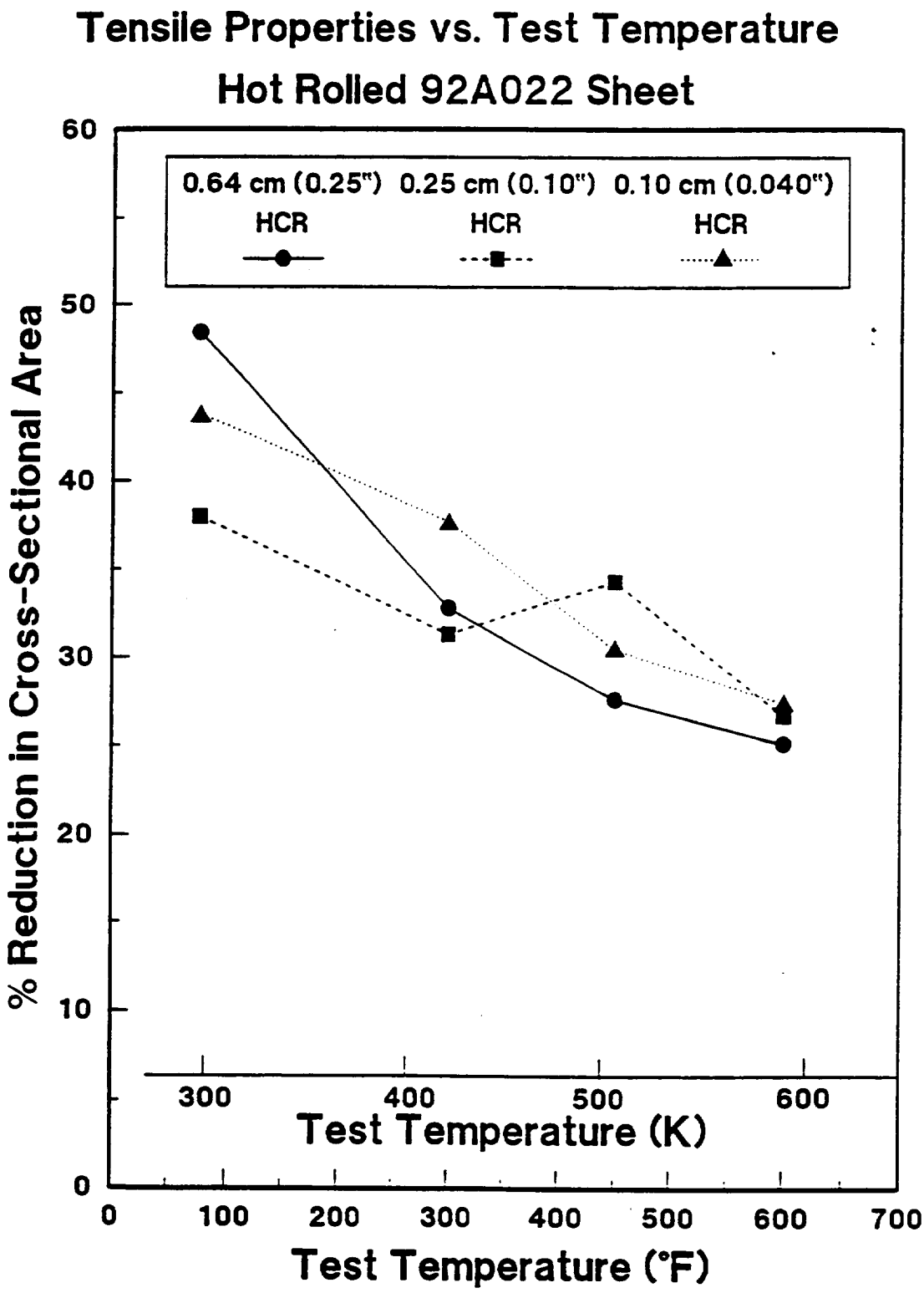
Tensile Properties vs. Test Temperature
Hot Rolled 92A022 Sheet
0.64 cm (0.25") HCR
0.25 cm (0.10") HCR
0.10 cm (0.040") HCR
% Reduction in Cross-Sectional Area
60
50
40
30
20
10
0
300
400
500
600
Test Temperature (K)
0
100
200
300
400
500
600
700
Test Temperature (°F)

Fig. 37

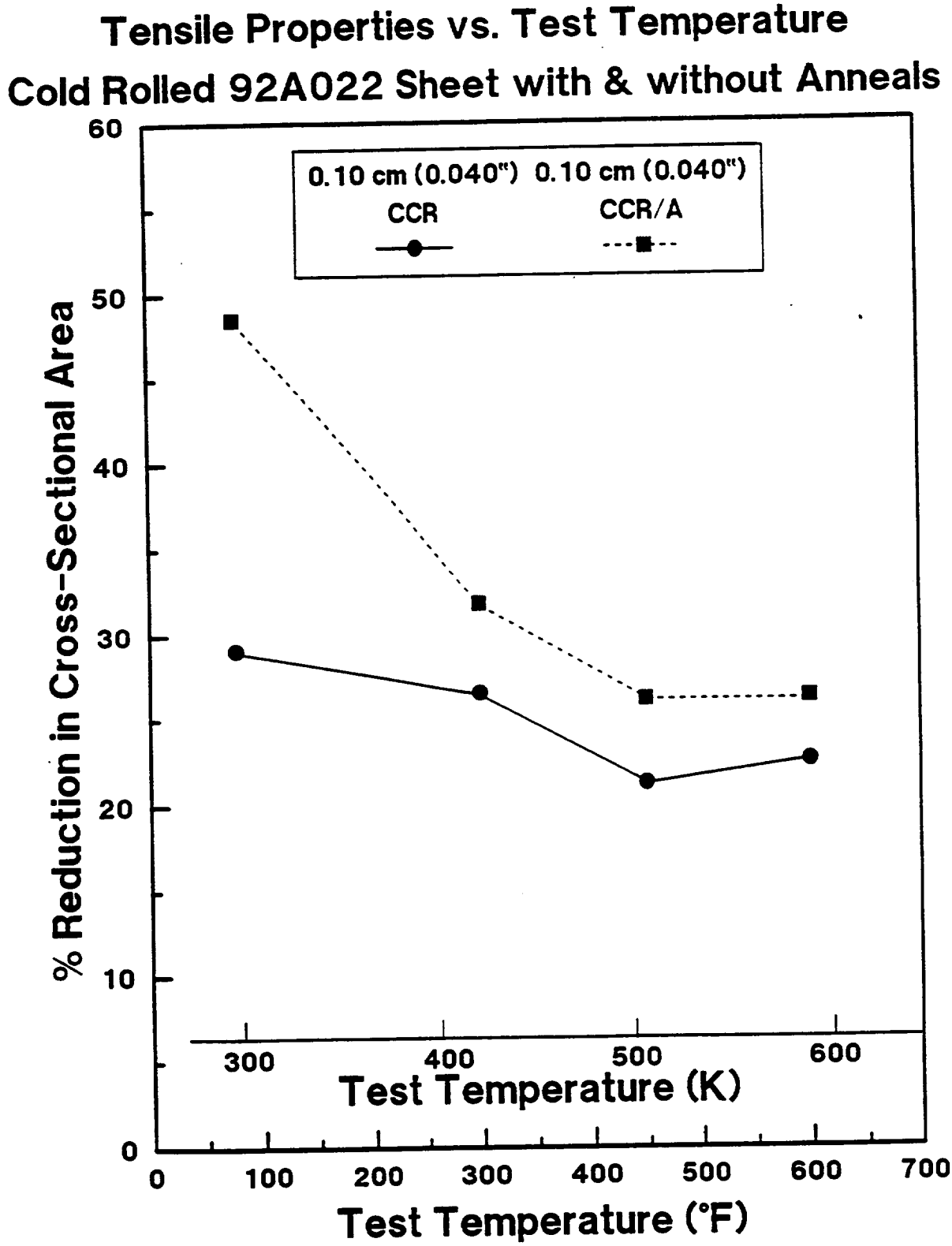
Tensile Properties vs. Test Temperature
Cold Rolled 92A022 Sheet with & without Anneals
0.10 cm (0.040") 0.10 cm (0.040")
CCR
CCR/A
% Reduction in Cross-Sectional Area
60
50
40
30
20
10
0
300
400
500
600
Test Temperature (K)
0
100
200
300
400
500
600
700
Test Temperature (°F)

Fig. 38

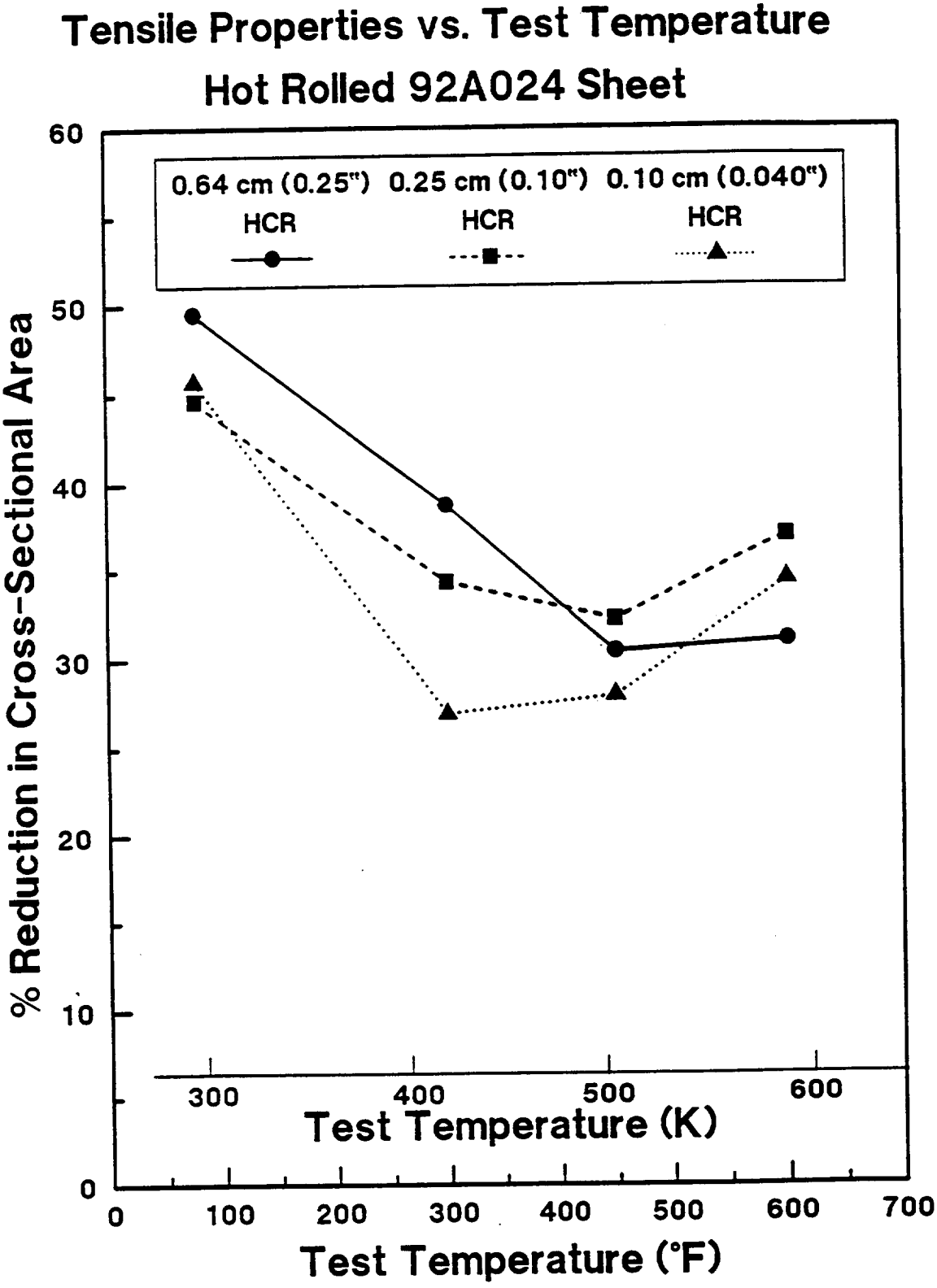
Tensile Properties vs. Test Temperature
Hot Rolled 92A024 Sheet
0.64 cm (0.25") HCR
0.25 cm (0.10") HCR
0.10 cm (0.040") HCR
% Reduction in Cross-Sectional Area
0
10
20
30
40
50
60
300
400
500
600
Test Temperature (K)
0
100
200
300
400
500
600
700
Test Temperature (°F)

Fig. 39

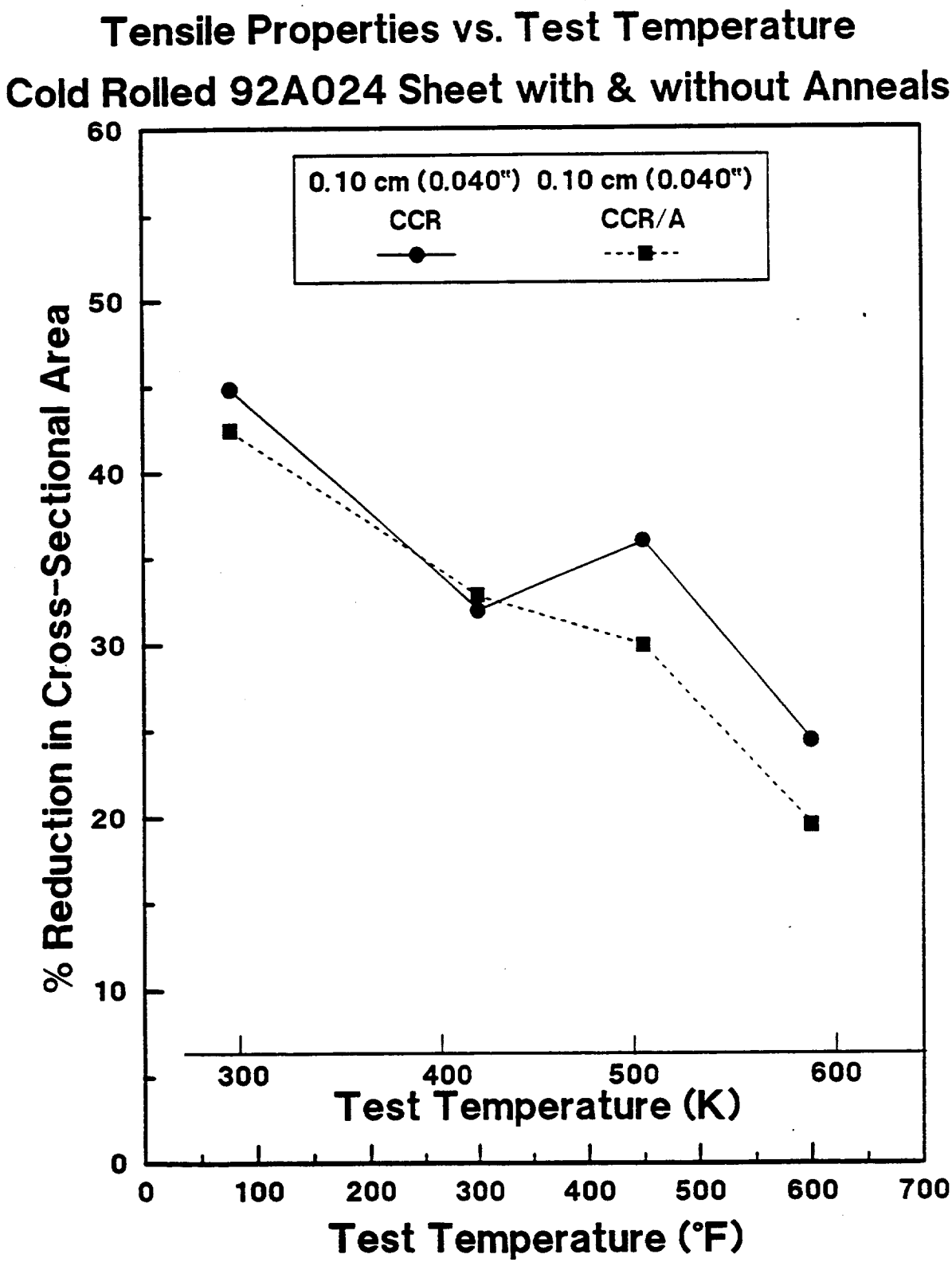
Tensile Properties vs. Test Temperature
Cold Rolled 92A024 Sheet with & without Anneals
0.10 cm (0.040") 0.10 cm (0.040")
CCR
CCR/A
% Reduction in Cross-Sectional Area
60
50
40
30
20
10
0
300
400
500
600
Test Temperature (K)
0
100
200
300
400
500
600
700
Test Temperature (°F)

Fig. 40

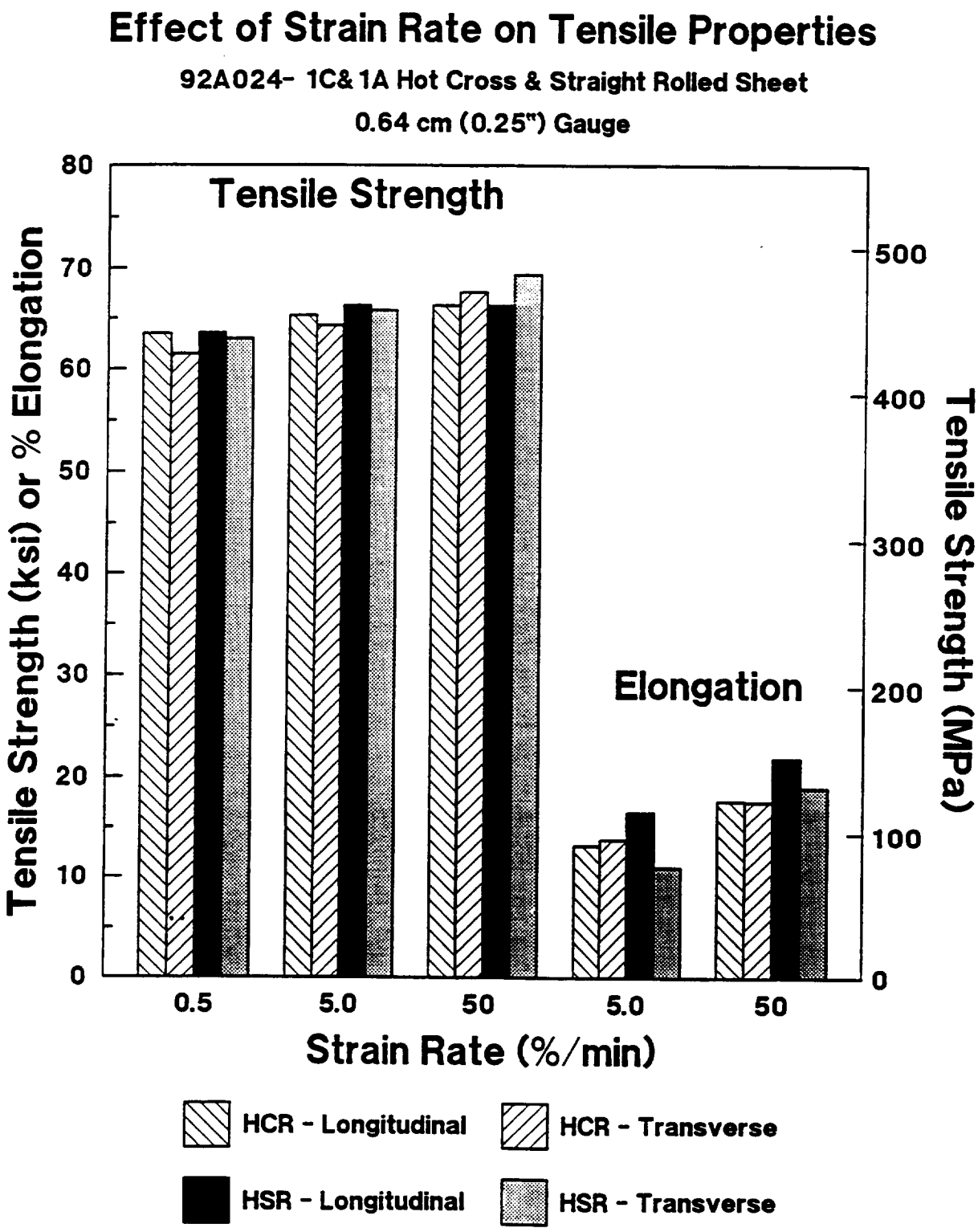
Effect of Strain Rate on Tensile Properties
92A024- 1C& 1A Hot Cross & Straight Rolled Sheet
0.64 cm (0.25") Gauge
Tensile Strength
Elongation
Tensile Strength (ksi) or % Elongation
Tensile Strength (MPa)
0
10
20
30
40
50
60
70
80
0
100
200
300
400
500
0.5
5.0
50
5.0
50
Strain Rate (%/min)
HCR - Longitudinal
HCR - Transverse
HSR - Longitudinal
HSR - Transverse

Fig. 41

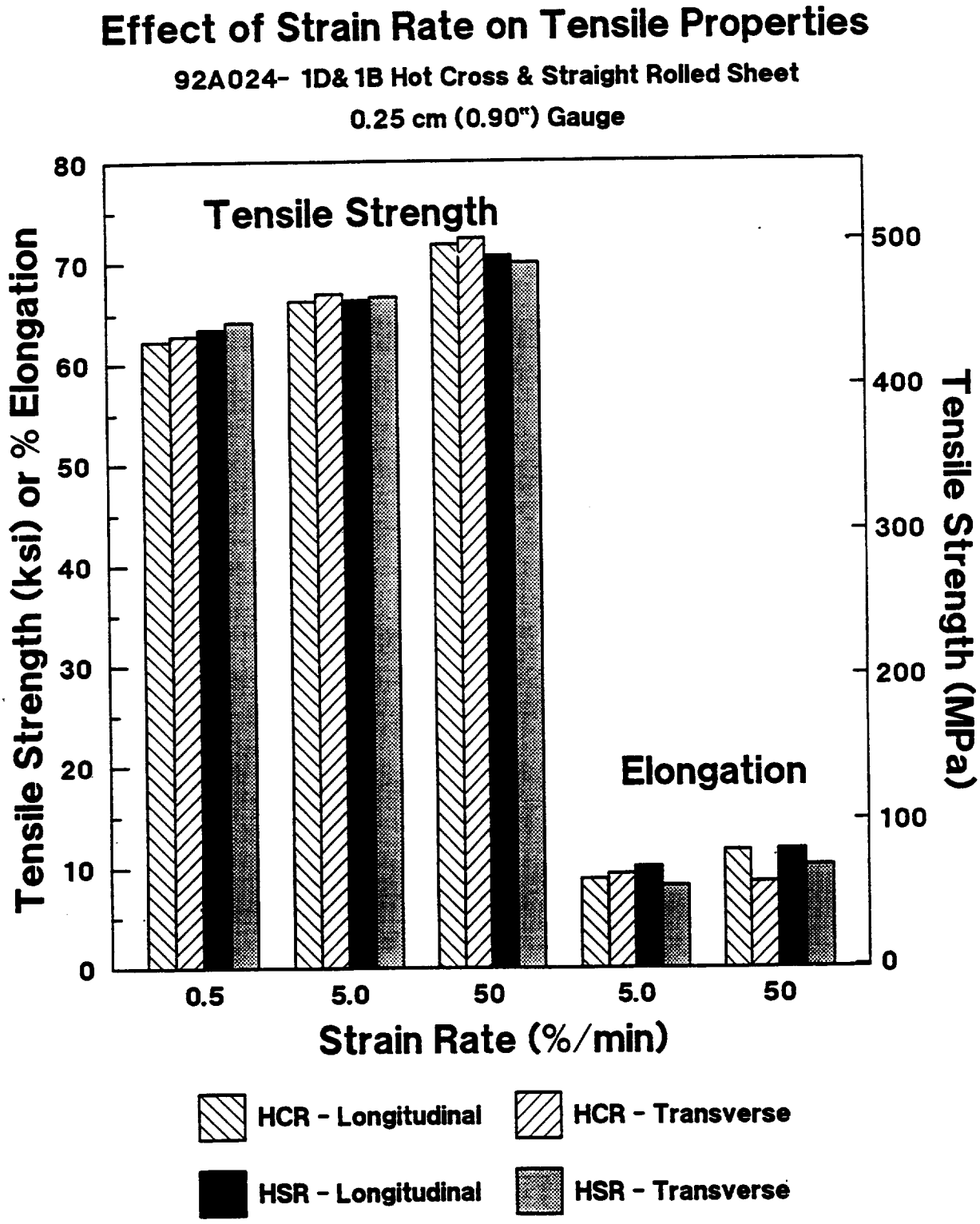
Effect of Strain Rate on Tensile Properties
92A024- 1D& 1B Hot Cross & Straight Rolled Sheet
0.25 cm (0.90") Gauge
Tensile Strength
Elongation
Tensile Strength (ksi) or % Elongation
Tensile Strength (MPa)
80
70
60
50
40
30
20
10
0
500
400
300
200
100
0
0.5
5.0
50
5.0
50
Strain Rate (%/min)
HCR - Longitudinal
HCR - Transverse
HSR - Longitudinal
HSR - Transverse

Fig. 42

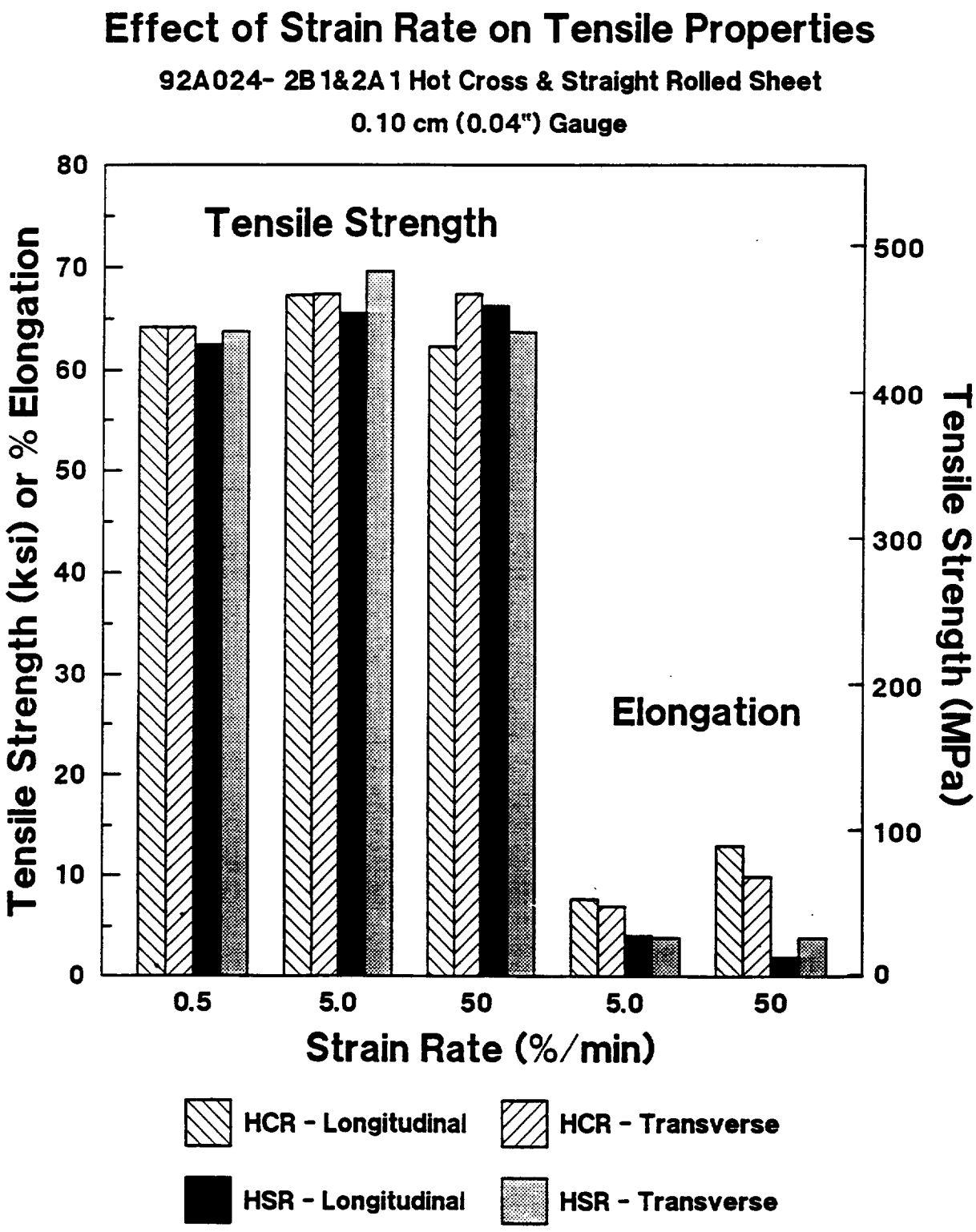
Effect of Strain Rate on Tensile Properties
92A024- 2B1&2A1 Hot Cross & Straight Rolled Sheet
0.10 cm (0.04") Gauge
Tensile Strength
Elongation
Tensile Strength (ksi) or % Elongation
Tensile Strength (MPa)
0
10
20
30
40
50
60
70
80
0
100
200
300
400
500
0.5
5.0
50
5.0
50
Strain Rate (%/min)
HCR - Longitudinal
HCR - Transverse
HSR - Longitudinal
HSR - Transverse

Fig. 43

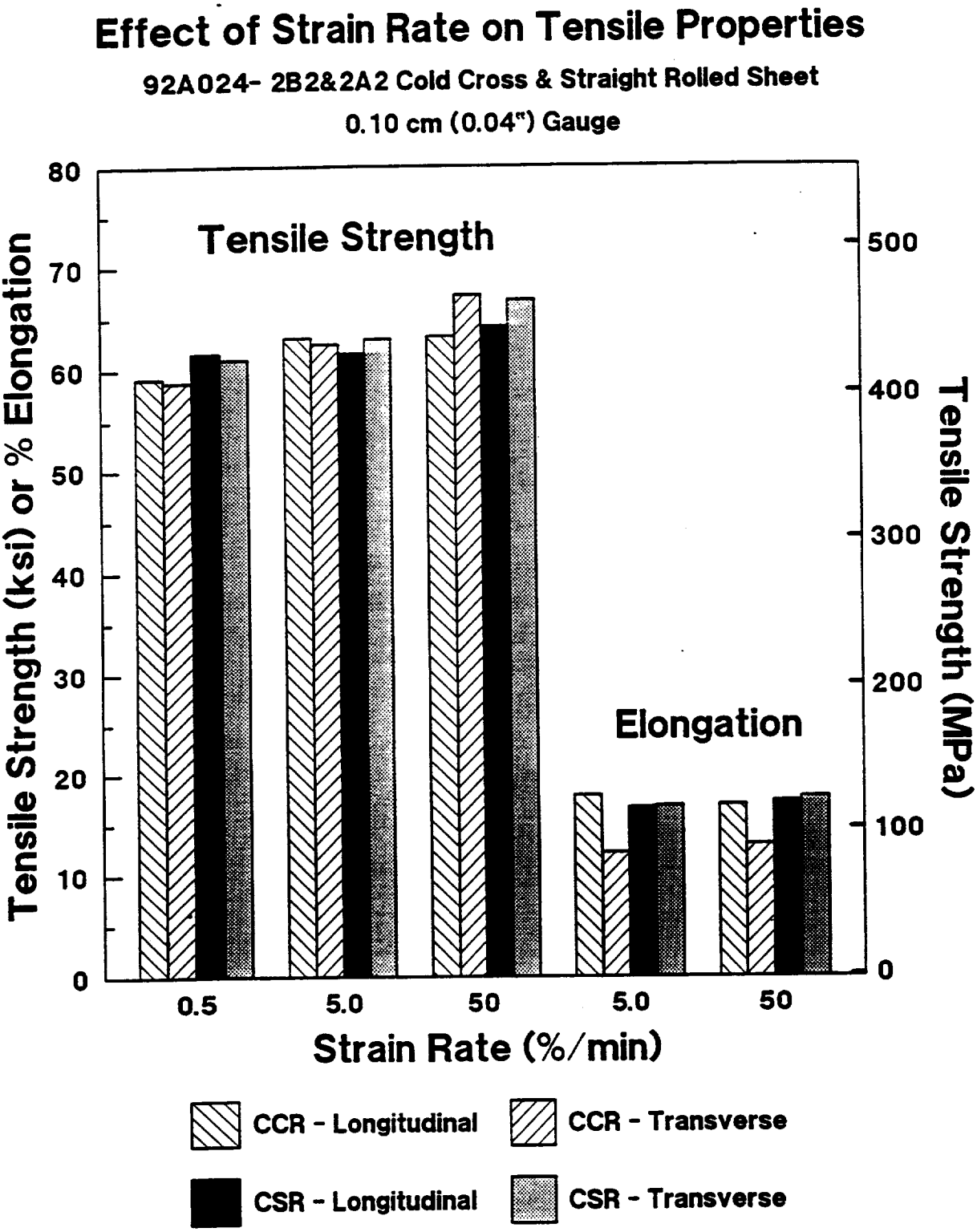
Effect of Strain Rate on Tensile Properties
92A024- 2B2&2A2 Cold Cross & Straight Rolled Sheet
0.10 cm (0.04") Gauge
Tensile Strength
Elongation
Tensile Strength (ksi) or % Elongation
Tensile Strength (MPa)
80
70
60
50
40
30
20
10
0
500
400
300
200
100
0
0.5
5.0
50
5.0
50
Strain Rate (%/min)
CCR - Longitudinal
CCR - Transverse
CSR - Longitudinal
CSR - Transverse

Fig. 44

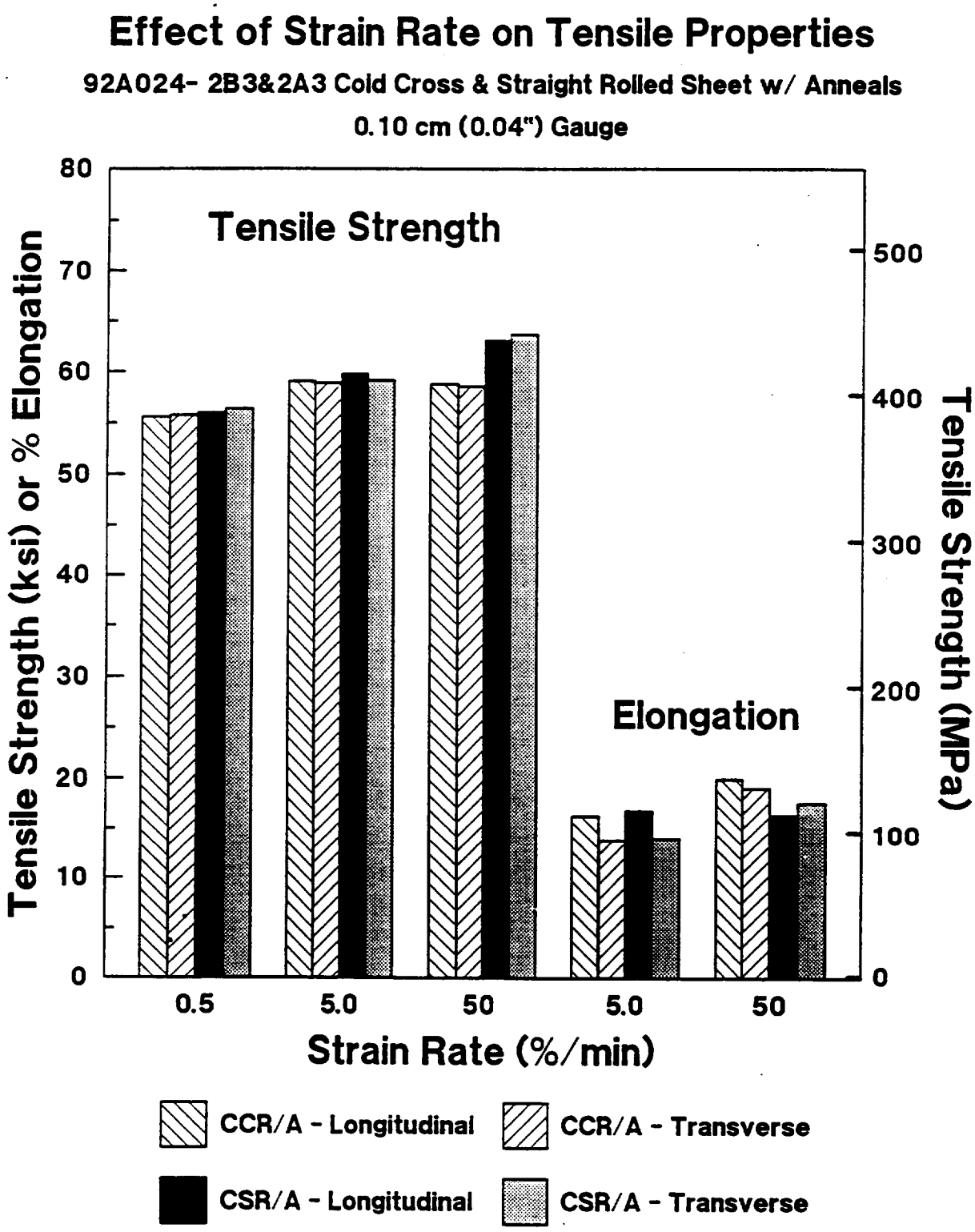
Effect of Strain Rate on Tensile Properties
92A024- 2B3&2A3 Cold Cross & Straight Rolled Sheet w/ Anneals
0.10 cm (0.04") Gauge
Tensile Strength
Elongation
Tensile Strength (ksi) or % Elongation
Tensile Strength (MPa)
80
70
60
50
40
30
20
10
0
500
400
300
200
100
0
0.5
5.0
50
5.0
50
Strain Rate (%/min)
CCR/A - Longitudinal
CCR/A - Transverse
CSR/A - Longitudinal
CSR/A - Transverse

Figure 45

Figure 46

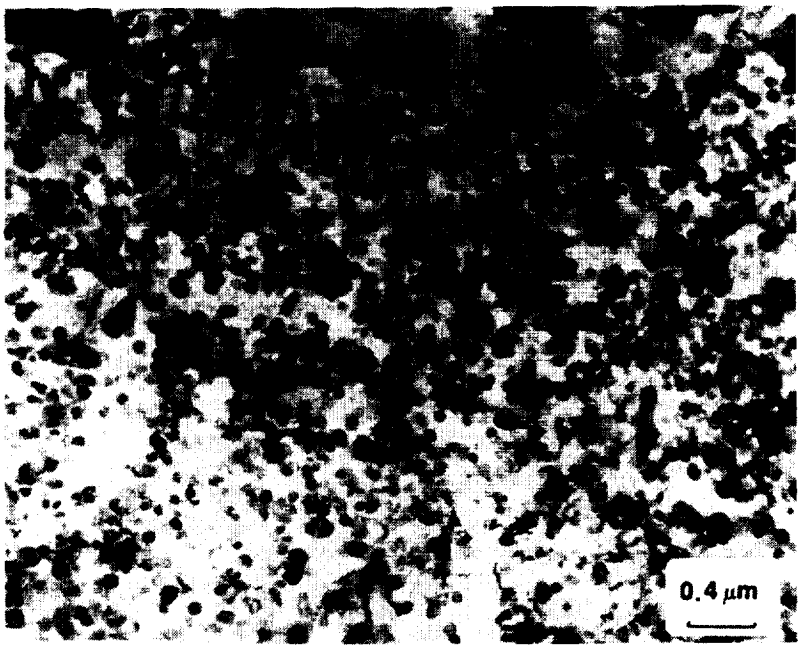

Figure 47

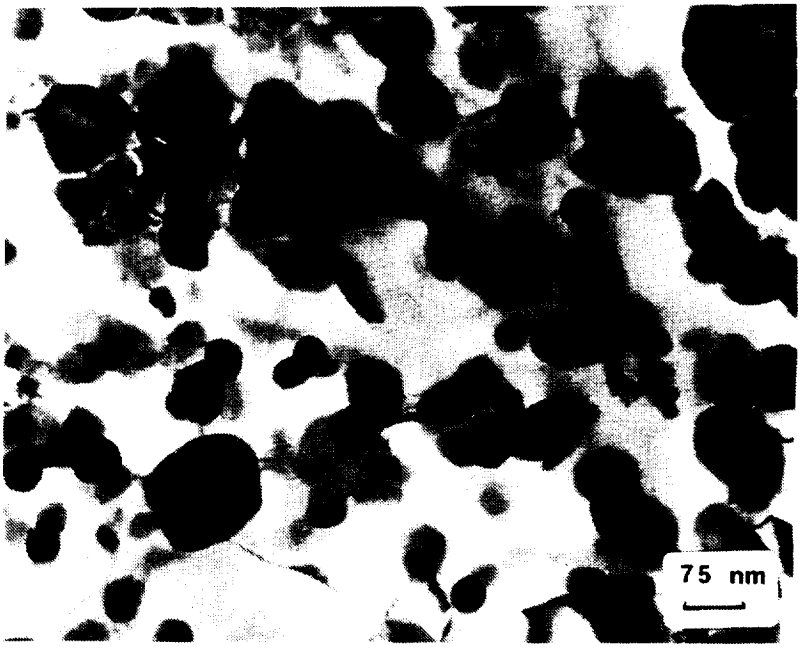

Figure 48

Figure 49

Figure 50

Figure 51

Figure 52

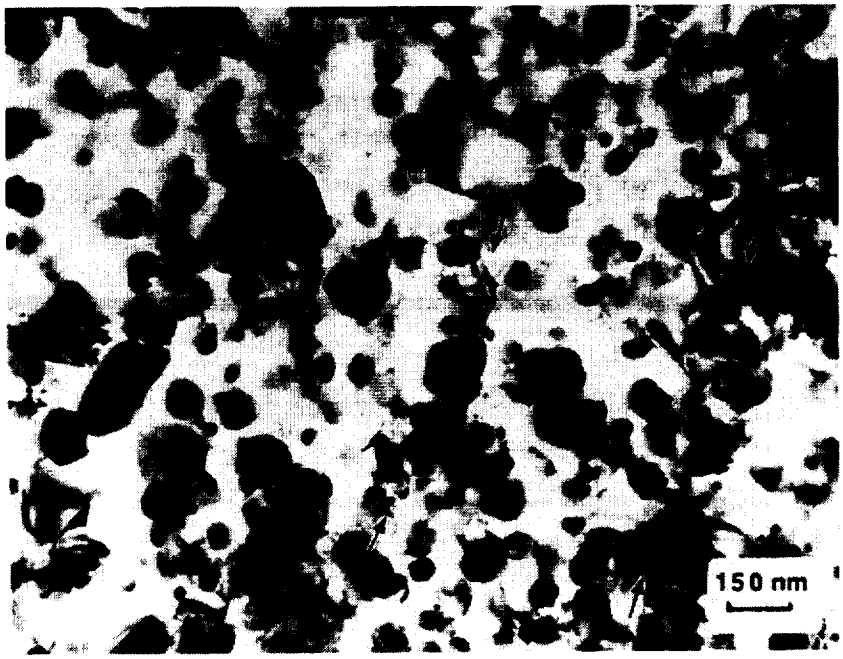

Figure 53

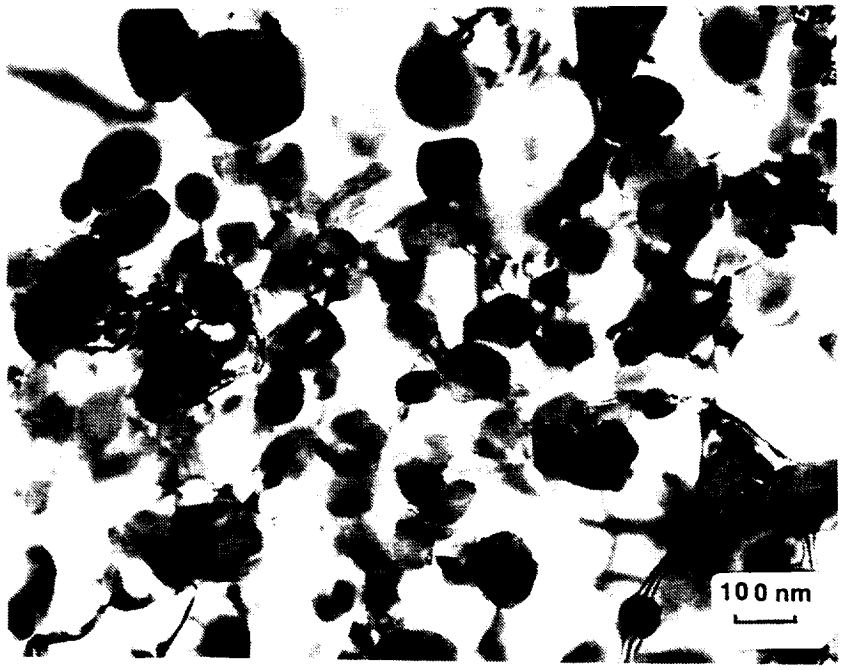

Figure 54

BOEING

Effect of Thermal Exposure and Test Temperature on Tensile Properties of Al-Cu-Li-Mg-Ag Alloys

Program Manager: W. E. Quist (Boeing)
Principal Investigator: F. S. Lin (Boeing)

Abstract

Boeing support for the Aluminum-Based Materials for High Speed Aircraft program was divided into two areas: 1) alloy characterization and 2) design studies.

Boeing has performed static fracture and fatigue crack growth rate (CGR) studies on Reynolds alloys RX818 and ML377 in sheet form. The static, fatigue and CGR property studies were performed on as-received material in the T8 condition as well as after exposure at 200°F, 225°F and 275°F for up to 1000 hrs, both at room temperature and at the exposure temperature. The results presented in this report just cover tensile properties. Fracture toughness, fatigue crack propagation and fractographic characterization of fracture surfaces wil be documented in the near future. The results of these studies showed that RX818 was the strongest of the two alloys both at room and elevated temperatures but that the ML377 alloy was the most thermally stable, based on several different interpretations of the data. This is generally consistent with the finds of other investigators supporting the program.

The design studies were performed using several different design concepts including skin/stiffener (baseline), honeycomb sandwich, integrally stiffened (including extruded stringers, orthogrid and isogrid concepts) and hybrid adaptations (conventionally stiffened thin-sandwich skins). The design concepts were exercised with respect to the wing box (upper), wing box (lower), wing strake, and the crown, window belt and keel areas of the fuselage. The results of these studies indicated that the preferred concept depended greatly upon the part of the aircraft being considered, but that many had advantages over the baseline skin-stringer design.

Objective

The primary objective of this task is to investigate both thermal stability and elevated temperature properties of two Al-Li sheet alloys which were recently developed by Reynolds Metals Company. One sheet alloy has an unrecrystallized grain structure with a composition of Al-3.5 Cu-1.0 Li-0.4 Mg-0.4 Ag-0.12 Zr (RX818), and another has a recrystallized structure with a composition of Al-3.5 Cu-1.0 Li-0.4 Mg-0.4 Ag-0.4 Mn-0.12 Zr (ML377).

Introduction

Al-Cu-Li-Mg-Ag alloys, which were recently developed by Reynolds Metals Company, and designated as RX818 and ML377 internally, have been recognized as potential materials for primary structural applications for the Mach 2 high speed civil transport (HSCT). This type of alloy in the T8 temper is strengthened primarily by T_1 (Al_2CuLi) plate shaped precipitates (1) and has both high strength and fracture toughness (2). The credit for achieving high fracture toughness is associated with the absence of shearable/coherent δ' precipitates since these precipitates have been found to be a primary factor in the low fracture toughness observed in commercial Al-Li alloys (2, 3, 4). However, the superior mechanical properties of these materials will deteriorate somewhat when subjected to thermal exposures between 200 - 275°F and/or tested in this temperature range (anticipated during Mach 2 HSCT aircraft service). The extent of degradation in the properties depends on both exposure temperature and time, and will also depend on both test temperature and strain rate.

Preliminary investigation from the NASA, HSR Metallic Materials Task, showed that RX818 was thermally stable (with respect to tensile properties) at 225°F for longer than 27,000 hours and had no significant degradation of the microstructures (1, 5). These intrinsic properties further indicate that this type of alloy is a potential candidate for structural materials for a Mach 2 HSCT aircraft which operates in this temperature range. However, there are two major concerns; one is the degradation of fracture toughness with thermal exposure, and another is the creep strain in the operation temperature range. The Aluminum Alloy Development Task undertaken by Boeing is to address the first item, i.e., the effect of thermal exposure on tensile properties, fracture toughness and fatigue crack growth rates. The results presented in this report just cover tensile properties. Fracture toughness, fatigue crack propagation and fractographic characterization of fracture surfaces will be documented in the near future.

Subtask 1

Procedures

Materials

Two pieces of each RX818-T8 and ML377-T8 Al-Li alloy sheet were received for property evaluation. Their dimensions are approximately 0.09"(T) by 47"(W) by 72"(L) where T, W, and L represent thickness, width and length, respectively. RX818 has an unrecrystallized grain structure and a typical composition of Al-3.5 Cu-1.0 Li-0.4 Mg-0.4 Ag-0.12 Zr; whereas ML377

has a recrystallized grain structure and a typical composition of Al-3.5 Cu-1.0 Li-0.4 Mg-0.4 Ag-0.4 Mn-0.12 Zr.

Thermal Exposure

Tensile specimens of each alloy were divided into seven groups. These seven groups were separately thermally-treated as : (a) no thermal exposure, (b) 200°F for 300 hours, (c) 200°F for 1000 hours, (d) 225°F for 300 hours, (e) 225°F for 1000 hours, (f) 275°F for 300 hours, and (g) 275°F for 1000 hours.

Tensile Tests

Tensile specimens of each alloy were machined to the following dimensions: thickness - 0.09 inch, gauge width - 0.25 inch, and gauge length - 1.13 inches. They were tested at four different temperatures: room temperature (R. T.), 200°F, 225°F., and 275°F. The test matrix is listed in Tables 1, 2 and 3. Each alloy in the T8 temper (no thermal exposure) was tested in longitudinal (L) , 45 degree and long transverse (LT) directions. Others were tested in both L and LT directions. Duplicate specimens were used for each case. Both elastic and plastic strains of each specimen were measured with a one inch gage length extensometer which was directly attached to the specimen being tested. The loading rate (cross-head-speed) of about 0.04 inch/minute was used. For specimens tested at elevated temperatures, the specimens were soaked at the specific temperature for 15 minutes prior to testing.

Results and Discussion

Grain Structure and Intermetallic Particles

The elevated temperature properties of all metals, such as strength and creep resistance, strongly depend on their grain structure. These properties are governed by dislocation interaction, dislocation climb and the rate of vacancy diffusion, and these three parameters are accelerated by the presence of grain and subgrain boundaries since both boundaries are the primary sources and sinks of dislocations and vacancies. Correspondingly, above a certain temperature the smaller the grain size, the lower the elevated temperature tensile properties and the higher the creep strain. In order to determine the difference in elevated temperature properties of Al-Li alloys having recrystallized and unrercrystallized grain structures, RX818 was processed to have an unrecrystallized grain structure, Figure 1(a) and 1(b), whereas, ML377 was intentionally processed to give a recrystallized grain structure, Figure 2(a) and 2(b). RX818 exhibits a thin recrystallized layer on the rolling surface, Figure 1(a). The straight line grain boundary pattern

with small interspacing (about 0.0005 inch) illustrated in Figure 1(a) and 1(b) indicates a thin pancake unrecrystallized grain structure for this Al-Li sheet. These straight lines represent high angle grain boundaries. As is obvious from Figure 2(a) and 2(b), ML377 has large, thick and elongated recrystallized grains.

The elevated temperature properties of aluminum alloys are profoundly influenced by the size, volume fraction, distribution and thermal stability of both strengthening precipitates and insoluble particles (dispersoid particles). The addition of 0.4% Mn to ML377, which forms thermally stable Mn dispersoids, was intended to improve the thermal stability, elevated temperature tensile properties and creep resistance.

Tensile Properties at Room Temperature

Tensile Properties in the L, 45 Degree and LT Directions

Tensile properties in these three orientations are important parameters for structural design. The 45 degree properties are directly related to shear strength of the material, and the shear strength becomes particularly critical when the body skin of an aircraft contains numerous rivets and fasteners. The tensile strength of both RX818-T8 and ML377-T8 are plotted as tensile yield strength (TYS) and ultimate tensile strength (UTS) vs test direction, i.e., 0 (L direction), 45 (45 degree angles with respect to L) and 90 (LT direction) as illustrated in Figure 3.

As can be seen from Figure 3, the 45 degree strength of RX818-T8 is substantially lower than both L and LT directions, while the strength in these three directions for ML377-T8 is comparable. The diffference between RX818 and ML377 is associated with crystallographic texture. RX818 with an unrecrystallized grain structure exhibits a strong deformation texture (5) resulting in a noticeably lower strength in the 45 degree angles; whereas, ML377 with a recrystallized structure develops a strong recrystallized texture (5) resulting in a comparable strength in the L, 45 degree and LT directions. This behavior is similar to that displayed by commercial Al-Li alloys when they have either unrecrystallized or recrystallized grain structures, i. e., alloys 2090, 2091 and 8090 in sheet form (8, 9).

When comparing the tensile strength between RX818 and ML377, both the TYS and UTS of RX818-T8 in the L and LT directions are higher than those for ML377-T8. The higher strength of RX818 is mainly due to the substructure strengthening effect. On the other hand, due to texture strengthening, the 45 degree strength of ML377-T8 is superior to RX818-T8. This higher 45 degree strength also implies that ML377-T8 has a greater shear strength than RX818-T8.

Separately, it is very interesting to note that the magnitude of strain hardening (in terms of the difference between UTS and TYS) is relatively constant for RX818 in all L, 45 degree and LT

directions; however, it is smaller in the L direction than both 45 degree and LT directions for ML377. The higher strain hardening in both 45 degree and LT directions of ML377-T8 is directly related to more slip systems operated which are, in turn, associated with crystallographic texture.

Tensile Properties of RX818-T8 and ML377-T8 With Thermal Exposure

The room temperature tensile properties of RX818-T8 and ML377-T8 after thermal exposure at temperatures of 200°F, 225°F and 275°F for both 300 hours and 1000 hours are listed in Tables 4 and 5 for RX818 and ML377 respectively. The data for TYS in the L direction are plotted against thermal exposure time at three temperatures; 200, 225 and 275°F (see Figure 4). This figure is plotted with a semilog axis in which "1" in the x-axis represents the T8 temper (no thermal exposure). Figure 4 shows that tensile yield strength of both RX818-T8 and ML377-T8 increases slightly with exposure time for all three temperatures studied. For example, the TYS of RX818-T8 increases 2-3 Ksi after exposure to each temperature (200, 225 and 275°F) for 1000 hours, but it increases only about 1 Ksi for ML377-T8. Additionally, Tables 4 and 5 also demonstrate that the TYS of both alloys in the LT direction have a similar response to thermal exposure as found for the L direction. The slight increase in tensile strength is associated with the formation of additional small amounts of S′ and δ′ precipitates (1).

It is surprising to note that the unrecrystallized RX818-T8 and recrystallized ML377-T8 have only a slightly different response to thermal exposure. This subtle difference between RX818 and ML377 implies that the presence of subgrain boundaries in RX818-T8 plays a small role in influencing aging kinetics during these thermal exposures, when the alloy is already in the T8 temper. It has been noted that subgrain boundaries in the unrecrystallized Al-Li alloys significantly accelerate the age hardening process when the materials are in the T3 condition (8). The different responses between T8 and T3 tempers may be due to a fact that T_1 precipitates form on subgrain boundaries in the T8 temper at the expense of vacancies along these boundaries. The lack of vacancies on subgrain boundaries slows down the diffusion process which, in turn, reduces aging kinetics. Likewise, precipitation of T_1 phase in the interior of subgrains reduces the diffusion rate.

This thermal exposure study clearly shows that both RX818-T8 and ML377-T8 are quite thermally stable at 200, 225 and 275°F up to 1000 hours, and that ML377-T8 has a slightly higher thermal stability than RX818-T8. In addition, another investigation from D. L. Dicus (5) demonstrated that RX818-T8 was thermally stable at 225F for more than 27,000 hours.

Effect of Test Temperature on Tensile Properties

Alloys RX818 and ML377 in the T8 temper were tested at 75, 200, 225 and 275°F. In addition, both alloys in the T8 plus various thermal exposures were tested at 200 and 225°F. These studies were undertaken to understand the interactions of thermally activated dislocations and, thus, dynamic recovery during tests at the elevated temperatures to which a Mach 2 HSCT airplane will be exposed.

T8 Temper

Tensile properties of RX818-T8 tested at 75, 200, 225 and 275°F are listed in Table 6, and these properties for ML377-T8, tested at the same conditions, are listed in Table 7. In order to facilitate the comparison of effect of both test temperature and orientation on tensile propeties for each sheet alloy, the data documented in Tables 6 and 7 are plotted as tensile strength vs test temperature, (see Figure 5). In addition, the same plot for the elongation is shown in Figure 6. These plots show three consistent results regardless of the alloys and test directions. They are: (i) both TYS and UTS decrease with increasing test temperature, (ii) strain hardening (in terms of the difference between UTS and TYS) decreases with increasing test temperature, and the difference becomes almost zero at a test temperature of 275°F, and (iii) elongation increases with increasing test temperatures except for the L direction of ML377 where its elongation decreases slightly.

These three temperature dependent properties can be explained by the dislocation interaction mechanisms. The reasons why tensile yield strength of both alloys decreases with increasing test temperature may include: (i) thermal activation reducing the pinning force between dislocations and solute atoms, (ii) screw dislocations and the screw components of the mixed dislocations having more opportunites to escape obstacles, i.e., precipitates, by cross slip resulting from thermal activation, and (iii) pre-existing dislocation loops and jogs that are introduced during stretching may climb and then become mobile as the test temperature increases, especially for dislocations on which no T_1 phase nucleates during artificial aging.

The decrease in ultimate tensile strength and strain hardening with increase in temperature can be explained by the decrease of dislocation interactions and dislocation/precipitate interactions. Besides, both dislocation loops and jogs that are formed by dislocation interactions are able to climb when tested at elevated temperature. The extent of reducing dislocation interactions and the intensity of dislocation climb and annihilation increase with increasing test temperature. At a temperature of 275°F, UTS is almost equal to TYS, i.e., little strain hardening. This indicates that the rate of strain hardening is almost equivalent to that of dynamic recovery. Separately, the

increasing rate of dynamic recovery with test temperatures, from 75 to 275°F, results in a higher elongation for the materials. The single abnormal case, in which longitudinal elongation of ML377-T8 decreases slightly when tested at these temperatures, may be associated with crystallographic texture which, in turn, influences the deformation behavior. This becomes an interesting topic for further investigation.

The effect of test orientation, L and LT, on the tensile strength for RX818-T8 is illustrated in Figure 5(a) and 5(b). Both TYS and UTS in the L direction are greater than those for the LT direction at the same test temperature. On the contrary, elongation in the L direction is lower than that in the LT direction (see Figure 6).

The effect of test orientation on tensile propeties for ML377 can be seen from Table 7 as well as Figure 5(c) and 5(d). TYS in the LT direction is lower than that in the L direction at the corresponding test temperature; whereas UTS is higher in the LT direction than that in the L direction. It is quite clear that the magnitude of strain hardening in the LT direction is noticeably greater than that for the L direction. This result is identical to that of the specimens tested at room temperature. The reason for this behavior was discussed earlier. As is obvious from Figure 6, elongation in the L direction decreases slightly when tested at these temperatures; whereas, that in the LT direction increases with increasing test temperatures.

Finally, tensile strength comparisons were made between RX818-T8 and ML377-T8 for test temperatures of 75, 200, 225 and 275°F. As noted earlier, the former has unrecrystallized grain structure, and the latter has recrystallized structure, with 0.4% Mn for dispersoid formation. For all four test temperatures, both the TYS and UTS of RX818-T8 are greater than those for the ML377-T8 counterparts. This reflects that substructure strengthening effects still dominate the tensile strength of RX818-T8 for test temperatures up to 275°F, when using a cross head speed of 0.04 inch/minute. In other words, the magnitude of the substructure strengthening effect is greater than that of the subgrain boundary contribution to dynamic recovery.

Another comparison method, which may give new insight regarding the dynamic recovery in RX818-T8 and ML377-T8, was to subtract the TYS tested at various elevated temperatures from that tested at 75°F, and also use these differences, divided by the 75°F TYS, for obtaining the percentage of change. The same calculation was also made for UTS and elongation. The resultant data are listed in Table 8 for both RX818 and ML377. The meaning of this calculation is that the smaller the difference betweeen the 75°F and the elevated temperature test results, the smaller the degree of dynamic recovery and, naturally, the better is the stability of elevated temperature tensile properties.

Based on this criterion, the data in Table 8 indicates that the LT direction performs slightly better than the L direction for both TYS and UTS of each alloy, except the UTS of ML377-T8 tested at 275°F. With regard to elongation, the LT direction performs noticeably better than the L direction for RX818-T8, but opposite is true for ML377-T8. Note that the elongation in the L direction of ML377 slightly decreases when tested at elevated temperatures. No relationship can be established between elongation and test temperature for this direction.

A comparison of both TYS and UTS between RX818-T8 and ML377-T8 was made using the same criterion just described. The data in Table 8 show that RX818-T8 performs, in general, slightly worse than ML377-T8. This slightly worse performance implies that subgrain boundaries in RX818-T8 play a small adverse role in dynamic recovery at the present test conditions. It is different from pure metals in that precipitates of T_1 phase on subgrain boundaries reduce the dynamic recovery process. A similar behavior was observed in Al-Li-Cu-Mg alloys by M. Pridham et al. (10), and they explained that precipitation of S phase (Al_2CuMg) along subgrain boundaries in alloy 8090 prevents the subgrain boundaries from acting as efficient dislocation sinks and hence, delays dynamic recovery.

With respect to the comparison of elongation between RX818 and ML377, the results of Table 8 clearly demonstrate that ML377-T8 performs significantly better than RX818-T8 in both L and LT directions, especially for the L direction for which its elongation decreases slightly when tested at these temperatures.

From this discussion of tensile test results at elevated temperatures, one concludes that ML377-T8 has a slightly better thermal stability than RX818-T8. This is in agreement with both the grain structure and chemical composition; ML377-T8 has large recrystallized grains and contains Mn dispersoids.

The elevated temperature test results and analysis present a most interesting topic from both a practical and research point of view. Does the magnitude of the difference in tensile properties between the 75°F test and the elevated temperature test have a correlation with the creep strain? If it does, this simple tensile test can be used to qualitatively rank both thermal stability and creep strain of these materials. This subject is reserved for further investigation.

T8 Temper Plus Various Thermal Exposures

The Elevated temperature tensile properties of RX818-T8, which were exposed to temperatures of 200 and 225°F for both 300 and 1000 hours and then tested at these two exposure temperatures, are listed in Table 9. Likewise, these properties for ML377-T8 are listed in Table 10. In addition, the properties of both alloys in the T8 condition when tested at 200 and 225°F are

included as baselines for comparison purpose. In order to facilitate a comparison of the effect of thermal exposure on the tensile properties for RX818 and ML377, the data listed in Tables 9 and 10 are plotted as strength vs thermal exposure time at 200 and 225°F in Figures 7 and 8.

Figures 7 and 8 show a consistent result that both the TYS and UTS of RX818-T8 and ML377-T8 increase slightly with thermal exposure time at each of the 200 and 225°F exposure temperatures. For example, both alloys increase their TYS and UTS of about 2 Ksi in both L and LT directions when exposed to each temperature of 200 and 225°F for 1000 hours, and then tested at these two exposure temperatures. This trend is similar to that of the same materials tested at room temperature after thermal exposure, described in the section *Tensile Properties of RX818-T8 and ML377-T8 With Thermal Exposure*. Therefore, the explanation used in the previous section can be applied to the present case. It is noted that elongation of both alloys is not affected by thermal exposure.

In conclusion, thermal exposure at temperatures of 200 and 225°F for up to 1000 hours is slightly beneficial to elevated temperature tensile strength for both alloys.

Conclusions

(1) In room temperature tests, RX818-T8 has both longitudinal and transverse tensile strengths greater than ML377-T8; whereas the opposite is true for the 45 degree direction. Correspondingly, the former alloy has a significantly lower strength in the 45 degree direction than both longitudinal and transverse directions, but the latter has a comparable strength in all three directions.

(2) The tensile strength for RX818 increases 2-3 Ksi and ML377-T8 increases its strength only about 1 Ksi when exposed to temperatures of 200, 225 and 275°F for 1000 hours and then tested at room temperature.

(3) The tensile yield strength, ultimate tensile strength and strain hardening effect for both RX818-T8 and ML377-T8 decrease with test temperatures from 75 to 275°F. On the other hand, the elongation of both alloys increases with increasing test temperature except for ML377-T8 in the longitudinal direction where it decreases slightly when tested at elevated temperatures.

(4) RX818-T8 exhibits a stronger tensile strength in the longitudinal and transverse directions than ML377-T8 when testing at 200, 225 and 275°F; while ML377-T8 has a slightly higher stability in its elevated temperature tensile properties compared to RX818-T8.

(5) The tensile strength for both RX818-T8 and ML377-T8 increases about 1 Ksi when exposed to temperatures of 200F and 225°F for 1000 hours and then tested at these two exposure temperatures.

Subtask 2

This task was subdivided into four Phases as shown in Fig. 1. As no materials properties were generated during the subject program that could be reduced to very preliminary property allowables for use in the design studies, it was not possible to initiate Phases I, III, and IV of the trade studies. However, substantial progress has been made in Phase II, particularly with respect to the development of structural/manufacturing concepts that would be particularly applicable to an "Aluminum" HSCT.

The aluminum structural/manufacturing design concepts for the wingbox, wing strake, and fuselage were developed with reference to projected materials properties from ongoing internal Boeing studies (Low-Cost Airplane Trade Study - LCATS). Aluminum material structural design concepts are summarized in the matrices shown in Figs. 2, 3 and 4. They are grouped into four major design families: (A) integrally stiffened, (B) sandwich, (C) hybrid concepts, and (D) conventional skin/stringer construction. The details are described below:

A. **Integrally Stiffened** Three arrangements are included: extruded stringers, orthogrid, and isogrid according to airplane location and type and magnitude of loading.

B. **Sandwich** Arrangements include two variations on sandwich edge treatments according to location and loading.

C. **Hybrids** (conventionally stiffened thin-sandwich skins) Included to study effects of hybrids on structural performance and cost. In addition, hybrids could provide redundant load paths, fail safety, and better damage tolerance, among other benefits.

D. **Conventional skin/stringer** Included to provide a baseline from which to measure concept improvements in terms of both performance and cost. (these concepts are not shown in Figs. 2, 3, and 4).

To make the best use of materials, a tailored structural approach was used. Materials possessing desired properties, along with novel structural arrangements that matched design and manufacturing process requirements at different locations, were selected. In developing each of the concepts, care was taken to address low-cost producible structure, as well as low weight and high performance.

Structural sizing of each of the design concepts was begun under this grant and continued under NASA contract NASI-19349. Sizing focused on refining the most promising concepts and processes to provide design data for weight and later cost estimation. To understand the sensitivity to material and structural concept changes, performance first was evaluated and compared at the concept level. The plan and schedule for these activities are shown in Figs. 5 and 6.

Six materials or structural concepts at the subcomponent level and four concepts at the component and airplane level were examined. For airplane level weights analysis, the concepts were not completed to the same degree of fidelity. A global (airplane) - local (panel) optimization iteration was used to determine minimum weight for each of the four airplane concepts. The global-local optimization process proved to be particularly difficult for the Mach 2.0 PMC skin-stringer concept and did not converge satisfactorily. In addition, the methods for determining fuselage weights for both the PMC skin-stringer and Titanium Honeycomb Sandwich concepts were based on data from Lockheed and Northrop, respectively. Both different from the Boeing method used for the PMC Honeycomb Sandwich concept. Therefore, the fuselage weights for the PMC skin-stringer and Titanium Honeycomb Sandwich concepts, and wing weights for the PMC skin-stringer concept are subject to significant revisions. The effect of durability and damage, and thermomechanical considerations on the overall weight were addressed in a preliminary fashion during the FY94 effort. Our plans during FY95 are to complete the airplane weight evaluation process to assure weights for the different concepts are consistent, and perform a more thorough assessment of durability, damage tolerance, and thermomechanical considerations. The details of this study can be found in NASA Contractor Report, Boeing Document Number D6-81508, "NASA Materials and Structures Design Integration Trade Study, First Year Written Report, January 1995" by Kumar G. Bhatia, Ludwig Suju, Stephen Sergev, David Gimmestad, Robert A. Seis, Bryan D. Johnson, Mark Nazari, James Fogleman, S. Eric Cregger, Terry Tsuchiyama, Kim Tran, Gene Arnold, Neil E. Zimmer, Jr., and Dennis Stogin.

References

1. Y. Mou, J. M. Howe and E. A. Starke, Jr., "Grain Boundary Precipitation and Fracture Behavior of an Al-Cu-Li-Mg-Ag Alloy" Met. Trans. A, Vol. 26A, P. 1591, 1995.
2. Alex Cho Presentation at Boeing, 1992.
3. E. A. Starke, Jr., T. H. Sanders and I. G. Palmer, "New Approaches to Alloy Development in the Al-Li Systems" J. of Metals, P. 24, Vol. 33, 1981.
4. S. Suresh, A. K. Vasudevan, M. Tosten and P. R. Powell, "Microscopic and Macroscopic Aspects of Fracture in Lithium-Containing Aluminum Alloys" A c t a Metall., P. 25, Vol. 35, 1987.
5. D. L. Dicus, "Overview of Aluminum Alloy Evaluation" in HSR Metallic Materials Task Reviews, April,1995.
6. ASTM E647 Standard Test Method for Measurement of Fatigue Crack Growth Rates, 1992.
7. ASTM E561 Standard Practice for R-Curve Determination, 1992.
8. F. S. Lin and W. E. Quist, "Development of Al-Li Sheet Alloys" The Boeing Company, 1990.
9. I. G. Palmer, W. S. Miller, D. J. Lloyd and M. J. Bull, "Effect of Grain Structure and Texture on Mechanical Propeties of Al-Li Base Alloys" in Al-Li Alloys III, Edited by C. Baker, P. J. Gregson, S. J. Jarris and C. J. Peel, P. 565, 1986.
10. M. Pridham, B. Noble and S. J. Harris, "Elevated Temperature Strength of Al-LI-Cu-Mg Alloys" in Al-Li Alloys III, Edited by C. Baker, P. J. Gregson, S. J. Jarris and C. J. Peel, P. 547, 1986.

Table 1. Test matrix for RX818 and ML377 sheet (no thermal exposure) tested at various elevated temperatures

Type of Specimen	Test at R. T.	Test at 200°F	Test at 225°F	Test at 275°F
L Tensile	RX-L-1 RX-L-2 ML-L-1 ML-L-2	RX-L-3 RX-L-4 ML-L-3 ML-L-4	RX-L-5 RX-L-6 ML-L-5 ML-L-6	RX-L-7 RX-L-8 ML-L-7 ML-L-8
LT Tensile	RX-LT-1 RX-LT-2 ML-LT-1 ML-LT-2	RX-LT-3 RX-LT-4 ML-LT-3 ML-LT-4	RX-LT-5 RX-LT-6 ML-LT-5 ML-LT-6	RX-LT-7 RX-LT-8 ML-LT-7 ML-LT-8
45° Tensile	RX-45-1 RX-45-2 ML-45-1 ML-45-2			

Table 2. Test matrix for RX818 and ML377 sheet (with various thermal exposures) tested at room temperature

Type of Specimen	Thermal Exposure					
	200°F/ 300 hrs	200°F/ 1000 hrs	225°F/ 300 hrs	225°F/ 1000 hrs	275°F/ 300 hrs	275°F/ 1000 hrs
L Tensile	RX-L-9 RX-L-10 ML-L-9 ML-L-10	RX-L-11 RX-L-12 ML-L-11 ML-L-12	RX-L-13 RX-L-14 ML-L-13 ML-L-14	RX-L-15 RX-L-16 ML-L15 ML-L-16	RX-L-17 RX-L-18 ML-L17 ML-L-18	RX-L-19 RX-L-20 ML-L19 ML-L-20
LT Tensile	RX-LT-9 RX-LT-10 ML-LT-9 ML-LT-10	RX-LT-11 RX-LT-12 ML-LT-11 ML-LT-12	RX-LT-13 RX-LT-14 ML-LT-13 ML-LT-14	RX-LT-15 RX-LT-16 ML-LT-15 ML-LT-16	RX-LT-17 RX-LT-18 ML-LT-17 ML-LT-18	RX-LT-19 RX-LT-20 ML-LT-19 ML-LT-20

Table 3. Test matrix for RX818 and ML377 sheet (with various thermal exposures) tested at two elevated temperatures of 200°F and 225°F

Type of Specimen	Thermal Exposure & Test Temperature			
	200°F/300 hrs Test at 200°F	200°F/1000 hrs Test at 200°F	225°F/300 hrs Test at 225°F	225°F/1000 hrs Test at 225°F
L Tensile	RX-L-21 RX-L-22 ML-L-21 ML-L-22	RX-L-23 RX-L-24 ML-L-23 ML-L-24	RX-L-25 RX-L-26 ML-L-25 ML-L-26	RX-L-27 RX-L-28 ML-L-27 ML-L-28
LT Tensile	RX-LT-21 RX-LT-22 ML-LT-21 ML-LT-22	RX-LT-23 RX-LT-24 ML-LT-23 ML-LT-24	RX-LT-25 RX-LT-26 ML-LT-25 ML-LT-26	RX-LT-27 RX-LT-28 ML-LT-27 ML-LT-28

Table 4. Tensile properties of RX818-T8 as affected by thermal exposure (R.T. test)

Properties		Thermal Exposure						
		T8	T8+200°F/ 300 hrs	T8+200°F/ 1000 hrs	T8+225°F/ 300 hrs	T8+225°F/ 1000 hrs	T8+275°F/ 300 hrs	T8+275°F/ 1000 hrs
TYS	L	83.6	83.8	85.5	83.9	86.0	86.6	86.8
(Ksi)	LT	80.1	80.6	81.7	81.6	82.9	82.2	84.1
UTS	L	87.9	88.3	88.4	88.2	89.5	90.1	90.1
(Ksi)	LT	84.9	85.3	85.9	86.0	86.7	85.9	87.5
Elong	L	8.9	9.3	8.7	8.9	8.8	8.6	8.1
(%)	LT	12.0	—	11.2	10.8	10.6	10.5	9.1

Table 5. Tensile properties of ML377-T8 as affected by thermal exposure (R.T. test)

Properties		Thermal Exposure						
		T8	T8+200°F/ 300 hrs	T8+200°F/ 1000 hrs	T8+225°F/ 300 hrs	T8+225°F/ 1000 hrs	T8+275°F/ 300 hrs	T8+275°F/ 1000 hrs
TYS	L	76.0	76.5	76.7	76.7	77.1	76.7	76.2
(Ksi)	LT	74.2	74.2	75.1	75.0	75.6	75.9	75.5
UTS	L	78.0	78.7	78.3	78.4	78.7	78.5	78.0
(Ksi)	LT	80.1	80.1	80.8	81.0	81.6	81.7	81.1
Elong	L	9.5	9.9	9.7	9.8	9.3	8.8	8.2
(%)	LT	9.7	9.5	8.9	8.9	9.0	9.0	7.9

Table 6. Tensile property variation of RX818-T8 (no thermal exposure) with test temperature

Tensile Properties		Test Temperature			
		75°F	200°F	225°F	275°F
TYS	L	83.6	79.4	78.5	75.7
(Ksi)	LT	80.1	77.0	76.0	73.2
UTS	L	87.9	81.1	79.7	75.6
(Ksi)	LT	84.9	79.2	77.5	73.2
Elong	L	8.9	11.0	11.9	13.1
(%)	LT	12.0	13.5	13.9	16.0

Table 7. Tensile property variation of ML377-T8 (no thermal exposure) with test temperature

Tensile Properties		Test Temperature			
		75°F	200°F	225°F	275°F
TYS (Ksi)	L	76.0	72.4	71.8	69.6
	LT	74.2	71.2	70.7	68.7
UTS (Ksi)	L	78.0	73.0	71.8	69.8
	LT	80.1	75.1	73.9	70.6
Elong (%)	L	9.5	9.1	8.6	9.1
	LT	9.7	10.6	10.9	12.0

Table 8 Tensile strength and elongation difference between the 75°F test and the elevated temperature tests for RX818 and ML377

Alloy	Tensile Properties		75°F	75°F-200°F	75°F-225°F	75°F-275°F
RX818	TYS	L	83.6	4.2 (5.0%)	5.1 (6.1%)	7.9 (9.4%)
		LT	80.1	3.1 (3.9%)	4.1 (5.1%)	6.9 (8.6%)
	UTS	L	87.9	6.8 (7.7%)	8.2 (9.3%)	12.3 (14.0%)
		LT	84.9	5.7 (6.7%)	7.4 (8.7%)	11.7 (13.8%)
	Elong	L	8.9	11.0 (24%)	3.0 (34%)	4.2 (47%)
		LT	12.0	1.5 (13%)	1.9 (16%)	4.0 (33%)
ML377	TYS	L	76.0	3.6 (4.7%)	4.2 (5.5%)	6.4 (8.4%)
		LT	74.2	3.0 (4.0%)	3.5 (4.7%)	5.5 (7.4%)
	UTS	L	78.0	5.0 (6.4%)	6.2 (7.9%)	8.2 (10.5%)
		LT	80.1	5.0 (6.0%)	6.2 (7.7%)	9.5 (11.9%)
	Elong	L	9.5	-0.4 (-4%)	-0.9 (-9%)	-0.4 (-4%)
		LT	9.7	0.9 (9%)	1.2 (12%)	2.3 (24%)

* Percent change from 75°F.

Table 9. Tensile property variations of RX818-T8 (T8 and T8 plus thermal exposure) with test temperature

Tensile Properties		Thermal Exposure & Test Temperature					
		T-8 200°F Test	200°F/300 hrs 200°F Test	200°F/1000 hrs 200°F Test	T-8 225°F Test	225°F/300 hrs 225°F Test	225°F/1000 hrs 225°F Test
TYS (Ksi)	L	79.4	80.0	80.7	78.5	79.5	80.5
	LT	77.0	77.4	78.2	76.0	76.3	78.3
UTS (Ksi)	L	81.1	81.5	82.2	79.7	80.0	80.8
	LT	79.2	79.5	80.0	77.5	77.4	79.1
Elong (%)	L	11.0	11.4	11.1	11.9	11.7	11.6
	LT	13.5	12.8	12.2	13.9	14.1	13.3

Table 10. Tensile property variations of ML377-T8 (T8 and T8 plus thermal exposure) with test temperature

Tensile Properties		Thermal Exposure & Test Temperature					
		T-8 200°F Test	200°F/300 hrs 200°F Test	200F/1000 hrs 200°F Test	T-8 225°F Test	225°F/300 hrs 225°F Test	225°F/1000 hrs 225°F Test
TYS (Ksi)	L	72.4	73.1	73.4	71.8	72.3	73.2
	LT	71.2	72.1	72.5	70.7	71.8	72.2
UTS (Ksi)	L	73.0	73.4	73.6	71.8	72.3	73.3
	LT	75.1	76.0	76.4	73.9	74.8	75.4
Elong (%)	L	9.1	9.4	9.4	8.6	8.7	8.8
	LT	10.6	10.3	10.1	10.9	10.4	10.6

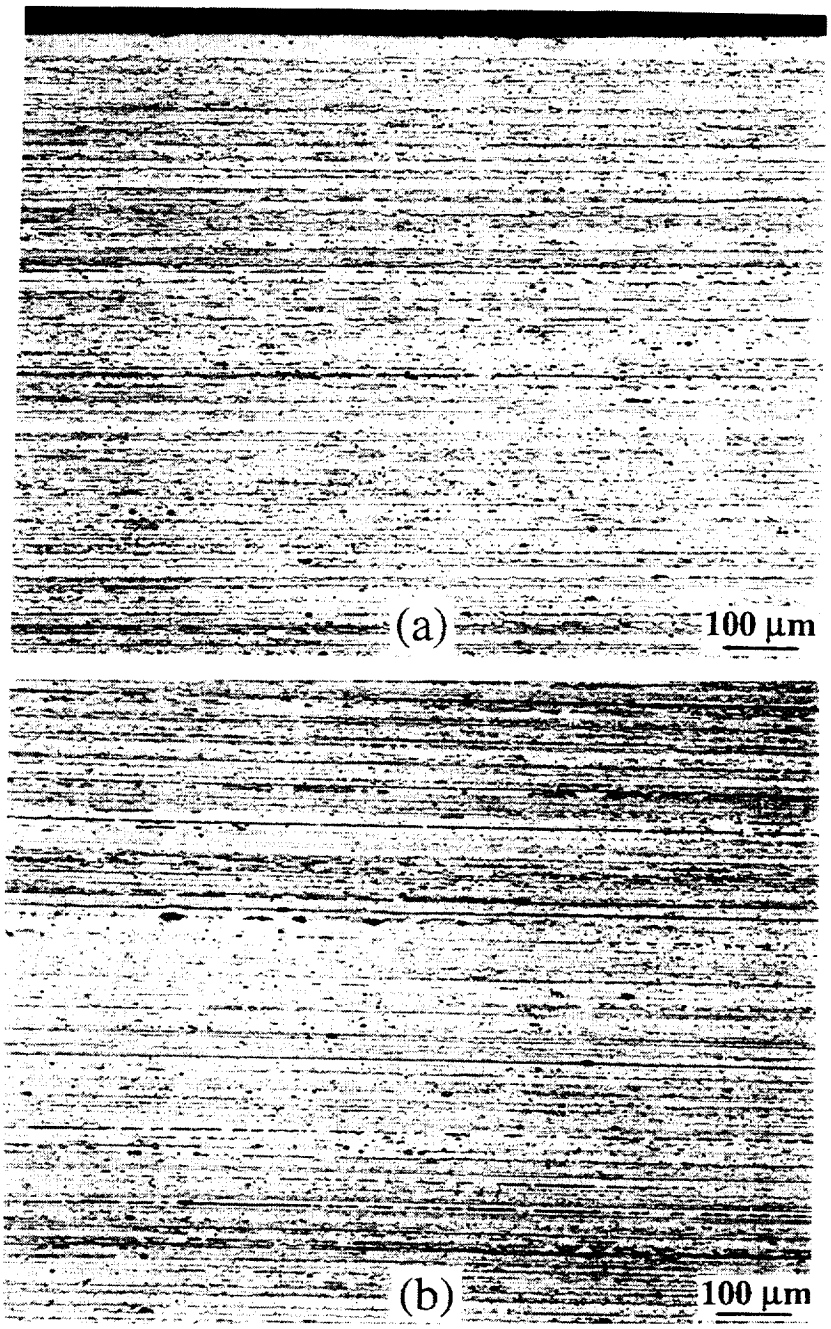

Figure 1. Optical micrographs showing unrecrystallized grain structure of RX818-T8; (a) near the surface area, and (b) the center region. 100X

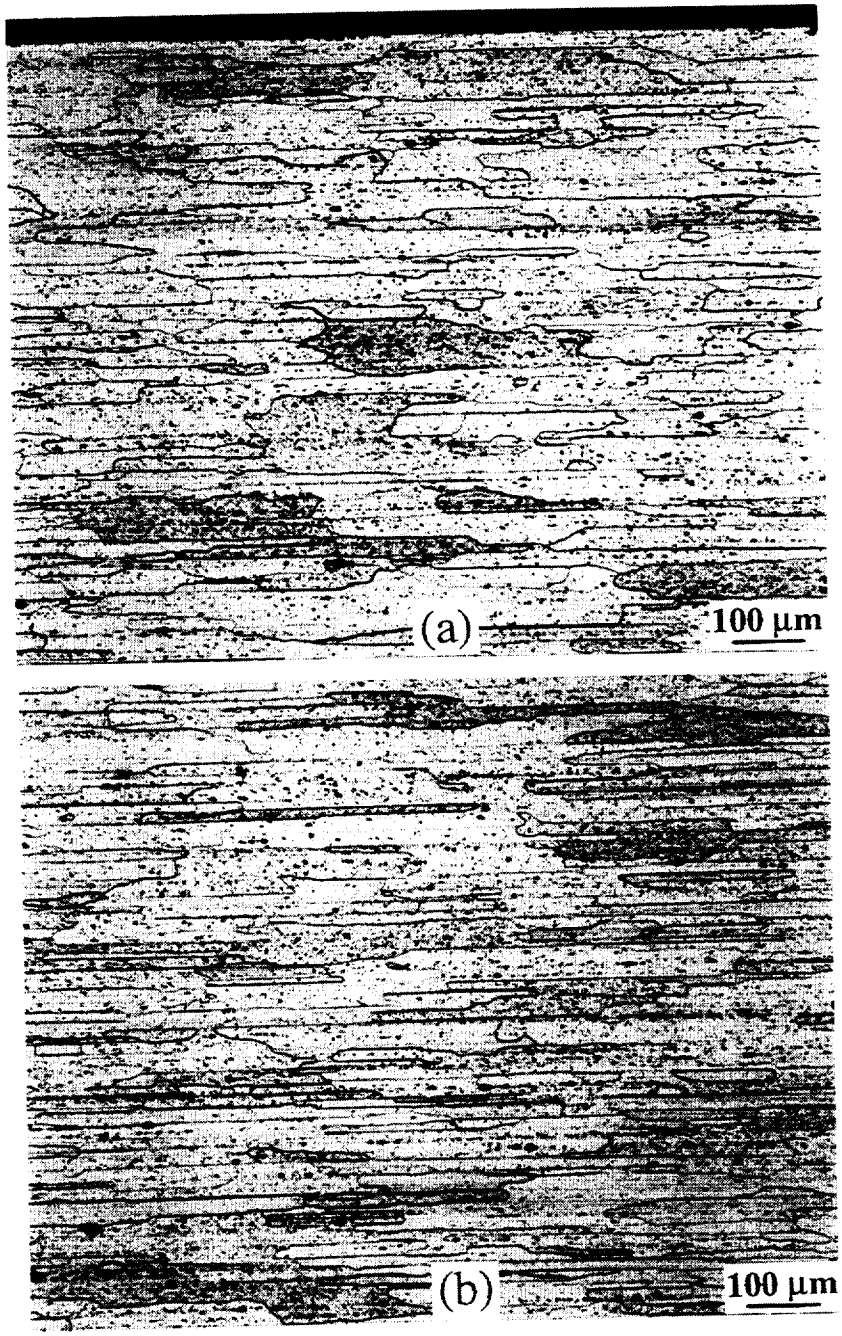

Figure 2. Optical micrographs showing recrystallized grain structure of ML377-T8; (a) near the surface area, and (b) the center region. 100X

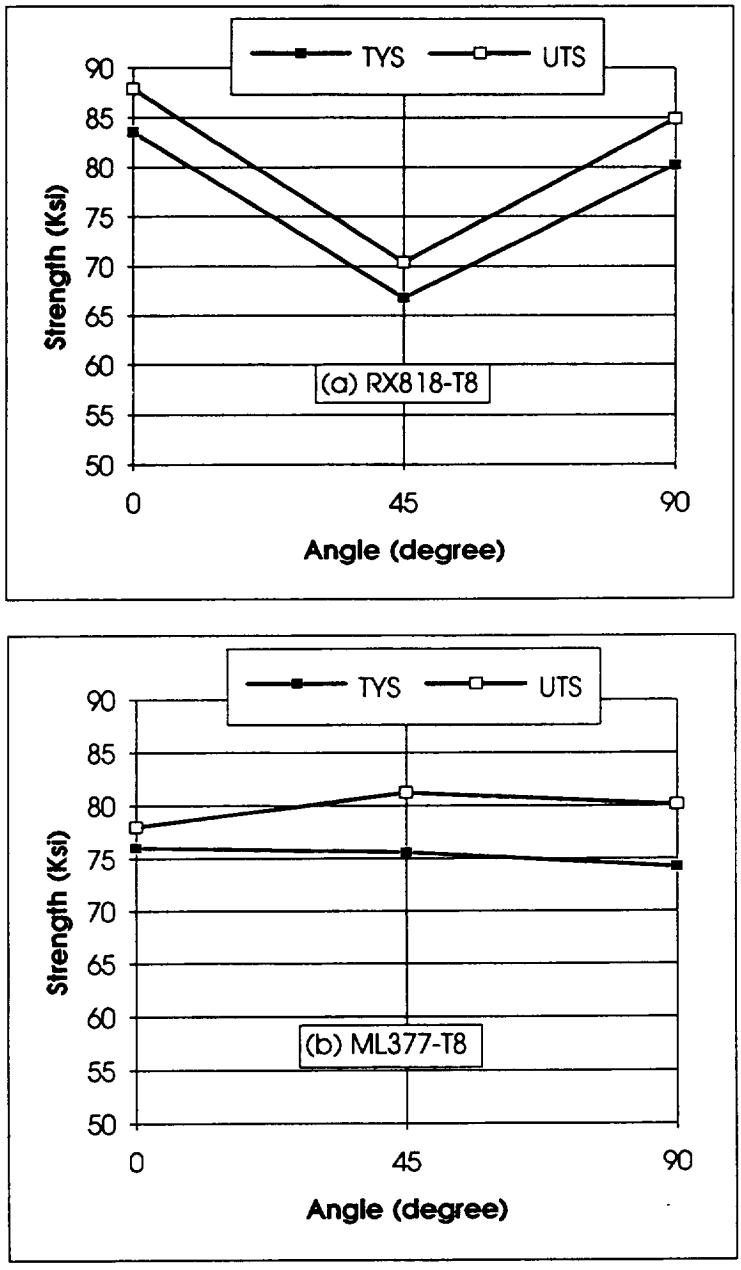

Figure 3. Two plots showing TYS and UTS in the L (0 degree), 45 degrees, and LT (90 degrees) directions : (a) RX818-T8 and (b) ML377-T8

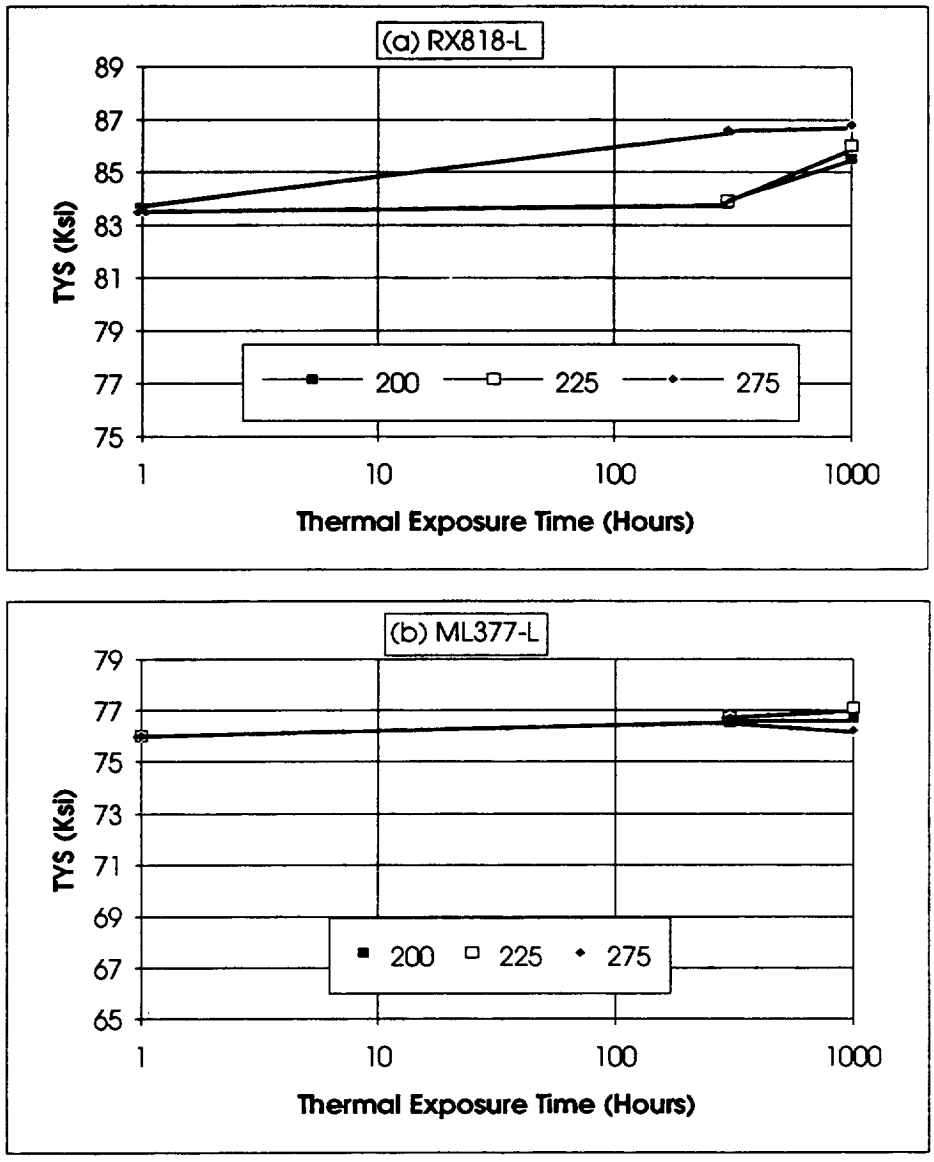

Figure 4. Two plots showing tensile yield strength in the L direction as a function of thermal exposure time at temperatures of 200F, 225F and 275F: (a) RX818-T8, and (b) ML377-T8

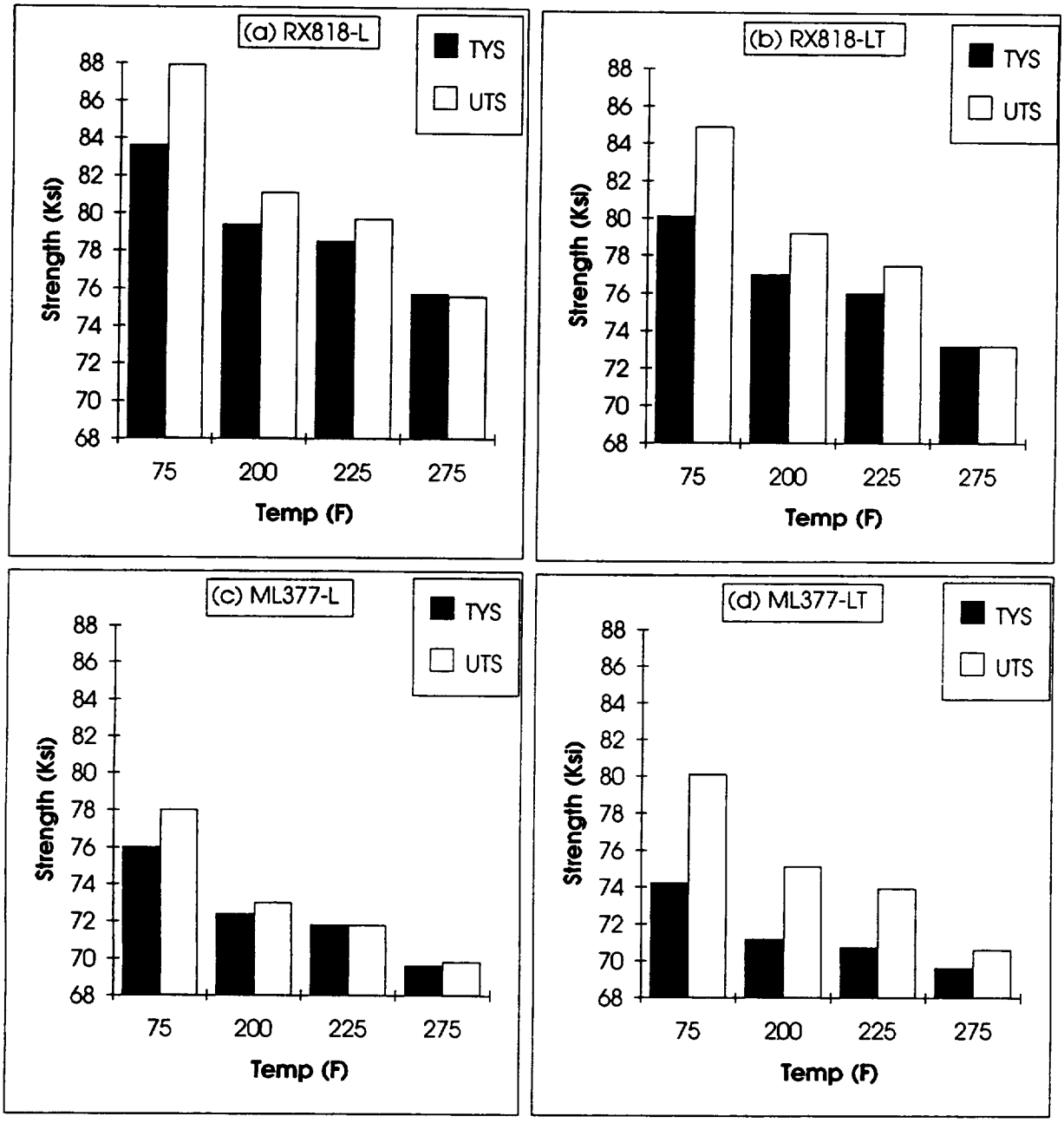

Figure 5. Four plots showing both TYS and UTS of RX818-T8 and ML377-T8 as affected by test temperature; (a) RX818-L, (b) RX818-LT, (c) ML377-L and (d) ML377-LT

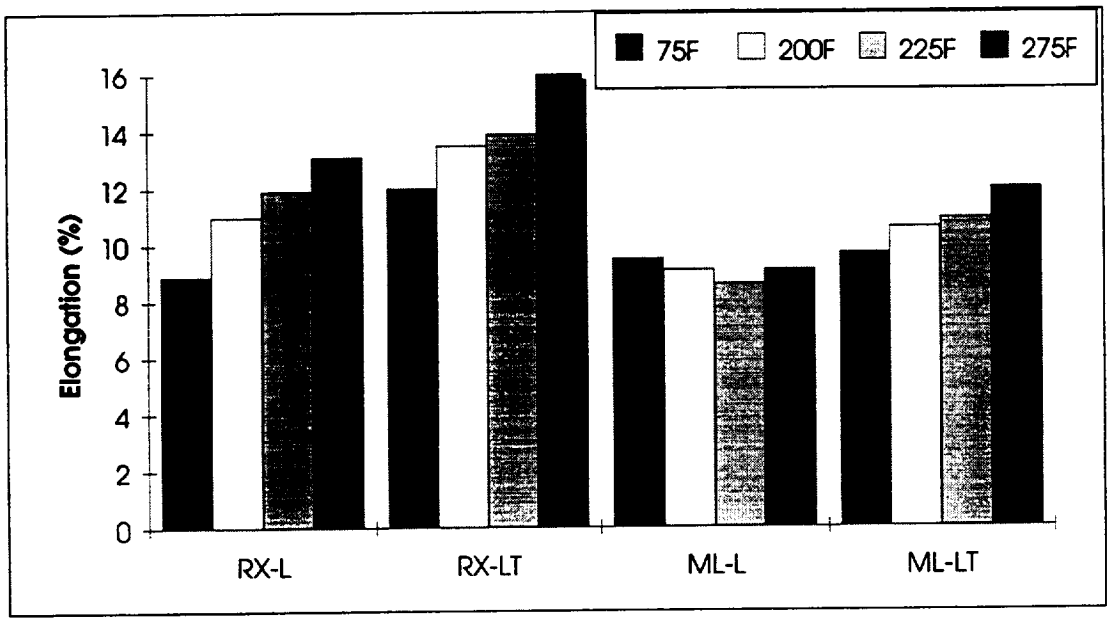

Figure 6. A plot showing elongation of RX818-T8 and ML377-T8 as affected by test temperature.

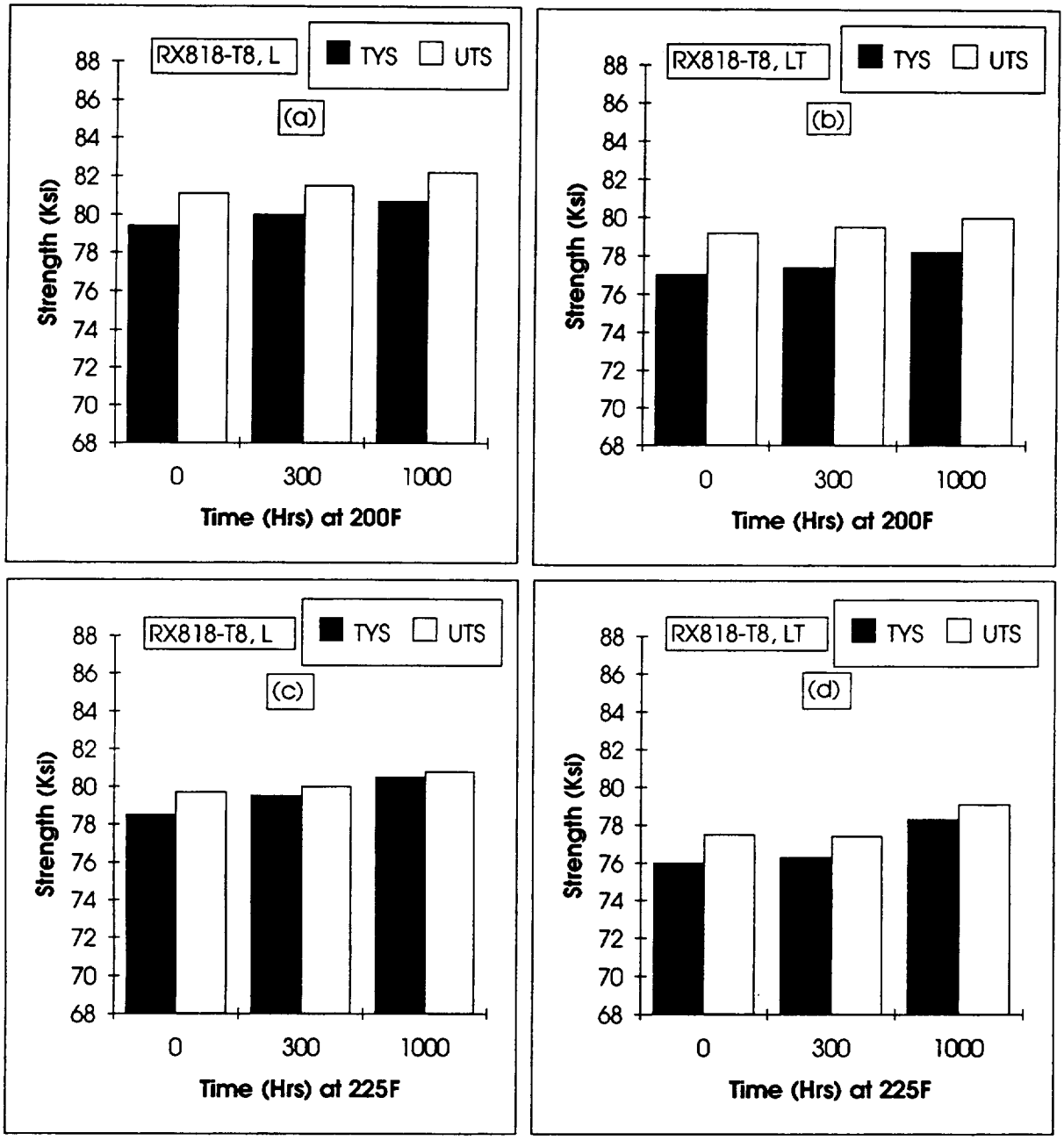

Figure 7. Four plots showing tensile strength vs thermal exposure time for RX818-T8; (a) a 200F tensile test in the L direction, (b) a 200F tensile test in the LT direction (c) a 225F tensile test in the L direction and (d) a 225F test in the LT direction.

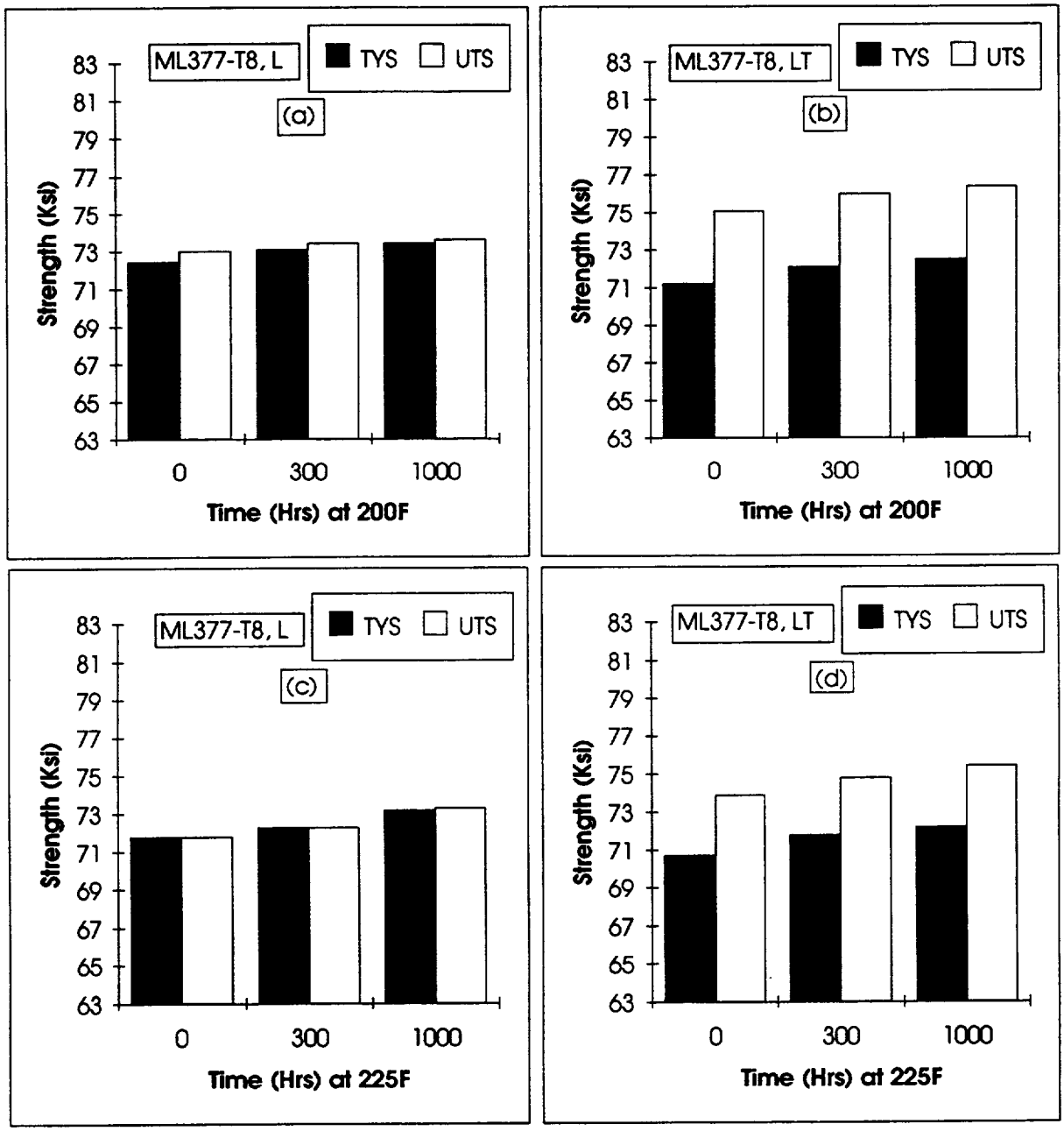

Figure 8. Four plots showing tensile strength vs thermal exposure time for ML377-T8; (a) a 200F tensile test in the L direction, (b) a 200F tensile test in the LT direction, (c) a 225F tensile test in the L direction, and (d) a 225F test in the LT direction.

Objectives:

(1) **To evaluate aluminum-based materials and processes in terms HSCT airplane performance.**

Approach:

Phase I—Material Property Projections

(1) Review/update LCATS property projections
(2) Develop property projections for non-LCATS alloys
(3) Develop pref. "allowables" for non-LCATS alloys

Phase II—Concept Weight Evaluation

(1) Select concepts
(2) Conduct structural analysis on selected concepts
(3) Develop weights data

Phase III—Airplane Performance Evaluation

(1) Develop three (3) airplane concepts/materials
(2) Develop point-design weights
(3) "Fly" airplanes for equivalent mission sizing

Phase IV—Technology Recommendations

(1) Prepare list critical technical needs
(2) Prepare technology recommendations

Deliverables:

Phase I—Material Property Projections

(1) Material property projections

Phase II—Concept Weight Evaluation

(1) Concept relative weights

Phase III—Airplane Performance Evaluation

(1) Airplane concepts/materials
(2) Mission-sized relative MTOWs

Phase IV—Technology Recommendations

(1) List of technical needs
(2) Technology recommendations

Figure 9. 1992 Material Technology Trade Studies for the Airframe

LCATS/UVA ALUMINUM CONCEPTS SUMMARY

Aluminum Concept Package Summary

WING CONCEPTS

CONCEPT TYPE	WING BOX UPPER PANELS	WING BOX LOWER PANELS	STRAKE WING LWR/UPPR
INTEGRALLY STIFFENED	1A	1B	1C
SANDWICH PANELS	2A	2A	2B
THIN SANDWICH STIFFENED	3A	3B	3A & 3B
SKIN/STRINGER CONVENTIONAL	N/A	N/A	N/A

FUSELAGE CONCEPTS

CONCEPT TYPE	WING BOX UPPER PANELS	WING BOX LOWER PANELS	STRAKE WING LWR/UPPR
INTEGRALLY STIFFENED	7A	7B	7A OR 7B
SANDWICH PANELS	8A	8B	8C
THIN SANDWICH STIFFENED	9A	9A	9B
SKIN/STRINGER CONVENTIONAL	N/A	N/A	N/A

N/A: *Pictorial representation of this concept family is not available at this moment. However extensive amount of information is available for this conventional type of structural arrangement.*

Figure 10. LCATS/UVA Aluminum Concepts Summary

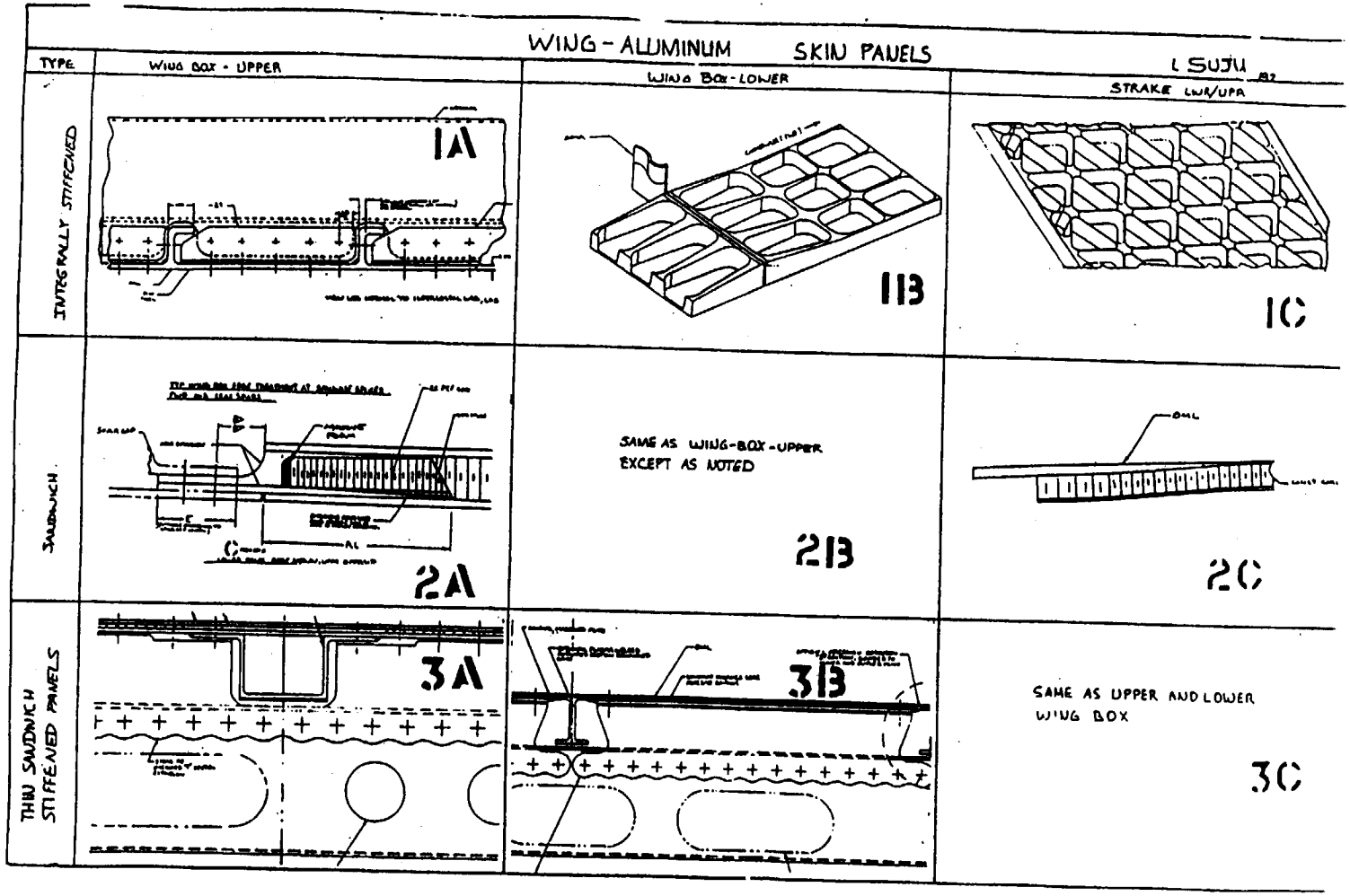

Fig. 11 HSCT Wing - Aluminum Skin Panel Concepts

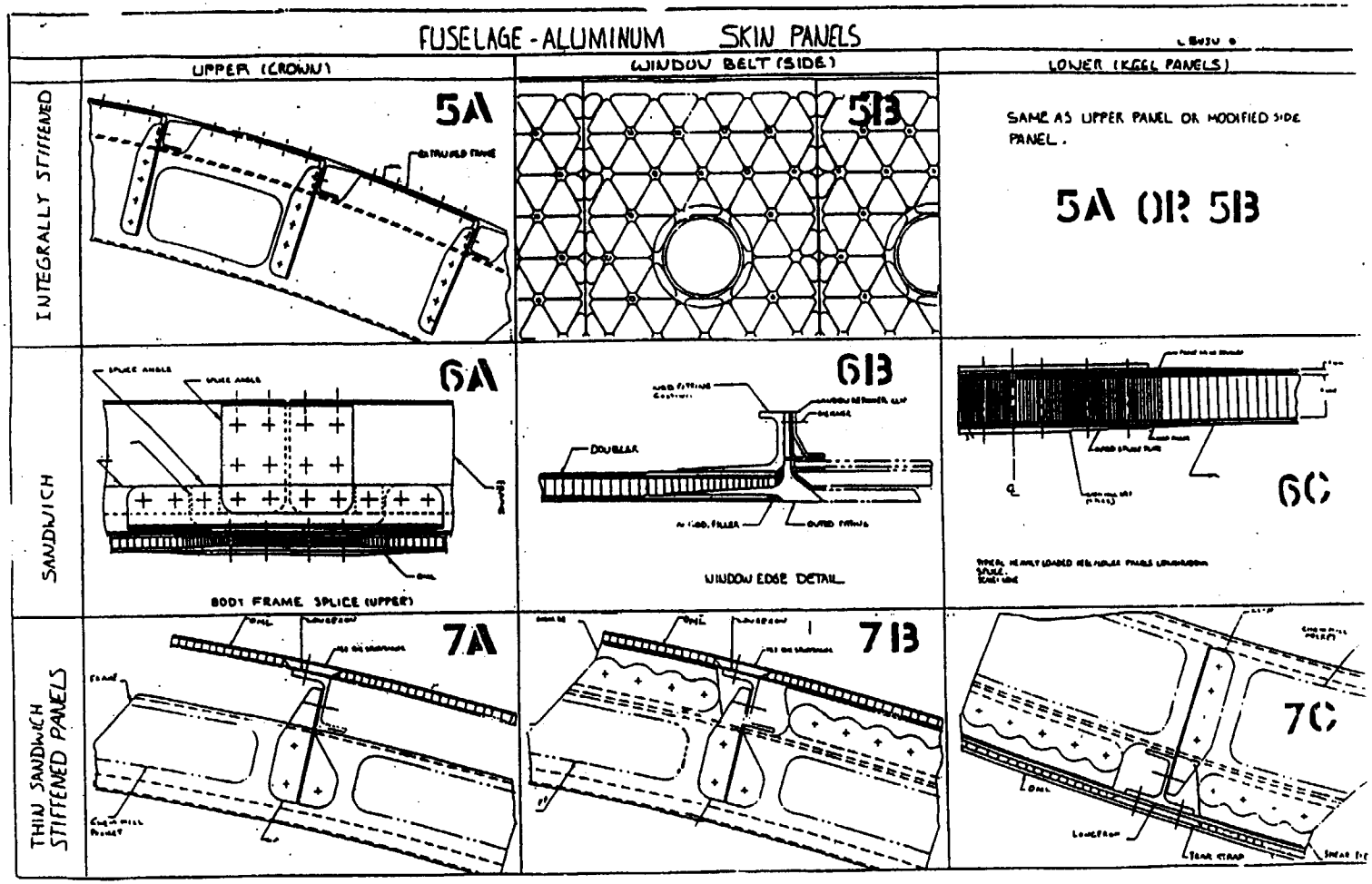

Fig. 12. HSCT Fuselage - Aluminum Skin Panel Concepts

Objectives:

(1) To evaluate aluminum-based materials and processes in terms HSCT airplane performance.

Approach:

Phase I—Material Property Projections

(1) Review/update LCATS property projections
(2) Review supplier updates

Phase II—Concept Weight Evaluation

(1) Develop/update/select design concepts
(2) Conduct structural analysis on selected concepts
(3) Develop concept-level weights data

Phase III—Technology Recommendations

(1) Prepare list critical technical needs
(2) Prepare technology recommendations

Deliverables:

Phase I—Material Property Projections

(1) Material property projections

Phase II—Concept Weight Evaluation

(1) Concept-level relative weights

Phase III—Technology Recommendations

(1) List of technical needs
(2) Technology recommendations

Figure 13. 1993 Material Technology Trade Studies for the Airframe

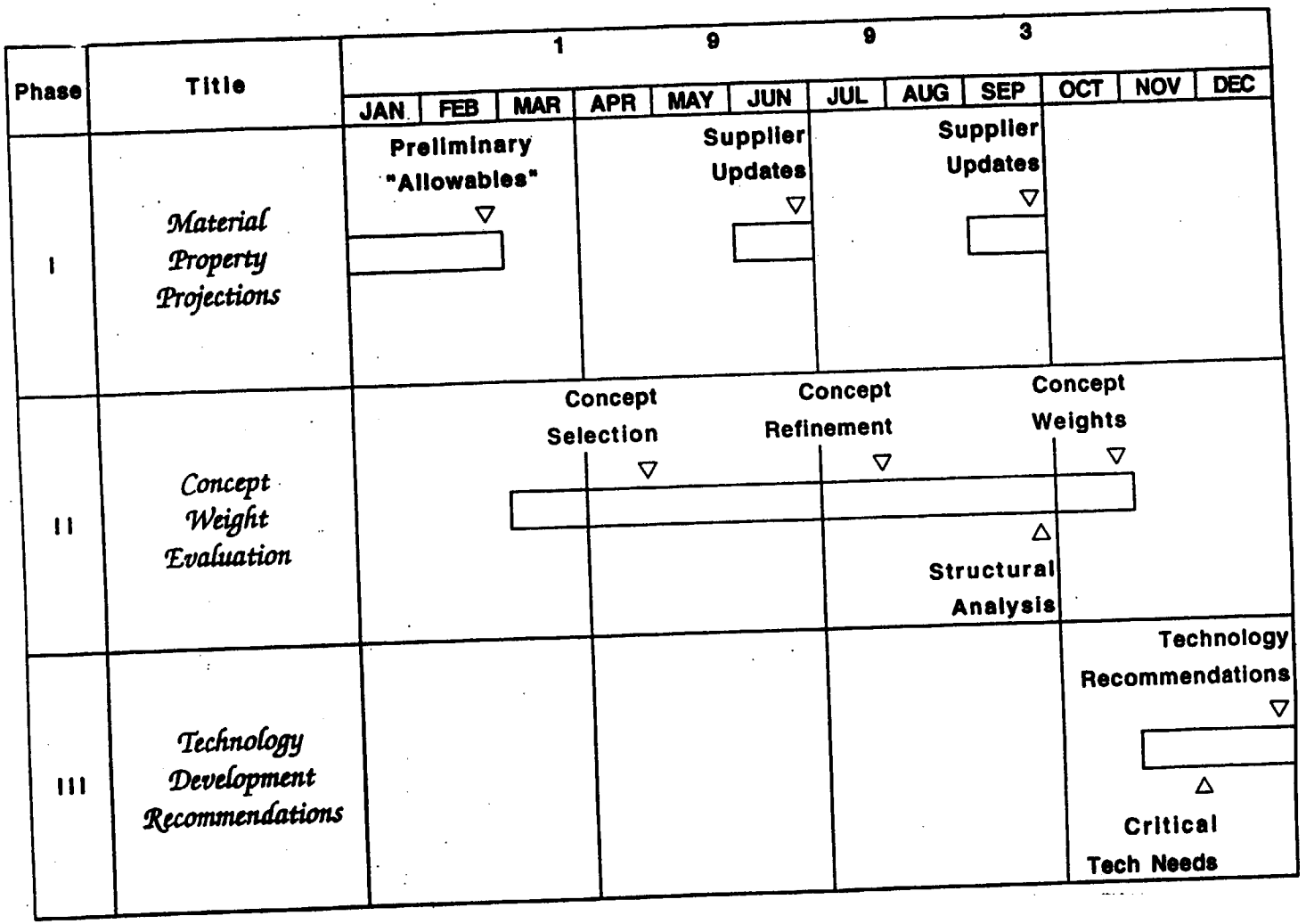

Fig. 14. Material Technology Trade Studies for the Airframe

McDONNELL DOUGLAS

Aluminum-Based Materials for High Speed Aircraft - Final Report

R.S. Kahandal

Senior Manager

Advanced Materials and Processes Laboratories

Abstract

NASA-LaRC has provided the University of Virginia (UVa) with a grant to investigate aluminum-based materials for use on future high speed aircraft. UVa has directed material suppliers to develop aluminum alloys and metal-matrix composites (MMCs), not included in this report, with improved elevated temperature properties and stability. McDonnell Douglas Aerospace (MDA) and Boeing have been selected by the University of Virginia to evaluate the design and material properties of these improved materials and conduct trade studies using these properties. This report focuses on four aluminum alloys. These alloys include: RX818-T8 and ML377-T8 from Reynolds Metals Company; and C415-T8 and C416-T8 from Alcoa.

Introduction

The economic viability of the next generation of supersonic transport depends on the timely development of materials and structures which can perform efficiently for extended periods in an elevated temperature environment. The University of Virginia (UVa), as directed by NASA-LaRC, has assembled a team of material suppliers experienced in alloy development in a program to address this challenge. The overall objective of this program is to investigate and develop improved aluminum alloys and metal matrix composites (MMCs) as candidates for application on a High Speed Civil Transport (HSCT). These will be developed to meet target properties supplied by HSCT airframe companies McDonnell Douglas Aerospace (MDA) and Boeing. The most promising candidates will be evaluated in baseline designs to obtain optimized material and structural vehicle concepts.

The RX818-T8 sheet and extrusion material was received in March 1994. An initial shipment of C415-T8 and C416-T8 was received in December 1994. An additional shipment of the C416-T8 was received in May 1995 to augment the previous C416-T8 material received. The ML377-T8 material was received in June 1995.

Approach

The approach for this program includes a six month material characterization and evaluation effort . This effort was to be performed according to the test matrix shown in Table 1. However, changes in the program necessitated a modification of the test matrix to that shown in Table 2.

Table 1. Original UVa Test Matrix[1]

TEST	ORIENTATION	TESTS
Fracture Toughness (ASTM E399)[2]	L-T; T-L	4
Salt Fog Corrosion ASTM (B117)[2]		
Blank Coupons	N/A	4
Interference-fit Fastener Panels[3]	N/A	4
Stress Corrosion Cracking (ASTM G49)[2,4]	LT	18
Machining Trials		
Cutting	N/A	6
Drilling/Reaming	N/A	6
Forming Trials		
Brake Forming[5]	L; 30; 45; 60; LT	50
Hydroforming	N/A	5
Joining Study		
Welding[6]	N/A	6
Adhesive Bonding	N/A	6
Chemical Processing		
Chemical Milling	N/A	2
Anodizing	N/A	2
Total Number of Tests per Alloy		**113**

(1) Material Required; 1,000 sq. in. per lot; multiple lots acceptable; 12-inch minimum sheet width
(2) Testing before and after thermal exposure
(3) Six each Ti fasteners installed wet and dry at standard interferences per specimen
(4) Spring-loaded flat tensile specimens tested by alternate immersion in substitute ocean water (ASTM D141)
(5) Minimum Bend Radius; 2 specimens/radii for 5 radii
(6) TIG, laser, capacitor discharge, and flash welding techniques used successfully until acceptable welds are produced

Table 2. Revised UVa Test Matrix

TEST	MATERIAL							No. of Tests
	RX818-T8		ML377	C415-T8		C416-T8		
	Sheet	Ext.	Sheet	Sheet	Ext. *	Sheet	Ext. *	
Corrosion Test								
Alternate Immersion ASTM G 44	5	1	1	2	2	2	2	15
Atmospheric ASTM G 50	5	1	1	1	2	1	2	13
Machining								
Drilling	6		12	6		6		30
Reaming	6		12	6		6		30
Milling		6			6		6	18
Chemical Processing								
Anodize	2		4	2		2		10
Chem Mill	4	2	4	2	2	2	2	18

* Note: These materials were not received.

CORROSION STUDY

Procedure

The corrosion study consisted of both atmospheric and alternate immersion interference fit test panels. The atmospheric tests followed the procedures of the American Society for Testing and Materials (ASTM) specification G 50 and the alternate immersion tests followed ASTM G 44.

The atmospheric testing is currently proceeding at the Douglas Aircraft Company (DAC) El Segundo Beach test site shown in Figure 1. This test requires two years to complete. The alternate immersion test is performed in the DAC Long Beach test laboratory facilities shown in Figure 2. This test requires 90 days for completion.

Figure 1. DAC El Segundo Beach Atmospheric Environment Corrosion Test Site Location

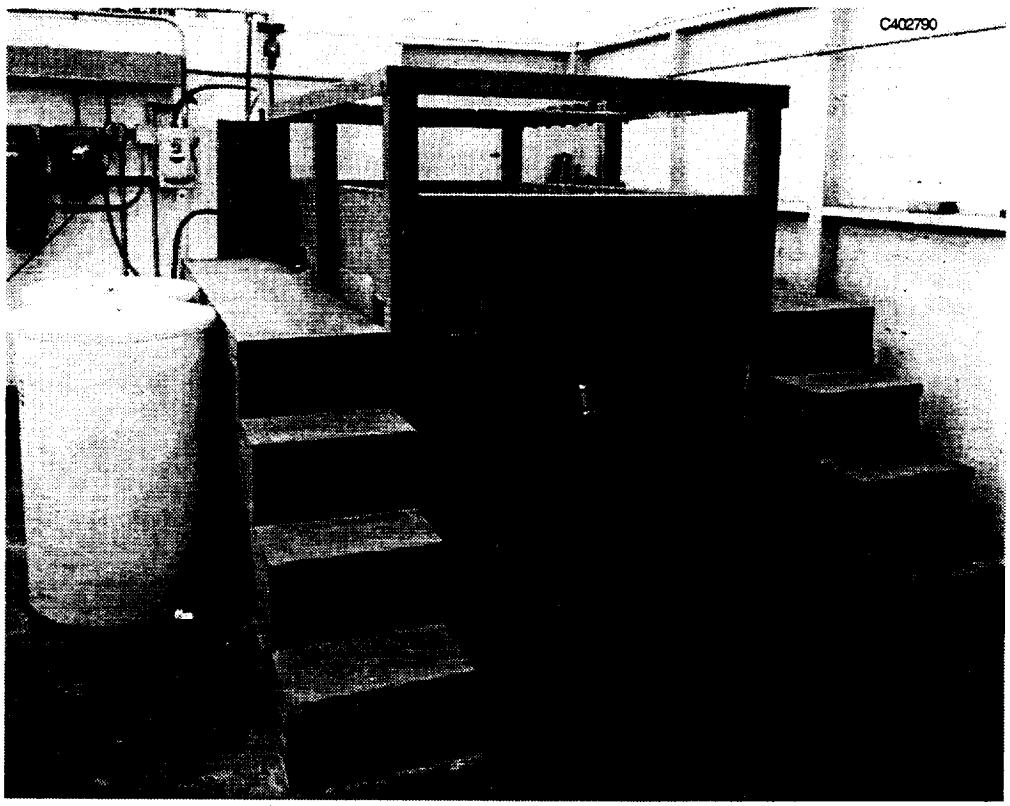

Figure 2. DAC Alternate Immersion Testing Facility

Ten panels were made from the RX818-T8 sheet and two from the extrusion. Six panels made from the RX818-T8 sheet were double panels where two sheets of material were mate drilled with holes 0.244 inch in diameter for 1/4 inch titanium lockbolts allowing for an interference fit of 0.0045 inch. The layout of fasteners is shown in Figure 3. Of these panels, two panels were bare, two were alodine coated, and two were anodized. One half of the surface area of each alodine coated and anodized panel was painted with primer. For details refer to the chemical processing section on page _ of this report. Four panels made from the RX818-T8 sheet were single panels with varying fastener interference fits. The layout pattern was modified to optimize testing and take advantage of additional interferences. These interferences were 0.003, 0.004, 0.005, and 0.006 inches. Figure 4 shows this new layout pattern, Table 3 shows the interferences, and Table 4 summarizes tests for all ten panels. Single sheet test panels were used for corrosion evaluation on the remaining alloys. Three panels each were made from the C415 and

C416 materials, one for alternate immersion and two for atmospheric testing. Two 4" x 10" subsized corrosion panels were made from the ML377 material. The panels for the C415, C416 and ML377 all used the same interference fit set-up parameters as those for the single sheet RX818-T8 panels.

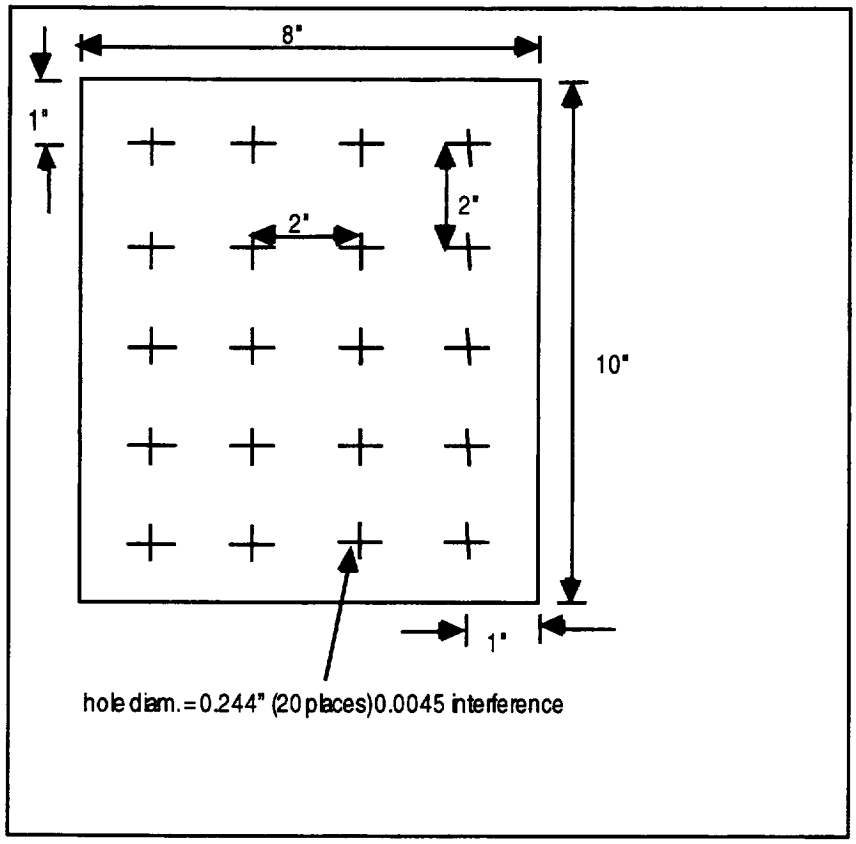

Figure 3. Built-up Two Sheet RX818-T8 Interference Fit Corrosion Panels, 6 each

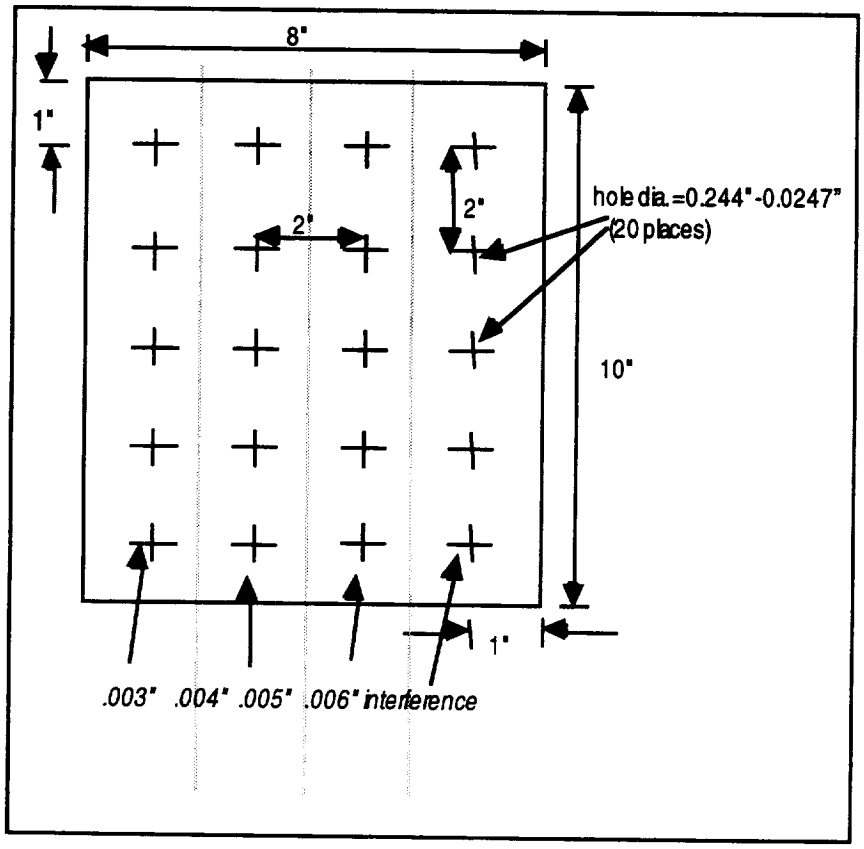

Figure 4. Single Sheet Interference Fit Corrosion Panels for RX818-T8, C415-T8, C416-T8, and ML377-T8 (Note various interference fits,)

Table 3. Interference Fit For RX818-T8 Sheet Corrosion Test Panels

COATING	TYPE	QUANTITY	INTERFERENCE
Bare	Double	2	0.0045
Bare	Single	4	0.003, 0.004, 0.005, 0.006
Alodine/Prime	Double	2	0.0045
Anodize/Prime	Double	2	0.0045

Table 4. Surface Condition Configuration For Atmospheric and Alternate Immersion Interference Fit Fastener Panels

ALLOY	No. of PANELS	TEST	CHEMICAL TREATMENT	COATING
RX818-T8	3	Atmospheric	Bare	Bare
RX818-T8	1	Atmospheric	Alodine	1/2 FR Prime
RX818-T8	1	Atmospheric	Anodize	1/2 FR Prime
RX818-T8	3	Alt Immersion	Bare	Bare
RX818-T8	1	Alt Immersion	Alodine	1/2 FR Prime
RX818-T8	1	Alt Immersion	Anodize	1/2 FR Prime
C415	2	Atmospheric	Bare	Bare
C415	1	Alt Immersion	Bare	Bare
C416	2	Atmospheric	Bare	Bare
C416	1	Alt Immersion	Bare	Bare
ML377	1	Atmospheric	Bare	Bare
ML377	1	Alt Immersion	Bare	Bare

Two RX818-T8 extrusions were also fabricated with 1/4 inch titanium lockbolts into corrosion specimens following the layout pattern in Figure 5. These included interference fits of 0.002, 0.0035, 0.0045, and 0.006 inches. One specimen was subjected to atmospheric testing and the other was subjected to alternate immersion testing. Since ML377-T8 extrustions were not available for evaluation, testing was not performed.

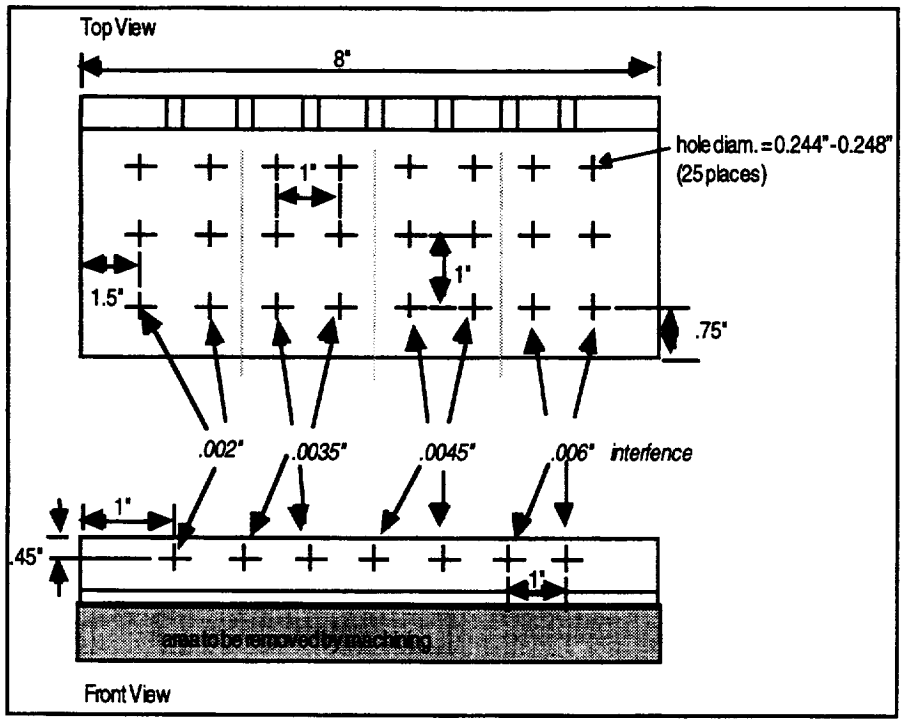

Figure 5. RX818-T8 Extrusion Interference Fit Corrosion Panels

Figure 6. RX818-T8 Extrusion Interference Fit Alternate Immersion Test Panels

Results and Discussion

Visual inspection was performed after completion of the alternate immersion test for the RX818-T8 test coupons and is summarized in Table 6. These results show that for the bare and alodine panels there is moderate, and slight to moderate pitting, with no cracking. For the panels that received alodine with primer and anodize with primer there was no visible corrosion or cracking. Figure 6 shows the RX818-T8 sheet alternate immersion panels after 90 days exposure and Figure 7 shows the RX818-T8 extrusion panels prior to test.

Table 5. Corrosion Panel Status

Material	Test	Length	Date of Completion
RX818-T8 Sheet	Atmospheric	2 Years	12/96
RX818-T8 Sheet	Alternate Immersion	90 Days	12/94
RX818-T8 Ext.	Atmospheric	2 Years	3/97
RX818-T8 Ext.	Alternate Immersion	90 Days	10/95
C415-T8 Sheet	Atmospheric	2 Years	8/97
C415-T8 Sheet	Alternate Immersion	90 Days	11/95
C416-T8 Sheet	Atmospheric	2 Years	8/97
C416-T8 Sheet	Alternate Immersion	90 Days	11/95
ML377-T8 Sheet	Atmospheric	2 Years	8/97
ML377-T8 Sheet	Alternate Immersion	90 Days	11/95

Table 6. RX818-T8 Corrosion Results

Material	Test	Visual Observation	Cracking
RX818-T8 Sheet	Bare	Moderate Pitting	none
RX818-T8 Sheet	Alodine	Slight to moderate pitting	none
RX818-T8 Sheet	Anodize	none	none
RX818-T8 Sheet	Alodine and Prime	none	none
RX818-T8 Sheet	Anodize and Prime	none	none

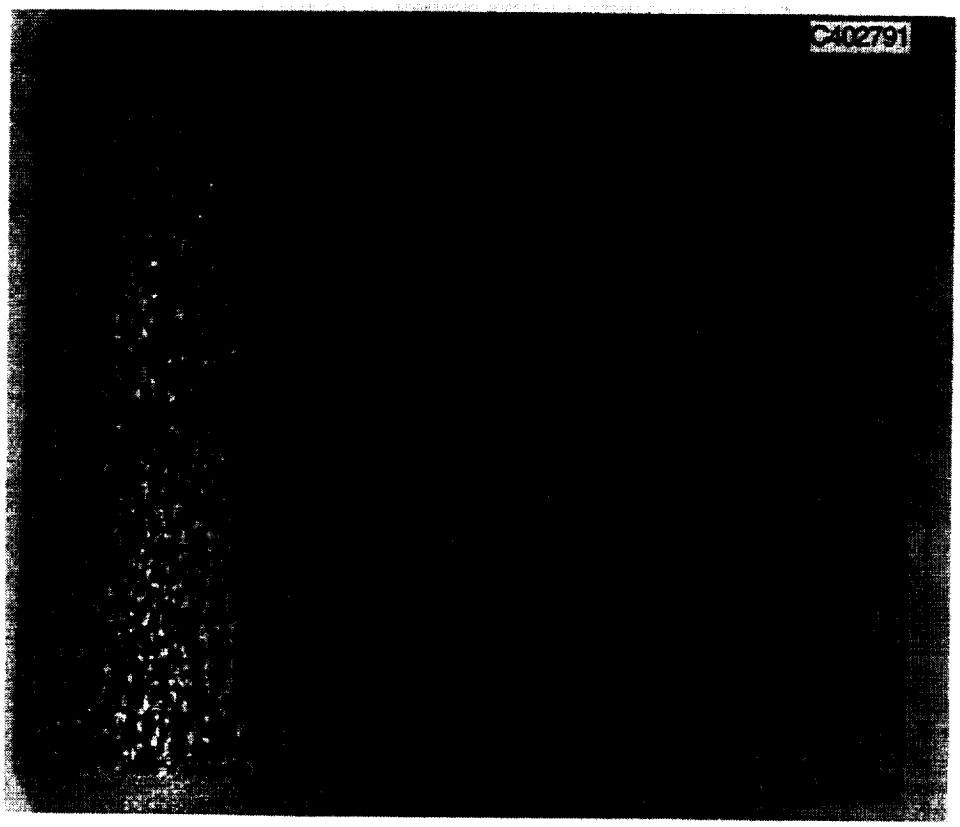

Figure 7. RX818-T8 Sheet After 90 Days Exposure

Microstructural examination of the RX818-T8 sheet shows pitting and moderate exfoliation corrosion at the exposed surfaces of the alternate immersion specimens, see Figures 8 and 9. Measurements of a typical pitting site for the alternate immersion specimens showed depths of 0.008 inch. This is typical for bare aluminum wrought products exposed to such a severe environment. Although pitting and exfoliation was evident on the RX818-T8 test panels, there were no signs of stress corrosion cracking detectable by dye penetrant inspection technique.

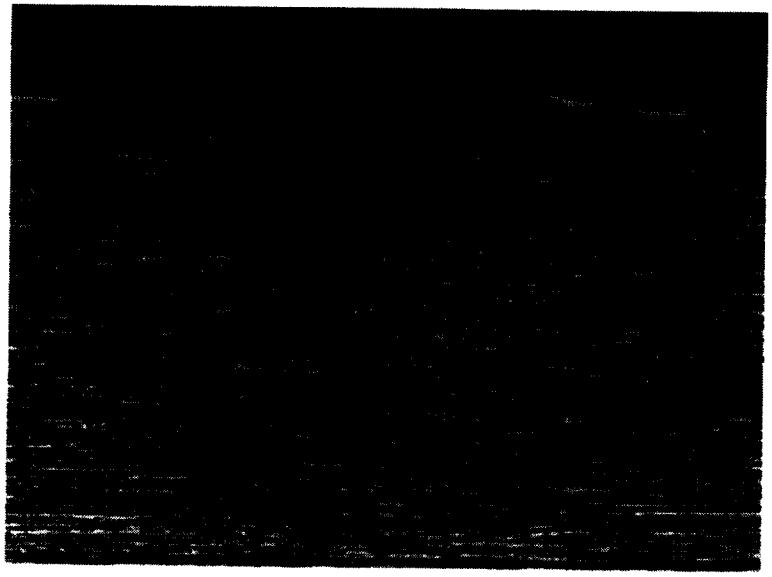

Figure 8. Photomicrograph Showing Pitting and Exfoliation Corrosion at the Surface of RX818-T8 Sheet Near a Countersunk Hole

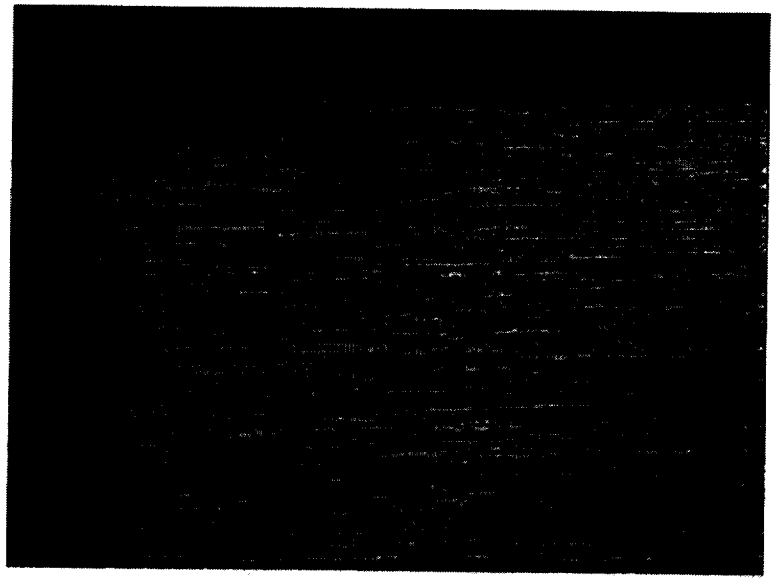

Figure 9. Photomicrograph Showing Pitting and Exfoliation Corrosion at the Surface of RX818-T8 Sheet Near the Edge of a Fastener Hole

MATCHING STUDY

Procedure

The machining study included determination of optimum speeds and feeds for routing, reaming, and milling and drill tool wear for hole preparation. The RX818-T8, C415-T8, C416-T8, and ML377-T8 materials were compared to both 2090-T6 aluminum lithium alloy and 7075-T8 aluminum alloy.

The drill wear study was done with two different drill bit types, a HSS twist drill and a double margin twist drill, both 3/16 inches diameter. The test of RX818-T8 material was performed on a CNC Mill. The other materials were tested by manual drill feed. Drilling speed parameters are from 1,000 to 3,000 rpm. Feed rate ranged from 4 to 32 inches per minute. Drill wear was measured with a microscope set at 40 power at the drill tips lip and margins as shown in Figure 10.

Routing was done with three router types: a two flute, straight fluted, HSS router; a three flute, right hand spiral, left hand cut router; and a two flute, right hand spiral, right hand cut router. The speeds ranged from 2,000 to 20,000 rpm. Feed rates ranged from 4 to 200 inches per minute.

Material hardness of each material was measured on a Rockwell hardness tester using the Rockwell B ($R_{b)}$ indentor.

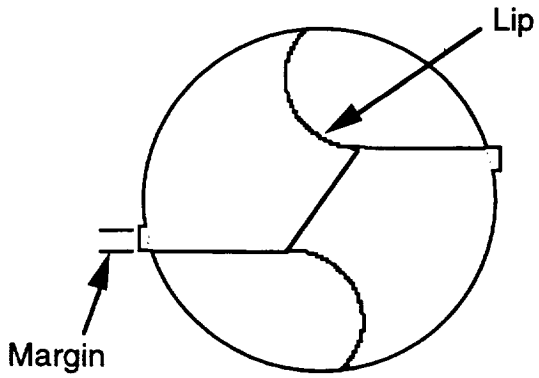

Figure 10. Drill Tip Showing Drill Wear Measurement Locations

Results and Discussion

With RX818-T8 material, the surface finish appeared good without the spalling seen when drilling softer aluminum alloys.

Routing tests showed that the RX818-T8 material can be routed at a wide variety of speeds and feeds without difficulty. Routing with light cuts produced fine surface finishes, according to visual inspection.

The drill wear study compared the RX818-T8 to 2090 and 7075 aluminum alloys. The spindle speed was 4,000 rpm and the feed rate was 32 inched per minute. Drilling was done dry without coolant. The results shown in Table 7 shows that drill wear from the RX818-T8 is greater than the wear of the 7075 and 2090 alloys. The drill bit used drilled 8,265 holes before reaching the DAC Manufacturing Research and Development internal department standard limit of 0.005 inches wear. The drill wear was consistent and regular with no sign of excessive physical or chemical abrasion.

Correlation of lab RX818-T8 test results to production line hand drilling applications indicate that the drill should last about 4,000 holes in production. This is approximately 80% of typical tool life for 7075-T6 aluminum.

In addition, drilling by hand, routing, reaming and milling were performed. The operator varied the speeds and feeds. During this no chipping, spalling or work hardening was observed, as with the 2090 aluminum. Tool life is slightly shorter than for 7075, but not significantly shorter. The material did not present any machinability problems that would require special tools or techniques in production. Figure 11 shows the RX818-T8 panels after the drill wear test was complete.

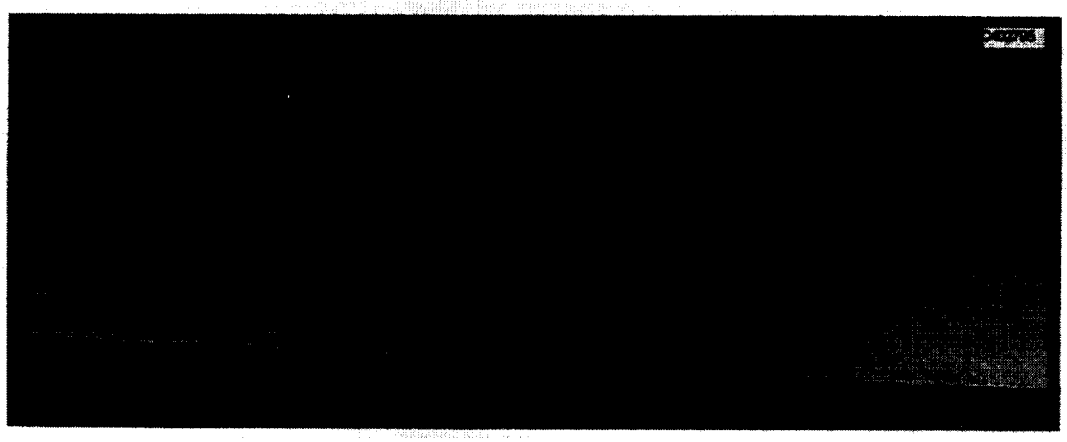

Figure 11. RX818-T8 Sheet Drill Wear Panels

The C415-T8, C416-T8, and ML377-T8 materials faired better in the drill study than did the RX818-T8. For all three materials the drill wear is consistently less than for the 2090, 7075, and RX818 materials, as documented in Table 7. The dominant wear mechanism for the C415-T8 and C416-T8 alloys is erosion rather than steady wear. However, the amount of erosion is significantly less than was seen with the 2090 drill tests. Some drills eroded the aluminum alloys more quickly than others probably due to the quality of tool grinding. Most of the drills showed erosive wear of the cutting edge from 0.001 to 0.002 inches, after that steady wear became the dominate wear mechanism. Erosive wear blunts the cutting edge caused by chipping of the lips whereas steady wear is further material removal such as rounding of the corners without blunting the cutting edge.

In the previous tests, CNC controlled equipment was used to reduce operator induced variation in drill tests. The CNC equipment was not available for this test so a manual milling machine was used. Manual drilling will lower drill life but it correlates closer to typical drill life in the shop.

Projecting the test data, C415-T8 would wear out drills after about 10,000 holes. Wear data for C416-T8 is less clear, showing drill bit would wear out anywhere from 5,000 holes to 15,000 holes. In neither case was there a notable tool problem. All four alloys have hardness values comparable to 2090-T8 and 7075-T6 per DPS 1.05. Hardness values are shown in Table 8.

Table 7. RX818-T8, C415-T8, C416-T8, and ML377-T8 Drill Wear Data (inches)

No.of Holes	RX818-T8 Wear	C415-T8 Wear	C416-T8 Wear	ML377-T8 Wear	2090-T8 Wear	7075-T6 Wear
0	0.000	0.000	0.000	0.000	0.000	0.000
159			0.008			
276	0.005			0.0005		
500					0.0026	0.0018
552	0.005			0.0005		
636			0.0013			
689		.0005				
828	0.005			0.0010		
927			0.0013			
1000					0.0026	0.0018
1104	0.005			0.0014		
1245			0.0013			
1320	0.005					
1380		.0005		0.0014		
1500					0.0026	0.0018
1563			0.0013			
1595	0.005					
1656				0.0014		
1669			0.0013			
1696		.0008				
1870	0.005					
1932				0.0014		
1987			0.0013			
2000		.0010			0.0026	0.002
2145	0.005					
2305			0.0013			
2332		.0010				
2420	0.005					
2500					0.0026	0.002
2623			0.0013			
2650	0.008	.0013				
2943			0.0013			
3000					0.0026	0.0021
3186		.0013				
3500					0.0026	0.0021
3926		.0013				
4000					0.0026	0.0021
4244		.0016				
4500					0.0026	0.0021
4562		.0016				

Table 8. Hardness Values

Material	Hardness, R_b
RX818-T8 Sheet	92
C415-T8	87
C416-T8	83
ML377-T8	90
2090-T8	85
7075-T6	90

CHEMICAL PROCESSING

Procedure

All materials were analyzed in 4L and 17L solutions, per Douglas Process Standard (DPS) 9.481-2, for chemical milling characteristics. The etch rate and surface roughness were measured with 7075-T6 and 2090-T8 used as baseline materials for comparison. See Table 9. The 4L and 17L solutions are typically used for chemical milling of 2000 and 7000 series aluminum alloys, per DPS 9.482-2. The chemical milling solution chemistries are described in Table 10.

Table 9. UVa Chemical Process Analysis Table

Alloy	**Bath**	**Comparison**	**Measure**
RX818-T8	4L, 17L	2090-T8, 7075-T6	Etch Rate, Roughness
ML377-T8	4L, 17L	2090-T8, 7075-T6	Etch Rate, Roughness
C415-T8	4L, 17L	2090-T8, 7075-T6	Etch Rate, Roughness
C416-T8	4L, 17L	2090-T8, 7075-T6	Etch Rate, Roughness

Table 10. Chemical Milling Solutions

Solution	Tank	Temperature, °F	Chemical Composition
4L	Mild Steel	190 to 195	40 gal. 4L solution (proprietary NaOH & S)
17L	Stainless	220 to 225	24.2 gal. NaOH, 2.0 gal. Triethanolamine, 3.3 gal. TFE #3

The other chemical processing tests include chromic acid anodize per DPS 11.01 and alodine 1500 coating per DPS 9.45. For the RX818-T8, these tests are being performed in conjunction with the alternate immersion and atmospheric tests as described in section 3.0. The other materials were tested with these chemical processes to evaluate adhesion but not subjected to corrosion testing.

Results and Discussion

DPS 9.482-2 requires that the average roughness measured in both parallel and perpendicular directions to be less than 100 microinches Ra, average roughness. The roughness for RX818-T8 sheet in the 17L solution meets this requirement. The roughness values for both the 17L and 4L solutions for the RX818-T8 extrusion, C415-T8 sheet, C416-T8 sheet, and ML377-T8 sheet all meet this DPS requirement. All four alloys are chemically milled resulting in less surface roughness values than for 2090-T8 sheet. Tables 11 though 14 show the details of this data. In these Tables, the parallel measurement for roughness is the first value and the perpendicular measurement is the second value.

The etch rate was measured in mils (thousands of an inch) per minute per surface. The etch rate for all four materials is comparable to the etch rate for the 7075-T6 aluminum. in these chemical milling solutions

Table 11. RX818-T8 Sheet Chemical Milling Results

Alloy	Solution	Etch Rate (mils/min. /surface)	Roughness (μin, Ra)
RX818-T8 Sheet	4L	0.82	130/140
2090-T8	4L	0.80	140/143
7075-T6	4L	0.70	76/94
RX818-T8 Sheet	17L	2.55	15/24
2090-T8	17L	2.50	22/31
7075-T6	17L	2.30	8/26

Table 12. RX818 Extrusion Chemical Milling Results

Alloy	Solution	Etch Rate (mils/min. /surface)	Roughness (μin, Ra)
RX818-T8 Ext	4L	0.9	74/65
2090-T8	4L	0.6	595/655
7075-T6	4L	1.2	29/32
RX818-T8 Ext	17L	2.6	47/55
2090-T8	17L	1.5	200/180
7075-T6	17L	2.6	30/36

Table 13. C415 and C416 Sheet Chemical Milling Results

Alloy	Solution	Etch Rate (mils/min. /surface)	Roughness ((in, Ra)
C415-T8 Sheet	4L	1.2	41/47
C416-T8 Sheet	4L	1.3	38/37
2090-T8	4L	0.6	595/655
7075-T6	4L	1.2	29/32
C415-T8 Sheet	17L	2.6	45/44
C416-T8 Sheet	17L	2.5	50/42
2090-T8	17L	1.5	200/180
7075-T6	17L	2.6	30/36

Table 14. ML377-T8 Sheet Chemical Milling Results

Alloy	Solution	Etch Rate (mils/min. /surface)	Roughness ((in, Ra)
ML377-T8 Sheet	4L	0.78	70/78
2090-T8	4L	0.88	380/410
7075-T6	4L	0.90	95/110
ML377-T8 Sheet	17L	2.1	53/59
2090-T8	17L	1.9	205/240
7075-T6	17L	1.9	53/55

For the RX818-T8 the chromic acid anodize and alodine tests were performed in conjunction with the alternate immersion and atmospheric tests. As discussed earlier, the results of corrosion testing was favorable, there was no visible corrosion damage found. For all four materials, adhesion of the coatings was visually inspected and considered equivalent to the adhesion on the 2090-T8 and 7075-T6 aluminum alloys. Figures 12 though 15 show the various chemical processing treatments on samples of RX818-T8 extrusion, C415-T8, C416-T8, and RX818-T8 sheet.

Figure 12. RX818-T8, C415-T8, C416-T8 Alodine Coupons

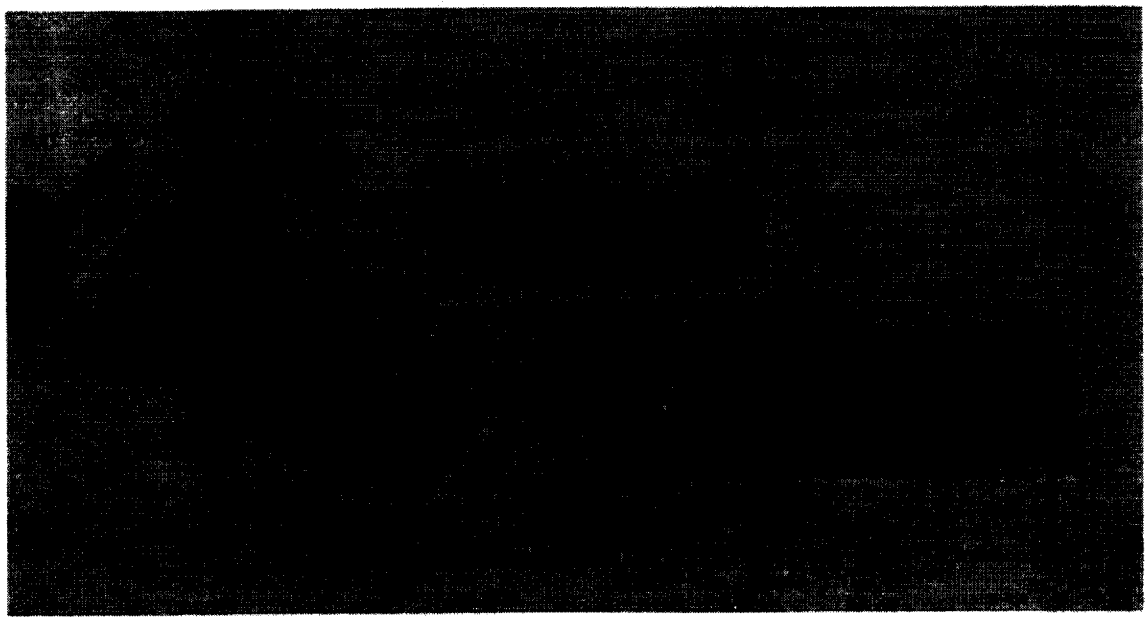

Figure 13. RX818-T8, C415-T8, C416-T8 Anodize Coupons

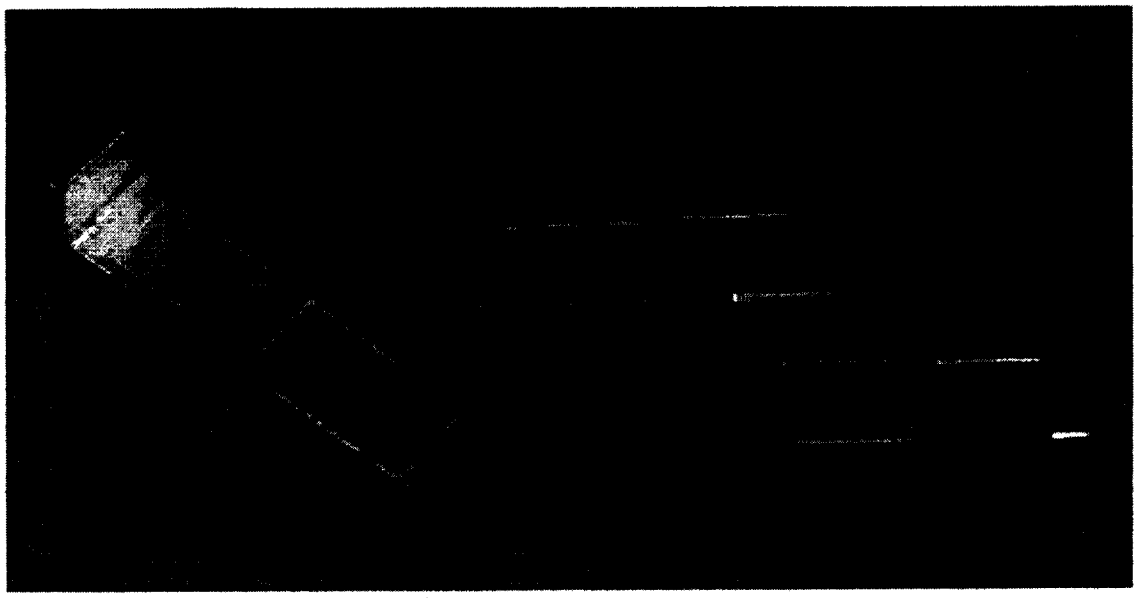

Figure 14. RX818-T8 Extrusion, C415-T8, C416-T8 Chem Mill Coupons

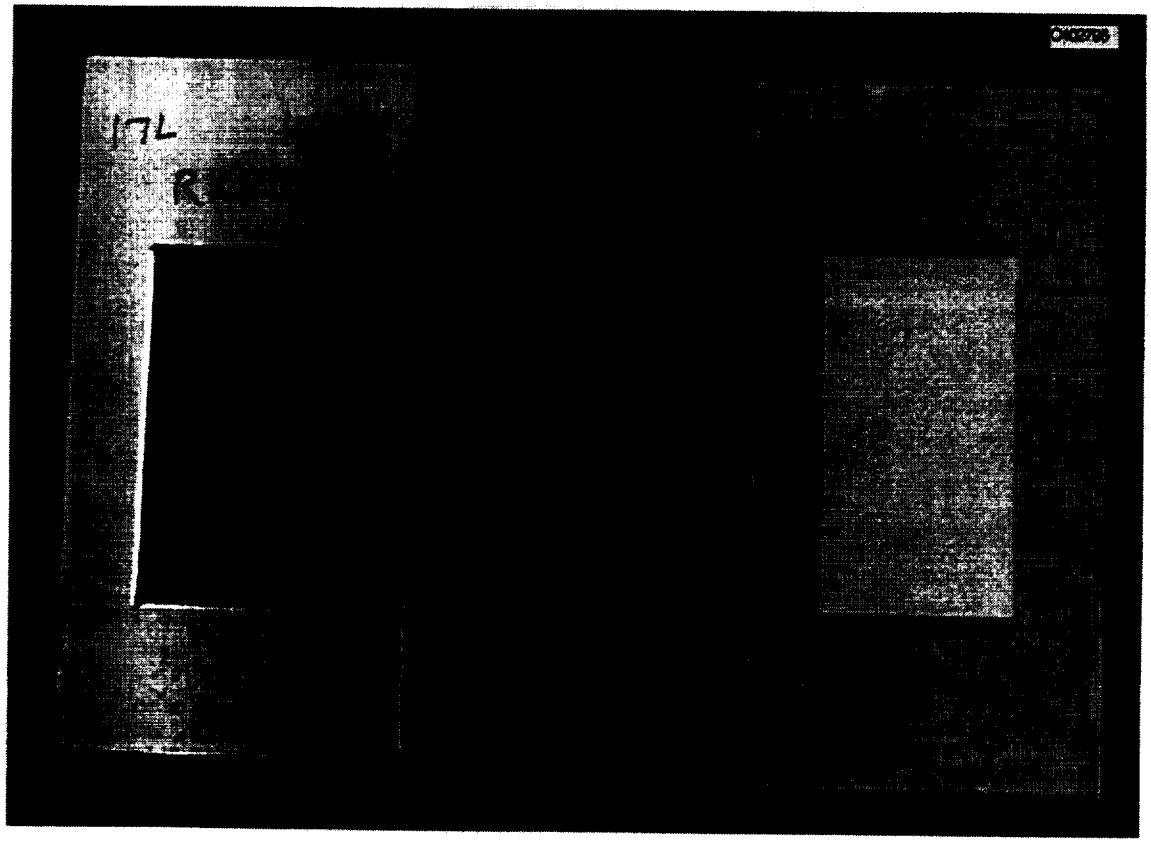

Figure 15. RX818-T8 Sheet Chem Mill Coupons

Conclusions

Preliminary corrosion test results are promising. Visual inspection of RX818-T8 revealed moderate, and slight to moderate pitting, with no cracks. The machinability characteristics are consistent with conventional aluminum alloys such as 7075-T6 and 2090-T8 and no difficulties such as those encountered with 2090-T8 were experienced. The drill wear of C415-T8, C416-T8, and ML377 is comparable to the wear from 2090 and 7075 alloys yet is less than the drill wear of RX818-T8. The chemical processes normally required for airframe manufacturing are successfully performed and meet DPS requirements. The roughness values for both the 17L and 4L solutions for the RX818-T8 extrusion, C415-T8 sheet, C416-T8 sheet, and ML377-T8 sheet all meet this DPS requirement.

REYNOLDS METALS COMPANY

NASA-UVA Light Aerospace Alloy and Structures Technology Program: Aluminum-Based Materials for High Speed Aircraft

Investigators:
Dr. Alex Cho (Principal Investigator) - Reynolds Metals Company
Mr. M.A.Cantrell - Reynolds Metals Company
Dr. James Howe - University of Virginia
Dr. William Quist - Boeing Aircraft Company
Mr. R. Kahandal - Douglas Aircraft Company

Abstract

Successful development of the high speed civil transport system (HSCT) depends on the availability of high performance elevated temperature materials. Among the ingot metallurgy aluminum alloys, Reynolds Metals Company selected an Al-Cu-Li-Mg-Ag alloy as a candidate alloy to meet the property and thermal stability requirements of the high speed civil transport research program. Initial evaluation of the Al-Cu-Li-Mg-Ag alloy (RX818) demonstrated excellent combinations of strength and fracture toughness in T8 temper condition. However, fracture toughness of these alloys after thermal exposure are lower than those in T8 temper. To minimize the thermal degradation of fracture toughness, a study was conducted to examine the effects of compositional and microstructural variations on the evolution of strength and fracture toughness during thermal exposure. The composition study included both major alloying elements such as Cu, Li, Mg and Ag and dispersoid forming elements such as Zr, V and Mn. To examine the effect of grain structure on thermal stability, 0.090δ gauge sheet with both unrecrystallized and recrystallized grain structures were produced and evaluated. For high strength applications, unrecrystallized grain structures were favored. For full scale characterization of these alloy variants, plant size ingots were cast for both recrystallized and unrecrystallized alloy variants. These ingots were rolled to .090δ gauge sheet and delivered to NASA and other HSCT team members for evaluation. In addition, a possible contamination by alkali elements were examined from the plant produced sheet products. The result showed that grain boundary segregation of alkali elements were not observed from the material even after thermal exposure.

Introduction

The objective of I/M Al-Cu-Li-Mg-Ag alloy development is to optimize a precipitate-strengthened ingot metallurgy alloy, based on the Al-Cu-Li-Mg-Ag system, to meet the property and thermal stability requirements of the High Speed Civil Transport Research Program. A concurrent goal is to understand the effects of thermal exposure on the microstructural/property evolution of the alloy as a function of time and temperature in order to help composition optimization and to develop techniques for predicting the evolution of the alloy during long term service environments.

Boeing Aircraft Company proposed several ambitious property goals for ingot metallurgy aluminum alloys for damage tolerant HSCT applications. It is desired that the combination of tensile yield strength and K_{app}. fracture toughness fall within the range between 70ksi/140/ksi-inch$^{1/2}$ to 80ksi/100 ksi-inch$^{1/2}$ after exposure to an anticipated elevated temperature service of up to 275°F (135°C).

Successful development of the high speed civil transport system (HSCT) depends on the availability of high performance elevated temperature materials. Among the conventional aluminum alloy systems, 2XXX series alloys are commonly used for elevated temperature applications because Cu bearing particles exhibit greater thermal stability. For example, alloys 2618 and 2519 contain a large volume fraction of coarse intermetallic particles, which not only enhance thermal stability, but also contribute to alloy strength. Unfortunately, coarse intermetallic particles are only marginally effective as strengthening agents while being deleterious on fracture toughness. Therefore, conventional 2XXX alloys offer limited strength and fracture toughness capability.

Among conventional aluminum alloy systems, only 7XXX series alloys could potentially meet the proposed property goals, but only prior to any thermal exposure. 7XXX series alloys are strengthened by a combination of metastable GP zones and $MgZn_2$ precipitates which provide a good combination of high strength and fracture toughness. However, these precipitate phases are not stable above 100°C, therefore, 7XXX series alloys are not suitable for elevated temperature applications.

Recent work at Reynolds Metals Company has demonstrated that a new proprietary Al-Cu-Li-Mg-Ag alloy (RX818) could potentially meet Boeing's requirements for high combinations of strength and fracture toughness. RX818 is mainly strengthened by thermodynamically stable phases which form extremely fine distributions of precipitates (i.e. T_1 and S'-like phases). These are effective in providing high combination of strength and fracture

toughness because the formation of large intermetallic particles is avoided. A high level of property stability in RX818 has been established in thermal exposure studies at Reynolds. Further improvement of thermal stability of the alloy could be achieved by adding optimum amounts of dispersoids in addition to the precipitate distribution. In TASK 2 program, the optimum amounts of precipitates and dispersoids will be established to improve the mechanical properties and thermal stability of RX818 alloy.

Procedures

To accomplish the above objectives, TASK 2 program consists of the following subtasks:

SUBTASK 2A: Evaluate RX818 Variation Alloys as Model Materials to Understand the Role of Various Strengthening Phases During Thermal Exposure.(Reynolds Metals Co.)

SUBTASK 2B: A study of the microstructural evolution of the Al-Li-Cu-Mg-Ag Systemwith RX818 alloy (UVa Participation)

SUBTASK 2C: Al-Cu-Li-Mg-Ag Alloy Evaluation (Boeing Participation)

SUBTASK 2D: Al-Cu-Li-Mg-Ag Alloy Evaluation (McDonnell Douglas Participation)

The SUBTASK 2A program consists of the following Subtasks:

Subtask 2A1:

Evaluate the three variants of RX818 alloy with modified Mg and Ag content to examine the effect of T_1 and S'-like phases on thermal stability and mechanical properties during the long term exposure.

Subtask 2A2:

Examine the effect of dispersoids on thermal stability and mechanical properties of RX818 alloy - moderate level of dispersoids for conventional casting.

Subtask 2A3:

Examine the effect of dispersoids on thermal stability and mechanical properties of RX818 alloy - high level of dispersoids by Spray Deposition Technique.

Subtask 2A4:

Examine the effect of recrystallization on thermal stability and mechanical properties of RX818 alloys.

Subtask 2A5:

Examine the alloy variants with very high Cu:Li ratio on thermal stability and mechanical properties.

Subtask 2A6:

Examine the grain boudary segregation of alkali metal elements during thermal exposure as a possible cause for the loss of fracture toughness.

SUBTASK 2A: Evaluate RX818 Variation Alloys as Model materials to understand the Role of Various Strengthening Phases During Thermal Exposure.

Subtask 2A1: Evaluate the three variants of RX818 alloy with modified Mg and Ag content to examine the effect of T_1 and S'-like phases on thermal stability and mechanical properties during long term thermal exposure.

Three levels of Mg and Ag contents were selected with fixed Cu and Li contents as three RX818 variant alloys. To meet the material reqiurement, four ingots (12" thick x 20" wide x 36" long) were cast and hot rolled to 0.125δ gauge unrecrystallized sheet for evaluation. Sheet products were solution heat treated at 990°F for 1 hour followed by cold water quench and 5% stretch. The sheet product were aged at 320°F for 16 hours as a standard age practice for all the RX818 variant alloys.

Compositions:

	Cu	Mg	Li	Zr	Ag	Si	Fe
(target)	3.6	.8	1.0	.14	.4	<.08	<.08
64627(actual)	3.8	.8	.9	.13	.4	.06	.06
(target)	3.6	.8	1.0	.14	.8	<.08	<.08
64641(actual)	3.6	.76	.8	.14	.8	.06	.07
(target)	3.6	.4	1.0	.14	.4	<.08	<.08
64653(actual)	3.6	.4	.8	.14	.4	.05	.07
64667(actual)	3.4	.4	.8	.14	.5	.04	.07

Tensile tests and plane stress fracture toughness test results by 16" wide center-notched panel tests in longitudinal direction are listed in Table 1. Also included are the tensile and fracture toughness properties after a thermal exposure of 1,000 hours at 275°F. After the thermal

exposure, tensile strengths increased by 2-3 ksi and the ductility (tensile elongation) by 3-4% at the same time. However, fracture toughness (K_c) decreased by 20-30 ksi-inch1/2. Tensile yield stress vs. fracture toughness values by K_c are plotted in Figure 1 to compare the results to the typical properties of 7075-T6, 2024-T3 and 2090-T8. The T8 temper fracture toughness values of the three alloys, S-64641, S-64667 and S-64627 are significantly higher than both 2090-T8 and 7075-T6 properties. Even after the thermal exposure, the K_c fracture toughness values of S-64667, S-64627 and S-64653 are still higher than that of 7075-T6. In order to compare the fracture toughness values to the property targets proposed by Boeing Aircraft Company, the K_{app}. values of RX818 type alloys are plotted in Figure 2. Prior to the thermal exposure, the K_{app}. fracture toughness values of the RX818 type alloys in T8 temper are higher than the proposed fracture toughness goal. However, after the thermal exposure, the fracture toughness values of the RX818 type alloys are lower than the proposed fracture toughness goal, even though the strengths are still higher than the proposed strength goal. This suggests that a further composition optimization is necessary to further improve the fracture toughness after the long term thermal exposures. Among the alloys tested, the best property combination was achieved by S-64627 which contains 0.8% Mg and 0.4% Ag.

TABLE 1

Tensile Test and Plane Stress Fracture Toughness Test Results from hot rolled 0.125" gauge sheet of four RX818 type alloys in T8 temper and in T8 after 1,000 h at 275°F.

S.No.	UTS(ksi)	TYS(ksi)	El.(%)	K_c	K_{app}
64627-T8	84.7	82.3	6.3	148.3	119.9
T8+1,000h	89.7	85.4	6.3	116.7	98.2
64641-T8	87.8	85.4	6.3	116.9	98.2
T8+1,000h	89.7	87.1	9.5	67.9	62.1
64653-T8	82.1	78.9	8.0	--	--
T8+1,000h	85.1	81.7	12.0	102.0	89.4
64667-T8	85.4	82.1	8.0	131.0	102.8
T8+1,000h	87.3	84.1	11.5	92.9	78.9

Note:

All the tensile properties are averaged from duplicates and K_c and K_{app}. values are from single tests.

K_c and K_{app}. values were tested by single 16" wide center notched and fatigue precracked specimens

K_c and K_{app}. values are in ksi-$(inch)^{1/2}$

FRACTURE TOUGHNESS OF RX818-T8 TYPE ALLOYS

Center Notched 16" Wide Panel (Fatigue Precrack)

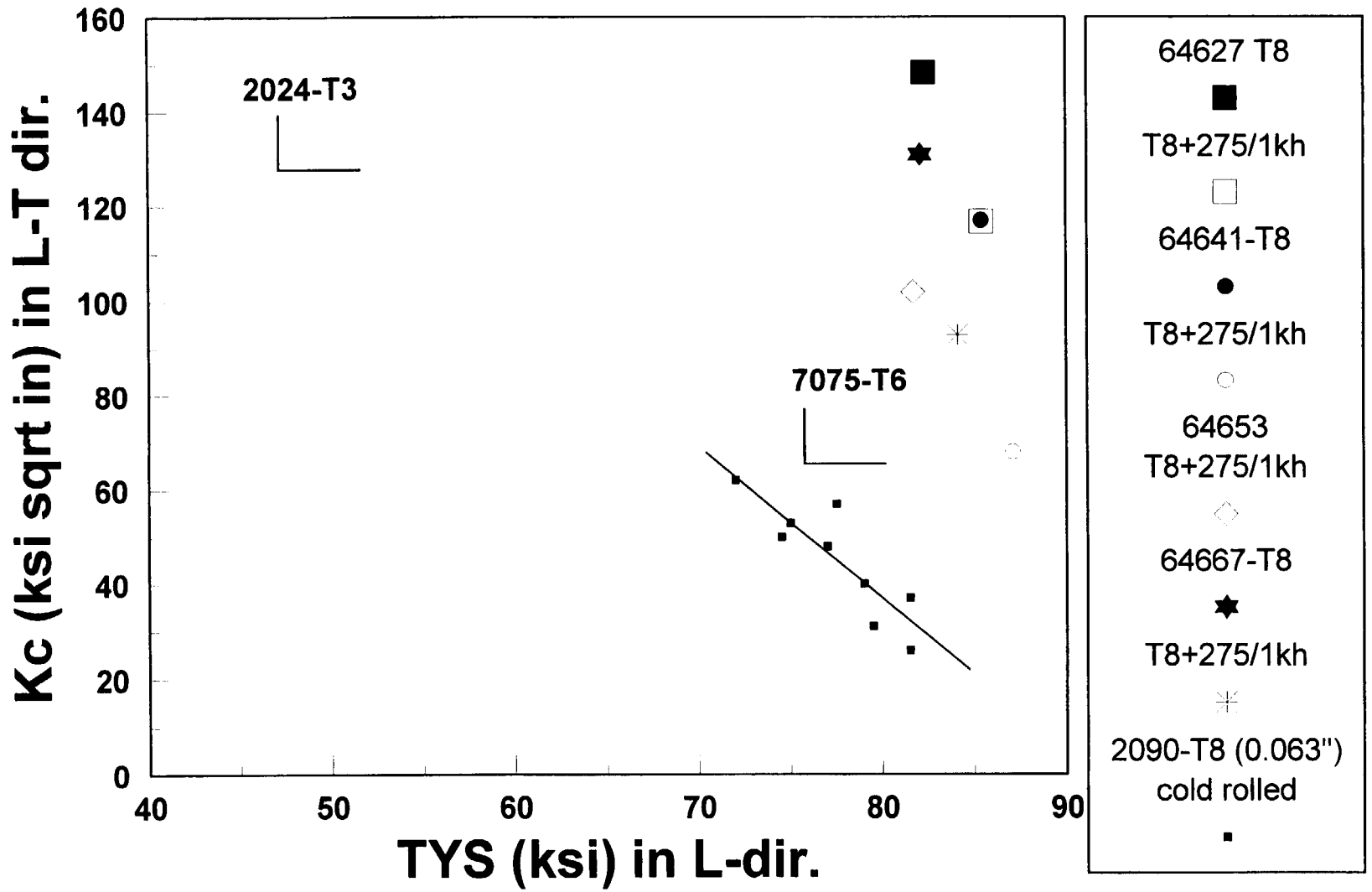

Figure 1 comparison of fracture toughness (K_C) of RX818 and other alloys.

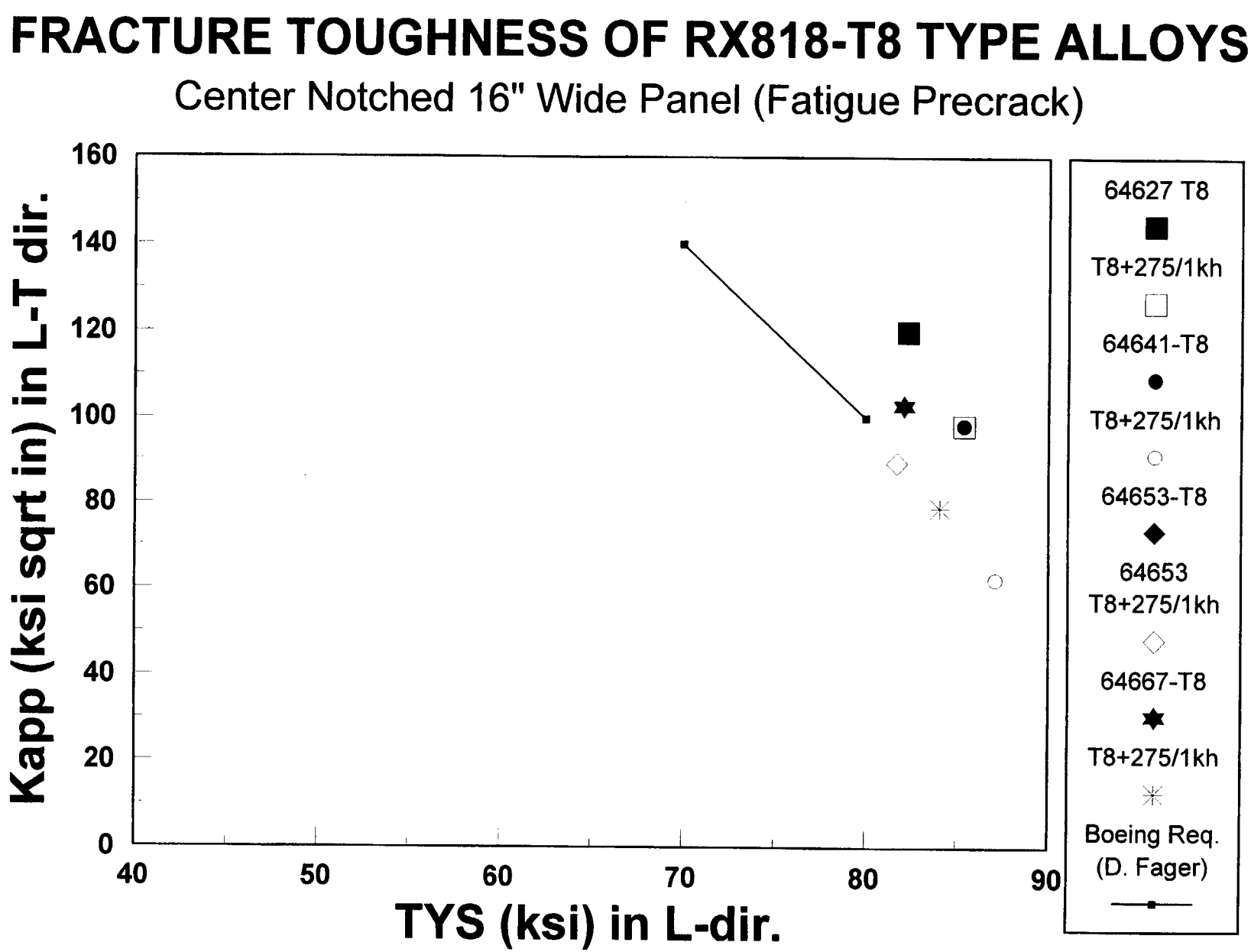

Figure 2 comparison of fracture toughness (K_{app}) of RX818 and Boeing requirment.

Subtask 2A2: Examine the effect of dispersoids on thermal stability and mechanical properties of RX818 alloy - moderate level of dispersoids for conventional casting.

The strength of RX818 alloy is based on precipitate strengthening. Further improvement of thermal stability of the alloy could be achieved by introducing optimum amount of dispersoids in addition to the precipitate distribution. The addition of dispersoids will improve thermal stability but could be deleterious to fracture toughness if too many are added. The key to the further improvement, therefore, would be identifying the optimum combination of precipitation strengthening and dispersoid strengthening. Two considerations were given in selecting alloying elements to form dispersoids: the first, its ability to form a thermally stable coherent phase to maximize strengthening effect; and the second, its cost to be economical enough for commercial scale production.

In this work, Zirconium, Vanadium and Manganese additions are being examined among the peritectic elements. For the initial five compositions of 30 lbs. permanent mold ingots were selected and cast. The target and actual compositions are as follows:

Compositions:

		Cu	Li	Mg	Ag	Zr	V	Mn
65836	(target)	3.5	1.0	.4	.4	.17	.1	.3
	(actual)	3.4	.99	.52	.34	.15	.12	.3
65837	(target)	3.5	0.8	.4	.4	.17	.1	.3
	(actual)	3.5	.86	.39	.22	.18	.12	.3
65638	(target)	3.0	1.2	.4	.4	.17	.1	.3
	(actual)	3.1	1.21	.4	.36	.15	.12	.29
65839	(target)	3.5	1.0	.4	.4	.17	.1	--
	(actual)	3.35	1.04	.4	.34	.17	.12	--
65840	(target)	3.5	1.0	.4	.4	.17	--	--
	(actual)	3.5	1.0	.39	.36	.16	.01	--

The ingots were homogenized, scalped and hot rolled to 0.125δ gauge sheet. The hot rolled sheet were then cold rolled to .090δ gauge sheet. The final gauge sheet products were solution heat treated at 990°F for 1 hour followed by cold water quench. T8 temper sheet were stretched by 5% and aged at 320°F for 16 hours as a standard T8 temper practice. Metallographic

examination of the .090δ gauge sheet samples in T8 temper showed various degrees of recrystallization depending on the alloy chemistry. The grain structures of the five alloys are shown in Figure 3. Four variant alloys containing Mn and V, S.No. 65836, 65837, 65838 and 65839, were recrystallized at various degrees. S.No. 65840, which contains only Zr, is not recrystallized. The tensile properties of all five variants in T8 temper material underwent complex property changes during the initial stage of the thermal exposures at 275°F. No significant changes occurred in strength or fracture toughness after exposure for 1,000 hours and 2,500 hours at 275°.

Additional Experiment

Among the five alloy variants examined, only S.No. 65840 was not recrystallized. The cause of the various degrees of recrystallization for the four other variants were not very clear at the time. To provide more information regarding the effect of dispersoid forming elements on the grain structure and fracture toughness after thermal exposure, additional five compositions of the 30 lbs. permanent mold ingots were cast. The five compositions are as follows:

	Cu	Li	Mg	Ag	Zr	V	Mn
66932 (target)	3.5	1.0	.4	.4	.16	.1	.3
(actual)	3.49	1.11	.43	.43	.17	.11	.19
66933 (target)	3.5	0.8	.4	.4	.16	.1	.3
(actual)	3.46	0.82	.42	.46	.19	.11	.34
66934 (target)	3.0	1.2	.4	.4	.16	.1	.3
(actual)	2.92	1.21	.4	.44	.18	.12	.33
66936 (target)	3.5	1.0	.4	.4	.16	--	--
(actual)	3.42	1.02	.39	.42	.17	--	--
66937 (target)	3.5	1.0	.4	.4	.16	--	.3
(actual)	3.50	1.0	.41	.43	.18	--	.32

The ingots were homogenized, scalped and hot rolled to 0.125δ gauge sheet. The hot rolled sheet were then cold rolled to .090δ gauge sheet. The final gauge sheet products were solution heat treated at 990°F for 1 hour followed by cold water quench. T8 temper sheet were stretched by 5% and aged at 320°F for 16 hours as a standard T8 temper practice. Metallographic examination of the .090δ gauge sheet samples in T8 temper showed various degrees of

recrystallization depending on the alloy chemistry. The grain structures of the five alloys are shown in the Figure 4. Alloys with Zr alone retained unrecrystallized grain structures after solution heat treatment. Other variants with additional dispersoids (Mn, V) were recrystallized after solution heat treatment at various degrees.

Tensile test and fracture toughness test results of the .090δ gauge sheet in T8 temper before and after a thermal exposure are listed in TABLE 3. Due to a mistake during the T8 test sample preparation, there were no tensile properties were available for S.No. 66936 in T8 temper. Fracture toughness values by K_c and K_{app}. values of all ten alloy variants after thermal exposure of 2500 hours at 275°F are plotted in Figure 5 and Figure 6. respectively. The data are presented in three groups by the degree of recrystallization. These observation suggests that materials with recrystallized grain structure would be favored for higher fracture toughness applications at a medium strength level, and materials with unrecrystallized microstructures would be favored for higher strength applications with a limited fracture toughness capability. Another observation is that alloy variant containing Zr and Mn without Vanadium exhibited better fracture toughness at a similar strength level than the alloy variants containing Zr, Mn and V.

TABLE 2

Tensile test (longitudinal direction) and plane stress fracture toughness test (L-T)* after thermal exposures at 275°F for 1,000 hours (-2) and 2,500 hours (-3).

S.No.	UTS(ksi)	TYS(ksi)	El(%)	K_c	K_{app}
65836-2	77.3	74.0	9.0	105.7	81.1
65836-3	76.6	74.0	8.5	93.3	77.4
65837-2	72.3	67.6	9.0	139.7	93.3
65837-3	72.3	68.5	8.5	126.0	88.1
65838-2	73.7	70.6	8.0	92.5	75.8
65838-3	73.6	70.7	5.5	91.2	72.9
65839-2	78.0	75.0	7.0	87.2	73.3
65839-3	78.2	75.1	7.0	82.4	67.7
65840-2	83.6	79.8	6.5	80.4	71.6
65840-3	82.8	78.4	8.5	88.7	73.2

Note:

All the tensile properties are averaged from duplicate test results.

K_c and K_{app} values are from single test results in ksi-$(inch)^{1/2}$

*10δ wide .090δ thick cold rolled center notched panels

TABLE 3

Tensile test (longitudinal direction) and plane stress fracture toughness test (L-T)* in the T8 temper (-1) and after thermal exposures at 275°F for 2,500 hours (-2).

S.No.	UTS(ksi)	TYS(ksi)	El(%)	K_c	K_{app}
66932-1	79.6	76.5	8.0	N.A.	N.A.
66932-2	81.5	78.5	8.5	76.9	67.6
66933-1	74.0	69.9	9.0	140.5	97.5
66933-2	76.5	73.2	10.2	114.8	83.9
66934-1	69.5	65.1	10.0	136.9	93.6
66934-2	73.2	70.8	10.5	91.0	74.4
66936-1	N.A.	N.A.	N.A.	N.A.	N.A.
66936-2	79.5	76.7	8.8	97.1	79.1
66937-1	75.4	70.9	9.0	150.0	100.3
66937-2	78.6	74.5	9.3	99.7	88.1

Note:

All the tensile properties are averaged from duplicate test results.

K_c and K_{app} values are from single test results in ksi-(inch)$^{1/2}$

*10δ wide .090δ thick cold rolled center notched panel

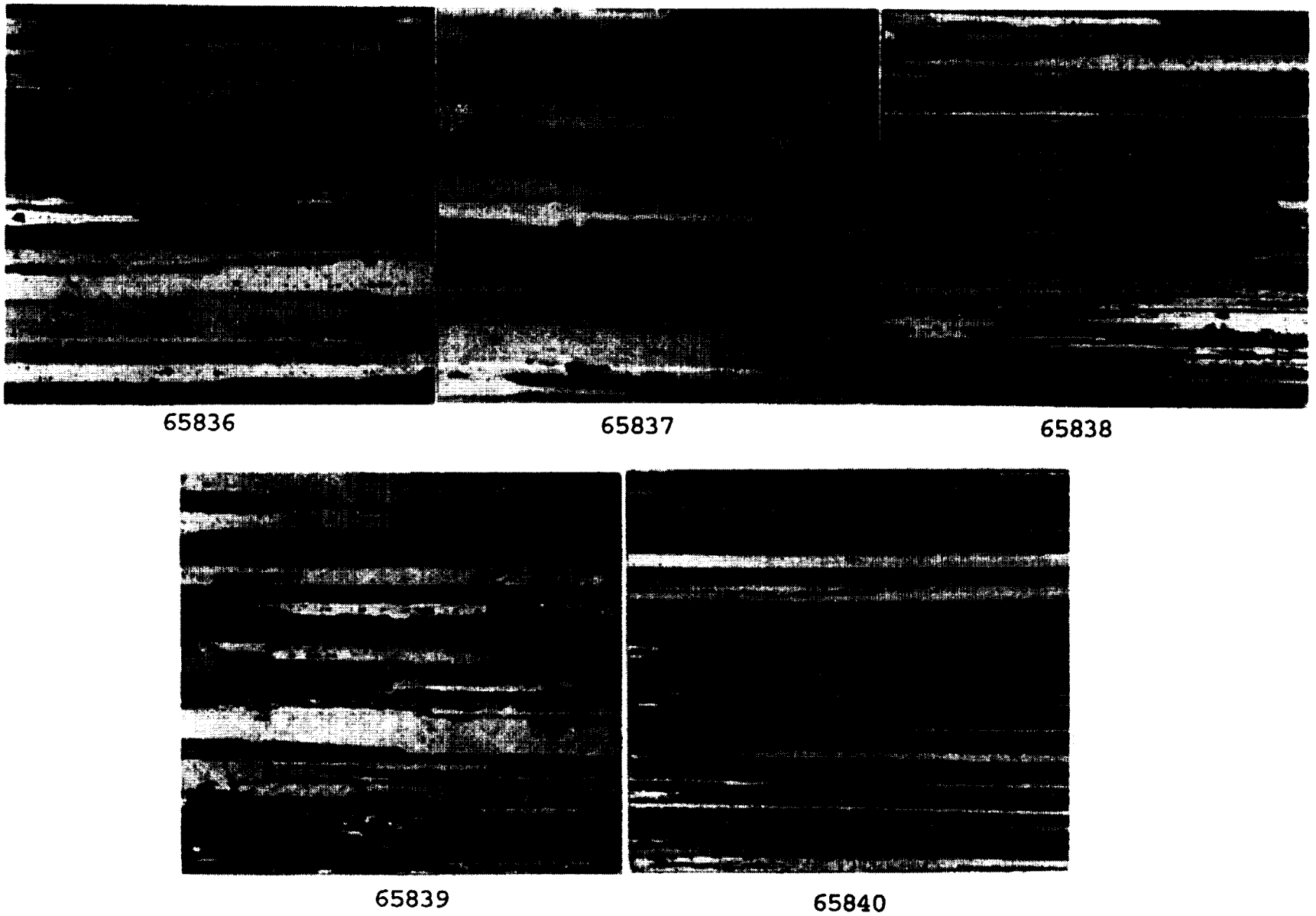

Figure 3. Photomicrographs of longitudinal cross sections of 0.090" gauge RX818-T8 type sheet, S.Nos. 65836, 65837, 65838, 65839 and 65840. Electro etched. Magnification: 100x.

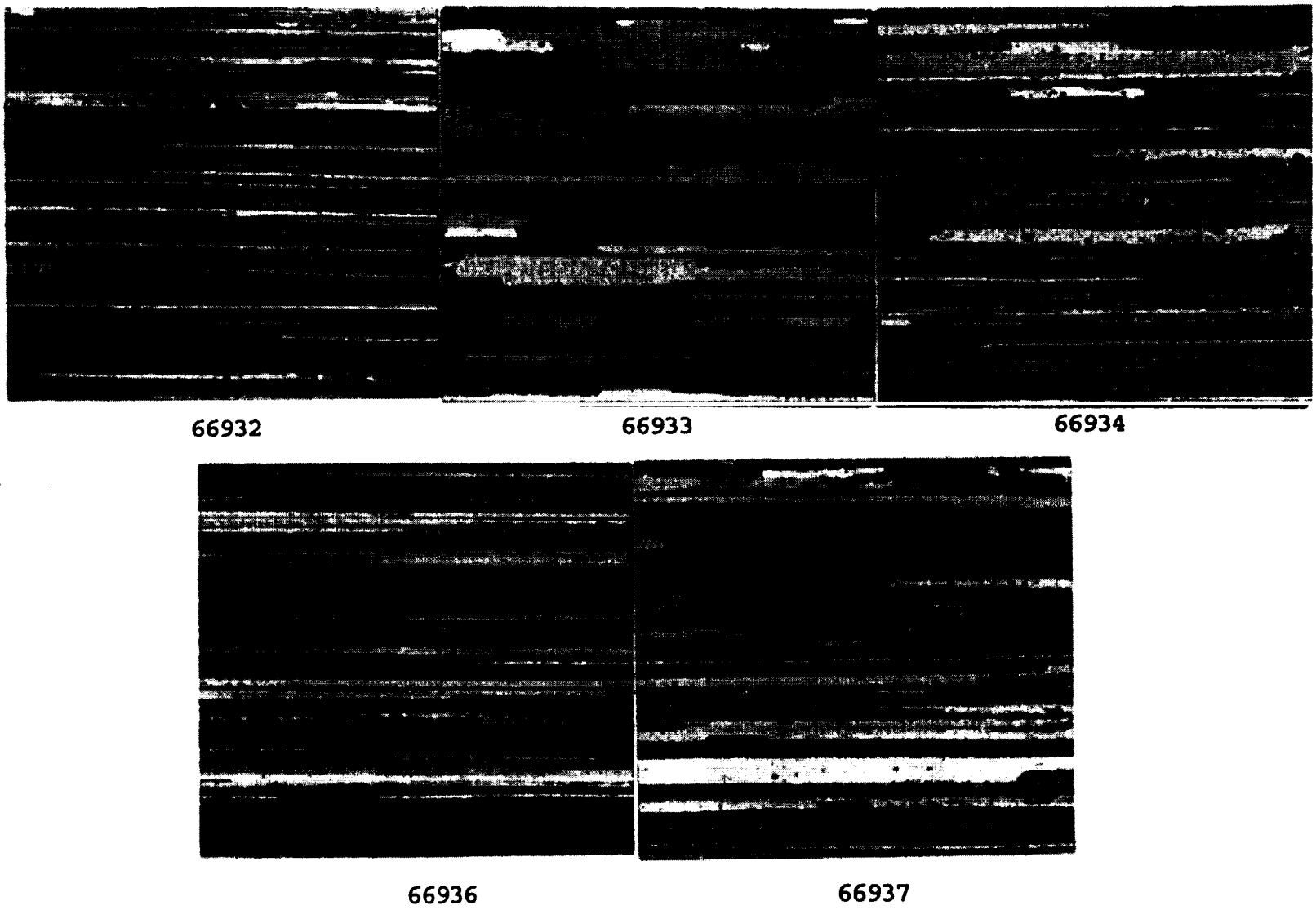

Figure 4. Photomicrographs of longitudinal cross sections of 0.090" gauge RX818-T8 type sheet, S.Nos. 66932, 66933, 66934, 66936 and 66937. Electro etched. Magnification: 100x.

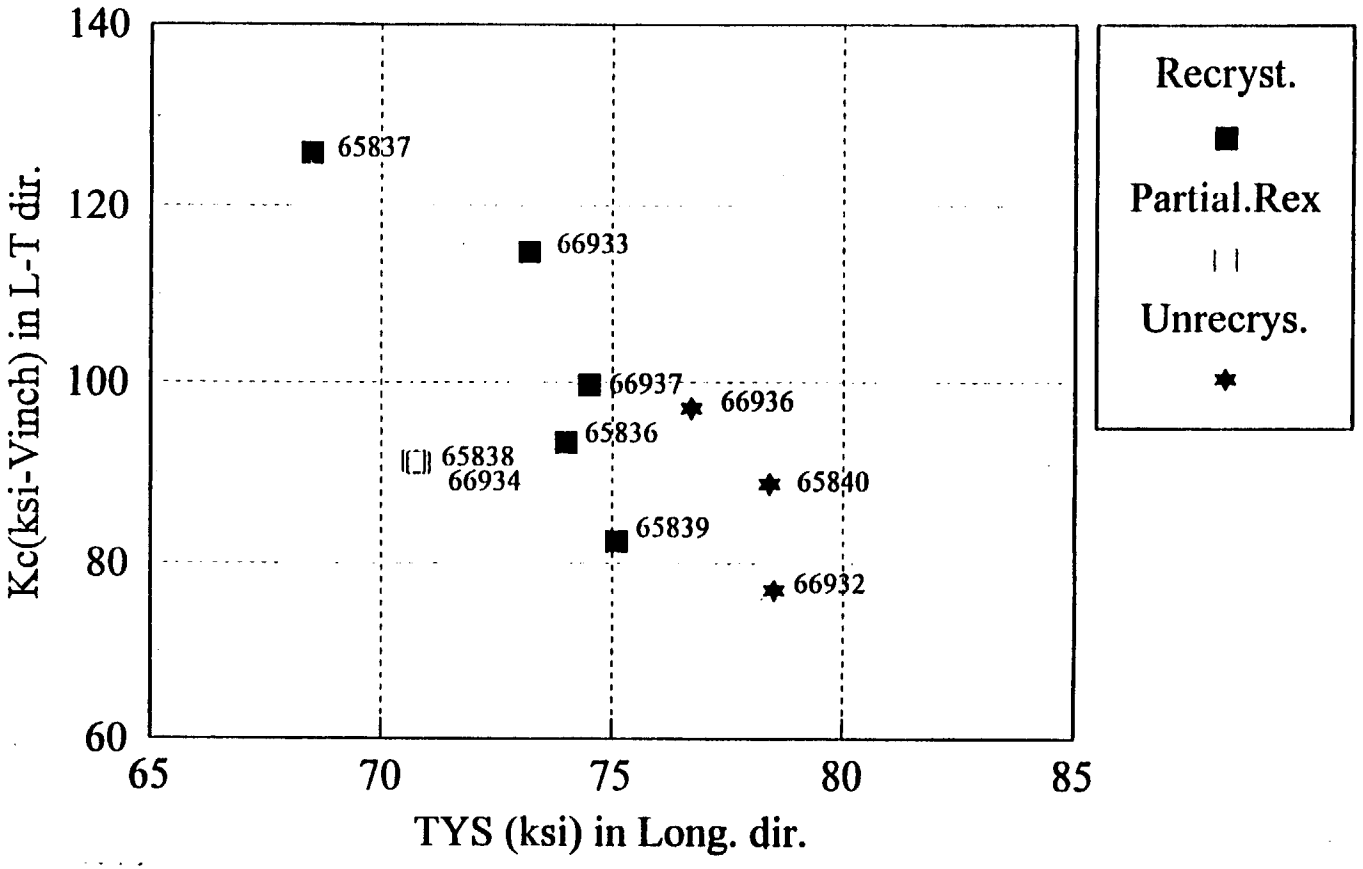

Fig. 5. **Fracture toughness of RX818-T8 type variants. K_c vs. TYS after 2500 hrs. Exposure at 275F.**

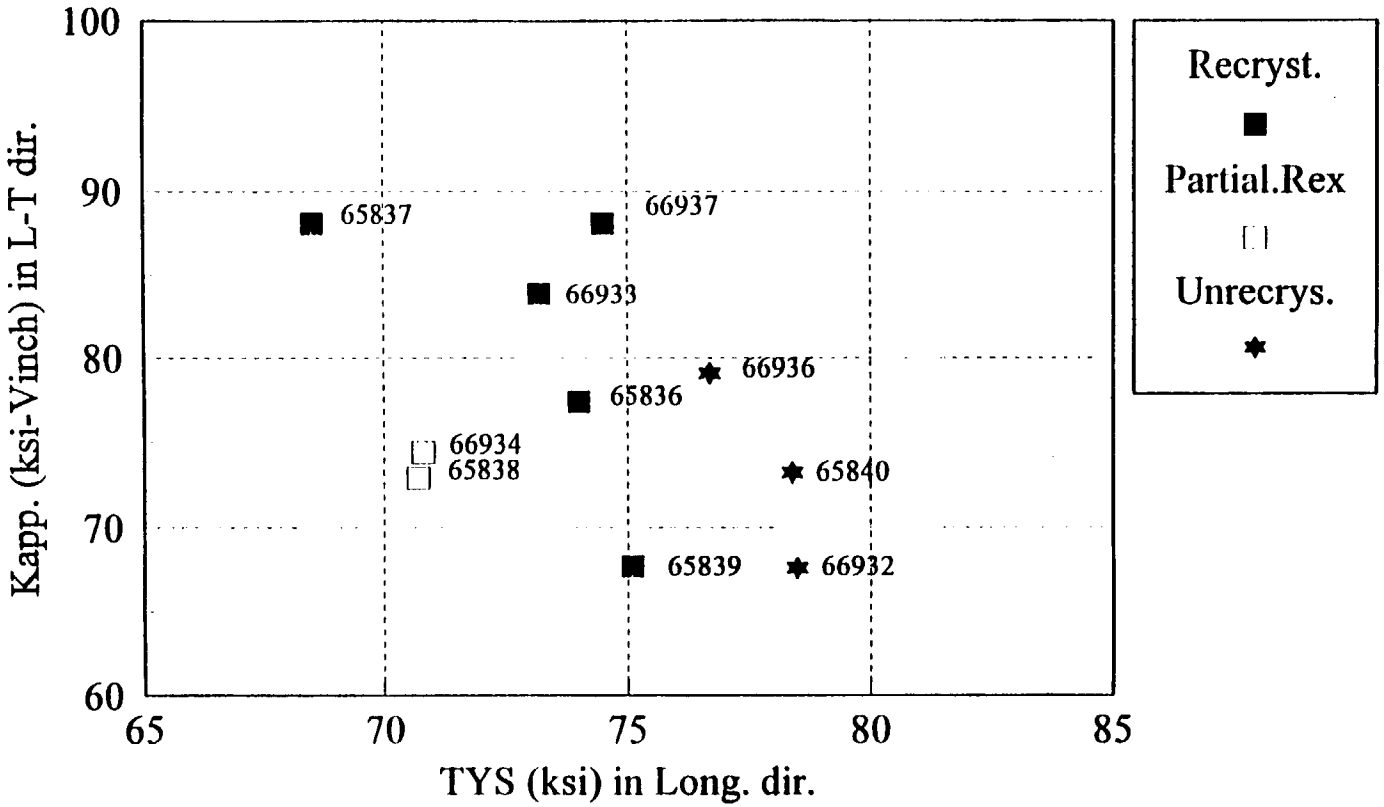

Fig. 6. **Fracture toughness of RX818-T8 type variants. K_{app} vs. TYS after 2500 hrs. Exposure at 275F.**

Subtask 2A3: Examine the effect of dispersoids on thermal stability and mechanical properties of RX818 alloy - high level of dispersoids by Spray Deposition Technique.

The dispersoid particles formed by Zr, V, and Mn are coherent phases which are effective strengthening agents. However, addition of too much of these elements would result in coarse incoherent particles which are extremely deleterious to fracture toughness.

Therefore, the total amount of these coherent dispersoid particles is very limited compared to the precipitate particles in RX818 alloy. One way to increase the amount of these coherent dispersoid particles is to employ a casting technique with a faster solidification rate.

In this work, RX818 variation alloys with a high volume fraction of dispersoids were evaluated with the billet cast by Spray Deposition Technique. Spray Deposition Technique was selected for its enhanced solidification rate and its economic feasibility for commercial scale production. Five compositions of 30 lbs permanent mold ingots were cast as starting stock material for Spray Deposition casting. The compositions are as follows:

S.No.		Cu	Li	Mg	Ag	Zr	V	Mn
65831	(target)	3.5	1.0	.4	.4	.3	.2	--
	(actual)	3.45	1.0	.43	.29	.29	.18	.01
65632	(target)	3.5	1.0	.4	.4	.3	.2	.5
	(actual)	3.6	1.04	.43	.38	.28	.18	.44
65833	(target)	3.5	1.0	.4	.4	.25	.2	.3
	(actual)	3.6	1.1	.43	.44	.26	.17	.32
65834	(target)	3.5	1.0	.4	.4	.25	.1	.3
	(actual)	3.39	1.02	.41	.43	.22	.09	.3
65835	(target)	3.0	1.2	.4	.4	.3	.2	--
	(actual)	3.58	1.21	.42	.46	.27	.17	--

The Spray deposited billets were machined to 3" diameter billets and extruded to .25" x 1.5" cross section bars. To compare the properties to the sheet from the conventionally cast ingots, these extrusions were hot rolled to 0.125" gauge and then cold rolled to 0.090δ gauge sheet. The final gauge sheet products were solution heat treated at 990°F for 1 hour followed by cold water quench. T8 temper sheet were stretched by 5% and aged at 320°F for 16 hours as a standard T8 temper practice.

The most surprising observation was that a Mn addition significantly increases the degree of recrystallization after heat treatment. Metallographic examination of the grain structures after solution heat treatment (Figure 7) revealed that the alloys containing Zr and no Mn are completely unrecrystallized and the alloys containing both Zr and Mn are fully recrystallized with coarse recrystallized grains. It appears that V content does not show a strong effect on the recrystallization behavior. It should be noted that the strengths of these alloys are strongly influenced by the degree of recrystallization.

Due to the narrow sheet samples from the spray deposited billets, it was decided to utilize Kahn Tear tests as a fracture toughness indicator test. The tensile and Kahn Tear test results of the samples in T8 and in T8 + thermal exposure conditions are listed in Table 4. Tensile yield stresses and Propagation Energy from Kahn tests from the five variants after thermal exposure at 275°F are plotted in Figure 8. As stated earlier, the material quality of these billets were very questionable, so we do not have enough confidence in the quality of the test results.

TABLE 4

Longitudinal Tensile Test and Kahn Tear test results of 0.090δ gauge sheet which were extruded and rolled from Spray Deposited billets and aged at 320°F for 16 hours.

S. No.	Exposure	UTS (ksi)	TYS (ksi)	El.(%)	Tear Strength (ksi)	Propagation Energy (in-lb/in2)
65831	as T8*	78.8	74.8	9.5	--	--
	500				18.1	297
	1000				16.7	342
	2500	78.6	73.1	7.0	18.7	419
65832	as T8	72.6	69.7	10.5	--	--
	500				17.9	417
	1000				16.9	360
	2500	73.3	69.1	9.0	16.7	290
65838	as T8	69.8	67.2	12.5	--	--
	500				16.0	187
	1000				8.2	36
	2500	66.8	63.0	7.5	9.1	21
65834	as T8	68.9	67.1	10.5	--	--
	500				19.0	270
	1000				18.8	266
	2500	69.5	67.2	10.5	18.3	270
65835	as T8	83.9	80.6	9.5	--	--
	500				13.7	186
	1000				13.0	135
	2500	79.6	73.3	6.5	13.4	135

* Aged at 320°F for 16 hours.

Note: tensile test results are averged values from duplicates.

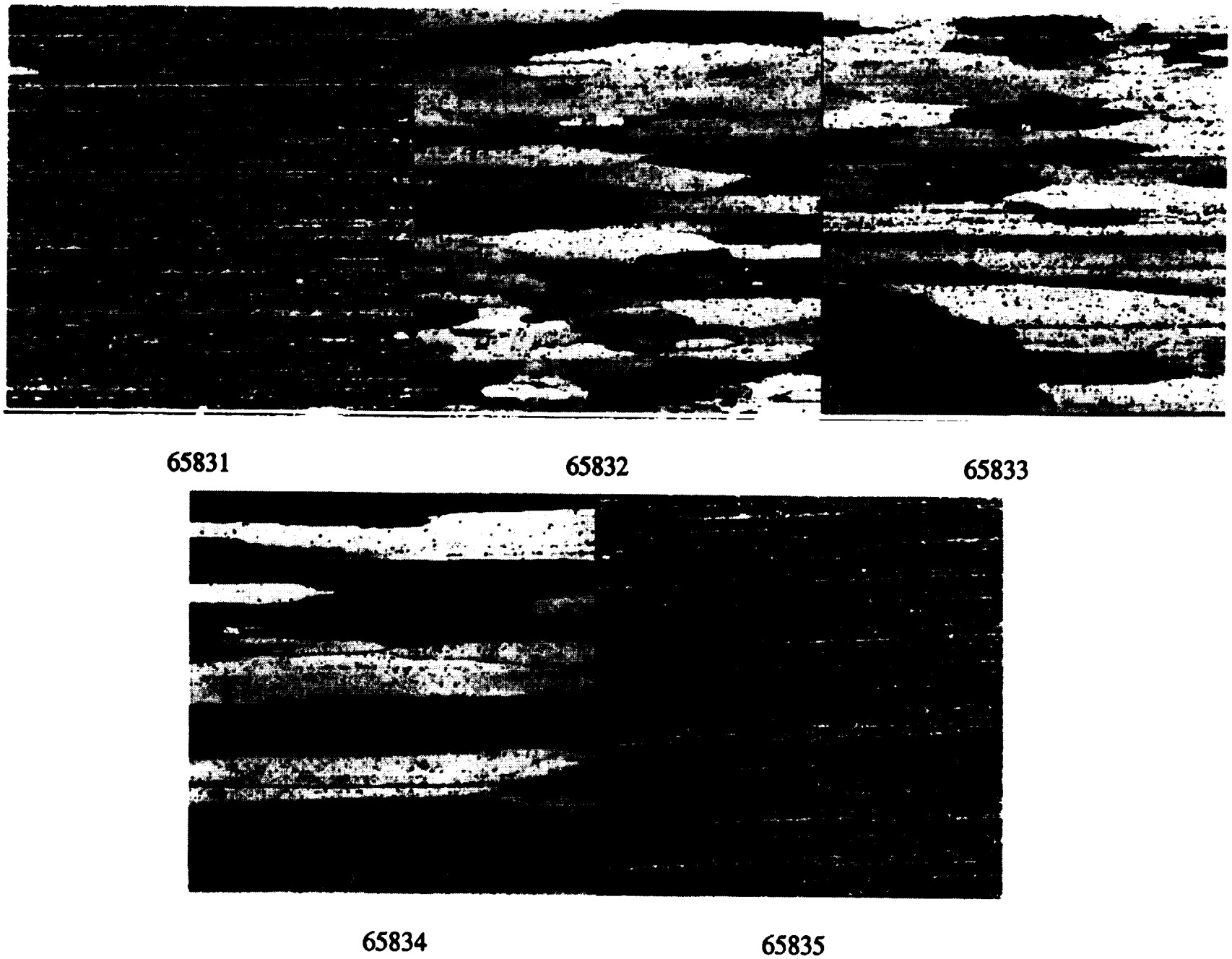

Figure 7. 100X Barkers Etch Micrographs of Spray Deposition Cast 0.090" RX818 Sheet in T8 Temper after Thermal Exposure at 275°F for 2500 hours.

Fracture Toughness of Spray Deposition Alloy Variants

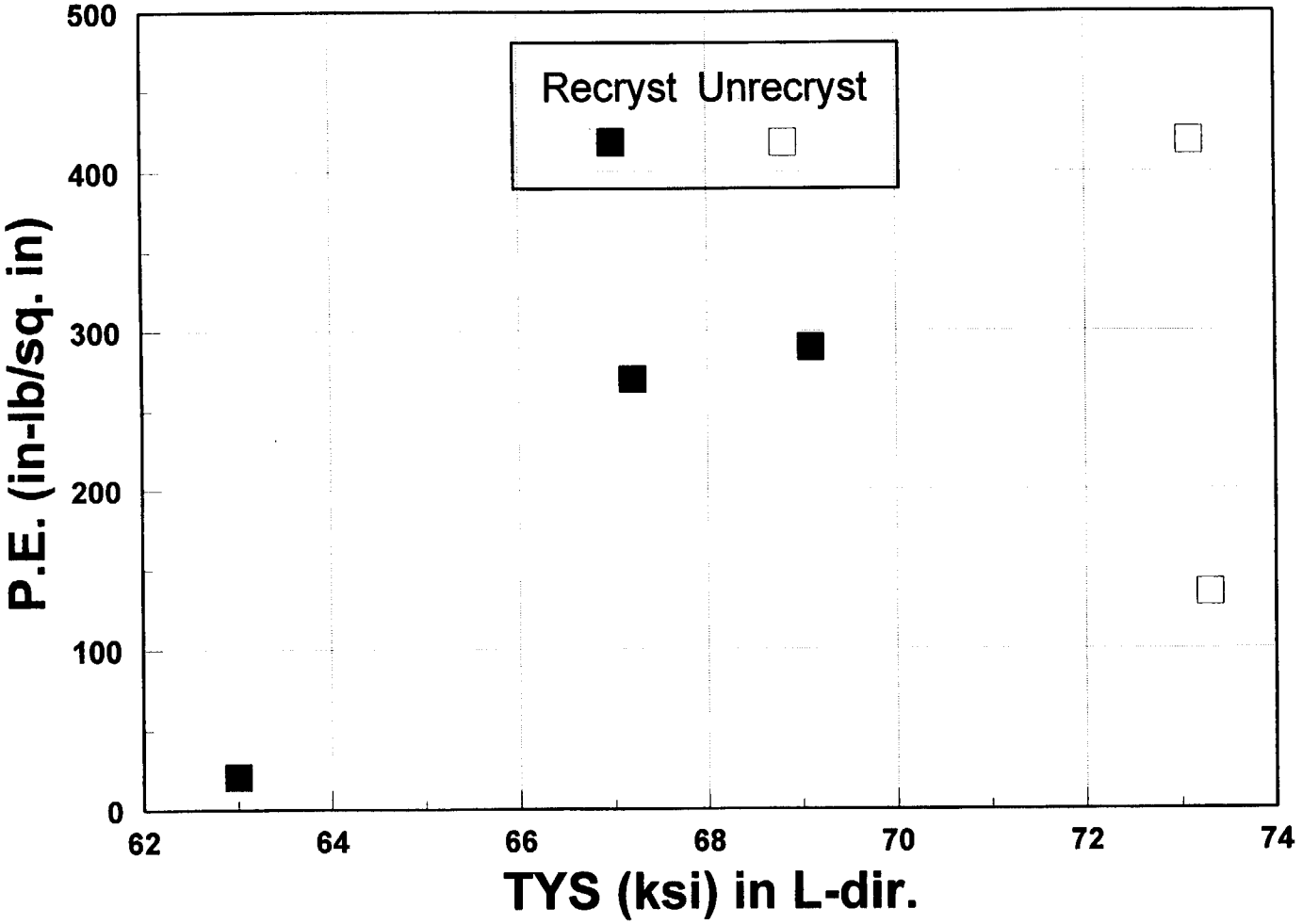

Figure 8 Propagation energy versus TYS after exposure 2500 hrs. at 275F of recrystallized and unrecrystallized alloys

Subtask 2A4: Examine the effect of recrystallization on thermal stability and mechanical properties of RX818 type alloys with full size inqots.

The earlier work showed promising strength-toughness results from RX818 alloy and also showed potential benefits of recrystallized variants. Therefore, RMC decided to cast four full size ingots to verify the full potential of these alloys for the future high speed aircraft applications. The unrecrystallized variant was designated as RX818 and the recrystallized variant was designated as ML377.

Four 10,000 pound ingots with 16" thick by 45" wide cross section were cast with RX818 chemistry (Ingot No. 13839-5 and 13839-6) and ML377 chemistry (Ingot No. 1385-2 and 1385-4). The actual chemistries are listed below:

RX818

Ingot No.	Lot No.	Final Gauqe	Cu	Li	Mg	Ag	Zr
13839-5	930K665B	.090 inch	3.76	.99	.51	.36	.14
13839-6	930K665A	scrapped	3.49	.96	.47	.33	.15

ML377

Ingot No.	Lot No.	Final Gauge	Cu	Li	Mg	Ag	Zr	Mn
1385-2	930K664A	.063 inch	3.53	.96	.44	.42	.14	.29
1385-4	930K664B	.090 inch	3.50	.95	.39	.42	.12	.30

Ingot 13839-5 (RX818) and the ingot 1385-2 (ML377) were rolled to .090δ gauge. Ingot 13839-6 (RX818) and 1385-4 (ML377) were rolled to .063δ gauge sheet. Ingot No. 13839-6 was scrapped after solution heat treatment due to the extremely coarse recrystallized grain structure. Sheet product were solution heat treated at 990°F for an hour followed by water quench and 3% stretch. The sheet product then aged at 320°F for 20 hours as a standard age practice for all RX818 variant alloys. Optical metallographic examination revealed that RX818 alloy sheet (930K665B) was not recrystallized, and ML377 alloy sheet (930K664B) was fully recrystallized (Figure 9) .

Crystallographic texture of both alloys are examined by X-ray diffraction method. Figure 10 shows the (111) Pole figures from RX818(930K665B) and ML377(930K664B) sheet. The Pole figure of RX818 sheet demonstrates the typical unrecrystallized texture with a strong

intensity of Brass component (110)[112]. Figure 11 shows volume fraction calculated from CODF (Crystallographic Orientation Distribution Function) from the two alloy sheet. The Pole figure from ML377 sheet, by contrast, shows a strong Goss component (110)[001] which is one of the typical recrystallized texture component. The effect of these differences in texture between RX818 and ML377 sheet resulted in the significant difference in strength anisotropy.

Tensile and plane stress fracture toughness test results from .090" gauge RX818 and ML377 sheet are listed in Table 5 and Table 6, respectively. Tensile tests were conducted with 2" gauge length sheet specimens in both T3 and T8 temper conditions. Mechanical properties in T3 temper are of interest because most sheet forming operations are perfomed in T3 temper.
In Figure 12, ML377 sheet shows high tensile elongation values in all three directions while unrecrystallized RX818 sheet shows limited ductility in the longitudinal direction. In T8 temper conditions, RX818 sheet shows a significant strength anisotropic behavior as can be seen in Figure 13. Even though the strength of ML377 in the longitudinal direction is not as high as that of RX818, the ML377 T8 temper sheet exhibited uniform strength in all three directions as a result of the fully-recrystallized grain structure with strong Goss component.

The plane stress fracture toughness tests were conducted in T8 temper with 16 inch wide, center notched, fatigue precracked panel specimens. Duplicate tests were conducted in the longitudinal direction for both RX818-T8 and ML377-T8 sheet. The test results are plotted in Figure 14 with typical strength fracture toughness values of 2024-T3 and 7075-T6 sheet. Both RX818-T8 and ML377-T8 show an excellent combination of strength and fracture toughness properties compared to these conventional alloys.

TABLE 5

Mechanical properties of .090" gauge cold rolled ML377 sheeet in T3 and T8 temper
(Ingot No. 1385-2, Lot No. 930K664B)

T3 temper (3% stretched)

Ga.	direction	UTS(ksi)	TYS(ksi)	El(%)	K_c(ksi(inch)1/2)	$K_{app.}$ (ksi(inch)1/2)
.090"	L	54.1	40.8	19.8	N.A.	N.A.
	45 deg.	52.7	38.3	18.0		
	LT	51.9	37.0	21.0		

T8 temper (3% stretched, aged at 320°F for 20 hrs.)

Ga.	direction	UTS(ksi)	TYS(ksi)	El(%)	K_c(ksi(inch)1/2)	$K_{app.}$ (ksi(inch)1/2)
.090"	L	79.0	75.1	8.3	136.1	105.9
					161.2	114.2
	45 deg.	81.4	75.8	8.5		
	LT	80.0	73.4	12.0		

Note:
All the tensile properties are averaged from duplicate test results.
K_c and $K_{app.}$ values are from single test results in Ksi-(inch)1/2

TABLE 6

Mechanical properties of .090" gauge cold rolled RX818 sheeet in T3 and T8 temper
(Ingot No. 13838-5, Lot No. 930K665B)

T3 temper (3% stretched)

Ga.	direction	UTS(ksi)	TYS(ksi)	El(%)	K_c(ksi(inch)1/2)	$K_{app.}$ (ksi(inch)1/2)
.090"	L	66.5	50.7	11.5	N.A.	N.A.
	45 deg.	53.8	40.5	23.3		
	LT	64.0	46.7	17.7		

T8 temper (3% stretched, aged at 320°F for 20 hrs.)

Ga.	direction	UTS(ksi)	TYS(ksi)	El(%)	K_c(ksi(inch)1/2)	$K_{app.}$ (ksi(inch)1/2)
.090"	L	85.4	83.1	7.5	119.6	92.3
					116.5	97.1
	45 deg.	70.4	68.3	11.6		
	LT	83.2	80.4	10.3		

Note:
All the tensile properties are averaged from duplicate test results.
K_c and $K_{app.}$ values are from single test results in Ksi-(inch)1/2

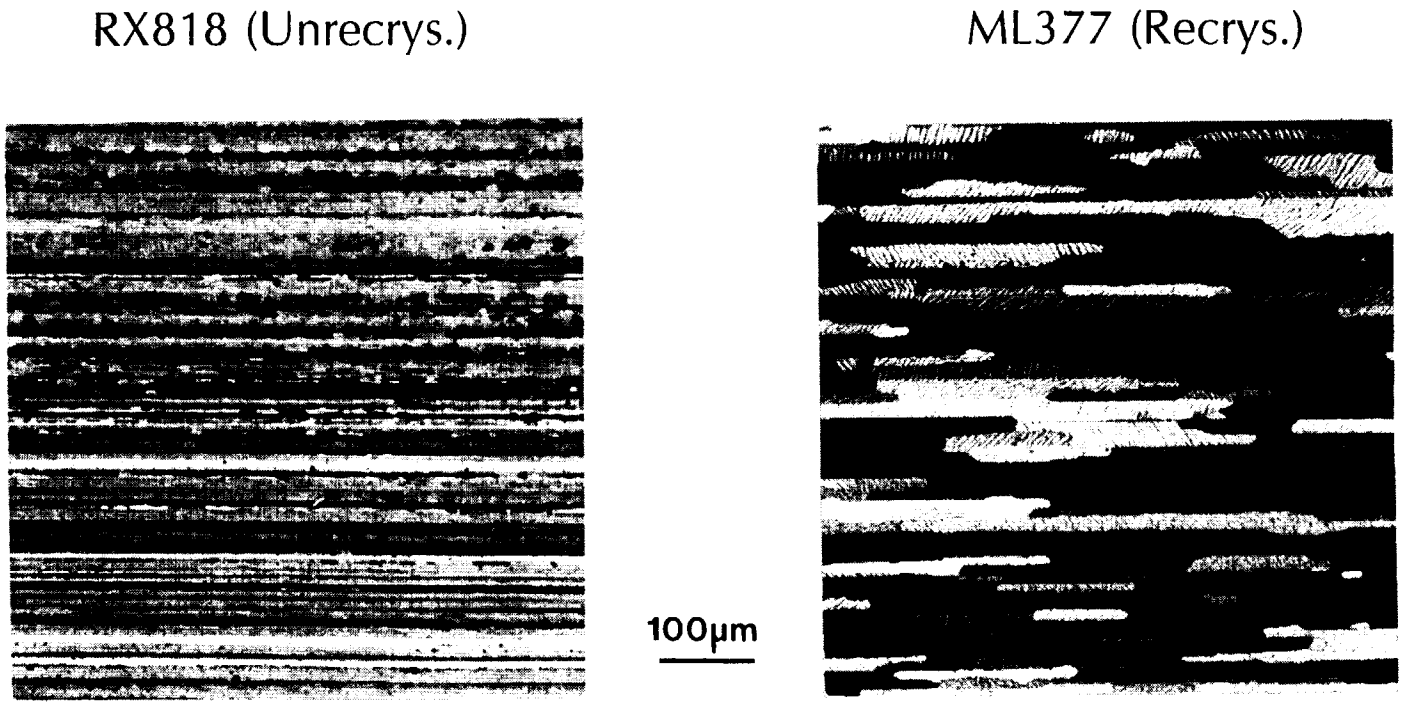

Figure 9 grain structure of RX818 and ML377 alloys sheet with gauge 0.090".

Pole Figures of two Al-Cu-Li-Mg-Ag Alloys

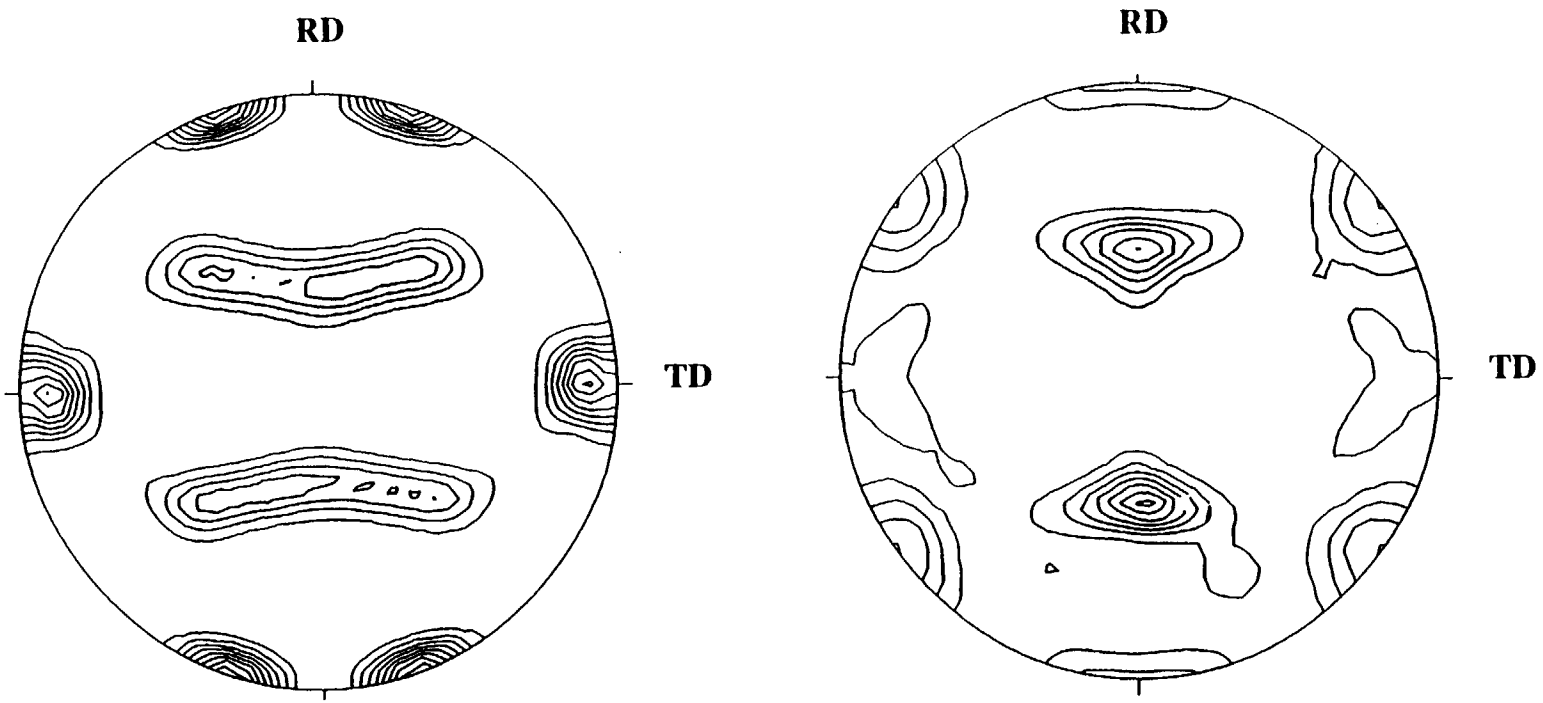

RX818 (Unrecrys.)

Maximum = 9.04
Contour(1) = 1.0
Contour(2) = 2.0
Contour(3) = 3.0
Etc.

ML377 (Recrys.)

Maximum = 7.35
Contour(1) = 1.0
Contour(2) = 2.0
Contour(3) = 3.0
Etc.

Figure 10 (111) pole figures of two sheet alloys (0.09 inch).

Quantitative Texture of Two Alloys with Different Grain Structure

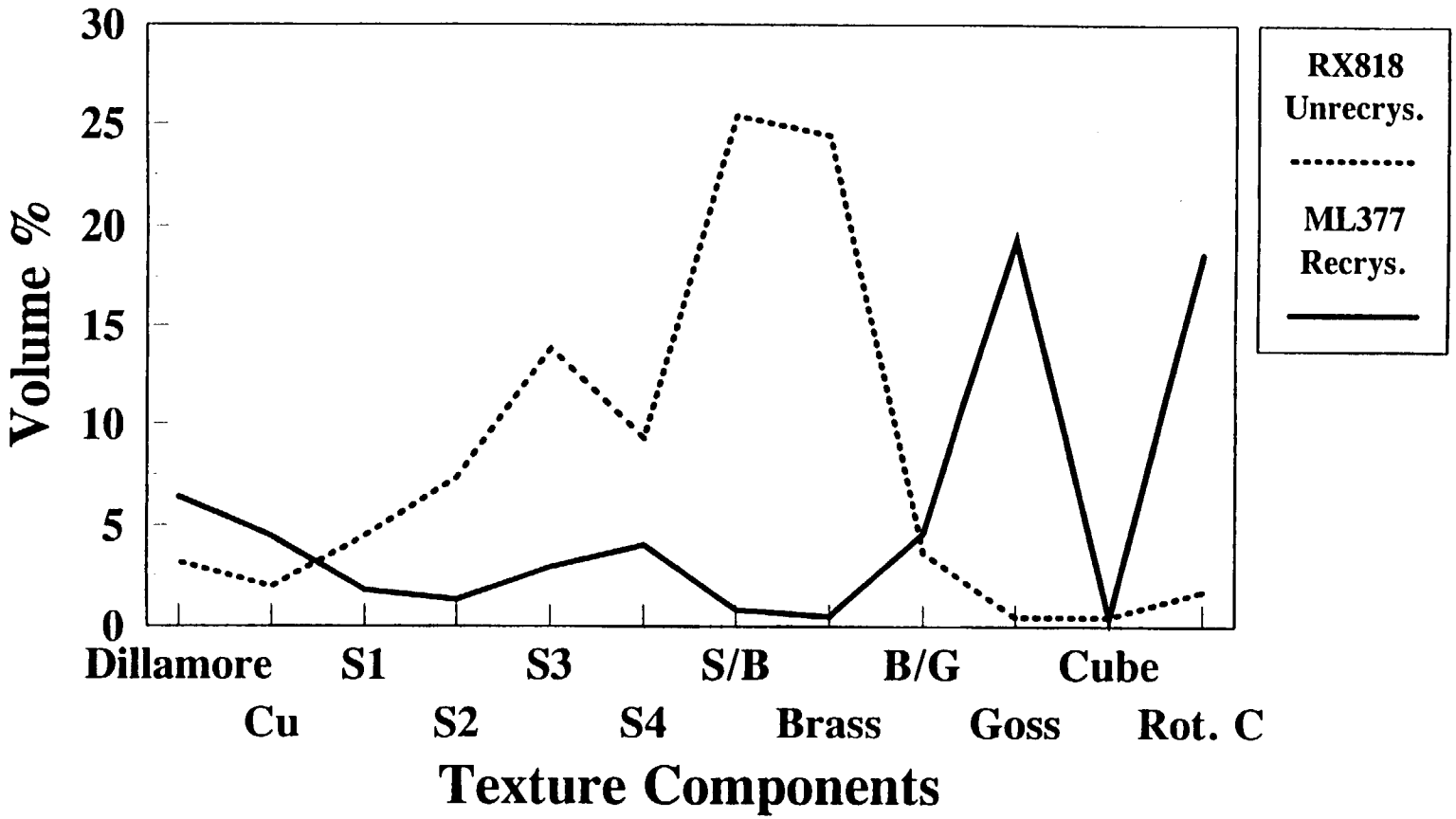

Figure 11 effect of recrystallization on the texture components.

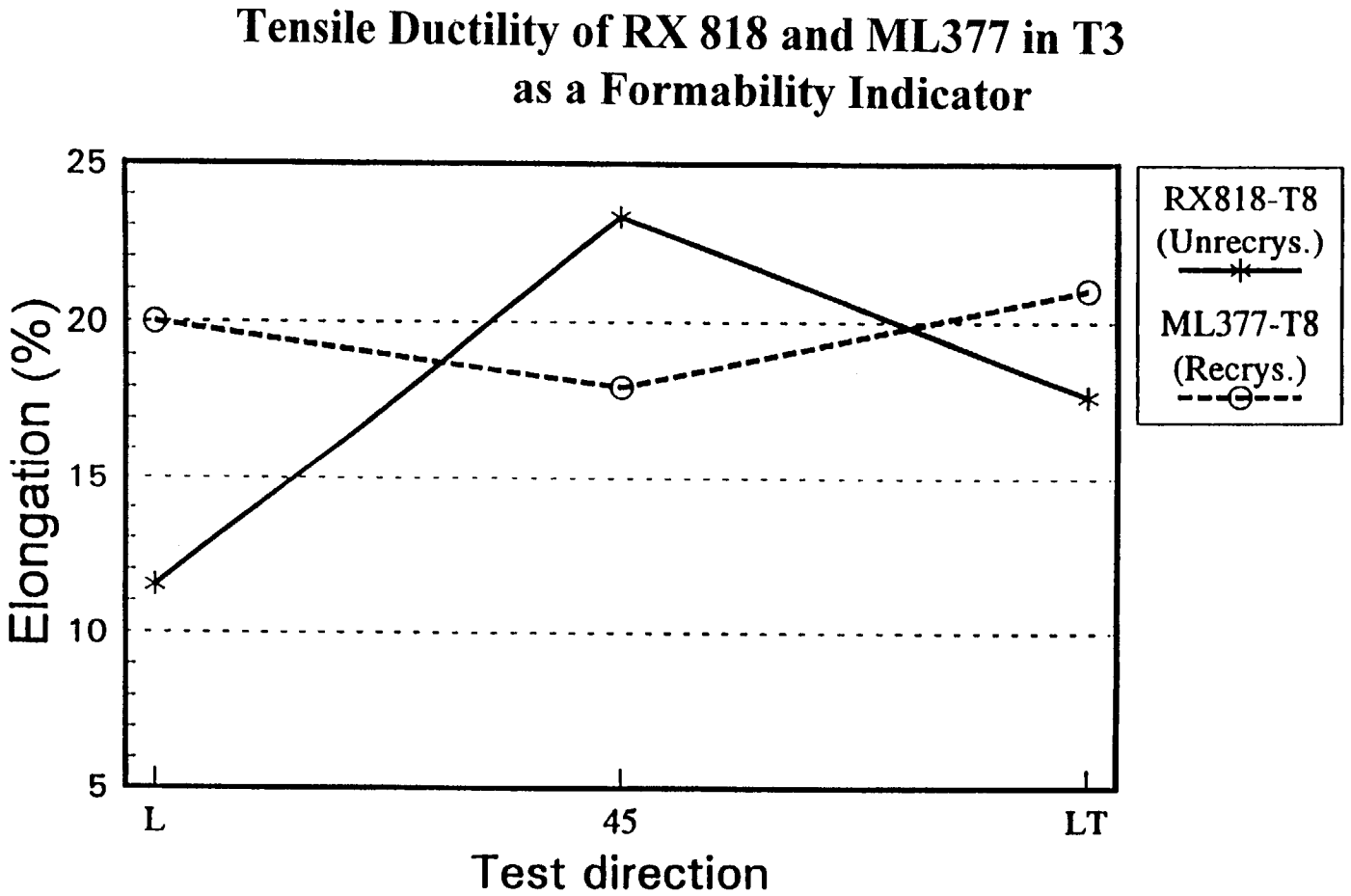

Figure 12 tensile ductility of two sheet alloys, 0.09" gauge (plant rolled & heat treated).

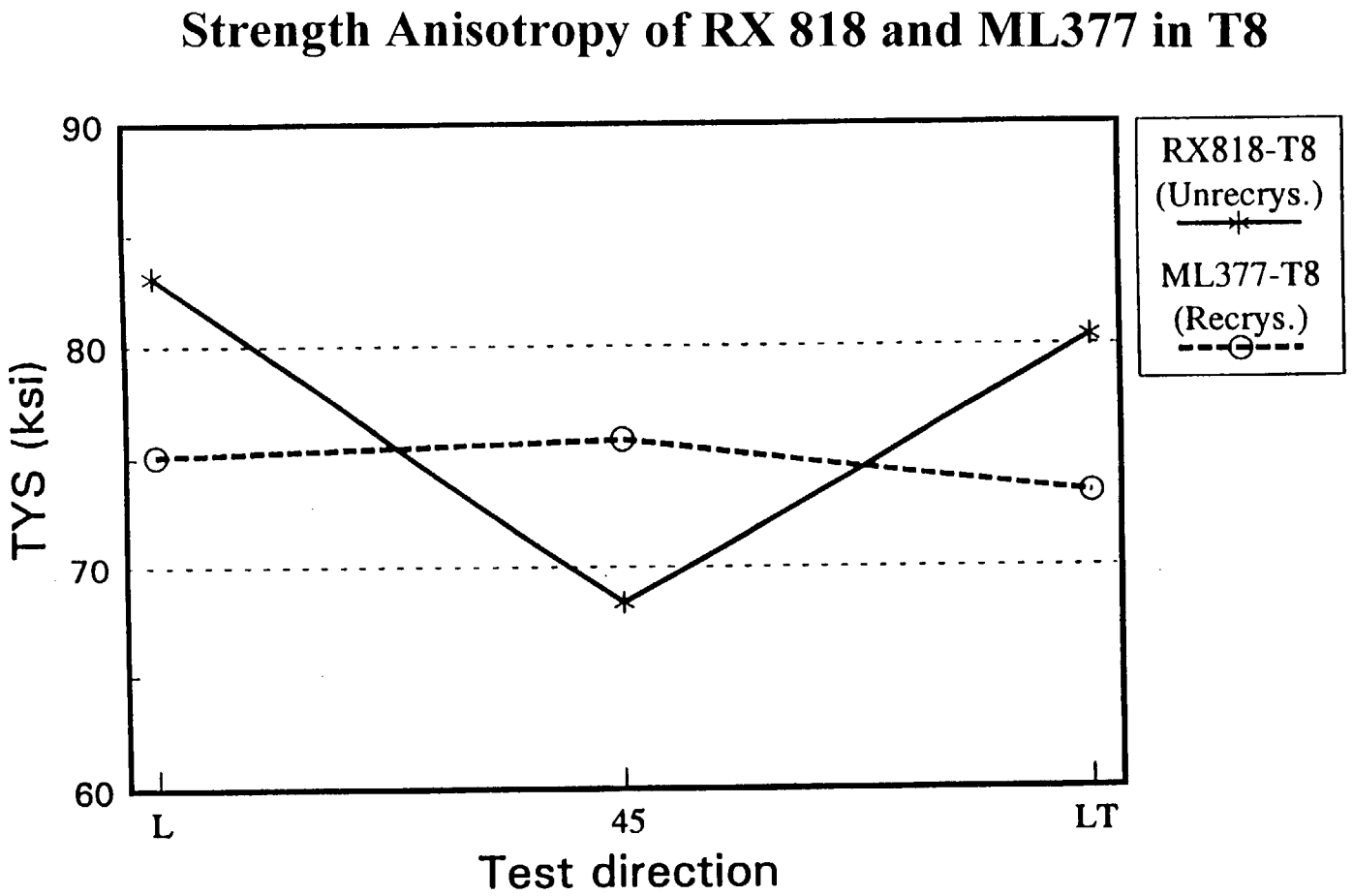

Figure 13 Strength Anisotropy of two sheet alloys, 0.09" gauge (plant rolled & Lab heat treated).

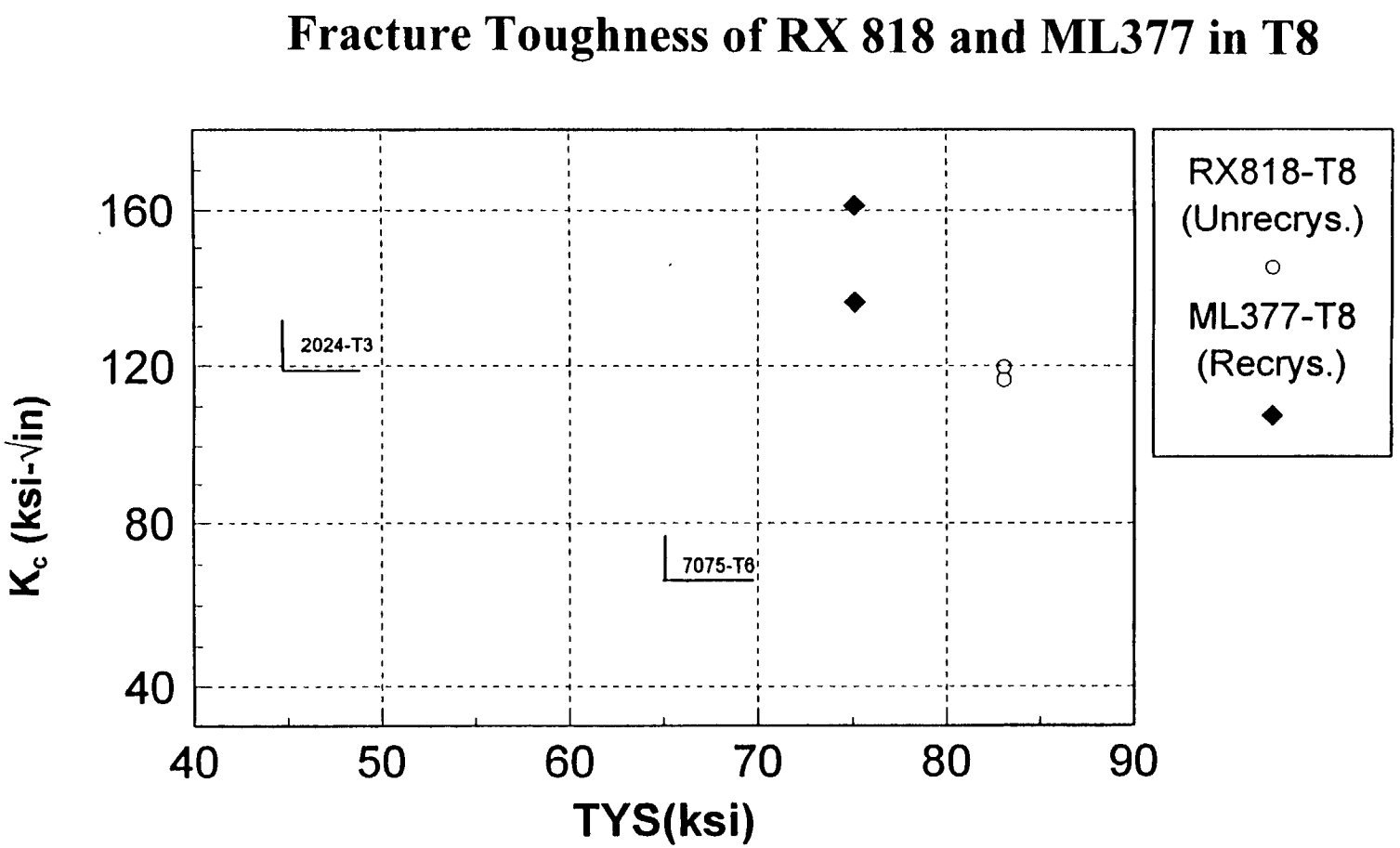

Figure 14 fracture toughness of two alloys, 0.09" gauge (center-notch precracked 16" wide specimen in L-T).

Subtask 2A5: Examine the the alloy variants with very high Cu:Li ratio on thermal stability and mechanical properties.

The alloys selected for this study (Variation #1 and Variation #2) are mainly strengthened by thermodynamically stable phases which form extremely fine distributions of plate-shaped precipitates (Tl phases) and also by theta' precipitates. Depending on the alloy compositions, different volume fractions of T1 (Al2CuLi) and theta' (Al2Cu) would precipitate according to the thermodynamic requirements. As a result, the overaging characteristics of the alloys would be determined by not only diffusion-controlled coarsening kinetics of the two strengthening phases and the solute partitioning between the two phases according to their solvus temperatures, but also by their relative grain structures. Two different Cu:Li ratios were selected for this study along with a standard RX818 alloy. Their compositions are as follows:

Composition (wt.%)

Alloy	Cu	Li	Mg	Ag	Zr	Cu:Li ratio
Variation #1	4.0	0.8	0.25	0.25	0.12	5.0
Variation #2	4.4	0.85	0.25	0.25	0.12	5.2
RX818	3.56	0.87	0.41	0.35	0.14	4.1

The material was cast as two 10,000 lb ingots. These ingots included Variation #1 and Variation #2. The ingots were homogenized, scalped and hot rolled to 0.090" gauge sheet. The sheet products were solution heat treated at 950°F for an hour followed by water quench and 3% stretch. The sheet products were then aged at 320°F for 20 hours as a standard age practice.

Figure 15 shows the strength-fracture toughness values of the two variant alloys and RX818 alloy before and after thermal exposures. After thermal exposure, there is no significant differences among the three alloys for post 275°F exposure only.

The evolution of strength and fracture toughness during thermal exposure

The evolution of strength and fracture toughness during thermal exposure at 275°F was studied with variation #1 alloy. The results are summarized in the TABLE 7. Figure 16 shows a sharp strength increase in the very beginning of the thermal exposure and decreases after 500 hours at 275° F. Figure 17 shows a sharp decrease in fracture toughness in the very beginning of the thermal exposure up to 200 hours at 275° F. The fracture toughness value after 1000 hours of

exposure is no lower than that at after 200 hours of exposure. This suggests that the severe loss of fracture toughness occurrs during the 200 hours at 275° F. The immediate next step would be to reproduce the result from the other sample alloys.

TABLE 7

The evolution of strength and fracture toughness during thermal exposure at 275°F for variation #1 alloy.

S.No.	Exposure at 275°F	UTS(ksi)	TYS(ksi)	El(%)	K_c(ksi-sqrt(inch))
70302-5	as T8	79.0	75.0	7.5	135.5
70302-5-1	T8+50h	80.7	76.6	8.3	117.9
70302-5-2	T8+100h	80.2	76.6	7.1	107.1
70302-5-3	T8+200h	80.0	77.5	6.3	99.8
70302-5-5	T8+500h	80.0	76.7	5.0	81.0
70302-5B	T8+1000h	80.1	75.7	7.3	102.0

NOTE:
Tensile test results are averaged values from duplicates
K_c values are from single test by 16" wide center notched, fatigue precracked panel specimens.

Effect of Cu:Li Ratio on Unrecrystallized Alloys

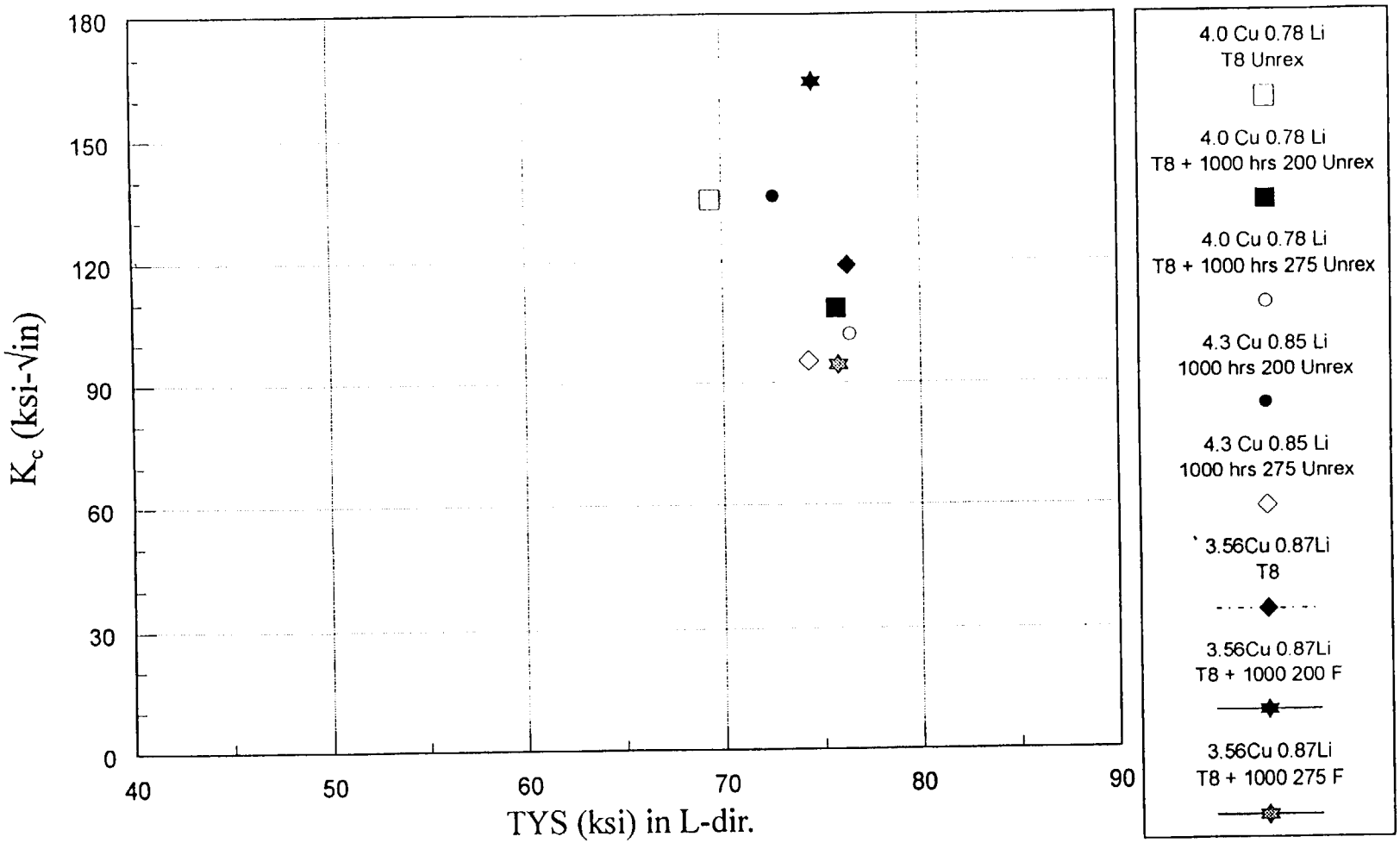

Figure 15 K_c (L-T) ~TYS (L) plot of three alloys: 4.0Cu-0.78Li-0.25Mg-0.25Ag-0.12Zr, 4.3Cu-0.85Li-0.25Mg-0.25Ag-0.12Zr, and RX818.

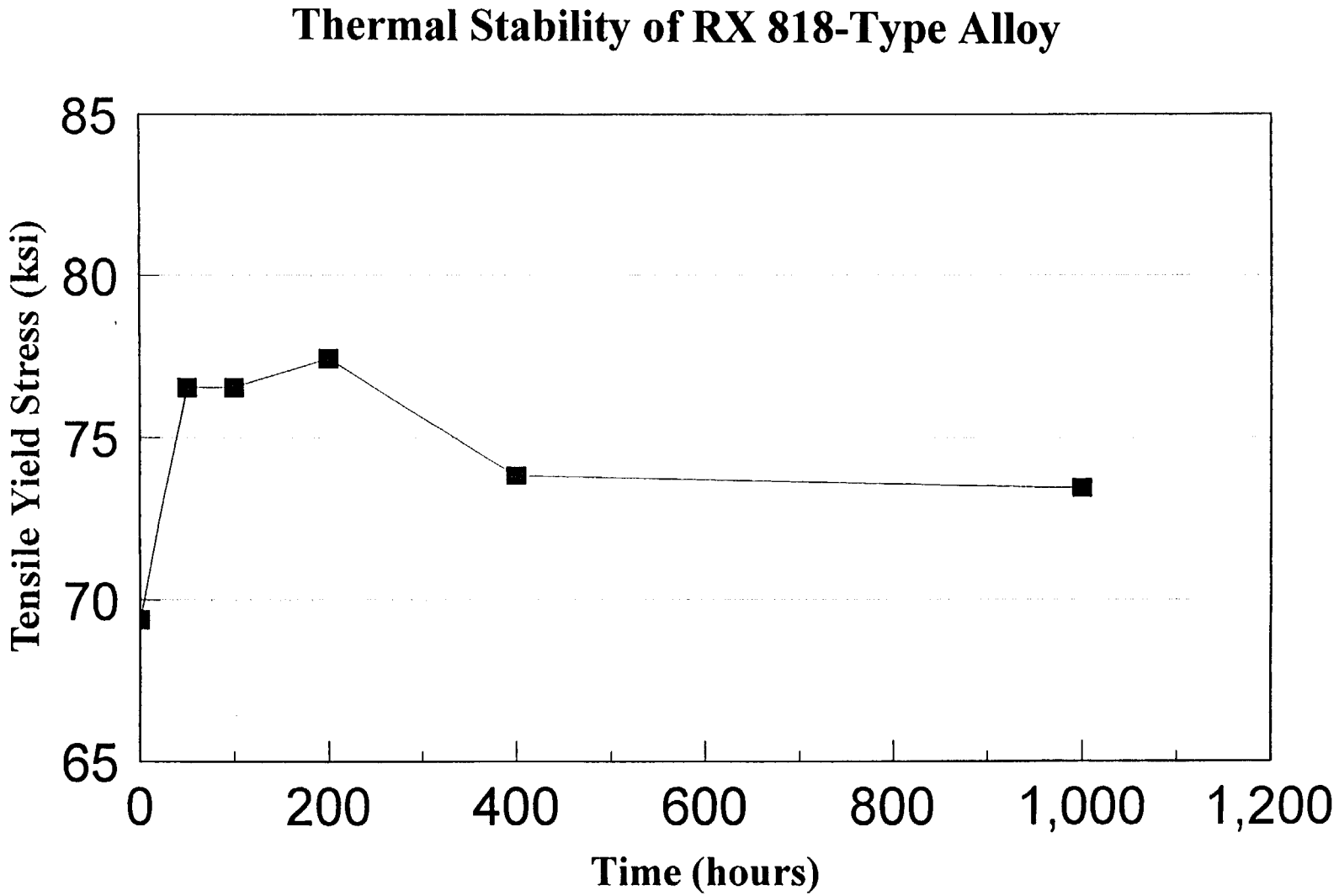

Figure 16 Tensile yield stress of alloy (4.0Cu-0.78Li-0.25Mg-0.25Ag-0.12Zr), 0.09″ gauge sheet, as a function of time at 275°F exposure .

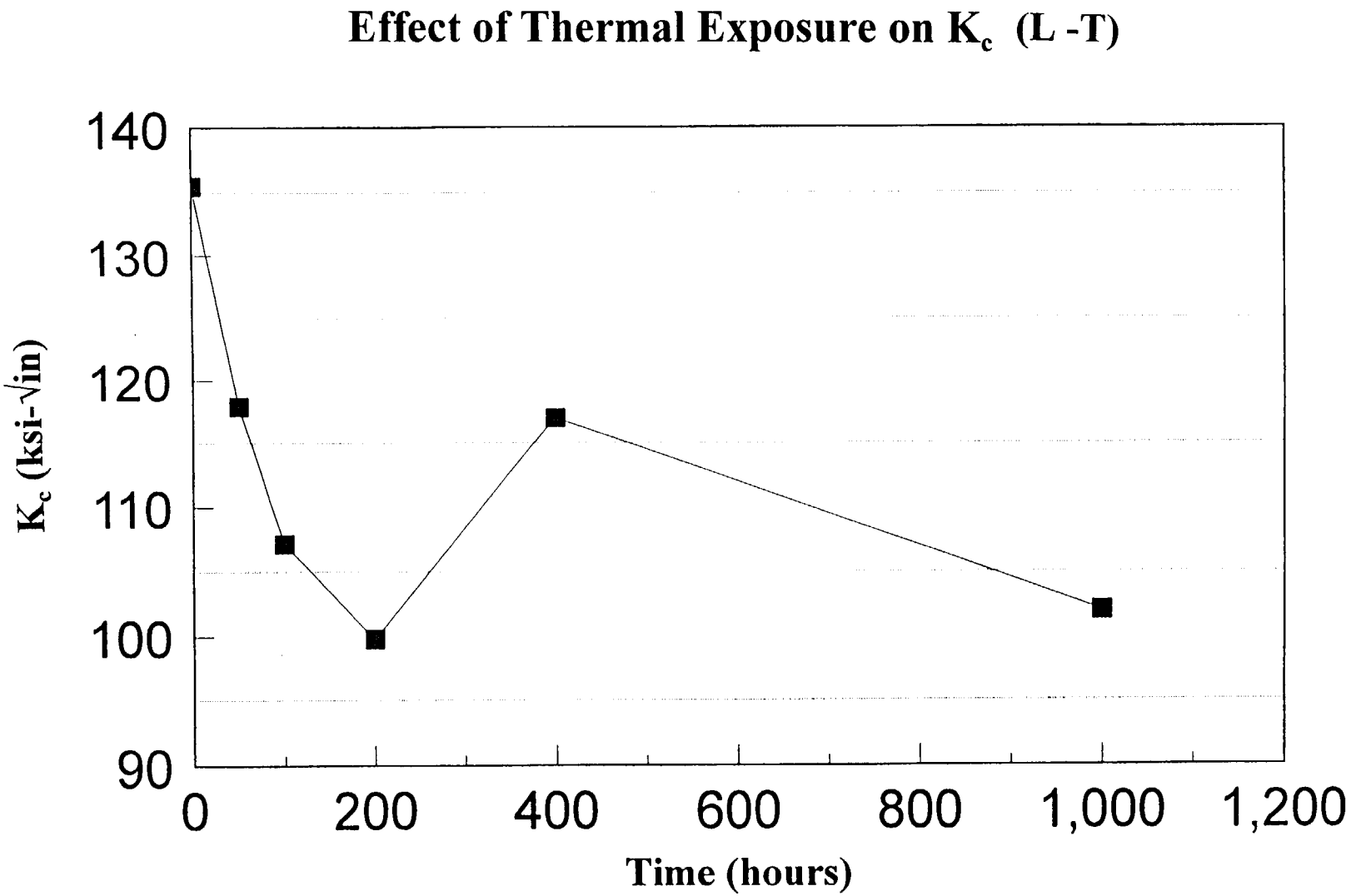

Figure 17 fracture toughness of alloy (4.0Cu-0.78Li-0.25Mg-0.25Ag-0.12Zr), 0.09″ gauge sheet, as a function of time at 275°F exposure .

Subtask 2A6: Examine the grain boundary segregation of alkali metal elements during thermal exposure as a possible cause for the loss of fracture toughness

Alkali metal elements such as Na and K are present in aluminum alloys as trace elements. It has been suggested by some researchers that these allkali metal impurties could diffuse through grain boundaries even at the very moderate temperatures and form eutectic phases. Such grain boundary particles would lower the surface energy and promote intergranular embrittlment. An experiment was conducted with ML377 alloy sheet to examine the grain boundary segregation of alkalai metal elements during thermal exposure as a possible cause for the loss of fracture tougness.

A sample of ML377 alloy sheet in T8 temper was exposed at 275°F for 500 hours. After the exposure, the sample was pre-pumped and fractured at a vacuum level in the low 10-8 torr range. Figure 18 shows the area where four particles, identified as A,B,C and D in the SEM micrograph, and the matrix, identified as M, were analyzed. The spectra indicate varied levels of oxygen for the particles, and may be related to reaction with air during the time between fracture and collection of the spectra. This can be attributed to the time elapsed at least 1 hour from fracture time and data collection for the spectra. Particle "A" , partcle "B" and partcle "C" appeared to be Al-Cu-Fe-Li partcles (Figure 19, Figure 20 and Figure 21) and particle "D" appeared to be Al oxide(Figure 22). Figure 23 shows the spectra of matrix detecting Al, Cu and Li. Na, K, P or Cl were not detected even though this technique has very good dectectability of those elements. Therefore, it was concluded that the grain boundary segregation of alkalai metal elements during thermal exposure is not a cause for the loss of fracture tougness after the thermal exposure for these alloys.

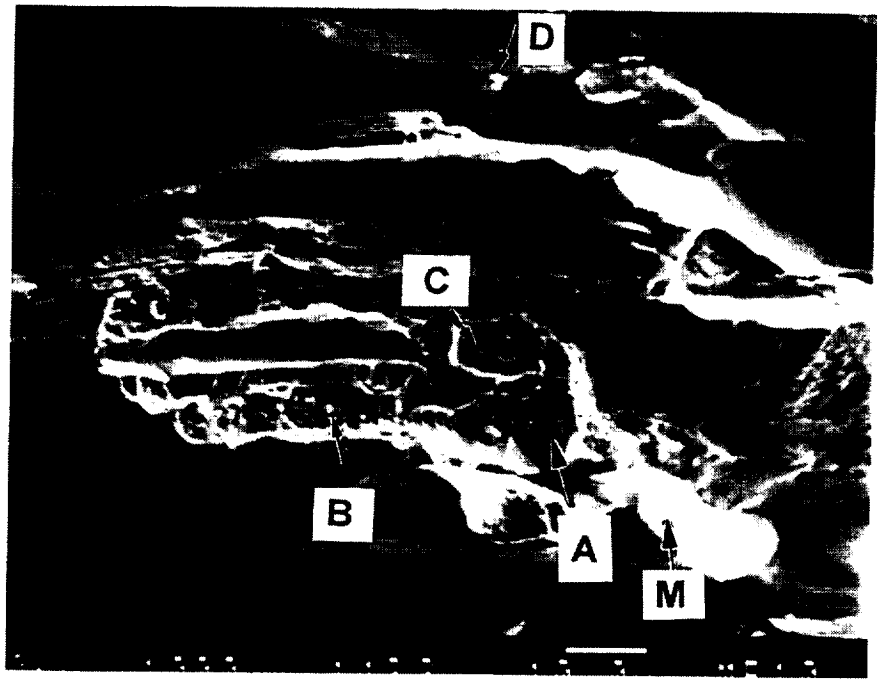

Figure 18 SEM micrograph (x1000) showing the area where four particles, identified as A,B,C and D, and the matrix, identified as M, were analyzed by Auger Spectroscopy.

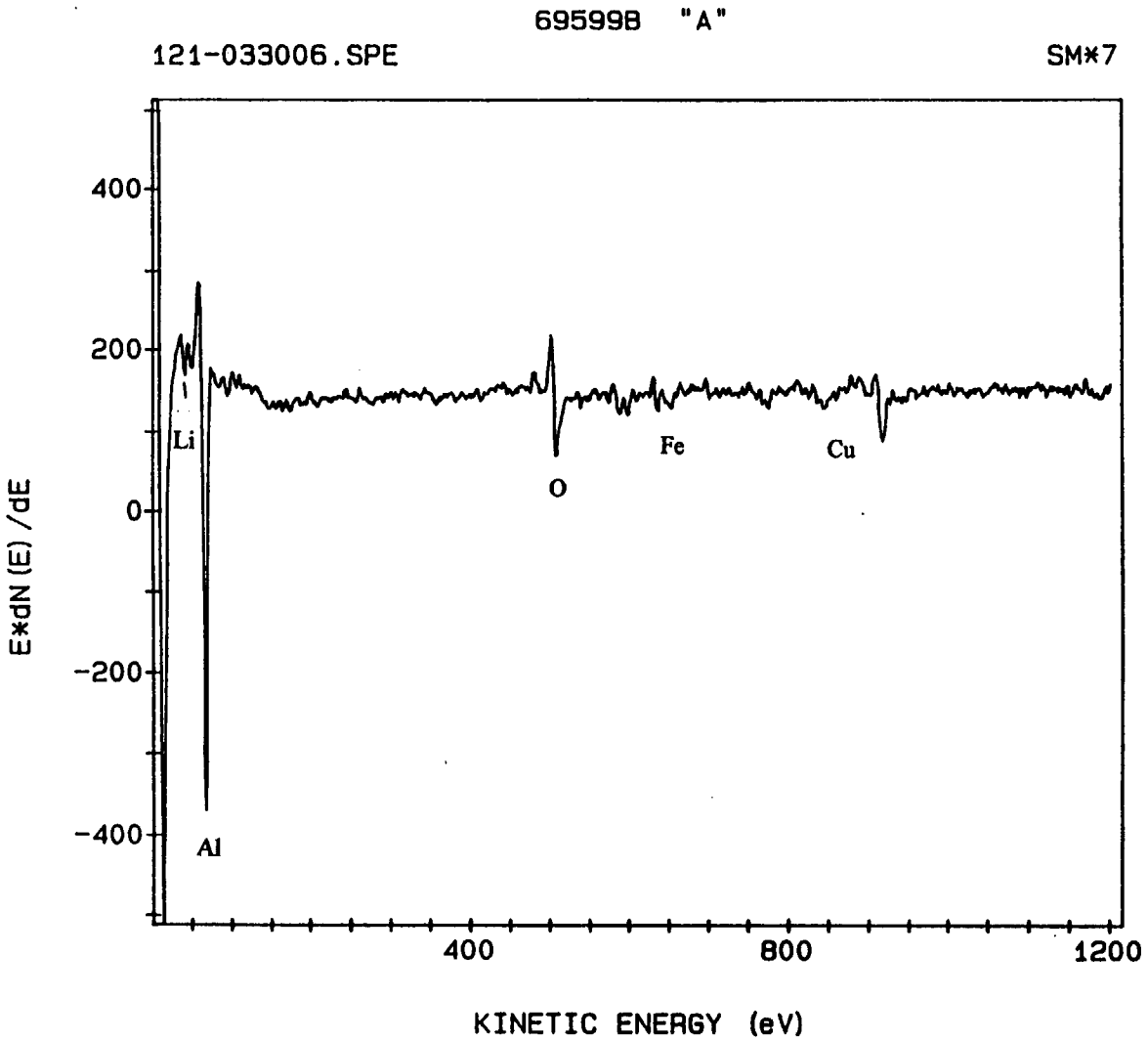

Figure 19 Auger spectrum of particle "A" on the in-situ fractured surface of ML377-T8 sheet after an exposure at 275°F for 500 hours. No Alkali elements were detected.

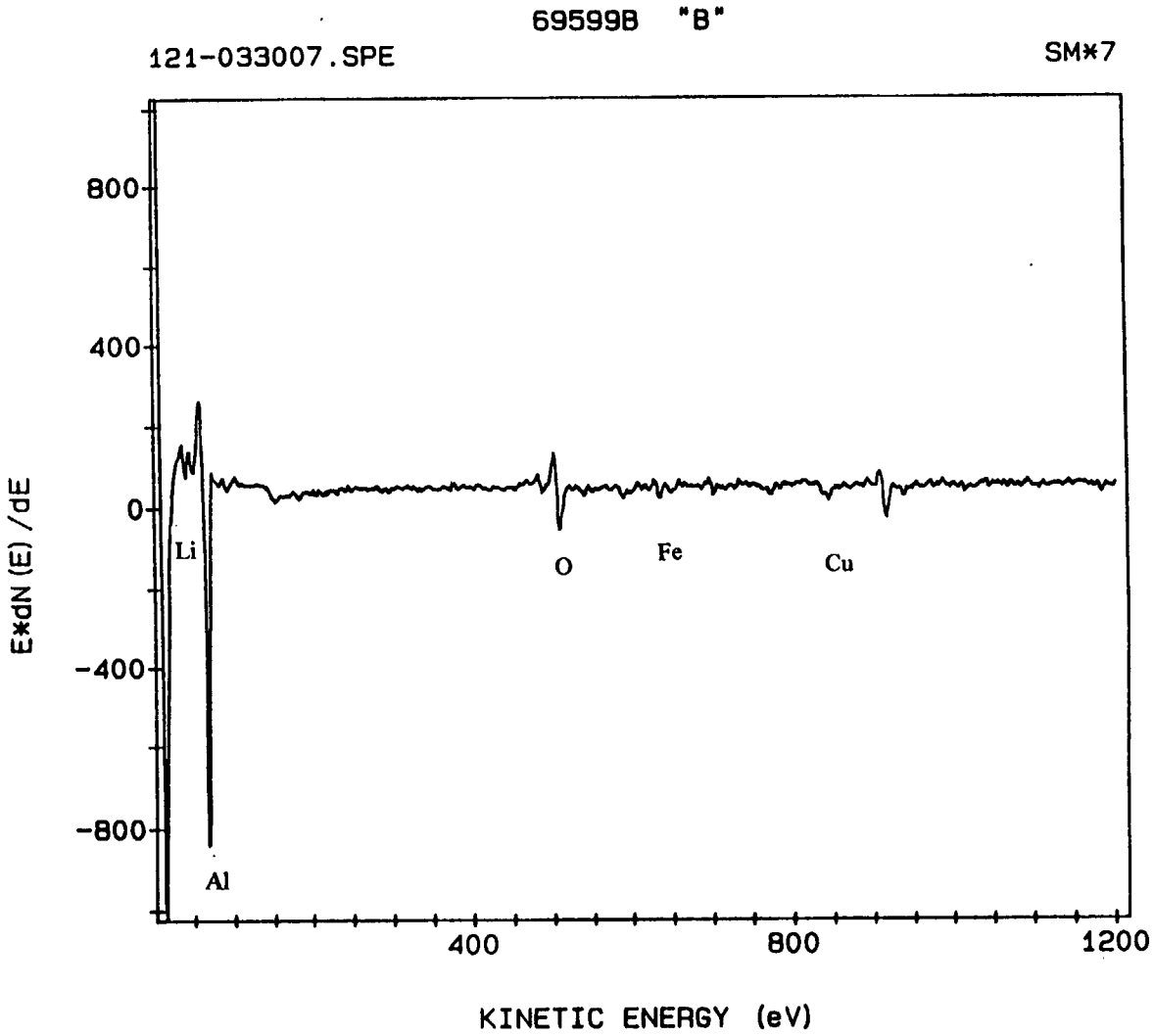

Figure 20 Auger spectrum of particle "B" on the in-situ fractured surface of ML377-T8 sheet after an exposure at 275 °F for 500 hours. No Alkali elements were detected.

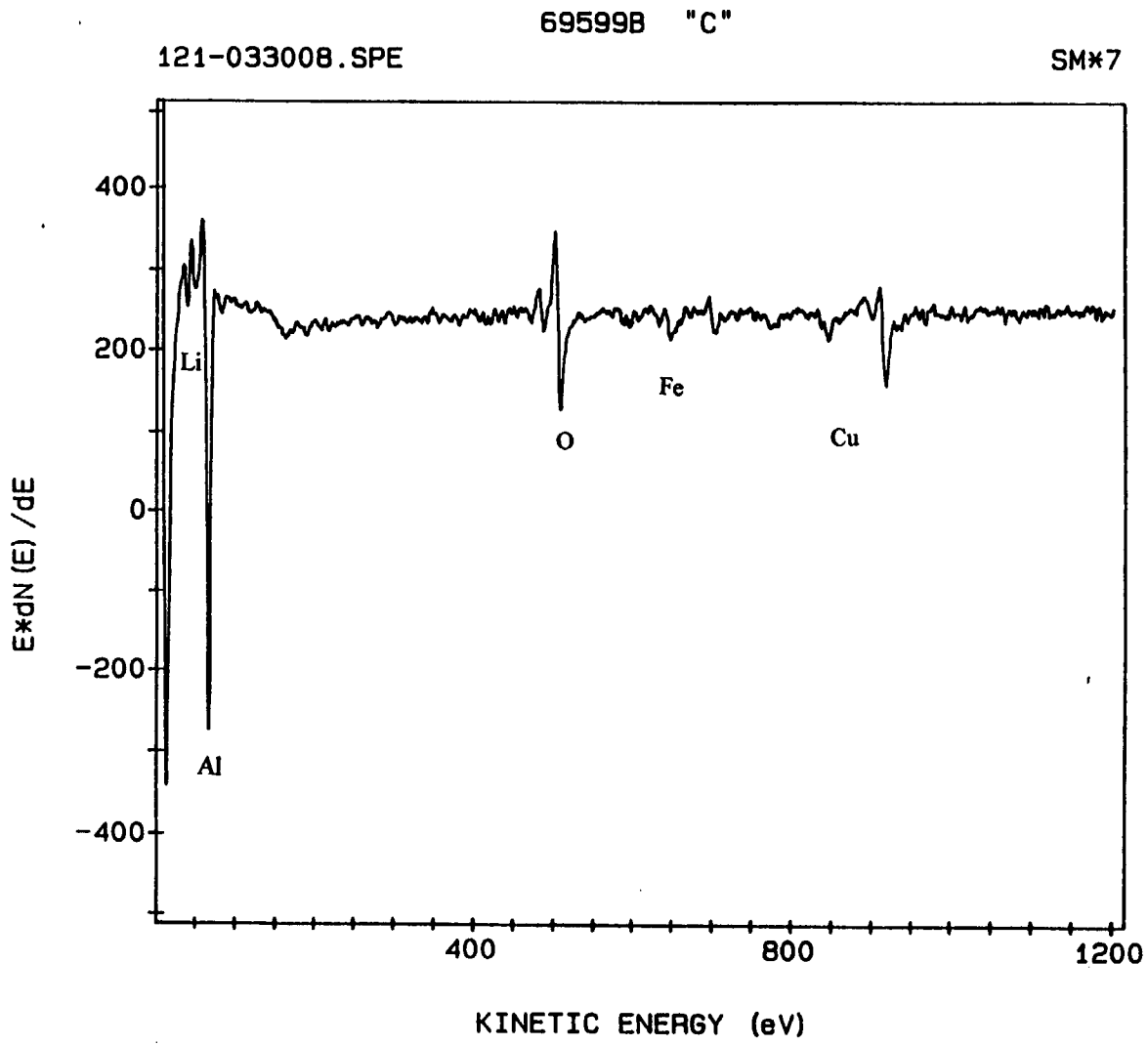

Figure 21 Auger spectrum of particle "C" on the in-situ fractured surface of ML377-T8 sheet after an exposure at 275 °F for 500 hours. No Alkali elements were detected.

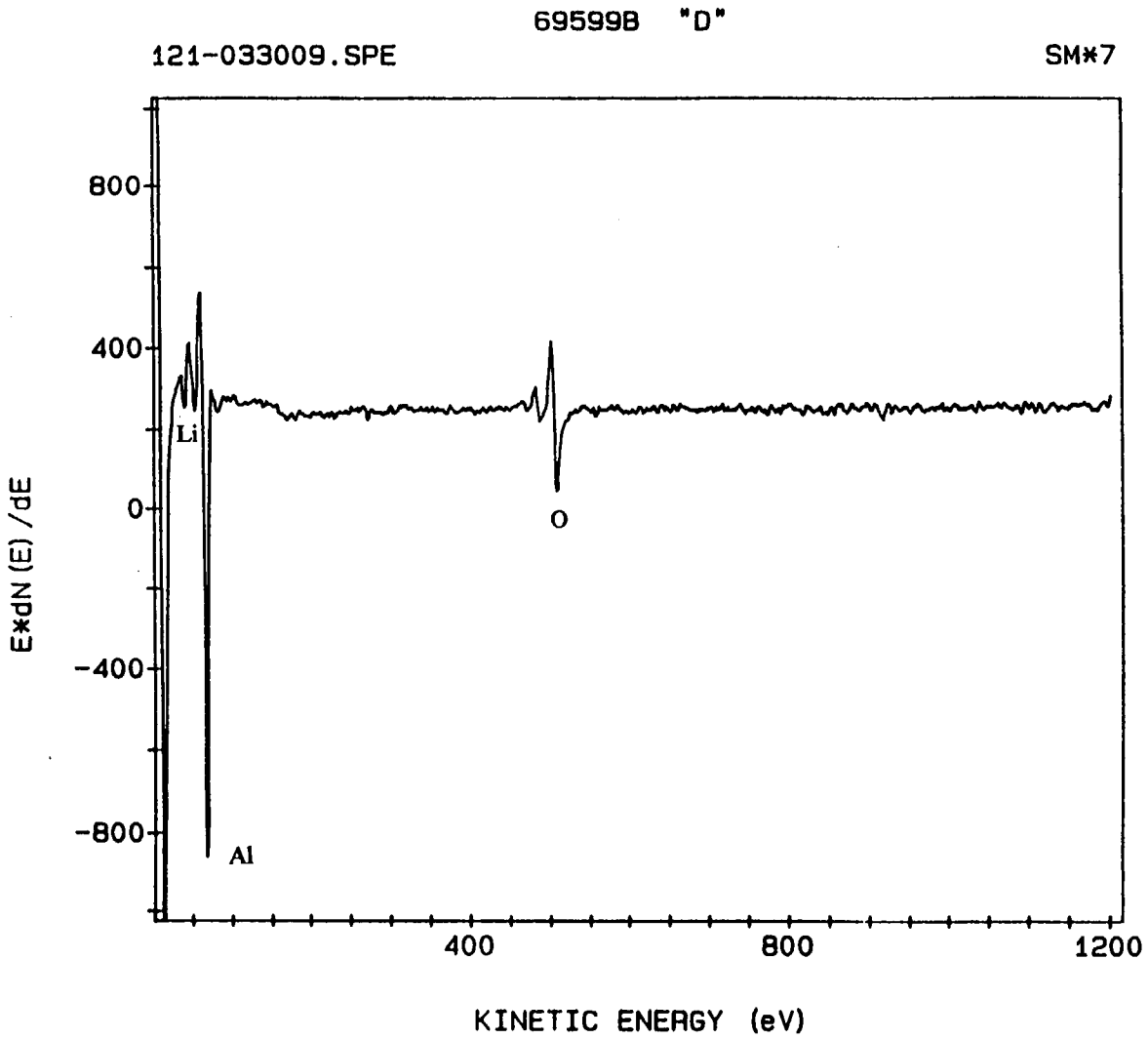

Figure 22 Auger spectrum of particle "D" on the in-situ fractured surface of ML377-T8 sheet after an exposure at 275°F for 500 hours. No Alkali elements were detected.

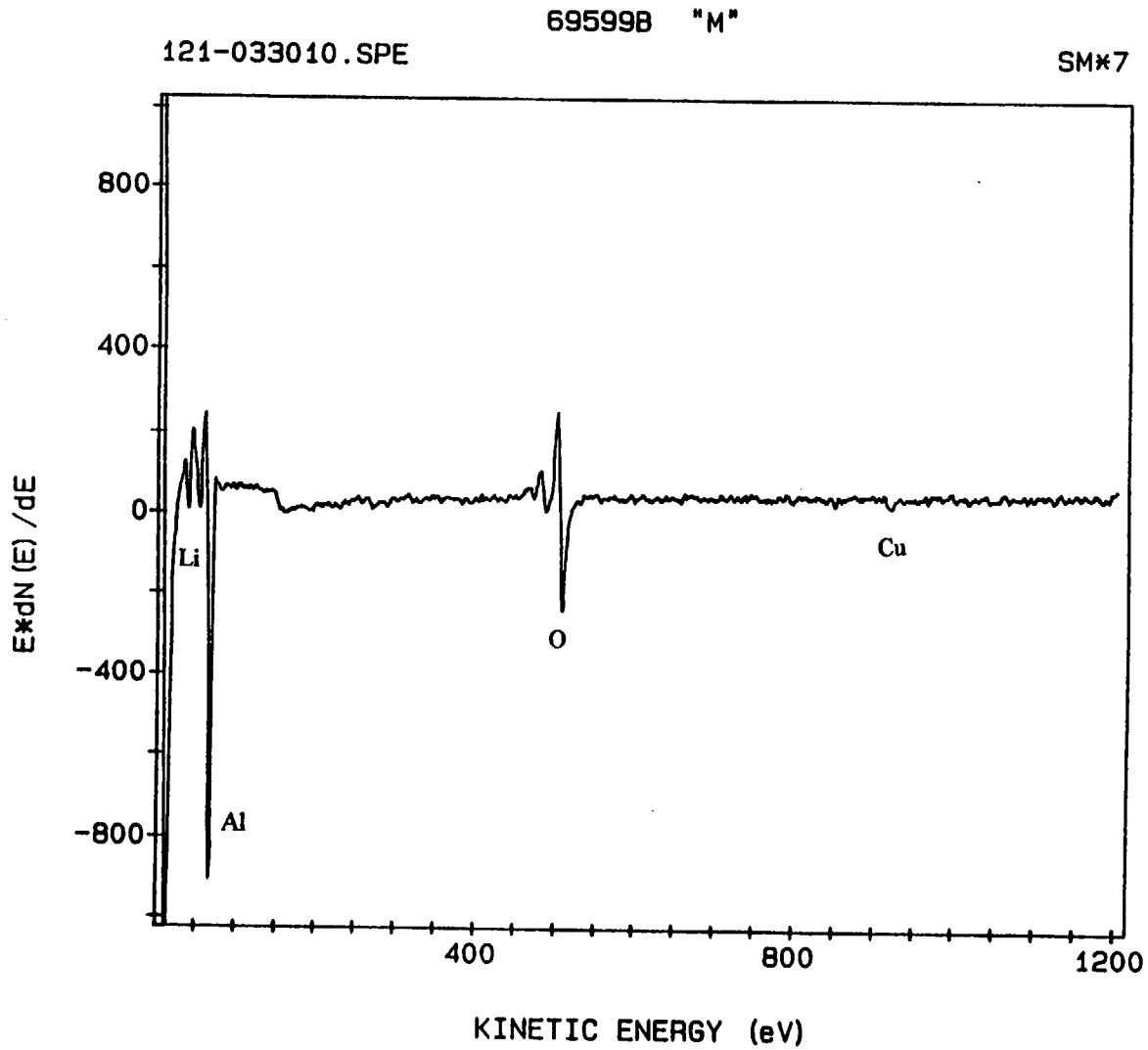

Figure 23 Auger spectrum of matrix on the in-situ fractured surface of ML377-T8 sheet after an exposure at 275 °F for 500 hours. No alkali elements were detected.

UNIVERSITY OF VIRGINIA

Elevated Temperature Fracture Toughness Of Advanced RS/PM And I/M Aluminum Alloys

Principal Investigator: R.P Gangloff

Abstract

Since January of 1992, research on deformation and fracture has been conducted at the University of Virginia to support aluminum alloy and process development for the High Speed Civil Transport Airframe. During 1992 and 1993, this work focused on rapidly-solidified (RS) powder metallurgy (PM) AA8009 and was conducted in conjunction with staff at Allied Signal. In 1994 and 1995, the emphasis changed to an investigation of the behavior of advanced ingot metallurgy (IM) AA2519 with silver and magnesium additions, as produced by Alcoa.

This work has aimed to: (a) develop a method to characterize the fracture toughness of plate and thin-sheet aluminum alloys, (b) establish the effects of test temperature and loading rate on fracture toughness, (c) establish the effects of alloy composition and thermomechanical processing on fracture toughness, (d) understand fundamental mechanisms of deformation and fracture, (e) improve models of fracture toughness, and (f) apply micromechanical modeling to predict the temperature dependence of fracture toughness from tensile properties. This research was carried out in five tasks; important findings are summarized.

A. Task I---High Resolution K-Δa Measurement of Fracture Toughness

The objective of Task I was to develop a laboratory method to characterize plane strain crack initiation and plane stress crack growth fracture toughnesses from a single small fracture mechanics specimen of thin sheet aluminum alloy. The direct current electrical potential difference method provided high resolution detection of the onset and subsequent stable growth of a fatigue precrack. The J-integral provided a rigorous measure of the crack tip driving force for fracture. The resulting K-Δa R-curve yielded K_{JICi}, K_{JIC}, and a measure of tearing resistance; these results compared reasonably to fracture toughnesses from thick specimens and from R-curves determined for large middle tension specimens from thin sheet. The small specimen method is an effective tool for studies pertaining to alloy development, environmental effects, and fracture mechanisms.

B. Task II---Elevated Temperature Deformation and Fracture of RS/PM AA8009

The objective of Task II was to employ modified melt-spinning and thermomechanical processing methods to solve two problems that limit some applications of RS/PM AA8009: (1) anisotropic fracture toughness, and (2) reduced fracture toughness at elevated temperatures or slow

loading rates. Extensive fracture toughness measurements demonstrated unequivocally the deleterious effect of increasing test temperature for several product forms of AA8009. Two modifications to the melt spinning process, designed to reduce oxides from particle surfaces, were ineffective in improving the fracture toughness of AA8009. The toughness for each modification of AA8009 decreased with increasing temperature, analogous to conventionally melt spun alloy. Processing to reduce the total dissolved hydrogen content of the alloy did not ameliorate the loss of damage tolerance in AA8009 at elevated temperature. Changes in thermomechanical processing (rolling reduction, temperature and direction) were ineffective in reducing the toughness degradation with increasing temperature. Thermomechanical processing adversely affected fracture toughness due to reduced oxide sheet spacing, and dynamic recovery and reduced work hardening. Thermomechanical processing eliminated anisotropy in toughess for AA8009. Plate and sheet exhibited isotropic (in-plane) fracture toughness in contrast to the extruded alloy.

C. Task III---Deformation and Fracture Mechanisms in Sub-micron Grain Size Aluminum Alloys

The objective of Task III was to determine the mechanism for the deleterious effects of increasing elevated temperature and decreasing loading rate on the fracture toughness of RS/PM alloys such as AA8009. This study employed a model aluminum alloy, cryogenically milled high purity aluminum, to establish that dynamic strain aging is not the sole cause of reduced fracture toughness at elevated temperature. Rather, an alternate mechanism was suggested that is generic to submicron grain-size alloys. In this new view, toughness is reduced at increased temperature (and reduced loading rate) because such conditions reduce work and strain-rate hardening between growing primary microvoids, leading to intravoid instability and coalescence at lowered strain. Decreased strain-rate hardening is attributed to increased mobile dislocation density due to dislocation emission and detrapping from dispersoids in dynamically recovered dislocation source-free grains.

D. Task IV---Elevated Temperature Fracture Toughness of AA2519 with Mg and Ag Additions

The objective of Task IV was to characterize the effects of Mg plus Ag additions and elevated temperature on the fracture toughness of an advanced I/M aluminum alloy, and to define the governing mechanisms of deformation and fracture. The fracture toughnesses of several alloys in this class are competitive with conventional 2000-series aluminum alloys. That fracture toughness is essentially constant with increasing temperature from 25°C to 175°C is explained by a micromechanical model. This behavior is governed by the fact that the intrinsic fracture resistance of this, and other I/M aluminum alloys, increases substantially with increasing temperature. This

behavior is traced to decreased intravoid strain localization, and decreased void-sheeting instability, with increasing temperature. Localization is governed by time-temperature-dependent microvoiding at dispersoids between growing primary microvoids. Such microvoiding declines with increasing temperature as dislocations are increasingly able to bypass dispersoids. Additionally, increased strain rate hardening with increasing temperature suppresses intravoid strain localization and coalescence.

E. Task V---Micromechanical Modeling of the Temperature Dependence of Fracture Toughness

The objective of Task V was to determine if a modern micromechanical model of ductile fracture can predict the effect of temperature on the fracture toughness of aluminum alloys. This study employed extensive data on the temperature dependence of fracture toughness for a large number of aluminum alloys in order to: (1) test the accuracy of micromechanical models, and (2) understand the continuum-mechanics factors that govern elevated temperature fracture toughness. A critical plastic strain controlled model successfully predicted initiation fracture toughness, confirming the micromechanical modeling approach. For each of eight alloys, the temperature dependence of fracture toughness was controlled by the temperature dependent interplay between alloy strength, elastic modulus, and intrinsic fracture resistance. The former two material properties determine the extent of crack tip plastic strain and hydrostatic stress, for a given applied stress intensity level. The latter material property determines the resistance of an alloy microstructure to the nucleation, growth and coalescence of microvoid damage. A correlation suggests a means to predict the temperature dependency and absolute value of fracture toughness, based only on measured tensile properties and microstructural features.

II. TASK I---HIGH RESOLUTION K-Δa MEASUREMENT OF FRACTURE TOUGHNESS

M.J. Haynes and R.P. Gangloff

Abstract

The plane strain initiation fracture toughness and plane stress stable crack growth resistance were determined with a single small compact tension (CT) specimen for each of three precipitation hardened aluminum alloy sheets (AA2024-T3, AA2519-T87 (+Mg+Ag), and AA2650-T6). Crack length was monitored precisely with direct current potential difference (DCPD) measurements, and specimen plasticity was accounted for with the J-integral. The DCPD technique resolves a small amount of crack-tip process-zone damage (≈ 20 μm) that constitutes crack initiation under plane strain constraint. Two measures of initiation toughness are calculated; the elastic-plastic fracture toughness detected by DCPD (J_{ICi}, K_{JICi}) and the toughness based on ASTM standard E 813 (J_{IC}, K_{JIC}). High resolution of fracture initiation is necessary to obtain a lower bound initiation toughness, K_{JICi}, because plane strain constraint is present ahead of the fatigue precrack, but is rapidly lost with crack extension in thin sheet. K_{JIC} overestimates toughness due to constraint loss coupled with the offset blunting line definition of fracture initiation. The J-integral/DCPD method provides a reproducible measure of the plane stress linear-elastic resistance curve (K_J-Δa) that compares reasonably to R-curves determined for large middle tension specimens. The small specimen method is effective for studies pertaining to alloy development, environmental effects, and fracture mechanisms.

Introduction

Accurate characterization of the fracture toughness of thin-sheet aluminum alloys is important to flaw-damage tolerant design of aerospace components such as airframes. For the next generation High Speed Civil Transport, the toughness of candidate aluminum alloy sheet is being evaluated by linear-elastic resistance curves determined from wide-panel, middle tension (MT) specimens, often according to the ASTM Standard Practice of R-Curve Determination (Designation E 561-92a). Use of the wide-panel MT specimen in alloy development is limited by the requirement for a large quantity of material and a high capacity load-frame. Application of the MT geometry is further complicated by complex experimental conditions including elevated temperature, thermal preexposure or aqueous environmental corrosion. Additionally, this test method does not define initiation fracture toughness.

Elastic-plastic fracture mechanics (EPFM) can characterize plane-strain initiation toughness and plane-strain or plane stress stable crack growth resistances for a single specimen which is small and not described accurately by linear-elastic fracture mechanics [1-3]. J-integral based

initiation toughness (J_{IC}) and resistance curve (J-Δa) measurements account for uncracked ligament plasticity and can be converted to the equivalent linear-elastic initiation toughness (K_{IC}) and the resistance curve (K_J-Δa) [3,4]. The ASTM Standard Test Method for J_{IC}, a Measure of Fracture Toughness (Designation E 813-89) and the ASTM Standard Test Method for Determining J-R Curves (Designation E 1152-92) encompass accepted methods for toughness characterization. Presently, these two standards are being consolidated [5].

Stress state effects on initiation and growth toughnesses must be considered carefully. J-integral resistance curves for ductile alloys are increasingly steep as specimen thickness declines, as represented schematically in Figure 1 [6,7]. Such sharp rises in the J-Δa curve are due to a loss in plane strain constraint as the crack extends, which results in increased alloy resistance to crack-tip process-zone fracture. Substantial crack growth in thin sheet occurs under plane stress deformation. Qualification of J_Q as a plane strain initiation toughness (J_{IC}), independent of specimen thickness, is based on the use of an offset blunting line and specimen size specified in ASTM standard E 813. Specifically, J_Q at the intersection of the 0.2 mm offset blunting line and the power law fit to the R- curve qualifies as J_{IC} if both the thickness and uncracked ligament exceed 25 J_Q/σ_{FL}. (σ_{FL} is the average of the yield and ultimate tensile strengths.) The E 813 standard is based on extensive experimentation with relatively thick (25 to 75 mm) specimens of ductile steels [8-10]. Its applicability to thin-sheet aluminum alloys, where constraint loss may influence J_{IC}, has not been investigated.

Based on Figure 1, it should be possible to determine plane strain initiation toughness by detecting the initial small amount of cracking at the mid-thickness point ahead of a fatigue precrack. As the resolution of measured crack extension increases, initiation toughness measurements will depend less on specimen thickness. Accurate and continuous high resolution measurement of crack extension during rising load is therefore a critical component of successful J-Δa toughness measurement. Direct current potential difference (DCPD) monitoring is well-suited for this purpose.

The objective of this study is to establish a small specimen-based method to characterize fracture toughness for aluminum alloy development. The aim is to develop data that are quantitative for alloy ranking and relevant to structural analysis. This paper evaluates the applicability and accuracy of EPFM and DCPD crack-length monitoring methods to determine plane strain initiation toughness and plane stress growth resistance with small compact tension (CT) specimens of thin sheet aluminum alloys. Three precipitation hardened alloys are studied (AA2024-T3, AA2650-T6, and AA2519-T87 (+Mg+Ag)). Fracture initiation is detected by DCPD, and experimentally verified through microstructural observations of process-zone damage.

Offset blunting line and high resolution DCPD measures of initiation toughness are compared based on observed crack-tip constraint and the ASTM E 813 thickness criterion. Resistance curves for AA2024-T3 are compared to the results of several laboratories using CT and MT geometries from the same material lot.

Procedure

Materials

The ambient and elevated temperature tensile properties of the ingot metallurgy aluminum alloys (AA) investigated are listed in Table 1. Boeing provided 3.2 mm thick sheet of AA2024-T3 (Al-4.4Cu-1.5Mg-0.6Mn by wt%), and the Aluminum Company of America provided 3.2 mm thick sheet of AA2519-T87 (+Mg+Ag) (Al-5.8Cu-0.5Mg-0.3Mn-0.5Ag-0.2Zr-0.1V by wt%), a variant of AA2519 with Mg and Ag additions. Pechiney Aluminum supplied 6.0 mm thick rolled plate of AA2650-T6 (Al-2.7Cu-1.6Mg-0.3Mn-0.2Fe-0.2Ni-0.2Si-0.1Ti by wt%), a low Fe and Ni variant of AA2618.

Fracture Toughness Experiments

Fracture toughness experiments were performed over a range of temperatures and loading rates. AA2024-T3 was tested at ambient temperature and a relatively rapid load-line displacement rate ($d\delta/dt$=15 μm/sec). AA2650-T6 and AA2519-T87 (+Mg+Ag) were tested at a slower load-line displacement rate (0.26 μm/sec) and at temperatures ranging from 25°C to 175°C. The rapid loading rate corresponds to crack initiation in 40 seconds, while the slower loading rate corresponds to initiation in roughly 45 minutes. Sample identifications and test temperatures are listed in Table 2.

Fracture toughness was characterized with J-integral based crack growth resistance (J-Δa) curves, utilizing fatigue precracked CT specimens tested under monotonically increasing load. Specimens were machined in the LT orientation, with a width (W) of 76.2 mm and a thickness (B) of 3.2 mm. An anti-buckling fixture with teflon sheet lubrication was placed around the CT specimen. Stainless steel spacers prevented lateral motion of the CT specimen at the loading-pin holes. For AA2650-T6, a sidegrooved CT specimen (6.0 mm gross thickness and a 4.8 mm net thickness) was tested to investigate the influence of constraint on aluminum alloy R-curve behavior. All specimens were precracked at a constant stress ratio ($R=K_{min}/K_{max}$) of 0.1 and under decreasing stress intensity (K) conditions to a K_{max} of 8.5 MPa$\sqrt{m}$ at the final crack length (Table 2).

Rising load fracture toughness experiments were performed on a closed-loop servoelectric testing system operated under constant grip-displacement rate control. A circulating air oven was mounted on the load frame, as shown in Figure 2, and temperature was regulated to ±1 °C with a

thermocouple attached to the CT specimen. The specimen was heated to temperature in 30 minutes and stabilized for 30 minutes prior to loading. A PC-based acquisition system continuously recorded applied load, electrical potential difference across the notch, notch mouth opening displacement, and time (Figure 2). A linear variable differential transformer (LVDT) measured notch mouth opening displacement for conversion to load-line displacement using a geometric relationship [11].

Crack Initiation and Growth Measurements

Crack initiation and growth in a precracked CT specimen were monitored continuously by the DCPD method [12]. A constant current of 7 to 10 A, stable to one part in 5000, was applied with a DC power supply and the electrical potential difference (V) was conditioned with a 10^4 gain amplifier. A 12 bit analog to digital (A/D) converter, with a full scale capability of 10 volts, averaged 144 readings per second of sampling time. For tests run at the slow displacement rate, 2880 readings were obtained per data point, while at the fast rate 144 readings were obtained. The large number of readings minimized random noise and reduced the error associated with the bit resolution of the A/D converter (0.24 μV/bit) [12]. In this study, a voltage resolution of 0.1 μV was reported. For experiments at the slow displacement rate, thermoelectric potentials were eliminated by periodically reversing the polarity of current flowing through the CT specimen. A thermally induced potential, equal to one-half the difference of measured positive and negative potentials, was subtracted from V. A reference probe was not employed in this study [12].

Ductile-fracture crack initiation is indicated by a rise in measured V because the electrical resistance of a cracked body increases as the crack extends. The definition of crack initiation is complicated by artificial rises in V (fictitious crack growth) or unexplained declines. Both of these artifacts were observed in this study and reported in the literature [13,14]. Bakker categorized fictitious crack growth in high toughness mild steel into components of crack-tip blunting, plasticity ahead of the crack tip, and void damage [13]. Plasticity is negligible, and blunting and void damage are invariant once the crack initiates [13]. Thus, ductile fracture initiation is defined reasonably by the first change in slope of the specimen potential difference versus load-line displacement (δ) record.

The variability in V- δ data dictates the resolution to which crack initiation can be detected. Variability is generally lowest for ambient temperature experiments at a rapid load-line displacement rate, as seen by comparing Figure 3(a) to 3(b). In practice, the DCPD technique resolves 0.1 μV to 0.2 μV changes, or 0.025% to 0.05% of the potential difference associated with the fatigue crack.

A standard method was developed to define crack initiation for each sample, using measurements of load (P) and V versus δ. Characteristic P- δ and V- δ curves for AA2024-T3 and

AA2519-T87 (+Mg+Ag) are shown in Figures 3(a) and 3(b), respectively. An estimated load-line displacement (δ') where the V- δ curve changes slope is used as a reference point for linear regressions to P- δ and V- δ data. The elastic compliance of the cracked plate is defined by least squares regression of P- δ data from 0.2 δ' to 0.8 δ'. Baseline V- δ data (i.e.- not associated with crack growth) are fit by linear regression from 0.5 δ' to 0.95 δ', while crack growth V- δ data are fit from 1.05 δ' to 1.30 δ'. From 0.0 δ' to 0.5 δ', V- δ data were excluded from the baseline regression because of artifacts such as closure contact of the fatigue crack surface. These three linear fits and the regression limits are indicated in Figure 3(a). The change in slope of the V- δ curve is dramatic from the baseline fit (-.48 μV/mm) to the crack growth fit (3.7 μV/mm). The intersection of the two linear fits indicates the transition from baseline response to crack growth, and the potential difference at this point (V_{ai}) is the potential difference associated with the fatigue precrack length, a_i.

A fracture initiation toughness, representative of about 20 μm of process-zone crack growth, is defined by a positive 0.2 μV vertical offset of the baseline V- δ regression. The intersection of the 0.2 μV offset fit and crack growth fit defines fracture initiation; the associated P_i, V_i, and δ_i measurements are shown in Figures 3(a) and 3(b). In Figure 3(b), 0.2 μV is the minimum offset that places the defined initiation point outside of the scatter band in the baseline V-δ trend. P_i, V_i, and δ_i are employed to calculate initiation fracture toughness. For all but two specimens, P_i deviated between 1.3% and 3.4% from linearity, as given by the load from the P- δ linear regression evaluated at δ_i. The average difference was 2.1%. Two exceptions were the AA2519-T87 (+Mg+Ag) specimens tested at 150°C and 175°C, where P_i deviated by 4.4% and 5.4% respectively, probably due to substantial plastic or creep deformation of the uncracked ligament. The narrow range of deviation from linearity supports the reproducibility of the 0.2 μV offset definition of initiation fracture toughness.

Crack length was determined from measured V using the calibration relationship of Hicks and Pickard [12,15]:

$$\frac{a}{W} = -0.5051 + 0.8857\left(\frac{V}{V_0}\right) - 0.1398\left(\frac{V}{V_0}\right)^2 + 0.0002398\left(\frac{V}{V_0}\right)^3 \qquad [1]$$

where V_0 is the reference potential for a/W = 0.241. The current input and potential wire placements are a compromise between high resolution and reproducibility [12,15]. As indicated in

Figure 2, the current is input along the load-line, from the top to the bottom of the CT specimen. The potential wires are positioned on the front face and are offset 1.7 mm (vertically) from the notch edge. With respect to thickness, the current leads are positioned at the midplane and the potential wires are placed at opposite edges of the CT specimen [12,15].

Equation 1 is based on finite element analysis and was verified experimentally for $0.24 < a/W < 0.70$ [15]. V_0 was determined iteratively [1] with Equation 1 from the measured potential immediately prior to crack initiation (V_{ai}) and the optically measured precrack (fatigue + notch) length a_i. The final crack length was marked by heat tinting or by growing a fatigue crack. Final crack lengths calculated with Equation 1 (Δa_{DCPD}) and measured optically ($\Delta a_{optical}$) are displayed in Table 2 for each sample.

EPFM Resistance Curves

The J-integral was utilized to account for uncracked ligament plasticity [3]. Applied J, equal to $J_{elastic} + J_{plastic}$, was calculated according to the ASTM Standard E 1152-92. $J_{elastic}$ is equal to K^2/E', where K is the applied elastic stress intensity factor for a CT specimen from the ASTM Standard Test Method for Plane-Strain Fracture Toughness of Metallic Materials (Designation E 399-90). E' equals E for plane stress and $E/(1-\nu^2)$ for plane strain, where E is elastic modulus and ν is Poisson's ratio [2].

Using the area method of ASTM E 1152, $J_{plastic}$ was determined from the measured load, load- line displacement, crack length, and the calculated unloading compliance. Using the compliance-crack length relationship for a CT specimen, an effective modulus was calculated from the initial measured slope of P-δ for a CT specimen with a fatigue precrack length a_i (Table 2). This value was used subsequently in calculating unloading compliance and $J_{plastic}$ from DCPD measured crack length. It was not necessary to partially unload the specimen during an

---

1 The exact solution for V_0 in Equation 1 involves complex numbers and is unwieldy. The following polynomial expression can be applied as an alternative to an iterative solution for V_0:

$$\frac{V}{V_0} = 0.60014 + 1.85514\left(\frac{a}{W}\right) - 1.93452\left(\frac{a}{W}\right)^2 + 6.24111\left(\frac{a}{W}\right)^3 - 7.66191\left(\frac{a}{W}\right)^4 + 4.28949\left(\frac{a}{W}\right)^5$$

2 According to ASTM E 1152, $(1-\nu^2)$ is always used to calculate $J_{elastic}$, which is not reasonable for plane stress crack tip deformation. In this study, $(1-\nu^2)$ is included for plane-strain-dominated fracture initiation toughness and is omitted for crack growth under plane stress.

experiment. To determine Δa for each J, DCPD measurements were corrected linearly to the optically observed final crack length, with zero error assumed for the fatigue precrack length.

Initiation and growth fracture toughness parameters were determined from J-Δa data. Plane strain deformation is assumed to control fracture initiation and plane stress deformation is assumed to dictate crack growth after an initial amount of mixed-mode growth. The applied J at DCPD-detected fracture initiation (J_{ICi}) was calculated from defined P_i, a_i, and δ_i. J_{ICi} was converted to a linear elastic initiation toughness, K_{JICi}, by the relation [3,4]:

$$K_{JICi} = \left(\frac{J_{ICi} E}{1 - \nu^2} \right)^{\frac{1}{2}} \qquad [2]$$

The ASTM E 813 standardized initiation toughness from an 0.2 mm offset blunting line (J_{IC}) was converted to K_{JIC} by the same relationship. The linear elastic R-curve (K_J-Δa) for small scale yielding was determined from J-Δa curves ($K_J = (J E)^{1/2}$), and generally described plane stress cracking. Figure 4(a) shows a- δ and P- δ traces for AA2024-T3 over 13 mm of crack growth at 25°C, which are used to calculate the K_J-Δa curve as well as K_{JICi} and K_{JIC}. A typical result of this analysis is shown in Figure 4(b).

Results

Microscopic Ductile Fracture Initiation

To test the capability of DCPD monitoring to detect process-zone damage associated with crack initiation, two rising load fracture toughness experiments were interrupted after a small, detectable increase in V. A CT specimen of aluminum alloy N203 [3] was loaded at 150°C and subsequently fatigued (K_{max}=21 MPa$\sqrt{m}$, R=0.65) to mark the extent of ductile crack growth. The specimen was separated to observe the variation in microvoid crack growth through the thickness (Figure 5(a)). For the second experiment, a CT specimen of AA2519+Mg+Ag was tested at 25°C and sectioned in profile to a depth of approximately 0.6 mm from the midplane. From the polished crack-tip profile, the micromechanism of ductile fracture initiation was directly observed (Figure 6(a)). V_{ai}, V_0, and the average final DCPD crack growth (Δa_{DCPD}) were calculated from potential versus time data for N203 (Figure 5(b)); load-line displacement is directly proportional to loading time. For AA2519+Mg+Ag at 25°C, V- δ data were used (Figure 6(b)). From the measured increase in V at the interrupt load, Δa_{DCPD} was calculated and compared to

[3] N203 is a developmental spray formed precipitation hardened alloy (Al-4.9Cu-0.5Mg-0.5Mn-0.4Ag-0.4Zr-0.2Ti-0.2V by wt%) similar to AA2519+Mg+Ag [16].

optical measurements of the average crack growth ($\Delta a_{optical}$).

Figure 5(a) shows that microvoid crack initiation associated with the rise in V (Fig. 5(b)) develops primarily in the center of the CT specimen, exceeding 200 μm at the midplane. The extent of crack growth rapidly declines away from the midplane and is essentially zero over 0.5 mm of thickness adjacent to either face of the CT specimen. If the region of microvoid damage is approximated as a triangle, then $\Delta a_{optical}$ is calculated as 103 μm from the area divided by the thickness of the CT specimen. The measurement of $\Delta a_{optical}$ includes the stretch zone width associated with crack tip blunting (roughly 10 μm). From Figure 5(b) and Equation 1, Δa_{DCPD} is calculated as 117 μm, which agrees reasonably with $\Delta a_{optical}$.

Crack initiation in AA2519+Mg+Ag developed by void nucleation at large constituent particles, followed by limited void growth and coalescence to the precrack tip (pt) by void-sheeting coalescence (Figure 6(a)). The large constituents are primarily undissolved Al_2Cu, and void sheeting coalescence involves void nucleation, growth, and coalescence at submicron dispersoids located between constituent-nucleated voids [17-19]. Optically measured crack growth of 86 μm is in excellent agreement with 88 μm of crack growth calculated from the increase in V (Figure 6(b)). In Figure 5(a), $\Delta a_{optical}$ at 0.6 mm from the midplane is 140 μm, indicating that this position represents a reasonable through thickness average of crack growth, consistent with the good agreement obtained from the crack tip profile. Measured crack extension should increase as the specimen is polished to the midplane.

Macroscopic Fracture Path

Crack initiation developed in the center of each CT specimen under plane strain conditions, as shown in Figure 5(a). The low magnification fractograph in Figure 7 demonstrates that flat fracture (normal to the Mode I applied load) occurs over approximately 80% of the thickness at the precrack tip, and changes to 45°-slant fracture as the crack extends. The interface between plane strain fracture and plane stress shear lips is indicated by arrows, and shows the gradual transition from flat to shear fracture that yields a triangular morphology for the former. Fracture was predominately plane stress after approximately 1.5 mm of crack growth. The results of Figures 5, 6, and 7 suggest that plane strain dominated for K_{JICi} from DCPD and plane stress was typical of K_J- Δa behavior, after a modest amount of mixed mode cracking.

Initiation Fracture Toughness

ASTM standardized toughness:

J_{IC} was calculated in accordance with ASTM Standard E 813. J-dominance was maintained for all Δa, and crack straightness and data spacing requirements were met. The thickness and original uncracked ligament always exceeded $25J_{IC}/\sigma_{FL}$, and the calculated effective

modulus was always within 10% of the elastic modulus (Table 2). Calculated crack growth (Δa_{DCPD}) was within 12% of $\Delta a_{optical}$ (Table 2). (In some cases, heat tinting was unsuccessful, and the final crack length was not determined). Five specimens (2024-#3, 2519-#1, 2519-#2, 2519-#5, and 2519-#6) did not satisfy the E 813 requirement that the absolute difference between Δa_{DCPD} and $\Delta a_{optical}$ must be less than 0.15 Δa_{max} for crack extensions larger than Δa_{max}, where Δa_{max} is given by the intersection of the 1.5 mm exclusion line and the R-curve. This requirement is not necessarily compatible with the generation of R-curves to large crack extensions. These 5 samples do meet the less stringent requirement from the proposed draft of the E813/E1152 combined standard; namely that the difference between Δa_{DCPD} and $\Delta a_{optical}$ does not exceed $0.15\Delta a_{optical}$ for crack extensions less than $0.2b_0$ and does not exceed $0.03b_0$ thereafter [5]. By comparing J_{IC} determinations from samples that met E 813 crack length accuracy requirements to samples that did not satisfy this requirement, we infer that DCPD crack length monitoring is sufficiently accurate to yield consistent J_{IC} values.

For each specimen, J_{IC} and the corresponding linear elastic initiation toughness (K_{JIC}) are given in Table 3. For the four replicate CT specimens of AA2024-T3, J_{IC} ranges from 27.0 to 36.2 kJ/m^2, and calculated K_{JIC} values from 45.2 to 52.4 MPa$\sqrt{m}$, with an average of 48.5 MPa$\sqrt{m}$. J_{IC} for 3.2 mm thick AA2650 (18.5 kJ/m^2) is 70% higher than J_{IC} for 6.0 mm thick AA2650 (10.9 kJ/m^2), and K_{JIC} of the thinner specimen is 31% higher than K_{JIC} of the thicker specimen. J_{IC} and K_{JIC} for AA2519-T87 (+Mg+Ag) are essentially temperature invariant, but are variable.

Electrical-potential-based initiation toughness:

Table 3 lists DCPD based initiation toughnesses, J_{ICi} and K_{JICi}, for each sample, which were verified by the same requirements as for a valid J_{IC}. Values of J_{ICi} and K_{JICi} for each sample were substantial lower than J_{IC} and K_{JIC}. For AA2024-T3, J_{ICi} ranges from 13.4 kJ/m^2 to 17.8 kJ/m^2, and K_{JICi} ranges from 31.9 MPa$\sqrt{m}$ to 36.7 MPa$\sqrt{m}$, with an average of 33.3 MPa$\sqrt{m}$. For AA2519-T87 (+Mg+Ag), K_{JICi} decreases mildly from 25°C (31.4 MPa$\sqrt{m}$) to 175°C (28.5 MPa$\sqrt{m}$), and shows considerably less scatter than K_{JIC} values. Least squares linear regression analysis of K_{JICi} versus temperature data yielded an intercept of 32.6 MPa $\sqrt{m}$ (at 0°C) and a slope of -0.016 MPa$\sqrt{m}$/°C. The 95% confidence interval of the slope (ß) implies a temperature invariant toughness ($-.044 < ß < +.011$). Values of J_{ICi} for 3.2 mm thick and 6.0 mm thick AA2650-T6 are 9.9 and 9.7 kJ/m^2 respectively, and K_{JICi} values are essentially equal (28.8 and 28.5 MPa$\sqrt{m}$).

Ratios of K_{JIC}/K_{JICi} are listed in Table 3 and range between 1.29 and 1.74 for 3.2 mm thick specimens. For the 6.0 mm thick AA2650 specimen, this ratio is reduced to 1.06. The thickness dependencies of K_{JICi} and K_{JIC} for AA2650-T6 are illustrated in Figure 8. Increasing K_{JIC} as thickness decreases is traced to a sharply rising R-curve for the 3.2 mm thick CT specimen, compared to a relatively shallow K_J-Δa curve for the 6.0 mm thick CT specimen. The sharply rising R-curve is likely due to a substantial loss in plane strain constraint (Figure 7) [4]. Presumably, K_{JICi} is thickness independent because similar plane strain constraint is maintained at the precrack tip for both thicknesses.

K_J-Δa Resistance Curves

Complete K_J-Δa resistance curves are presented in Figure 8 for AA2650, Figure 9 for AA2519, and Figures 4(b) and 10 for AA2024. The value of K_J at a crack extension of 3 mm is listed in Table 3 for each sample, and serves as a "figure of merit" in ranking plane stress crack growth resistance.

Qualification of Experimental Data:

For the J-Integral to be a valid crack tip parameter, microscopic fracture processes must be contained well within the annular zone of validity of the J-fields [1-3]. For all CT specimens tested, J-dominant conditions prevailed throughout loading, with J values well below the maximum allowed by ASTM E 1152. J-Δa curves are specific to a thickness of 3.2 mm, reflected by the applied J exceeding B $\sigma_{FL}/20$ at crack extensions between 1 and 2 mm. J-controlled growth occurs for $\Delta a < 3$ mm, corresponding to crack growth within one-tenth the original uncracked ligament. Applied loads in the crack growth regime are below the modified Green's fully plastic limit load (P_L) solution for plane stress [20]; below 0.4 P_L at initiation and increasing to a maximum of 0.86 P_L at the completion of J-controlled crack growth.

Displacement rate partitioning analysis suggests that J is the valid crack tip parameter for rising load experiments of AA2519-T87 (+Mg+Ag) between 25°C and 175°C. Saxena and Landes developed a displacement rate partitioning analysis that separates measured load-line displacement rate (v) into the sum of elastic (v_e), plastic (v_p), and creep (v_c) rate components [21]. v_c is determined from empirical values of v_e, v_p, and v. There is no established criteria for ascertaining the value of v_c above which creep is sufficiently extensive to compromise J, but Saxena and Landes argue that creep crack growth rates in stainless steel are not uniquely correlated by J when v_c/v exceeds 0.8. For AA2519, $v_e + v_p$ dominated the measured total displacement rate, and v_c/v

---

4 2650-#2 maintains plane strain constraint over the entire crack growth regime, but shows a rising R-curve due to a weaker strain singularity ahead of a moving crack tip [2].

was always below 0.8. Experiments on creep crack growth of AA2519-T87 at 135°C support the dominance of time independent crack tip fields [22]. Hamilton and Saxena found that v_c/v ratios varied from 0.0 to 0.8 and concluded that creep does not affect K-governed crack tip fields.

Interlaboratory R-Curve Characterization of AA2024-T3

Specimen geometry can affect the magnitude and validity limits of K_J-Δa. The J-integral/DCPD test method was employed with CT specimens to determine K_J-Δa data at 25°C for 3.2 mm thick AA2024-T3 sheet in the LT orientation (W=76.2 mm), as part of an interlaboratory R-curve characterization [23]. DCPD based measurements of K_J-Δa for a single specimen are represented by filled circles in Figure 10, and error bars represent the maximum variability associated with three additional replicate experiments, as quantified by 95% confidence interval estimates of K_J. K_J-Δa curves were measured for the same lot of 3.2 mm thick AA2024-T3 sheet by several laboratories employing different experimental methods and specimen geometries. Boeing employed a 1.5 m wide MT panel with visual observation of crack length. Fracture Technology Associates (FTA) used partial unloading compliance (PUC) measurements of crack length for a 30.5 cm wide MT panel as well as a 50.8 mm wide CT specimen. All the specimens were 3.2 mm thick. For modest crack extensions ($\Delta a < 7$ mm), the R-curves in Figure 10 are nearly identical for the CT and small MT specimens. The higher R-curve for the widest MT specimen is not understood, but may be due to underestimated crack length measurements [23].

Discussion

Results show that the J-Δa R-curve method, based on elastic-plastic fracture mechanics and high resolution DCPD monitoring of crack length, accurately characterizes the plane strain crack initiation toughness and the plane stress stable crack growth resistance of aluminum alloys. The thickness-independence of K_{JICi}, and the thickness-dependence of J_{IC} and the stable crack growth portion of the R-curve (Figure 1), are established by experimental results. The small specimen used in this method enables efficient yet quantitative alloy development. This method is also relevant to mechanistic studies of elevated temperature and aqueous environment effects on fracture toughness [24-27]. Several factors are critical to the correct application and interpretation of results from the J-integral/DCPD method.

Microscopic Fracture Initiation

High resolution detection of ductile fracture initiation is the crucial component of accurate K_{JICi} measurement. Initiation in precipitation hardened aluminum alloys evolves under high constraint at the midplane of the CT specimen, as established by fractographic studies of microvoid damage associated with small increases in measured V (Figures 5 and 6). Consequently, K_{JICi} is a relevant measure of plane-strain initiation toughness.

Crack growth is averaged over the specimen thickness when calculated based on the DCPD calibration relationship (Equation 1). Based on potential difference data for N203 and AA2519 (Figures 5 and 6), a 0.1 μV increase in V corresponds to 8 μm and 13 μm of average crack extension, respectively. Consistent with the 0.2 μV offset from the baseline V-δ trend (Figures 3, 5(b), and 6(b)), initiation fracture toughness based on DCPD is thus associated with average crack extensions of 16 and 26 μm, respectively. A similar resolution is reported elsewhere [14]. The higher sensitivity (dV/da) for N203 is due to a smaller a/W ratio after fatigue precracking relative to AA2519-T87 (+Mg+Ag).

In principle, partial unloading compliance is more sensitive to crack tip damage compared to DCPD. The percentage increase in specimen compliance for a small change in crack length, (dC/C)/da, is higher than the percentage increase in V from DCPD, (dV/V)/da. For example, 50 μm of crack extension in a CT specimen of N203 (a_i/W=0.493, W=48.26 mm, B=3.2 mm) results in a 0.5% increase in specimen compliance versus a 0.1% increase in V. However, a 0.1% change in V can be discerned by DCPD monitoring, while a 0.5% in compliance may be difficult to resolve. Precise compliance measurements may be obscured by complications due to friction at the loading pins, clip gage misalignment, and hysteresis in the unload/reload cycle [14]. Additionally, the number of crack length measurements by compliance during a rising load test is limited to the number of unloadings, which effectively limits the resolution of process-zone damage that constitutes crack initiation.

In practice, DCPD more effectively resolves fracture initiation [14]. However, artifacts in the V-δ signal due to thermal fluctuations and the initial elastic loading must be minimized. Thermal fluctuations affect measured V by altering the resistivity of the alloy and by changing the potential difference across dissimilar metal junctions within the DCPD circuit. The latter is accounted for by switching the polarity of the current, while the former requires a reference probe to eliminate drift in the V-δ signal. In addition, the environment should be maintained at a nearly constant temperature. Initial elastic loading can affect the potential signal by separating crack faces that are electrically contacted and by providing a parallel current path through the load frame. The magnitude of the latter effect depends on the resistance through the test sample versus the resistance through the load frame. If the resistances are similar, then the specimen must be electrically isolated from the load frame.

Initiation Fracture Toughness in Thin Sheet

Three measures of initiation fracture toughness are discussed in this section; K_{JIC}, K_{JICi}, and K_{IC} from ASTM standard E 399. The discussion focuses on precision (variability) and accuracy (absolute values) of K_{JIC} and K_{JICi}.

Variability:

Table 3 reveals that K_{JICi} may be a more precise measure of initiation fracture toughness relative to K_{JIC}. The discrepancy in precision is small for AA2024-T3, with differences of 15.0% and 15.9% between the maximum and minimum measurements of K_{JICi} and K_{JIC}, respectively. For AA2519+Mg+Ag, results presented in TASK IV show that initiation toughtness is temperature-independent. Additionally, the discrepancy in K_{JICi} and K_{JIC} is significant, with differences of 14.4% and 32.8% between the maximum and minimum values of K_{JICi} and K_{JIC}.

The definition of crack initiation must be objective and reproducible to obtain precise initiation toughness measurements. The 0.2 μV vertical offset definition of fracture initiation adheres to both requirements and minimizes scatter in K_{JICi}. The 15% variability may be related to variations in constituent particle distributions ahead of the fatigue precrack tip or to artifacts in the V-δ signal that appear concurrent with fracture initiation. The 0.2 mm offset blunting line definition of crack initiation for K_{JIC} is objective but not reproducible. The lack of reproducibility is traced to variability of DCPD-based K_J-Δa measurements between crack extensions of 0.0 mm and 0.7 mm, as illustrated in Figure 9. The reason for this scatter is not known, but may be related to artifacts in measured electrical potential during initial crack growth, or to variation in the proportions of plane strain and plane stress crack growth.

Absolute measures of initiation fracture toughness:

A comparison of K_{IC} data for 2000 series aluminum alloys [28] to K_{JICi} and K_{JIC} values in Table 3 suggests that K_{JICi} approximates the true initiation toughness for a thin sheet, while K_{JIC} is an overestimate. The average K_{JICi} and K_{JIC} for AA2024-T3 sheet from Table 3 are 33.3 MPa$\sqrt{m}$ and 48.5 MPa$\sqrt{m}$, respectively. The published plane strain fracture toughness of AA2024-T3 (from E 399) varies from 31 MPa$\sqrt{m}$ to 44 MPa$\sqrt{m}$ at the strength level studied (σ_{YS}=390 MPa) [28]. Bucci reported a K_{IC} of 36 MPa$\sqrt{m}$ for AA2024-T351 with a yield strength of 325 MPa [29].

For 20 mm thick CT specimens of AA2024-T351, Schwalbe and coworkers determined a J-integral initiation toughness J_{lin}, similar to J_{ICi} [14]. From Equation 2, K_{lin} values of 33.2 and 36.9 MPa$\sqrt{m}$ were calculated. Griffis and Yoder employed three thicknesses of three point bend specimens (B=6.4 mm, 12.7 mm, and 23.6 mm) and a multi-specimen technique to determine J-Δa curves for 25 mm thick AA2024-T351 plate [30]. The applied K at fracture initiation, K_{IC}^0, was determined by extrapolating the J-Δa curve to zero crack extension and converting the extrapolated J value to a linear-elastic initiation toughness. Average K_{IC}^0 for the three specimen thicknesses

was 33.5 MPa$\sqrt{m}$. Based on these results, literature values of initiation toughness for naturally aged AA2024 are about equal to K_{JICi} and are well below K_{JIC}. In Figure 11 K_{JICi}, K_{lin}, and K_{IC}^0 are plotted versus thickness for naturally aged AA2024. This plot strongly suggests that initiation fracture toughness based on high resolution detection of crack tip process-zone damage is thickness independent, at least to a thickness of 3.2 mm.

From a metallurgical perspective, it is unclear whether the initiation toughness for 3.2 mm sheet should equal the toughness of thick AA2024 plate. Hot rolling might increase strength to lower toughness, but the subsequent solution heat treatment could cause substantial recovery or recrystallization to counterbalance the effect of rolling. Large constituent particles would break and redistribute during rolling to alter the toughness. Measurements of initiation toughness for the two CT thicknesses of metallurgically identical AA2650-T6 (Table 3 and Figure 8) confirm the thickness independence of K_{JICi} suggested in Figure 11.

Comparisons between K_{JICi}, K_{JIC}, and K_{IC}:

Using the same experimental technique applied in this study, but a slightly different definition of K_{JICi}, Somerday et. al. determined K_{JICi}, K_{JIC}, and K_{IC} from sidegrooved CT specimens of AA2009/SiC that maintained plane strain constraint and met all the geometry requirements in ASTM E 399 and ASTM E 813 [25]. The three measures are compared in Figure 12, where K_{JIC} and K_{JICi} are plotted versus K_{IC}. The solid line represents a one-to-one relationship between the elastic and elastic-plastic measurements, while the dashed line represents initiation toughness measurements which are 15% below K_{IC}. Both K_{JIC} and K_{JICi} correlate with K_{IC}. K_{JIC} is slightly higher than K_{IC}, and K_{JICi} is consistently less than K_{IC}. (The average difference is 17%.) K_{JICi} represents the lower bound initiation toughness associated with an early stage of process-zone damage [25]. K_{JIC} and K_{IC} are higher than K_{JICi} because the former are each defined based on an arbitrary amount of stable crack extension. If fracture in an E399-valid specimen is truly unstable at $K=K_{IC}$, then K_{IC} and K_{JICi} (from a thinner specimen) should be equal.

In thin sheet alloys where constraint is lost with crack extension (Figure 7), initiation toughness is overestimated by K_{JIC} and well represented by K_{JICi}, as shown in Table 3 and Figure 8. Values of K_{JIC} (solid triangles) and K_{JICi} (open triangles) for the two (metallurgically identical) thicknesses of AA2650-T6 are plotted in Figure 12, with the provisional fracture toughness from ASTM E 399 (K_Q) assumed to approximate K_{IC}. (Sample 2650-#2 did not meet the E 399 requirements that B exceed $2.5(K_Q/\sigma_{YS})$ and that P_{max}/P_Q be less than 1.1. Sidegrooves added constraint not recognized by ASTM E 399.) For the thick sidegrooved specimen, K_{JIC}, and to a

lesser extent K_{JICi}, correspond closely to K_Q and conform with the data for AA2009/SiC. As thickness is decreased to 3.2 mm (2650-#1), K_{JICi} is unchanged while K_{JIC} is increased to well above the standardized plane strain initiation toughness. Hence, K_{JICi} best represents initiation toughness in CT specimens of sheet aluminum alloys. As specimen thickness declines and/or alloy toughness increases, K_{JIC} becomes increasingly larger than the true initiation toughness.

The thickness independence of K_{JICi} (Figures 8 and 11) is consistent with the argument that fracture initiation toughness is constant, given a predominantly plane strain crack tip stress state [28]. A plane-strain stress-state was present directly ahead of the fatigue precrack in both thicknesses of AA2650-T6, but some plane-strain constraint was lost near the specimen edges after 0.2 mm of crack growth in the thinner CT specimen. For single edge-notched bend specimens of mild steel, Green and Knott reported thickness invariant crack tip opening displacements at fracture initiation under plane strain constraint, and a higher crack tip opening displacement for a thin specimen where constraint was lost [31].

Applicability of ASTM E 813 Thickness Criterion:

K_{JIC} overestimates the initiation toughness in thin sheet AA2650-T6, even though the thickness criterion from ASTM E 813 ($B > 25\ J_Q/\sigma_{FL} = 1.09$ mm) was easily satisfied. As thickness increases and constraint is maintained to larger crack extensions, K_{JIC} presumably approaches a thickness independent value that is comparable to K_{IC} and 5 to 20% higher than K_{JICi}. K_Q for 2650- #2 is nearly equal to K_{JIC} (30.1 MPa$\sqrt{m}$), which suggest that a 6.0 mm thick, sidegrooved specimen yields a J_{IC} that is thickness independent. If J_{IC} for 3.2 mm thick AA2650-T6 is assumed invalid, and J_{IC} for the 6.0 mm thick specimen is valid (Figure 12), then bounds can be estimated for the constant M in a generalized thickness criterion ($B > M\ J_Q/\sigma_{FL}$). Based on this argument, M must be between 75 and 225 for aluminum alloys and the CT geometry. K_{JICi} from high resolution DCPD measurements is independent of thickness to 3.2 mm for CT specimens of aluminum alloys with flow strengths as low as 420 MPa and toughnesses as high as 40 MPa$\sqrt{m}$ (Figure 11). This implies that M is less than 65 for this case.

K_J-Δa Curves:

Over a substantial crack extension, the K_J-Δa resistance curve determined by the J-integral/DCPD method for AA2024-T3 compares favorably to K_J-Δa determined by the J-integral and PUC for MT specimens (Figure 10). The general equivalence of DCPD and PUC in measuring crack lengths for R-curve determination is reported elsewhere [23,32]. K_J-Δa data for MT specimens are valid to significantly higher crack lengths relative to the CT geometry, probably

due to a loss of J-dominance in the latter [1,3].

K_J-Δa curves, determined from small specimens with significant ligament plasticity, are relevant to linear elastic R-curves determined from large specimens that satisfy small scale yielding conditions. For 1.6 to 2.0 mm thick sheet of AA2024-T3, K-Δa is plotted in Figure 10 for various specimen sizes [23,32,33]. R-curves determined from elastic analysis (K_R-Δa) are indicated by lines, while those determined from elastic plastic analysis (K_J-Δa) are represented by symbols. An excellent correspondence is observed between K_J-Δa curves from small specimens (50.8 mm wide CT [23] and 30.5 cm wide MT [23]) and K_R-Δa curves from large specimens that satisfy small scale yielding conditions (60.0 cm wide MT [32] and 1.52 m wide MT [23]).

Crack growth resistance can be ranked by K_J^{3mm}, an arbitrary point on the R-curve. K_J^{3mm} is less than K_C, the critical plane stress fracture toughness, but is a relative indicator of K_C for different alloys and testing conditions. The geometry, width, thickness, and initial precrack length of the test specimen affect K_C, so K_C determined from small CT or MT specimens is not relevant to K_C determined from large center cracked panels [32]. The K_J-Δa curve from a small specimen could be combined with an accurate extrapolation procedure to predict K_J at longer crack lengths. K_C for a wide panel could then be estimated with the extrapolated K-Δa result and a tangency condition for crack instability [32]. A K_J-Δa curve determined from a CT specimens thus provides a potential means of characterizing K_C for alloy development.

K_J-Δa resistance curves, generated from CT specimens by the J-integral/DCPD method, are useful for screening purposes and testing under complex experimental conditions, such as elevated temperature or aqueous environments. For example, the resistance curve behavior of AA2519-T87 (+Mg+Ag) as a function of temperature is displayed in Figure 9. These data illustrate the temperature independence of K_{JICi}, as well as the peak crack growth resistance at 75°C, and the decreased crack growth resistance at 150°C and 175°C. The superior room temperature crack growth resistance of AA2519-T87 (+Mg+Ag) alloy sheet relative to AA2650-T6 and AA2024-T3 is seen from Table 3. Determining these results with MT specimens would be material-intensive and expensive.

Conclusions

The results presented in this paper establish the accuracy, reproducibility, and relevance of initiation fracture toughness and K_J-Δa measurements determined from thin compact tension (CT) specimens by the J-integral/DCPD method.

1. Direct current potential difference (DCPD) monitoring is an effective technique for detecting microvoid fracture initiation in precracked CT specimens of aluminum alloy sheet, with a resolution of 20 μm of crack tip damage. Crack initiation develops under plane strain constraint at the midplane of the thin CT specimen, and is thus representative of plane strain initiation toughness.

2. For 3.2 mm sheet of precipitation hardened 2xxx Al alloys, the plane strain initiation toughness measured according to ASTM E813 is thickness-dependent and 50% higher than the plane strain initiation toughness based on DCPD monitoring (K_{JICi}). The thickness criterion for geometry-independent initiation toughness is non-conservative for thin sheet aluminum alloys.

3. The plane strain initiation toughnesses of AA2024-T3 and AA2650-T6 are independent of specimen thickness, when K_{JICi} is defined based on high resolution detection of an early stage of crack tip process-zone damage.

4. Ambient temperature J-Δa resistance curves of 3.2 mm thick AA2024-T3 sheet, measured from CT specimens by the J-integral/DCPD method, compare closely with data from larger middle tension (MT) and smaller CT geometries.

5. Results from the small specimen J-integral/DCPD method are relevant to prediction of large specimen R-curve behavior, alloy development, and mechanistic studies.

III. TASK II---ELEVATED TEMPERATURE DEFORMATION AND FRACTURE OF RS/PM AA8009

S.S. Kim and R.P. Gangloff

Abstract

The objective of this work was to evaluate the effects of processing variables on two problems that limit the performance of AA8009 (Al-8.5%Fe-1.3%V-1.7%Si, by weight): (1) decreasing fracture toughness with increasing elevated temperature and decreasing loading rate, and (2) anisotropic fracture toughness for extruded AA8009. Modified rapid-solidification processing, including inert gas shrouding of the ribbon surface and mechanical obstruction of the gas boundary layer, reduced oxide thickness on prior ribbon particle boundaries and the hydrogen content associated with oxides. The expected improvement in elevated temperature fracture toughness was not observed. AA8009 was processed thermomechanically (TMP) by a variety of rolling and annealing schedules. Substantial improvement in toughness isotropy was obtained by homogenization of the microstructure. K_{IC} tended to decrease with rolling reduction, independent of fracture temperature and due to microstructural changes during rolling. Reduced oxide sheet spacing and enhanced dynamic recovery, that reduces work hardening, each acted to reduce fracture toughness. Considering all TMP conditions, the expected improvement in elevated temperature fracture toughness was not realized.

A second objective was to improve understanding of time-temperature-dependent deformation and fracture in AA8009. AA8009 failed by microvoid processes, regardless of the processing route and testing temperature/loading rate. Low toughness was associated with a single size of shallow dimples, while igh toughness was correlated with a bimodal distribution of spherical dimples. The likely mechanism for the time-temperature-dependent fracture behavior of AA8009 is localized plastic deformation between growing microvoids. This flow instability truncates stable void growth and is attributed to reduced work hardening characteristic of the unique dislocation substructure in submicron grain-size aluminum alloys.

Introduction

Background and Problem Statement

Future high speed civil transportation systems, aimed at speeds of Mach 2.0 to 2.4, require new high performance airframe materials that are stable microstructurally and mechanically at temperatures up to 350°C, and as low as -80°C, with expected service lives on the order of 100,000 hours [34,35]. A variety of aluminum-based compositions and novel processing techniques have been considered. Among the emerging materials, rapid solidification/powder metallurgy (RS/PM) processed Al-Fe-X alloys have received significant attention due to their high volume fraction of dispersoids and ultrafine grain size, which are stable to 425°C [36-38].

It was demonstrated, however, that the fracture toughness, crack growth resistance and tensile ductility of RS/PM Al-Fe-X alloys are reduced significantly at temperatures between 175 and 200°C [24,39-47]. For example, results for AA8009 (an alloy based on Al-Fe-Si-V) show that tensile ductility and fracture toughness may be anisotropic and further decrease with decreasing strain rate at elevated and ambient temperatures [24,39-43]. Similar results were reported for Al-Fe-Ce and other elevated temperature aluminum alloys which contain submicron grain size and a high volume fracture of small (of order 50 nm diameter) dispersoids [44-47].

Improved Elevated Temperature Damage Tolerance

Fracture toughness may be improved by modifications to the planar flow RS casting procedure as well as to subsequent thermomechanical processing. During solidification and compaction, oxides form along the prior ribbon particle boundaries of many RS/PM alloys. Porr demonstrated that AA8009 fails by microvoid coalescence and the oxide-matrix interfaces serve as the first void nucleation sites, regardless of testing temperature [24,39]. Therefore, oxide decorated prior ribbon particle boundaries are potentially detrimental to fracture toughness and provide a likely cause for toughness anisotropy.

Several processing modifications were proposed to improve the elevated temperature damage tolerance and toughness isotropy of AA8009 [48]. As a first attempt, thermomechanical processing (TMP) was performed on extruded AA8009 to refine the oxide layers and homogenize the microstructure by pulverizing oxide films on prior ribbon particle boundaries. A recent study indicates that TMP effectively reduces toughness anisotropy [24]. Alternately, the planar flow RS-casting process was modified, including dry inert gas shrouding of ribbons and mechanical obstruction of surface boundary gas layer, to reduce the overall oxide population [48].

The effects of processing variables on time-temperature-dependent deformation and fracture in AA8009 need to be further examined. Understanding of micromechanical mechanism for time-temperature dependent fracture behavior of AA8009-type alloys is limited. This poor mechanistic understanding has further limited the effectiveness of processing variations.

Proposed Mechanisms for Time-Temperature Dependent Fracture of Ultrafine Grain Sized Materials

Several mechanisms have been proposed to explain the reduction in tensile ductility and fracture toughness for dispersion strengthened, ultrafine grain sized alloys at elevated temperatures and/or slow strain rates. Delamination toughening was believed to be responsible for the reduced elevated temperature damage tolerance of AA8009, since compact tension specimens from extrusion delaminated significantly at 25 and 300°C, but not at 175°C [49-52]. Boundary failure can lead to a loss of through-thickness specimen constraint to increase the initiation and growth fracture toughness of a delaminating alloy. Low magnification SEM fractographs of AA8009 plate and sheet products, however, demonstrated a total lack of delamination, regardless of test temperature, suggesting that delamination is not a central factor in reduced fracture toughness at elevated temperature.

Kim argued that residual atomic hydrogen associated with powder surface oxides is responsible for reduced tensile ductility in PM aluminum alloys [53]. This argument is based on the relatively high total dissolved hydrogen content in RS/PM processed aluminum alloys, as a result of the low degassing temperature compared to IM-processed alloys. Porr and Gangloff, however, demonstrated that reduced hydrogen content in AA8009 did not improve fracture [39]. It was concluded that hydrogen in AA8009 is strongly trapped in the form of hydrated oxides, independent of the starting level or alloy product form. Heating between 25°C and 175°C is insufficient to detrap this hydrogen and thus to provide a source for alloy embrittlement. This hypothesis was confirmed by limited thermal-desorption spectroscopy experiments [54]. Experiments with AA8009 demonstrated that fracture toughness was degraded similarly with increasing temperature for precracked specimens loaded in either moist air or ultra-high vacuum [39,55]. Accordingly, hydrogen produced by environmental reactions is not responsible for elevated temperature embrittlement of AA8009.

It was suggested that dynamic strain aging (DSA) occurs in AA8009-type alloys at intermediate temperatures due to the sluggish diffusion of substitutional Fe and V present in the matrix. DSA was argued to cause the loss of tensile ductility and possibly fracture toughness [40,41,56]. Even though DSA is a broadly accepted mechanism for Al-Fe-X alloys, it can be challenged for several reasons. Lloyd and Westengen proposed that a decrease in tensile ductility for ultrafine grain sized materials at elevated temperature is the result of a thermally accelerated dynamic recovery process and the formation of Lüders band [46,47,57,58]. Kim et al. advocated the dynamic recovery mechanism for the reduced elevated temperature damage tolerance based on TEM micrographs of tensile deformed AA8009 [59]. It was demonstrated that dislocation density in as-received and elevated temperature tensile deformed AA8009 is extremely low; in each case, any presence of dislocations was in the form of subgrain boundaries which segment the existing

solidification-produced subgrains. Dynamic recovery would be, in general, favored at high temperature and/or slow strain rate, either by dislocation climb or diffusional relaxation [60]. Porr et al. suggested that reduced tensile ductility and fracture toughness at elevated temperature for AA8009-type alloys is related to dislocation climb over the particles at elevated temperature, leading to localized plastic deformation between growing microvoids [39].

Objective

The objectives of the present study were: (1) to precisely characterize the effects of planar flow-RS casting variables and thermomechanical processing conditions on the temperature-dependent toughness of AA8009, and (2) to establish micromechanical mechanisms for time-temperature dependent deformation and fracture of AA8009-type alloys.

Procedures

Materials

RS/PM AA8009 (Al-8.5%Fe-1.3%V-1.7%Si, by wt pct) plate and sheet, produced with a variety of processing routes, were supplied by Allied Signal Inc. for the present study. These alloys were rapidly quenched from the melt into ribbons using the planar flow casting process, either in a moist air atmosphere (Conventional AA8009) or a dry-inert gas atmosphere (Modification A AA8009). Ribbons produced by Modification A were further modified by mechanical obstruction of the surface boundary gas layer (Modification B).

During powder solidification and compaction, a considerable amount of oxides form as flakes which align predominantly along the prior powder particle boundaries which are parallel to the rolling direction. These oxides contain hydrogen in the form of $Al_2O_3 \cdot H_2O$. XPS/AES measurements of oxide thicknesses on ribbons from each process were obtained by Allied Signal. Hydrated oxide thickness decreased from 4.5 nm for Conventional AA8009 to 2.9 nm for Modification B.

Ribbons were pulverized mechanically into -32 mesh powders, and consolidated into bulk compacts by vacuum hot pressing followed by hot extrusion. Gas analysis of extruded AA8009 established that the hydrogen content varied from 3.5 ppm for Conventional AA8009 to 2.1 ppm for Modification A and 1.5 ppm for Modification B. Oxide thickness, oxygen content, and hydrogen content associated with the final product from each ribbon are summarized in Table 4.

Modification B of AA8009 was found to have a high carbon content in the form of coarse quasicrystalline icosahedral particles, which were provided by erosion of the component used to obstruct the surface gas boundary layer. Therefore, the present study concentrated on Conventional and Modification A of AA8009.

Extrusions from each processing route were rolled into plate and sheet with gauge thicknesses of 6.3, 2.3 and 1.0 mm. Rolling direction (straight and cross rolling) and temperature

(hot, cold and cold/anneal) were varied systematically.

The microstructures of as-received AA8009 plate and sheet were characterized elsewhere [35,48,59]. Thermomechanical processing practice refined the oxide layers and reduced the interplanar spacing between these layers. (See Figure 23). The planar separation of oxide stringers averaged approximately 7 μm for 6.3 mm thick plate, while it deceases to approximately 2 to 5 μm for 1.0 mm thick sheet. The average grain size of AA8009 varied between 0.1 μm and 0.3 μm depending on product form. Most grain boundaries observed in AA8009 were low-angle boundaries, with the angle between adjacent boundaries estimated to be less than 5°. AA8009 had approximately 25% volume fraction of nearly spherical $Al_{12}(Fe,V)_3Si$ particles. The average particle diameter ranged from 50 to 100 nm. Dispersoid particles were mainly located along subgrain boundaries. Clusters of small silicide particles were often observed within the subgrain interiors.

Fracture Toughness Experiments

Compact tension (CT) specimens, with a width of 38.1 mm, were prepared from each plate and sheet product of AA8009. CT specimens of 6.3 mm thick AA8009 plate had a 6.3 mm gross thickness with sidegrooves of 19.8% of the gross specimen thickness (5.05 mm net thickness) to increase through-thickness constraint. CT specimens without sidegrooves were machined from each AA8009 sheet. All specimens were fatigue precracked at a K_{max} of 9 MPa$\sqrt{m}$ to an a/W ratio of approximately 0.5. For 1.0 mm thick C(T) specimen, the fatigue precrack was grown to an a/W ratio of 0.7 in order to prevent buckling. Fracture toughness tests were conducted on a servo-electric testing machine, employing direct current electrical potential measurements to yield crack extension (Δa) and computed unloading compliance to determine J-integral values. The initiation fracture toughness was determined by the first nonlinearity in direct current potential versus load line displacement data. As established in Task I, this is a sensitive measure of the first stage of crack tip process zone damage, at the center of the specimen under plane strain constraint.

Elevated temperature fracture toughness experiments were conducted in a circulating air oven mounted on the testing system. All specimens were heated to temperature in 45 minutes and held at temperature for 60 minutes prior to loading. All experiments were conducted at constant applied actuator displacement rate; selected rates varied from 2.5×10^{-2} mm/sec to 5.1×10^{-6} mm/sec.

Results

Effect of Temperature on Fracture Toughness of Conventional AA8009

Figure 13 shows the effect of temperature on the initiation fracture toughness (K_{JCi} from Task I) of Conventional AA8009 (1991 Vintage), in three thicknesses of 6.3, 2.3 and 1.0 mm, at a

displacement rate of 2.5 x 10^{-3} mm/sec. 6.3 mm thick plate was produced by hot cross-rolling, while 2.3 and 1.0 mm thick sheets were prepared with cold cross-rolling. Regardless of product form, fracture toughness decreases with increasing temperature within the range studied. For example, K_{JICi} for 6.3 mm thick AA8009 plate decreases from 35 MPa$\sqrt{m}$ to 10 MPa$\sqrt{m}$ with increasing temperature from 25 to 175°C. Due to the limited data, each point is connected with straight line. A detailed temperature dependence of K_{JICi} for extruded AA8009, reported by Porr and Gangloff [24], showed a similar trend to the present results. Unlike tensile elongation which shows a minimum at near-175°C [42], an initiation toughness minimum is not observed for each product form within the temperature range studied.

The strong effect of temperature on the complete K *vs* Δa crack growth resistance curve is shown in Figure 14. This plot presents the results of replicate fracture toughness experiments, conducted with AA8009 plate at 25 and 175°C. Both the direct current electrical potential (pot) and compliance (com) methods were utilized to monitor crack growth in middle-cracked tension (MT) and compact tension (CT) specimens. These various experimental procedures yielded essentially identical R-curve data.

The R-curves shown in Figure 14 can be analyzed to yield the tearing modulus ($T_R \alpha$ $dJ/d\Delta a$), a measure of the resistance of an alloy to stable crack growth [24,50,51]. The temperature dependence of T_R is presented in Figure 15 for the forms of AA8009 represented in Figure 13. T_R exhibits a minimum with increasing temperature. This trend is not necessarily indicative of an intrinsic effect of temperature on fracture resistance because T_R is extremely sensitive to stress state; which is governed by yield strength, specimen thickness and delamination.

Figures 13 and 15 indicate that the absolute fracture toughness values for AA8009 vary with thermomechanical processing from plate to sheet. At 25°C, for example, K_{JICi} for 6.3 mm thick plate is 35 MPa$\sqrt{m}$, while initiation toughness decreases to 19 MPa$\sqrt{m}$ for 1.0 mm thick sheet.

Figure 16 shows SEM fractographs of cracks in 6.3 mm thick AA8009 plate fractured at: (a) 25°C, (b) 175°C and (c) 300°C at an actuator displacement rate of 2.5 x 10^{-3} mm/sec. The crack growth direction is from left to right, and the fractograph is located adjacent to the fatigue precrack at the specimen mid-thickness position. Regardless of test temperature, the fracture mode in AA8009 appears to be microvoiding. This notion is based on a stereoimaging fractographic analysis of matching fracture surfaces conducted by Porr [39]. Notably, the size, morphology and distribution of voids vary with the testing temperature. At 25°C, the fracture surface is characterized by a bimodal distribution of spherical dimples. The size of the large spherical dimples ranges from 2 to 5 μm, while that of the small dimples is about 1 μm. At 175°C, on the

other hand, a uniform distribution of shallow dimples is observed with an average diameter of 3 μm. The morphology of voids at 300°C is similar to that at 175°C.

Effect of Loading Rate on Fracture Toughness

Figure 17 shows the effect of actuator displacement rate on the fracture toughness of 6.3 mm thick conventionally processed AA8009 plate (1991 Vintage) at 25°C and 175°C. For comparison, fracture toughness data for 10.0 mm thick AA8009 extrusion, obtained by Porr and Gangloff [24], is included in Figure 17. Decreasing loading rate has a similar effect on the fracture toughness of AA8009 as increasing temperature; that is, initiation fracture toughness decreases with decreasing displacement rate at both 25 and 175°C. For example, the toughness of 6.3 mm thick AA8009 plate at 25°C decreases from 41 MPa$\sqrt{m}$ to 16 MPa$\sqrt{m}$ with decreasing actuator displacement rate from 2.5×10^{-2} to 5.1×10^{-6} mm/sec. The time taken from the start of the test to unstable crack growth was 20 seconds for the test at 2.5×10^{-2} mm/sec and two days for 5.1×10^{-6} mm/sec.

The data in Figure 17 clearly demonstrate that the fracture toughness of AA8009 depends on both temperature and time; low toughness fracture can be produced at 25°C provided that sufficient time is provided. This time-dependent fracture behavior is not normally observed in ingot metallurgy processed aluminum alloys such as AA2618.

The trend lines in Figure 17 indicate that the magnitude of the loading rate dependence of K_{JICi} for 6.3 mm thick plate changes at a critical loading rate of about 10^{-5} mm/sec for fracture at 25°C. Due to limited data for plate at 175°C, such a critical loading rate can not be determined with accuracy. However, the data for AA8009 extrusion show that the critical loading rate equals 10^{-2} mm/sec for fracture at 175°C [39]. The significance of the temperature dependence of this critical or transition loading rate is discussed in an ensuing section.

Figure 18 shows SEM fractographs of 6.3 mm thick conventionally processed AA8009 plate fractured at: (a) 25°C and 5.1×10^{-6} mm/sec, (b) 25°C and 2.5×10^{-2} mm/sec, (c) 175°C and 5.1×10^{-6} mm/sec, and (d) 175°C and 2.5×10^{-2} mm/sec. Decreasing loading rate has a similar effect on the fracture mode of AA8009 as increasing temperature; that is, a bimodal distribution of spherical dimples for short-term tests compared to and a uniform size of shallow dimples for the long term test at each temperature. At 175°C and 5.1×10^{-6} mm/sec, for example, dimples are uniformly distributed and aligned along a certain direction (Figure 18c), while the size and distribution of the dimples are not as uniform for the fast loading rate case at 175°C (Figure 18d). Moreover, comparing Figures 16 and 18, there exists a close resemblance in fracture mode between the room temperature-very slow loading rate case and the high temperature-standard loading rate case.

Effect of Modified RS and Thermomechanical Processing on Fracture Toughness

In order to understand the effect of each RS process modification on the fracture toughnesses of AA8009, K_{JICi} values at 25, 175, and 300°C are plotted in Figure 19 for differently processed 6.3 mm thick hot cross-rolled plates of AA8009. Data are presented for Conventional AA8009 (1991 Vintage), as well as for Modifications A and B, all from the present study. For comparison, fracture toughness data are plotted for extruded AA8009 and rolled plate of AA8009 (1990 Vintage), as reported previously by Porr and Gangloff [24,39]. Similar tearing modulus results are presented in Figure 20 for these materials. All toughness data in Figure 19 represent the LT orientation initiation toughness, except for Modification A results which represent the TL case. (The final rolling direction in cross rolling is always perpendicular to the initial extrusion direction. Accordingly, if an orientation is expected to be lower toughness, it would be LT.)

Average initiation fracture toughnesses are represented with the bars in Figures 19 and 20, and individual toughness values are indicated by filled circles to indicate the range of experimental error. The initiation toughness changes from 35 MPa$\sqrt{m}$ for Conventional AA8009 to 22 and 29 MPa$\sqrt{m}$ for Modifications A and B, respectively, at 25°C. The toughness at 175°C varies from 15 MPa$\sqrt{m}$ for extruded AA8009 to 10 MPa$\sqrt{m}$ for the AA8009 plates, including Conventional and Modifications A and B. For each processing condition, the initiation fracture toughness decreases with increasing temperature from 25 to 300°C. A weak toughness minimum is suggested only for the 1990 Vintage plate case.

Metallogaphic analyses suggested that eachmodified process method reduced the oxide population somewhat. Quantitative metallography was not conducted. Despite the reduced oxide thickness and total dissolved hydrogen content, as reported by Allied Signal Inc. (Table 4), the modified processes do not improve elevated temperature fracture toughness. Delamination, and possible associated toughening, was only observed for LT-oriented fatigue precracked specimens from the extrusion, and then only for fracture at 25°C.

Figure 21 shows SEM fractographs of 6.3 mm thick AA8009 plate, produced with (a) Modification A and (b) Modification B, respectively, and fractured at 25°C and 2.5 x 10^{-3} mm/sec. The modified processes did not alter the basic fracture mode of microvoid coalescence. There is, however, a subtle difference in fracture morphology between conventional and modified-processed AA8009. The dimples in Modification A appear to be shallower; a void impingement-type coalescence process is evidenced. The fracture surface of Modification A at 25°C is similar to that of Conventional 8009 at elevated temperature and/or slow loading rate. Modification B, on the other hand, has a featureless surface with occasional large dimples, aligned along the crack propagation direction.

The effect of temperature on the fracture toughness of three thicknesses of hot-cross-rolled Modification A AA8009 is represented in Figure 22. Despite the modified RS and thermo-mechanical processing, K_{JICi} decreases significantly at 175°C compared to the toughness at 25°C. The toughness difference between each thickness appears to be reduced for Modification A of AA8009, compared to that of Conventional AA8009 (see Figure 13). An SEM fractographic examination of the various sheet/plate thicknesses of Modification A showed a change in fracture mode with increasing temperature. This change was identical to that discussed for Conventional AA8009 (Figure 16). Figure 22 demonstrates that the fracture toughness of the 6.3mm and 2.3mm thicknesses of AA8009 decreases with decreasing temperature from 25°C to -60°C. The toughness of 1.0mm sheet increased modestly with this decrease in temperature.

For both conventionally and modified-processed AA8009, rolling reduction from 6.3mm to 1.0mm resulted in a reduced spacing of oxide layers, as well as a reduced oxide size. Typical microstructures are presented in Figure 23 for three thicknesses of conventionally processed AA8009.

Effect of TMP on Fracture Toughness of 8009

Figure 24 shows the effect of plate/sheet thickness on the initiation fracture toughnesses, K_{JICi}, for Conventional AA8009 and hot cross-rolled Modification A of AA8009, at three test temperatures. 6.3 mm thick Conventional AA8009 plate was produced with hot cross-rolling, while 2.3 and 1.0 mm thick Conventional AA8009 sheets were produced with cold cross-rolling. Each thickness of Modification A was produced by hot cross-rolling. For any rolling reduction and specimen thickness, K_{JICi} decreases with increasing temperature, regardless of processing route. For example, for 1.0 mm thick Conventional AA8009 sheet, the initiation toughness decreases from 20 MPa$\sqrt{m}$ at 25°C to 5 MPa$\sqrt{m}$ at 175°C.

Previously, it was demonstrated that tensile strength increases, while tensile ductility decreases, for Conventional AA8009 with increasing rolling reduction, regardless of test temperature [48]. For each test temperature, the initiation toughness for Conventional AA8009 reflects this trend in tensile properties; K_{JICi} decreases with thermomechanical processing from 6.4 mm thick plate to 1.0 mm thick sheet. The effect is particularly pronounced at 25°C for Conventional AA8009. For Modification A, the thickness dependence at 25°C is less clearly defined. K_{JICi} tends to decrease with increasing rolling reduction for Modification A fractured at 175°C. These initiation toughness differences at 25°C and 175°C appear to be significant for Modification A 8009, but are approaching the order of the expected variability in toughness from replicate experiments.

Two points are important with regard to the data in Figure 24. First, the J-integral R-curve method reasonably establishes the plane strain initiation fracture toughness (K_{JICi}) for AA8009

specimens as thin as 1.0 mm. This point is supported by the extensive experiments reported in Task I and by the presence of a plane strain region, at the fatigue precrack and in the center of each specimen of AA8009 examined at each test temperature. Typical low magnification fractographs are presented in Figure 25 for 1 mm thick CT specimens of Modification A of AA8009, tested at 25°C (a) and 175°C (b). Second, the processing of Conventional AA8009 represented in Figure 24 was hot, however, the 2.3 mm and 1.0 mm thick sheets were subjected to final cold rolling. Neither the amount of rolling deformation, nor a final cold pass, mitigated the deleterious effect of increasing test temperature on fracture toughness.

Figure 26 shows SEM fractographs of Conventional AA8009 sheet, with a gauge thickness of 2.3 mm fractured at (a) 25°C and (b) 175°C compared to 1.0 mm sheet fractured at (c) 25°C and (d) 175°C. The actuator displacement rate was 2.5×10^{-3} mm/sec. Compared to the 6.3 mm thick Conventional AA8009 plate represented in Figure 16, the distribution of dimples typical of the thinner gauges of AA8009 appear to be more uniform with less evidence of void sheeting-type microvoiding at 25°C. At 175°C, dimples of less than 1 μm in size are shallower than those produced at 25°C and are aligned along the crack propagation direction.

The effects of rolling reduction on the tensile yield strength and elongation of Modification A of AA8009 plate and sheet tested at 25°C and 150°C were obtained by Allied-Signal Inc. and presented elsewhere [48]. Modified AA8009 showed similar trends in tensile behavior compared to Conventional AA8009; mechanical processing to reduced thickness slightly enhances yield strength, but reduces tensile elongation for each temperature. The more relevant tensile ductilities of Modifications A and B of AA8009 are presented in Figures 27 and 28, respectively, as a function of gauge thickness for the L orientation at four tensile-test temperatures from 25 to 316°C. Three cases were hot cross rolled, without final cold reduction, in contrast to the data presented in Figure 24. Two of the 1.0 mm thick sheets were cold rolled to final thickness. For each of the AA8009 product forms represented in Figures 27 and 28, ductility is high at 25°C, sharply decreases with increasing temperature to 150°C, and only exhibits a weak minimum for four of the ten cases examined. None of the processing conditions affected a reduction in the deleterious effect of increasing temperature from 25°C to 150°C, for both modifications to the RS processing method.

Considering the tensile tests at 25°C of Modifications A and B, ductility decreased with increasing rolling from 6.3 mm to 2.3 mm, consistent with the data in Figure 24. Further reduction to 1.0 mm produced a modest ductility increase for each modification.

Figure 29 shows the initiation fracture toughness for 1.0 mm thick Modification A AA8009 sheet, produced by cross-rolling at different rolling temperature (hot and cold) or with intermediate annealing. Each toughness value represents K_{JICi} for the TL orientation and an applied displacement rate of 2.5×10^{-3} mm/sec. Regardless of rolling temperature and intermediate

annealing, the initiation fracture toughness decreases with increasing temperature from 25 to 175°C. Toughnesses at 25 and 175°C are unaffected by rolling temperature or intermediate annealing.

Effect of Long Term Heat Treatment

Selected specimens from cold rolled 1.0 mm thick Modification A AA8009 sheet were thermally exposed at 370°C for 100 hours without stress. Fracture toughness data are compared with as- received AA8009 sheet in Figure 30. High temperature exposure has no effect on toughness for AA8009 regardless of testing temperature, analogous to a previous study of high temperature exposure on the fracture toughness of AA8009 extrusion [39]. Temperature alone is not sufficient to induce a damaging microstructural change in 8009. This result is notable because uniaxial tensile experiments at Allied Signal. demonstrated that the 370°C annealing treatment substantially reduced the elongation to fracture (necking) of cold rolled 8009 sheet [48].

Summary of Fracture Toughness Measurements

Figure 31 provides a summary plot of the temperature dependencies of the initiation fracture toughness for many of the RS and thermomechanical processing conditions examined in this study. Data are also provided for ultra-fine grain size aluminum (Exxon DS Al), AA2618, and AA2519 (Ag + Mg), studied in Tasks III and IV. The results for SiC reinforced AA2009 were obtained at UVa under a separate NASA grant program [61-63]. The fracture toughness of several forms of AA8009 is excellent at 25°C, compared to the IM alloys and the metal-matrix composite. Increasing temperature to 150°C and above results in the same substantial fracture toughness degradation for each form of AA8009 studied. Toughness minima were not observed. The fracture toughnesses of the thin-sheet forms of AA8009 are particularly low compared to plate at each temperature.

Discussion

The results of this study are interpreted in order to understand: (a) the mechanism for brittle fracture of AA8009 at elevated temperatures or slow loading rates, and (b) the effects of processing variables on elevated temperature fracture of RS/PM AA8009.

Mechanism for Time-Temperature Dependent Fracture of AA8009

It has been well established that tensile ductility and fracture toughness decrease with increasing temperature and decreasing strain rate for submicron grain sized, dispersion strengthened aluminum alloys [24,39-47]. Several mechanisms were proposed for this unique time-temperature dependent fracture and deformation behavior, including: (1) macroscopic delamination toughening [50-52], (2) hydrogen or oxygen environment embrittlement [55,64], (3) internal hydrogen embrittlement from processing [53], (4) dynamic strain aging (DSA)

[40,42,43,56], and (5) slip localization with nil work hardening due to dislocation-dispersoid interaction [39].

Each proposed mechanism is reviewed here. Emphasis is placed on plastic instability and flow localization which appears to be most relevant to deformation and fracture of AA8009-type alloys. Additional work in this regard is reported in Task III.

Macroscopic Delamination Toughening:

A delamination-toughening mechanism to explain reduced toughness in AA8009 at elevated temperature was advocated by Chan [50,51] and Jata [52] based on SEM observations of extruded AA8009 showing significant delamination at 25 and 300°C, but not at 175°C. Such boundary failure results in a loss of through-thickness specimen constraint if the height of the out-of-plane cracks are on the order of the crack tip plastic zone, and if the height exceeds spacing so that shear operates under plane stress on planes at 45° to the Mode I crack. Delamination can therefore increases the initiation and growth fracture toughness, as originally proposed for improved toughness of Al-Li alloys at cryogenic temperatures [65].

Delamination toughening of AA8009 was examined by Porr and Gangloff [24]. They concluded that this mechanism is not a central factor to explain the time-temperature dependence of K_{ICi}, and does not necessarily contribute to the excellent ambient temperature fracture toughness. Unlike extruded AA8009, plate and sheet product forms do not delaminate, regardless of the loading rate or test temperature. Macroscopic SEM fractographs of Conventional AA8009 sheet with gauge thickness of 1.0 mm fractured at 25°C and 175°C, shown in Figure 25, further confirm this notion. Regardless of test temperature, sheet AA8009 does not delaminate, but fracture toughness declines with increasing temperature. Porr and Gangloff also demonstrated that, independent of specimen constraint or the occurrence of delamination, the effective strain to fracture decreases from 25 to 175°C [24]. This result indicates that the intrinsic fracture resistance of AA8009 declines with increasing temperature, independent of stress state effects. The same conclusion is established in Task III for a different ultra-fine grain size PM aluminum alloys.

Internal and External Hydrogen Embrittlement:

Compared to ingot metallurgy counterparts, AA8009 contains an extremely high hydrogen content due to the relatively low degassing temperature employed to avoid formation of a detrimental intermetallic phase and coarsening of silicide particles. Consequently, the possibility exists for hydrogen-induced damage at elevated temperatures [53,64]. The effect of internal and external hydrogen on fracture toughness of 8009 was examined by Porr et al. [55]. Prolonged heating in vacuum, or reduced total dissolved hydrogen content by autoclaving, has no effect on fracture toughness. They concluded that hydrogen in 8009 is similarly strongly trapped in each

product form at both 25°C and 175°C. Very high temperature, perhaps 400°C, is required to chemically produce atomic hydrogen in the AA8009 microstructure.

As summarized in Table 4, Modified AA8009 has two- or three-fold less hydrogen content compared to Conventional AA8009. Despite this significantly reduced hydrogen content, elevated temperature fracture toughness was not improved. A recent, thermal desorption spectroscopy study of AA8009 plate confirmed that hydrogen is strongly bonded up to 350°C [54]. It is likely that hydrogen in AA8009 is beneficially chemically trapped by strongly bonded hydrated oxides and is not released in atomic form for embrittlement at relatively low temperature on the order of 175°C.

Dynamic Strain Aging:

Skinner et al. suggested that dynamic strain aging (DSA) occurs in AA8009 at intermediate temperatures due to the sluggish diffusion of substitutional Fe and V present in the matrix. DSA was proposed as the mechanism for the loss of tensile ductility with increasing temperature and/or decreasing strain rate.

The DSA arguments focuses on work hardening and strain rate sensitivity effects on flow localization and necking. While elongation to fracture in a uniaxial tensile specimen may decline due to DSA-induced plastic instability, it is unclear how this relates to the more relevant crack tip or notch root process zone that is under complex triaxial deformation and elastic constraint. The dislocation structure of deformed AA8009 is unique in that classical forest dislocation structures are not formed. Interaction between solute atoms and forest dislocation networks, which is the cause of DSA, is thus questionable. Experiments with high purity fine grain size aluminum, reported in Task III, demonstrate that DSA is not responsible for the time-temperature dependent fracture behavior observed in AA8009.

Plastic Instability and Flow Localization:

The present SEM fractographic examination demonstrates that 8009 fails by microvoiding. Based on a systematic fractographic study by Porr [39], several factors interact to affect the fracture resistance of 8009-type alloys. Fracture initiates by microvoid nucleation at prior ribbon particle boundary oxides, followed by void growth through ribbon particles, either by secondary microvoid nucleation and growth or by cracking of locally intense deformation bands. AA8009 fractures by a different void coalescence process depending on the testing condition; results suggest void sheeting at 25°C and/or fast loading rates, and void impingement at 175°C and/or slow loading rate. An alteration in the void coalescence process is likely due to the change in the magnitude of plastic instability and flow localization in AA8009 with different testing conditions. Flow instability may be governed by complex dislocation-particle interactions that vary with test temperature.

Plastic flow localizes for several reasons. Dynamic strain aging can cause a negative strain rate sensitivity, within some temperature range that can lead to plastic instability and flow localization, as proposed by Thomason [66]. Since AA8009 appears to have a negative strain rate sensitivity within the temperature range between 175 and 200°C, it can be argued that plastic flow localization would be possible in this temperature range due to DSA. However, as proposed by Edwards et al. for zinc, containing a large volume fraction of small Al_2O_3 or W particles and with a typical grain size of 1 to 3 μm, generation of mobile dislocations at particles and limited matrix recovery can cause a similar strain rate sensitivity [67].

Lloyd and Westengen proposed that a high rate of dynamic recovery at elevated temperature in ultrafine grain sized materials can enhance plastic instability and flow localization [46,47,57,58]. They attributed the lack of intragranular dislocation substructure during deformation to the annihilation and redistribution of dislocations due to enhanced dynamic recovery process in ultrafine grain sized materials. When the grain size is similar to the mean free path for the dislocations (1 to 2 μm), the formation of dislocation cell structures is not favored within the grain interior, unlike medium to coarse grain size I/M aluminum alloys. Dynamic recovery rate increases with increasing temperature and/or decreasing strain rate. TEM micrographs of tensile deformed AA8009 supports the occurrence of dynamic recovery [59]. At elevated temperatures, oxide and silicide particles are free of dislocations and overall dislocation density is extremely low. Characteristic of recovery, any remaining dislocations are neatly arranged in arrays after high temperature deformation.

Porr suggested that flow localizes due to dislocation climb over particles at elevated temperatures in AA8009 resulting in intense shear bands between primary voids nucleated at oxide layers along the prior ribbon particle boundaries. Porr's dislocation climb mechanism in AA8009 is based on the Humphrey and Kalu model which considers that the rate of dislocation accumulation at nonshearable spherical particles is balanced by the rate of dislocation climb and/or diffusional relaxation around particles [68]. The HK model predicts that the critical strain rate, above which dislocations accumulate at particles and below which climb can dominate, is approximately 4×10^{-6} sec^{-1} at 25°C and 2×10^{-1} sec^{-1} at 175°C for AA 8009 with an average silicide particle size of 80 nm. A four to five order of magnitude increase in the critical strain rate is predicted for increasing temperature from 25°C to 175°C.

As demonstrated in Figure 17, K_{JICi} for 6.3 mm thick AA8009 plate is significantly reduced at a loading rate of about 10^{-5} mm/sec for fracture at 25°C. Data from Porr for a similar AA8009 extrusion show that such a toughness decrease occurs at a critical loading rate of about 10^{-2} mm/sec for fracture at 175°C. Accordingly, the toughness experiments indicate that the critical strain rate is increased by three orders of magnitude for increasing temperature from 25°C to

175°C. It is necessary to compare actuator displacement rates in this analysis because of uncertainties associated with calculating crack tip strain rate.

The HK model prediction of "critical" strain rate versus temperature, along with data representing AA8009, are plotted in Figure 32. For conditions where strain rate, temperature and particle diameter result in a value of $\ln(\dot{\varepsilon}Td^3)$ to the left of the deformation transition lines, dislocations climb (or diffusional relaxation occurs) around particles faster than they accumulate; when right of the line, particle-dislocation interactions result in hardening, and presumably, more homogeneous slip. Even though there is a substantial discrepancy between the predictions of the climb-based model for flow localization, and the time dependence of K_{JICi} measured at 25°C compared to 175°C, overall agreement is encouraging.

Evolution of Fracture in Al 8009

Regardless of processing route and testing condition, AA8009 fails by dimpled rupture. Void impingement-type coalescence is evidenced at elevated temperature and/or slow strain rate, in contrast to void sheeting at ambient temperature and/or fast strain rate. At 25°C, microvoids nucleated and grew from oxide-matrix interfaces, then coalesced by formation of a second population of smaller spherical voids. These secondary voids initiated at dispersoids between oxide nucleated voids, forming void sheets between oxides. At elevated temperatures, on the other hand, coalescence of voids occurred by void impingement after shear instability from intense shear that developed between oxides or growing voids on different parallel planes.

The change in microvoid coalescence may be attributed to localized plastic deformation between growing microvoids, perhaps due to the weakened dislocation-particle interactions. Weakened dislocation-particle interactions may result from dislocation climb, as proposed by Porr [24]. Dislocation climb over silicide particles has not been evidenced in deformed Al-Fe-X alloys. As demonstrated in tensile deformed AA8009 at elevated temperature [59], however, most dislocations after deformation are in the form of subgrain boundaries with neater, less ragged arrays, indicating a high rate of dynamic recovery. At 25°C, on the other hand, a high density of dislocations is evidenced around oxide and silicide particles. The lack of dislocation structures at elevated temperatures would lead to low work hardening and enhanced plastic instability.

Effect of Different Processing Route

A variety of product forms of AA8009, produced by modified planar flow casting as well as different thermomechanical processing routes, were examined in the present study. Despite reduced oxide population and homogenized microstructure from modified processing, improvements in elevated temperature fracture toughness was not observed. Beneficial dislocation structures with thermomechanical processing was not evidenced.

Effects of Modification Processes:

Modified RS processes, including Modifications A and B, successfully reduced the thickness of the hydrated oxide layer, percent oxygen and hydrogen content in AA8009, as summarized in Table 4. None-the-less, AA8009 still suffered from degraded fracture toughness at elevated temperature and slow strain rate. Moreover, the ambient temperature fracture toughnesses for Modifications A and B of AA 8009 plate are substantially lower than that of Conventional AA8009 plate. Even though the RS process modifications substantially reduced the oxide thickness on AA8009 ribbon, a considerable amount of oxide can form during compaction. Therefore, the reduced oxide population from the modified processes may not be sufficient to improve elevated temperature fracture toughness. Alternately, void nucleation at oxide-matrix interfaces, which should be affected by the change in oxide population, may not significantly affect the overall fracture toughness, especially at elevated temperature. The second notion is reasonable since the present study suggests that void coalescence, rather than void nucleation, controls the fracture behavior of AA8009. This notion is controversial, since Porr suggested that void nucleation, rather than void coalescence, is a controlling factor, based on SEM micrographs of interrupted and sectioned notched tensile specimens [39].

Modification A of AA8009 plate has a lower room temperature fracture toughness compared to both Conventional AA8009 and Modification B at the same gauge thicknesses. The explanation for this effect is uncertain. SEM fractographs in Figures 16, 21 and 26 indicate that the fracture surface of Modification A is similar to that of Conventional AA8009. A considerable amount of carbon was present in Modification B, due to contamination from the modified RS equipment. As shown in Figure 21, Modification B plate has a featureless surface with occasionally large dimples at 25°C. This fracture surface may reflect the reduced oxide population in Modification B 8009, which would provide less void nucleation sites. The large dimples may be associated with coarse quasicrystalline icosahedral carbide particles.

Effect of Thermomechanical Processing:

Thermomechanical processing was performed on extruded AA8009 at Allied-Signal to improve: (1) fracture toughness isotropy by obtaining a uniform microstructure, and (2) elevated temperature fracture resistance by both refining oxide layers on prior ribbon particle boundaries and introducing beneficial dislocation structure by cold deformation.

Thermomechanical processing has been proven to effectively reduce the fracture toughness anisotropy in AA8009 [24]. Porr reported that LT oriented AA8009 extrusion has approximately 50% higher initiation toughness than that for the TL orientation at 25°C. The TL orientation is intrinsically less tough because of prior ribbon boundary cracking and a lack of beneficial delamination which does not occur because K_{IC} is low for TL orientation. Delamination for the LT extrusion magnifies the difference in toughness. The degree of toughness anisotropy for extruded

AA8009 decreased with increasing test temperature.

Figure 33 shows blunting line offset fracture toughness values for 2.6 mm thick Modification A of AA8009 sheet at 25 and 175°C for the LT and TL orientations. These data were obtained by Fracture Technology Associates (FTA) employing the ASTM-standard unloading compliance method to define J-Δa. This figure shows that the TL orientation has approximately 30% higher toughness than LT for the 2.6 mm thick sheet. The final rolling direction for cross-rolling is always perpendicular to the initial extrusion direction. Accordingly, if an orientation is expected to be lower toughness, it would be the LT case in cross-rolled plate, as controlled by fracture along the original extrusion-aligned prior ribbon boundaries. Compared to the AA8009 extrusion, however, toughness anisotropy is substantially diminished with thermomechanical processing.

Thermomechanical processing did not induce beneficial dislocation structure that lead to improved elevated temperature fracture toughness. As shown in Figures 24 and 29, thermomechanical processing to increasingly thin sheet slightly degraded fracture toughness at each test temperature. Increased rolling reduction, either hot and cold, affects the oxide population and perhaps the dislocation substructure. These factors are likely to each influence the intrinsic deformation, flow localization, and fracture resistance of AA8009-type alloys. Additionally, rolling affects yield strength and work hardening; these factors, coupled with intrinsic fracture resistance, affect temperature-dependent K_{IC}.

Refined oxide layers and reduced spacing between those layers with increasing rolling reduction to sheet was demonstrated for AA8009 (Figure 23) [59]. SEM studies on as-received Conventional AA8009 plate and sheet showed that the average interplanar spacing between the oxide stringers on prior ribbon particle boundaries was reduced from 7 μm for 6.3 mm thick plate to 2 to 5 μm for 1.0 mm thick sheet. Refined oxide layer should increase the applied strain required for void nucleation. On balance, void growth could be facilitated by rolling reduction, because of decreased intra ribbon particle spacing between the void nucleating oxides at 25°C. At elevated temperature, rolling reductions in prior ribbon particle thickness may not affect void growth if governed by local shear.

Cold rolling to 1.0 mm thick sheet from 10.0 mm thick extrusion forms subgrain boundaries within the existing solidification-produced subgrains, resulting in a further refined subgrain structure [59]. Such subgrain boundaries may act as sinks for dislocation annihilation during deformation, and dynamic recovery would be generally favored for the finer subgrain structure. The enhanced dynamic recovery would lead to lower work hardening and intensify the localized deformation. Reduced work hardening and flow localization would, in turn, induce strong shear bands between voids formed at oxide layers. SEM fractographs of thinner gauges of Conventional AA8009 sheet, as shown in Figure 26, suggest enhanced flow localization with

increased thermomechanical processing. Void impingement-type coalescence process is notable on the fracture surface of thinner gauges of 8009 even at 25°C.

If the aforementioned notion is correct, the same gauge thickness of cold rolled AA8009 should have higher ductility and fracture toughness at each temperature, compared to hot rolled sheet. Dynamic recovery is favored during hot rolling and should promote a fracture-prone microstructure. Notably, however, any difference in tensile ductility and fracture toughness between cold rolled and hot rolled AA8009 sheet is within experimental error as shown in Figures 27, 28, and 29. Moreover, intermediate annealing after cold rolling had no effect on tensile ductility or fracture toughness. A plausible speculation is that with such a severe rolling of almost 1000% reduction, the microstructure of each sheet was fully recovered.

Conclusively, cold rolling does not enhance the fracture toughness of AA8009. In contrast Westengen observed that a 4% cold prestrain by rolling produced a 50% increase in the tensile elongation to fracture for an ultra-fine grain size aluminum alloy [46]. He suggested that this is due to suppressed plastic instability by activating dislocation sources throughout the grains which otherwise do not have a mobile dislocation density to enable work hardening. Such dislocation sources within the small grains were neither specified nor evidenced. Additionally, uniaxial tensile elongation data, governed by necking instability, may not be relevant to ductility and fracture toughness. In the present study, the magnitude of the rolling reduction was between 100% and 1000% of the original thickness. Dislocations which are activated at a relatively early stage of rolling deformation may be annihilated during the final stage of rolling.

Dynamic recovery would be favored with refined microstructure due to the rolling reduction. Enhanced dynamic recovery would lead to lower work hardening and intensify localized deformation. Accordingly, tensile ductility and fracture toughness decrease with increasing rolling reduction, producing a decreasing size of subgrain structure, superimposed on the effect of rolling reduction on the oxide population. It is presently not possible to establish the relative contributions of oxide-based factors and slip localization/work hardening-based factors.

Conclusions

The effects of temperature and loading rate on the fracture toughness of AA8009 plate and sheet, processed by either conventional rapid solidification or modified RS and by a range of thermomechanical routes, were examined by using J-integral fracture mechanics. Several conclusions were drawn.

1) The initiation fracture toughness of AA8009 decreases with increasing temperature and decreasing loading rate, regardless of processing route and product form.

2) Time-temperature-dependent degradation in AA8009 fracture toughness is not due to delamination toughening, hydrogen embrittlement, or dynamic strain aging.

3) AA8009 fracture is by microvoid processes initiated at boundary oxides, regardless of processing route and test condition; a single size of shallow dimples characterizes low toughness cracking.

4) The likely mechanism for time-temperature-reduced toughness is localized plastic deformation between growing microvoids; flow instability truncates stable void growth.

5) The flow localization appears to be promoted by several factors, including low work hardening without dislocation substructure, dynamic recovery, dislocation evasion of silicides, and discontinuous dislocation emission.

6) The lack of dislocation structure in AA8009 is attributable to dislocation-climb assisted dynamic recovery at elevated temperature, leading to low work hardening and plastic flow localization developing locally intense shear bands between oxide particles.

7) Thermomechanical processing degrades fracture toughness due to the reduced oxide sheet spacing coupled with dynamic recovery and reduced work hardening.

8) Modified processes to reduce the oxide population and total dissolved hydrogen content of AA8009 do not ameliorate the loss of damage tolerance at elevated temperature.

IV. TASK III---DEFORMATION AND FRACTURE MECHANISMS IN SUB-MICRON GRAIN SIZE ALUMINUM ALLOYS

S.S. Kim, M.J. Haynes, and R.P. Gangloff

Abstract

Advanced aluminum alloys with thermally-stable submicron grains, fine dispersoids, and metastable solute are limited uniquely by reduced ductility and toughness at elevated temperatures. The mechanism is controversial. Experimental results for cryogenically milled oxide dispersion strengthened pure aluminum (CM Al) extrusion; with 3 volume pct of 20 nm Al_2O_3, and a 0.5 μm grain size, establish that uniaxial tensile ductility, plane strain crack initiation fracture toughness (K_{JICi}), and tearing resistance (T_R) decrease monotonically with increasing temperature from 25 to 325°C. Fracture is by microvoid processes at all temperatures; reduced toughness correlates with changed void shape from spherical to irregular with some faceted walls. Strain-based micromechanical modeling predicts fracture toughness, and shows that temperature-dependent decreases in K_{JICi} and T_R are due to reduced yield strength, elastic modulus, and intrinsic fracture resistance. Since CM Al does not contain solute such as Fe, dynamic strain aging is not necessary for low-toughness fracture at elevated temperature. Rather, increased temperature reduces work and strain-rate hardening between growing primary voids, leading to intravoid instability and coalescence at lowered strain. Decreased strain-rate hardening is attributed to increased mobile dislocation density due to dislocation emission and detrapping from dispersoids in dynamically recovered dislocation source-free grains.

Introduction

Advanced rapidly solidified (RS) or mechanically alloyed (MA) powder metallurgy (PM) aluminum alloys, with submicron grain size and a substantial volume fraction (5 to 30 vol pct) of small (20 to 200 nm diameter) dispersoids, are candidates for next generation light-weight elevated temperature structures [69-71]. The microstructures and ambient-temperature tensile properties of such alloys are stable after prolonged high temperature exposure, however, tensile elongation and fracture toughness decrease with increasing deformation temperature above 25°C, and with decreasing strain rate, in sharp contrast to ingot metallurgy (IM) precipitation hardened aluminum alloys [42,49].

For example, sheet, plate and extrusion of melt spun RS aluminum alloy (AA) 8009 [5] exhibit a 50% decrease in tensile ductility and an 80% or more decrease in fracture toughness with increasing test temperature from 25 to 200°C [24,39,42,49,72]. Preexposure at 350°C for hundreds of hours has no effect on strength or ductility measured at 25°C. Reduction-in-area and total elongation-to-fracture are a minimum at a temperature that increases with increasing strain rate [24,39,42,49,72], but the initiation fracture toughness of AA8009 declines without a minimum [24]. The temperature dependence of fracture toughness was traced to a degradation in intrinsic fracture resistance, rather than an extrinsic change in the crack tip stress and strain distributions that drive fracture [24].

Several mechanisms have been proposed for the unique time-temperature-dependent fracture behavior of submicron grain size, dispersoid-bearing Al alloys. Changes in the amount of crack tip constraint (so-called delamination toughening) [51,73,74], as well as embrittlement due to dissolved hydrogen from RS-powder processing or environmental exposure, were shown to be unlikely causes of reduced intrinsic ductility and toughness at elevated temperatures [24,39,55]. Rather, reduced fracture resistance was attributed speculatively to strain localization between growing microvoids [24,39,72]; due to reduced work hardening (or softening) [75], reduced strain rate hardening, or dislocation-particle-boundary interactions. Such behavior is unique to submicron grain size aluminum alloys, with dispersoids but without intragranular dislocation cell structure due to dynamic recovery [46,57,58].

Alternately, dynamic strain aging (DSA) was reported to govern deformation and, by inference, fracture of Al-Fe-X alloys [40,42,56]. Mg promotes DSA in cast and wrought aluminum alloys at temperatures below about 100°C; DSA in-turn causes plastic flow localization and shear fracture at reduced uniform tensile elongation [77,78]. Skinner et al. argue that Fe and V similarly interact with dislocations, and that this DSA is most apparent at temperatures above 100°C due to the sluggish diffusion of substitutional solute such as iron [42]. This view was supported by Scanning Transmission Electron Microscopy (STEM) measurements of a high (~1 atom percent) solid solution Fe concentration in RS AA8009, correlation between temperature-dependent minima in tensile elongation to failure and strain rate sensitivity, and comparison of activation energies for deformation and Fe diffusion. Fracture of AA8009-type alloys was not, however, defined sufficiently to prove the role of DSA.

The fracture mechanism uncertainty is, therefore, centered on the cause of flow localization between growing microvoids [24,39]; be it derived from DSA, dislocation-dispersoid-grain

---

5 AA8009 (Al-8.5%Fe-1.3%V-1.7%Si, weight pct) has a grain size of 0.3 to 0.5 μm and contains 25 volume pct of 50 to 100 nm diameter al_{13} $(Fe,V)_3Si$ particles [43].

boundary interactions, or both processes. Luton and coworkers produced ultrafine grain aluminum by ball-milling elemental Al and alumina powders at cryogenic temperatures [79]. Grain size is refined by Al_2O_3 and AlN particles from reactive mechanical alloying, and is stable during subsequent powder compaction and hot extrusion processing. Supersaturated Fe, Cr, Si or V are not present in solid solution. Accordingly, this material provides a means to isolate the contributions of DSA and fine grain size/dispersoids to elevated temperature deformation and fracture. These features are coupled in RS alloys such as AA8009.

The objective of this research is to characterize the time-temperature-dependent fracture resistance of cryogenically milled oxide dispersion strengthened pure aluminum (CM Al), at temperatures between ambient and the moderately elevated levels where ductility and fracture toughness could decrease. Goals are to test the importance of DSA compared to the grain size/dispersoid-based mechanism for fracture, and to model fracture toughness.

Procedures

Extruded plate (6.4 mm thick) of CM Al was provided by Exxon Research and Engineering Co. Elemental aluminum powder (99.99% pure) was mixed with 3 volume pct of Al_2O_3 powder and ball-milled in a liquid nitrogen slurry for five hours at -196°C. Milled powders were degassed at an elevated temperature, compacted, and extruded at 460°C to form plate. Extrusions were not heat treated.

Uniaxial tensile experiments were conducted at temperatures between 25 and 325°C. Round specimens were prepared with the loading axis parallel to the extrusion (L) direction. A capacitance extensometer was used to measure L-direction displacement over a 25.4 mm uniform gauge length at 25, 175 and 250°C. A grip displacement rate of 12.7 μm/sec was employed, yielding a nominal strain rate of 5×10^{-4} sec^{-1}.

Compact tension (CT) specimens with a width of 38.1 mm were prepared from the extrusion in the L-T orientation. Sidegrooves (gross specimen thickness = 6.3 mm and net thickness = 5.1 mm) were used to increase through-thickness constraint. Specimens were fatigue precracked at a maximum stress intensity (K_{max}) of 7 MPa$\sqrt{m}$ to an a/W ratio of 0.5 ± 0.05.

Resistance-curve fracture toughness experiments were conducted with a closed-loop servo-electric machine under constant grip displacement rate control, as detailed elsewhere [19,24,39,62]. Crack growth (Δa) was determined by direct current electrical potential difference (dcEPD) measurements, as a function of the applied J-integral. The plastic component of J was determined from calculated unloading compliance, and the elastic component from a standard stress intensity (K) solution. J-Δa data were analyzed to establish: (1) the small-scale yielding stress

intensity at the first dcEPD detection of crack propagation (the plane strain initiation toughness, J_{ICi}, or $K_{JICi} = \{[J_{ICi}E]/[1-\nu^2]\}^{1/2}$), (2) a standard measure of the initiation fracture toughness (K_{JIC}) [80], and (3) the plane strain tearing modulus (T_R). [81] [6] Fracture toughness experiments were conducted at temperatures between 25 and 325°C in a forced-circulating air oven mounted on the testing system. CT and tensile specimens were heated to temperature in 45 minutes and maintained for 60 minutes prior to loading.

Results

Microstructure

The composition of CM Al in Table 5, measured by LECO and atomic absorption spectroscopy, is consistent with the processing route. The addition of 3.0 volume pct of Al_2O_3 provides a calculated elemental oxygen concentration of 2.05 weight pct compared to the measured level of 2.04 weight pct. The high level of nitrogen is probably due to AlN formation during cryogenic milling. Since less than 0.01 weight pct Fe was present in the starting powders, the high Fe content is most likely from contamination by fractured particles from the stainless steel milling balls and vessel wall. The optical micrograph of as-polished CM Al in Figure 34 shows infrequent large particles, sized between 2 and 20 μm. Image analysis established that the amount of these inclusions is 0.43 volume pct. Energy dispersive X-ray analysis of particles with the Scanning Electron Microscope (SEM) (e.g., the SEM micrograph in the inset of Figure 34) showed that these particles contain 32 weight pct Fe in addition to Al, Si and Cr. This composition is consistent with stainless steel contamination. These results account quantitatively for the measured iron level of 0.12 weight pct, consistent with the view that there is no reason for iron to be present in solid solution in CM Al powders, above the solubility limit of about 10^{-4} weight pct. Other than the few iron-based inclusions, the microstructure of CM Al is free of micron or larger constituent phases. The submicron-sized particles suggested in Figure 34 were not identified by optical or scanning electron microscopy, and the grain size was not resolvable.

The grain size of CM Al is 0.4 to 1 μm, as shown by the TEM micrograph in Figure 35a. Figure 35b shows that the diameter of individual Al_2O_3 dispersoids is about 10 to 20 nm, and that clusters of dispersoids are present with an effective diameter of about 100 nm. Occasional rod-type carbides are apparent, as determined by STEM of several particles. (These larger carbides may correspond to the small-particle structure suggested in Figure 34.) Neither AlN nor

---

6 $T_R = [dJ/d\Delta a][E/\sigma_o^2]$, where E is modulus, v is Poisson's ratio, σ_o is flow strength, and $dJ/d\Delta a$ is determined by linear regression of Δa data from 0.15 to 1.5 mm.

submicron sized iron-chrome particles were observed by TEM. The total fraction of Al_2O_3, plus unresolved AlN dispersoids was not measured, however, it may exceed the amount of alumina added, 3 volume pct, due to powder reactions during milling.

Tensile Properties

Figure 36 presents true tensile stress-true strain (σ-ε) data for CM Al, deformed to maximum load at 25, 175 and 250°C. The work hardening parameter (n) was determined by regression analysis of the slope of the linear relation between log σ and log plastic strain (ε_p), consistent with the Ramberg-Osgood flow curve [41]. Table 6 shows the 0.2 pct offset tensile yield strength (σ_{YS}), ultimate strength (σ_{UTS} or σ_{TS}), ductility (reduction in area at fracture, RA), total strain at maximum load, and n for CM Al at test temperatures of 25 to 325°C and a nominal strain rate of 5×10^{-4} sec^{-1}. The temperature dependencies of σ_{YS}, σ_{UTS} and RA are shown in Figure 37. CM Al exhibited a relatively low proportional limit, high work hardening rates at low ε_p, and low average work hardening thereafter. Serrated flow was not observed. While the n values in Table 6 indicate temperature-independent hardening, the data in Figure 36 suggest that the average hardening capacity of CM Al decreased with increasing temperature. Since necking occurred at decreased and low uniform strains at 175 and 250°C, data are insufficient for accurate assessment of the temperature dependence of hardening, and of the possibility that work softening occurred beyond maximum load [75]. (The n values in Table 6 include a contribution from the low strain regime where log ε_p depends nonlinearly on log σ.) Compression experiments are required to better define the flow properties of CM Al over a range of strain, strain rate and temperature.

Unlike conventional large grain-size aluminum alloys, which exhibit improved tensile ductility at elevated temperatures, the ductility (as well as the modulus and yield strength) of CM Al decrease with increasing temperature to 325°C, as shown in Figure 37. RA for CM Al does not exhibit a minimum for temperatures between 25 and 325°C; similar to the behavior of AA8009, but contrary to the temperature-dependent minimum of total elongation to fracture for RS Al-Fe-X alloys [24,39,40,42]. The limited data in Figure 36 suggest that uniform elongation to necking declines with increasing temperature, but may exhibit a minimum or plateau below 250°C.

Figure 38 shows macroscopic side-views of CM Al tensile specimens fractured at: (a) 25°C and (b) 175°C. For this uniaxial tensile geometry, necking and a cup-cone fracture mode occurred at 25°C; however; at 175°C, the fracture surface was slanted to the tensile (L) axis at an approximate angle of 40°, indicating a localized shear instability. Figure 39 shows SEM

fractographs of CM Al tensile specimens fractured at: (a) 25°C and (b) 175°C. The fracture mode is dimpled rupture, regardless of testing temperature, but the dimple morphology appears to change with increasing temperature. Detailed analysis of the CM Al fracture morphology is deferred to the section on the SEM study of CT crack surfaces.

Fracture Toughness

Table 7 and Figure 40 present plane strain fracture initiation toughness, K_{JICi}, and tearing modulus, T_R, results for the L-T orientation of CM Al at two constant grip displacement rates, and as a function of temperature to 325°C. K_{JICi} data for ingot metallurgy AA2618 [39], as well as standard-based K_{JIC} for CM Al [80], are included. The J-integral characterization of toughness accounted accurately for plastic deformation and provided reasonable measurements of plane strain initiation and plane strain tearing-resistance fracture toughnesses [19,24,62,80,81]. Plane strain constraint was substantial for all toughness levels examined and fracture was normal to the Mode I load without shear elements.

K_{JICi} underestimates plane strain fracture toughness compared to elastic (K_{IC} from ASTM Standard E399 [82]) or elastic-plastic (K_{JIC} from ASTM Standard E813 [80]) methods with an offset blunting line definition of crack initiation. The room temperature K_{JIC} value of 24 MPa$\sqrt{m}$ for CM Al is reasonably high, and K_{JIC} is greater than K_{JICi} at each temperature between 25°C and 325°C (Table 7). K_{JICi} is emphasized here because it is independent of alloy tearing resistance and mixed mode plane strain-plane stress cracking, and is relevant to modeling [19,24,61,62]. The temperature dependencies of K_{JICi} and K_{JIC} are identical for CM Al (Table 7).

The temperature dependencies of the fracture toughnesses of CM Al mirror that of tensile ductility; K_{JICi}, K_{JIC}, T_R and RA each decrease with increasing temperature. Temperature-dependent minima in these properties are not observed, at least between 25°C and 325°C. The tendency for reduced toughness with decreasing crack tip strain rate is indicated in Table 7; K_{JICi} for CM Al decreases from 13.6 MPa$\sqrt{m}$ to 11.0 MPa$\sqrt{m}$, and T_R from 22.1 to 4.7, with decreasing grip displacement rate from 2.5 μm/sec to 0.005 μm/sec at 25°C.

Microscopic Crack Surface Morphology

CM Al compact tension specimens fractured at 25°C exhibited several (2 to 6) large delaminations, approximately perpendicular to the fatigue and Mode I fracture toughness crack planes, as illustrated by the low magnification SEM fractograph in Figure 41a. This behavior is typical of extruded RS PM aluminum alloys and may be caused by oxide inclusions on powder particle surfaces [73,74]. The number of delaminations is less for CM Al compared to extruded AA8009, for the same side-grooved CT specimen geometry [24,39]. This difference is probably

due to the large amount of ribbon surface oxide, produced during melt spinning of AA8009 in moist air, compared to limited powder surface oxidation during cryogenic milling and subsequent powder handling for CM Al.

The number of delaminations decreased and the amount of stable crack growth prior to delamination increased with increasing test temperature. Delaminations were similar at 25°C and 80°C (e.g., Figure 41a). Delaminations occurred at 125°C and 175°C, but only after 0.5 mm of crack advance, as shown by the SEM fractograph in Figure 41b. (Delamination at 25°C occurred closer to, but not precisely at, the fatigue precrack front (Figure 41a).) CM Al did not delaminate during loading to K_{JICi} at either 215, 250, or 325°C, as illustrated in Figure 41c.

Fracture of CM Al evolves during straining by microvoid nucleation, growth and coalescence at all temperatures. Figure 42 shows SEM fractographs of CT fracture surfaces produced at a single grip displacement rate of 2.5 μm/sec, and at either 25°C (a, b and c) or 175°C (d, e and f). These fractographs were obtained at the specimen mid-thickness, for Δa between 50 and 200 μm, and represent the plane strain initiation toughness. Dimple morphology changes significantly with increasing temperature. At 25°C a bimodal distribution of dimples is observed; 1 to 3 μm diameter dimples are interspersed with 0.5 μm dimples. Figure 42a shows evidence of surface roughness, manifest as walls on the fracture surface and inclined 50° to 90° from the average Mode I crack plane. These walls are visible in Figure 42a as bright regions and are covered by the smaller dimples. Dimples produced by plastic deformation at 25°C are spherical and well-developed, as demonstrated in Figures 42b and 42c. Stereofractographic observations, not reproduced here, confirmed that the 25°C dimples are spherical holes. Microscopic delaminations were not observed on CM Al fracture surfaces produced at 25°C or any higher temperature.

The CM Al fracture surface produced at 175°C shows significant roughness on the microscopic scale, Figure 42d. Dimples range in diameter from 1 to 2 μm, but are less well-developed compared to the 25°C case. For example, note the discontinuous dimple perimeters and walls that form triple-point junctions in Figures 42e and 42f. The morphology shown in the upper-right portion of Figure 42f is the dominant feature of elevated temperature fracture in CM Al. When dimples are well developed (e.g., the lower left of Figure 42f), the perimeters form polygonal shapes (pentagonal or hexagonal), dimple walls are faceted and triple-point features are present when wall-facets intersect. The 175°C dimples were often elongated in the Mode I crack opening direction. The comparison between Figures 42c and 42f shows the difference between the 25 and 175°C dimpled-fracture morphologies.

The features shown in Figure 42f could be interpreted as intergranular fracture, however, this is not the case. Figure 43 summarizes a high-magnification, matching crack surface,

stereofractographic analysis of the CM Al CT fracture surface produced at 175°C. Figures 43a and 43b are a stereo-pair of a single area on one-half of the crack surface, while Figures 43c and 43d are a stereo-pair of the identical area on the matching half of the fracture. (These four images are viewable simultaneously in a stereo-viewer.) By inverting Figures 43a and 43b, top-to-bottom, over the bottom two images, the three-dimensional character of microscopic fracture features is revealed. For example, the three areas marked a, b and c in Figures 43a and 43c match across the crack plane. Stereo-viewing of either 43a/b or 43c/d showed that holes are the predominant feature on each fracture surface. In all cases examined, a hole on one-half of the crack surface matched a hole on the mating half. Interlocking features that are typically produced by intergranular cracking were never observed for CM Al at 175°C (or at 25°C).

Dimpled rupture is confirmed as the dominant fracture mode for CM Al at elevated temperatures. Reduced toughness at 175°C correlates with the mixture of poorly developed dimple-like features and the unusual faceted nature of the dimples, with no interspersed small dimples, compared to the bimodal distribution of well-defined spherical holes formed at 25°C. A similar result was reported for AA8009 based on a detailed matching-surface stereofractographic analysis [39]. A bimodal distribution of spherical dimples was produced at 25°C; while a single population of shallow lenticular dimples, with a depth to diameter ratio of about 0.3, correlated with reduced toughness at 175°C. The dimple geometry in RS PM AA8009 sheet was affected by the spacing of sheets of prior (ribbon) particle boundary oxide that are not present in CM Al. Intergranular fracture was not observed for AA8009 at any temperature [39].

CM Al fracture behavior at 250 and 325°C was examined by SEM, but not in detail because the toughness reduction of interest occurred between 25 and 175°C. The morphologies shown in Figures 42d through 42f, as well as in Figure 43, were typically observed for CM Al cracks produced at 250 and 325°C. Additionally, there was evidence of localized superplastic deformation between dimples growing at the highest two temperatures. This phenomenon was reported previously for creep crack growth in submicron grain size RS PM aluminum alloys, including AA8009 [83,84], and is not a central feature of the decline in fracture toughness up to about 200°C.

Discussion

The plane strain crack initiation and growth fracture toughnesses (Figure 40 and Table 7) as well as the tensile ductility (Table 6) of submicron grain size, oxide-dispersion-strengthened, cryogenically milled aluminum decrease monotonically with increasing temperature and perhaps with decreasing loading rate. This behavior is analogous to that of RS and MA PM aluminum alloys [24,39,40,42,49,55,56,72,76], at least for temperatures up to 325°C, and is in sharp

contrast to the fracture of IM aluminum alloys with coarser microstructures. This discussion will establish that DSA is not the sole cause of this behavior; rather, dislocation interactions with dispersoids in submicron grains lead to localized plastic deformation and reduced toughness.

The extent to which fracture properties exhibit a temperature-dependent minimum is important for mechanistic interpretation [42]. The intrinsic fracture resistance of CM Al, approximated by tensile RA, declines with increasing temperature, but does not exhibit a minimum below 325°C. The minima reported in the tensile elongation of AA8009, at strain rate-dependent temperatures between 150°C (9×10^{-5} sec^{-1}) and 225°C (9×10^{-2} sec^{-1}), and of an Al-Fe-Si-V with a lower volume fraction of silicide between 100°C (9×10^{-5} sec^{-1}) and 200°C (9×10^{-2} sec^{-1}) [42], are not directly representative of ductility. The more relevant RA exhibited a very mild minimum near 200°C for extruded AA8009, and a low ductility plateau above 200°C without a minimum for plate AA8009 (at least to 316°C) [24]. The initiation toughness is a simple fracture mechanics parameter to consider; K_{JICi} decreased monotonically, without a minimum for extruded CM Al between 25°C and 325°C, similar to both extrusion and plate of AA8009 at temperatures between 25°C and 316°C [24]. The tearing modulus of CM Al declined monotonically over this temperature range, however, T_R passed through a minimum at about 175°C for extrusion and plate of AA8009 [24].

Micromechanical Modeling

Continuum fracture mechanics concepts provide a first step to understand the factors that control temperature-dependent toughness.

Delamination Toughening:

Extrinsic delamination toughening of CM Al complicates interpretation of temperature dependent K_{JICi}, K_{JIC} and T_R [51,65,73,74,85,86]. The issues are: (a) the extent to which delamination at 25°C elevates toughnesses above intrinsic plane strain values, and (b) the likelihood that the elimination of this mechanism with increasing temperature (Figure 41), explains decreasing toughness trends.

Results for CM Al indicate that delamination does not govern intrinsic fracture initiation toughness and the deleterious effect of elevated temperature, but may affect K_{JIC} and T_R. Electrical potential measurements indicate the precise value of the critical stress intensity level, K_{JICi}, corresponding to between 25 μm and 50 μm of crack extension localized in the mid-50% of the CT specimen. SEM analysis of the CM Al specimens represented in Figure 41 showed that delamination did not occur within this region for any temperature examined. Rather, delamination occurred after the initiation event, as easily seen in Figure 41b. Since T_R and K_{JIC} reflect stable

crack growth, delamination at 25°C possibly elevated these toughnesses above intrinsic values. This contribution declined with increasing temperature. For the 25°C case in Table 7, the low value of K_{JICi}, and the higher values of K_{JIC} and T_R are consistent with this argument. As the extent of delamination increases, T_R decreases to zero and K_{JIC} approaches K_{JICi}. This secondary role of delamination is consistent with the relatively low values of toughness for CM Al compared to results for classic delaminating alloys such as Al-Li-Cu [65].

Three factors contribute to declining delamination with increasing temperature; increasing boundary strength, decreasing alloy flow strength and decreasing intrinsic fracture resistance [24,65]. There is no mechanism or data showing that boundary fracture resistance increases with increasing temperature for PM Al alloys. Second, σ_{YS} for CM Al declines by 40% between 25 and 325°C (Table 6), suggesting a similar decrease in crack tip process zone stresses, normal to the delamination plane and existing over a critical distance.[7] Third, an intrinsic low-toughness fracture process intervened to limit applied stress intensities to below the level necessary for delamination. The secondary importance of delamination toughening was substantiated for AA8009; K_{JICi} and T_R decreased with increasing temperature for plate and sheet alloys which did not delaminate at any temperature [24].

Prediction of Initiation and Growth Fracture Toughnesses:

Micromechanical modeling of several IM and RS PM aluminum alloys demonstrated that K_{JICi} and T_R are governed by the interplay between the temperature-dependent crack tip strain distribution (alloy modulus, n and σ_{YS}-dependent), and process zone damage resistance (related to alloy RA) [19,24,61,85,86]. Temperature-dependent K_{JICi} and T_R were well-predicted with a single adjustable parameter.

The toughness of CM Al was predicted by strain-based crack tip modeling.[8] Input parameters included temperature-dependent E, n, σ_{YS}, and the critical effective plastic strain to nucleate crack tip microvoid damage (ε_f^P). Temperature-dependent elastic modulus was based on

---

7 Each normal component of the crack tip stress field within the plastic zone is proportional to a work hardening- dependent multiple of σ_{YS}, while the distance over which such stresses are elevated scales with stress intensity [85].

8 The detailed fracture mechanics basis, assumptions, specific equations and shortcomings of the models for K_{JICi} and T_R are detailed elsewhere [19,61,85,86]. The purpose of the analysis here is to show the roles of temperature- dependent tensile properties in affecting fracture toughness.

data for pure aluminum (E = 72, 68, 66, 64, 63, 62 and 58 GPa at 25, 80, 125, 175, 215, 250 and 325°C, respectively) [87]. ε_f^P was approximated by -ln(1 - pct RA/100) divided by a plane strain constraint factor (r) of 7 [19,61,86]. Three mildly temperature-dependent constants (C_1, C_2 and d_N) were used to describe the crack tip strain field [61].[9] The critical distance over which crack tip damage is produced (l*) was calculated to equal 10 μm from the measured K_{JICi} at 25°C (Table 7). This distance is of the correct order of magnitude and is assumed to be constant with increasing temperature because of the invariant CM Al microstructure and microvoid fracture mode. l* is not relatable to a specific microstructural feature because of modeling uncertainties [61].

With these values, the strain-based initiation toughness model reasonably predicted absolute values and the monotonic decline in K_{JICi} with increasing temperature for CM Al, without a minimum for temperatures between 25 and 325°C. These model predictions are compared with experimental results in Table 7 and Figure 44. Predicted toughnesses are within 30% of measured values for any temperature between 25 and 325°C. The plane strain tearing modulus model [86] predicts declining T_R with increasing temperature, without adjustable parameters. Predicted values are lower than measured T_R, particularly for the 25°C case where the measurement is high due to delamination toughening that is not included in the model. For the higher temperature cases, predicted T_R is less than zero, indicating unstable crack growth without resistance to tearing. As indicated by the values in parentheses in Table 7, predicted T_R is increasingly negative with increasing temperature, as controlled by the constant, Ω, ($\Omega = E\ \varepsilon_f^P / r\ \sigma_{YS}$) that decreased with increasing temperature. A modest change in the constants in the tearing modulus model (e.g., r) would result in excellent agreement between the measured and predicted tearing modulus. This model suggests either a low T_R plateau or minimum at a temperature near 175°C.

For conventional aluminum alloys, E, n and σ_{YS} decrease with increasing temperature, tending to reduce K_{JICi} and T_R; however; ε_f^P increases, with the net effect of a constant or increasing toughness with increasing temperature [19]. In contrast the adverse effect of temperature on the initiation and growth fracture toughnesses of CM Al is traced to the

---

9 C_1 and C_2 are curve fitting constants that describe the distribution of plastic strain with distance ahead of the crack tip. d_N is the proportionality constant relating blunted crack tip opening displacement to applied J. These parameters depend mildly on work hardening, and hence on temperature. Single values of C_1 (0.126) and C_2 (1.23) were employed because CM Al is essentially elastic-perfectly plastic at each temperature considered. For the highest work hardening level (n = 0.03, Table 6) to the lowest (n = 0), d_n varies from 0.68 to 0.78. This constant was equated to 0.70 for each temperature.

temperature-dependent decline in intrinsic ε_f^P, analogous to the behavior of RS AA8009 [24]. Either K_{JICi} or T_R could exhibit a temperature-dependent minimum or plateau, because of the relative temperature dependencies of the material flow and fracture properties. From a mechanistic perspective, the inverse temperature dependence of the intrinsic fracture resistance of CM Al and 8009-type alloys is centrally important; the mechanism for this behavior is controversial.

Dynamic Strain Aging

The results in Tables 6 and 7, as well as in Figures 37 and 40, demonstrate that dynamic strain aging is not the sole cause of elevated temperature reductions in tensile ductility and fracture toughness for submicron grain PM Al alloys. The temperature dependencies of RA, K_{JICi} and T_R are identical for CM Al and RS alloys such as AA8009 between 25 and 325°C. The former alloy does not contain Fe, V or Cr in metastable solid solution, while the latter may. If DSA is the only mechanism for reduced intrinsic fracture resistance, then ε_f^P, K_{JICi} and T_R should not decrease with increasing temperature for low solute CM Al, counter to the experimental results. A mechanism other than DSA, or acting in concert with DSA, causes reductions in ductility and toughness at elevated temperature for submicron grain PM Al alloys.

In the literature, DSA has not been linked irrefutably to fracture in Al-Fe-X alloys. STEM measurements revealed about 1 atomic percent of iron in the matrix of RS Al-Fe-Si-V [42,56], however, such experiments were not documented in detail and may be complicated by the large amount of $Al_{12}(Fe,V)_3Si$ particles relative to the volume of electron beam-affected matrix. The DSA argument for RS PM alloys was not supported by fracture surface and microscopic fracture mechanism analyses or modeling [42,56]. Rather, DSA was inferred from uniaxial tensile elongation data which are not necessarily relevant to intrinsic fracture resistance. Temperature-reduced RA-ductility and intrinsic toughness parameters for CM Al (and AA8009) did not exhibit the minima observed for elongation-to-fracture and analyzed to support DSA in Al-Fe-Si-V alloys. The mechanism for DSA in the dislocation substructure unique to ultrafine grain size alloys, particularly the lack of intragranular dislocation cells [46,57,58,69,72,75,76], has not been considered in contrast to forest dislocation and vacancy models of strain aging in conventional alloys [78,88-90]. The temperature and strain rate dependencies of flow stress; taken as indicative of DSA in Al-Fe-Si-V, Al-Cr-Zr and Al-Fe-Ce alloys [40,42,56]; are equally rationalized based on dislocation interactions with dispersoids in submicron grains, as developed in an ensuing section.

Localized Plastic Deformation and Instability

Hypothesis:

A new hypothesis is presented for the deleterious effect of increasing temperature on the intrinsic fracture resistance of CM Al, and possibly other RS PM alloys. Primary voids, growing from oxide or dispersoid-cluster nucleation sites, coalesce at reduced strains with increasing temperature because of increasing intravoid plastic instability. Elevated temperature, and the tendency for increased strain rate between microvoids in any microstructure, promote strain localization due to: (1) thermally activated recovery that eliminates dislocation cell and source structure within ultrafine grain interiors, and (2) dispersoids in ligaments between growing microvoids providing a mobile dislocation source and hence decreasing flow resistance with increasing strain rate.

In essence dislocation-dispersoid interactions in cell-free submicron grains provide a means, other than DSA, for enhanced void growth and coalescence within a window of temperature and time. Outside of this window, or for large grains with many dislocation sources, work and strain rate hardening are sufficient for stable growth of primary microvoids, resulting in high ductility and fracture toughness that increase between 25°C and 350°C. This hypothesis is supported, as follows, by results for CM Al and AA8009 coupled with literature on flow localization and dispersoid-particle interactions in submicron size grains.

Plastic Instabilities in CM Al and RS 8009:

Results for CM Al indicate the importance of shear instability and localized deformation in microvoid fracture. The flat (cup and cone) to slant fracture mode transition for uniaxial tensile specimens of CM Al (Figure 38) suggests that a macroscopic plastic instability is favored at higher temperatures. This behavior was reported for RS AA8009 [39] and Al-Si [73] as well as certain IM alloys [78], but is not typically observed for IM precipitation hardened aluminum alloys. Second, the transition from a bimodal distribution of spherical dimples to the irregularly formed and faceted dimples in CM Al (Figures 42 and 43), or to the shallow lenticular dimples in AA8009 (7), suggests that stable microvoid growth is truncated by intravoid ligament flow localization at elevated temperatures.

Evolution of Microvoid Fracture in Ultrafine Grain Al Alloys:

Thomason argues that, with increasing temperature: a) microvoid nucleation at particle interfaces requires higher applied strain since matrix recovery reduces interface stress, b) microvoid growth rate increases due to reduced work hardening, and c) microvoid coalescence is retarded by increasingly strain rate ($\dot{\varepsilon}$)-sensitive flow strength, σ_o (increasing m in the relation $\sigma_o = K \dot{\varepsilon}^m$) [66]. Thomason estimates that intravoid strain rates are 100 to 10,000-fold higher than

the average macroscopic deformation rate [66]. Increasing m promotes void-ligament hardening to stabilize void growth for IM aluminum alloys, causing fracture resistance to rise, all with increasing temperature. In contrast microstructures that favor low work or strain rate hardening promote microvoid growth and flow localization between defects including primary microvoids [91-93]. Low-elongation shear-fracture in solution treated and quenched IM 7000-series aluminum alloys [78], as well as in IM AA3004 [77], was attributed to intravoid plastic instability caused by Mg-DSA.

The following scenario is proposed for fracture of CM Al. At all temperatures, primary microvoids nucleate at the larger clusters of Al_2O_3 dispersoids, iron-rich constituents, carbides, and weakly bonded prior particle boundaries. At 25°C, microvoids grow spherically with increasing strain until secondary small voids nucleate at smaller particles, leading to primary void coalescence. At elevated temperatures, irregular regions of dimple-like fracture, and faceted dimples, are produced because primary void growth is truncated by intravoid plastic instability and cracking in this ligament subjected to locally intense deformation. The former fracture features are typical of cracking along regions of local deformation. The cause of facets on the dimple walls (Figures 42 and 43) is not clear, but may involve slip band cracking or interaction with the growing primary void. Intrinsic ductility and plane strain fracture toughness are reduced if void growth ceases due to low-strain coalescence. The question is why increasing temperature causes this plastic instability in ultrafine grain dispersion-strengthened aluminum alloys, in contrast to the behavior of coarse-grain IM alloys.

A calculation based on spherical particles, with average spacing estimated from volume fraction, establishes that about 40 Al_2O_3 (20 nm diameter) and 30 $Al_{12}(Fe,V)_3Si$ (50 nm diameter) dispersoids intersect a primary void diameter (2 μm length), while 31,000 oxides and 15,000 silicides are contained within the volume of such a spherical void for CM Al and AA8009, respectively. About 50 equiaxed grains of 0.5 μm diameter are contained within this size of spherical dimple. Rather than DSA, we propose that dislocation interactions with dispersoids and boundaries govern low work and strain rate hardening, causing intravoid flow instability and premature microvoid coalescence in submicron grain alloys.

Dislocation-Dispersoid Interactions and Flow Localization:

Westengen and Lloyd concluded that dynamic recovery in submicron grain size aluminum is high and responsible for nil strain hardening, inhomogeneous flow localization (Luders banding), plastic instability, and reduced elongation to fracture [46,57,58]. TEM observations showed that intragranular dislocation cell structure does not evolve with straining when grain size is less than the low energy cell size, typical of equilibrium and between 0.5 to 2 μm for aluminum [46,57,58]. Straining is accommodated by emission and trapping of dislocations by grain and

particle interfaces. Transient work softening was observed and predicted for several submicron grain size aluminum alloys with dispersoids [71,75,94,95]. This phenomenon was not observed in all cases [24,96], and is not well understood.

Considering strain rate-sensitive flow, m for IM aluminum alloys without DSA is about 0.01 at 25°C and increases monotonically to 0.04 at a homologous temperature of 0.5 [19,66]. In contrast m for RS AA8009 decreases from 0.025 at 25°C to a negative value (-0.005) at 150°C, then increases to 0.04 at 300°C [42]. Mitra argued that m is near zero at 25°C, increases to 0.01 at 75°C, declines through a minimum (at 0.002) near 150°C, and achieves 0.02 at 300°C for a similar RS Al-Fe-Si-V alloy [56]. This behavior was attributed to Fe-DSA. For Al-Fe-Mn (1.2 μm grain size, but not RS and presumably without Fe in solid solution), m increased monotonically from 0.008 at 25°C to 0.025 at 150°C and 0.06 at 250°C [46]. Negative m was reported for both melt-spun and spray deposited Al-Si at 25°C [74]. It is difficult to interpret small changes in m values that are near-zero, however, this exponent does not appear to increase strongly with temperature between 25 and 200°C, and a minimum in strain rate sensitivity occurs at about 150°C for RS aluminum alloys.

Edwards et al. clarified these strain rate hardening trends [67]. The flow strength of PM zinc (with a 2 μm grain size and 5, 15 or 30 volume pct of 300 or 600 nm diameter Al_2O_3 dispersoids) is approximately strain rate-independent for T_m between 0.3 and 0.7, particularly in the near- threshold stress regime, with small positive and negative m suggested. Low-m stress-strain rate behavior was explained based on the argument that dispersoids are the major source of mobile dislocations for submicron grain microstructures which are otherwise dislocation-source deficient due to a lack of cells from dynamic recovery [67]. The emission of mobile dislocations from particles is triggered when the local interface stress exceeds a threshold level. The intermediate temperature strain rate insensitivity ($m = 0 \pm 0.05$) in such materials is attributed to the balance between dislocation emission from particles and local matrix recovery by diffusional processes. At increased strain rate, particle interface stresses increase due to reduced local recovery; enhanced dislocation emission increases the mobile dislocation density (ρ_m) to accommodate the applied strain rate at lower stresses according to dislocation dynamics models [97]. Increasingly smaller particles emit mobile dislocations with increasing local strain rate because the threshold stress for emission increases with decreasing particle size [67]. This model explains flow strength behavior that mimics a DSA-type response.

In a similar vein, Arzt and Rösler emphasize that dislocations climb over impenetrable dispersoids, but are trapped and must detach from the particle to continue glide [98]. Dislocation trapping, due to reduced line energy from diffusional relaxation at the incoherent particle-matrix

interface, was evidenced experimentally and predicted theoretically for Al alloys similar to CM Al [98,99]. A detachment stress (σ_D) and activation energy must be exceeded for the dislocation to escape the particle and become mobile. Dislocation detachment provides a basis for understanding the threshold stress, as well as a mechanism for low or negative m. At increased strain rates, particle interface stresses are higher due to reduced local recovery, and dislocations detach from particles at lower applied stress to increase ρ_m and accommodate the strain rate. Larger particles emit more mobile dislocations with increasing strain rate because σ_D increases with increasing particle size [98]. Reduced diffusion near the particle interface increases the energy of the trapped dislocation (reduces the benefit of particle-interface capture) and promotes detrapping [99].

These dislocation-particle interactions provide a mechanism for time-temperature-reduced m, and in turn for intravoid plastic instability and coalescence for submicron grain alloys such as CM Al, but not for larger grain size microstructures. The role of the small grain size is to preclude dislocation cells at times and temperatures where intragranular recovery occurs, and thus to preclude alternate sources of mobile dislocations. The role of the thousands of dispersoids between cluster or inclusion nucleated primary voids is to provide a means for intravoid strain rate softening, and flow instability, in response to the local strain rate increase that accompanies void growth.

Uncertainties:

Results for CM Al suggest a plausible mechanism for intravoid flow localization and reduced fracture toughness in ultrafine grain dispersoid-bearing aluminum at elevated temperatures, when DSA-solute are absent. Whether DSA is ever operative in RS aluminum alloys remains to be defined. In principle both mechanisms may contribute to the mechanical behavior of alloys with submicron grain size, dispersoids and metastable solute.

Both the dislocation-dispersoid and DSA mechanisms for reduced elevated temperature fracture toughness remain speculative. The kinetics and microstructural details of void nucleation, growth and coalescence have not been determined sufficiently for submicron grain aluminum microstructures [17]. The relationship between deformation mode , intravoid instability and void shape is not well understood. The temperature dependence of m is not established for CM Al. Analysis of strain rate hardening in fracture is complicated by the uncertain levels of strain and deformation rate in the ligament between growing voids ahead of a crack tip under triaxial tension. For example, the strain rate sensitivity exponent varies with stress, as does the importance of the dispersoid-source mechanism [67]. Compressive deformation and TEM studies are required to

better define temperature-dependent interactions between dislocations and dispersoids.[10]

Since the grain size of CM Al is less than 1μm, and ductility is low at homologous temperatures between 0.40 and 0.55, it is necessary to consider the contribution of time-dependent plastic deformation, particularly Coble creep, to fracture. Microvoid wall facets (Figures 42 and 43) could be interpreted based on stress-driven vacancy transport along grain boundaries, leading to cavity formation and growth at boundaries that are prevented from sliding by particles (Figure 35) [100]. Deformation mechanism map calculations using parameters for aluminum indicate that Coble creep is insufficient to affect fracture of CM for the conditions examined [101]. For a 0.5 μm grain size at 175°C, dislocation creep progresses at much faster strain rates compared to Coble creep and explains the high stresses that were achieved in the CM Al tensile experiments (Figure 37). For Coble creep to dominate at these conditions, grain size would have to be less than about 0.07 μm, well below the actual grain size of CM Al. Neither stress-strain rate data nor constitutive law parameters have been published for CM Al; limited creep experiments with submicron-grain size AA8009 showed that strain rate depends on stress raised to the 5 to 10 power for the temperature-stress regime pertinent to tensile and CT fracture [83]. The linear stress dependence expected for Coble creep was not observed. While the slow loading rate toughness data in Table 7 are limited, experiments with AA8009 demonstrated that K_{JICi} and T_R are reduced at 25°C, analogous to the higher temperature case, provided that loading rate is reduced 100-fold [39]. In total it is unlikely that Coble creep contributed to deformation and fracture of CM Al.

Differences in σ_{YS} and dispersoid characteristics (volume fraction, size, composition, crystal structure and interface properties) between CM Al and AA8009 do not compromise the conclusions of this work. The dispersoid volume fraction and size of CM Al are significantly less than that of both AA8009 [42,43] and PM zinc-alumina [67]. If CM Al had not exhibited temperature-reduced toughness, as did AA8009, then poor elevated temperature fracture resistance of the latter would be traced to either DSA or the high volume fraction of dispersoids. Since the toughness of CM Al declined upon heating, without Fe-DSA, the combination of submicron grain size and dispersoids are implicated as argued. Similar large numbers of dispersoids were within the ligament defined by two growing microvoids for CM Al (31,000) and AA8009 (15,000). While the effect of dispersoid size and spacing on dislocation emission, intravoid flow localization and fracture is unknown, there is no reason to believe that differences will cause dramatically

---

10 Porr speculated on a different deformation-based mechanism for fracture of AA8009, as an alternative to DSA [76]. Building on a dislocation model by Humphries and Kalu [68], he argued that deleterious flow localization results when dislocations evade impenetrable dispersoids by climb at a sufficiently elevated temperature or low strain rate.

different behavior. Skinner and coworkers reported similar temperature-dependent deformation and fracture behavior for Al-Fe-Si-V alloys with silicide contents between 10 and 40 volume pct, and sizes between 40 and 200 nm [42,43]. Edwards et al. found that dislocation emission from Al_2O_3 particles promoted low strain rate hardening at elevated temperatures for an Al_2O_3 volume fraction as low as 5 pct at the 300 nm dispersoid size [94].

A route to improve the intrinsic ductility and fracture toughness of advanced aluminum alloys such as CM Al and AA8009 may be to modestly increase the grain size to provide intragranular dislocation cell structure and mobile dislocation sources that improve work and strain rate hardening. Limited results for spray deposited Al-Fe-Si-V showed flow localization, including transient work softening for submicron grain sizes [94]. The same alloy, but with a 5 μm grain size, deformed homogeneously with increased work hardening and tensile elongation. The temperature-dependence of deformation and fracture was not defined. Additionally, inclusions, dispersoid clusters and microdelaminations that nucleate primary voids should be reduced for improved toughness. Solute such as Si, Mg or Fe should be minimized.

Conclusions

The fracture behavior of cryogenically milled, powder compacted and hot extruded aluminum; with a submicron grain size and 3 volume pct of 20 nm-sized Al_2O_3 dispersoids, but free of solute such as iron; was examined as a function of temperature. The goal was to determine the mechanism for elevated temperature/low strain rate degradation of fracture toughness by separating the contributions of Fe-dynamic strain aging and microstructurally localized plastic deformation.

1. The uniaxial tensile ductility, plane strain crack initiation fracture toughness (K_{JICi}), and plane strain stable-tearing resistance (T_R) of CM Al decrease monotonically with increasing temperature between 25°C and 325°C. Delamination does not affect the magnitude or temperature dependence of K_{JICi}.

2. Continuum micromechanical models of K_{JICi} and T_R show that temperature-dependent toughnesses decrease because of declining yield strength, elastic modulus and intrinsic fracture resistance. This latter property is controlling for submicron grain alloys, but increases with increasing temperature for conventional aluminum alloys. Toughness-minima or plateau behavior is due to the relative temperature dependencies of alloy flow and fracture resistances.

3. Fracture in CM Al is by microvoid processes at all temperatures, however, reductions in fracture resistance correlate with a change in primary void morphology from spherical to irregularly shaped and occasionally faceted.

4. Dynamic strain aging, due to diffusing solute such as iron, is not a necessary element of the elevated temperature reduction in intrinsic tensile ductility and fracture toughness for submicron grain size, dispersoid-strengthened Al.

5. Speculatively, the intrinsic fracture resistance of alloys such as CM Al is degraded by temperature-reduced work and strain rate hardening which promote plastic instability between growing primary microvoids and exacerbate low-strain coalescence.

6. Plasticity localizes between primary voids at elevated temperatures due to dynamic recovery, which eliminates work hardening dislocation cell and source structures in submicron grains, coupled with reduced strain-rate hardening or softening. Decreased strength with increasing strain rate is due to increased mobile dislocation density from the emission or detrapping of dislocations from dispersoids in the source-deficient microstructure.

V. TASK IV---ELEVATED TEMPERATURE FRACTURE TOUGHNESS OF AA2519 WITH Mg AND Ag ADDITIONS

M. J. Haynes and R.P. Gangloff

Abstract

The plane strain initiation fracture toughness (K_{JICi}) and plane stress tearing modulus (T_R^{ps}) of an ingot metallurgy Al-Cu-Mg-Ag alloy are characterized as a function of temperature by a J-integral method. Ω-strengthened AA2519+Mg+Ag exhibits mildly decreasing fracture toughness (K_{JICi}≈31 MPa√m) from 25°C to 175°C, while T_R^{ps} increases monotonically to 7 at 100°C and subsequently declines as temperature increases. A critical plastic strain-controlled micromechanical model of initiation toughness successfully predicts temperature independent K_{JICi}. Constant initiation toughness is due to rising intrinsic fracture strain (ε_f^*) with temperature, which balances the effects of decreasing flow strength, work hardening, and elastic modulus on the crack-tip strain distribution. Microvoids nucleate at cracked constituent particles, with growth truncated by void sheeting associated with dispersoids. Intravoid strain localization (ISL) between primary voids is a precursor to void sheet coalescence, and is retarded by alloy strain and strain rate hardening. Modeling predicts a transition from dislocation accumulation at dispersoids at low temperature to dislocation bypassing by climb at elevated temperature, implying that void nucleation and flow softening in the ISL band are reduced, and strain to fracture (ε_f^*) increases. Decreased void sheeting and increased primary void growth at 150°C versus 25°C are consistent with the proposed ISL mechanism of microvoid fracture.

Introduction

A significant effort is currently aimed at the development of advanced aluminum alloys for the airframe of the high speed civil transport (HSCT). Airframe materials will be required to maintain strength and toughness at temperatures ranging from 100°C to 200°C for a projected life of 60,000 hrs. [102] Advanced ingot metallurgy (IM) alloys, rapidly solidified powder metallurgy (RS/PM) alloys, and metal matrix composites (MMC) are candidate aluminum-based materials. Selection of HSCT materials hinges on at least three critical issues: 1) intermediate loading rate fracture toughness at elevated temperatures, 2) slow loading rate or creep crack growth fracture resistance at elevated temperatures, and 3) elevated temperature thermal exposure effects on ambient temperature fracture toughness. The first issue is considered here for an advanced IM aluminum alloy.

Ductile fracture of metals typically occurs by microvoid nucleation, growth, and coalescence, as reviewed in general [17,66,103-106] and specifically for aluminum alloys (AA) [29,107-109]. Important microstructural variables affecting the three stages of microvoiding in aluminum alloys, and hence the intrinsic fracture resistance, include: size, spacing, and fracture behavior of brittle constituent phases; [29,107,108] composition and volume fraction of dispersoids; [17,107] slip mode as affected by precipitation hardening; [108,110] and grain boundary precipitation. [108,109] Continuum factors; including alloy yield strength, [17,29,66,103,106] work hardening, [17,66,103,104,108] strain rate hardening, [66] and stress state triaxiality; [17,66,103] dictate the local stresses and strains that control the rates of void nucleation, growth and coalescence. The effects of these factors on plane strain fracture toughness are well defined for precipitation hardened aluminum alloys deformed at cryogenic to ambient temperatures [29,107], but not sufficiently at elevated temperatures [39,111,112].

Polmear and Couper showed that certain IM Al-Cu-Mg-Ag alloys possess superior elevated temperature yield strength and creep/stress rupture properties over conventional AA2024, AA2219, and AA2618 [113]. This improvement was attributed to the formation of a coherent precipitate phase, Ω, promoted by small Ag additions to an alloy with a sufficiently high Cu/Mg ratio. The Ω phase is believed to be a metastable variant of the equilibrium Θ (Al_2Cu) phase, forming on {111} Al matrix planes as a uniform dispersion of thin hexagonal shaped plates [114]. Polmear and Couper concluded that Ω is more coarsening resistant than Θ', but provided no evidence. This hypothesis was recently confirmed [115,116]. The elevated temperature fracture behavior of Ag-modified Al-Cu-Mg alloys has not been defined.

Understanding of ductile fracture within the crack-tip process-zone is derived through coupled micromechanical modeling and microstructural studies. The most developed models of microvoid fracture initiation toughness combine crack tip stress and strain distributions with a microstructural based, critical strain - critical distance failure criterion [24,61,111,117,118]. These models are effectively tested by predicting and measuring the temperature dependence of fracture toughness [24,61,111], but additional work is required. Experimental estimates of a constraint-sensitive intrinsic failure strain [24,61,111,117,119,120], and the use of an adjustable critical distance parameter in modeling, must be supplemented by detailed microstructural studies of the strain-dependent progression of void nucleation, growth, and coalescence [18,119,121]. Results on stress-based void nucleation [122-124] and strain-based void growth to coalescence [17,121,125] must be related to crack tip damage and toughness prediction.

The objective of the current study is to quantitatively characterize plane strain initiation and

plane stress growth fracture toughnesses as a function of temperature for an IM Al-Cu-Mg-Ag alloy. A second goal is to test the capability of a strain-controlled micromechanical model to predict elevated temperature initiation-toughness. To understand the mechanisms of fracture, interrelationships between microstructure, continuum flow properties, and the progression of microscopic ductile fracture damage are considered. Prior thermal exposure effects on the toughness of IM aluminum alloys, as well as static-load crack growth at elevated temperature, are considered elsewhere [22,112,126-128].

Procedures

Material

The Aluminum Company of America (ALCOA) supplied experimental AA2519, with Ag and Mg additions (denoted AA2519+Mg+Ag), as 3.2 mm thick hot rolled sheet. Composition was specified as Al-5.75Cu-0.52Mg-0.49Ag-0.30Mn-0.16Zr-0.09V by weight percent. A second sheet, Al-5.83Cu-0.52Mg-0.30Mn-0.14Zr-0.10V (AA2519+Mg), was also supplied. Both alloys were solution treated at 529°C for 1 hr, cold water quenched, stretched 7% and aged at 177°C for 3 hours, producing a peak strength (T87) condition [129].

The microstructure of AA2519+Mg+Ag was characterized with optical and electron microscopy. Constituent particles were qualitatively identified through scanning electron microscopy (SEM) with energy dispersive spectroscopy (EDS). Constituent area fraction (A_f) and size distribution were measured by optical microscopy and image analysis on polished surfaces of the three principal planes of the sheet. The average radius (r) and A_f were used to determine the constituent volume fraction ($V_f=A_f$) and the nearest neighbor spacing between randomly distributed spherical particles in a volume ($\Delta_3=1.18r\ (\pi/6V_f)^{1/3}$) [130]. Based on particles observed on fracture surfaces, only constituents larger than 2.0 μm in diameter were counted. Grain structure was revealed by a 45 second Graff-Sargent etch followed by a 10 second exposure to Keller's etch. Dispersoids and precipitates were resolved through Transmission Electron Microscopy (TEM). TEM disks were mechanically reduced to a thickness of 150 μm and subsequently thinned by electrolytic polishing at -30°C in 30% HNO_3 and 70% methanol solution.

Elastic-Plastic Fracture Toughness Experiments

Fracture toughness was characterized with the J-integral based crack growth resistance (J-Δa) curve method detailed elsewhere [81,131]. Compact tension (CT) specimens were machined in the LT orientation[11], with a width (W) of 76.2 mm and a 3.2 mm thickness (B). To

11 For sheet, the rolling direction is L, the width is T, and the thickness is S.

prevent buckling, CT specimens were fatigue precracked to a final crack length (a) corresponding to an a/W ratio of $0.6 \pm .001$, and an anti-buckling fixture with teflon sheet lubrication was placed around the specimen. Specimens were precracked at a constant stress ratio ($R=K_{min}/K_{max}$) of 0.1 and under decreasing stress intensity (K) conditions from a K_{max} of 19.4 MPa$\sqrt{m}$ at a/W of 0.4 to 8.5 MPa$\sqrt{m}$ at the final crack length.

Rising load fracture toughness experiments were performed on a closed-loop servoelectric testing system operated under constant grip-displacement rate control. A circulating air oven was mounted on the load frame, and temperature was regulated to ±1 °C with a thermocouple attached to the CT specimen. The specimen was heated to temperature over a 30 minute interval and stabilized for 30 minutes prior to loading. A PC-based acquisition system continuously recorded applied load, crack length, notch mouth opening displacement, and time. Crack length was continuously monitored by the direct current electrical potential difference (DCPD) method [12,39]. A linear variable differential transformer (LVDT) measured notch mouth opening displacement for conversion to load-line displacement using a geometric relationship [11].

The J-integral elastic-plastic crack tip parameter was utilized with relatively small specimens to obtain both plane strain initiation toughness and plane stress crack growth resistance data, accurately accounting for uncracked ligament plasticity[12] [132]. J-Δa resistance curves were calculated according to ASTM Standard E1152, and all requirements of the standard were met. Initiation and growth fracture toughness parameters were determined from J-Δa data, as detailed elsewhere [131]. Initiation fracture toughness (J_i) was defined at the first change in the slope of potential difference versus load-line displacement data. The stress state at initiation was plane strain for all cases examined. J_i was converted to a plane strain linear elastic initiation toughness (K_{JICi}) by the relation [132]:

$$K_{JICi} = \left(\frac{J_i E}{1 - \upsilon^2} \right)^{\frac{1}{2}} \qquad [3]$$

12 At higher temperatures, creep deformation ahead of the crack-tip could invalidate J and necessitate the use of creep- based crack-tip parameters (C* or C(t)). Saxena and Landes developed a displacement rate partitioning analysis that separates measured load-line displacement rate (v) into the sum of elastic (v_e), plastic (v_p), and creep rate (v_c) components [21]. There is no established criteria for ascertaining the value of v_c/v above which J is compromised as a crack-tip parameter, but creep crack growth rates in stainless steels do not correlate with J when v_c/v exceeds 0.8 [21]. J is the valid crack-tip parameter for AA2519+Mg+Ag at all temperatures. v_c/v was always less than 0.8. Partitioning analysis applied to creep crack growth experiments of AA2519-T87 at 135°C supports the dominance of time independent crack-tip fields [22].

The DCPD method detects early stage crack initiation, with a small level of crack tip damage compared to that embodied in the ASTM E399 standardized definition of K_{IC} [62,82,131]. The linear elastic R-curve (K_J-Δa) for small scale yielding was determined from J-Δa curves ($K_J = [J^*E]^{1/2}$), and generally described plane stress cracking for Δa above about 1.5 mm. A plane stress tearing modulus (T_R^{ps}) was defined from the average slope ($dJ/d\Delta a$) of the linear portion of the J-Δa curve over a range of crack growth (2 mm < Δa < 3 mm) [13] [85].

Four measures of toughness were determined for AA2519+Mg+Ag: 1) K_{JICi}, 2) T_R^{ps}, 3) J at a crack length of 3 mm (J^{3mm}), and 4) the corresponding K_J at 3 mm (K_J^{3mm}). Toughnesses were measured at a CT load-line displacement rate ($d\delta/dt$) of 0.26 μm/s and at temperatures of 25°C, 75°C, 100°C, 125°C, 150°C, and 175°C. This displacement rate corresponded to crack initiation in about 40 minutes and 3 mm of crack growth in 2.4 hours. Limited experiments were conducted on AA2519+Mg.

Uniaxial Compression Experiments

The compressive flow properties of AA2519+Mg+Ag, including the 0.2% offset yield strength (σ_{ys}^c) and the strain hardening exponent (N), were measured at the same temperatures as the fracture toughness experiments. Compression specimens, with a 2.6 mm by 2.6 mm square base and a height of 5.2 mm, were machined with the long axis parallel to L. The compression fixture consisted of two aligned and interlocking four post cages that converted tensile motion to compressive force. An LVDT, mounted on the inner two compression plates measured total displacement to a resolution of 1 μm. The specimen was centered between two Al_2O_3 platelets, lubricated with colloidal graphite to minimize barreling, and deformed to 5% true strain at a constant cage displacement rate of 0.33 μm/sec. The displacement rate corresponded to an average true strain rate of $6x10^{-5}$ sec^{-1} over the full strain range.

Calculating the true total strain (ε) was complicated by compliant deformation between the inner compression plates. The measured LVDT displacement equaled sample plastic displacement plus sample and fixture elastic displacements. A correction procedure involved subtraction of the total measured elastic displacement to give load versus sample plastic displacement data, that were converted to true stress (σ) versus true plastic strain by the usual relations. The temperature

---

13 $T_R^{ps} = [E/\sigma_{fl}^2](dJ/d\Delta a)$, where the flow stress (σ_{fl}) equals the average of the yield and ultimate tensile strengths.

dependence of the AA2519+Mg+Ag elastic modulus (E) was estimated with published E versus temperature for pure aluminum [87], scaled to the ambient temperature modulus of AA2519+Mg+Ag specified by ALCOA (E=72.4 GPa). Elastic strain, based on the estimated modulus, was added to plastic strain to obtain ε.

The Ramberg-Osgood (R-O) constitutive equation ($\varepsilon/\varepsilon_0 = \sigma/\sigma_0 + \alpha(\sigma/\sigma_0)^n$) was fit to compression σ - ε data [41]. Fitting parameters include a reference stress (σ_0), a reference strain (ε_0) given by σ_0/E, a constant (α), and the R-O plasticity exponent (n). From 1.0% to 5.0% true strain, n was determined from the linear regression slope of true plastic strain versus true stress plotted logarithmically [133]. The work hardening exponent (N) equals the inverse of n. The parameters σ_o and α are not independent; assuming a value of one for α yielded reasonable σ_0 values and accurate curve fits.

Tensile Experiments

L-oriented smooth tensile bars, with a 19.1 mm gauge length and a 1.6 mm diameter, were strained to failure at a grip displacement rate of $1x10^{-3}$ mm/sec; corresponding to an initial true strain rate of $6x10^{-5}$ sec^{-1}. 0.2% offset tensile yield strength (σ_{ys}^t), ultimate tensile strength (σ_{uts}), and the percentage reduction in area (RA) were ascertained at each fracture toughness testing temperature.

L-oriented, circumferentially notched round-tensile-specimens, with varying notch acuity, were fractured to establish the effect of macroscopically imposed triaxial stress-state on the tensile ductility of AA2519+Mg+Ag. Stress-state triaxiality was expressed as the ratio of mean stress (σ_m) to effective stress (σ) and depended on notch geometry according to [24,63,120,134,135]:

$$\left(\frac{\sigma_m}{\sigma}\right) = \frac{1}{3} + \ln\left(\frac{d_o}{4R} + 1\right) \qquad [4]$$

The initial notch root profile radius (R) for a semi-circular notch was varied, at a constant initial notch-root diameter (d_0) of 1.6 mm, to obtain five constraint levels: σ_m/σ values of 1.54, 1.13, 0.77, 0.55 and 0.33; where the later ratio corresponds to a smooth (uniform gauge) tensile specimen. The small size of the notch precluded continuous measurement of notch-root contraction with a diametral extensometer. The effective diameter at failure (d_f) was determined to

a resolution of 2.5 μm from four equally spaced diametral measurements of the fracture surface. Effective plastic strain at fracture (ε_f^p) depends on diametral contraction, or equivalently, RA according to [120]:

$$\overline{\varepsilon_f^p} = 2\ln\left(\frac{d_o}{d_f}\right) = -\ln\left(1 - \frac{RA}{100}\right) \qquad [5]$$

Since d_0 and R were not monitored during testing, ε_f^p was related to the initial stress state triaxiality.

Results

Microstructure

Inhomogeneously distributed constituent particles are present in AA2519+Mg+Ag (Figure 45(a)); the volume fraction is 1.2%, the average diameter is 5.7 μm, and the 3-D nearest neighbor spacing (Δ_3) is 11.9 μm. Based on EDS, most constituents are undissolved Θ (Al_2Cu), although Al- Cu-Mn-Fe particles were also detected. This Θ originates from the high Cu content (5.75 wt%), which exceeds the solubility limit of 5.25 wt% for Cu in Al+0.5 wt% Mg at the solution heat treatment temperature [136]. Large Θ particles form during ingot solidification, break into smaller particles and redistribute during thermomechanical processing, and do not dissolve during solution treatment. Constituents are clustered along the sheet rolling direction, and constituent cracks are oriented normal to L (Figure 45(b)).

Flattened-and-elongated grains are observed in the etched microstructure of AA2519+Mg+Ag as shown in Figure 46, with grain dimensions on the order of 50 to 200 μm or larger in the L-direction. X-ray diffraction pole figures and orientation distribution function (ODF) calculations, performed by ALCOA to determine if the alloy is recrystallized, produced conflicting evidence. ODF values imply small components of recrystallization textures (Cube=2.40, Goss=0.30 times random) and large components of deformation textures (Brass=6.60, Copper=3.50) [129]. However, <111> and <200> pole figures did not correspond to experimentally observed hot rolling textures of aluminum alloys [137]. Despite the anisotropic grains and deformation components of the texture, the alloy is essentially recrystallized. TEM detected only two subgrains within a large sample area. Recrystallization is expected in this alloy. The high volume fraction of large Θ particles and hot rolling reduction (≈98%) promote particle

stimulated nucleation of recrystallization [138]. Some subgrains may be present in AA2519+Mg+Ag, because submicron dispersoids inhibit recrystallization [139].

TEM resolved Mn- and Zr-containing dispersoids in AA2519+Mg+Ag, which were identified using EDS. Both dispersoids are around 0.2 to 0.4 μm in diameter and contain significant levels of Cu. The dominant strengthening precipitate in AA2519+Mg+Ag is Ω, as indicated by the brightfield TEM image in Figure 47 and the diagonal streaks (perpendicular to the precipitate plates) in the selected area diffraction pattern. Small volume fractions of Θ' plates and S' (Al_2CuMg) laths were also observed. In AA2519+Mg, Θ', S', and Ω are present in comparable volume fractions, with no one precipitate dominating. Grain boundary precipitation and precipitate free zones (PFZs) were observed, with PFZ widths on the order of 0.05 μm.

Fracture Toughness

Macroscopic Fracture Path:

Crack initiation develops in the center of each CT specimen under plane strain conditions, and flat fracture occurs over approximately 80% of the thickness. As the crack extends, the proportion of flat plane strain fracture decreases and that of slant plane stress increases, yielding a triangular morphology of the former [131]. Fracture is predominately plane stress after approximately 2.0 mm of crack growth. These results establish that plane strain dominates K_{JICi} and plane stress is typical of T_R^{ps}.

Effect of Temperature:

K_J-Δa resistance curves for LT oriented CT specimens of AA2519+Mg+Ag, tested at a load- line displacement rate of 0.26 μm/sec, are displayed in Figure 48 as a function of temperature. The K_J-Δa curve of AA2519+Mg at 175°C is also shown. The dotted line located at a crack extension of 3 mm represents one-tenth the original uncracked ligament or the estimated limit of J-controlled crack growth from ASTM E1152, but the data are well behaved and the trends remain unchanged up to Δa of at least 4 mm. K_{JICi} is plotted versus temperature in Figure 49 for AA2519+Mg+Ag and AA2519+Mg. Crack growth resistance, quantified by T_R^{ps}, is plotted versus temperature in Figure 50 K_{JICi} and three growth toughness parameters (T_R^{ps}, J^{3mm}, K_J^{3mm}) are listed in Table 8 for both AA2519+Mg+Ag and AA2519+Mg at each test temperature.

K_{JICi} is variable, most likely due to the inhomogeneous distribution of Θ constituent within the crack-tip process-zone. At 25°C, K_{JICi} is 30.5 MPa$\sqrt{m}$ for AA2519+Mg and varies from 29.6

MPa√m to 37.1 MPa√m for AA2519+Mg+Ag. The Ag-bearing alloy has plane stress tearing moduli of 5.4 and 4.0 at 25°C, while T_R^{ps} is 5.4 for AA2519+Mg. Values of J^{3mm} are 127.8 kJ/m^2 and 134.6 kJ/m^2 for AA2519+Mg+Ag and AA2519+Mg, respectively. The corresponding K_J^{3mm} values for small scale yielding are 96.2 MPa√m and 98.7 MPa√m. K_J^{3mm} approximates, but is always substantially less than the critical plane stress fracture toughness from a wide-center-cracked plate experiment [131].

AA2519+Mg+Ag exhibits a mildly decreasing initiation fracture toughness with increasing temperature at a load-line displacement rate of 0.26 μm/sec (Figure 49). Least squares linear regression analysis of K_{JICi} versus temperature yielded an intercept of 33.1 MPa√m (at 0°C) and a slope of -0.013 MPa√m/°C. The 95% confidence interval of the slope (ß) implies a temperature invariant toughness ($-.043 < ß < +.018$). Limited K_{JICi} data for 2519+Mg show toughness rising slightly as temperature increases to 100°C and declining to 25.4 MPa√m at 175°C. The plane stress tearing moduli for 2519+Mg and 2519+Mg+Ag increase monotonically to peak values near 100°C, and subsequently decline as temperature increases (Figure 50). Table 8 shows that J^{3mm} and K_J^{3mm} exhibit similar trends, increasing to 75°C and declining above 125°C.

Microscopic Fracture Processes

The midplane region of plane strain fracture surfaces, within 500 μm of the fatigue precrack tip, was analyzed by SEM. For the relatively rapid loading rate examined, microvoid coalescence is the operating fracture mechanism in AA2519+Mg+Ag at both ambient and elevated temperatures, as illustrated in Figures 51(a) & 51(b). A bimodal distribution of dimple sizes characterizes each surface. Larger dimples (5 to 30 μm in diameter) are associated with primary void initiation and growth from undissolved Θ particles, with some contribution from manganese and iron bearing constituents. Microscopically flat fracture facets were observed on undissolved Θ, consistent with cracked particles in the as received material.

Sheets of small voids (0.5 to 5 μm in diameter, depending on temperature) nucleate from smaller second phase particles in strain localized regions between primary voids [17,18]. Void sheets, marked by "vs" in Figures 51(a) and 51(b), truncate the growth of primary voids and connect primary void clusters in AA2519+Mg+Ag. Stereographic fracture surface observations show that sheets propagate at angles ranging between 45 and 80° from the Mode I crack plane. Void sheets are seen directly ahead of the fatigue precrack tip [131], underlying their importance to fracture initiation toughness. High magnification SEM tilt fractography was employed to

characterize the morphology of dimples on void sheets (Figures 52(a) and 52(b)). At 25°C and 150°C, the sheet surfaces are covered by dimples of shear character, and the shear nature is more dominant at 150°C, as indicated by the shallower dimples (Figure 52(b)). Dimples within void sheets increase in size as temperature increases. Submicron dispersoid particles are observed within void sheet dimples at 25°C, but less often at 150°C. TEM observations of dispersoid size, shape, and composition; correlated to particles observed in void sheet dimples; suggest that Mn-bearing dispersoids are likely void nucleation sites.

As temperature increases, stereographic observations show that void sheeting is retarded in AA2519+Mg+Ag. The area fraction of void sheets at 150°C markedly declines relative to the area fraction formed at room temperature. Metallographic profile sections of crack tips formed at ambient temperature and 150°C, shown in Figures 53(a) and 53(b) respectively, corroborate both crack growth due to Θ particle fracture and the character of void sheeting. Crack growth was interrupted at a K_J level of approximately 80 MPa$\sqrt{m}$ for each CT specimen (corresponding to approximately 900 μm of crack growth), and was subsequently polished to the midplane or plane strain region. Arrows indicate void sheets, which are confirmed as less prevalent at 150°C; indicated by shorter "canals" between primary voids and also by areas ahead of the crack tip with high amounts of local damage that are not yet linked by the void sheet mechanism.

The effect of temperature on the stable growth of primary voids was evaluated by quantitative fractography. The radius of primary dimples (r_D) was measured from a montage of 30 1000X magnification fractographs which covered a 500 μm by 500 μm area in the plane strain region. At 25°C, average r_D equals 9.2 μm or 3.2 times the average constituent radius, r. At 150°C, average r_D equals 10.7 μm or 3.8r. An increased extent of primary void growth (r_D/r) at 150°C in AA2519+Mg+Ag implies an enhanced resistance to void sheeting, consistent with qualitative fractographic evidence (Figure 53) and increased intrinsic alloy ductility [103].

A limited amount of small dimples oriented within the mode I crack plane was observed on the 150°C fracture surface (represented by the upper left-corner of Figure 51(b)). This was interpreted as grain boundary ductile fracture (GBDF) [109]. The area fraction of GBDF is small at the loading rate employed in this study.

Deformation and Tensile Fracture

Uniaxial mechanical properties of AA2519+Mg+Ag are listed in Table 9 as a function of deformation temperature, and the temperature-dependencies of σ_{ys} and N are plotted in Figure 54. With increasing temperature, σ_{ys}^t, σ_{ys}^c, σ_0, σ_{uts}, N, and estimated E decrease, while RA increases

monotonically. Compressive yield strength is 17-40 MPa below the tensile yield strength, and both decline by about 20% between 25°C and 175°C. Values of N approach zero (perfectly plastic behavior) as temperature increases.

Experimental measurements of ε_f^p versus σ_m/σ for AA2519+Mg+Ag at 25°C and 150°C are plotted in Figure 55 along with a theoretical prediction of ε_f^p versus σ_m/σ obtained by integrating the Rice and Tracey void growth law [103,120,125]. Fracture strain decreases dramatically with increasing triaxiality at each temperature. For high triaxiality ($\sigma_m/\sigma \approx 1.7$) the ductility approaches an intrinsic fracture strain, denoted ε_f^*, and described in detail elsewhere [111]. Figure 56 plots ε_f^p versus temperature for two constraint levels; $\sigma_m/\sigma=0.33$ and 1.13. As temperature increases, ε_f^p rises. A smooth-to-notched ratio, r_{sn}, is defined as ε_f^p at $\sigma_m/\sigma=0.33$ divided by ε_f^p at $\sigma_m/\sigma=1.13$. Based on the linear regression fits to ε_f^p versus temperatures at the two constraint levels, r_{sn} is essentially constant at 4.2 between 25°C and 175°C. The effect of triaxial constraint on ε_f^p is independent of temperature, at least for these two constraint levels. This information is necessary for micromechanical predictions of K_{JICi} and T_r^{ps}.

Discussion

Engineering Implications

The average initiation fracture toughnesses of experimental AA2519+Mg+Ag (K_{JICi}=32.9 MPa$\sqrt{m}$) and AA2519+Mg (30.5 MPa$\sqrt{m}$) at 25°C are comparable to or exceed that of conventional aluminum alloys [140]. K_{JICi} for AA2024-T3 is 32.4 Mpa$\sqrt{m}$ [131], but the yield strength of this alloy is 100 MPa less than that of the AA2519 variants. K_{IC} of AA2024-T851 (σ_{ys}=460 MPa) ranges from 23 to 28 MPa$\sqrt{m}$ for the LT orientation, while equal strength but higher purity AA2124-T851 exhibits improved toughness (K_{IC}=27 to 36 MPa$\sqrt{m}$). K_{IC} values of AA2219-T851 are high (36 to 41 MPa$\sqrt{m}$), but strength levels are low (σ_{ys}=345 to 360 MPa). Considering high strength AA7075- T651 (σ_{ys}=515 to 560 MPa), K_{IC} varies from 27 to 31 MPa$\sqrt{m}$.

Elevated temperature fracture toughness comparisons between competing aluminum alloy

systems are important in materials selection for HSCT applications. Figure 57 is a summary plot of initiation fracture toughness versus temperature for conventional IM alloys (AA2219-T851 [112] and AA2618-T851 [39]) and advanced alloys (AA2519+Mg+Ag, AA2090-T81 [141], AA2009/SiC/20p-T6 [62], and RS/PM AA8009 [24]). ASTM E399 K_{IC} is used to characterize initiation toughness for AA2219-T851 and AA2090-T81, and these measurements are slightly higher than a K_{JICi} measurement [131]. All specimens were tested in the LT orientation, except for TL oriented AA2090-T81. AA2519+Mg+Ag displays ambient and elevated fracture toughness behavior similar to AA2219-T851, but with yield strength levels 130 to 160 MPa higher [112]. K_{IC} increases mildly with temperature for AA2090-T81 [141], and the strength and absolute toughness levels are similar to AA2519+Mg+Ag. AA2618-T851 and AA2009/SiC/20p-T6 possess essentially constant fracture toughness with temperature, but absolute toughnesses are degraded by high volume fractions of $FeNiAl_9$ and SiC particles, respectively [39,62]. A marked decrease in K_{JICi} with temperature is observed for RS/PM aluminum alloys; the unique mechanisms responsible for this trend are discussed elsewhere [39]. The good toughness of AA2519+Mg+Ag is notable given the significant volume fraction of undissolved Al_2Cu. A modest decrease in the Cu content should reduce the amount of this phase and increase the fracture toughness.

AA2519+Mg shows a significant decrease in K_{JICi} at 175°C, corresponding to widespread grain boundary ductile fracture (GBDF). The Ag-bearing alloy did not display significant amounts of GBDF. K_{JICi} degradation by GBDF may be due to an increasing contribution of creep fracture or environmental effects. This fracture mechanism was not explored.

Two approaches must be coupled to understand and predict temperature dependent K_{JICi} and T_R^{ps} for use in damage tolerant life prediction and alloy development. First, micromechanical modeling of the crack tip process zone defines the temperature-dependent contributions of alloy deformation and fracture properties to initiation and growth fracture toughnesses. Second, strain-driven evolution of microscopic void damage must be related to microscopic plasticity and microstructural features.

The Critical Plastic Strain-Controlled Model

Components of the Model:

The critical plastic strain-controlled model of initiation fracture toughness, for alloys that fail by dimpled rupture, couples the following three elements: 1) the intrinsic fracture resistance of the alloy, 2) the strain distribution ahead of a stationary crack-tip that drives microscopic fracture

processes, and 3) a microstructural distance (l^*) necessary for the fracture process. The model is discussed in detail elsewhere [61,85,111,117].

Plane strain K_{JICi} corresponds to the applied stress intensity (K) level required for the crack- tip plastic strain field (ε^p versus distance ahead of the crack tip, x) to exceed the position-dependent fracture resistance (ε_f^p versus x) over l^*. At $K=K_{JICi}$, the ε^p-x curve exceeds the ε_f^p-x curve at $x \leq l^*$, and the intersection of these two curves defines the intrinsic fracture strain, ε_f^* [111].

(1) Fracture Resistance: For AA2519+Mg+Ag, fracture is by microvoid nucleation, growth, and coalescence. Strain is assumed to characterize fracture resistance because it explicitly drives void growth [17,103,125] and implicitly controls the void nucleation stage [61,122,124]. Microvoid fracture resistance is affected by σ_m/σ; a stress state-dependent failure-strain, $\varepsilon_f^p(\sigma_m/\sigma)$, must therefore be predicted or measured and coupled with $\sigma_m/\sigma(x)$ to obtain fracture resistance as a function of distance ahead of the crack tip, $\varepsilon_f^p(x)$ [85,111,120].

The constraint-sensitivity of ε_f^p was not measured at each temperature studied, so simplifying assumptions were employed to model K_{JICi}. A smooth bar constraint ratio (r_s) was defined as ε_f^p at $\sigma_m/\sigma=0.33$ divided by ε_f^*, and a notched bar constraint ratio (r_n) was defined as ε_f^p at $\sigma_m/\sigma=1.13$ divided by ε_f^*. The model failure criterion was employed in conjunction with the measured failure locus for AA2519+Mg+Ag at 25°C (Figure 55) to determine an ε_f^* of 0.08, an r_s of 6.5, and an r_n of 1.5 [111]. Measurements of ε_f^p versus σ_m/σ at 150°C, or any other test temperature, are not sufficient to repeat these calculations with confidence. Both constraint ratios are assumed to be temperature independent, which is consistent with temperature invariant r_{sn} observed in Figure 56.

The precise intrinsic fracture strain for toughness modeling is that required to produce microvoid damage in the notch root corresponding to damage in the crack-tip process-zone at K_{JICi}. Measurements of fracture strain based on RA, instead of the strain at the critical damage event, result in overestimated ε_f^*. Experimental and computational studies suggest that this error is small because reduction of the minimum cross-sectional area is limited after a critical damage event

corresponding to K_{JICi}, such as void sheet coalescence [120,142].

(2) Crack-Tip Strain Field: For ε^p, a finite element-based elastic-plastic strain field was used, derived by McMeeking from the finite-strain flow theory of plasticity [143]. The strain field was calculated for large deformation geometry changes and a smoothly blunting crack. The function, $\varepsilon^p = C1(\delta/x)^{C2}$, was fit to McMeeking's results for N values of 0, 0.1, and 0.2, and an angular orientation of 45° from the crack plane [61,111]. The variable δ is the crack tip opening displacement and C1 and C2 are curve-fitting constants. The magnitude of ε^p for a given x increases as δ and K increase.

(3) Critical Distance: A critical distance over which microvoid damage occurs is an essential model element since the crack-tip strain singularity precludes defining the failure criterion at the point of maximum strain [61,85,120]. An accepted definition of l^* for initial crack extension is some multiple of the nearest-neighbor interparticle spacing [85,117]. It is not correct to equate l^* with the average spacing of void-nucleating particles, because more than one void ahead of the crack tip can participate in void link-up. It is not possible presently to determine l^* *a priori* by metallographic or fractographic measurements, thus this parameter is used as a curve-fitting constant to match experimental toughness data [61,85,111,117,144]. If the microvoid fracture mechanism is constant as temperature varies, then l^* may be invariant, enabling model predictions of temperature-dependent toughness. This assumption must be critically examined.

The three components of the critical plastic strain controlled model are combined to yield [61,111]:

$$K_{JICi} = \sqrt{\frac{\sigma_{ys} E l^*}{(1-\nu^2)\, d(N)} \left(\frac{-\ln(1-RA)}{r\ Cl} \right)^{\frac{1}{\alpha}}} \qquad [6]$$

where ε_f^* is estimated by -ln(1-RA)/r, r is either r_s or r_n depending on available data, υ is Poisson's ratio, and σ_{ys} is the average of tensile and compressive yield strengths. The parameter d(N) is a proportionality constant between δ and J/σ_{ys}, and is a function of N, stress state, σ_{ys}/E, and the definition of δ. Values of d(N) are related linearly to N between 0 and 0.2 (d(N) = 0.58-1.4N) [143], and are similar to those given by analytical solutions [145]. The parameters C1 and C2 are obtained for any N by interpolating linearly between curve fits of FEM results for N =

0, 0.1, and 0.2 [61,111]. Measured N at each temperature (Table 9) was employed to determine d(N), C1, and C2. Poisson's ratio was assumed to equal 0.3 at all temperatures. The remaining alloy deformation properties can be measured. Table 10 shows the input parameters for modeling of AA2519+Mg+Ag at each temperature.

Because the tensile properties of AA2519+Mg+Ag are strain-rate sensitive, the crack tip strain rate is estimated for a CT specimen fractured at a load-line displacement rate of 0.26 μm/sec (dK/dt=1.2 x 10^{-3} MPa$\sqrt{m}$/sec). Differentiation of McMeeking's crack tip strain field, for the stationary crack at $K \leq K_{JICi}$, yields a crack tip strain rate gradient, dependent on K, dK/dt, and the distance ahead of the crack tip [146]. For the specimen fractured at room temperature, at $K=K_{JICi}$, and at a process zone distance of 30 μm, the crack tip strain rate is estimated as $6x10^{-5}$ sec^{-1}. Uniaxial tension and compression specimens were deformed at this strain rate to obtain flow properties (Table 9) for input to the micromechanical model.

Model Predictions:

With the parameters; σ_{ys}, E, ε_f^*, d(N), C1, and C2; determined as a function of temperature, K_{JICi} for AA2519+Mg+Ag is predicted through Eq. 6. The constant l^* is the single adjustable parameter. Equal values of l^* (20.5 μm) were calculated from average measured K_{JICi} at 25°C for both the smooth- and notched-tensile cases, and were used to predict K_{JICi} from 75°C to 175°C. The calculated value of l^* is nearly twice as high as the calculated spacing of Al_2Cu and Fe-bearing constituent particles in a volume (Δ_3= 11.9 μm).

The temperature dependence of K_{JICi} for AA2519+Mg+Ag is predicted successfully as shown in Figure 58, with ε_f^* based on both smooth- and notched-tensile bar RA. Variability in the measured tensile properties leads to variability in predicted K_{JICi}. A linear-regression fit to K_{JICi} measurements (K_{JICi} = 33.1 MPa$\sqrt{m}$ - 0.013*T) agrees well with fits to predictions from both smooth (K_{JICi} = 32.7 + 0.001*T) and notched-specimen (K_{JICi} = 32.9 MPa$\sqrt{m}$ - 0.001*T) data, where T is the temperature in Celsius. A 95%-confidence-interval estimate of the slope (ß) using the student-t-distribution indicates that there is no significant difference between ß for the measurements (-0.043< ß <0.018), smooth-specimen predictions (-0.026< ß <0.027) and notched-specimen predictions (-0.028< ß < 0.026). Both measured and predicted K_{JICi} are essentially temperature-independent from 25°C to 175°C (ß°0).

The strain-controlled model quantifies the interplay between crack-tip ε^p, ε_f^*, and l^* that

governs initiation fracture toughness. Microvoid-rupture K_{JICi} does not scale solely with either the intrinsic fracture resistance (ε_f^*) or the deformation properties (σ_{ys}, E, N) that govern ε^p in terms of K. Rather, both elements must be combined with a fracture initiation criteria to predict the "composite" property of K_{JICi}. The relative sensitivities of crack-tip ε^p and ε_f^* to temperature dictate the temperature dependence of K_{JICi}, when l^* is assumed to be temperature-invariant. As σ_{ys}, E, and N decline with increasing temperature, which is observed in AA2519+Mg+Ag and other IM aluminum alloys, crack tip strain increases for a fixed x and K [61,111]. Crack-tip ε^p is thus enhanced at elevated temperatures, resulting in a lower applied K necessary for ε^p to exceed a given ε_f^* over l^*. Increased ε_f^* for AA2519+Mg+Ag at elevated temperatures essentially offsets enhanced crack-tip strain, resulting in a constant predicted K_{JICi} with temperature.

The experimental verification of predicted K_{JICi} versus temperature for AA2519+Mg+Ag (Figure 58) provides a strong confirmation of the plastic-strain based model of crack-tip initiation toughness. The model is verified similarly based on measured and modeled K_{JICi} versus temperature in other aluminum alloy systems [24,61,111,144].

Modeling Difficulties:

Strain-based micromechanical modeling of initiation fracture toughness yields reasonable values of l^*, as well as accurate temperature dependencies of K_{JICi}. Absolute values of K_{JICi} are not predicted, however, due to uncertainties in ε_f^* and l^*. Accurate determination of ε_f^* is complicated by the need to correlate damage at the critical microvoid damage (or coalescence) event, within the notch root of tensile specimens and the process-zone ahead of a crack-tip. The Bridgman approximation of ε_f^p and uncertainty in the effect of stress-state-constraint on ε_f^p also hinder accurate measurements of ε_f^*. These issues are discussed elsewhere [63,111].

Ultimately, l^* must be determined independently for absolute toughness prediction. l^* might be measured independently from measured particle spacings on a polished microstructural section, measured void spacings on a polished section of a notched tensile bar interrupted at the critical fracture event, or measured dimple spacings in the high constraint region of a CT fracture surface. For example, model evaluations for several aluminum alloys and steels indicate an empirical relationship between Δ_3 from microstructural sections and l^* calculated from measured

fracture toughness [111]. l^* ranges from 1 to 6 times Δ_3.

Notched-tensile experiments of AA2519+Mg+Ag at 25°C were interrupted at peak load and sectioned longitudinally to independently determine l^*. The nearest neighbor spacings of voids nucleated from constituent particles within the cross section of the notch were measured from a metallographic section of one unloaded tensile bar. Void spacing measurements were confined to a longitudinal distance of 150 μm above and below the minimum notch root diameter. The nearest neighbor void spacing in a plane (Δ_2^{void}) varied from 11.8 μm to 163.4 μm, reflecting severe clustering of the constituents. Average Δ_2^{void} equals 43 μm, and is converted to an average 3-D nearest neighbor void spacing (Δ_3^{void}) of 28 μm by the relation $\Delta_3^{void}/\Delta_2^{void} = 1.23(1/V_f)^{-1/6}$, with V_f equal to 0.02 [130]. Δ_3^{void} was equated to l^* for an absolute prediction of initiation toughness. The measured diametral contraction of the notch and Eq. 5 were used to calculate an average ε_f^p of 0.071, which was divided by r_n to obtain an ε_f^* of 0.047. Predicted K_{JICi} from Eq. 6 with these estimates of l^* and ε_f^* equals 31.0 MPa$\sqrt{m}$ for AA2519+Mg+Ag at 25°C.

This absolute prediction agrees well with the average measured K_{JICi} of 32.9 MPa$\sqrt{m}$, but is not rigorous. Peak load probably represents a lower amount of microvoid damage relative to that in the crack-tip process-zone at K_{JICi}. Moreover, l^* does not necessarily equal Δ_3 or Δ_3^{void}. Rather, the ratio of calculated l^* (for agreement between measured and predicted initiation toughness) to Δ_3 depends directly on the extent of primary void growth, r_D/r [111]. Thus, measured constituent spacings from a metallographic section are not necessarily sufficient to determine l^* independently. The ratio r_D/r, and its influence on the multiple of particle or void spacings that constitutes the critical distance, must be determined.

Void size and spacing measurements from CT fracture surfaces or sectioned notched tensile bars appear to be the most promising method of independently determining l^*, since information on both Δ_3^{void} and r_D/r can be obtained. Caution is dictated. More detailed microscopic studies of the evolution of microvoid fracture is required to understand the relationships between l^*, Δ_3^{void}, and r_D/r. Quantitative tilt fractography is necessary to obtain the true nearest neighbor spacing of particles from a 3-D fracture surface. Moreover, the strong distance and angular dependencies of crack-tip ε^p, coupled with a heterogeneous distribution of void-nucleating particles, makes

independent determination of l^* a formidable problem that is beyond the scope of this work.

The Moving Crack Model of Tearing Resistance

Chan formulated an expression for the plane strain tearing modulus ($T_R^{p\varepsilon}$) based on Rice's continuum analysis of the strain field ahead of a moving crack [86]. The temperature-dependent material parameter, $\Omega = E\,\varepsilon_f^*/\sigma_{fl}$, governs plane strain tearing resistance. Both absolute values and the temperature dependence of $T_R^{p\varepsilon}$ for AA8009 were reasonably predicted by this model, including a minimum in tearing resistance at 200°C [24].

A simple modification to Chan's micromechanical model for $T_R^{p\,\varepsilon}$ does not yield accurate predictions of either the absolute values of the plane stress tearing modulus, or the temperature-maximum in plane stress T_R^{ps}, for AA2519+Mg+Ag. Specifically, the constraint factor was reduced from r of 6.5 for plane strain to unity for plane stress, and mildly temperature dependent constants (α, ß, and λ in Chan's model) were assumed to equal the values for AA8009 [24,86]. Measured (Table 8) versus predicted T_R^{ps} are 4.7/40, 7.2/83, and 3.7/142 for AA2519+Ag+Mg fractured at 25°C, 100°C, and 175°C, respectively. This poor agreement may be traced to the notion that stable crack growth under plane stress involves a local shear-based failure criterion, while the model for $T_R^{p\varepsilon}$ was derived by equating the critical Mode I crack opening to the principle fracture strain for uniaxial tensile loading, reduced to account for increased plane strain constraint [86]. Further work is needed to model plane stress tearing resistance, and the associated temperature and microstructural dependencies of the deformation and fracture properties that constitute T_R^{ps}.

Elevated Temperature Fracture Evolution

Understanding of temperature-dependent K_{JICi} also requires basic analysis of the temperature- dependent factors that govern the intrinsic resistance of the alloy to microvoid nucleation, growth, and coalescence. Mechanism-based study of elevated temperature microvoid fracture in IM aluminum alloys is limited [66,147], counter to the ambient temperature case [29,107,108,148]. Increasing temperature greatly affects ε_f^* by promoting stress relaxation around second phase particles and by altering flow properties such as yield strength, work hardening and strain rate hardening [147].

Higher temperature or lower strain rate enhances recovery at particle/matrix interfaces,

lowering the stresses on the interface and postponing void nucleation to higher applied strains, provided that interfacial strengths are not severely degraded [147]. Microvoid nucleation from a dilute volume fraction (<5%) of large constituents in aluminum alloys occurs at a small fraction of the strain required for dimpled rupture [17]. A large fraction of constituent particles in AA2519+Mg+Ag were cracked prior to testing (Figure 45), and the polished crack tip profiles show that all large particles eventually cracked (Figure 53). Because microvoid nucleation occurs at low strain, the temperature dependence of the nucleation rate is not significant in describing the temperature dependence of fracture toughness.

Temperature affects microvoid growth rates and the strain at the onset of void coalescence [147]. Strain-based rates of void growth increase with higher stress state triaxiality and lower work hardening [125,149]. The global stress state triaxiality did not change from ambient temperature to 175°C, based on fracture surface appearance. Work hardening decreases markedly with temperature for 2519+Mg+Ag (Figure 54), and the void growth rate is expected to increase. Since ε_f^* increases with increasing temperature for AA2519+Mg+Ag (Figure 56), counter to an increasing void growth rate with temperature, temperature-dependent void coalescence must dominate fracture.

Increasingly strain rate sensitive plastic deformation at elevated temperatures retards void coalescence [66,147,150,151]. Fractography of AA2519+Mg+Ag shows clusters of Θ nucleated voids separated by void sheets associated with submicron dispersoids (Figure 52). At elevated temperature, fractographic evidence indicates that void sheeting is retarded (Figure 53). A necessary precursor to void sheeting is intravoid strain localization (ISL) of shear deformation between large, primary voids nucleated at Θ. The onset of ISL depends on stress state triaxiality [121,152], strain hardening [151,153,154], strain rate sensitivity [66,147,150,151], constituent particle spacing and distribution [153,154], slip mode [108,119], and microvoid nucleation at dispersoids within the strain localized band [17,148]. The critical strain for ISL rises with increasing strain hardening and strain rate sensitivity. Increasing triaxiality, clustering of constituents, planar slip (from cutting of precipitates), or a higher volume fraction of submicron dispersoids in the intravoid ligament should decrease this critical strain.

Speculatively, reduced void sheeting in AA2519+Mg+Ag at elevated temperatures (Figure 53) is responsible for increasing ε_f^*. The change in void sheeting is not due to changes in triaxiality, second phase particle distributions, or slip mode. Macroscopic fracture surface observations suggest that triaxiality did not change with temperature, and constituent and

dispersoid particle spacing distributions remain unchanged to 175°C. Slip is not localized due to dislocation cutting of Ω and does not exacerbate ISL. Li found that Ω precipitates are not fully sheared during plastic deformation at 25°C or 150°C; rather, dislocation cutting disperses evenly along Ω [155]. Because the effects of these factors appear negligible, the propensity for void nucleation at dispersoids, as well as changes in strain hardening and strain rate hardening of AA2519+Mg+Ag, are believed to be responsible for retarded ISL and reduced void sheeting at elevated temperatures.

Intravoid Strain Localization

Factors Controlling ISL:

As strain accumulates and primary voids grow in the crack-tip process zone, the critical condition for microscopic ISL is attained due to: 1) a high volume fraction and non-homogenous distribution of second phase particles and associated voids, 2) a reduction in cross sectional area between primary microvoids, and 3) stress-state triaxiality. Strain rate within an ISL band (ε_{ISL}) increases, and because the global strain rate must be conserved, strain rate in the surrounding continuum (ε_{surr}) decreases. ε_{ISL} is estimated as two to four orders of magnitude greater than ε_{surr} [66,151]. Here, ε_{ISL} is assumed to increase by 1 to 3 orders of magnitude, and ε_{surr} decreases by an order of magnitude, relative to the global strain rate.

The progression or abatement of ISL depends on competition between flow hardening and softening in the ISL band. Void nucleation and growth at dispersoids within the band contribute to softening and promote continued localization. Strain and strain rate hardening, coupled with the accelerated strain rate in the intravoid shear band, produce ISL band flow hardening relative to the flow strength of the surrounding material. If the band hardens enough to overcome flow softening, then ISL is abated and shifted to other primary voids [151]. Hardening is governed by time and temperature dependent dynamic recovery.

Temperature and Strain Rate Dependence of Flow Stress:

Time-dependent dynamic recovery occurs in aluminum alloys at ambient and elevated temperatures, and lowers flow stress. The kinetics of dislocation recovery, the imposed strain rate, and temperature dictate the amount of dynamic recovery and the associated flow stress decrease. Reduced recovery in the ISL band, due to amplified strain rates relative to the surrounding continuum, is a substantial source of band hardening.

Figure 59 summarizes the temperature and strain rate sensitivity of flow stress for AA2519+Mg+Ag, AA2219-T851 [156], and low solute aluminum alloys [157,158] in terms of the

Zener-Hollomon parameter[14]. For a strain rate of $6x10^{-5}$ s^{-1}, the equivalent temperature corresponding to a given Z is plotted as a second ordinate. At constant temperature, an order of magnitude decrease in Z is equivalent to an order of magnitude reduction in strain rate. Consequently, the strain rate sensitivity of flow stress (m in the relation $\sigma_0 \alpha \varepsilon^m$) is estimated at constant temperature from the slope of each curve, over the strain rates of interest.

Flow stress depends uniquely on Z for each alloy, and depends similarly on temperature and strain rate within two regimes. For Z larger than about 10^{16} s^{-1}, the flow stress is relatively insensitive to changes in temperature or strain rate. For Z less than 10^{15} s^{-1}, dynamic recovery is enhanced and the flow stress decreases markedly with decreasing Z (decreasing ε or increasing T). These two regimes correspond to changes in the equilibrium subgrain size during steady state deformation of pure aluminum [159]. Of importance to fracture is the result that m increases with increasing temperature and is substantial for Z less than 10^{15} s^{-1} or T greater than 100°C.

Temperature Dependence of ISL and ε_f^*:

With increasing temperature, m increases and N decreases. For example, at 25°C and the strain rate employed in this study ($\varepsilon=6x10^{-5}$ s^{-1}), flow stress is in the strain rate insensitive regime of Figure 59 (Log Z=20.6 s^{-1}) and m is 0.020 for AA2219-T851. At 150°C, flow stress is in the strain rate sensitive regime (Log Z=13.3 s^{-1}) and m is 0.035. Conversely, N decreases from 0.05 at 25°C to 0.03 at 150°C, based on work hardening data from uniaxial compression of 2519+Mg+Ag, modified to reflect work hardening within the ISL band.

When the strain rate is amplified within an ISL band, strain and strain-rate hardening are responsible for band hardening and abatement of strain localization. As temperature increases, the change in ISL band hardening is difficult to predict due to uncertainties in strain, strain rate, and the constitutive law for ISL band material. It is possible to approximate combinations of strain

---

14 The Zener-Hollomon parameter (Z), a temperature-compensated strain-rate, is given by:

$$Z = \dot{\varepsilon} \exp\left(\frac{\Delta H}{RT}\right)$$

where ΔH is the activation energy associated with the temperature dependence of flow stress and is assumed to equal the activation energy for self diffusion in aluminum (140 kJ/mol) [68]. R is the universal gas constant and T is temperature in Kelvin. The parameter Z represents conditions for constant dislocation recovery; at equal Z, decreased temperature or increased strain rate equivalently increases flow strength.

enhancement ($\Delta\varepsilon=\varepsilon_{ISL}-\varepsilon_{surr}$) and strain rate enhancement ($\lambda=\varepsilon_{ISL}/\varepsilon_{surr}$) for which ISL band hardening, due to m and N, is equal at 25°C and 150°C[15]. For example, increased strain rate hardening within the ISL band for λ=100 and higher m at 150°C versus 25°C, is counterbalanced by reduced strain hardening for $\Delta\varepsilon$=0.08 and lower N at 150°C compared to 25°C. For λ equal to 1000 and 10000, ISL band hardening is equal at 25°C and 150°C for $\Delta\varepsilon$ equal to 0.25 and 0.64, respectively. The quantitative contributions of strain and strain rate hardening to ISL band hardening can not be determined because λ and $\Delta\varepsilon$ are not known. Reasonable choices of $\Delta\varepsilon$ (0.08) and λ (100) suggest that ISL band hardening, void sheeting behavior, and ε_f^* may be temperature independent. However, the softening effect of void nucleation at dispersoids must be considered.

Temperature and strain-rate dependent bypassing of dispersoids controls the rate of dislocation accumulation at the dispersoid/matrix interface and therefore should control the rate of secondary void nucleation and flow softening in the ISL band between growing primary voids. Humphreys and Kalu modeled the critical strain rate for dislocation bypassing by climb around particles, as influenced by particle size and temperature-dependent bulk and interface diffusion [68]. A critical temperature versus strain rate prediction is plotted in Figure 60 for AA2519+Mg+Ag and measured dispersoid sizes ranging from 0.1 to 0.3 μm. (The average size of 0.2 μm is plotted as a solid line.) The plot is a "micro-deformation mechanism map", where dislocation bypassing of dispersoids is predicted at all temperature/strain-rate combinations below a line and dislocation accumulation is predicted for combinations above a line. Superimposed on the plot are the temperature and applied global strain rate conditions (•) for AA2519+Mg+Ag tensile testing. The dashed lines represent local strain rate enhancements (λ) in an ISL band of two, three, and four orders of magnitude, while the lower horizontal line represents a 10-fold reduction in the surrounding matrix strain rate.

During tensile fracture at ambient temperature, dislocations do not bypass 0.1 to 0.3 μm diameter dispersoids, even at the reduced strain rate outside the ISL bands. Dislocation

---

[15] The Hollomon constitutive law $\sigma_0=K\,\varepsilon^N\,\varepsilon^m$ was assumed,[73] and the incremental increase in σ_0 due to increased strain and strain rate within the ISL band relative to the surrounding material was calculated. K values at 25°C and 150°C were calculated at 5% strain and the global strain rate, using N values from Table 9 and m values given in the text.

accumulation and void nucleation at dispersoids should be abundant and lead to significant flow softening, enhanced ISL, and relatively low strain fracture involving void sheeting. For a given dispersoid size and λ, bypassing occurs above a critical temperature. For example, with 0.2 μm diameter dispersoids and a λ of 100, the model predicts that dislocation bypassing within the band occurs at temperatures above 120°C. Above the critical temperature, dislocation accumulation and void nucleation at dispersoids are reduced, flow softening diminishes, and ISL is retarded. This critical temperature rises with increasing dispersoid size and λ. The critical temperature for bypassing of at least the smaller dispersoids is between 25°C and 175°C, regardless of λ. Therefore, dislocation bypassing of dispersoids is augmented in AA2519+Mg+Ag between ambient and elevated temperature, leading to reduced flow softening and retarded ISL.

In summary, dislocations do not bypass dispersoids at 25°C in alloys such as AA2519+Mg+Ag, void nucleation is abundant within the ISL band, flow softening between primary constituent-nucleated voids is significant, and ISL is catalyzed. Void sheeting is prevalent since strain rate hardening and work hardening are not sufficient to overcome substantial flow softening. At elevated temperatures (150°C), dislocations bypass dispersoids, void nucleation within the ISL band decreases, and flow softening is reduced. Speculatively, void sheeting is retarded and ε_f^* is higher at 150°C because ISL band hardening overcomes the reduced flow softening and delays ISL. This hypothesis is consistent with retarded void sheeting (Figure 53), the change in morphology of void sheet dimples (Figure 52), and the increase in measured primary void growth (r_D/r) as temperature is increased from 25°C to 150°C.

The effects of m, N, and void nucleation at dispersoids on ISL, void sheeting, and ε_f^* must be quantified. The void-filled band can be represented by a Gurson yield potential [161]; but the strain, strain rate, and criteria for void nucleation within an ISL band are uncertain. Two studies have addressed these issues. Becker and Smelser's finite element simulation of strain localization and fracture between 2 mm diameter holes in an aluminum sheet quantified strain and strain rate enhancements within ISL bands under plane stress, as well as abatement of ISL due to m and N [151]. Pan and coworkers analyzed the localization of deformation within a porous band using Gurson's yield potential and found that strain to failure increased with increasing strain rate hardening [150]. These results are insufficient to predict the temperature-dependence of ε_f^* necessary to model K_{JICi} and to develop fracture resistant aluminum alloys.

Correlations Between m and ε_f^*:

The intrinsic fracture resistance of AA2519+Mg+Ag (and AA2618) correlates with strain rate sensitivity, as expected based on the discussion of ISL. Values of m for AA2519+Mg+Ag are assumed equal to the slopes of the curve for AA2219-T851 in Fig. 15, and ε_f^* for smooth- and notched-bars is obtained from Table III. ε_f^* for AA2618, calculated from smooth-tensile-bar RA[47] using a r_s value of 7, are correlated to m determined from creep data [156]. Figure 61 displays the linear correlations for each alloy and supports the role of increasing m in retarding ISL. Increasing ε_f^* is not due solely to m since reduced void nucleation at dispersoids also retards ISL as deformation temperature increases.

ε_f^* is less dependent on m for AA2618 and absolute fracture resistance is lower at any temperature, compared to AA2519+Mg+Ag. The fracture resistance of AA2618 is lower due to a significantly higher volume fraction of more closely spaced constituents (V_f=0.08, Δ_3=8.3 μm), resulting in reduced primary void spacing and growth to coalescence. Speculatively, the reduced sensitivity of ε_f^* to m in AA2618 reflects a lower amount of void sheeting due to the higher volume fraction of constituents. Void sheeting may occur in AA2618 [39], but microvoids nucleate and grow from a higher density of sites and therefore coalesce by impingement at lower strains relative to AA2519+Mg+Ag in the absence of void sheeting. The abatement of ISL at elevated temperatures in AA2618 does not affect alloy ductility as strongly as it does in AA2519+Mg+Ag. Alternately, ε_f^* for AA2618 is not less dependent on m, but rather is less dependent on temperature due to the lower volume fraction of submicron particles and the absence of Mn and Zr containing dispersoids that contribute to ISL band softening.

Woodford correlated strain rate hardening and total elongation to fracture for several superplastic alloys based on Fe, Ni, Mg, Pb, Ti, and Zr [162]. While total elongation is a poor indicator of intrinsic fracture strain, this correlation shows a qualitatively similar m-dependence to Figure 61. In contrast, mechanisms such as dynamic strain aging (DSA) produce a negative strain rate sensitivity and associated reduction in elongation or ε_f^*. Parks and Morris related low post-uniform strain to negative m values and DSA in AA3004 [77]. King et. al. attributed low ductility in a solutionized 7000 series AA to DSA producing ISL and void sheeting [78]. Kim et. al. cited low m as the cause of elevated temperature ductility and fracture toughness degradation in cryogenically milled ultra-fine grain size Al with Al_2O_3 dispersoids [144].

Conclusions

1. Fracture initiation toughness is high (K_{JICi} > 30 MPa$\sqrt{m}$) for AA2519+Mg+Ag with a substantial volume fraction (1.2%) of large undissolved Al_2Cu particles, and decreases slightly with increasing temperature from 25°C to 175°C. AA2519+Mg possesses a significantly lower K_{JICi} than its Ag-bearing counterpart at 175°C.

2. Fracture of AA2519+Mg+Ag involves a bimodal distribution of microvoids. Fracture evolves by primary void initiation at processing-cracked Al_2Cu particles, followed by limited void growth and unstable coalescence through propagation of fine dimpled void sheets nucleated at dispersoids. Void sheeting is retarded and primary void growth is enhanced as temperature increases.

3. Yield strength and strain hardening decrease monotonically with increasing temperature for AA2519+Mg+Ag, consistent with increasing dynamic recovery.

4. The effective plastic strain to fracture of AA2519+Mg+Ag decreases markedly with increasing triaxial constraint, and increases with increasing temperature for two levels of constraint.

5. The critical plastic strain-controlled micromechanical model of initiation toughness accurately predicts the measured temperature dependence of K_{JICi} regardless of whether smooth or notched bar reduction in area is employed to estimate the intrinsic fracture strain, ε_f^*. As temperature increases, toughness is temperature invariant due to decreasing σ_{ys}, E, and N which enhance crack-tip strain, balanced by increasing ε_f^*.

6. The flow stress of IM 2000 series aluminum alloys and pure aluminum shows two regimes: a relatively temperature/strain rate insensitive region above a Zener-Hollomon parameter of 10^{16} s^{-1} and a relatively temperature/strain rate sensitive region below 10^{15} s^{-1}. Flow strength at the standard strain rate employed in this study is within the strain rate sensitive region for temperatures above about 100°C.

7. The propensity for strain localization between growing primary microvoids (intravoid strain localization or ISL) has a major influence on ε_f^*. Strain and strain rate hardening between primary microvoids act to retard ISL, but the net retardation may be temperature independent.

8. As temperature increases from 25°C to 175°C, modeling of stress relaxation at a particle/matrix interface predicts a transition from dislocation accumulation at dispersoids to dislocation bypassing in AA2519+Mg+Ag. Dislocation bypassing results in decreased void nucleation at dispersoids, decreased flow softening within an ISL band, reduced void sheeting, and hence increased ε_f^*. This hypothesis is consistent with fractographic evidence of retarded void sheeting and increased primary void growth at 150°C.

9. ε_f^* increases linearly with strain rate hardening in AA2519+Mg+Ag and AA2618.

VI. TASK V---MICROMECHANICAL MODELING OF THE TEMPERATURE DEPENDENCE OF FRACTURE TOUGHNESS

M.J. Haynes, B.P. Somerday, C.L. Lach, and R.P. Gangloff

Abstract

The temperature dependence of initiation fracture toughness (K_{JICi}) is modeled micromechanically for a variety of advanced aluminum alloys; including precipitation-hardened-ingot metallurgy, spray formed, rapidly-solidified or mechanically-alloyed powder metallurgy, and metal-matrix composite alloys; that fail by microvoid processes. A critical-plastic-strain-controlled model, employing tensile yield strength, elastic modulus, work hardening, and reduction-in-area measurements, successfully predicts K_{JICi} *vs* temperature for eight alloys, providing a strong confirmation of this approach. In each case, temperature-dependent K_{JICi} is controlled by the interplay between the temperature dependencies of the intrinsic microvoid-fracture resistance and the crack-tip stress/strain fields governed by alloy flow properties. This model quantifies these microstructure-sensitive contributions to temperature-dependent fracture toughness. Uncertainties in the triaxial-stress-modified critical fracture strain, as well as the critical distance (volume) for crack-tip-damage evolution, hinder absolute predictions of fracture toughness. The critical distance, calculated with the model from measured K_{JICi}, correlates with the nearest-neighbor spacing of void nucleating particles determined by quantitative metallography, as well as with the extent of stable void growth determined from quantitative fractography. These correlations suggest a means to predict absolute fracture toughness.

Introduction

Problem Statement and Objective

Recent research has focused on measuring the plane-strain fracture-initiation toughness, and plane-strain as well as plane-stress crack-growth resistances, of advanced plate and sheet aerospace Al alloys [19,24,25,39,62,144]. Experimental J-integral (J) vs. crack extension (Δa) curves were established using elastic-plastic fracture mechanics (EPFM) and precision crack length monitoring by direct-current potential difference (DCPD) or unloading compliance [12]. The DCPD technique detected more effectively microscopic damage constituting initial crack extension compared to standardized offset methods, particularly in thin-sheet or high-tearing-resistance alloys [62,131]. The linear-elastic plane-strain fracture toughness calculated from J at the DCPD-detected initial crack extension (K_{JICi}), as well as the J vs. Δa (or equivalently K vs. Δa) curves, were

reported as a function of temperature for experimental and commercial Al alloys; including advanced 2XXX precipitation-hardened alloys [19,39], submicron-grain-size powder-metallurgy alloys [24,144], a spray-formed 2XXX alloy, and a 2XXX alloy reinforced with SiC particulate [62]. In all cases, fracture was based on microvoid damage.

It is important to model fracture toughness in order to understand K_{JICi} and K vs. Δa, particularly with regard to the temperature dependencies of the basic microstructural and deformation properties that govern fracture toughness. Measured K_{JICi} vs. temperature data for Al alloys vary widely. In addition K_{JICi} and tensile ductility for an alloy can depend on temperature differently. These trends must be understood. The critical-plastic-strain-controlled model is most pertinent for predicting Al-alloy fracture toughness, and is detailed below. Although this model is simple conceptually, model accuracy over a range of flow properties and microstructures has not been established. Some model parameters are difficult to define unambiguously.

The objective of this work is to apply the strain-controlled model to predict the temperature dependencies of fracture-initiation toughness for Al alloys. This study aims to understand the fundamental elements of the measured temperature dependencies of fracture toughness. In addition the variation of model parameters with temperature and microstructure offers a unique opportunity to critically test the model. Temperature-dependent K_{JICi} is modeled for eight advanced Al alloys, based on measured deformation and fracture properties, with one adjustable parameter. In one alloy, microstructure is altered to examine the influence of slip mode and particle spacing on model parameters and K_{JICi}.[16]

Background on Strain-Controlled Fracture-Toughness Model

Advanced micromechanical models of fracture toughness couple the following three elements [85]: 1) an estimate of the intrinsic fracture resistance, 2) solutions for the crack-tip stress and strain fields which drive the microscopic fracture process, and 3) a microstructural distance necessary for the fracture process. These models overcome the limitations of earlier work which only considered the crack-tip driving force and critical distance [108,163]. Including the fracture resistance is critical for understanding the effects of temperature and microstructure on fracture toughness.

---

16 In this paper, only the initiation toughness is characterized and modeled. Plane-strain growth toughness (tearing modulus, T_R) was measured for the metal-matrix composite and submicron-grain-size alloys, and was predicted successfully using a micromechanical model which coupled the moving crack-tip displacement field with a local criterion for crack propagation [24,61,86,144].

Fracture Resistance:

For the Al alloys considered, fracture is by microvoid nucleation, growth and coalescence (MNG) involving second-phase particles. Strain should characterize the fracture resistance regardless of the relative contributions of void nucleation and growth. While strain is shown explicitly to drive void growth [17,66,103,120,125], void-nucleation criteria are couched typically in terms of a critical stress. The stress which concentrates near the particle/matrix interface is, however, a function of the remote strain [61,122,123].

There are two approaches for estimating the critical fracture strain: modeling and direct measurement. Each stage of MNG is affected by triaxial stress (characterized by σ_m/σ_{fl}, where σ_m is mean stress and σ_{fl} is flow stress) [17,66,103], as well as plastic strain. A gradient of σ_m/σ_{fl} exists ahead of a crack tip [85,163]. A stress state-dependent failure-strain locus ($\varepsilon_f^p(\sigma_m/\sigma_{fl})$) must therefore be predicted or measured. Ideally, the effective plastic strain to failure, ε_f^p, is the sum of the void-nucleation strain, plus the strain required to grow the voids to the critical event characterized by K_{JICi}.

The modeling approach must derive $\varepsilon_f^p(\sigma_m/\sigma_{fl})$ from considering the detailed MNG processes for an alloy. Models exist for predicting both the nucleation and growth strains [17,66,103]; however, calculating $\varepsilon_f^p(\sigma_m/\sigma_{fl})$ is complicated. MNG model elements, such as the void-nucleating- particle fracture strength or interface decohesion strength, and the solution for stress local to a particle, are uncertain [122,123,124]. Second, for "growth-controlled" MNG, where stable void growth contributes substantially to $\varepsilon_f^p(\sigma_m/\sigma_{fl})$, voids coalesce by two means: void impingement or shear-based strain localization [17,18]. Strain-localized coalescence criteria are uncertain and depend on the spacing of "primary" void-nucleating particles [153,154], strain-hardening and strain rate-hardening exponents [66,150,151,153,154], stress-state triaxiality [120,125], and the volume fraction of smaller "secondary" void-nucleating particles (i.e., dispersoids) [17,19]. Third, the contribution of each MNG stage to $\varepsilon_f^p(\sigma_m/\sigma_{fl})$ can vary among alloys. For example, $\varepsilon_f^p(\sigma_m/\sigma_{fl})$ may be governed by the nucleation strain if voids coalesce spontaneously upon nucleation, as is likely for a metal-matrix composite with a high volume fraction of large void-nucleating reinforcement particles [61]. An alloy with few large inclusions may behave differently under void-growth control.

In addition to these complications associated with "isolated" particles and voids, particle-particle and void-void interactions must be considered, as well as local triaxial stress which evolves from elastic constraint on matrix plastic flow, if the alloy contains a high volume fraction of primary void-nucleating particles and/or the particles are distributed heterogeneously. Furthermore, the primary void-nucleating particles may have a range of sizes and shapes and, as a result, the nucleation strain varies from site to site. Void nucleation and growth may not be uniform among the population of particles in three dimensions throughout the microstructure.

Direct measurement of $\varepsilon_f^p(\sigma_m/\sigma_{fl})$ avoids the complexities associated with MNG modeling. The $\varepsilon_f^p(\sigma_m/\sigma_{fl})$ locus is typically measured by straining notched-tensile specimens, which impose a range of σ_m/σ_{fl} values [117,120]. A second experimental technique used to estimate $\varepsilon_f^p(\sigma_m/\sigma_{fl})$ is measurement of fracture-surface microroughness [85,164]. While measured values of $\varepsilon_f^p(\sigma_m/\sigma_{fl})$ include the three stages of MNG, and thus cannot offer insight into MNG mechanisms, such values are reliable inputs for micromechanical fracture-toughness models.

Crack-Tip Strain Field:

The solution for effective plastic strain (^{p}) should be consistent with the observed mode I crack-tip profile geometry, as well as the angular orientation of void-damage sites ahead of the stationary crack tip. Hutchinson, Rice, and Rosengren (HRR) derived the stress and strain fields for a crack tip undergoing small geometry change (i.e., no blunting) where J-dominance prevails [165,166]. Solutions for ε^p ahead of a crack tip undergoing substantial blunting [118,143,163,167] are assumed to be more relevant for fracture of high-strength Al alloys. McMeeking's finite-strain, flow-theory, finite-element-modelling (FEM) results for a smoothly blunting crack tip are used in this study [143]. The following function is fit to McMeeking's results for a σ_{ys}/E ratio of 0.003:

$$\bar{\varepsilon}^p = C1\left(\frac{\delta}{x}\right)^{C2} \qquad [7]$$

The variable, x, is radial distance from the crack tip, δ is Mode I crack-tip-opening displacement, and C1 and C2 are curve-fitting constants. The function is fit to FEM results reported for work-hardening exponents (N from $\sigma \alpha \varepsilon^N$) of 0, 0.1, and 0.2. The FEM solution for an angular orientation of 45° from the crack plane is used since ε^p is maximum in this plane for all x [143].

Critical Distance:

A critical distance (l^*) over which MNG-damage occurs is an essential model element since the crack-tip strain singularity precludes defining the failure criterion at the point of maximum strain [120,121,149]. An accepted definition of l^* for initial crack extension by MNG is some multiple of the nearest-neighbor interparticle spacing [85,103,117]. It is not correct to equate l^* with the average spacing of void-nucleating particles, because every particle does not participate in void link-up during crack extension and coalescence may depend on particle properties. It is presently not possible to determine l^* *a priori* by metallographic or fractographic measurements, thus this parameter is often used as a curve-fitting constant to match experimental toughness data [19,24,61,117,144]. If the MNG mechanisms are constant as temperature varies, then l^* may be invariant, enabling model predictions of temperature-dependent toughness trends. This assumption must, however, be critically examined.

Model Formulation

The strain-controlled fracture-toughness model is based on the assumption that the plane-strain initiation toughness corresponds to that applied stress-intensity (K) level required for the crack-tip plastic strain to exceed the pertinent fracture resistance over a finite distance. A graphical illustration of this model is shown in Figure 62, where ε^p,$\varepsilon_f^p(\sigma_m/\sigma_{fl})$, and σ_m/σ_{fl} are plotted as a function of distance ahead of the crack tip, x. The ε^p and σ_m/σ_{fl} crack-tip distributions, both derived for N equal to 0, are from the FEM and slip-line continuum analyses of McMeeking [143] and Rice and Johnson [163], respectively. The $\varepsilon_f^p(\sigma_m/\sigma_{fl})$ locus is plotted given ε_f^p vs. σ_m/σ_{fl} (measured or calculated) for the alloy coupled with the continuum relationship between σ_m/σ_{fl} and x. Represented schematically below the abscissa of Figure 62 are the crack tip, blunted to an opening displacement of δ, the critical distance, l^*, and void-nucleating particles. As δ increases with increasing remote loading, the ε^p field shifts as indicated by the solid arrow in Figure 62. The σ_m/σ_{fl} field shifts in a similar manner as σ increases, but is also affected by yield strength and work hardening levels [85,143]. The δ increases until the ε^p and $\varepsilon_f^p(\sigma_m/\sigma_{fl})$ curves intersect and ε^p exceeds $\varepsilon_f^p(\sigma_m/\sigma_{fl})$ at $x \leq l^*$. This applied δ corresponds to the fracture initiation toughness, δ_{IC}, and defines the associated critical value of ε_f^p (ε_f^*).

A predictive equation is derived from Eq. 7, given that $\varepsilon^p = \varepsilon_f^*$ and $x = l^*$ for $\delta = \delta_{IC}$:

$$\delta_{IC} = l^* \left(\frac{\overline{\varepsilon_f^*}}{Cl} \right)^{\frac{1}{C2}} \qquad [8]$$

δ_{IC} is the product of intrinsic ductility and the critical size scale for microvoid processes, similar to an expression derived based on the extent of stable void growth [103]. Equation 8 is expressed in terms of K through the following relationships between J, K and δ [132,143,145]:

$$\delta = d_n \frac{J}{\sigma_{ys}} \qquad [9]$$

$$J = \frac{K^2 (1 - \nu^2)}{E} \qquad [10]$$

The dimensionless constant, d_n, is a function of N, stress state, σ_{ys}/E, and the definition of δ. The quantity, ν, is Poisson's ratio. For plane-strain constraint, $K = K_{JICi}$ corresponding to $\delta = \delta_{IC}$:

$$K_{JICi} = \sqrt{\frac{\sigma_{ys} E l^*}{(1 - \nu^2) d_n} \left(\frac{\overline{\varepsilon_f}}{Cl} \right)^{\frac{1}{C2}}} \qquad [11]$$

Values of d_n are related linearly to N between 0.0 and 0.2 (Table 11; $d_n = 0.58 - 1.4N$), and are similar to those given by analytical solutions [143,145]. The parameters, C1 and C2, are obtained for any N by interpolating linearly between curve fits (Eq. 7) of FEM results for N = 0, 0.1, and 0.2 (Table 11). The remaining alloy deformation properties can be measured. Each of these parameters (C1, C2, d_n), as well as σ_{ys}, E and ε_f^* in Eq. 11, are temperature-dependent.

Procedures

Alloy Systems

Extensive data on microstructure, as well as temperature-dependent deformation properties, stress state-governed fracture strains and fracture-initiation toughnesses were obtained for nine Al alloys. The nine alloys belong to four systems: 1) ingot metallurgy (I/M) [19,39,119], 2) spray formed (SF), 3) powder-metallurgy (P/M), SiC-particulate-reinforced metal-matrix composite

(MMC) [61-63], and 4) P/M, submicron-grain-size (SM/GS) [24,144]. Alloy designation, product form, and nominal composition are listed in Table 12. The I/M alloys, MMC matrix, and SF alloy are precipitation-hardened, and the tempers are indicated. AA2134 was characterized in both the underaged (UA) and overaged (OA) conditions [119]. The composition of N203 is similar to AA2519+Mg+Ag, differing mainly in the Mn and Zr contents. The SM/GS alloys were processed by two different P/M techniques, cryogenic milling (CM Al) or rapid solidification by melt spinning (AA8009), followed by powder compaction, hot extrusion, and rolling [24,144]. Thicknesses of sheet, plate, and extrusion range from 3.2 mm to 25.4 mm. Processing and microstructural details for each alloy are reported elsewhere [16,19,24,39,62,144,168].

Fracture Toughness

Longitudinal-transverse-oriented (LT) compact-tension (CT) specimens were precracked by fatigue to crack length-to-width ratios (a/W) between 0.5 and 0.6. The CT thickness was 3.2 mm for AA2519+Mg+Ag and N203, 3.9 mm for AA2095 and AA2195, 6.3 mm for CM Al and AA2009/SiC/20p, and 7.6 mm for AA2618 and AA8009. The 6.3 mm- and 7.6 mm-thick specimens were sidegrooved by 20% of the gross thickness. Fracture-toughness temperatures ranged from -185°C to 325°C, depending on the alloy system. Specimens were tested at a constant actuator displacement rate of between 0.26 μm/s and 2.5 μm/s, and the duration of each experiment ranged from 15 minutes to 3 hours.

The J vs. Δa behavior for AA2618, AA2519+Mg+Ag, N203, CM Al, AA8009, and AA2009/SiC/20p was characterized using the ASTM Standard Test Method for Determining J-R Curves (E 1152) and the DCPD technique without partial unloading [12,25,39,131]. Initial crack extension was associated with the first deviation from the baseline trend of the DCPD vs. load-line displacement data. Values of K_{JICi} were calculated at this point from the applied J using Eq. 10. J- dominance and plane strain prevailed for each alloy at initial crack extension according to the criteria of ASTM E 1152 [132]. Details of these experiments are reported elsewhere [19,24,39,62,144].

The J vs. Δa curves for AA2095 and AA2195 were measured using ASTM E 1152 and unloading-compliance-based crack-length measurements. The 0.2 mm-offset-blunting-line construction from the ASTM Standard Test Method for J_{IC}, A Measure of Fracture Toughness (E813) defined the applied J associated with initial crack extension. Significant crack extension accompanies the blunting-line definition of fracture-initiation toughness (K_{JIC}), leading to an overestimate of K_{JICi} compared to values from the DCPD method [62]. The provisional fracture-

initiation toughness (K_Q) from the ASTM Standard Test Method for Plane-Strain Fracture Toughness of Metallic Materials (E 399) was reported for AA2134 [119].

Deformation Properties

Based on uniaxial-tensile tests, the 0.2%-offset yield strength, σ_{ys}, elastic modulus, E, work- hardening exponent, N, and percent reduction of area, %RA, were reported for each alloy as a function of temperature [19,24,39,41,61,119,144,169]. Recent results for N203 are listed in Table 13. Table 14 summarizes values of σ_{ys}, E, N, and %RA corresponding to the lowest and highest test temperatures for each alloy. Values of σ_{ys}, E, and N decrease monotonically for each alloy as temperature increases, with the rate of decline dependent on the specific alloy. Values of %RA show two temperature dependencies: increasing %RA as temperature increases for the I/M, SF and MMC systems [19,41,61,169]; and decreasing %RA as temperature increases for SM/GS alloys [24,49,144].

Void-Nucleating Particle Spacings

The size and spacing of primary void-nucleating particles were evaluated, as these influence ductility and fracture toughness strongly, and are correlated with l^* [17,103,163]. Measured volume- fraction (f_v) and average radius (r) data for void-nucleating particles in AA2618, AA2134, and AA2009/SiC/20p were taken from the original studies [39,62,119]. For AA2095, AA2195, AA2519, and N203, measurements of r and f_v were averaged over longitudinal, transverse, and through- thickness metallographic sections. With the exception of AA2195, particles smaller than 2 μm in diameter were assumed not to participate in primary void nucleation and were ignored. In AA2195, constituent particles were small, and the lower-bound diameter was 0.5 μm.

Three measures of interparticle spacing were obtained for each alloy. The mean free path (λ), which is independent of particle shape and distribution, is equal to $(4/3)r(1-f_v)/f_v$ [130]. The center-to-center nearest-neighbor spacings of a random distribution of spherical particles on a plane (Δ_2) and in a volume (Δ_3) are given by [130]:

$$\Delta_2 = \bar{r}\left(\frac{\pi}{6f_v}\right)^{\frac{1}{2}} \qquad [12]$$

$$\Delta_3 = 1.18\ \bar{r}\left(\frac{\pi}{6f_v}\right)^{\frac{1}{3}} \qquad [13]$$

The area fraction measured by image analysis is assumed to equal f_v. For AA2134, the average constituent-particle radius for the four different Mn contents was calculated from published values of f_v and λ [119]. The results of the particle-spacing analysis are summarized in Table 15. The types and compositions of constituent particles are listed for each alloy, and discussed elsewhere [19,39,62,119,168].

Stress State-Governed Intrinsic Fracture Resistance

In order to determine ε_f^* for input into the strain-controlled model (Figure 62), the effective plastic failure strain, ε_f^p, must be measured or calculated for a wide range of σ_m/σ_{fl}. Failure in this context is defined as the measured strain for a critical level of void damage [120,142]. The $\varepsilon_f^p(\sigma_m/\sigma_{fl})$ loci considered here were constructed by testing notched-tensile specimens for selected alloy systems and deformation temperatures.

Values of ε_f^p are calculated from the following expression [120,134,135,170]:

$$\bar{\varepsilon}_f^p = 2\ln\left(\frac{d_o}{d_f}\right) = -\ln\left(1-\frac{\%RA}{100}\right) \qquad [14]$$

The initial and final diameters at the minimum cross section, d_o and d_f, respectively, are measured for each smooth- or notched-round-tensile specimen [19,24,61,120,121]. In this study, the easily-measured %RA at fracture was used in Eq. 14, instead of the diametral strain at the critical damage event, resulting in an overestimated ε_f^p. Experimental and computational studies suggest that this error is small because reduction of the minimum cross-sectional area is limited after the critical damage event [120,142]. The stress state, σ_m/σ_{fl}, is governed by the ratio of the initial notch-root diameter, d_o, to the profile radius of the notch (R) [120,121,135,170]:

$$\left(\frac{\sigma_m}{\sigma_{fl}}\right) = \frac{1}{3} + \ln\left(\frac{d_o}{4R}+1\right) \qquad [15]$$

Figure 63 shows a failure locus for AA2519+Mg+Ag measured at 25°C, compared to a model prediction of the locus based on a void-growth law [19,125]. The ratio of uniaxial-tensile ε_f^p ($\sigma_m/\sigma_{fl} = 0.3$) to ε_f^* is defined as the constraint ratio (r), and is determined rigorously by the construction shown in Figure 62. The value of r for AA2519+Mg+Ag at 25°C is 6.5 (Figures 62

and 63) [19]. The ratio, r, is used to reduce uniaxial-tensile fracture strains to high-constraint values of ε_f^p, representative of the crack-tip process zone.

The dependence of ε_f^p on σ_m/σ_{fl} varies significantly for different aluminum alloys, as illustrated in Figure 64 for AA2009/SiC/20p as well as UA and OA 2134 (0.6% Mn) [63,119]. Values of ε_f^p for OA 2134 are more sensitive to σ_m/σ_{fl} (r = 8, from the construction in Figure 62) compared to those for UA 2134 (r = 3). This difference may relate to localized slip in the UA temper which promotes strain-localized void nucleation and/or void coalescence at low σ_m/σ_{fl} [119]. Values of ε_f^p for AA2009/SiC/20p are insensitive to global σ_m/σ_{fl} up to 175°C (i.e., r = 1) because local constraint on matrix plastic flow dominates ε_f^p [63]. These systems illustrate that r can vary from 1 to as high as 8, depending on alloy microstructure and the mechanisms of void nucleation through coalescence.

Failure loci do not exist for the widely varied temperatures of interest; it is necessary to employ simplifying assumptions to facilitate modeling of K_{JICi}. In most cases, ε_f^p is measured from uniaxial-tensile specimens (σ_m/σ_{fl} = 0.3) as a function of temperature and divided by r to obtain ε_f^*. For alloys where a failure locus was measured for only one temperature, r was determined from the construction in Figure 62 and was assumed to be temperature-invariant. Temperature-independent r was observed for 2519+Mg+Ag and AA2009/SiC/20p up to a temperature of 175°C, as shown in Figures 65 and 66 [19,63]. The value of r for AA8009 was measured as seven from the $\varepsilon_f^p(\sigma_m/\sigma_{fl})$ locus at 25°C [24]. For the remaining systems, r was estimated as seven [17].

Values of ε_f^* are plotted in Figures 67 through 69 for the I/M and SM/GS Al alloys over the temperature ranges given in Table 14, and the appropriate r values are indicated. Fracture strains for AA2519+Mg+Ag and N203 rise sharply as temperature increases, and are significantly higher than the values for AA2618 which increase only modestly with increasing temperature (Figure 67). Values of ε_f^* increase monotonically from cryogenic to elevated temperatures for

---

17 A constraint ratio of 7 is a reasonable choice, based on void-growth laws [103,125] and measured failure loci for Al alloys and steels [19,24,63,117,120].

AA2195, but exhibit a possible minimum for AA2095 (Figure 68). Fracture strains decrease significantly from 25°C to 175°C for CM Al and AA8009 (Figure 69), consistent with observations for other SM/GS Al alloys [70,171]. Values of ε_f^* for AA2009/SiC/20p are inferred from Figure 66 Up to 175°C, r equals 1 and thus ε_f^* equals ε_f^p, while for temperatures above 200°C r is greater than 1. Values of r above 175°C cannot be determined using the construction in Figure 62 since only one notched- tensile constraint level (σ_m/σ_{fl} = 1.0) was tested, and ε_f^* is assumed to equal notched-specimen ε_f^p. The mechanisms controlling the temperature dependencies of ε_f^* for the various Al alloys are considered elsewhere [19,24,61,144].

Results

With the parameters; σ_{ys}, E, ε_f^*, d_n, C1, and C2; determined as a function of temperature, K_{JICi} is predicted through Eq. 11. Uniaxial-tensile properties are the sole inputs for AA2095, AA2195, AA2618, N203, and CM Al [39,41,144,169]. Notched-specimen experiments are used to augment these inputs for AA2519+Mg+Ag, AA2009/SiC/20p-T6, AA8009, and AA2134 [19,24,61,119]. A single adjustable parameter, l^*, is calculated by equating measured and predicted K_{JICi} at a single temperature. This constant is assumed to be temperature-independent.

Precipitation-Hardened Alloys

AA2519-T87 (+Mg+Ag):

The temperature dependence of K_{JICi} for AA2519+Mg+Ag is predicted successfully by Eq. 11, as shown in Figure 70 and with ε_f^* based on both uniaxial- and notched-tensile %RA (Figure 67) [19]. Variability in the measured tensile properties (e.g., %RA) leads to variability in predicted K_{JICi}. A linear-regression fit to the K_{JICi} measurements agrees reasonably with fits to predictions from both uniaxial- and notched-specimen data, as shown in Table 16. A 95%-confidence-interval estimate of the slope (ß) using the student-t-distribution indicates that there is no significant difference between ß for the measurements ($-0.043 < ß < 0.018$), uniaxial-specimen predictions ($-0.026 < ß < 0.027$), and notched-specimen predictions ($-0.028 < ß < 0.026$).

Both measured and predicted K_{JICi} of AA2519+Mg+Ag are essentially temperature-invariant from 25°C to 175°C (ß≈0). Equal values of l^* (20.5 μm) were calculated from average measured K_{JICi} at 25°C, for both the uniaxial- and notched-tensile cases, and were

used to predict K_{JICi} from 75°C to 175°C. The calculated value of l^* correlates with the planar nearest-neighbor spacing of undissolved Al_2Cu and Fe-bearing constituent particles for AA2519 (Δ_2 = 18.8 μm), and is nearly two times greater than their nearest-neighbor spacing in a volume (Δ_3 = 11.9 μm).

AA2618-T851 and N203-T6:

The strain-controlled fracture-toughness model (Eq. 11) predicts effectively the temperature dependence of K_{JICi} for AA2618 and N203. Figure 71 shows modeling results based only on uniaxial-tensile tests of AA2618 and N203. Linear-regression fits to measurements and predictions are in excellent agreement, and show that K_{JICi} increases as temperature increases for N203 (Figures 71 and Table 16). For AA2618, predicted K_{JICi} is nearly constant from 25°C to 175°C (ß = -0.012), compared to a temperature-invariant measured K_{JICi} (ß = -0.0004). Both predicted and measured K_{JICi} increase mildly between 175°C and 225°C. From measured K_{JICi} at 25°C, l^* values of 14.8 μm and 20.3 μm were calculated for AA2618 and N203, respectively. These l^* values are from 1 to 2 times the nearest-neighbor spacing ($l^* = 1.5\Delta_2 = 1.8\Delta_3$), and 1 to 3 times the nearest-neighbor spacing ($l^* = 1.7\Delta_2 = 2.4\Delta_3$), for AA2618 and N203, respectively.

AA2095-T8 and AA2195-T8:

Considering a wider temperature range including cryogenic levels, modeling using uniaxial-tensile properties predicts that K_{JICi} is constant for AA2095, and increases monotonically for AA2195, as temperature increases (Figure 72 and Table 16). For AA2095, Table 16 shows that the temperature dependencies of predicted (ß = 0.003) and measured (ß = 0.005) K_{JICi} agree. Predicted and measured K_{JICi} for AA2195 agree only for selected temperatures (i.e., 135°C and -140°C; Figure 72). Values of K_{JICi} are predicted to increase as temperature increases (ß = 0.023), which does not agree with a linear-regression fit to measured K_{JICi} data (ß = -0.006). However, measured K_{JICi} for AA2195 shows broad scatter, resulting in uncertainty in the measured temperature dependence. The variability of measured K_{JICi} could be associated with the offset definition of initiation toughness coupled with the difficulty in measuring precisely the steeply rising J vs. Δa curve for small crack- growth increments [131]. Calculated values of l^* are 29.6 μm for AA2195 (from measured K_{JICi} at 25°C), and 21.9 μm for AA2095 (from measured

K_{JICi} at -75°C). A value of l^* is not calculated at 25°C for AA2095 because of the erratically low ε_f^*.

AA2009/SiC/20p-T6:

Prediction of K_{JICi} is perhaps most challenging for the complex microstructure of the MMC, which contains a high volume fraction of void-nucleating SiC particles [61]. Values of ε_f^p (Figure 66) are insensitive to global σ_m/σ_{fl} (i.e., r = 1) only below 175°C, but ε_f^p is assumed to equal ε_f^* at all temperatures due to a lack of %RA data for high constraint levels (i.e., $\sigma_m/\sigma_{fl} \approx$ 1.5). Due to the inherent variability in measured K_{JICi} from SiC-particle clustering, upper-bound and lower-bound l^* values were calculated at 25°C from Eq. 11, and used for toughness predictions from 50°C to 316°C. Upper-bound and lower-bound predictions of K_{JICi} vs. temperature are plotted in Fig. 73 [61]. Two symbols are used for measured K_{JICi}; error bars represent the maximum variability among replicate results, and solid squares show single measurements. While upper-bound predictions exceed measured K_{JICi} at all temperatures, the lower-bound predictions agree with the measured values. The measured temperature dependence is predicted for both l^* values. Upper- and lower- bound l^* values (6.4 μm and 11.3 μm) are reasonable, corresponding to between 3 and 4 times the nearest-neighbor SiC-particle spacing. The unique issues associated with modeling K_{JICi} of an MMC are considered elsewhere [61].

Submicron Grain Size Alloys:

Submicron-grain-size alloys suffer losses in σ_{ys}, E, N, and ε_f^* as temperature increases, as demonstrated by uniaxial-tensile results (Table 14 and Figure 69) [24,144]. Because each of these material properties decreases as temperature increases, K_{JICi} is predicted to decrease. Predicted temperature dependencies correlate with those measured, as established in Figure 74 [24,144]. The temperature dependence of predicted K_{JICi} for CM Al (ß = -0.037 for 25<T<175°C and ß = -0.017 for 175<T<325°C) agrees reasonably with measured trends (ß = -0.045 for 25<T<175°C and ß = - 0.015 for 175<T<325°C), as presented in Table 16. The model also predicts the temperature dependence of measured K_{JICi} for AA8009 (Figure 74 and Table 16), but the magnitude of K_{JICi} is overpredicted at 175°C and above. At 25°C, l^* is calculated as 8.0 μm for CM Al and 16.8 μm for AA8009. If a second l^* (7.2 μm) is calculated for AA8009 from

measured K_{JICi} at 175°C, then predicted and measured values of K_{JICi} agree for temperatures from 200°C to 316°C [24]. A change in deformation mode was postulated, and a change in dimple morphology (from spherical and well-developed at 25°C to shallow above 175°C) was observed, which may correspond to a change in l^*. A similar but more subtle change in dimple morphology from spherical at 25°C to faceted at 175°C was observed in CM Al [144]. If a second l^* (6.6 μm) is calculated for CM Al at 175°C, predicted K_{JICi} agrees with measured values. A varying l^* with a change in the dominant stage of MNG is possible.

Microstructural Influences on K_{JICi}

In addition to temperature effects, the strain-controlled model can provide understanding of microstructure and yield-strength effects on K_{JICi}. Literature results on UA and OA AA2134-type alloys provide data for the toughness dependence on Mn content and aging condition [119] Measured values of K_Q are plotted for both aging conditions as a function of Mn content in Figure 75; such values exceed K_{IC} because the thickness criterion from ASTM E 399 was not satisfied. Values of K_Q increase mildly as Mn is added in amounts up to 0.6 wt%, then decrease sharply as the Mn content is increased to 1.0% [119]. The initial rise in K_Q was attributed to the formation of submicron Mn-rich dispersoids that homogenized slip, while K_Q declined as excess Mn formed large constituents [119]. This trend was observed in both the UA and OA conditions, with a lower measured K_Q in the overaged condition.

Predicted K_Q from measured uniaxial- and notched-tensile properties for the UA and OA tempers is plotted in Figure 75. The model (Eq. 11) predicts the maximum and subsequent decline in K_Q as Mn content is increased, as well as the lower toughness in the OA temper. Agreement between predicted and measured values is adequate for the OA temper and exceptional for UA AA2134. Values of l^* were not calculated by equating measured and predicted K_Q at one Mn content, rather, such values were assumed to be a constant multiple of Δ_3, and the constant was adjusted until the best agreement was obtained at $l^* = 4\Delta_3$. The spacing, Δ_3, is identical for the UA and OA tempers because constituent size and distribution are not affected by aging. The l^* corresponding to each Mn content is listed on the top abscissa in Figure 75. At the three lower Mn contents, voids nucleated at undissolved Al_2CuMg particles. For 1.0% Mn, the volume fraction of Mn containing constituents increased, voids nucleated from these particles, and Δ_3 and l^* decreased [119].

Lower toughness is measured and predicted for the OA temper, despite higher uniaxial-tensile ε_f^p compared to the UA temper, because ε_f^p is less sensitive to stress-state triaxiality in the UA condition (Figure 64). This complexity illustrates the danger in predicting K_Q solely from uniaxial-tensile data. Microstructural changes may alter the shape of the $\varepsilon_f^p(\sigma_m/\sigma_{fl})$ locus and r may not equal seven.

Discussion

Accuracy of Strain-Controlled Model

Comparison between predicted and measured K_{JICi} shows that the plastic-strain-based model accurately predicts the temperature dependencies of initiation toughness for Al alloys. Once l^* was determined for each of the nine alloys systems modeled, K_{JICi} was predicted for 57 conditions of changing temperature or microstructure. The 57 conditions do not include the single temperature at which the measured and predicted K_{JICi} were equated. Of the 57 predictions, 49 are directly comparable to measured K_{JICi} from identical test temperatures and microstructures.

The average difference between predicted and measured K_{JICi} for the 49 conditions is 16%. Notably, 17 predictions are within 5% of the measured values, 10 predictions are within 10%, and 11 predictions range between 10% and 20% difference. The 11 predictions which differ from the measurements by more than 20% are among four alloys: AA8009, AA2009/SiC/20p, CM Al, AA2195. The average difference between predicted and measured K_{JICi} is 28% for these four alloys with a total of 22 predictions. The average difference between predicted and measured K_{JICi} is only 7% for the other five systems (AA2095, AA2618, AA2519+Mg+Ag, AA2134, and N203).

The model is least accurate for the two alloys with the most complex microvoid fracture mechanisms; viz., AA8009 and AA2009/SiC/20p. AA8009 shows a change in dimple morphology (attributed to a change in deformation mode) as temperature increases from 25°C to 175°C [24,39]. If two values of l^* are employed, corresponding to these two microvoid fracture modes, then model predictions of K_{JICi} are accurate. The physical interpretation of l^* in this case, however, is complex and uncertain [39]. AA2009/SiC/20p contains a high volume fraction of inhomogenously distributed SiC particles that may compromise the continuum nature of the crack-tip strain field and thus affect model accuracy, as detailed elsewhere [61]. Model accuracy is better for CM Al and AA2195, with an average difference between predicted and measured K_{JICi} of 16%. In AA2195 the variability in measured K_{JICi} accounts for the difference. The difference in

CM Al is attributed speculatively to a subtle change in dimple morphology as temperature increases from 25°C to 175° C, analogous to the AA8009 case [144].

These experimental verifications provide a strong confirmation of the plastic-strain based model of crack-tip initiation toughness.

Temperature Dependence of K_{JICi}

The strain-controlled model identifies the interplay between crack-tip ε^p, ε_f^*, and l^* that governs initiation fracture toughness. Microvoid-rupture K_{JICi} does not scale solely with either the deformation properties (σ_{ys}, E, N) that govern crack-tip stress and strain or the intrinsic fracture resistance (ductility). Rather, both elements must be combined with a fracture initiation criteria to predict the "composite" property of K_{JICi}. This analysis provides a basis for a more fundamental understanding of temperature-dependent toughness.

The relative sensitivities of crack tip ε^p and $\varepsilon_f^p(\sigma_m/\sigma_{fl})$ to temperature dictate the temperature dependence of K_{JICi}, when l^* is assumed to be temperature-invariant. The parameters; σ_{ys}, E, d_n, C1, and C2; describe crack-tip strain for a given K (Eqs. 7, 9, and 10). Values of σ_{ys} and E decline monotonically with increasing temperature for each Al alloy. In addition d_n, C1, and C2 depend on N (Table 11), and hence indirectly on temperature. Values of d_n increase monotonically with increasing temperature due to decreasing work hardening (decreasing N) for all alloys. Values of C1 decrease, while C2 increases, with rising temperature.

The interplay between $\varepsilon_f^p(\sigma_m/\sigma_{fl})$ and crack-tip ε^p is illustrated by the two terms in Eq. 11 which represent the temperature dependencies of these elements, viz., $\{l^*[\varepsilon_f^*/C1]^{1/C2}\}$ and $\sigma_{ys}E/[d_n(1-\nu^2)]$, respectively. The former term is δ_{IC} from Eq. 8 and the latter term represents the conversion of δ_{IC} to K_{JICi} (denoted δ-K) from Eqs. 9 and 10. The temperature dependence of the former term is controlled by ε_f^*, since l^* may be temperature-invariant and temperature effects on C1 and C2 offset[18]. In the latter term and as temperature increases, σ_{ys} and E decrease, and d_n increases; δ-K and K_{JICi} decline. Physically, crack tip strain is increased with increasing

---

18 Calculations show that predicted K_{JICi} differ by less than 3% regardless of the C1-C2 pair selected within the limits given in Table 11.

temperature for a fixed x and K[19]. The applied K to initiate fracture is decreased.

Temperature insensitive K_{JICi} arises when δ_{IC} and δ-K counterbalance. For AA2519+Mg+Ag, uniaxial-tensile ε_f^* increases by 63%, from 0.08 at 25°C to 0.13 at 175°C. The absolute values of C1 and C2 in Eq. 8 lead to a moderated increase in δ_{IC} of 50%, from 13.9 μm at 25°C to 20.9 μm at 175°C. Over the same temperature range, σ_{ys} and E decrease by 20% and 12%, respectively (Table 14), while d_n increases by 8%. The parameter δ-K decreases by 35%, from 7.7×10^7 MPa^2 at 25°C to 5.1×10^7 MPa^2 at 175°C. Values of K_{JICi}, expressed as $(\delta_{IC} \times \delta\text{-}K)^{1/2}$, are nearly equal at 25°C and 175°C; the ratio of predicted K_{JICi} from uniaxial-tensile data at 25°C to that at 175°C is 1.002. The increased fracture resistance at 175°C is effectively offset by the enhanced crack-tip strain field at a given K. A similar competition between the temperature dependencies of δ_{IC} and δ-K results in approximately temperature insensitive K_{JICi} for AA2618 and AA2095.

Values of K_{JICi} decrease above 200°C for AA2009/SiC/20p, despite the dramatically increasing intrinsic fracture resistance (Figure 66), which demonstrates the strong influence of temperature-dependent crack-tip ε^p on K_{JICi}. From 25°C to 316°C, ε_f^* changes from 0.03 to 0.26 (a 910% increase), corresponding to increased δ_{IC} from 1.7 μm to 11.9 μm (for the lower-bound l^* of 6.5 μm). The term δ-K decreases by an order of magnitude, from 1.3×10^8 MPa^2 at 25°C to 1.1×10^7 MPa^2 at 316°C. The K_{JICi} prediction at 316°C (11.6 MPa$\sqrt{m}$) is 21% lower than the prediction at 25°C (14.6 MPa$\sqrt{m}$), despite the 7-fold increase in δ_{IC}, because enhanced crack-tip ^{p}

---

19 Crack-tip ε^p is derived in terms of K by substituting Eqs. 9 and 10 into Eq. 7 to yield:

$$\bar{\varepsilon}^p = C1 \left(\frac{d_n K^2 (1 - \upsilon^2)}{\sigma_{ys} E x} \right)^{C2}$$

which demonstrates the effects of temperature-dependent σ_{ys}, E, and d_n.

results in a lower applied K necessary for ε^p to exceed ε_f^* over l^*.[20]

Interplay between δ_{IC} and δ-K also governs the elevated-temperature degradation of K_{JICi} for SM/GS Al alloys. Because of uniquely decreasing ε_f^* as temperature increases (counter to large- grained precipitation-hardened Al alloys), δ_{IC} and δ-K cooperatively degrade K_{JICi}. For AA8009, predicted δ_{IC} declines from 13.9 μm at ambient temperature to 10.6 μm at 316°C, while δ-K decreases from 7.7×10^7 MPa^2 to 3.5×10^7 MPa^2. The combined effects of the degradation in ε_f^* at elevated-temperature and increased crack tip strains at a given K, cause predicted K_{JICi} to decline, from 32.7 MPa$\sqrt{m}$ at 25°C to 19.2 MPa$\sqrt{m}$ at 316°C. When temperature is increased from 25°C to 325°C in CM Al, predicted δ_{IC} decreases from 4.9 μm to 1.7 μm, δ-K declines from 3.8×10^7 MPa^2 to 1.7×10^7 MPa^2, and hence K_{JICi} is predicted to decline from 13.6 MPa$\sqrt{m}$ to 5.5 MPa$\sqrt{m}$.

The temperature-dependent interplay between δ_{IC} and δ-K is crucial for successfully predicting and understanding temperature-dependent K_{JICi}. Micromechanical models that consider only the temperature-dependent plastic-strain field [108,163] predict declining fracture toughness with increasing temperature for precipitation-hardened AA2519+Mg+Ag, AA2618, AA2095, AA2195, and N203, counter to the mildly rising, mildly declining, or temperature-insensitive K_{JICi} measured for these alloys. For the SM/GS alloys, AA8009 and CM Al, only a mild decline in K_{JICi} would be predicted. For AA2009/SiC/20p, the temperature dependence of K_{JICi} is reasonably predicted solely from declining σ_{ys}, E, and N, due to the dominance of crack-tip ε^p in controlling initiation toughness [61], but this agreement is fortuitous.

---

20 The functionality of the crack tip strain field (Eq. 7), described by the absolute values of C1 and C2, diminishes the impact of temperature dependent ε_f^* on K_{JICi}. For AA2009/SiC/20p, ε_f^* increased by 910% from 25°C to 316°C, but predicted δ_{IC} (Eq. 8) increased by only 600% If ε_f^* and δ_{IC} were linearly related as has been proposed [85,103,117], then ε_f^* would have a stronger effect on K_{JICi}. Equation 11, rederived based on this linear relationship, would not predict the decrease in K_{JICi} above 200°C for AA2009/SiC/20p (K_{JICi} at 316°C would be predicted as 14.1 MPa$\sqrt{m}$). The relationship between ε_f^* and δ_{IC} is important for alloys where ε_f^* is strongly temperature-dependent.

The strain-controlled model is an effective tool for screening alloys for further fracture toughness characterization. For example, AA2195 is a candidate alloy for cryogenic tank applications. The predicted decline in K_{JICi} from 38.1 MPa$\sqrt{m}$ at ambient temperature to 30.2 MPa$\sqrt{m}$ at -185°C indicates that initiation toughness characterization at cryogenic temperatures is warranted. For this case, the deformation properties increase as temperature decreases to -185°C, and δ-K increases from $9.8x10^7$ MPa^2 to $1.3x10^8$ MPa^2. However, predicted δ_{IC} decreases sharply from 14.7 μm to 7.3 μm, resulting in the predicted decrease in K_{JIC}. Modelling traces the predicted decrease in cryogenic temperature K_{JIC} of AA2195 to a decline in ε_f^*. Because the microstructure does not change from ambient to cryogenic temperatures, the likely cause of the rapid degradation in ε_f^* is either an insufficient increase in work hardening, a decrease in strain-rate sensitivity, or increased yield strength as temperature decreases. The mechanism for this effect must be established.

Microstructural Influences on K_{JICi}

The effect of microstructure on initiation toughness is understood from the strain-controlled model, via the interplay between the deformation-property-dependent crack-tip strain-field term, δ-K, and the intrinsic crack initiation resistance term, δ_{IC}. δ_{IC} does not mirror changes in ε_f^* because l^* is not constant. For AA2134, δ-K changes mildly with the addition of manganese, in either the underaged ($5.9x10^7$ MPa^2 < δ-K < $6.8x10^7$ MPa^2) or overaged ($6.9x10^7$ MPa^2 < δ-K < $7.3x10^7$ MPa^2) tempers. Effects of Mn on K_Q thus reflect trends in δ_{IC}. For Mn contents of 0.0%, 0.3%, 0.6%, and 1.0%, δ_{IC} equalled 43.3, 48.0, 44.3, and 20.3 μm for the underaged (UA) temper and 23.5, 26.9, 20.7, and 11.9 μm for the overaged (OA) temper.

The success of the strain-controlled fracture toughness model in predicting K_Q for UA and OA tempers of AA2134 with varying Mn (Figure 75) illustrates model flexibility. The peak in K_Q between 0.3% and 0.6% Mn was predicted without explicit modelling of slip localization and its effect on each stage of MNG [119]. The failure locus for each temper (Figure 64) and its role in fracture initiation ahead of a crack (with a σ_m/σ_{fl} gradient) offers insight into fracture micromechanics. Fracture of OA AA2134 is sensitive to stress-state triaxiality, while fracture of UA AA2134 (prone to slip localization) is less sensitive to triaxiality [119].

Uncertainties in ε_f^*

Strain-based micromechanical modeling of initiation fracture toughness yields reasonable values of l^*, as well as accurate temperature-dependencies of K_{JICi}. Absolute values of K_{JICi} are not predicted, however, due to uncertainties in ε_f^* and l^*. Three uncertainties in ε_f^* are discussed.

Damage Correlation:

Initiation-toughness models predict the K level for initial crack-tip process-zone damage. Standard measures of initiation toughness may not be modeled accurately if the measurement reflects stable crack extension [61,62,131]. Rather, model predictions are best compared to a high-resolution indication of the K level for initial crack extension. Initiation toughness determined from DCPD measurements, K_{JICi}, is well suited for this purpose. In contrast the temperature dependencies of K_Q and K_{IC} (from ASTM E 399) or K_{JIC} (from ASTM E 813) are predicted from Eq. 11 (Figures 72 and 75), but l^* values may be overestimated. Fracture initiation defined by the 95% secant line (K_Q, K_{IC}) or 0.2 mm-offset-blunting line (K_{JIC}) leads to increased measured K at fracture initiation due to stable crack growth along a finite-sloped R-curve. For example, an overestimated initiation toughness in AA2134 may have resulted in the higher calculated l^* value of $4\Delta_3$, compared to $1.7\Delta_3$ for AA2519+Mg+Ag and $1.8\Delta_3$ for AA2618. The extent of the error in l^* increases with increasing plane strain-tearing resistance and with decreasing specimen thickness (due to an increased amount of stable plane stress crack growth with rising K).

Ultimately, the comparison between measured and modeled initiation toughness is an exercise in equating damage for different stress and strain fields, particularly those for a crack tip vs. a blunt notch or uniaxial-tensile specimen. The most relevant experiments are those that detect equivalent levels of microvoid damage at ε_f^* for a tensile bar and at K_{JICi} for a precracked specimen. A technique was developed to detect the formation of a central flaw within uniaxial- and notched-tensile specimens deformed at a constant strain-gage extensometer rate [120,125], but this procedure was not correlated with the microvoid damage levels in the crack-tip process-zone at detected fracture initiation. In principle direct current potential difference monitoring can detect equivalent levels of microvoid damage in a tensile specimen and ahead of a crack tip, but this has not been accomplished. Rather, ε_f^* is approximated by a more global measurement such as %RA.

Approximation of ε_f^P:

The use of Bridgman's [134] analysis to calculate ε_f^P (Eq. 15) may overestimate the actual strain required to damage and fracture a notched tensile specimen by up to a factor of 2 [25,63,170]. Finite element modelling demonstrated that strains on the surface of a notched specimen and in the center are overestimated and underestimated, respectively, by Bridgman's equations [170]. The degree of error is insensitive to work hardening [25], but increases for larger strains and more severe notch acuity [170]. Since this error is independent of work hardening and, hence, temperature, it is accounted for by calculating l^* at 25°C and does not affect significantly the predicted absolute values of K_{JICi} at elevated temperatures[21]. If the ε_f^P values in Figures 66 through 69 are corrected based on FEM results [170]; then ε_f^* decreases significantly, calculated l^* is larger, and process zone damage at K_{JICi} is predicted over more average particle spacings.

Stress-State Triaxiality Sensitivity:

Measurements for Al alloys [19,63,119,120,172] demonstrate differences in the stress-state-triaxiality dependence of ε_f^P. A smooth-to-notched constraint ratio, r_{sn}, is defined as $\varepsilon_f^P(0.3)/\varepsilon_f^P(1.0)$, since some of these alloys were characterized over a limited range of σ_m/σ_{fl}. The ratio, r_{sn}, equals 0.9 for global stress-state-insensitive AA2009/SiC/20p [63] and 3.9 for highly sensitive AA2519+Mg+Ag [19]. A range of sensitivities exist between these limits; with r_{sn} values of 1.4, 1.7, 1.9, 2.0, 2.2, and 3.0 for AA7075 [120], UA AA2134 [119], AA2024 [63], AA2090 [172], AA2618 [63], and OA AA2134 [119] respectively. Values of r_{sn} do not necessarily scale with the constraint ratio relevant to micromechanical modelling (r) because the sensitivity of ε_f^P to σ_m/σ_{fl} can change at higher constraint levels leading to crossovers between the failure loci. For example, r for AA2519+Mg+Ag is 6.5 (r_{sn}=3.9) while r for overaged 2134 equals 8.0 (r_{sn}=3.0). Experimental variability in failure loci, as well as mechanisms of MNG correlating to r, have not been defined.

The value of r for a given alloy depends on the stress-state-triaxiality sensitivity of each MNG stage, as well as the strain dissipated during each stage [173]. An exponential dependence of ε_f^P on σ_m/σ_{fl} derived from void-growth modelling (Figure 63) results in a theoretical r of 5.8

---

21 This error in fact depends on the magnitude of applied strain, which varies with test temperature.

between σ_m/σ_{fl}=0.33 and σ_m/σ_{fl}=1.5 [103,125]. If void nucleation is promoted by σ_m [122,124], then $\varepsilon_f^p(\sigma_m/\sigma_{fl})$ should change since an additional stress state dependence is involved in fracture evolution [173]. This effect is not significant in alloys where large, brittle particles nucleate voids at small strains [18,119], but may be significant in alloys where smaller particles nucleate voids by interface cohesion at relatively high strains [122,124]. A high volume fraction of large brittle void-nucleating particles precludes global stress-state-triaxiality sensitivity because local constraint on matrix deformation promotes high levels of local σ_m/σ_{fl} (i.e., AA2009/SiC/20p) [63]. Mean stress can affect the critical condition for void coalescence, limiting the strain evolved during stable void growth and altering the stress-state-triaxiality sensitivity [121,152].

Because the shape of the stress-state-dependent failure locus varies significantly from alloy to alloy, rigorous fracture toughness modeling must include ε_f^p measurements over a wide range of global σ_m/σ_{fl}. Determining ε_f^* from a single global-constraint level; as for AA2618, AA2095, AA2195, N203, and CM Al; is an oversimplification for correlating microvoid damage in a σ_m/σ_{fl} gradient. Even for alloys where a failure locus was measured at one or two temperatures [19,24,63], there is no guarantee that r is invariant with increasing temperature.

Interpretation of Calculated l^*

The critical distance, the sole adjustable parameter in the strain-controlled model (Eq. 11), is calculated by equating the measured and predicted K_{JICi} at a single temperature, and hence depends on accurate determination of this measured initiation toughness and each model input. Measurements or estimation of σ_{ys}, E, C1 and C2 do not affect significantly calculated l^*. Values of d_n vary modestly depending on whether analytical [145] or FEM [143] solutions are employed, affecting calculated l^* by about 20%. The strongest effect on calculated l^* is uncertainties in measuring ε_f^*; generally ε_f^* is overestimated, causing l^* to be underestimated.

Ultimately, l^* must be determined by an independent means for absolute toughness predictions. This distance should relate to the primary void-nucleating particle spacing for alloys that fail by microvoid fracture, and may represent the distance required for void coalescence at $K=K_{JICi}$. Calculated l^* for each Al alloy is given in Figures 70 through 75, while primary void-nucleating particle spacings are given in Table 15. The mean free path, λ, from a randomly placed

straight line on a polished metallographic section, is not relevant because damage does not evolve in random directions. Rather, microvoiding is confined to directions dictated by heterogeneous microstructural features and the crack tip strain field. The nearest-neighbor spacing of primary void-nucleating particles, randomly distributed in a plane (Δ_2) or in a volume (Δ_3), should relate to l^*, because the nearest neighbor particles govern the direction and size scale of void coalescence.

Complex microvoid fracture mechanisms and microstructural features obscure the relationship between l^* and Δ_3. For example, the majority of void damage in AA8009 likely accumulates within planar oxide sheets, oriented parallel to the plane defined by the loading and crack-growth directions in an LT CT specimen [24]. Void damage coalescence may occur by transverse ligament shear parallel to the crack front. Although the planar spacing of these oxide sheets is approximated as 12 μm [39], the relationship of this spacing with l^* is unclear. Similarly, clusters of Al_2O_3 dispersoids in CM Al and SiC in the MMC are speculated to nucleate void damage, but cluster spacing is difficult to define.

Figure 76 shows correlations between l^* and Δ_3 for steels [174-176] (solid symbols) and six of the Al alloys included in this work (open symbols). The distance, l^*, was calculated at each temperature where K_{JICi} was both measured and predicted. The standard deviation of l^* is given for AA2009/SiC/20p, AA2519+Mg+Ag, and AA2195 in Figure 76[22]. The error bars also include the effect of temperature, if any, on l^*. Sufficient data were available in the literature for steels to calculate l^* from Eq. 11 and measured K_{IC} [174-176]. For each Al alloy except AA2195, voids nucleated at 2 to 20 μm diameter and widely spaced particles identified in Table 15. Voids nucleated at smaller (0.5 to 1.0 μm) and more closely spaced particles in AA2195, and at large (3 μm) and closely spaced particles in the MMC. For each steel but one, microvoid fracture was governed by small (0.2 μm to 0.4 μm diameter), closely spaced sulfides or carbides. The exception is a Fe-0.4C low-alloy steel with additions of Ni and Si (•) which promoted the formation of larger 0.7 μm diameter sulfide particles that served as more widely spaced void-nucleation sites [175].

Figure 76 suggests two trends between l^* and Δ_3 for steels and aluminum alloys: one for alloys where microvoid fracture is controlled presumably by both widely spaced (large) particles as

---

22 Values of K_{JIC} for AA2195 at -75°C and -185°C are erratic and result in overestimated l^* values which are not included in the calculation of the standard deviation.

well as a second population of interdispersed submicron particles[23], and another for alloys where microvoid fracture is controlled by void damage associated with a single size distribution of relatively closely spaced particles. For the former case, l^* is nearly proportional to Δ_3, while for the latter case, l^* is about 5 times Δ_3. The two trends in Figure 76 are only reasonable if it is possible to explain the physical significance of the intercept. The linear regressions show that l^* is not zero for the two correlations, but rather equals 11 μm and -4 μm at a Δ_3 of zero. While a positive intercept could be rationalized, the negative value is meaningless. These correlations remain reasonable at about $1.8\Delta_3$ and $3.8\Delta_3$, if forced through zero. Alternately, l^* may not be a fixed multiple of Δ_3; the relationship may depend on microstructure and the details of MNG.

The data in Figure 76 are analyzed further based on the extent of primary void growth prior to coalescence. Data points with a diagonal slash represent alloys where the extent of stable void growth was quantified by the measured ratio of the final void radius (R_V) to the nucleating-particle radius (R_I). Values of R_V and R_I were measured from fracture-surface dimples in high constraint regions, directly ahead of the specimen fatigue precrack [174,175]. Figure 77 displays a unique relationship between R_V/R_I and l^*/Δ_3. The function $l^*/\Delta_3 = 1.6 + 0.025(R_V/R_I)^2$ was obtained by least squares curve fitting, with a coefficient of determination (r^2) equal to 0.92. (A linear fit, $l^*/\Delta_3 = 0.06 + 0.42(R_V/R_I)$, was also calculated from regression, but the fit is less accurate (r^2 equals 0.78).) For no stable void growth ($R_V/R_I=1$), voids coalesce spontaneously upon nucleation, and l^*/Δ_3 might be expected to equal one. The linear and quadratic fits yield l^*/Δ_3 values of 0.48 and 1.63, respectively, at R_V/R_I equal to one. Because these values are reasonably close to one, they provide a physical basis for the correlation.

The effect of stable void growth on l^* in Figure 76 is interpreted as follows. The data are divided into alloys with relatively high R_V/R_I ratios favored by a unimodal size distribution of particles and low R_V/R_I ratios determined by the bimodal size distribution of particles. The critical distance for each alloy is a fixed multiple of Δ_3, with the multiple dependent on R_V/R_I. For the high R_V/R_I case, stable void growth allows particles further from the crack tip to nucleate voids as K increases and the plastic strain distribution spreads. Since more particles are involved in the

---

23 Voids nucleated from submicron particles soften the ligament between large microvoids growing from primary particles and promote the onset of strain-localized coalescence [19].

critical coalescence event that constitutes K_{JICi}, l^* is a larger multiple of Δ_3. For the R_V/R_I case (such as in AA2519+Mg+Ag), the void-coalescence conditions are satisfied before void damage accumulates over more than one or two particle spacings. The bimodal particle distribution favors this behavior because secondary void damage from smaller second-phase particles promotes void sheeting between primary voids [17,19]. The ratio, l^*/Δ_3, is relatively low due to this strain-localized coalescence.

The correlations shown in Figures 76 and 77 may provide a means of defining l^* *a priori*, and hence predicting absolute values of K_{JICi} from microstructural and fractographic observations. Caution is dictated. More detailed microscopic studies of the evolution of MNG, as a function of alloy microstructure and temperature, are required to understand the correlations suggested in Figures 76 and 77. Measurements of Δ_3 are complicated by the three-dimensional distribution of primary void-nucleating particles that can be nonuniform due to particle clustering or banding from processing. Spitzig and others employed a Dirichlet cell tessellation procedure to describe the local geometric properties of inclusions in a steel [177,178]. While this method is encouraging, it has not been integrated with a model of crack-tip deformation and fracture. The strong distance and angular dependencies of crack-tip ε^p, coupled with a heterogeneous distribution of one or more populations of void-nucleating particles, make this a formidable problem.

Because ε_f^* and R_V/R_I are both measures of intrinsic alloy fracture resistance, critical strain and critical distance are not independent. It is reasonable to speculate that l^*/Δ_3 is a unique monotonically increasing function of ε_f^*, analogous to the trend in Figure 77. Accordingly, it may be possible to eliminate l^* in Eq. 11 by substituting the dependence of this parameter on ε_f^* and Δ_3. If future studies confirm this relationship, then absolute predictions of temperature and microstructure effects on K_{JICi}; through measured ε_f^*, σ_{ys}, E, N, and Δ_3; will be enabled.

F. Conclusions

1. The critical plastic strain-controlled model successfully predicts the temperature dependence of initiation fracture toughness (K_{JICi}) for a variety of advanced aluminum alloys that crack by microvoid processes. Predictions are based on smooth bar tensile deformation properties, an estimate of the reduction in smooth bar fracture strain for triaxial stress state constraint corresponding to the crack tip, and a single adjustable parameter. Results for 50 experiments effectively demonstrate the ability and accuracy of this modelling approach.

2. Approximately temperature insensitive K_{JICi} is predicted and observed for 2000 series precipitation-hardened alloys from cryogenic to elevated temperatures, while a degradation of K_{JICi} with increasing temperature is correctly modeled for submicron grain size alloys.

3. The temperature dependencies of K_{JICi} are traceable to the interplay between thermally-sensitive intrinsic fracture resistance and the crack tip strain field that is temperature dependent through σ_{ys}, E, and N. Both components are necessary to predict temperature insensitive initiation toughness in precipitation hardened aluminum alloys, where the critical fracture strain (ε_f^*) generally rises with temperature and σ_{ys}, E, and N decline.

4. The model correctly accounts for the effect of manganese on the toughness of AA2134, including changes in the nearest neighbor particle spacing as Mn-rich constituents form, varying ε_f^* due to slip mode changes, and varying dependencies of ε_f^p on stress-state constraint.

5. Uncertainties in ε_f^* and l^* preclude predictions of absolute values of K_{JICi}. Accurate determination of ε_f^* is complicated by the need to correlate damage at the initiation event, within tensile specimens and the process zone ahead of a crack tip. The Bridgman approximation of ε_f^p and uncertainty in the alloy-dependent effect of stress-state constraint also hinder accurate measurements of ε_f^*.

6. Model calculated critical distance, l^*, correlates with the nearest neighbor spacing in a volume (Δ_3) for several aluminum alloys and steels, and l^*/Δ_3 correlates with the extent of primary void growth (R_V/R_f). Both correlations suggest an approach to predict absolute toughness values from tensile properties coupled with microstructural and fractographic observations.

VII. References

1. McMeeking, R.M. and Parks, D.M., "On Criteria for J-Dominance of Crack-Tip Fields in Large Scale Yielding," in Elastic-Plastic Fracture, ASTM STP 668, J.D. Landes, J.A. Begley and G.A. Clarke, Eds., American Society for Testing and Materials, Philadelphia, PA, 1979, pp. 175-194.

2. Ritchie, R.O. And Thompson, A.W., "On Macroscopic and Microscopic Analyses for Crack Initiation and Crack Growth Toughness in Ductile Alloys," Metallurgical Transactions A, Vol. 16A, 1985, pp. 233-248.

3. Hutchinson, J.W., "Fundamentals of the Phenomenological Theory of Nonlinear Fracture Mechanics," J. of Appl. Mech. Trans. ASME, Vol. 50, 1983, pp. 1042-1051.

4. Underwood, J.H., "The Equivalence of K_{IC} and J_{IC} Fracture Toughness Measurements in NiCrMoV Steel," Experimental Mechanics, Vol. 18, No. 9, 1978, pp. 350-355.

5. Joyce, J.A. and Hackett, E.M., "Standard Test Method for J-Integral Characterization of Fracture Toughness," Draft Version, American Society for Testing and Materials, Philadelphia, PA, 1995.

6. Schwalbe, K.-H., "Influence of Stress State on Static Crack Growth in AlZnMgCu0.5," Engineering Fracture Mechanics, Vol. 9, 1977, pp. 557-583.

7. Schwalbe, K.-H. and Heerens, J., "Suggestions for a Modification of ASTM E 813," in Elastic-Plastic Fracture Test Methods: The User's Experience, ASTM STP 856, E.T. Wessel and F.J. Loss, Eds., American Society for Testing and Materials, Philadelphia, PA, 1985, pp. 411-416.

8. Clarke, G.A., "Evaluation of the J_{IC} Testing Procedure by Round Robin Tests on A533B Class 1 Pressure Vessel Steel," Journal of Testing and Evaluation, JTEVA, Vol. 8, 1980, pp. 213-220.

9. Clarke, G.A., Landes, J.D., and Begley, J.A., "Results of an ASTM Cooperative Test Program on the J_{IC} Determination of HY130 Steel," Journal of Testing and Evaluation JTEVA, Vol. 8, 1980, pp. 221-232.

10. Landes, J.D., and Begley, J.A., "Recent Developments in J_{IC} Testing," in Developments in Fracture Mechanics Test Methods Standardization, ASTM STP 632, W.F. Brown, Jr., and J.G. Kaufman, Eds., American Society for Testing and Materials, Philadelphia, PA, 1977, pp. 57-81.

11. Landes, J.D., "J Calculation from Front Face Displacement Measurement on a Compact Specimen," International Journal of Fracture, Vol. 16, 1980, pp. R183-R186.

12. Donald, J.K. and Ruschau, J., "Direct Current Potential Difference Fatigue Crack Measurement Techniques," in Fatigue Crack Measurement: Techniques and Applications, K.J. Marsh, R.O. Ritchie, and R.A. Smith, Eds., EMAS, West Midlands, UK, 1991, pp. 11-37.

13. Bakker, A., "A DC Potential Drop Procedure for Crack Initiation and R-Curve Measurements During Ductile Fracture Tests", in Elastic-Plastic Fracture Test Methods: The User's Experience, ASTM STP 856, E.T. Wessel and F.J. Loss, Eds., American Society for Testing and Materials, Philadelphia, PA, 1985, pp. 394-410.

14. Schwalbe, K.-H., Hellmann, D., Heerens, J., Knaack, J., and Muller-Roos, J., "Measurement of Stable Crack Growth Including Detection of Initiation of Growth Using the DC Potential Drop and the Partial Unloading Methods," in Elastic-Plastic Fracture Test Methods: The User's Experience, ASTM STP 856, E.T. Wessel and F.J. Loss, Eds., American Society for Testing and Materials, Philadelphia, PA, 1985, pp. 338-362.

15. Hicks, M.A. and Pickard, A.C., "A Comparison of Theoretical and Experimental Methods of Calibrating the Electrical Potential Drop Technique for Crack Length Determination," International Journal of Fracture, Vol. 20, 1982, pp. 91-101.

16. Chellman, D.J., Bayha,T.D., Li, Q., and Wawner, F.E., Jr., "Microstructure/Properties of High Temperature Spray Deposited Al-Cu-Mg-X Alloys," in Proceedings of the Fourth International Conference on Aluminum Alloys, Vol II, T.H. Sanders, Jr. And E.A. Starke, Jr., Eds., Georgia Institute of Technology, Atlanta, GA, 1994, pp. 2-9.

17. Van Stone, R.H., Cox, T.B., Low, J.R., Jr., and Psioda, J.A., "Microstructural Aspects of Fracture by Dimpled Rupture," International Metallurgical Reviews, Vol, 30, 1985, pp. 157-179.

18. Cox, T.B. and Low, J.R., Jr., "An Investigation of the Plastic Fracture of AISI 4340 and 18 Nickel--200 Grade Maraging Steels," Metallurgical Transactions A, Vol. 5A, 1974, pp. 1457-1470.

19. Haynes, M.J. and Gangloff, R.P., "Elevated Temperature Fracture Toughness of an Al-Cu-Mg-Ag Alloy", Metallurgical Transactions A, in press, 1997.

20. Hu, J.M. and Albrecht, P., "Limit Load Solution and Loading Behavior of C(T) Fracture Specimen," International Journal of Fracture, Vol. 52, 1991, pp. 19-45.

21. Saxena, A. and Landes, J.D., "Characterization of Creep Crack Growth in Metals," in Advances in Fracture Research, P Rama Rao, K.N. Raju, J.F. Knott, D.M.R. Taplin, Eds., Pergamon Press, Oxford, UK, 1984, pp. 3977-3988.

22. Hamilton, B.C. and Saxena, A., "Elevated Temperature Crack Growth of Aluminum Alloy 2519," in The 4th International Conference on Aluminum Alloys, T.H. Sanders, Jr. and E.A. Starke, Jr., Eds., Georgia Institute of Technology, Atlanta, GA, 1994, pp. 749-756.

23. Reynolds, A.P., "Multilab Comparison of R-Curve Methodologies: Alloy 2024-T3," NASA CR 195004, NASA-Langley Research Center, Hampton, VA, 1994.

24. Porr, W.C, Jr. and Gangloff, R.P., "Elevated Temperature Fracture of RS/PM Alloy 8009: Part I. Fracture Mechanics Behavior," Metallurgical Transactions A, Vol. 25A, 1994, pp. 365-379.

25. Somerday, B.P., "Elevated Temperature Fracture Toughness of a SiC Particulate-Reinforced 2009 Aluminum Composite," Masters Thesis, University of Virginia (1992).

26. Young, L.M., Young, G.A., Scully, J.R., and Gangloff, R.P., "Aqueous Environmental Crack Propagation in High-Strength Beta Titanium Alloys," Metallurgical Transactions A, Vol. 26A, 1995, pp. 1257-1271.

27. Dietzel, W., Schwalbe, K.H., and Wu, D., "Application of Fracture Mechanics Techniques to the Environmentally Assisted Cracking of Aluminum 2024," Fatigue and Fracture of Engineering Materials and Structures, Vol. 12, 1989, pp. 139-165.

28. Hertzberg, R.W., Deformation and Fracture Mechanics of Engineering Materials, 3rd Edition, John Wiley & Sons, New York, NY, 1989, pp. 410-413.

29. Bucci, R.J., "Selecting Aluminum Alloys to Resist Failure by Fracture Mechanisms," Engineering Fracture Mechanics, Vol. 12, 1979, pp. 407-441.

30. Griffis, C.A. and Yoder, G.R., "Initial Crack Extension in Two Intermediate Strength Aluminum Alloys," Journal of Engineering Materials and Technology, Vol. 98, 1976, pp. 152-158.

31. Green, G. and Knott, J.F., "On Effects of Thickness on Ductile Crack Growth in Mild Steel," Journal of Mechanics and Physics of Solids, Vol. 23, 1975, pp. 167-183.

32. Schwalbe, K.-H. and Setz, W., "R Curve and Fracture Toughness of Thin Sheet Materials," Journal of Testing and Evaluation, JTEVA, Vol. 9, No. 4, 1981, pp. 182-194.

33. Yeh, J.R., Bray, G.H., Bucci, R.J., and Macheret, Y., "Prediction of R-Curves from Small Coupon Tests," in Proceedings, FAA/NASA International Symposium on Advanced Structural Integrity Methods for Airframe Durability and Damage Tolerance, C.E. Harris, Ed., NASA Conference Publication 3274, Part 2, NASA-Langley Research Center, Hampton, VA, 1994, pp. 999-1013.

34. W.E. Quist and R.E. Lewis, "The Need for Rapidly Solidified Powder Metallurgy Aluminum Alloys for Aerospace Applications", in Rapidly Solidified Powder Aluminum Alloys for Aerospace Alloys, ASTM STP 890, M.E. Fine and E.A. Starke, Jr., Eds., ASTM, Philadelphia, PA, 1986, pp. 1-38.

35. E.A. Starke, Jr., "NASA-UVA Light Aerospace Alloy and Structures Technology Program Supplement: Aluminum-Based Materials for High Speed Aircraft," NASA Contractor Report 4645, NASA-Langley Research Center, Hampton, VA, February, 1995.

36. Y-W. Kim and W.M. Griffith, Eds., Dispersion Strengthened Aluminum Alloys, TMS-AIME, Warrendale, PA, 1988.

37. M.E. Fine and E.A. Starke, Jr., Eds., Rapidly Solidified Powder Aluminum Alloys, ASTM STP 890, ASTM, Philadelphia, PA, 1986.

38. M.J. Koczak and G.J. Hildeman, Eds., High Strength Powder Metallurgy Aluminum Alloys II, TMS-AIME, Warrendale, PA, 1982.

39. W.C. Porr, Jr., Elevated Temperature Fracture of Advanced Powder Metallurgy Aluminum Alloy 8009, PhD Dissertation, University of Virginia, 1992.

40. E. Bouchaud, L. Kubin, and H. Octor, et al., "Ductility and Dynamic Strain Aging in Rapidly Solidified Aluminum Alloys," Metall. Trans. A, Vol. 22A, 1991, pp. 1021-1028.

41. Y. Leng, W.C. Porr, Jr. and R.P. Gangloff, "Tensile Deformation of 2618 and Al-Fe-Si-V Aluminum Alloys at Elevated Temperatures," Scripta Metall et Matl., Vol. 24, 1990, pp. 2163-2168.

42. D.J. Skinner, M.S. Zedalis and P. Gilman, "Effect of Strain Rate on Tensile Ductility for a Series of Dispersion-Strengthened Aluminum-Based Alloys," Mat. Sci. And Engr., Vol. A119, 1989, pp. 81-86.

43. D.J. Skinner, "The Physical Metallurgy of Dispersion Strengthened Al-Fe-V-Si Alloys", in ref. 34, pp. 181-197.

44. J.A. Hawk, P.K. Mirchandani, R.C. Benn and H.G.F. Wilsdorf, "Evaluation of the Elevated Temperature Strength and Microstructural Stability of Dispersion Strengthened MA Aluminum Alloys", in ref. 35, pp. 517-537.

45. S.L. Lagenbeck, W.M. Griffith, G.J. Hildeman and J.W. Simmon, "Development of Dispersion-Strengthened Aluminum Alloys", in ref 35, pp. 410-422.

46. H. Westengen, "Plastic Instability During Tensile Deformation of a Fine Grained Al-Fe-Mn Alloy", in Microstructural Control in Aluminum Alloys: Deformation, Recovery and Recrystallization, E.A. Chia and H.J. McQueen, Eds., TMS-AIME, Warrendale, PA, 1986, pp. 109-122.

47. H. Westengen, "Tensile Deformation of a Fine Grained Al-Alloy", in Strength of Metals and Alloys, R.C. Gifkins, Ed., ICSMA 6, Melbourne, Australia, 1982, 461-466.

48. E.A. Starke, Jr., "NASA-UVa Light Aerospace Alloy and Structures Technology Program Supplement: Aluminum-Based Materials for High Speed Aircraft", NASA Contractor Report 4517, NASA-Langley Research Center, Hampton, VA, June, 1993.

49. W.C. Porr, Jr., Y. Leng, and R.P. Gangloff, "Elevated Temperature Fracture Toughness of P/M Al-Fe-V-Si", in Low Density, High Temperature Powder Metallurgy Alloys, W.E. Frazier, M.J. Koczak, and P.W. Lee, Eds., TMS-AIME, Warrendale, PA, 1991, pp. 129-155.

50. K.S. Chan, "Evidence of a Thin Sheet Toughening Mechanism in Al-Fe-X Alloys," Metall. Trans. A, Vol. 20A, 1989, pp. 155-164.

51. K.S. Chan, "Confirmation of a Thin Sheet Toughening Mechanism and Anisotropic Fracture in Al-Fe-X Alloys," Metall. Trans. A, Vol. 20A, 1989, pp. 2337-2344.

52. P. Krawczyk and K.V. Jata, "Influence of Strain Rate on the Fracture Toughness of Al-8Fe-1V-2Si at 315 deg C," Scripta Metall. et Mater., Vol. 24, 1990, pp. 1009-1013.

53. Y.-W. Kim, "Effect of Non-Uniform Microstructure and Hydrogen in High Temperature PM Aluminum Alloy Al-8.4Fe-7.2Ce," Progress in Powder Metallurgy, Vol. 43, 1987, pp. 13-31.

54. S. Smith and J.R. Scully, Unpublished Research, University of Virginia, 1993.

55. W.C. Porr, Jr., A.P. Reynolds, Y. Leng and R.P. Gangloff, "Elevated Temperature Cracking of RSP Aluminum Alloy 8009: Characterization of the Environmental Influence," Scripta Metal. et Matl., Vol. 25, 1991, pp. 2627-2632.

56. S. Mitra, "Elevated Temperature mechanical Properties of a Rapidly Solidified Al-Fe-V-Si Alloy," Scripta Metall. et Matl., Vol. 27, 1992, pp. 521-526.

57. D.J. Lloyd, "Deformation of Fine-Grained Aluminum Alloys," Metal Science, May, 1980, pp. 193-198.

58. D.J. Lloyd and L.R. Morris, "Luders Band Deformation in a Fine Grained Aluminum Alloy," Acta Metall., Vol. 25, 1977, pp. 857-861.

59. S.S. Kim, Y.B. Xu, E.A. Starke, Jr. And R.P. Gangloff, "Elevated Temperature Tensile Deformation and Fracture of a Dispersion-Strengthened Al 8009", Unpublished Research, University of Virginia, 1992.

60. Strengthening Methods in Crystals, A. Kelly and R.B. Nicholson, Eds., John Wiley and Sons, Inc., New York, NY, 1971.

61. B.P. Somerday, Yang Leng and R.P. Gangloff, "Elevated Temperature Fracture of Particulate-Reinforced Aluminum Part II: Micromechanical Modelling," Fatigue and Fracture of Engineering Materials and Structures, Vol. 18, 1995, pp. 1031-1050.

62. B.P. Somerday, Yang Leng and R.P. Gangloff, "Elevated Temperature Fracture of Particulate-Reinforced Aluminum Part I: Fracture Toughness," Fatigue and Fracture of Engineering Materials and Structures, Vol. 18, 1995, pp. 565-582.

63. B.P. Somerday and R.P. Gangloff, "Global Constraint - Insensitive Fracture in SiC Particulate-Reinforced AA 2009," Metall. and Matls. Trans. A, Vol 25A, 1994, pp. 1471--1479.

64. C.D.S. Tuck, "The embrittlement of Al-Zn-Mg and Al-Mg Alloys by Water Vapor," Metall. Trans. A, Vol. 16A, 1985, pp. 1503-1514.

65. K.T. Venkateswara Rao and R.O. Ritchie, "Mechanisms Influencing the Cryogenic Fracture-Toughness Behavior of Aluminum-Lithium Alloys," Acta Metallurgica, Vol. 38, 1990, pp. 2309-2326.

66. P.F. Thomason, Ductile Fracture of Metals, Pergamon Press, Oxford, England, 1990, pp. 94-114.

67. G.R. Edwards, T.R. McNelley and O.D. Sherby, "Diffusion-Controlled Deformation of Particulate Composites," Phil. Mag., Vol. 32, 1975, pp. 1245-1264.

68. F.J. Humphreys and P.N. Kalu, "Dislocation-Particle Interactions During High Temperature Deformation of Two Phase Aluminum Alloys," Acta Metallurgica, Vol. 35, 1987, pp. 2815-2829.

69. H.G.F. Wilsdorf, "Dispersion Strengthening of Aluminum Alloys," Dispersion Strengthened Aluminum Alloys, Y.-W. Kima nd W.M. Griffith, Eds., TMS-AIME, Warrendale, PA, 1988, pp. 3-29.

70. P.S. Gilman, "Light High-Temperature Aluminum Alloys for Supersonic and Hypersonic Vehicles," Thermal Structures and Materials for High Speed Flight, E.A. Thornton, Ed., Progress in Astronautics and Aeronautics, Vol. 140, A.R. Seebass, Editor-in-Chief, AIAA, Washington, DC, 1992, pp. 141-160.

71. E.A. Starke, Jr. And H.G.F. Wilsdorf, "New Low-Density and High-Temperature Aluminum Alloys," Thermal Structures and Materials for High Speed Flight, E.A. Thornton, Ed., Progress in Astronautics and Aeronautics, Vol. 140, A.R. Seebass, Editor-in-Chief, AIAA, Washington, DC, 1992, pp. 113-139.

72. S.S. Kim and R.P. Gangloff, "NASA-Uva Light Aerospace Alloy and Structure Technology Program Supplement: Aluminum-Based Materials for High Speed Aircraft," Contractor Report 4517, NASA-Langley Research Center, Hampton, VA, 1993.

73. D.M. Li and A. Bakker, "Shear Fracture of a Rapidly-Solidified Aluminum Scrap Alloy in Tension," Scripta Metall. et Mater., Vol. 30, 1994, pp. 343-348.

74. D.M. Li and A. Bakker, "Strain Rate Dependence on Flow and Fracture Behavior for a Rapidly-solidified Al alloy," Scripta Metall. et Mater., Vol. 30, 1994, pp. 1171-1176.

75. D. Kuhlmann-Wilsdorf and H.G.F. Wilsdorf, Phys. Stat. Sol., Vol 172, 1992, pp. 235-248.

76. S. Mitra and T.R. McNelley, "Temperature Dependence of Strain Hardening in a Dispersion-Strengthened Al-Fe-V-Si Alloy," Metall. Trans. A, Vol. 25A, 1993, pp. 2589-2593.

77. D. Park and J.G. Morris, "The Tensile Deformation Behavior of AA 3004 Aluminum Alloy," Metall. Trans. A, Vol. 25A, 1994, pp. 357-364.

78. J.E. King, C.P. You and J.F. Knott, "Serrated Yielding and the Localized Shear Failure Mode in Aluminum Alloys," Acta Metall., Vol. 29, 1981, pp. 1553-1566.

79. M.J. Luton, C.S. Jayanth, M.M. Disko, S. Matras and J. Vallone, "Cryomilling of Nano-Phase Dispersion Strengthened Aluminum," Multicomponent Ultrafine Microstructures, L.E. McCandish, B.H. Kear and D.E. Polk, Eds., Mater. Res. Soc., Pittsburgh, PA, 1989, pp. 79-86.

80. *Standard Test Method for J_{IC}, A Measure of Fracture Toughness*, Designation E813-89, Annual Book of ASTM Standards, Vol. 3.01, ASTM, Philadelphia, PA, 1992, pp. 732-746.

81. *Standard Test Method for Determining J-R Curves,* Designation E1152-87, Annual Book of ASTM Standards, Vol. 3.01, ASTM, Philadelphia, PA, 1992, pp. 847-857.

82. *Standard Test Method for Plane Strain Fracture Toughness of Metallic Materials*, Designation E399-90, Annual Book of ASTM Standards, Vol. 3.01, ASTM, Philadelphia, PA, 1992, pp. 506-536.

83. Yang Leng, W.C. Porr, Jr. And R.P. Gangloff, "Time Dependent Crack Growth in P/M Al-Fe-V-Si at Elevated Temperatures," Scripta Metallurgica et Materialia, Vol. 25, 1991, pp. 895-900.

84. S.F. Claeys, J.W. Jones and J.E. Allison, "A Fractographic Study of Creep Crack Growth in Rapidly Solidified Al-Fe-X Alloys," Dispersion Strengthened Aluminum Alloys, Y.W. Kim and W.M. Griffith, Eds., TMS-AIME,Warrendale, PA, 1987, pp. 323-336.

85. R.O. Ritchie and A.W. Thompson, "On Macroscopic and Microscopic Analyses for Crack Initiation and Crack Growth Toughness in Ductile Alloys," Metall. Trans. A, Vol. 16A, 1985, pp. 233-248.

86. K.S. Chan, "A New Criterion for Brittle-to-Ductile Fracture Transition," Acta Metall., Vol. 37, 1989, pp. 1217-1226.

87. L.F. Mondolfo, Aluminum Alloys: Structure and Properties, Butterworth and Company, Woburn, MA, 1976, p. 82.

88. U.F. Kocks, R.E. Cook and R. A. Mulford, "Strain Aging and Strain Hardening in Ni-C Alloys," Acta Metall., Vol. 33, 1985, pp. 623-638.

89. R.B. Schwartz and L.L. Funk, "Kinetics of the Portevin-Le Chatelier Effect in Al 6061 Alloy," Acta Metall., Vol. 33, 1985, pp. 295-307.

90. L.P. Kubin, Y. Estrin and C. Perrier, "On Static Strain Aging," Acta Metall. Mater., Vol. 40, 1992, pp. 1037-1044.

91. Y. Huang and J.W. Hutchinson, "A Model Study of the Role of Nonuniform Defect Distribution on Plastic Shear Localization," Modeling of Material Behavior and Its Relation to Design, J.D. Embury and A.W. Thompson, Eds., TMS-AIME, Warrendale, PA, 1990, pp. 129-147.

92. Y.W. Chang and R.J. Asaro, "An Experimental Study of Shear Localization in Aluminum-Copper Single Crystals," Acta Metall., Vol. 29, 1981, pp. 241-257.

93. A.K. Ghosh, "Tensile Instability and Necking in Materials with Strain Hardening and Strain Rate Hardening," Metall. Trans. A, Vol. 8A, 1977, pp. 1221-1232.

94. S. Hariprasad. S.M.L. Sastry and K.L. Jerina, "Deformation Characteristics of the Rapidly solidified Al-8.5% Fe-1.2%V-1.7%Si Alloy," Scripta Metall. et Matl., Vol. 29, 1993, pp. 463-466.

95. Anthony Reynolds, private communication, NASA-Langley Research Center, Hampton, VA, 1994.

96. M.A. Rowley, Characterization of the Viscoplastic Response of High Temperature alloys, MS Thesis, University of Virginia, Charlottesville, VA, 1993.

97. G.M. Pharr and W.D. Nix, "Application of the Methods of Dislocation Dynamics to Describe Plastic Flow in Both B.C.C. And F.C.C. Metals," Acta Metall., Vol. 27, 1979, pp. 433-444.

98. E. Arzt and J. Rosler, "High Temperature Deformation of Dispersion Strengthened Aluminum Alloys," Dispersion Strengthened Aluminum Alloys, Y.W. Kim and W.M. Griffith, Eds., TMS-AIME, Warrendale, PA, 1988, pp. 31-55.

99. D.J. Srolovitz, M.J. Luton, R. Petkovic-Luton, D.M Barnett, and W.D. Nix, "Diffusionally Modified Dislocation Particle Elastic Interactions," Acta Metall., Vol. 32, 1984, pp. 1079-1088.

100. A.G. Evans and T.G. Langdon, "Structural Ceramics," Prog. Matls. Sci., Vol. 21, 1976, pp. 171-193.

101. H.J. Frost and M.F. Ashby, Deformation-Mechanism Maps, Pergamon Press, Oxford, UK, 1982, pp. 1-27.

102. W.B. Lisagor, "Advanced Metallics for High-Temperature Airframe Structures," Thermal Structures and Materials for High Speed Flight, Vol. 140, E.A. Thornton, Ed., AIAA, Washington, DC, 1992, pp. 141-160.

103. W.M. Garrison, Jr. And N.R. Moody, "Ductile Fracture," J. Phys Chem. Solids, Vol 48, 1987, pp. 1035-1074.

104. H.G.F. Wilsdorf, "The Ductile Fracture of Metals: A Microstructural Viewpoint," Mater. Sci. Eng., Vol. 59, 1983, pp. 1-39.

105. I.C. Howard and A.A. Willoughby, "Mechanics and Mechanisms of Ductile Fracture," Advances in Fracture Mechanics, G.G. Chell, Ed., Applied Science Publishers, London, 1984, pp. 39-99.

106. K.-H. Schwalbe, "On the Influence of Microstructure on Crack Propagation Mechanisms and Fracture Toughness of Metallic Materials," Eng. Fract. Mech., Vol. 9, 1977, pp. 795-832.

107. J.G. Kaufman and J.S. Santner, "Fracture Properties of Aluminum Alloys," Applications of Fracture Mechanics for Selection of Structural Materials, J.E. Campbell, W.W. Gerberich, and J.H. Underwood, Eds., ASM International, Metals Park, OH, 1982, pp. 169-211.

108. G.T. Hahn and A.R. Rosenfield, "Metallurgical Factors Affecting Fracture Toughness of Aluminum Alloys," Metall. Trans. A, Vol. 6A, 1987, pp. 653-670.

109. A.K. Vasudevan and R.D. Doherty, "Grain Boundary Ductile Fracture in Precipitation Hardened Aluminum Alloys," Acta Metall., Vol. 35, pp. 1193-1219.

110. C.P. Blankenship, Jr., E. Hornbogen, and E.A. Starke, Jr., "Predicting Slip Behavior in Alloys Containing Shearable and Strong Particles," Mater. Sci. Eng., Vol. 169, 1993, pp. 33-41.

111. M.J. Haynes, B.P Somerday, C.L. Lach, and R.P. Gangloff, "Micromechanical Modeling of Temperature-Dependent Initiation Fracture Toughness in Advanced Aluminum Alloys", in Elevated Temperature Effects on Fatigue and Fracture, ASTM STP 1296, R.S. Piascik, R.P. Gangloff, N.E. Dowling and A. Saxena, Eds., ASTM, Philadelphia, PA, 1997, pp. 165-190.

112. J.G. Kaufman, K.O. Bogardus, D.A. Mauney and R.C. Malcolm, "Creep Cracking in 2219-T851 Plate at Elevated Temperatures," in Mechanics of Crack Growth, ASTM STP 590, J.R. Rice and P.C. Paris, Eds., ASTM, Philadelphia, PA, 1976, pp. 49-168.

113. I.J. Polmear and M.J. Couper, "Design and Development of an Experimental Wrought Aluminum Alloy for Use at Elevated Temperatures," Metall. Trans. A, Vol. 19A, 1988, pp. 1027-1035.

114. Y.C. Chang, and J.M. Howe, "Composition and Stability of Omega Phase in an Al-Cu-Mg-Ag Alloy," Metall. Trans. A, Vol 24A, 1993, pp. 1461-1470.

115. S.P. Ringer, W. Yeung, B.C. Muddle and I.J. Polmear, "Precipitate Stability in Al-Cu-Mg-Ag Alloys Aged at High Temperatures," Acta Metall., Vol 42, 1994, pp. 1715-1724.

116. Q. Li and F.E. Wawner, Jr., "Investigation of the Formation of the Coherent Precipitate Phases in Al-Cu-Mg-Ag Alloys and Characterization of the Alloy's Properties," in Control of Interface in Metal and Ceramic Composites, R. Lin and S. Fishman, Eds., TMS-AIME, Warrendale, PA, 1993, pp. 107-118.

117. R.O. Ritchie, W.L. Server and R.A. Wullaert, "Critical Fracture Stress and Fracture Strain Models for the Prediction of Lower and Upper Shelf Toughness in Nuclear Pressure Vessel Steels," Metall. Trans. A, Vol 10A, 1977, pp. 1557-1570.

118. R.C. Bates, "Mechanics and Mechanisms of Fracture," Metallurgical Treatises, J.K. Tien and J.F. Elliot, Eds., TMS-AIME, Warrendale, PA, 1982, pp. 551-570.

119. J.A. Walsh, K.V. Jata, and E.A. Starke, Jr., "The Influence of Mn Dispersoid Content and Stress State on Ductile Fracture of 2134 Type Al Alloys," Acta Metall., Vol. 37, 1989, pp. 2861-2871.

120. A.C. Mackenzie, J.W. Hancock, and D.K. Brown, "On the Influence of State of Stress on Ductile Fracture Initiation in High Strength Steels," Eng. Fract. Mech., Vol. 9, 1977, pp. 167-188.

121. J.W. Hancock and A.C. Mackenzie, "On the Mechanisms of Ductile Failure in High-Strength Steels Subjected to Multi-Axial Stress-States," J. Mech. Phys. Solids, Vol. 24, 1976, pp. 147-169.

122. A.S. Argon, J. Im, and R. Safoglu, "Cavity Formation from Inclusions in Ductile Fracture," Metall. Trans. A, Vol. 6A, 1975, pp. 825-837.

123. S.H. Goods and L.M. Brown, "The Nucleation of Cavities by Plastic Deformation," Acta Metall., Vol. 27, 1979, pp. 1-15.

124. G. LeRoy, J.D. Embury, G. Edwards and M.F. Ashby, "A Model of Ductile Fracture Based on the Nucleation and Growth of Voids," Acta Metall., Vol. 29, 1981, pp. 1509-1522.

125. J.R. Rice and D.M. Tracey, "On the Ductile Enlargement of Voids in Triaxial Stress Fields," J. Mech. Phys. Solids, Vol. 17, 1969, pp. 201-217.

126. A.P. Reynolds and D.M. Royster, "Retained Mechanical Properties of a New Al-Li-Cu-Mg-Ag Alloy as a Function of Thermal Exposure Time and Temperature," Scripta Metall. Mater., Vol. 30, 1994, pp. 1485-1490.

127. P.L. Bensussan, D.A. Jablonski, and R.M. Pelloux, "A Study of Creep Crack Growth in 2219-T851 Aluminum Alloy Using a Computerized Testing system," Metall. Trans. A, Vol. 15A, 1984, pp. 107-120.

128. K.M. Nikbin and G.A. Webster, "Temperature Dependence of Creep Crack Growth in Aluminum Alloy RR58," in Micro and Macro Mechanics of Crack Growth, K. Sadananda, B.B. Rath, and D.J. Michel. Eds., TMS-AIME, Warrendale, PA, 1982, pp. 137-148.

129. L.M. Karabin, ALCOA Technical Center, Alcoa Center, PA, unpublished research, 1993.

130. C.W. Corti, P. Cotterill, and G.A. Fitzpatrick, "The Evaluation of the Interparticle Spacing in Dispersion Alloys," Int. Met. Rev., Vol 19, 1974, pp. 77-88.

131. M.J. Haynes and R.P. Gangloff, "Fracture Toughness Characterization of Thin Sheet Aluminum Alloys with Electrical Potential-Based Crack Initiation Detection and Crack Length Measurements, JTEVA, 1997, vol. 25, pp. 82-98.

132. J.W. Hutchinson, "Fundamentals of the Phenomenological Theory of Nonlinear Fracture Mechanics," J. of Appl. Mech. Trans. ASME, Vol. 50, 1983, pp. 1042-1051.

133. *Annual Book of ASTM Standards*, Vol. 3.01, Designation E646-91, ASTM, Philadelphia, PA, 1991, pp. 647-653.

134. P.W. Bridgman, Studies in Large Plastic Flow and Fracture, McGraw-Hill Book Co., New York, NY, 1952, pp. 9-37.

135. J.C. Earl and D.K. Brown, "Distribution of Stress and Plastic Strain in Circumferentially Notched Tension Specimens," Eng. Fract. Mech., Vol. 8, 1976, pp. 599-611.

136. C.R. Brooks, Heat Treatment, Structure and Properties of Nonferrous Alloys, ASM International, Metals Park, OH, 1982, p. 123.

137. W.G. Fricke, Jr. And M.A. Przystupa, "Texture," in Treatise on Materials Science and Technology, Vol. 31, Aluminum Alloys-Contemporary Research and Applications, A.K. Vasudevan and R.D. Doherty, Eds., Academic Press, New York, NY, 1989, pp. 563-578.

138. F.J. Humphreys, "The Nucleation of Recrystallization at Second Phase Particles in Deformed Aluminum," Acta Metall., Vol 25, 1978, pp. 1323-1344.

139. J.A. Wert and L.K. Austin, "Modeling of Thermomechanical Processing of Heat-Treatable Aluminum Alloys," Metall. Trans. A, Vol 19A, 1988, pp. 617-625.

140. R.W. Hertzberg, "Deformation and Fracture Mechanics of Engineering Materials, 3rd Ed., John Wiley & Sons, New York, NY, 1989, pp. 410-413.

141. R.J. Bucci, R.C. Malcolm, E.L. Colvin, S.J. Murtha, and R.S. James, "Cooperative Test Program for the Evaluation of Engineering Properties of Al-Li Alloy 2090-T8X Sheet, Plate, and Extrusion Products, NSWC TR 89-106, Naval surface Warfare Center, Dahlgren, VA, 1989, p. 66.

142. V. Tvergaard and A. Needleman, "Analysis of the Cup-Cone Fracture in a Roung Tensile Bar," Acta Metall., Vol. 32, 1984, pp. 157-159.

143. R.M. McMeeking, "Finite Deformation Analysis of Crack-Tip Opening in Elastic-Plastic Materials and Implications for Fracture," J. Mech. Phys. Solids, Vol. 25, 1977, pp. 357-381.

144. S.S. Kim, M.J. Haynes, and R.P. Gangloff, "Localized Deformation and Elevated-Temperature Fracture of Submicron-Grain Aluminum with Dispersoids," Mat. Sci. and Eng., Vol. A203, 1995, pp. 256-271.

145. C.F. Shih, "Relationships Between the J-Integral and the Crack Opening Displacement for Stationary and Extending Cracks," J. Mech. Phys. Solids, Vol. 29, 1981, pp. 305-326.

146. L. Young, "Environment Assisted Cracking in ß-Titanium Alloys," Master's Thesis, University of Virginia, Charlottesville, VA, 1992.

147. M.F. Ashby, C. Gandhi, and D.M.R. Taplin, "Fracture-Mechanism Maps and their Construction for F.C.C. Metals and Alloys," Acta Metall., Vol 27, 1979, pp. 699-729.

148. D. Broek, "Particles and Crack Growth in Aluminum Alloys," Prospects of Fracture Mechanics, G.C. Shih, H.C. Van Elst, and D. Broek, Eds., Noordhoff, Netherlands, 1974, pp. 19-34.

149. F.A. McClintock, "A Criterion for Ductile Fracture by the Growth of Holes," J. of Appl. Mech. Trans. ASME, Vol. 35, 1968, pp. 363-371.

150. J. Pan, M. Saje, and A. Needleman, "Localization of Deformation in Rate Sensitive Porous Plastic Solids," Int. J. Fract., Vol. 21, pp. 261-278.

151. R. Becker and R.E. Smelser, "Simulation of Strain Localization and Fracture Between Holes in an Aluminum Sheet," J. Mech. Phys. Solids, Vol. 42, 1994, pp. 773-796.

152. N. Ohno and J.W. Hutchinson, "Plastic Flow Localization Due to Non-Uniform Void Distribution," J. Mech. Phys. Solids, Vol. 32, 1984, pp. 63-85.

153. E.M. Dubensky and D.A. Koss, "Void/Pore Distributions and Ductile Fracture," Metall. Trans. A, Vol. 18A, 1987, pp. 1887-1895.

154. H. Yamamoto, "Conditions for Shear Localization in the Ductile Fracture of Void-Containing Materials," Int. J. Fract., Vol 14, 1978, pp. 347-365.

155. Q. Li, "Interaction Between Dislocations and the SL Phase During Deformation of Al-Cu-Mg-Ag Alloys," in Proceedings Microscopy Society of America, Fifty-Second Annual Meeting, G.W. Bailey and A.J. Garratt-Reed, Eds., San Francisco Press, San Francisco, CA, 1994, pp. 694-695.

156. Metals Handbook, Ninth Edition, Vol. 2, ASM International, Metals Park, OH, 1987, pp. 79-84.

157. J.E. Hockett, "On Relating the Flow Stress of Aluminum to Strain, Strain Rate, and Temperature," Transactions of AIME, Vol. 239, 1967, pp. 969-976.

158. E.W. Hart and H.D. Solomon, "Load Relaxation Studies of Polycrystalline High Purity Aluminum," Acta Metall., Vol 21, 1973, pp. 295-307.

159. H.J. McQueen and J.J. Jonas, "Recovery and Recrystallization During High Temperature Deformation," in Treatise on Materials Science and Technology, Vol. 6, Plastic Deformation of Materials, R.J. Arsenault, Ed., Academic Press, New York, NY, 1975, pp. 393-493.

160. A.K. Ghosh, "Tensile Instability and Necking in Materials with Strain Hardening and Strain-Rate Hardening," Acta Metall., Vol. 25, 1977, pp. 1413-1424.

161. A.L. Gurson, "Continuum Theory of Ductile Rupture by Void Nucleation and Growth: Part I - Yield Criteria and Flow Rules for Porous Ductile Media," Journal of Engineering Materials and Technology, Transactions of ASME, Vol. 99, 1977, pp. 2-15.

162. D.A. Woodford, "Strain-Rate Sensitivity as a Measure of Ductility," Trans. ASM, Vol. 62, 1969, pp. 291-293.

163. Rice, J.R. And Johnson, M.A., "The Role of Large Crack Tip Geometry Changes in Plane Strain Fracture," Inelastic Behavior of Solids, M.F. Kanninen et al., Eds., McGraw-Hill, New York, NY, 1970, pp. 641-672.

164. Thompson, A.W. And Ashby, M.F., "Fracture Surface Microroughness," Scripta Metallurgica et Materials, Vol. 18, 1984, pp. 127-130.

165. Hutchinson, J.W., "Singular Behavior at the End of a Tensile Crack in a Hardening Material," Journal of Mechanics and Physics of Solids, Vol. 16, 1968, pp. 13-31, 337-347.

166. Rice, J.R. And Rosengren, G.F., "Plane-Strain Deformation Near a Crack Tip in a Power-Law Hardening Material," Journal of Mechanics and Physics of Solids, Vol. 16, 1968, pp. 1-12.

167. McMeeking, R.M., "Blunting of a Plane Strain Crack Tip into a Shape with Vertices," Journal of Engineering Materials and Technology, Transactions of the ASME, Vol. 99, 1977, pp. 290-297.

168. Blankenship, C.P., Jr. And Starke, E.A., Jr., "Structure-Property Relationships in Al-Li-Cu-Mg-Ag-Zr Alloy X2095," Acta Metallurgica, Vol. 42, 1994, pp. 845-855.

169. Gangloff, R.P., "NASA-Uva Light Aerospace Alloy and Structures Technology Program," UVA Report No. UVA/528266/MS94/117, University of Virginia, Charlottesville, VA, 1995, pp. 65-79.

170. Hancock, J.W. And Brown, D.K., "On the Role of Strain and Stress State in Ductile Fracture," Journal of Mechanics and Physics of Solids, Vol. 31, 1983, pp. 1-24.

171. Wilsdorf, H.G.F., Wawner, F.E., Jr., and Wert, J.A., "Very High Temperature Aluminum Materials Concepts", Wright Laboratory Report No. WL-TR-91-4022, Wright Patterson Air Force Base, OH, 1991.

172. Venkateswara Rao, K.T., Uy, W., and Ritchie, R.O., "Cryogenic Toughness of Commercial Aluminum-Lithium Alloys: Role of Delamination Toughening," Metallurgical Transactions, Vol. 20A, 1989, pp. 485-497.

173. Miller, T.C. And Anderson, T.L., "A Void Growth Model Relating Fracture Toughness and Constraint," Fracture Mechanics: Twenty-Fourth Volume, ASTM STP 1207, J.D. Landes, D.E. McCabe, and J.A.M. Boulet, Eds., ASTM, Philadelphia, PA, 1994, pp. 87-107.

174. Bray, J.W., Handerhan, K.J., Garrison, W.M., Jr., and Thompson, A.W., "Fracture Toughness and the Extents of Primary Void Growth," Metallurgical Transactions A, Vol. 23A, 1992, ppl. 485-496.

175. Garrison, W.M., Jr., "The Effect of Silicon and Nickel Additions on the Sulfide Spacing and Fracture Toughness of a 0.4 Carbon Low Alloy Steel," Metallurgical Transactions A, Vol. 17A, 1986, pp. 669-678.

176. Lee, S., Majno, L., and Asaro, R.J., "Correlation of Microstructure and Fracture Toughness in Two 4340 Steels," Metallurgical Transactions A, Vol. 16A, 1985, pp. 1633-1648.

177. Spitzig, W.A., "Effect of Various Sulfide Stringer Populations on the Ductility of Hot-Rolled C-Mn Steels," Acta Metallurgica, Vol. 33, 1985, pp. 175-184.

178. Spitzig, W.A., Kelly, J.F., and Richmond, O., "Quantitative Characterization of Second-Phase Populations," Metallography, Vol. 18, 1985, pp. 235-261.

VIII. Tables

Table 1 - Mechanical Properties of Aluminum Alloys.

Material	Test Temperature (°C)	Elastic Modulus (GPa)	σ_{YS} 0.2% offset (MPa)	σ_{UTS} (MPa)	σ_{FL} (MPa)
AA2024-T3	25	68.9	390	466	428
AA2650-T6	25	75.8	405	445	425
AA2519-T87 (+Mg+Ag)	25	72.4	515	566	541
	75	68.4	505	536	521
	100	67.6	489	510	500
	125	66.3	479	487	483
	150	64.9	451	453	452
	175	63.7	420	422	421

Table 2 -Fatigue Precrack Length, Effective Modulus, and a Comparison of Calculated and Observed Crack Extensions for Each CT Specimen Experiment; Width = 76.2 mm, Thickness = 3.2 mm.

Sample Identification	Test Temperature (°C)	Precrack Length a_i (mm)	Calculated Crack Growth Δa_{DCPD} (mm)	Measured Crack Growth $\Delta a_{optical}$ (mm)	Effective Modulus E_{eff} [1] (GPa)
2024-#1	25	38.5	14.49	...	71.4
2024-#2		38.6	12.92	12.99	66.1
2024-#3		46.4	4.06	4.52	72.7
2024-#4		45.4	4.14	...	69.0
2650-#1	25	45.4	8.17	8.22	75.8
2650-#2 [2]		44.3	7.77	...	71.6
2519-#1	25	45.9	6.40	7.08	72.1
2519-#2	75	45.7	5.96	5.30	71.6
2519-#3	100	45.5	5.22	5.25	66.4
2519-#4	125	44.2	5.70	5.70	65.8
2519-#5	150	45.4	6.90	7.46	71.8
2519-#6	175	45.8	6.42	6.77	69.3

(1) Calculated from a_i, the initial slope of the load versus load-line-displacement curve, and the compliance versus crack length calibration relationship for a CT specimen.

(2) Sidegrooved; gross thickness = 6.0 mm; net thickness = 4.8 mm

Table 3 - Elastic-Plastic and Equivalent Linear-Elastic Initiation and Growth Fracture Toughnesses for 3.2 mm Thick Sheet of Ingot Metallurgy Aluminum Alloys.

Sample Id.	Test Temperature (°C)	J_{ICi} [1] (kJ/m²)	J_{IC} [2] (kJ/m²)	K_{JICi} [1] (MPa√m)	K_{JIC} [2] (MPa√m)	K_{JIC}/K_{JICi}	K_J^{3mm} (MPa√m)
2024-#1	25	14.0	27.7	32.6	45.8	1.40	85.5
2024-#2		17.8	36.2	36.7	52.4	1.43	86.9
2024-#3		13.5	27.0	32.0	45.2	1.41	86.9
2024-#4		13.4	33.6	31.9	50.5	1.58	83.4
2650-#1	25	9.9	18.5	28.8	39.3	1.36	77.7
2650-#2 [3]		9.7	10.9	28.5	30.1	1.06	46.8
2519-#1	25	12.4	20.7	31.4	40.6	1.29	96.2
2519-#2	75	14.1	32.7	32.6	49.6	1.52	103.0
2519-#3	100	12.2	33.5	30.2	49.9	1.65	99.9
2519-#4	125	13.6	29.0	31.5	46.0	1.46	96.7
2519-#5	150	13.4	40.8	31.0	53.9	1.74	86.2
2519-#6	175	11.6	29.8	28.5	45.6	1.60	72.7

(1) DCPD detected crack initiation

(2) Crack initiation based on ASTM standard E 813

(3) Sidegrooved; gross thickness = 6.0 mm; net thickness = 4.8 mm

Table 4 - Oxide thickness, hydrogen content and oxygen content of conventionally processed AA8009 compared to process-modifications A and B

	Oxide thickness (nm)	Total Hydrogen (ppm)	Percent Oxygen
Conventional 8009	4.0 - 5.0	3.5 - 4.5	0.12 - 0.13
Modification A	3.2 - 3.3	1.6 - 2.5	0.084 - 0.09
Modification B	2.8 - 3.0	1.3 - 1.7	0.076 - 0.082

Table 5 - Chemical Composition of Cryogenically Milled Pure Aluminum (weight pct).

O	N	Fe	Si	V	Mg	Cr	Y	Al
2.04	0.78	0.12	0.036	0.005	0.002	< 0.002	< 0.002	Bal.

Table 6 - Tensile Properties of CM Aluminum as a Function of Temperature.

Temperature (°C)	σ_{YS} (MPa)	σ_{UTS} (MPa)	RA (%)	Strain @ P_{max}	n
25	260	281	38.9	0.037	0.029
25	270	284	36.5		
80	251	261	24.6		
125	240	247	22.7		
175	230	242	15.6	0.011	0.025
215	211	216	17.9		
250	200	209	13.2	0.013	0.03
325	150	151	12.7		

Table 7 - Fracture Toughness of CM Al as a Function of Temperature and Grip Displacement Rate.

Temp. (°C)	Grip Disp. Rate (μm/sec)	Measured K_{JICi} [1] (MPa√m)	Predicted K_{JICi} (MPa√m)	Measured T_R	Predicted T_R	Measured K_{JC} [2] (MPa√m)
25	2.5	13.6	13.6 [3] 13.4 [4]	22.1	6.7 3.8	24.1
25	0.005	11.0		4.7		14.5
80	2.5	12.7	10.3	14.5	0 (-3.0)	19.1
125	2.5	9.5	9.6	6.1	0 (-3.8)	14.3
175	2.5	7.1	7.8	3.3	0 (-5.5)	10.0
215	2.5	6.5	7.9	1.6	0 (-4.9)	8.4
250	2.5	5.0	6.6	1.30	0 (-5.1)	6.9
325	2.5	4.9	5.5	0.70	0 (-5.0)	5.4

(1) Based on dcEPD definition of J_{ICi} [24,25].

(2) Based on ASTM Standard E813 [80].

(3) Measured toughness was employed to define l* for RA = 38.9% and σ_{YS} = 260 MPa.

(4) Predicted based on RA = 36.5% and σ_{YS} = 270 MPa (See Table 6).

Table 8 - Initiation and Growth Toughnesses of AA2519+Mg+Ag and AA2519+Mg.

Temperature (°C)	Variant of 2519-T87	K_{JICi} (MPa√m)	T_R^{ps}	J^{3mm} (kJ/m²)	K_J^{3mm} (MPa√m)
25	+ Mg + Ag	29.6 30.9 33.8 37.1	5.4 4.0	127.8 125.9	96.2 95.5
75	+ Mg + Ag	32.0	7.0	155.1	103.0
100	+ Mg + Ag	31.8	7.2	147.5	99.9
125	+ Mg + Ag	31.5	6.6	140.7	96.6
150	+ Mg + Ag	31.1 31.4 31.7	6.4	114.4	86.2
175	+ Mg + Ag	30.9	5.5	82.9	72.7
25	+ Mg	30.5	5.4	134.6	98.7
100	+ Mg	34.1	7.9	155.0	102.4
175	+ Mg	25.4	3.7	61.5	62.6

Table 9 - Uniaxial Tensile and Compressive Flow Properties of AA2519+Mg+Ag.

Temperature (°C)	E[87] (GPa)	σ_{ys}^{t} (MPa)	σ_{uts} (MPa)	RA (%)	σ_{ys}^{c} (MPa)	σ_o (MPa)	N
25	72.4	515	566	40	493	524	0.045
75	68.4	505	536	40	485	510	0.036
100	67.6	489	510	50	469	497	0.030
125	66.3	479	487	49	440	474	0.023
150	64.9	451	453	52	434	450	0.016
175	63.7	420	422	57	388	407	0.013

Table 10 - Critical Plastic Strain-Controlled Model Parameters for AA2519+Mg+Ag.

Temperature (°C)	d(N)	C1	C2	σ_{ys} (MPa)	E[87] (GPa)	ε_f^* Smooth r_s=6.5 (%)	ε_f^* Notched r_n=1.5 (%)
25	0.52	0.1264	1.219	504	72.4	7.9	8.1(1)
75	0.53	0.1262	1.221	495	68.4	7.8	9.4
100	0.54	0.1261	1.222	475	67.6	10.8	9.8
125	0.55	0.1260	1.223	459	66.3	10.3	9.9
150	0.56	0.1259	1.225	443	64.9	11.4	10.4
175	0.56	0.1258	1.226	404	63.7	12.9	14.8

(1) Average of 3 measurements

Table 11 - Fracture Toughness Model Parameters as a Function of N (after McMeeking [143]).

Work Hardening Exponent (N from $\sigma \alpha \varepsilon^N$)	C1	C2	d_n
0.0	0.1256	1.228	0.58
0.1	0.1274	1.208	0.44
0.2	0.1302	1.130	0.30

Table 12 - Chemical Compositions of Ingot Metallurgy, Spray Formed, Ultra Fine Grain-Size, and Metal Matrix Composite Aluminum Alloys.

Alloy Designation	Alloy System	Product Form	Nominal Alloy Composition (weight %)
AA2095-T8	I/M	Plate	Al-4.6Cu-1.5Li-0.4Ag-0.4Mg-0.15Zr
AA2195-T8	I/M	Plate	Al-4.0Cu-1.0Li-0.4Ag-0.4Mg-0.15Zr
AA2618-T851	I/M	Plate	Al-2.6Cu-1.6Mg-1.0Fe-1.2Ni-0.2Si
AA2519-T87(+Mg+Ag)	I/M	Sheet	Al-5.8Cu-0.5Mg-0.5Ag-0.3Mn-0.15Zr-0.1V
AA2134-type (+Mn)	I/M	Plate	Al-4.0Cu-1.5Mg-0.15Zr (0, 0.3, 0.6, 1.0 Mn)
N203-T6	SF	Extrusion	Al-5.0Cu-0.5Mg-0.5Mn-0.4Zr-0.4Ag-0.2Ti-0.2V
CM Al	SM/GS	Extrusion	Al + 2.5 vol%Al_2O_3
AA8009	SM/GS	Extrusion	Al-8.5Fe-1.3V-1.7Si
2009/SiC/20p-T6	PM/MMC	Plate	Al-3.6Cu-1.3Mg + 19.5 vol% SiC

Table 13 - Tensile Properties for Spray Formed N203.

Temperature (°C)	σ_{ys} (MPa)	E (GPa)	N	%RA
25	447	72.1	0.085	28.2
100	432	70.7	0.063	42.5
150	392	68.9	0.045	46.3
190	342	66.0	0.028	61.2

Table 14 - Temperature-Dependent Tensile Properties for Aluminum Alloys.

Alloy Designation	Temperature Range (°C)	σ_{ys} (MPa)	E (GPa)	N	%RA
AA2095-T6 [169]	-140 / 135	621 / 524	79.3 / 69.0[2]	.059 /.005	11 / 22
AA2195-T6 [169]	-185 / 135	693 / 538	80.3 / 69.0[2]	.066 /.005	15 / 44
AA2618-T851 [41]	25 / 225	450 / 365	75.3 / 60.0	.05 /.005	23 / 35
AA2519-T87(Mg+Ag) [19]	25 / 175	504 / 404[1]	72.4 / 63.7[3]	.045 /.013[4]	40 / 57
N203-T6	25 / 190	447 / 342	72.1 / 66.0	.085 /.028	28 / 61
CM Al [144]	25 / 325	265 / 150	72.0 / 58.0[3]	...	38 / 13
AA8009 [24]	25 / 316	395 / 270	83.4 / 61.5	.077 / .040	51 / 39
2009/SiC/20p-T6 [61]	25 / 316	410 / 90	108 / 60[3]	.125 / .042	2.6 / 23

(1) Average of tensile and compressive yield strengths
(2) Based on precision modulus measurements at 25°C and -180°C
(3) Based on temperature dependency of E for pure aluminum [251]
(4) Determined from uniaxial compression tests

Table 15 - Interparticle Spacing of Primary Void-Nucleating Particles.

Alloy Designation	Primary Void Nucleating Particles	εf_v	r (μm)	λ (μm)	Δ_2 (μm)	Δ_3 (μm)
AA2095-T8 [168]	T_1, Al_7Cu_2Fe	0.037	3.80	132	14.3	10.8
AA2195-T8 [168]	C	0.0066	1.39	279	12.4	7.0
AA2618-T851 [39]	$FeNiAl_9$	0.08	3.75	58	9.6	8.3
AA2519-T87(Mg+Ag) [19]	Θ, C	0.012	2.85	313	18.8	11.9
N203-T6	...	0.022	2.44	145	11.9	8.3
AA2134 (+0.00 wt%Mn)	S, C'	0.0175	2.55	190	13.9	9.3
AA2134 (+0.31 wt%Mn)	S, C'	0.0196	2.65	180	13.7	9.3
AA2134 (+0.61 wt%Mn)	S, C'	0.0220	2.50	150	12.2	8.5
AA2134 (+1.02 wt%Mn)	S, C'	0.0407	2.90	91	10.4	8.0
2009/SiC/20p-T6 [25]	SiC	0.195	1.5	8.3	2.5	2.5

T_1: Primary Al_2CuLi
Θ: Primary Al_2Cu
C: Impurity (Fe,Si) constituents
S: Primary Al_2CuMg [119]
C': Mn bearing constituents [119] ($Al_{20}Cu_2Mn_3$, $Al_{20}Cu_2(Mn,Fe)_3$

Table 16 - Linear Least Squares Regression Fits to Predicted and Measured K_{JICi} Versus Temperature.

Alloy Designation	Temperature Range (°C)	Predicted Fit K_{JICi} =	Measured Fit K_{JICi} =
AA2095-T6	-185/135°C	20.9 MPa√m + 0.003*T[1]	21.4 MPa√m + 0.005*T
AA2195-T6	-185/135°C	35.9 MPa√m + 0.023*T	38.6 MPa√m - 0.006*T
AA2618-T851	25/175°C	20.4 MPa√m - 0.0004*T	20.4 MPa√m - 0.012*T
AA2519-T87(+Mg+Ag) Smooth Bar Notched Bar	25/175°C	 32.7 MPa√m + 0.001*T 32.9 MPa√m - 0.001*T	33.1 MPa√m - 0.013*T
N203-T6	25/190°C	26.4 MPa√m + 0.028*T	25.4 MPa√m + 0.038*T
CM Al	25/175°C	14.1 MPa√m - 0.037*T	15.3 MPa√m - 0.045*T
CM Al	175/325°C	11.0 MPa√m - 0.017*T	9.6 MPa√m - 0.015*T
AA8009	25/100°C	34.2 MPa√m - 0.055*T	34.5 MPa√m - 0.068*T
AA8009	175/316°C	27.7 MPa√m - 0.027*T	22.5 MPa√m - 0.037*T

(1) T is temperature in degrees celsius

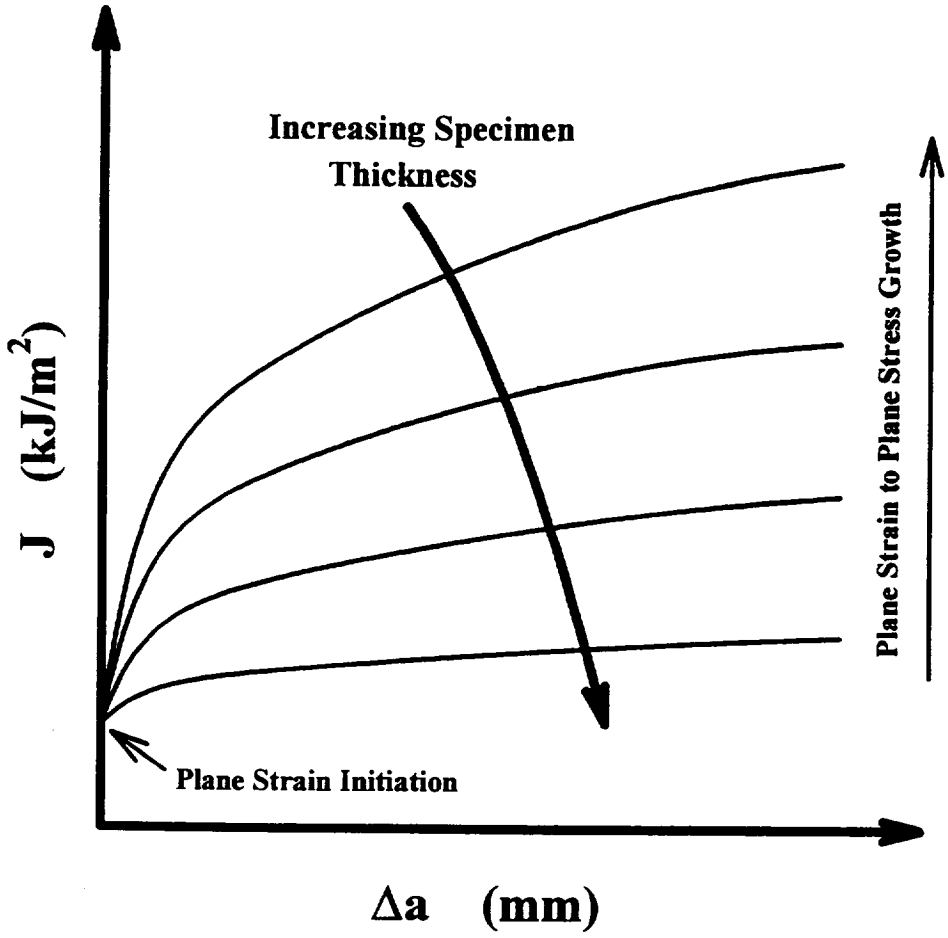

Figure 1: Schematic J-Δa curves illustrating the effect of increasing specimen thickness on ductile fracture toughness.

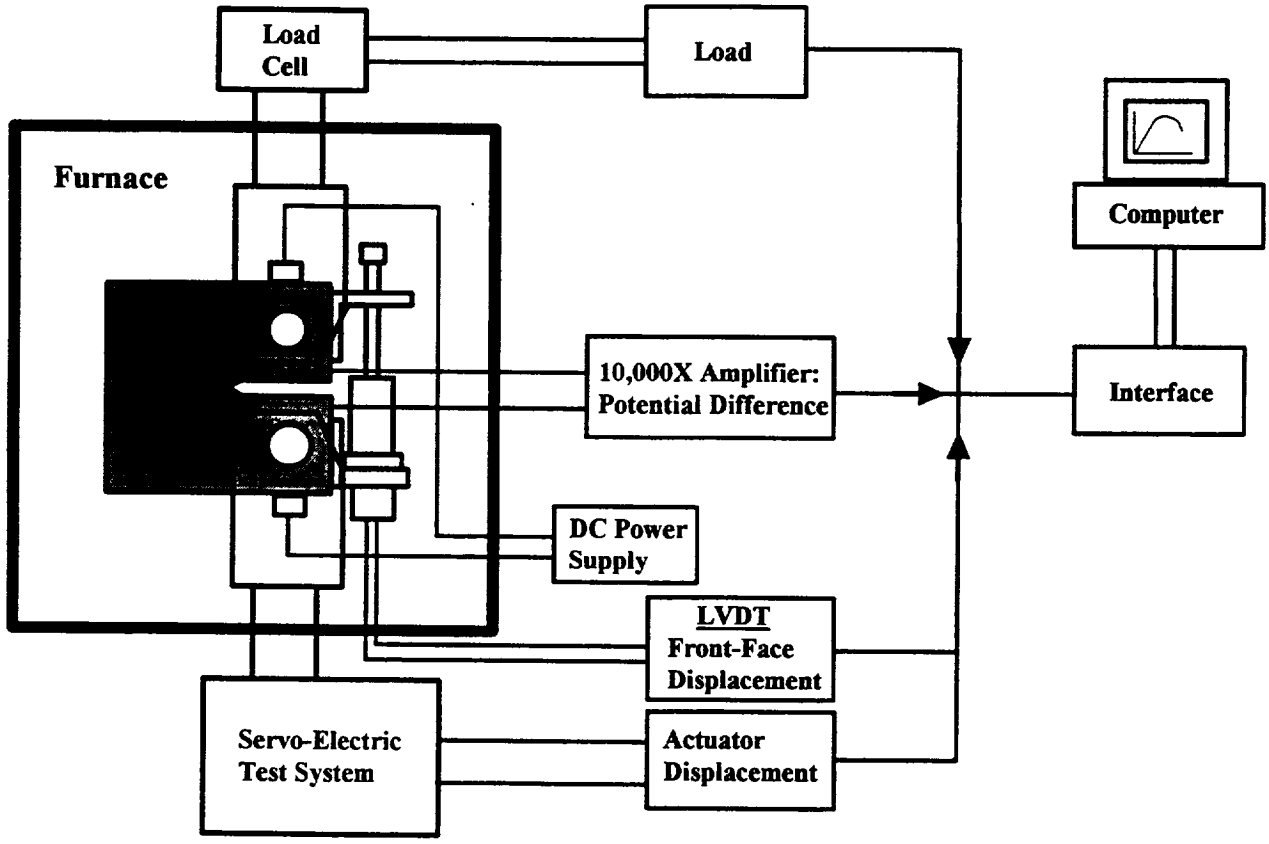

Figure 2: Schematic of a rising-load fracture toughness experiment with a CT specimen; displaying load, displacement, and crack length measurement equipment.

(a)

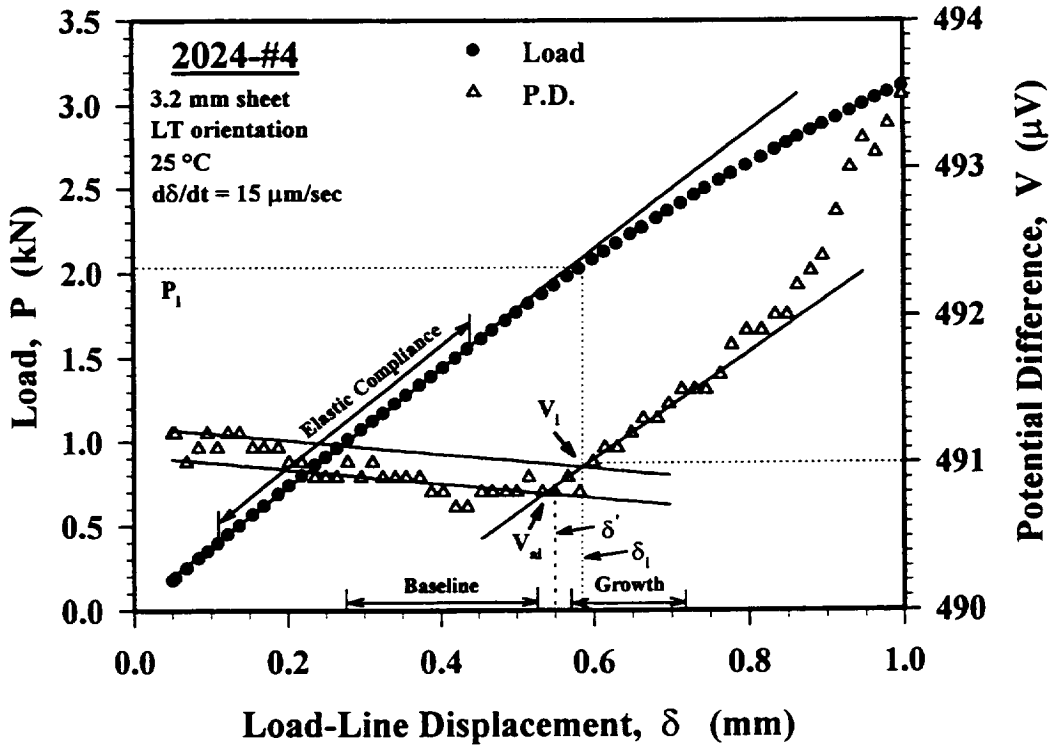

(b)

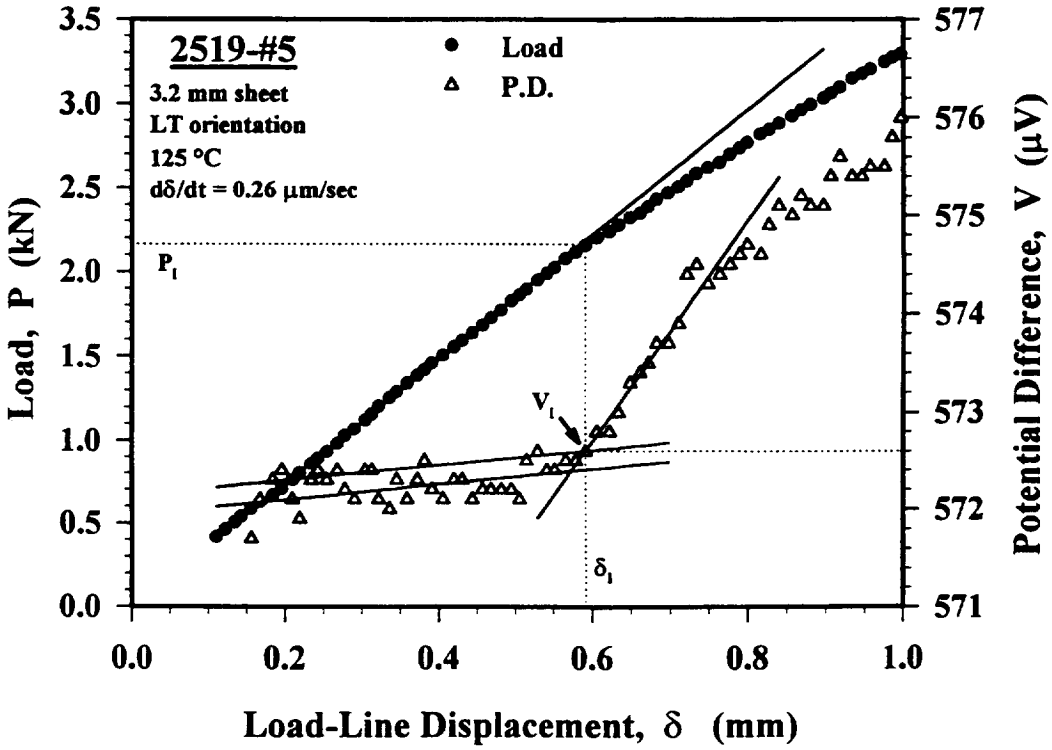

Figure 3: Load-displacement and potential-displacement records illustrating the method employed to determine initiation fracture toughness for: (a) AA2024-T3 at 25°C and a displacement rate of 15 μm/sec, and (b) AA2519-T87 (+Mg+Ag) at 125°C and a displacement rate of 0.26 μm/sec.

(a)

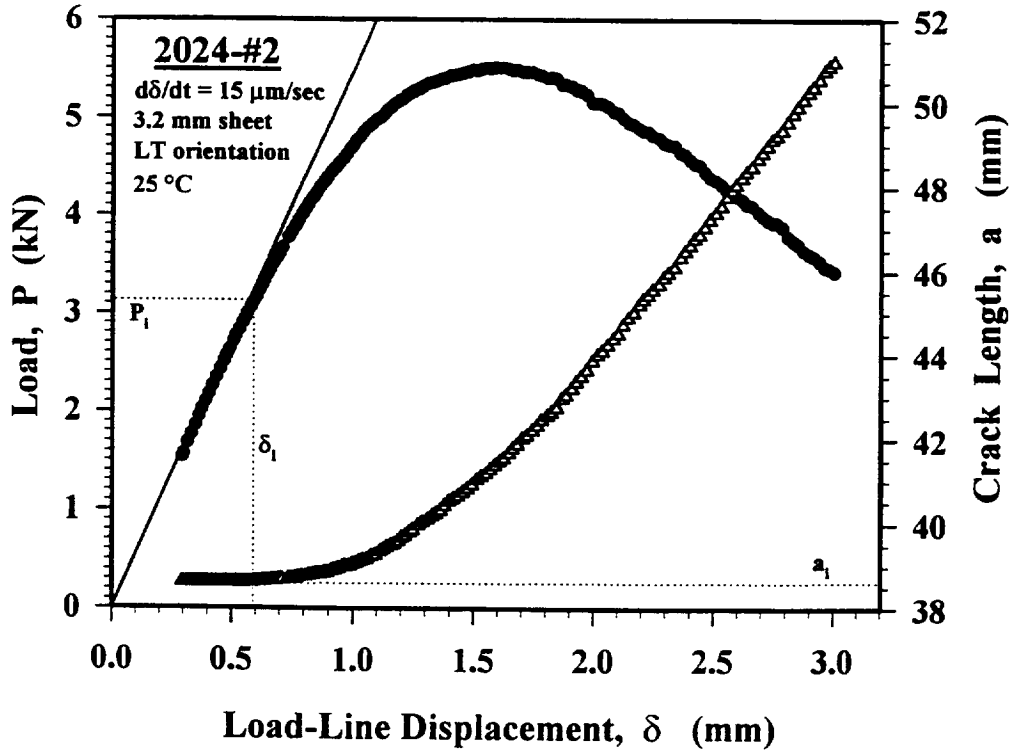

(b)

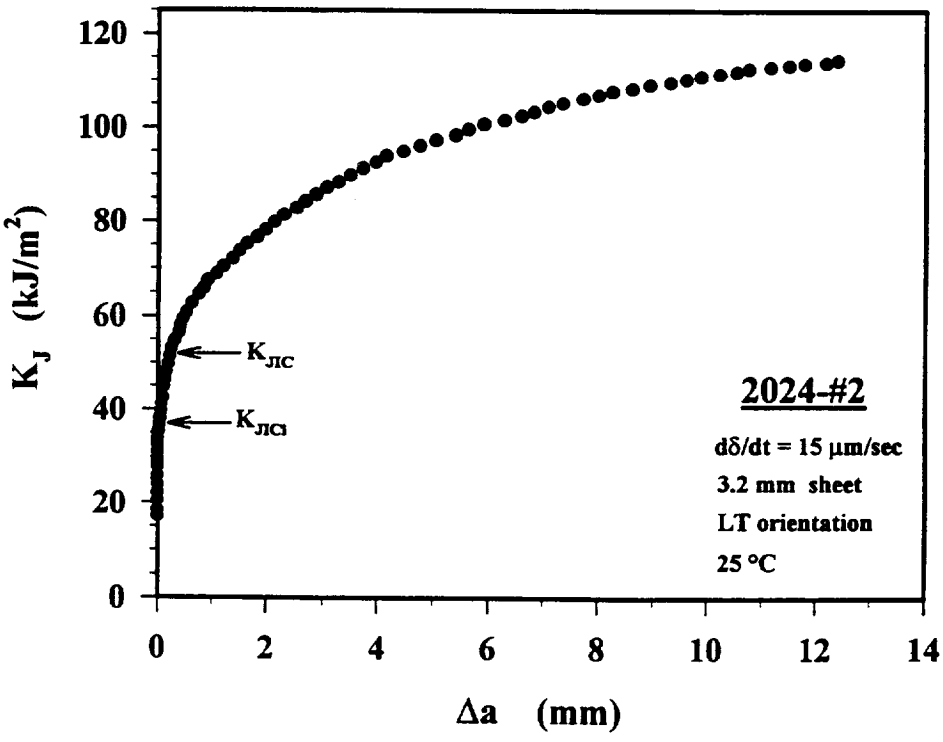

Figure 4: (a) Ambient temperature load-displacement and crack growth-displacement data for AA2024-T3. P-δ and a-δ data are input into a J-integral expression to obtain the J-Δa curve. (b) The corresponding K_J-Δa curve, calculated from J-Δa by $K_J = (J\,E)^{1/2}$.

(a)

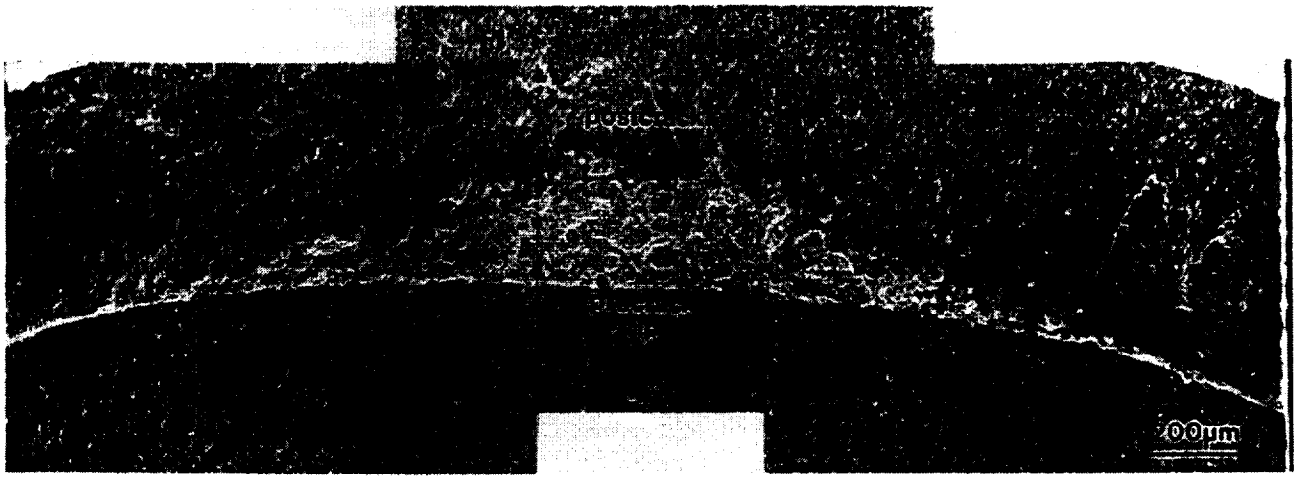

(b)

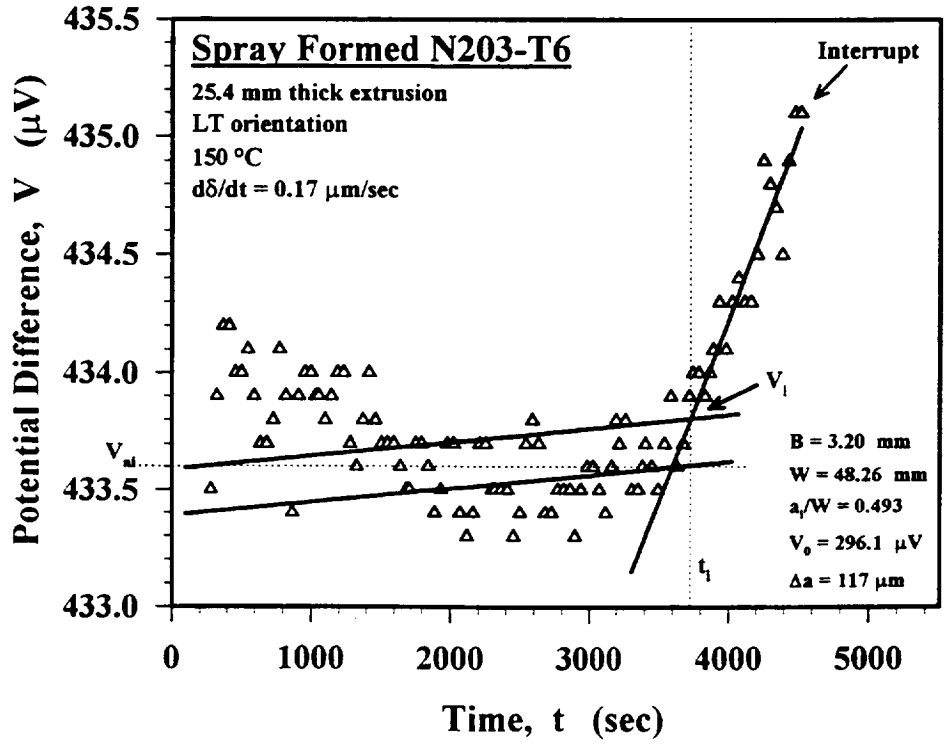

Figure 5: (a) SEM fractograph showing microscopic process-zone damage at the midplane of a spray formed N203 CT specimen. (b) The corresponding potential versus time curve that resolves the crack-tip damage from (a). Full scale on the Y-axis represents a 0.58% increase in V.

(a)

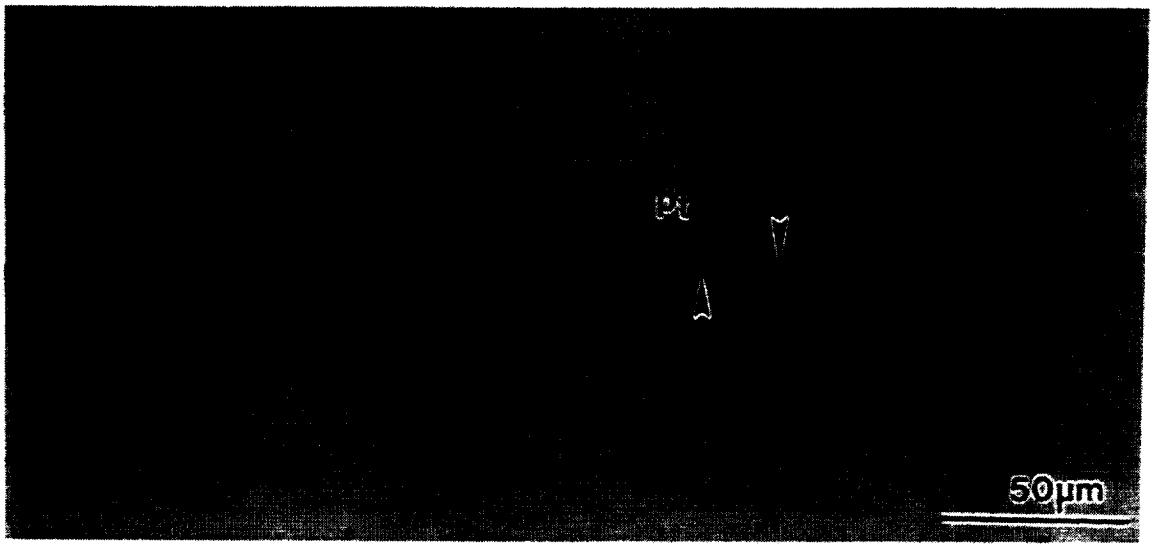

(b)

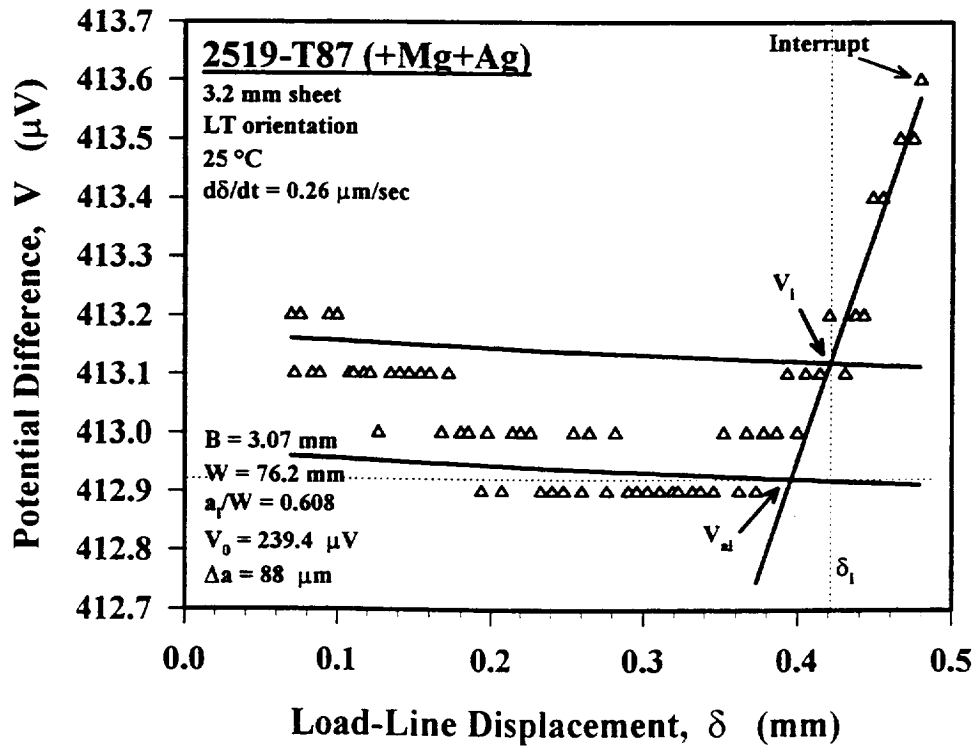

Figure 6: (a) Polished crack tip profile of AA2519-T87 (+Mg+Ag) illustrating the process-zone damage associated with ductile fracture initiation near K_{JICi}. Voids nucleate at large second phase particles and coalesce with the precrack tip (pt) by void sheet coalescence (arrows). (b) The corresponding potential versus displacement curve. Full scale on the Y-axis represents a 0.24% increase in V.

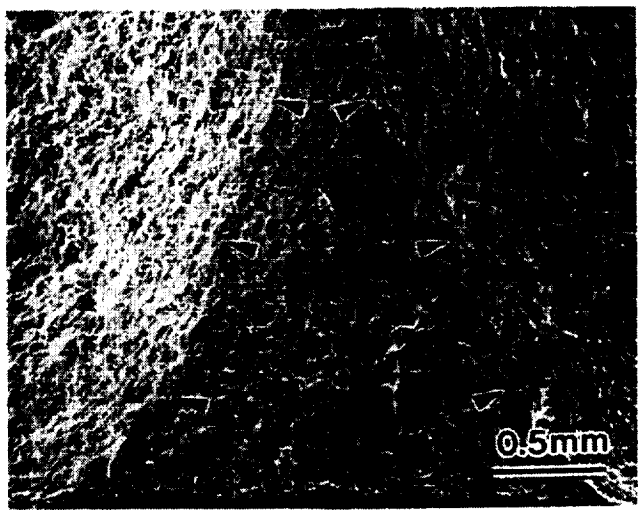

Figure 7: Low magnification SEM fractograph of an AA2519-T87 (+Mg+Ag) fracture surface produced at 25°C showing the plane strain flat fracture at initiation from the fatigue precrack and the transition to plane stress cracking. The shear lip - flat fracture interface is indicated by arrows, with the fatigue precrack just visible parallel to the bottom edge of the photo and with crack growth from bottom to top.

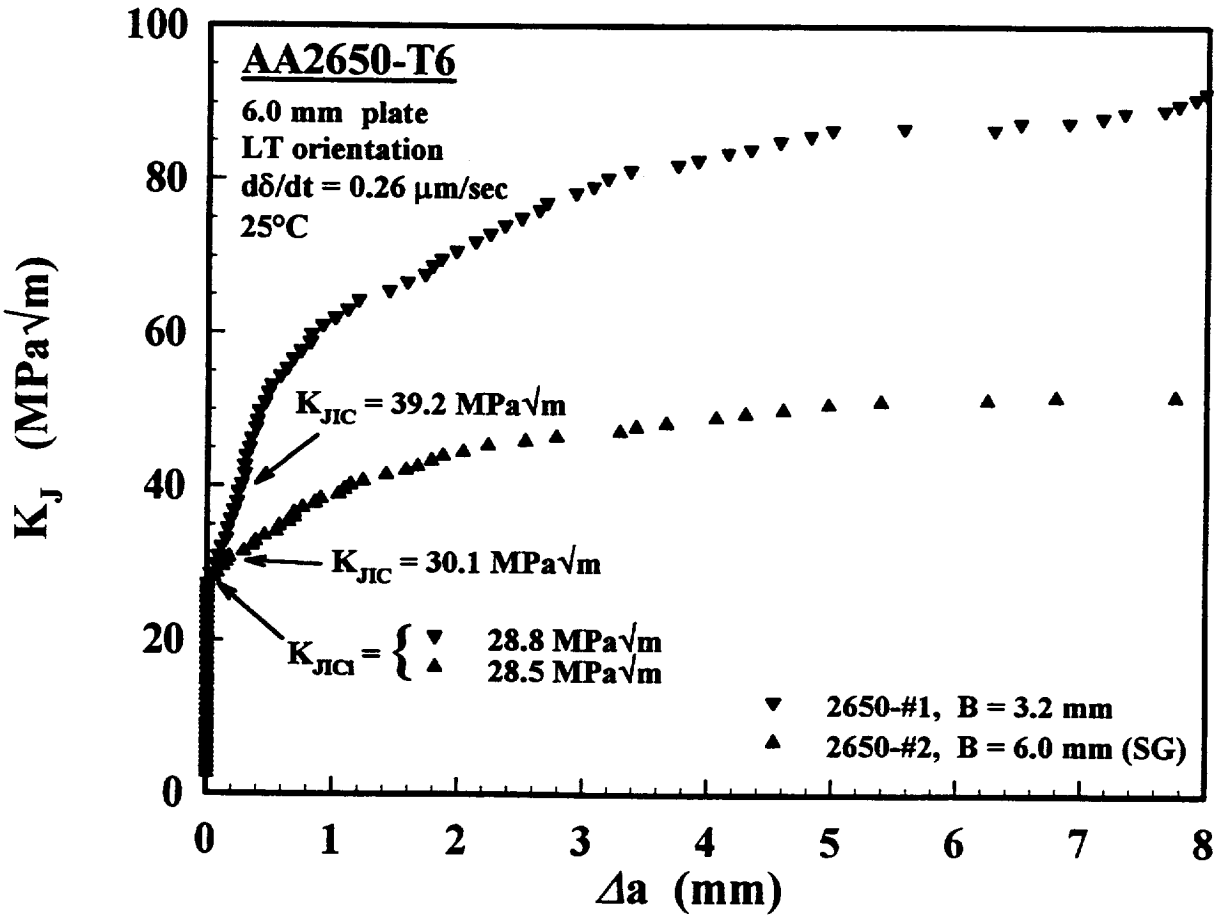

Figure 8: K_J-Δa curves for two CT thicknesses of AA2650-T6, illustrating the thickness dependence of K_{JIC} and the thickness independence of K_{JICi}. (SG denotes a sidegrooved CT specimen.)

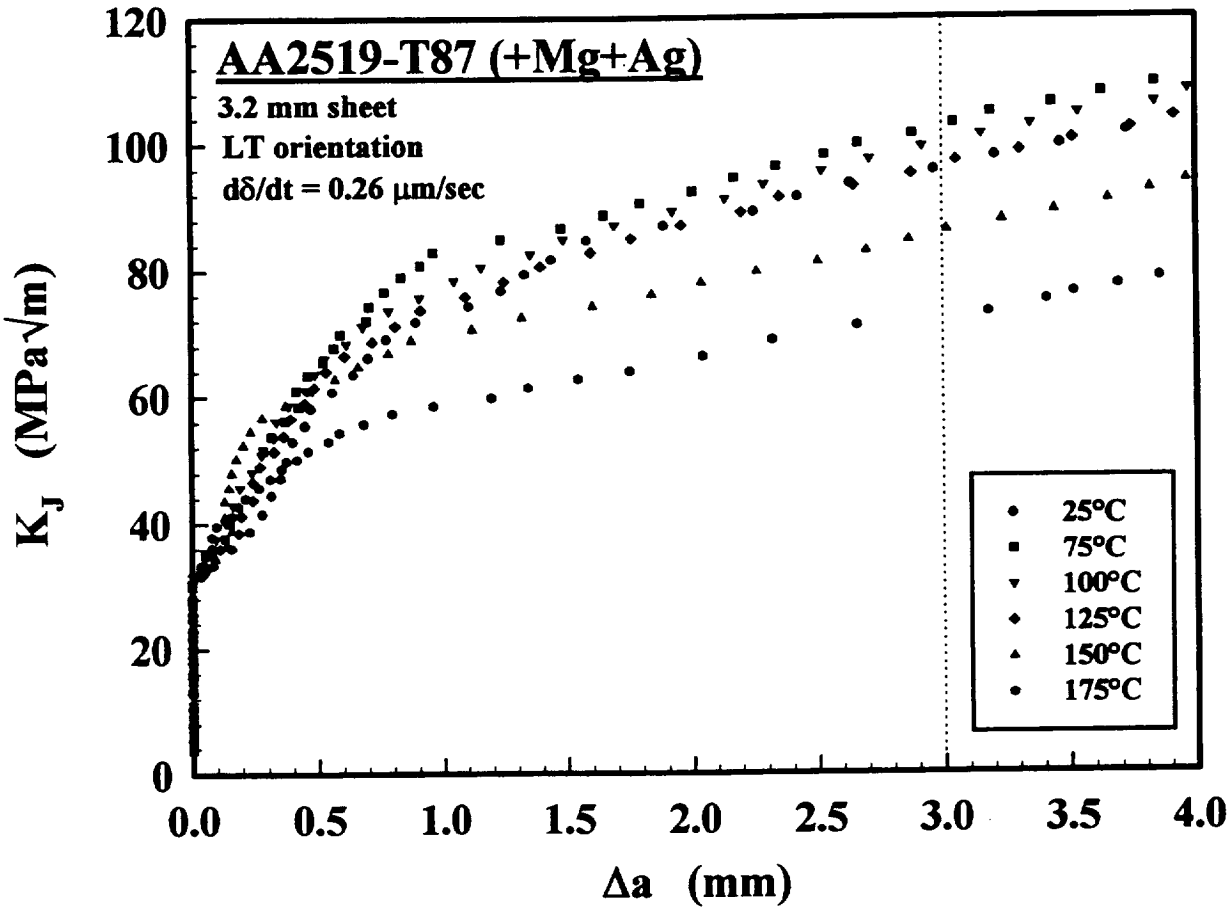

Figure 9: K_J-Δa as a function of temperature determined from CT specimens of AA2519-T87 (+Mg+Ag); $d\delta/dt = 0.26$ μm/sec.

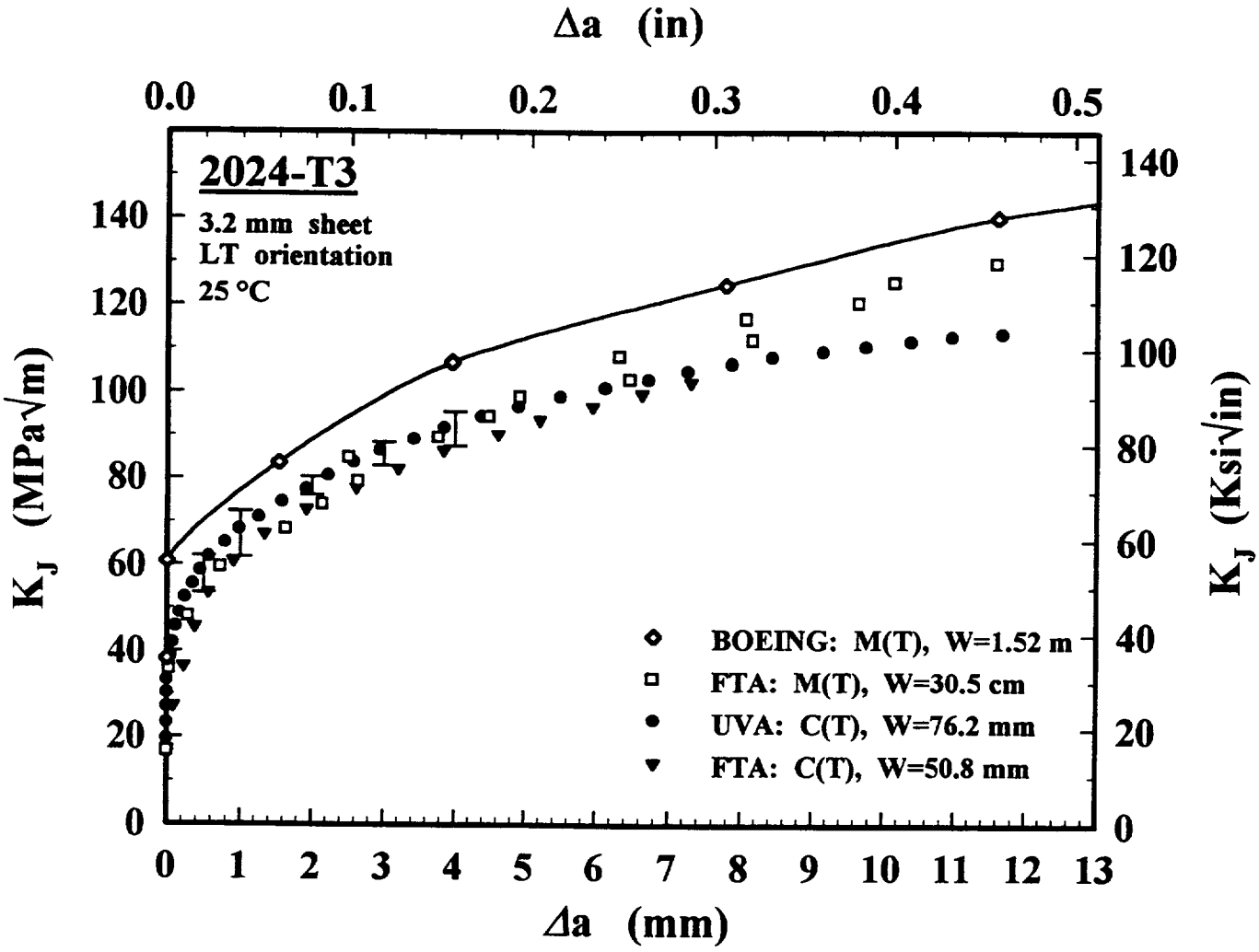

Figure 10: Room temperature K_J-Δa curve (•) for AA2024-T3 CT specimen determined by the J-integral/DCPD method compared to literature results for AA2024-T3 CT and MT specimens. Specimen thickness = 3.2 mm.

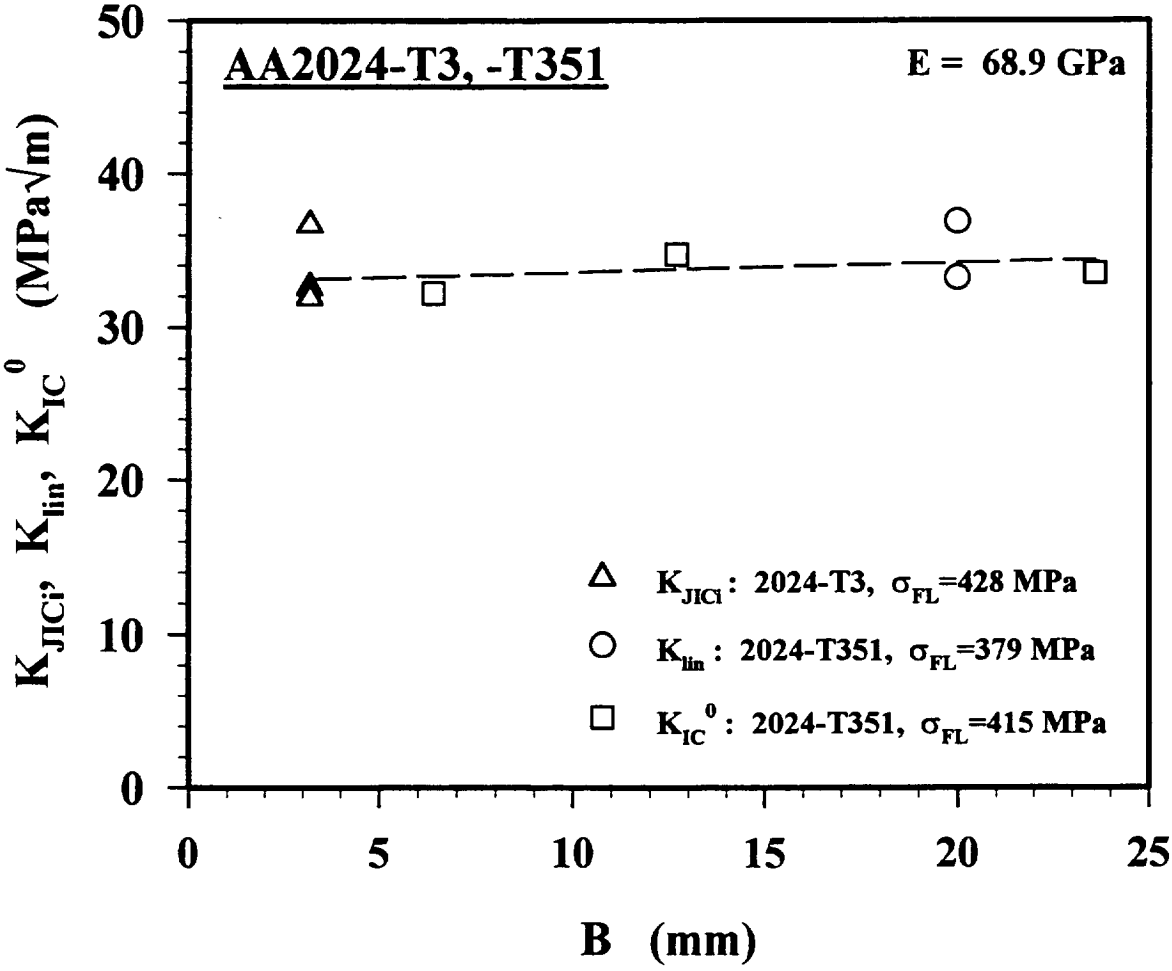

Figure 11: Thickness dependence of initiation fracture toughness measurements for naturally aged AA2024, based on early detection of crack tip process-zone damage.

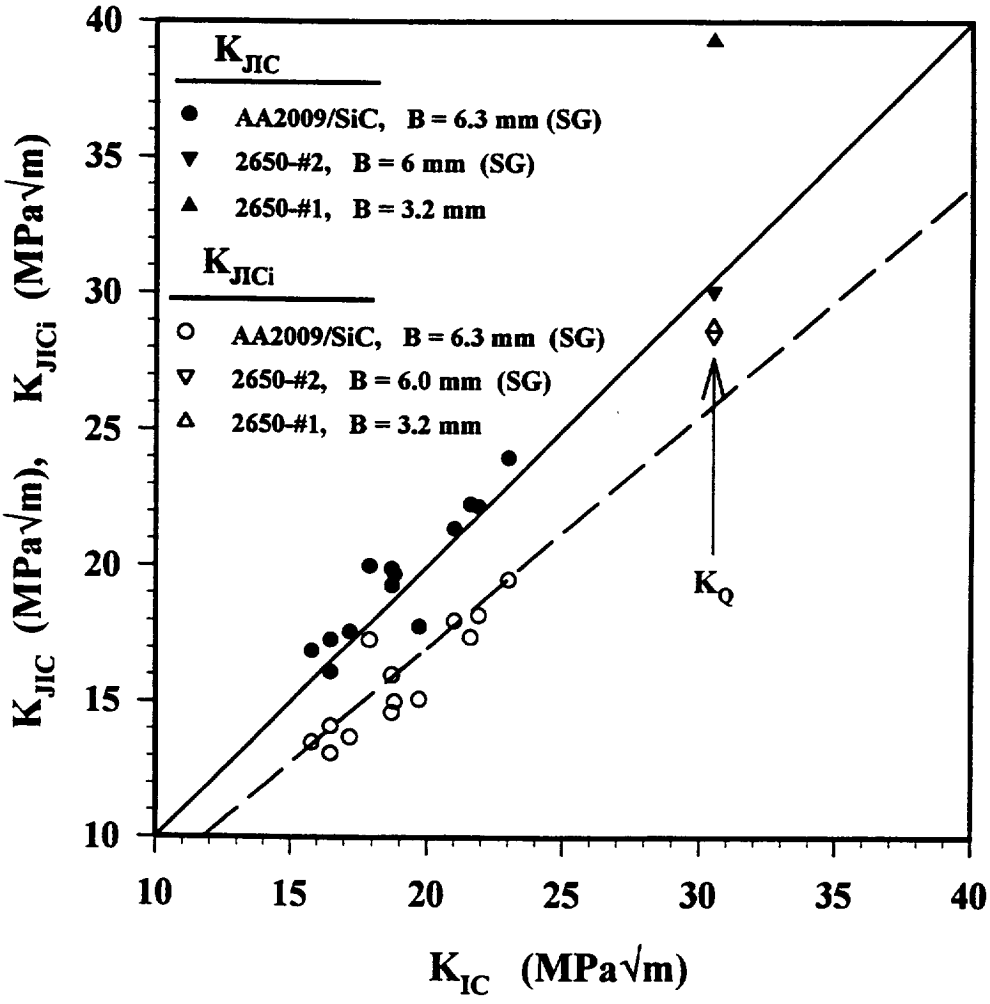

Figure 12: Comparison of K_{JIC}, K_{JICi}, K_{IC} measurements for AA2009/SiC [25] and AA2650-T6. (SG denotes sidegrooved CT specimens.)

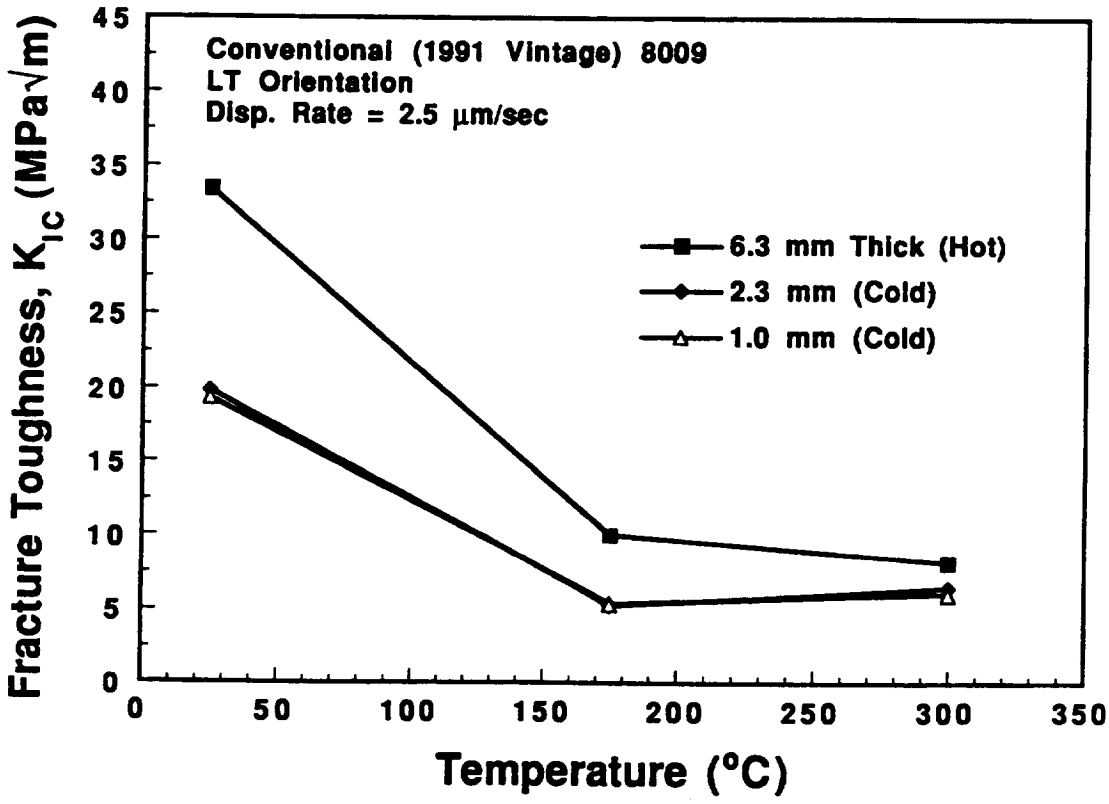

Figure 13: Effect of temperature on the initiation fracture toughness, K_{JICi}, of Conventional AA8009 plate and sheet (1991 Vintage) in gauge thicknesses of 6.3, 2.3 and 1.0 mm.

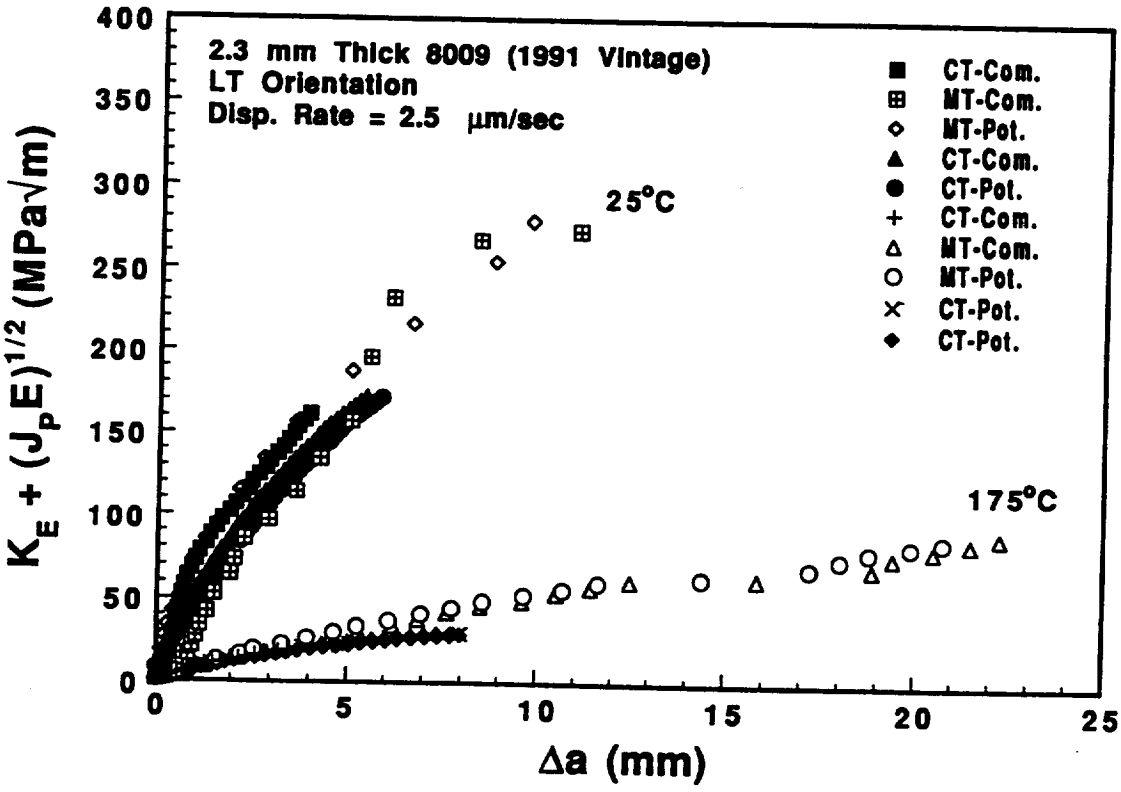

Figure 14: Applied stress intensity from the J-integral *vs* Δa R-curves for 2.3 mm thick Conventional AA8009 sheet (1991 Vintage) at 25 and 175°C, determined by C(T) and M(T) specimens with unloading compliance and electric potential.

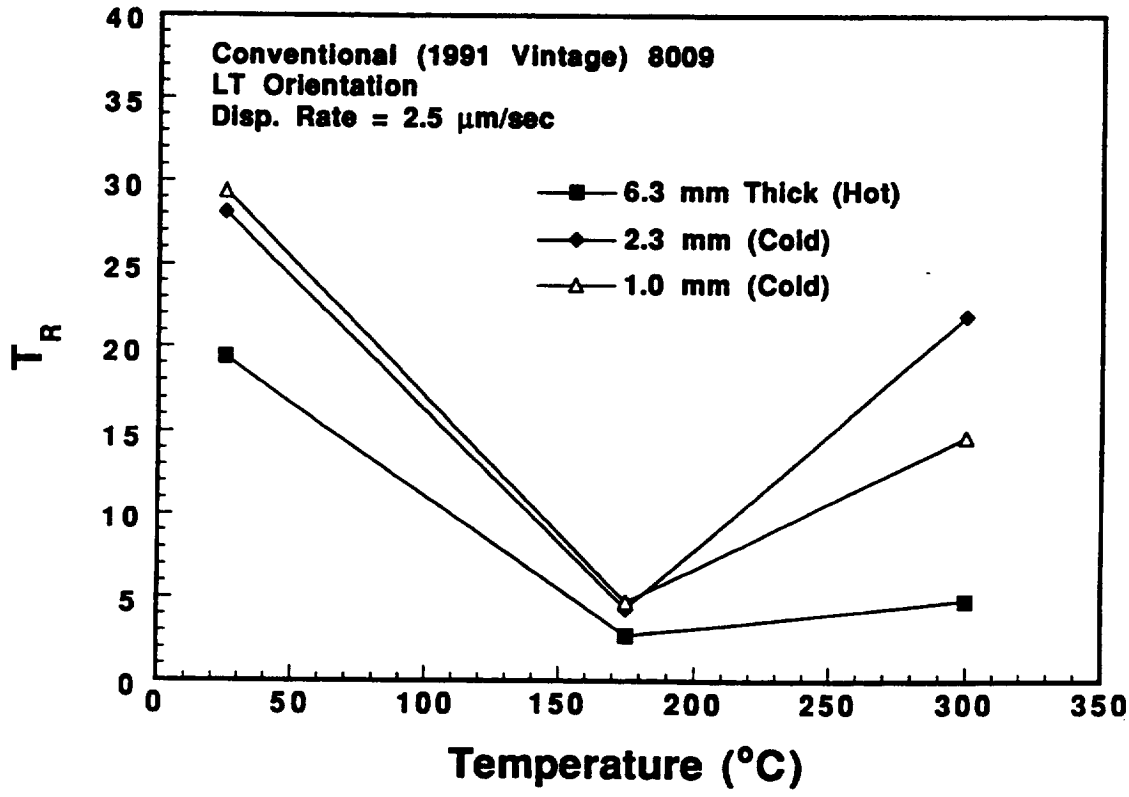

Figure 15: Effect of temperature on the tearing modulus of Conventional AA8009 plate and sheet (1991 Vintage) at gauge thicknesses of 6.3, 2.3 and 1.0 mm, respectively, and a fixed displacement rate of 2.5×10^{-3} mm/sec.

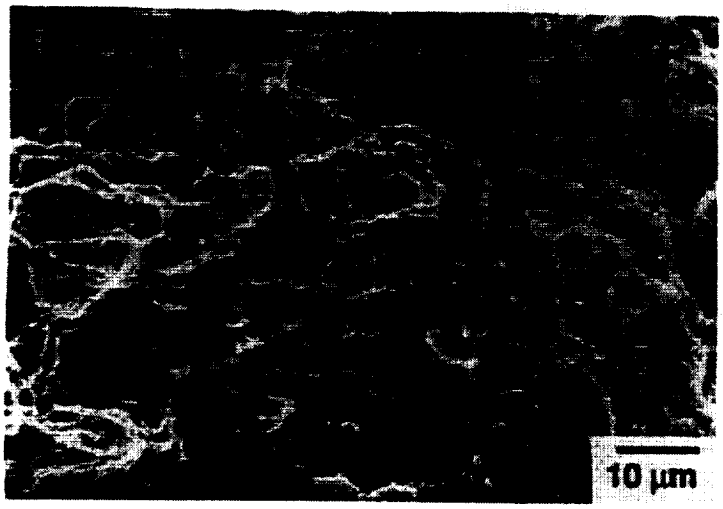

(a)

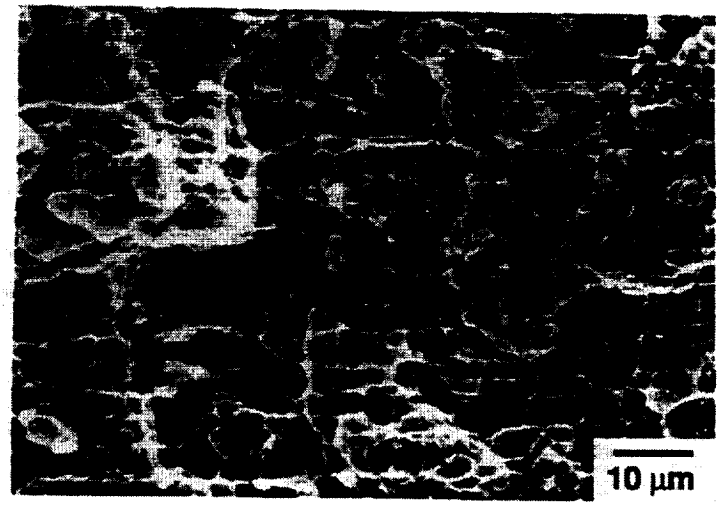

(b)

(c)

Figure 16: SEM fractographs of 6.3 mm thick Conventional AA8009 plate (1991 Vintage) fractured at: (a)25°C, (b) 175°C and (c) 300°C, at a displacement rate of 2.5 x 10^{-3} mm/sec.

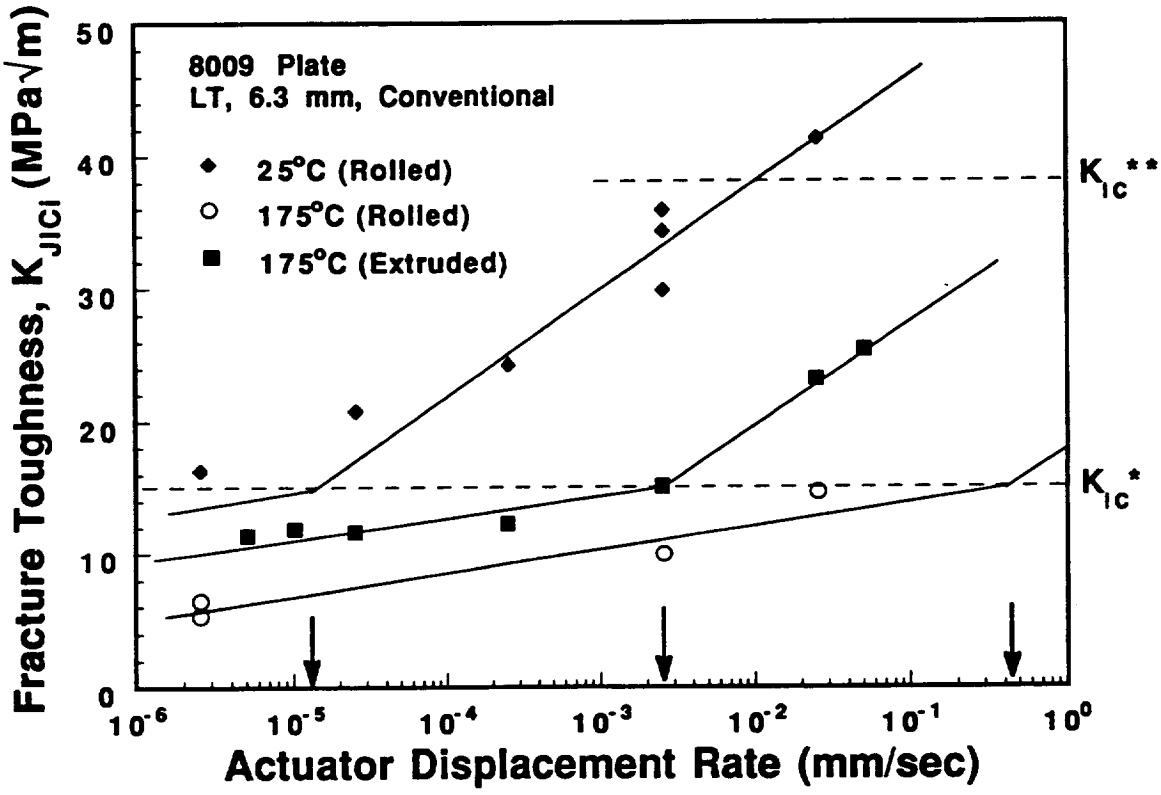

Figure 17: Effect of actuator displacement rate on the fracture toughness of 6.3 mm thick Conventional AA8009 plate (1991 Vintage) at 25 and 175°C.

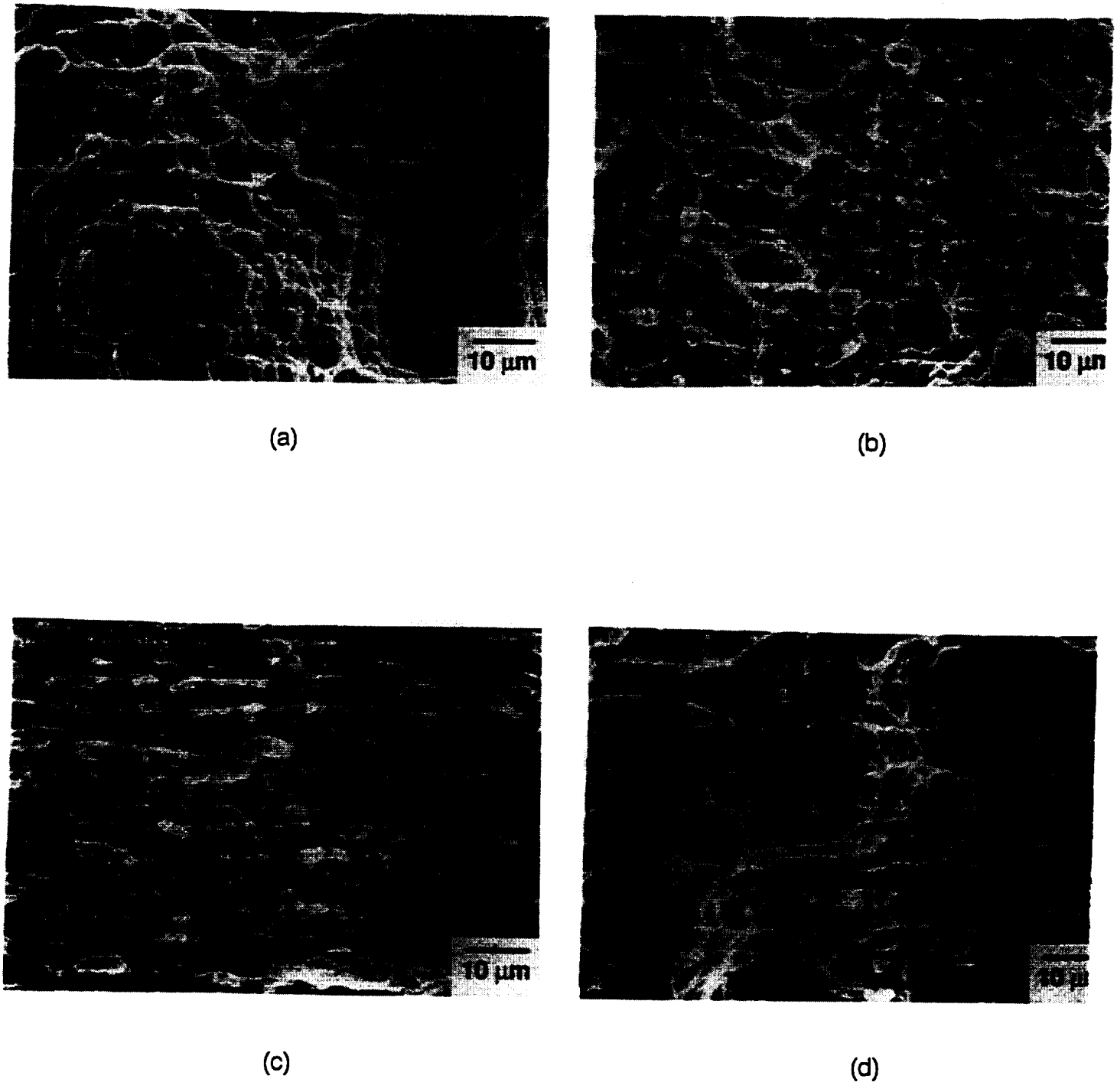

Figure 18: SEM fractographs of 6.3 mm thick Conventional AA8009 plate (1991 Vintage) fractured at: (a) 25°C and 5.1×10^{-6} mm/sec, (b) 25°C and 2.5×10^{-2} mm/sec, (c) 175°C and 5.1×10^{-6} mm/sec, and (d) 175°C and 2.5×10^{-2} mm/sec.

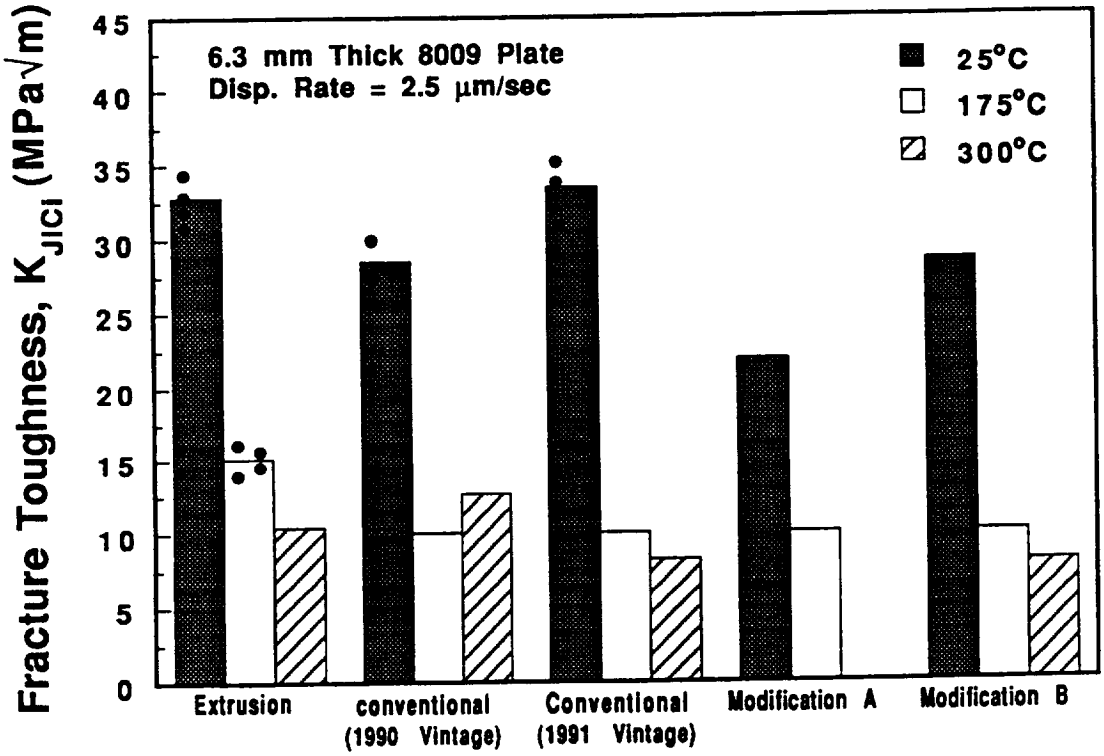

Figure 19: Effect of processing procedure on the initiation fracture toughness of 6.3 mm thick AA8009 plate.

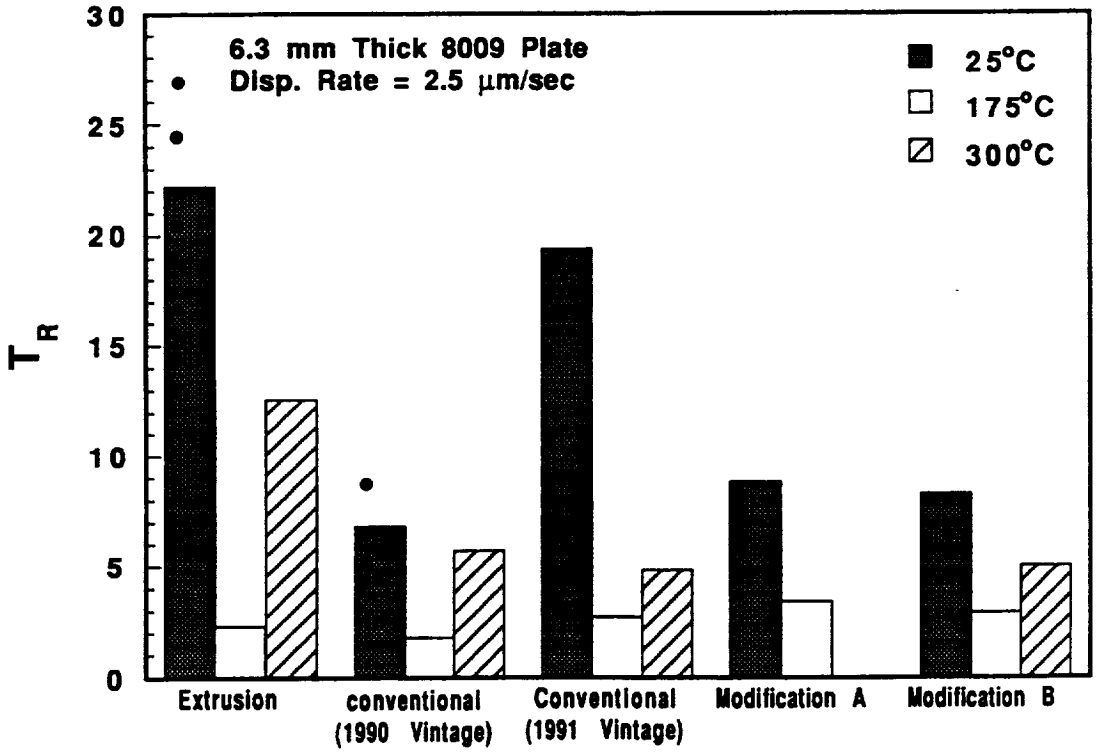

Figure 20: Effect of processing procedure on the tearing modulus of 6.3 mm thick AA8009 plate.

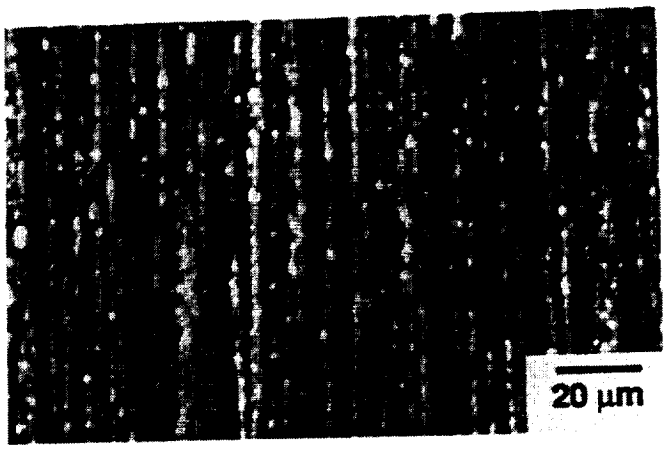

(a)

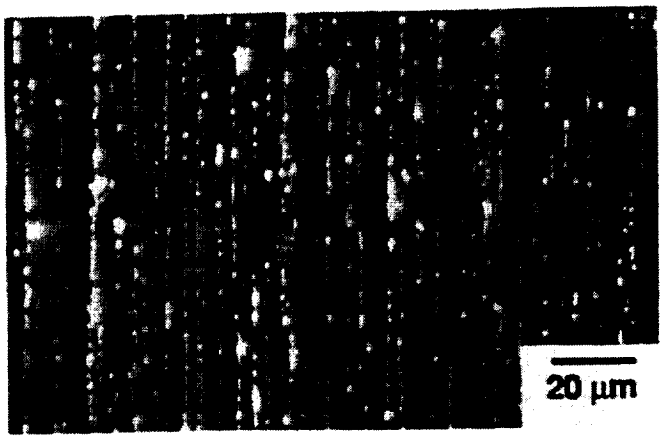

(b)

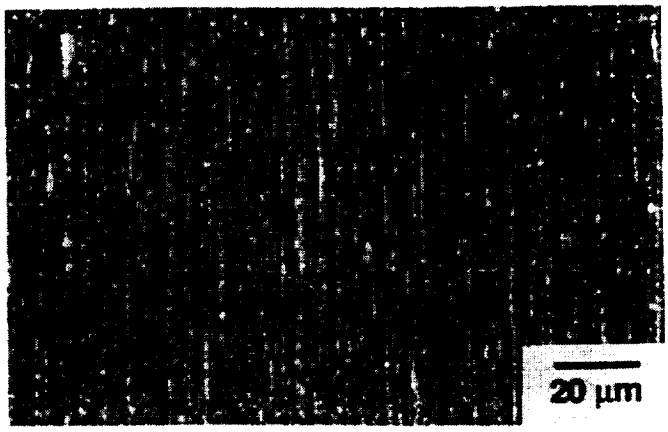

(c)

Figure 21: SEM micrographs of etched, as-received Conventional AA8009 plate and sheet (1991 Vintage) with gauge thicknesses of: (a) 6.3 mm, (b) 2.3 mm and (c) 1.0 mm, showing stringers of oxides along prior ribbon particle boundaries.

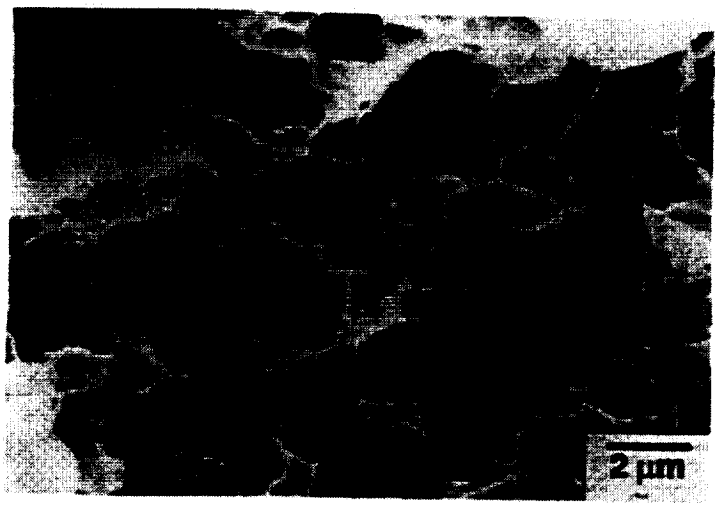

(a)

(b)

Figure 22: SEM fractographs of 6.3 mm thick (a) Modification A and (b) Modification B of AA8009 fractured at 25°C and 2.5 x 10^{-3} mm/sec.

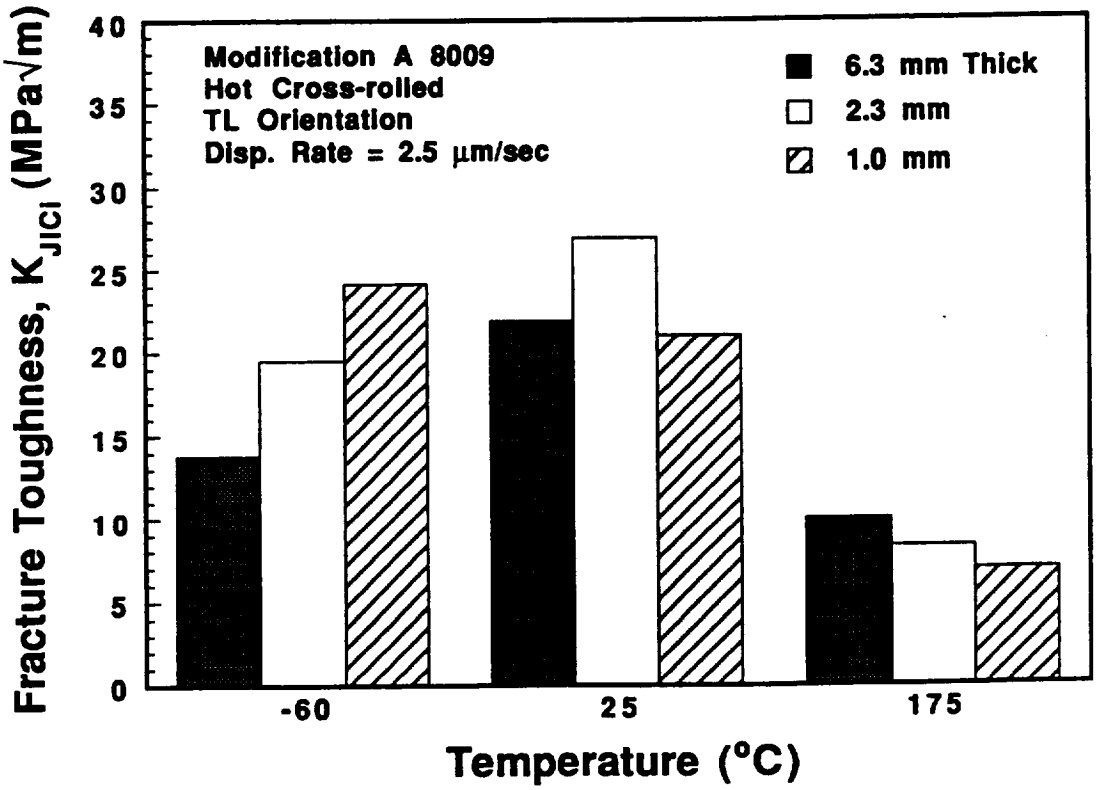

Figure 23: Effect of cryogenic to elevated test temperature on the fracture toughness of Modification A of AA8009 with gauge thicknesses of 6.3, 2.3 and 1.0 mm.

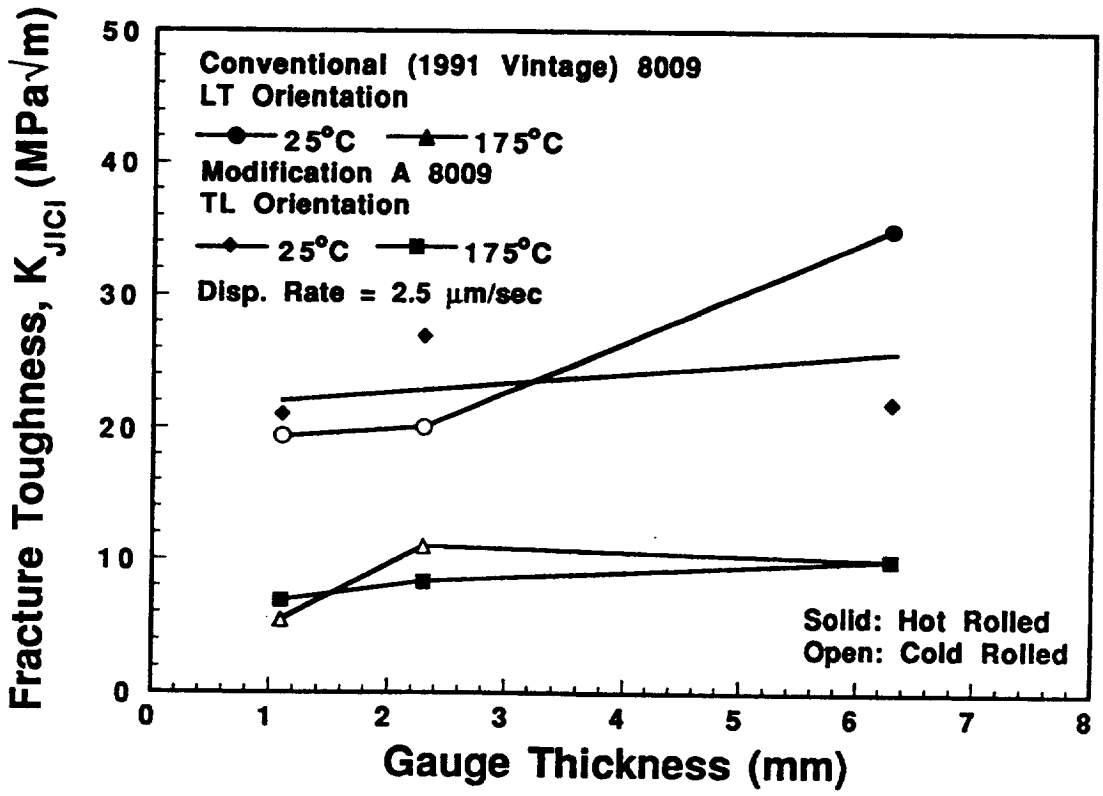

Figure 24: Effect of thermomechanical processing on the fracture toughness of Conventional (1991 Vintage) and Modification A of AA8009 fractured at 25°C and 175°C at a fixed grip displacement rate of 2.5×10^{-3} mm/sec.

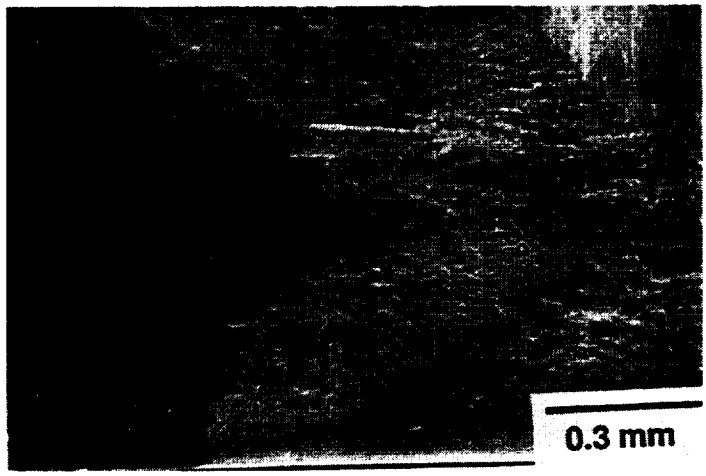

(a)

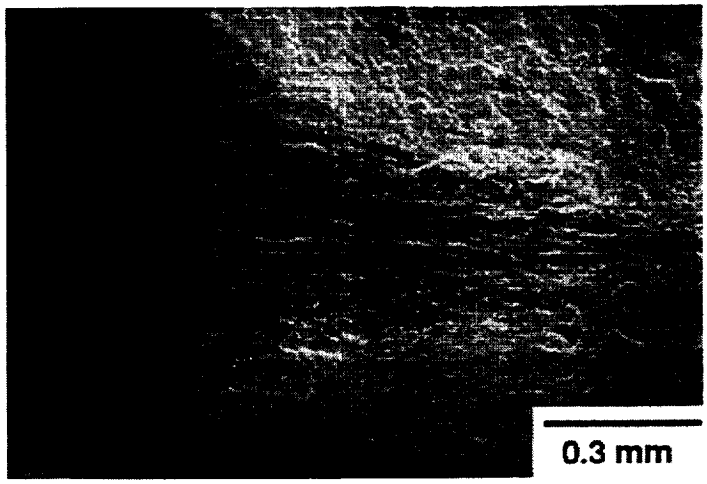

(b)

Figure 25: Low magnification SEM fractographs of 1.0 mm thick Conventional AA8009 sheet (1991 Vintage) fractured at: (a) 25 °C and (b) 175 °C at 2.5 x 10^{-3} mm/sec.

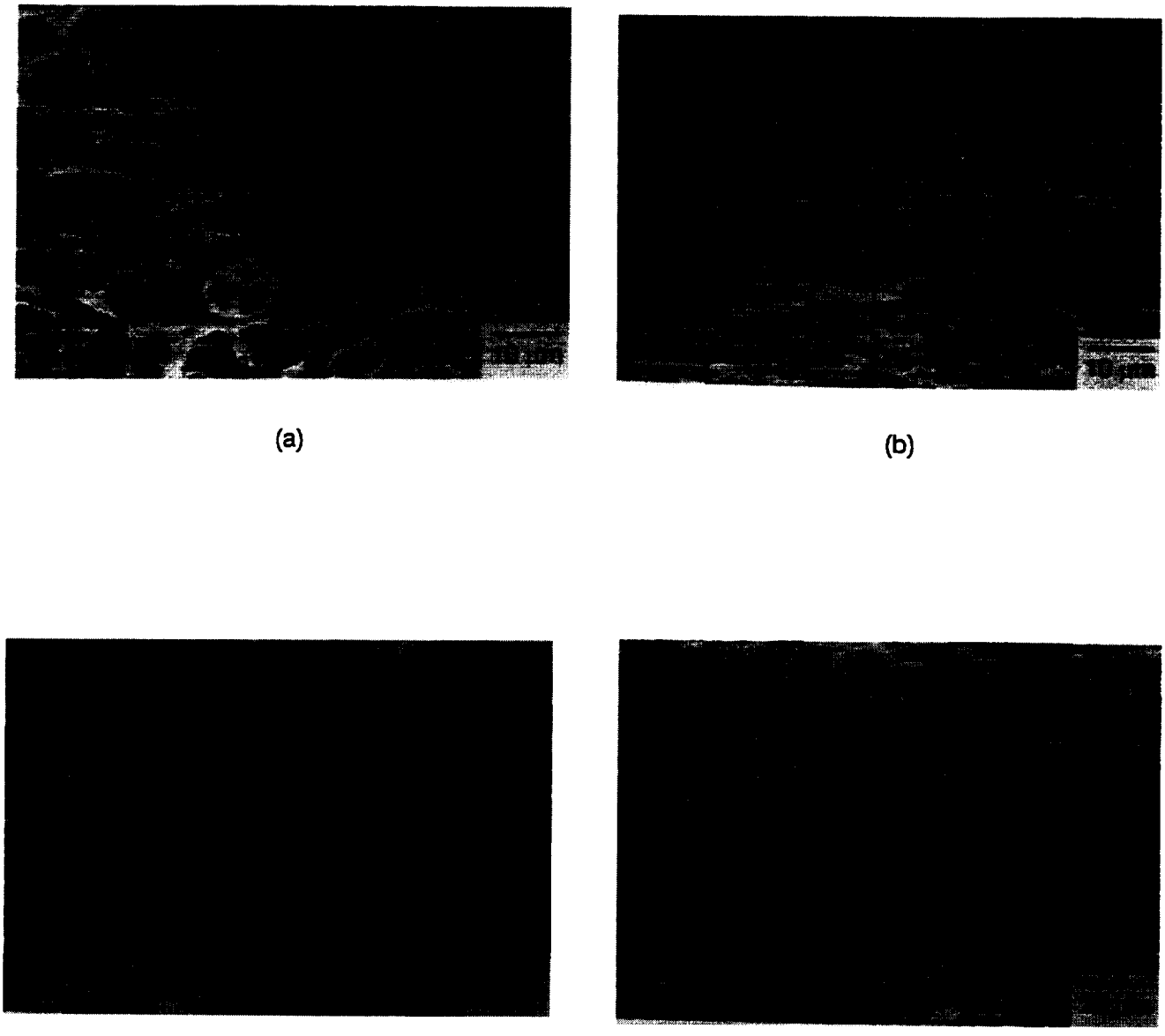

Figure 26: SEM fractographs of Conventional AA8009 sheet (1991 Vintage) with a gauge thickness of 2.3 mm fractured at: (a) 25 °C and (b) 175 °C, compared to 1.0 mm thick sheet fractured at: (c) 25 °C and (d) 175 °C, all at 2.5 x 10^{-3} mm/sec.

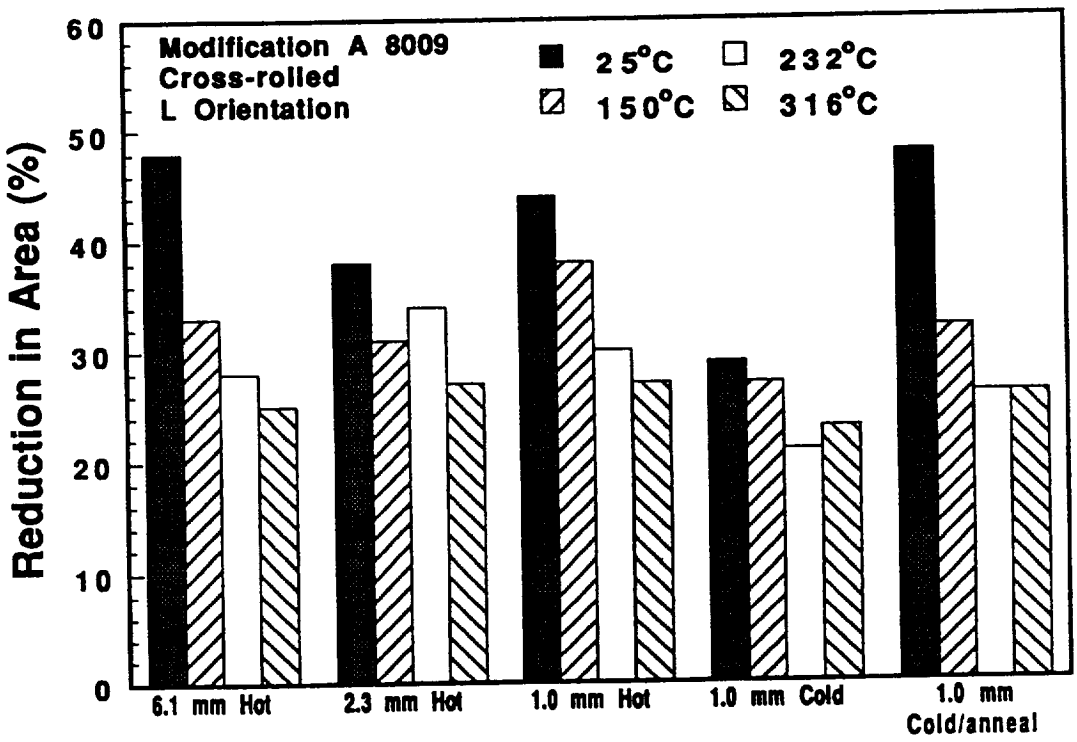

Figure 27: Effect of thermomechanical processing on the tensile reduction-in-area at fracture for Modification A of AA8009 fractured at temperatures between 25°C and 316°C.

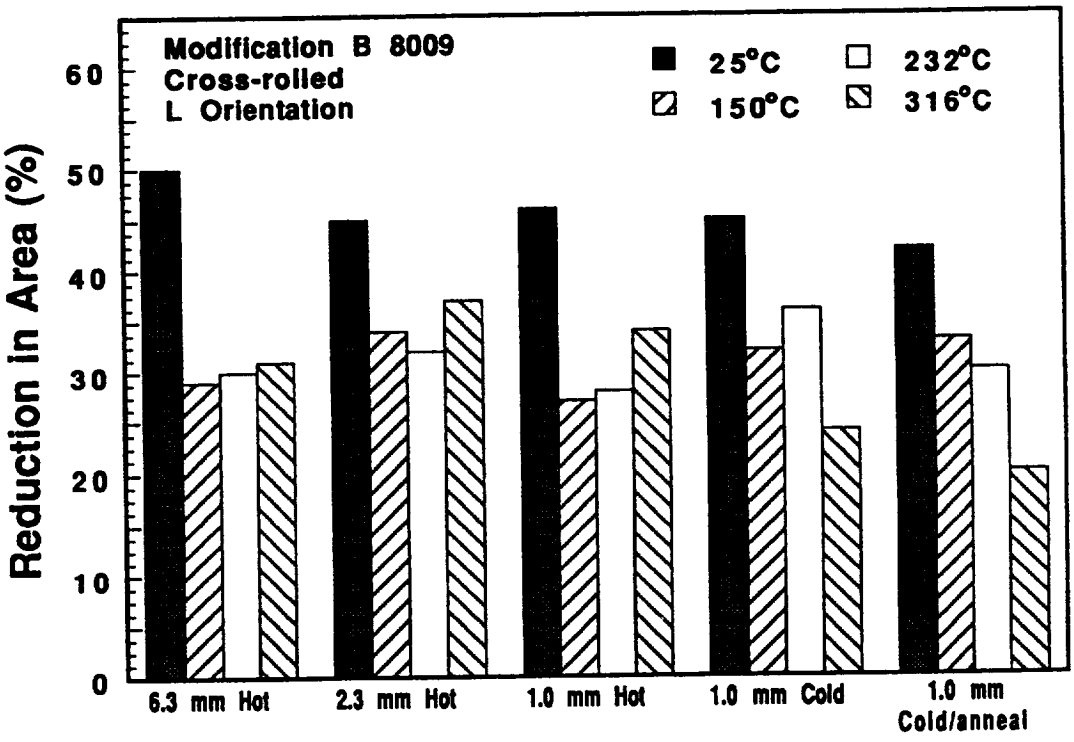

Figure 28: Effect of thermomechanical processing on the tensile reduction-in-area at fracture for Modification B of AA8009 fractured at temperatures between 25°C and 316°C.

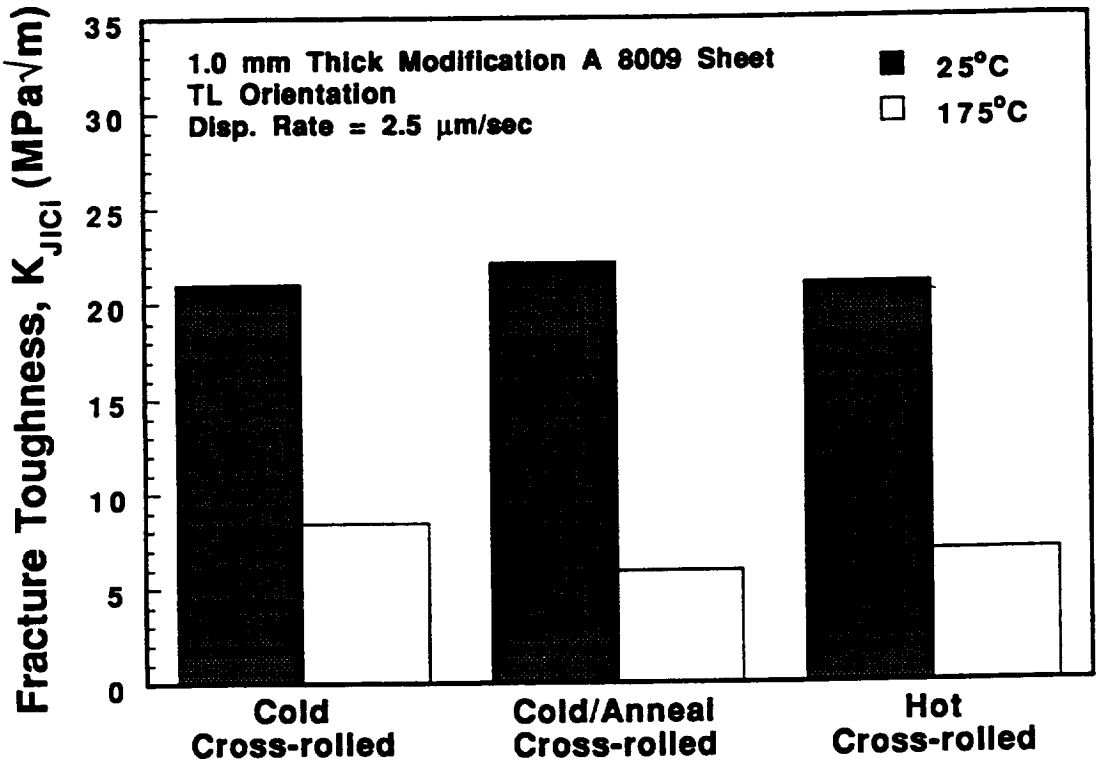

Figure 29: Effect of rolling temperature and annealing on the initiation fracture toughness of 1.0 mm thick sheet of Modification A of AA8009 sheet.

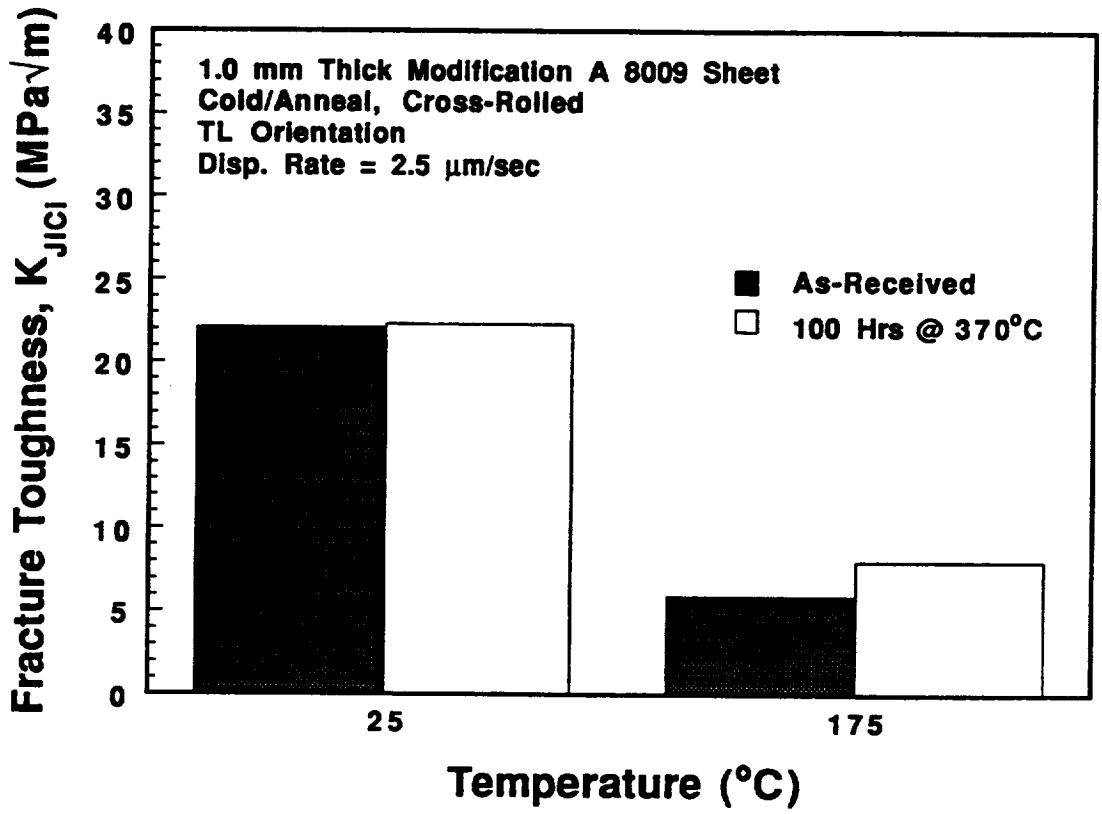

Figure 30: Effect of high temperature exposure on the fracture toughness of 1.0 mm thick Modification A of AA8009 sheet.

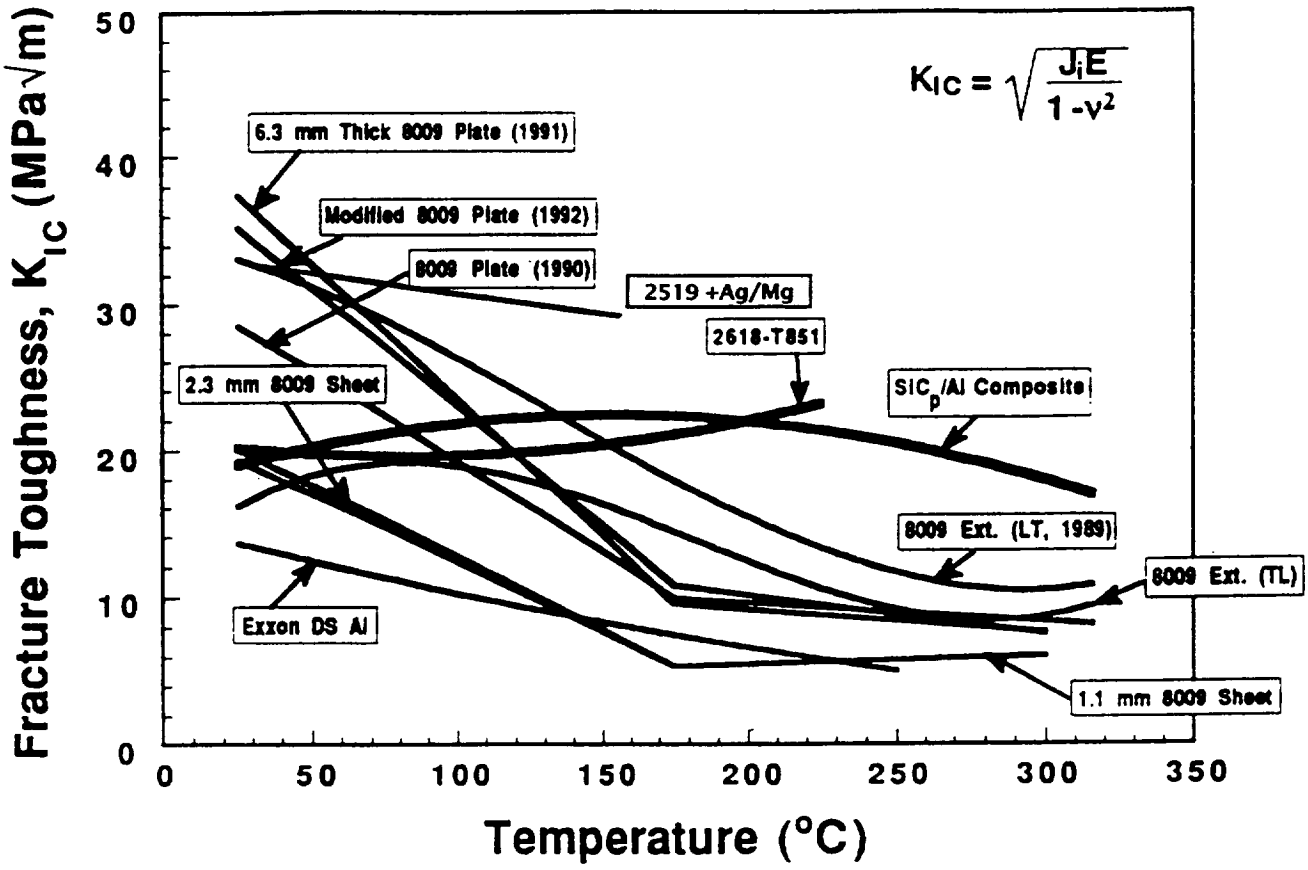

Figure 31: The temperature dependencies of initiation fracture toughness for a wide variety of elevated temperature aluminum alloys, including conventional IM alloys (AA2618 and AA2519), advanced RS/PM AA8009, and a metal matrix composite.

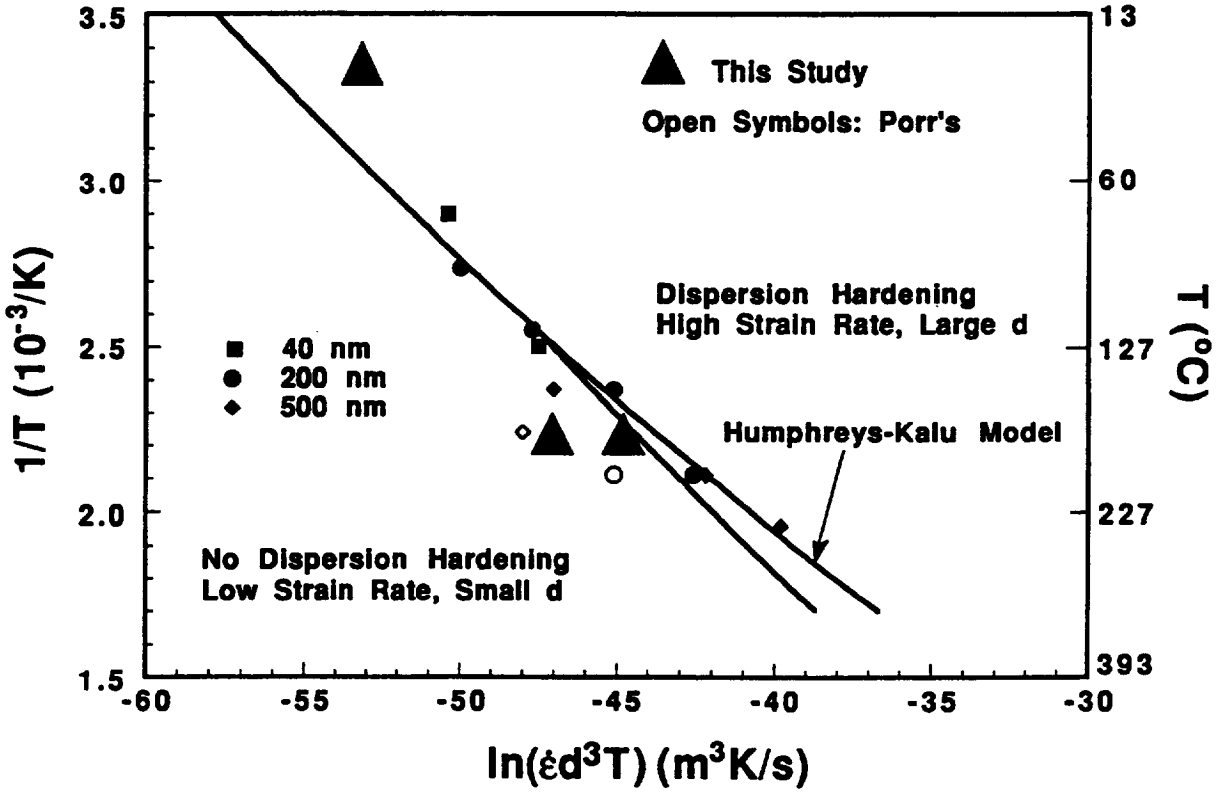

Figure 32: The transition for climb-assisted dislocation bypassing of dispersoids in AA8009; predicted as a function of particle size, temperature, and strain rate by the HK model and compared to values inferred from fracture toughness experiments.

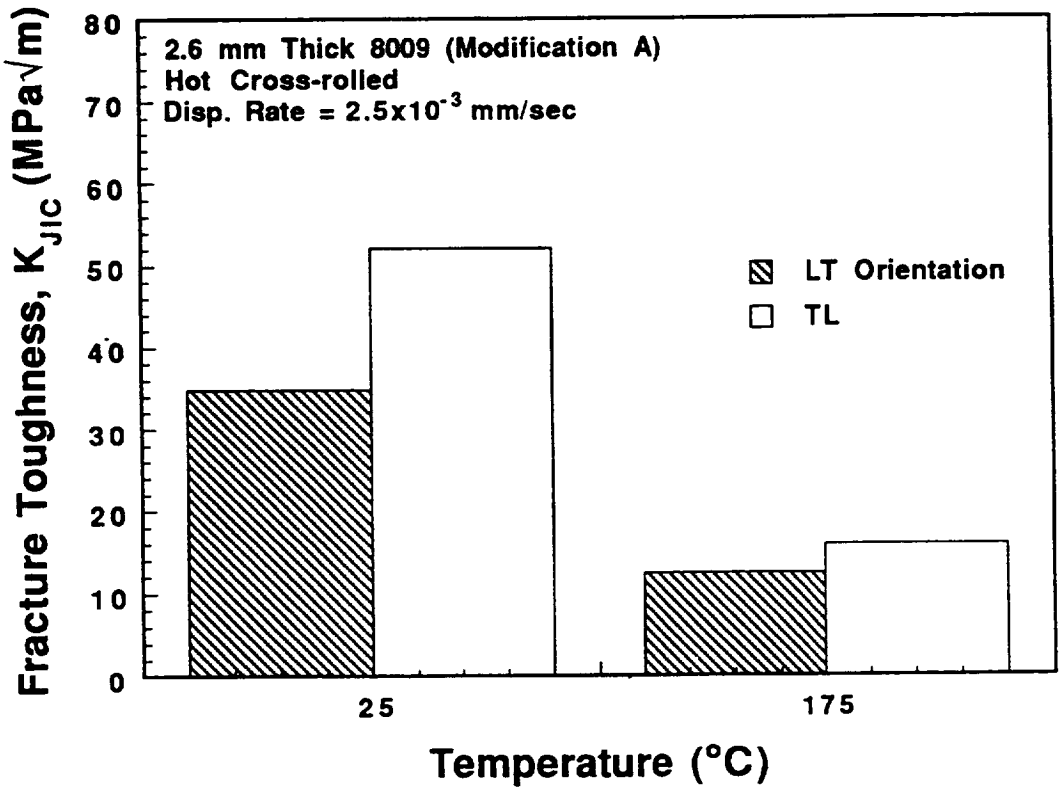

Figure 33: Effect of crack orientation on the fracture toughness of 2.6 mm thick Modification A of AA8009 sheet, tested at 25 and 175°C.

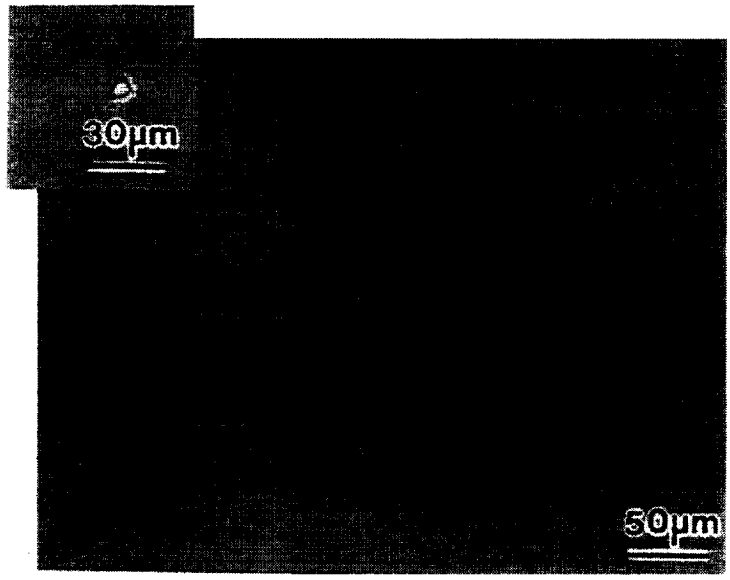

Figure 34: Optical micrograph of mechanically polished and unetched CM Al showing infrequent, but large constituent particles. The inset shows an SEM-secondary electron image of an inclusion. The plane of polish is parallel to the transverse (vertical) and longitudinal-extrusion (horizontal) directions.

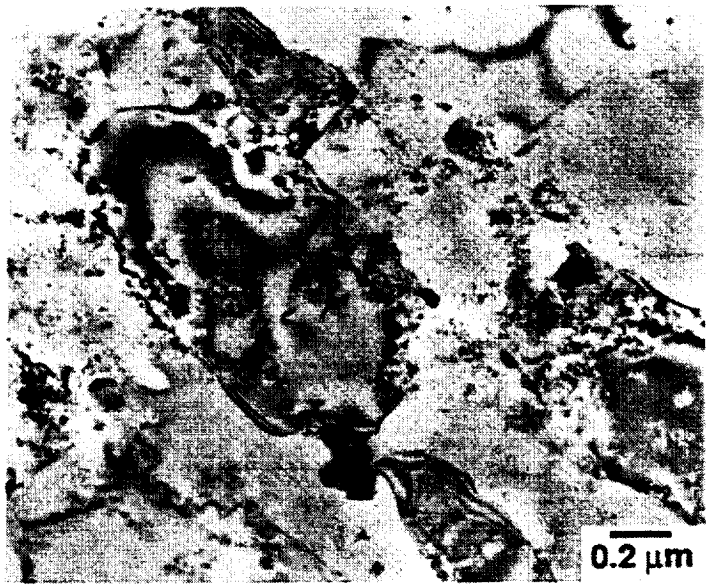

(a)

(b)

Figure 35: TEM micrographs of CM Al showing: (a) the submicron grain size and (b) clusters of fine Al_2O_3 dispersoids.

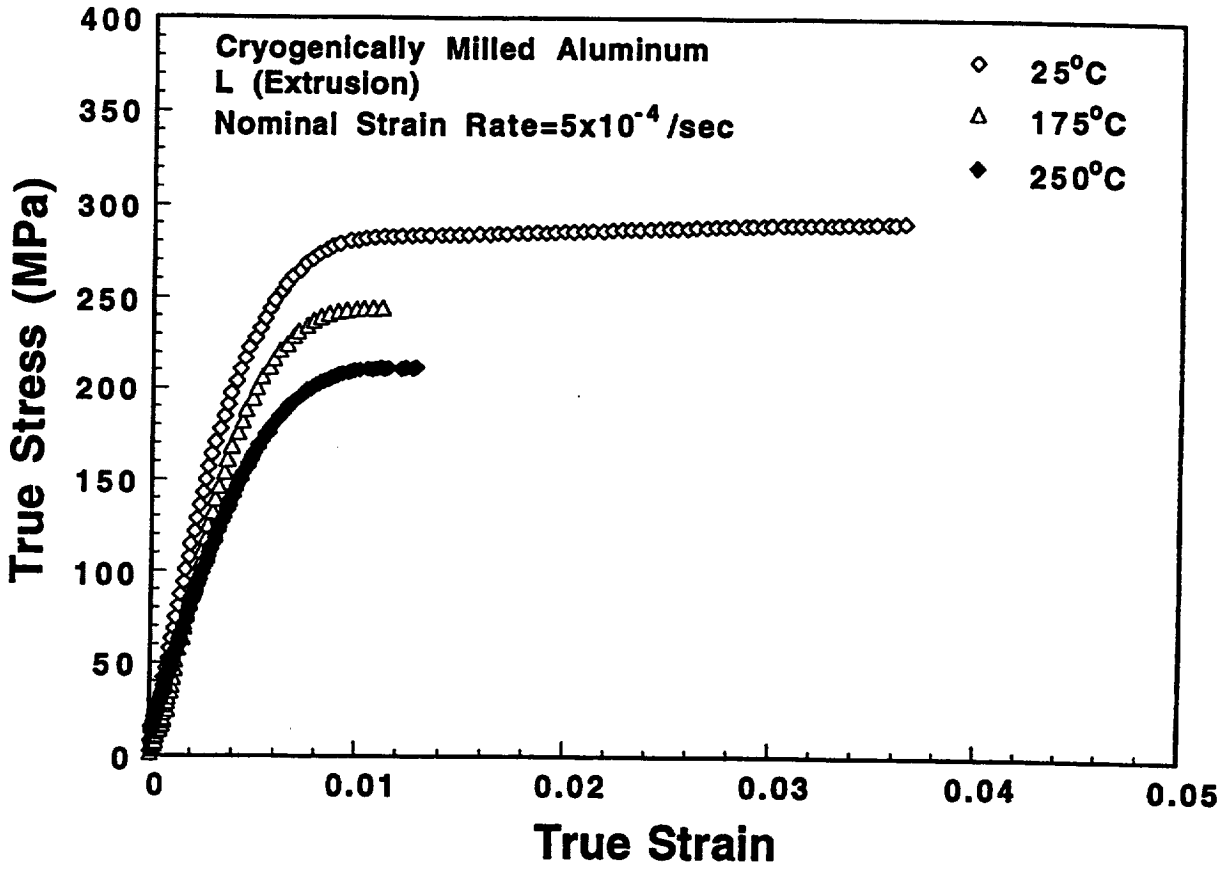

Figure 36: Uniaxial true tensile stress vs true total strain for CM Al prior to necking, as a function of temperature.

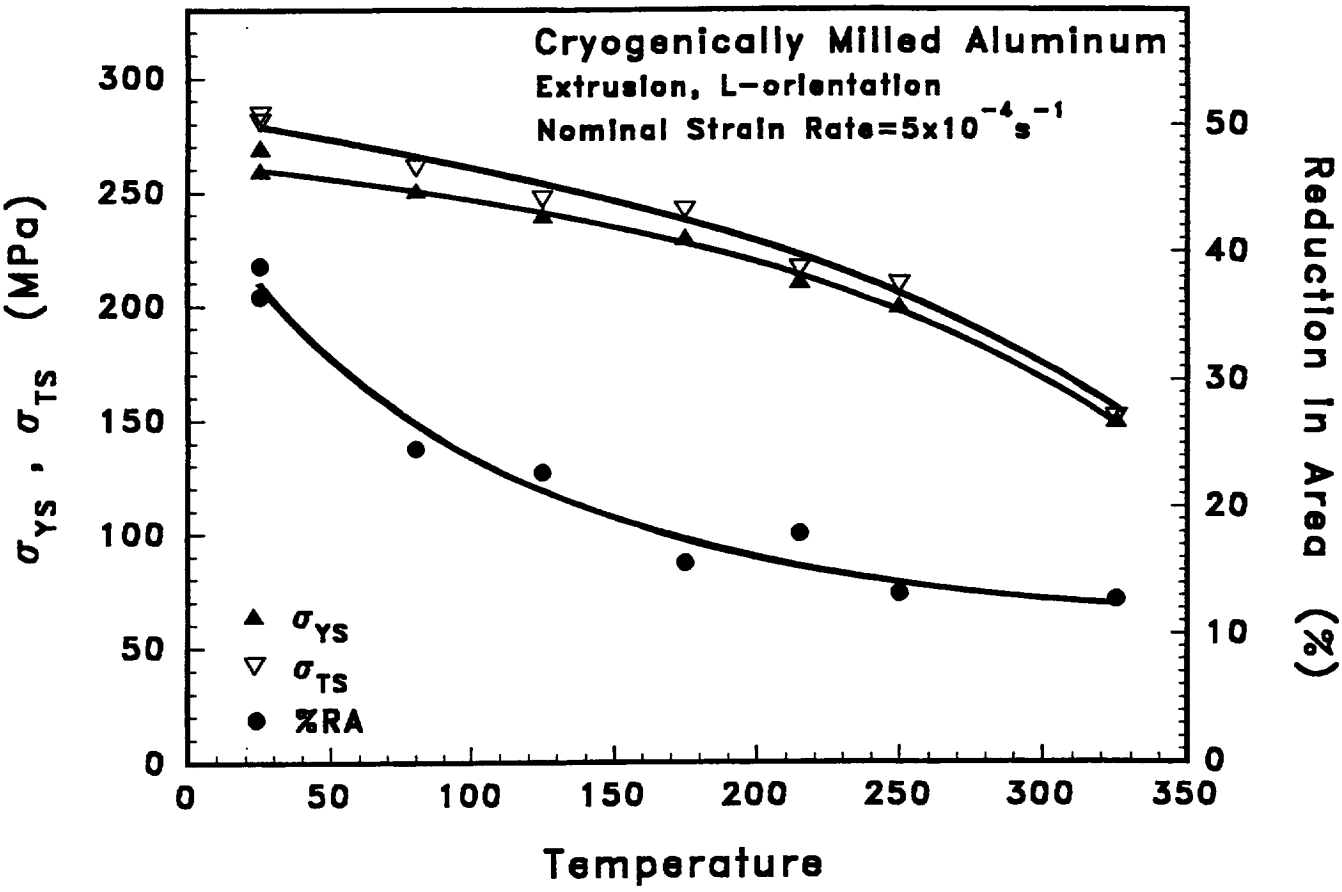

Figure 37: The temperature dependencies of tensile yield strength, ultimate tensile strength and ductility (%RA) of CM Al at a single loading rate.

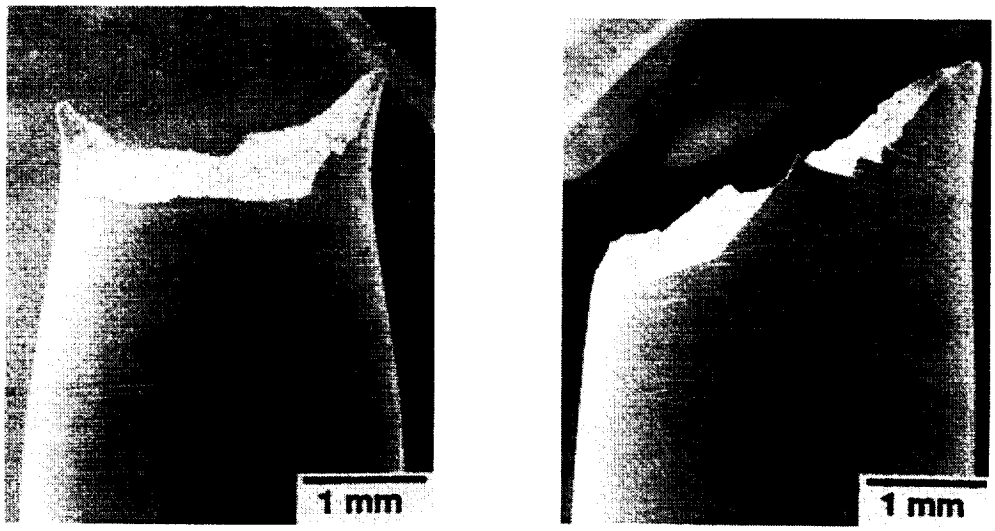

Figure 38: Macroscopic side-views of CM Al tensile specimens fractured at: (a) 25°C and (b) 175°C.

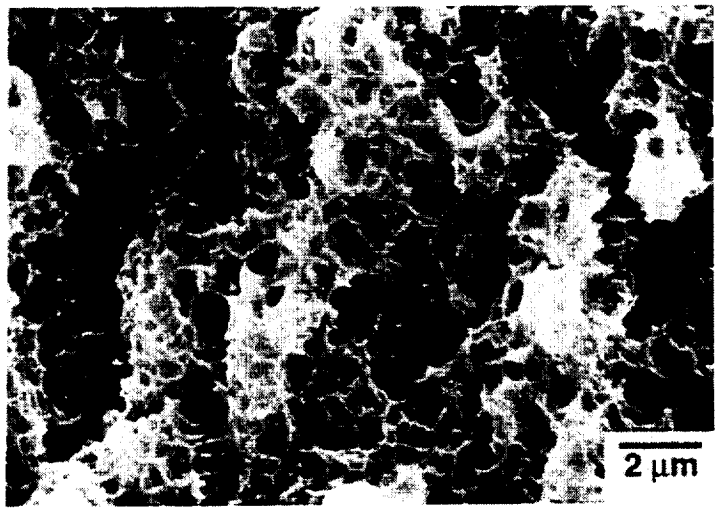

(a)

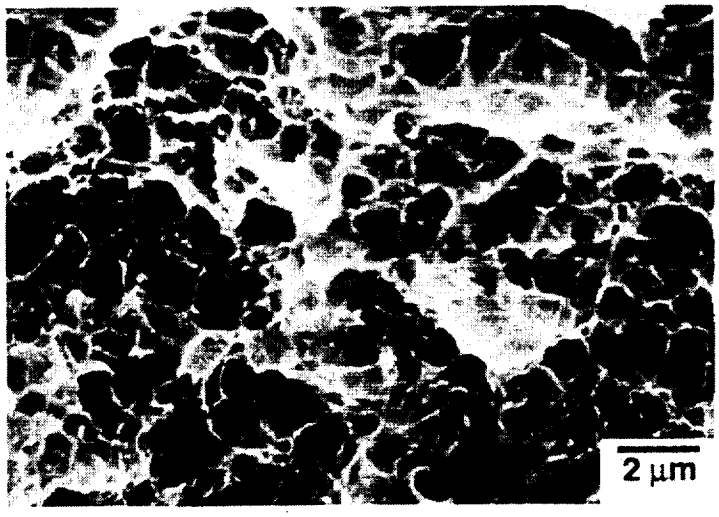

(b)

Figure 39: SEM fractographs of CM Al tensile fracture surfaces produced at: (a) 25 °C and (b) 175 °C, and a nominal strain rate of 5 x 10^{-4} sec^{-1}.

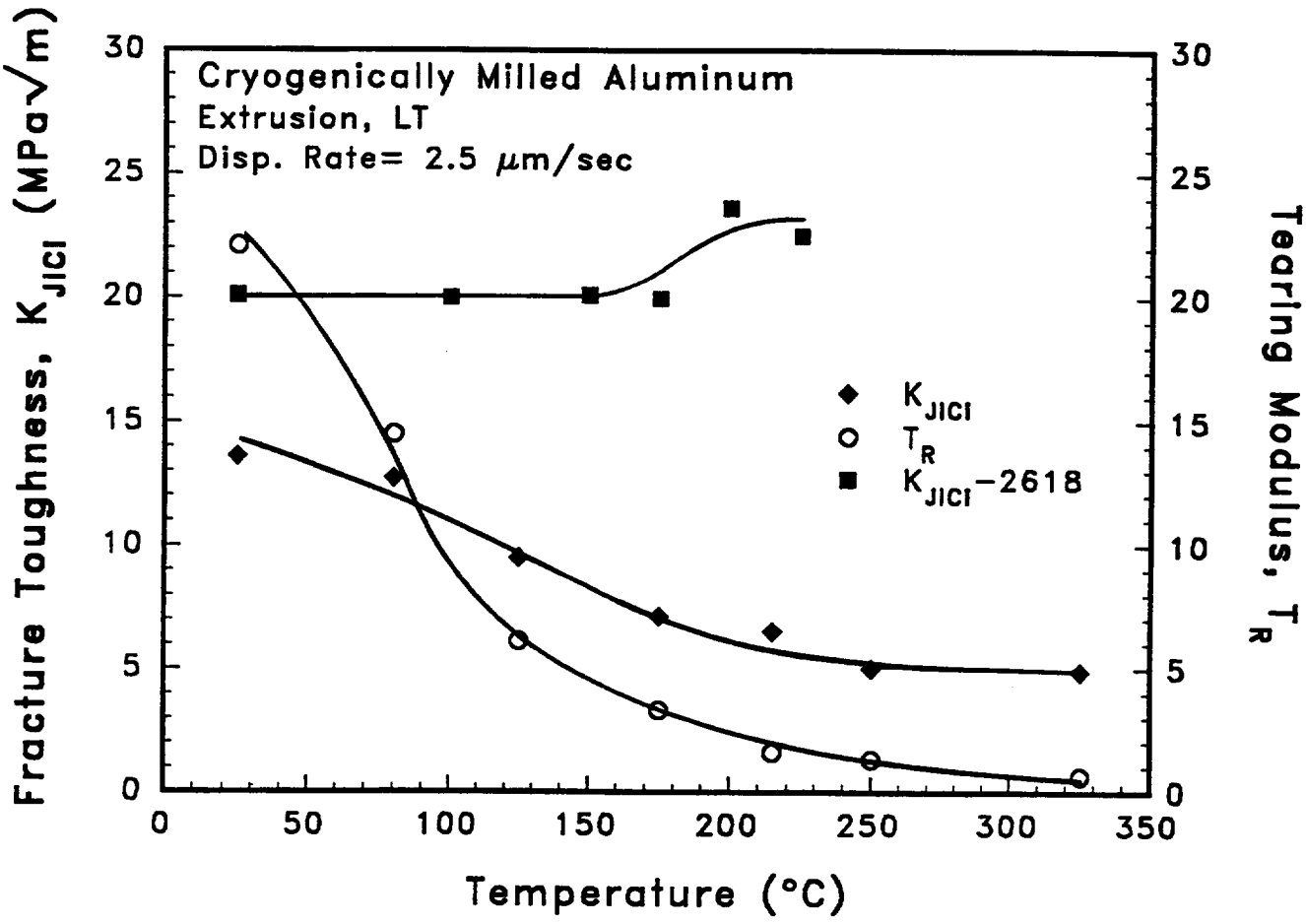

Figure 40: Initiation fracture toughness (K_{JICi}) and tearing modulus (T_R) for CM Al and AA2618 (8), as a function of temperature.

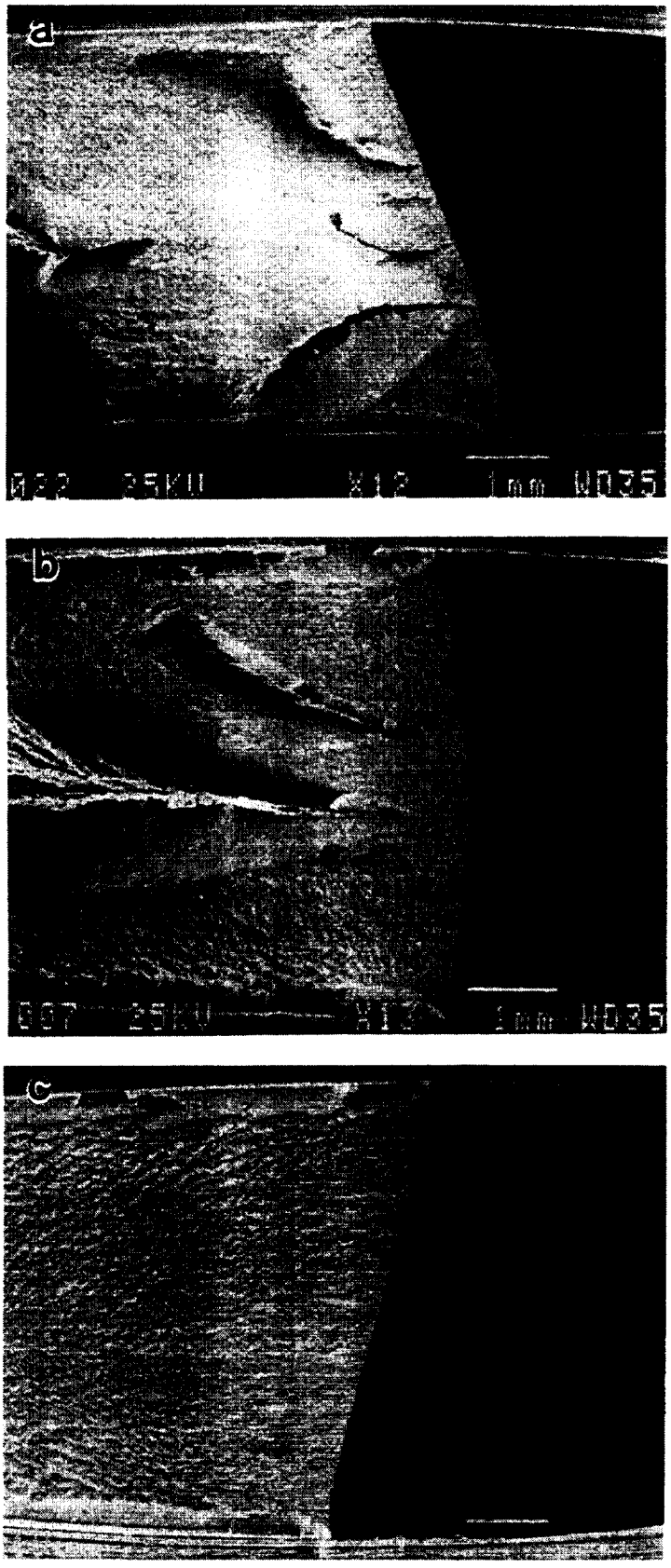

Figure 41: Low magnification SEM fractographs of macroscopic delaminations in CM Al fractured at: a) 25°C, b) 175°C, and (c) 250°C. Each crack grew from right to left, and the fatigue crack-fast fracture interface is shown by the contrast and roughness changes right-of-center.

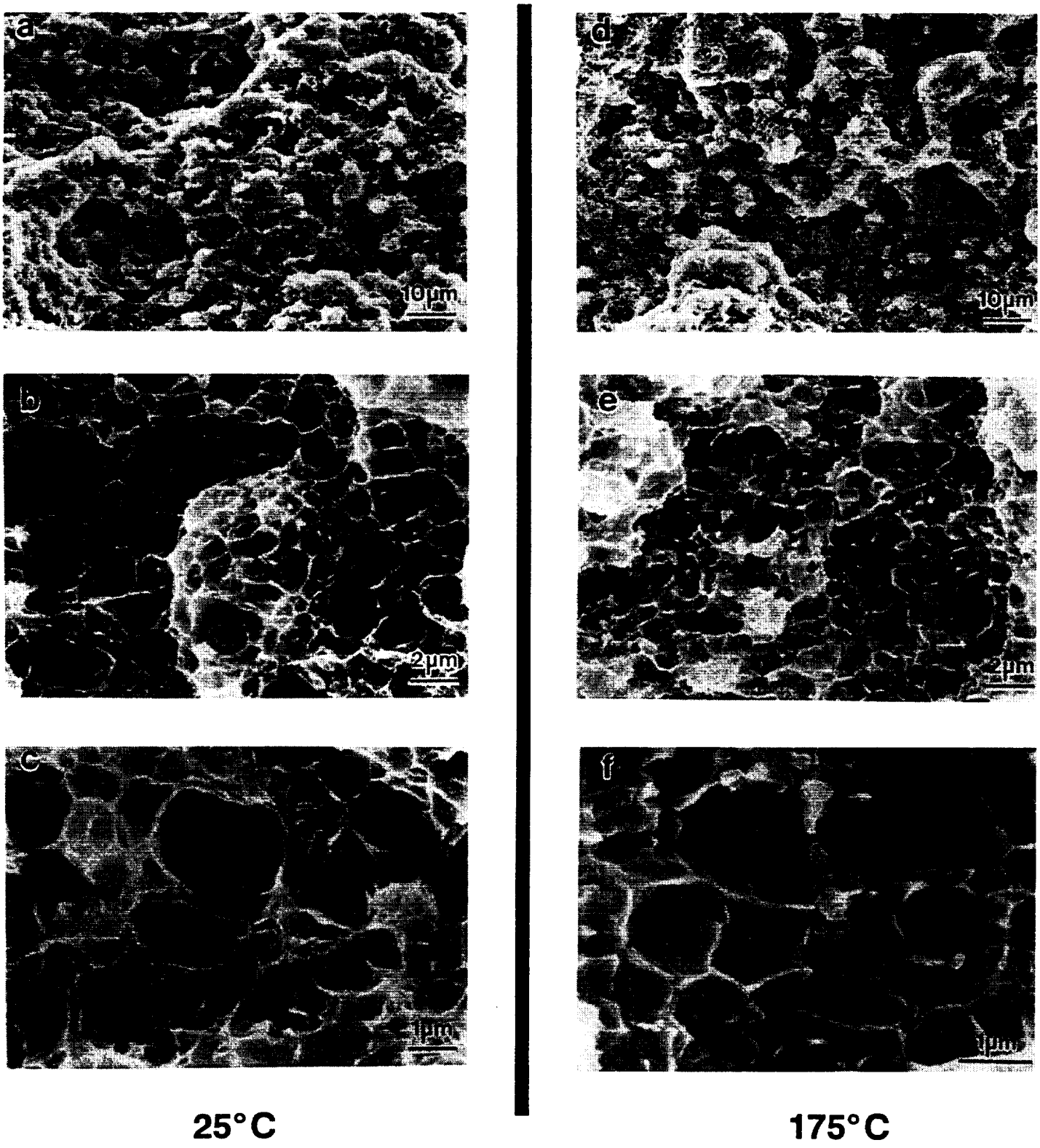

Figure 42: SEM fractographs of CM Al compact tension specimen fracture surfaces, at mid-thickness and for $\Delta a = 0.4 \pm 0.2$ mm, produced at: (a), (b) and (c) 25°C; and (d), (e) and (f) 175°C. Fractographs are arranged vertically in order of increasing magnification and the crack grew from right to left.

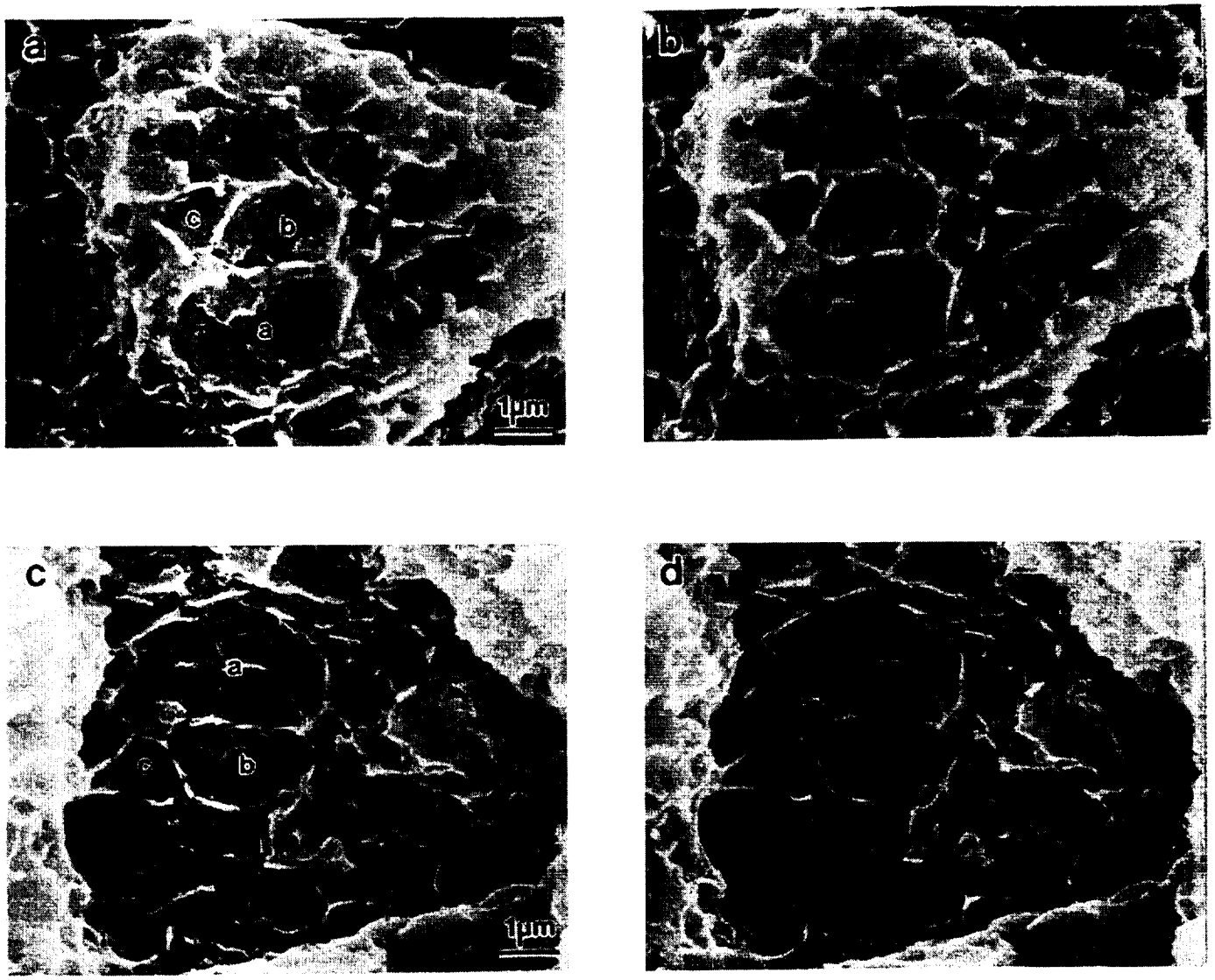

Figure 43: High magnification, matching-surface, stereofractographic analysis of a CM Al CT fracture surface, for $\Delta a = 0.4 \pm 0.2$ mm and produced at 175°C. (a) and (b) show one-half of the crack surface, and are tilted 7° and 0° (respectively) from the normal to the fracture plane. (c) and (d) show the matching half of the crack surface and are tilted 7° and 0°, respectively. The crack grew from right to left.

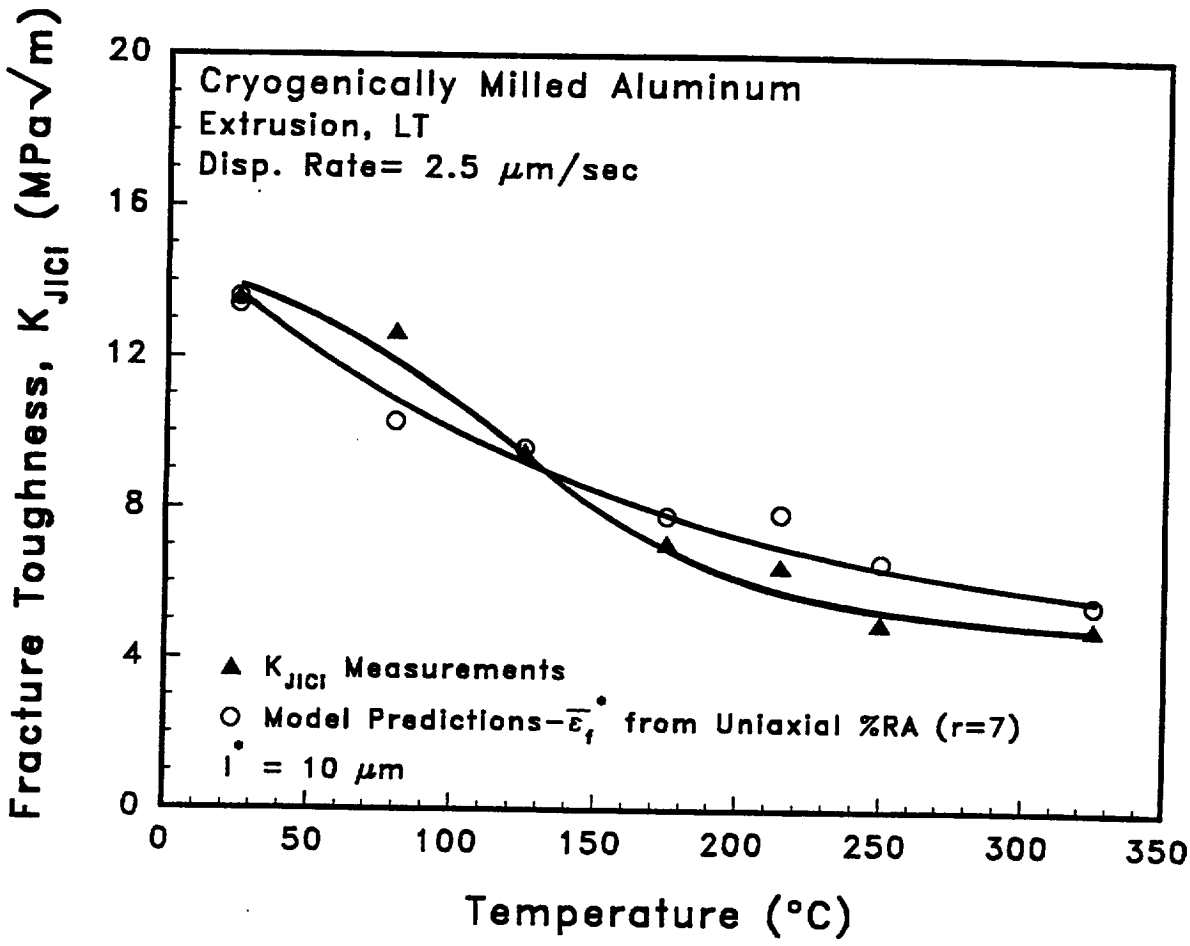

Figure 44: Critical plastic strain-controlled model predictions compared to experimentally measured values of the plane strain crack initiation toughness for CM Al as a function of temperature.

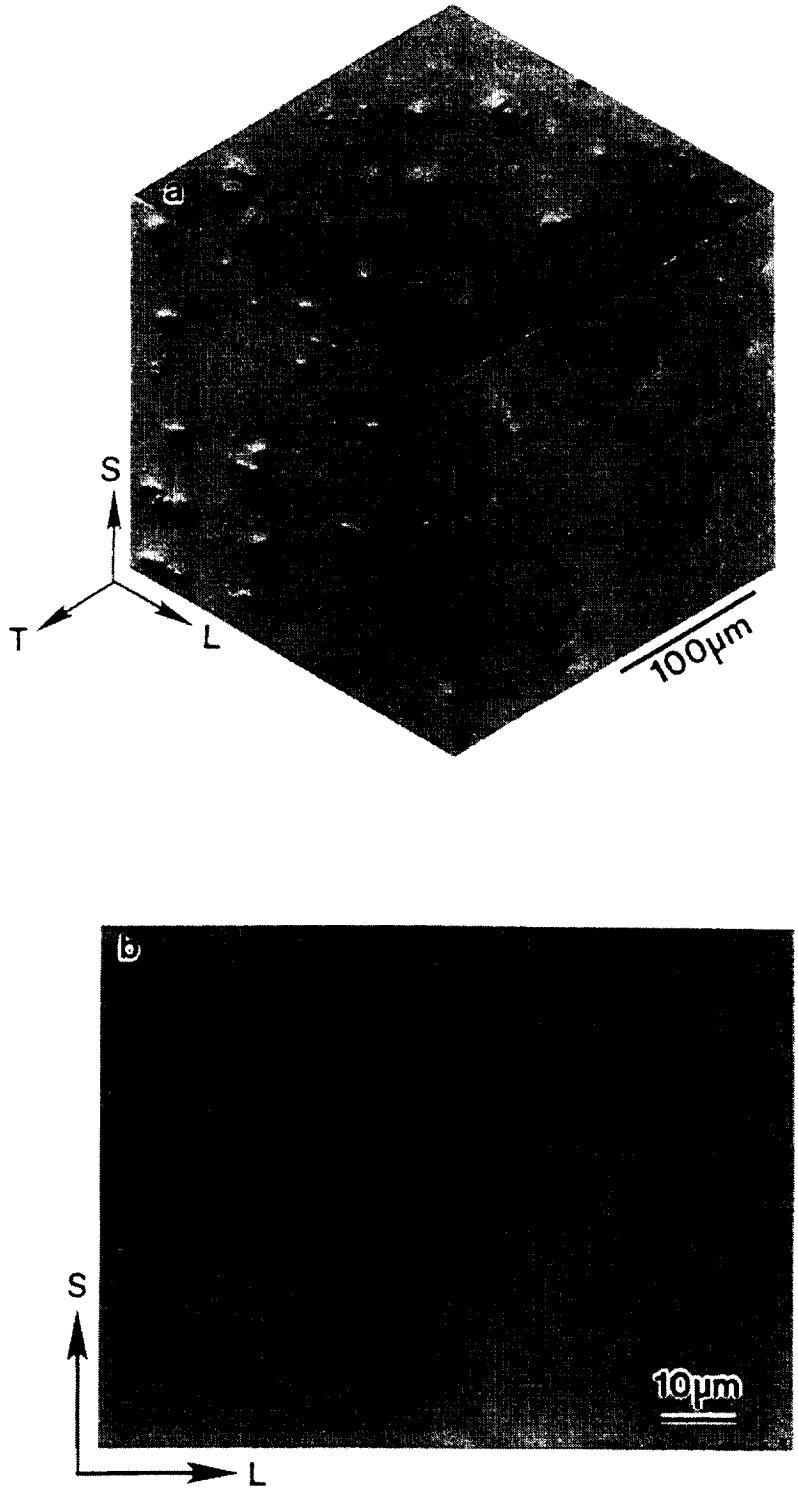

Figure 45: Optical micrographs of AA2519-T87 (+Mg+Ag) demonstrating: (a) an inhomogeneous distribution of undissolved θ (Al_2Cu) particles, and (b) processing-induced cracks in θ.

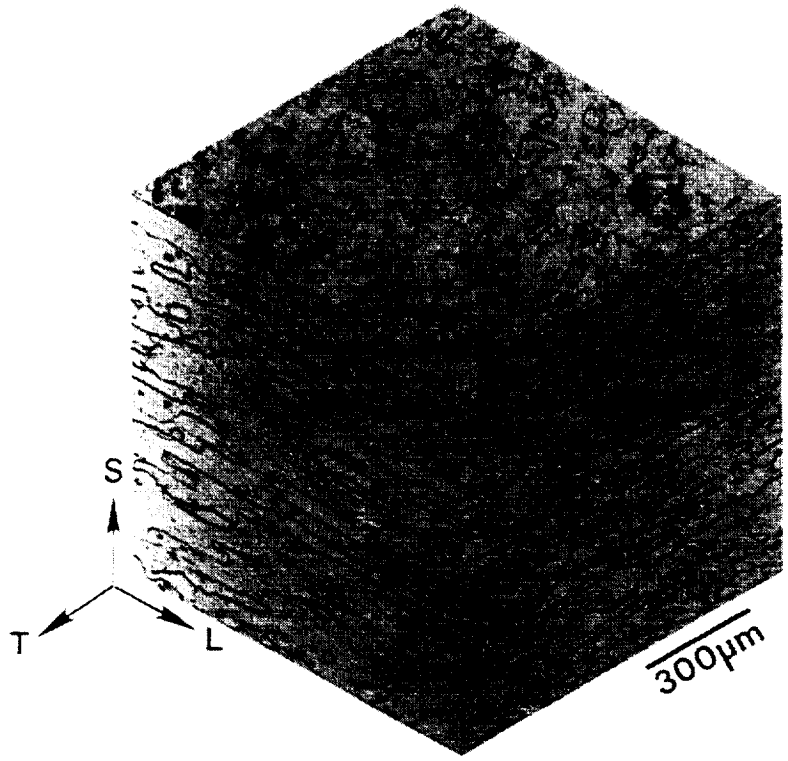

Figure 46: Optical micrograph of AA2519-T87 (+Mg+Ag) grain structure.

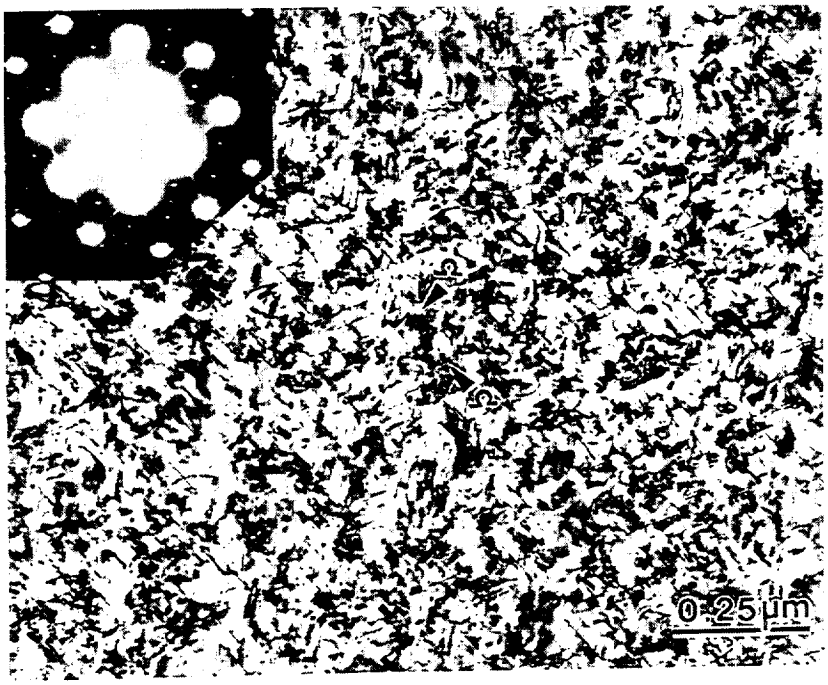

Figure 47: Transmission electron micrograph of AA2519-T87 (+Mg+Ag), with Ω precipitate plates indicated by arrows. The dominance of Ω is indicated by the bright diagonal streaks in the selected area diffraction pattern, each oriented perpendicular to one variant of Ω. The electron beam is approximately parallel to <110>.

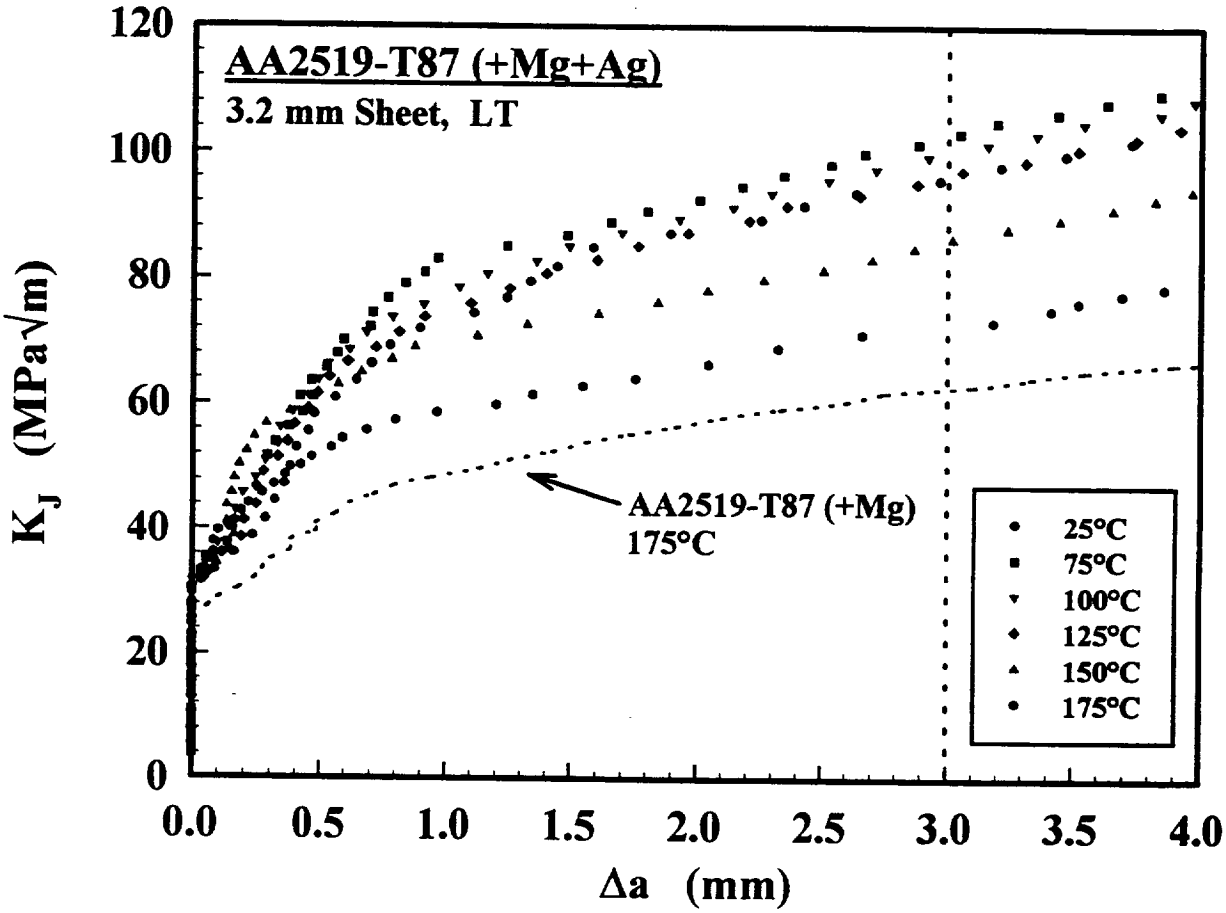

Figure 48: K_J-R curves as a function of temperature determined from CT specimens of AA2519+Mg+Ag; load-line displacement rate = 0.26 μm/sec. The K_J-Δa curve for a CT specimen of AA2519+Mg is included.

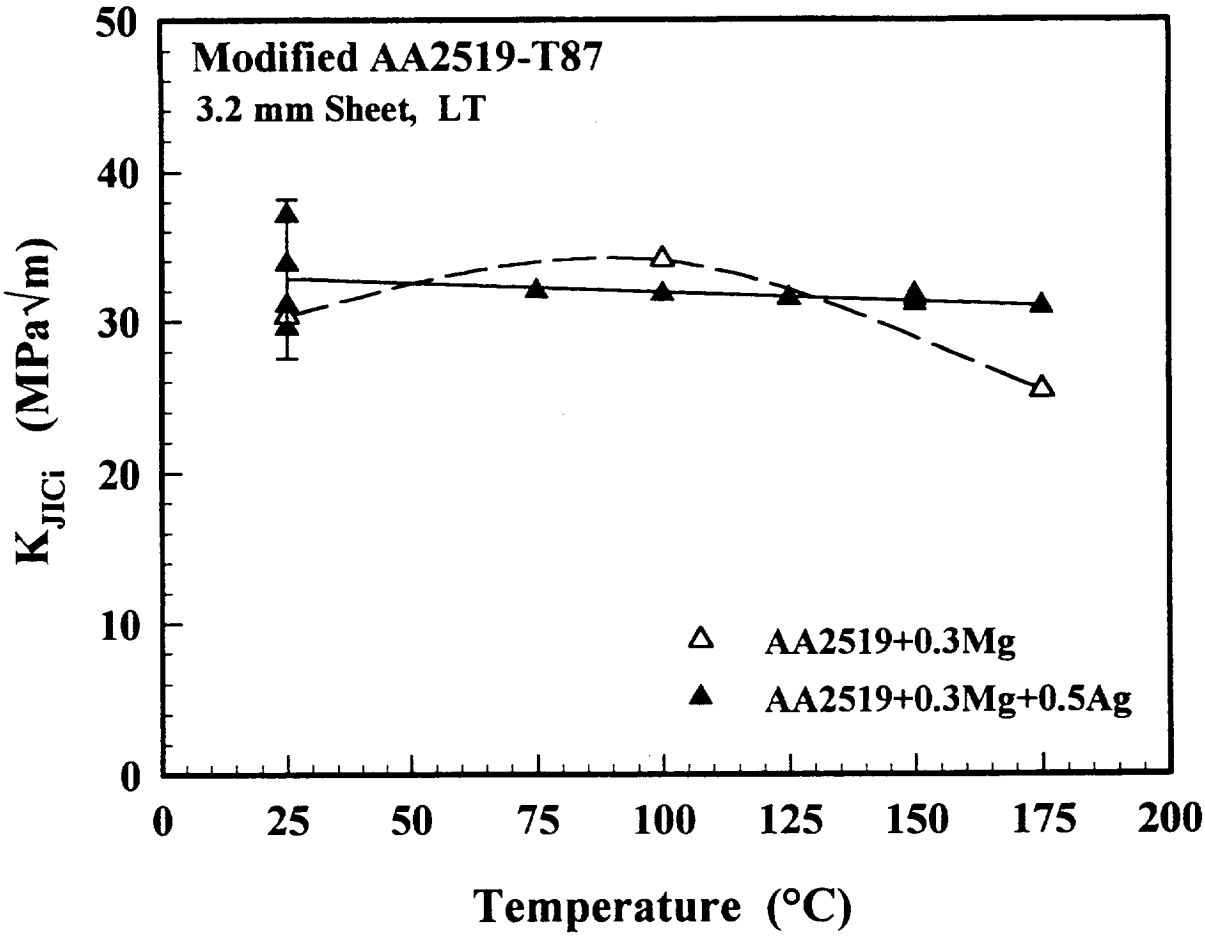

Figure 49: Initiation fracture toughness, K_{JICi}, as a function of temperature for AA2519+Mg+Ag and AA2519+Mg; load-line displacement rate = 0.26 μm/sec.

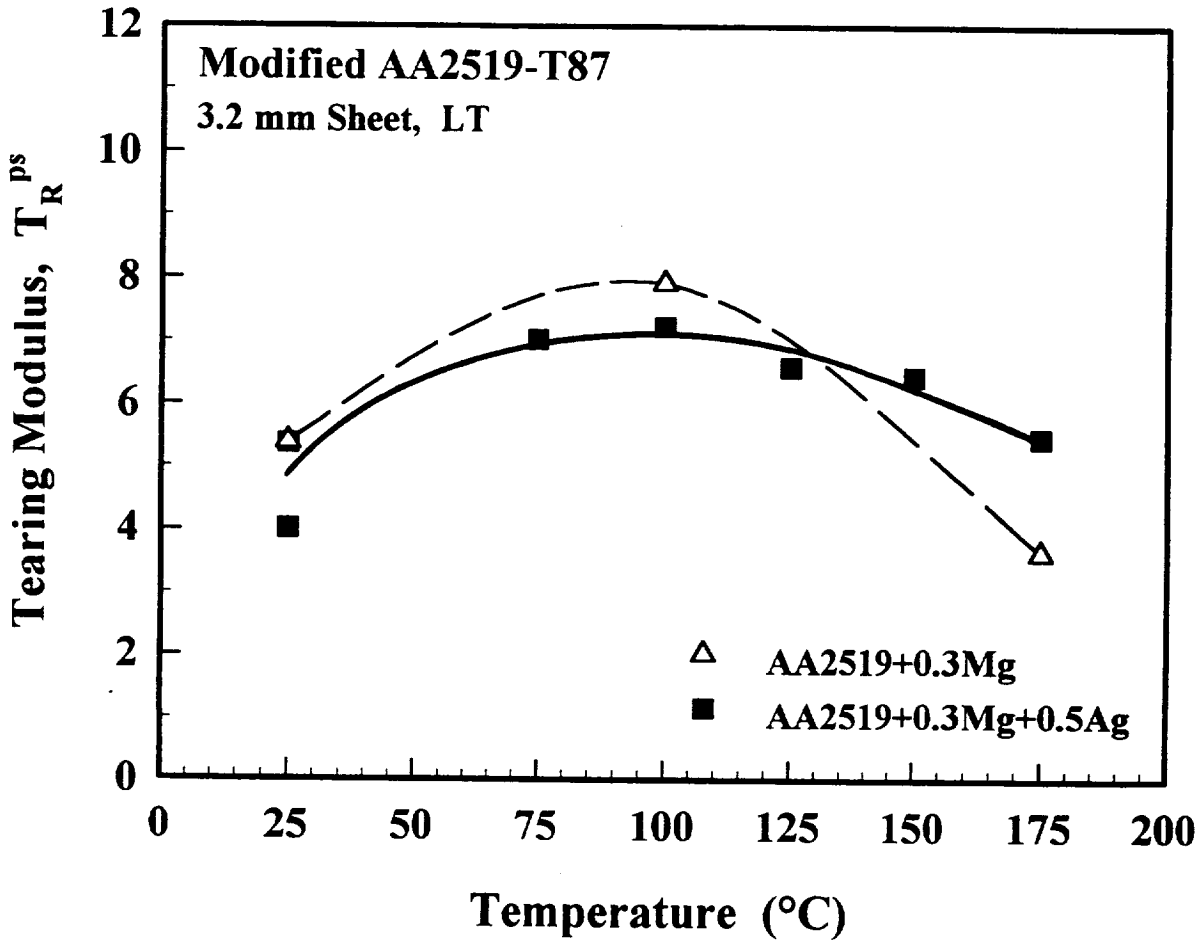

Figure 50: Plane stress tearing modulus, T_R^{ps}, as a function of temperature for AA2519+Mg+Ag and AA2519+Mg; load-line displacement rate = 0.26 μm/sec.

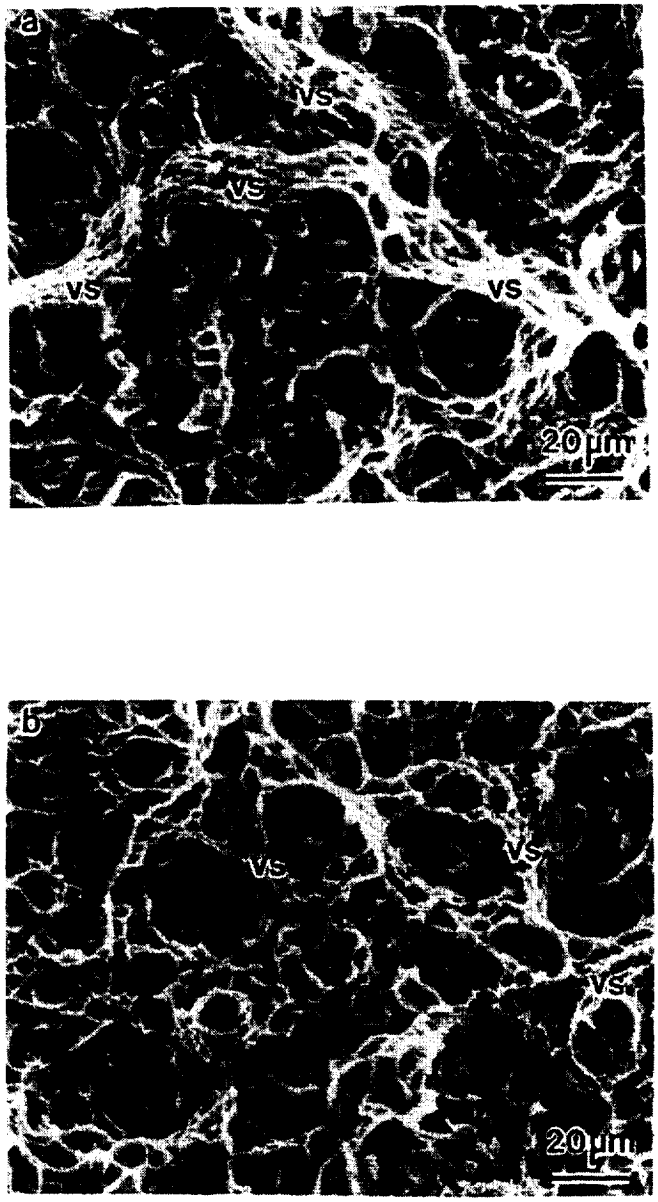

Figure 51: SEM fractography of AA2519+Mg+Ag demonstrating: (a) primary voids nucleated at undissolved θ with void sheeting at 25°C and (b) θ-nucleated voids with reduced void sheeting at 150°C. Micrographs were taken from the midplane of the plane strain fracture surface and just beyond the fatigue precrack. The crack growth direction is from bottom to top and void sheets are marked by "vs".

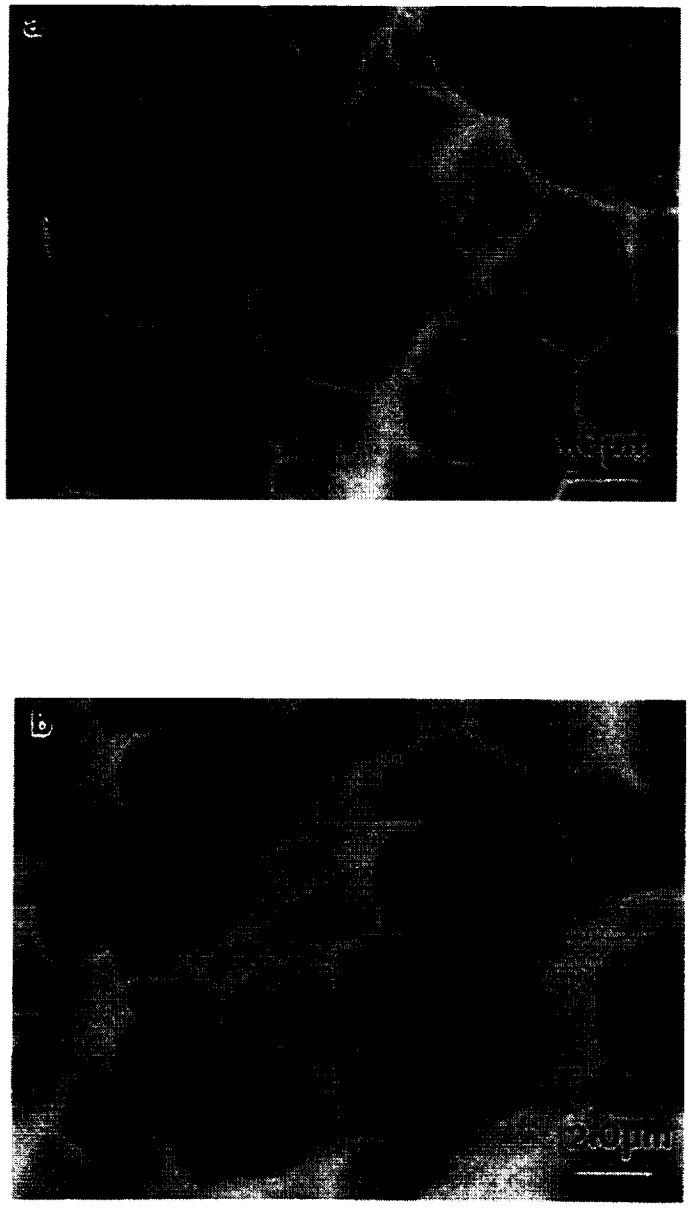

Figure 52: SEM tilt fractography of AA2519+Mg+Ag showing dimple morphology within void sheets produced at: (a) 25°C and (b) 150°C. The fracture surfaces in (a) and (b) were tilted 75°C and 45°C respectively, in the direction of crack growth and about a line parallel to the crack front. The crack growth direction is from right to left and into the plane of the fractograph.

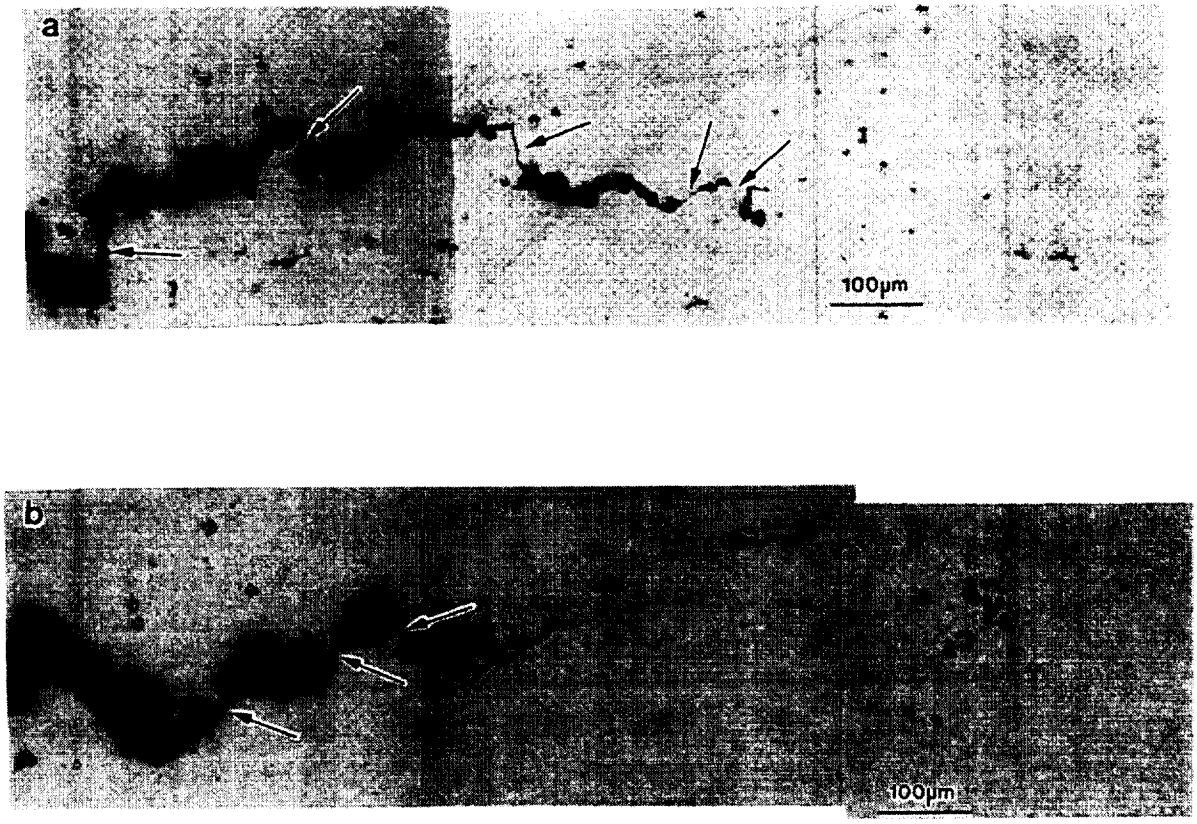

Figure 53: Crack tip profiles from midplane of AA2519+Mg+Ag CT specimens fractured at: (a) 25°C and (b) 150°C; load-line displacement rate = 0.26 μm/sec. The arrows indicate void sheets. The estimated plane strain plastic zone diameter is 2670 μm at 25°C and 3460 μm at 150°C. Microvoid damage is localized within a portion of the plastic zone adjacent to the crack tip.

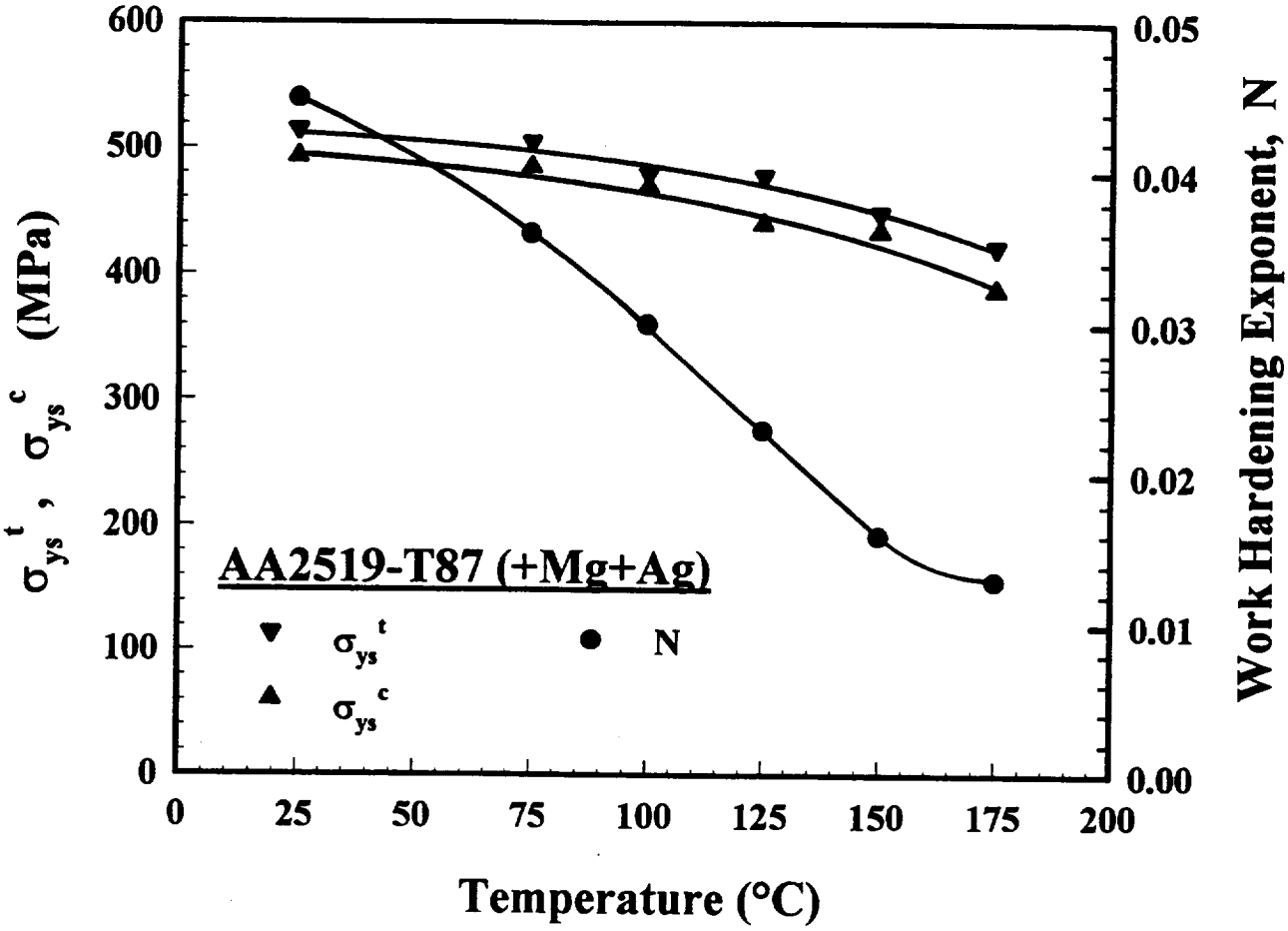

Figure 54: Tensile yield strength, compressive yield strength, and work hardening exponent of AA2519+Mg+Ag as a function of temperature; $\dot{\varepsilon} \approx 6x10^{-5}$ sec^{-1}.

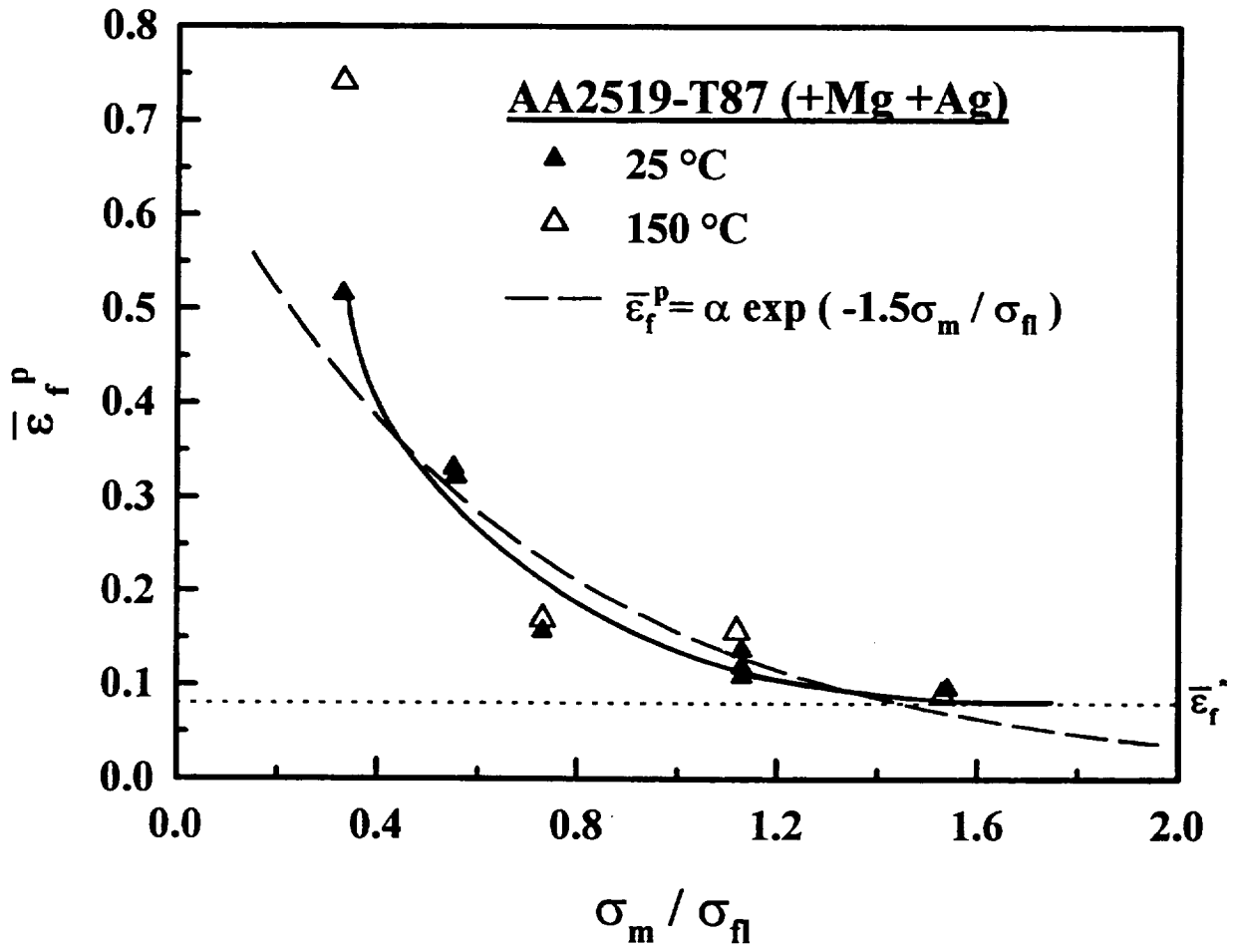

Figure 55: Failure loci for AA2519+Mg+Ag at 25°C and 150°C. A theoretical prediction from integration of Rice and Tracey's void growth law is indicated by the large-dashed line [103,125].

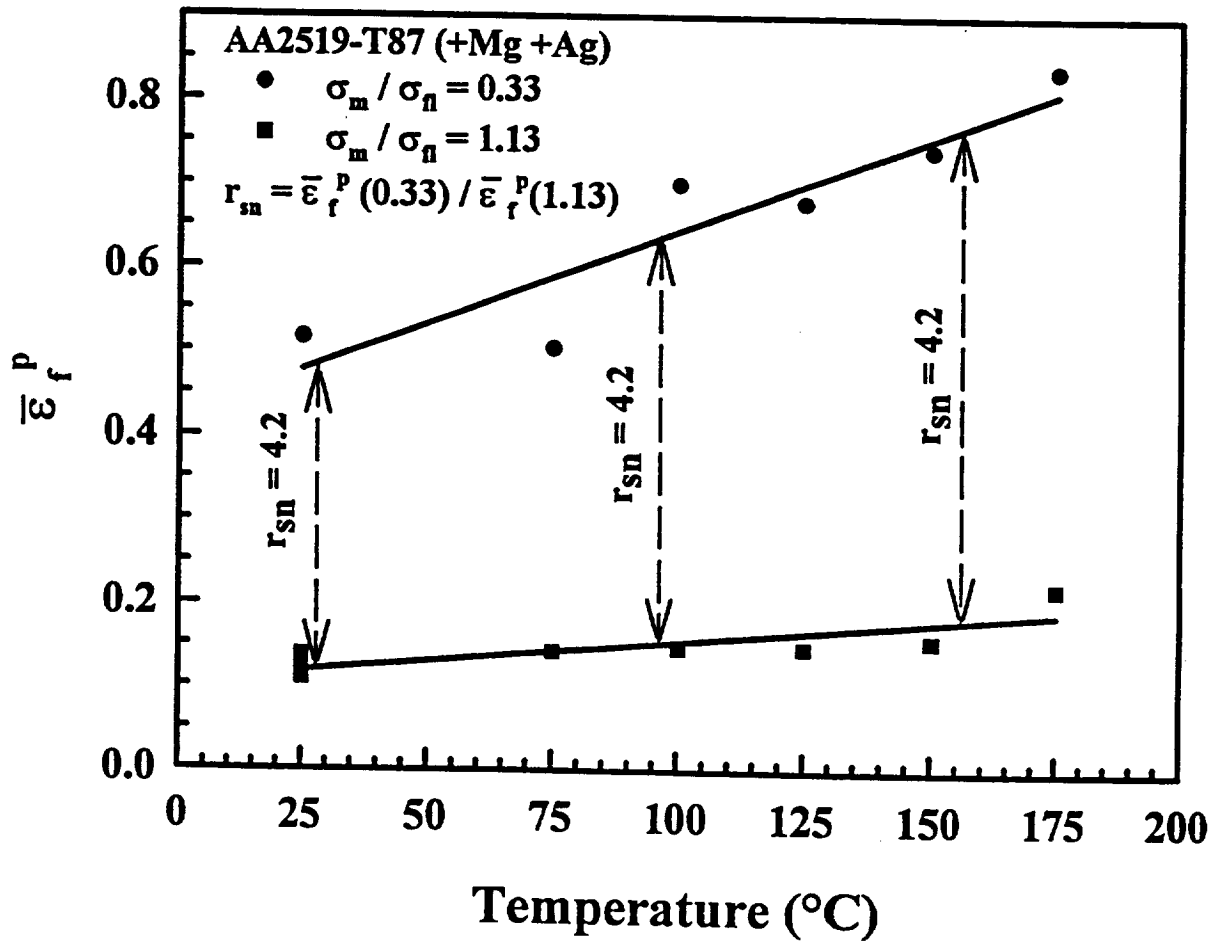

Figure 56: Effective plastic strain to fracture of smooth and notched bars of AA2519+Mg+Ag as a function of temperature, demonstrating the temperature independence of the constraint ratio, r_{sn}.

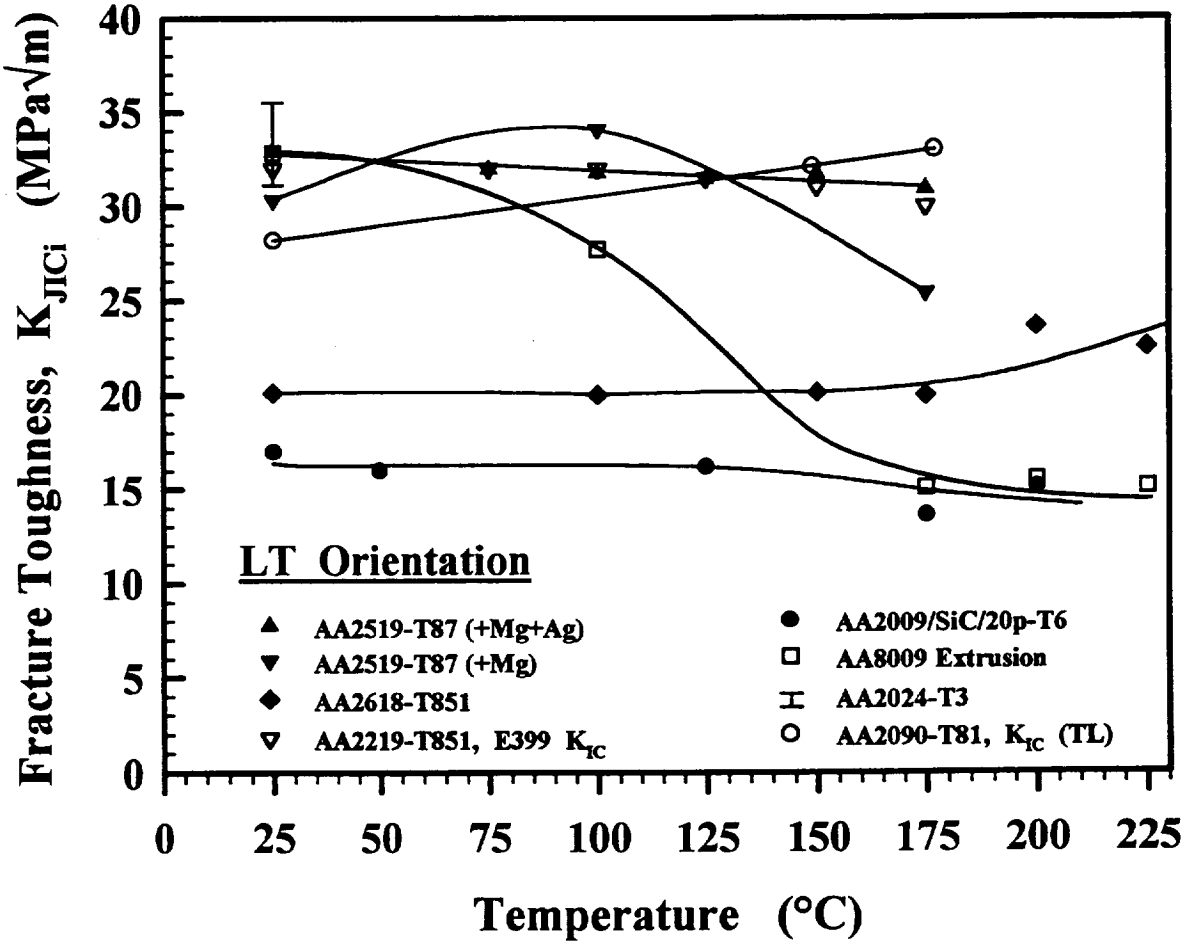

Figure 57: Initiation fracture toughness as a function of temperature for AA2519+Mg+Ag, AA2519+Mg, AA2618-T851 [39], AA2219-T851 [112], AA2090-T81 [141], AA2009/SiC/20p-T6 [62], and AA8009 [24]. The range of K_{JICi} for AA2024-T3 at 25°C is indicated by the error bar [131].

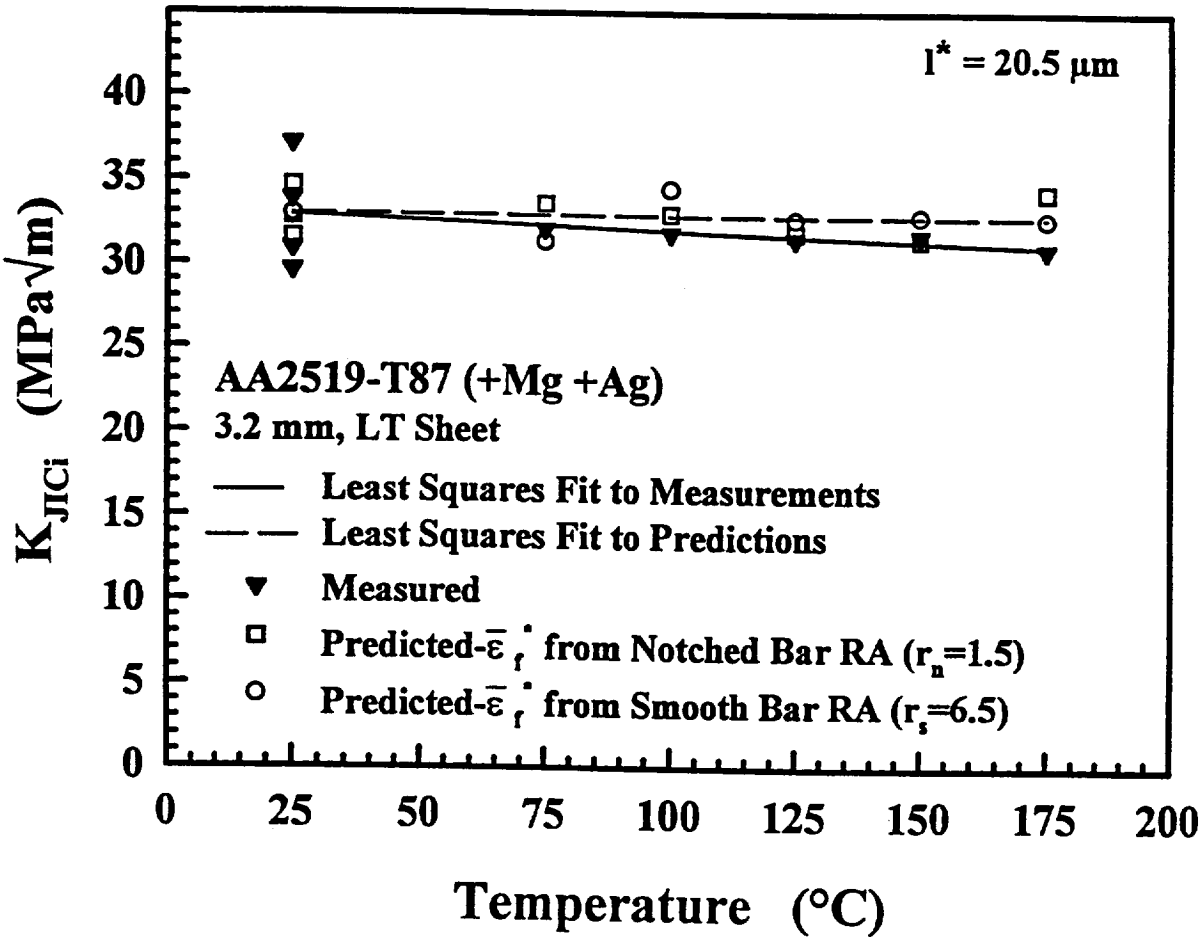

Figure 58: Critical plastic strain-controlled model predictions and experimentally measured values of the initiation fracture toughness as a function of temperature for AA2519+Mg+Ag.

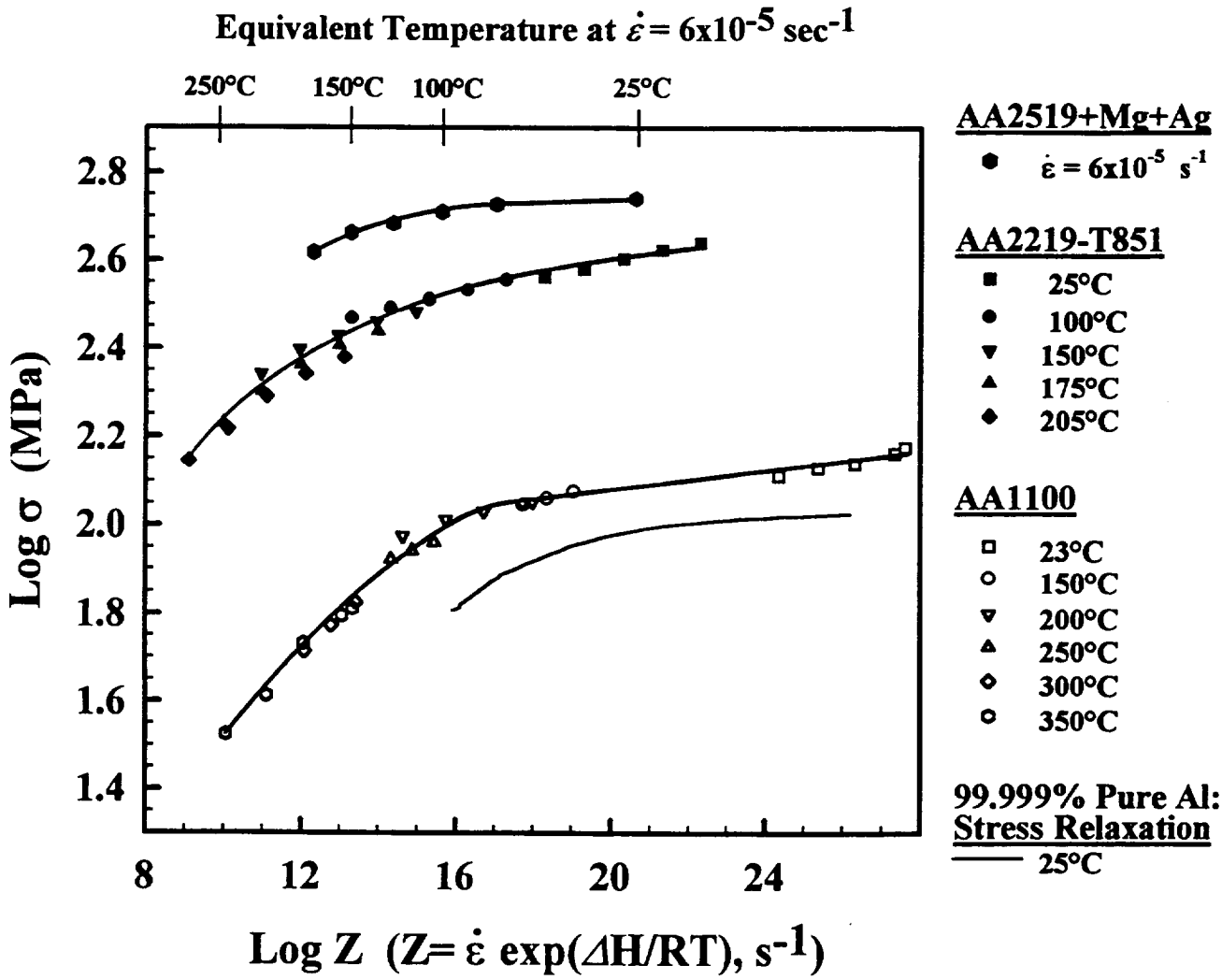

Figure 59: Temperature/strain rate dependence of flow stress for AA2519-T87, AA2219-T851 [156], AA1100 [157], and 99.999% pure aluminum [158].

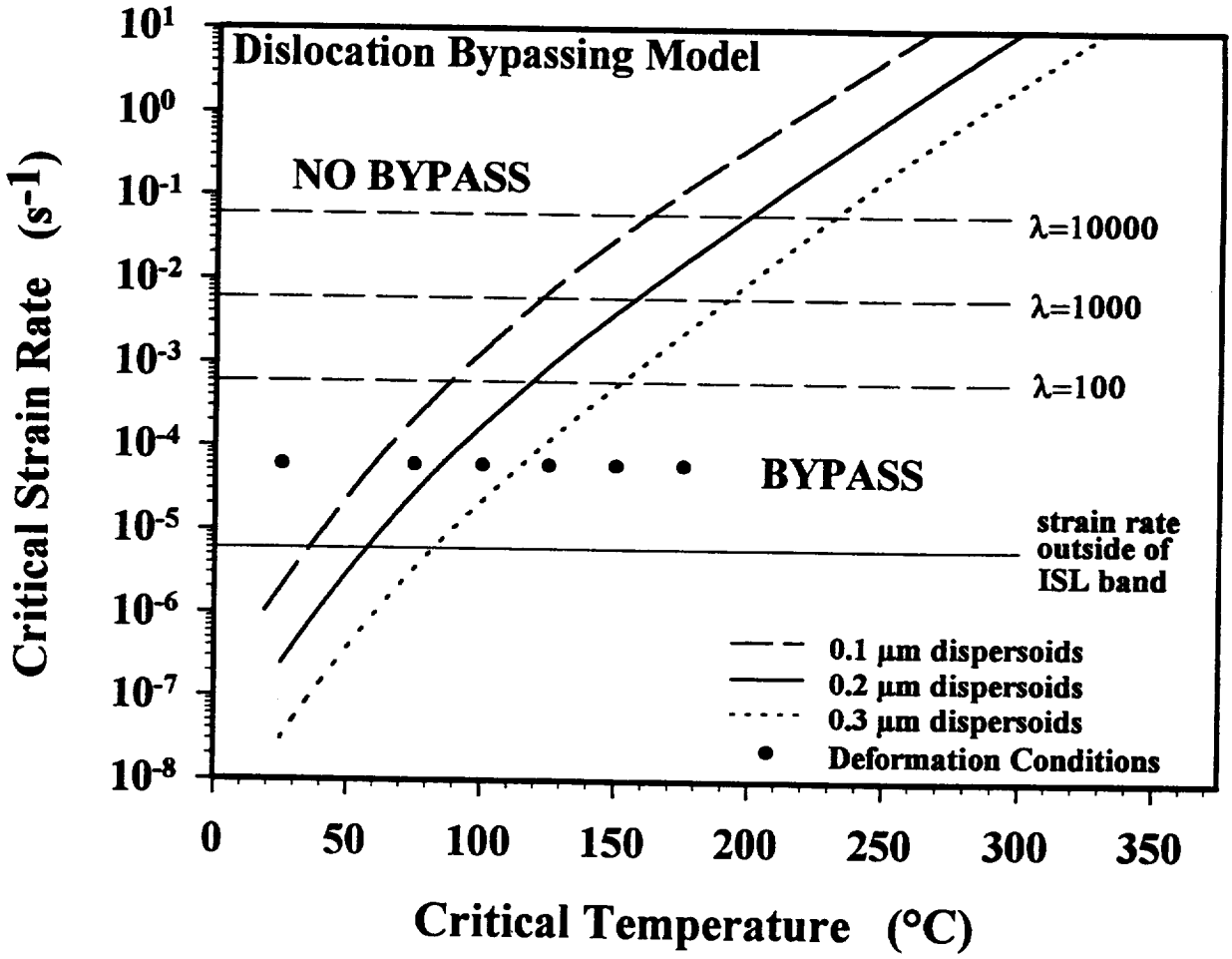

Figure 60: Model for dislocation bypassing of submicron dispersoids (after Humphreys and Kalu) [68]. The region below each curve represents deformation conditions where dislocations climb around dispersoids, and the region above the curve represents dislocation accumulation at dispersoids. The solid dots represent deformation conditions for AA2519+Mg+Ag. The dashed horizontal lines represent strain rates within an ISL band for λ of 10^2, 10^3, and 10^4.

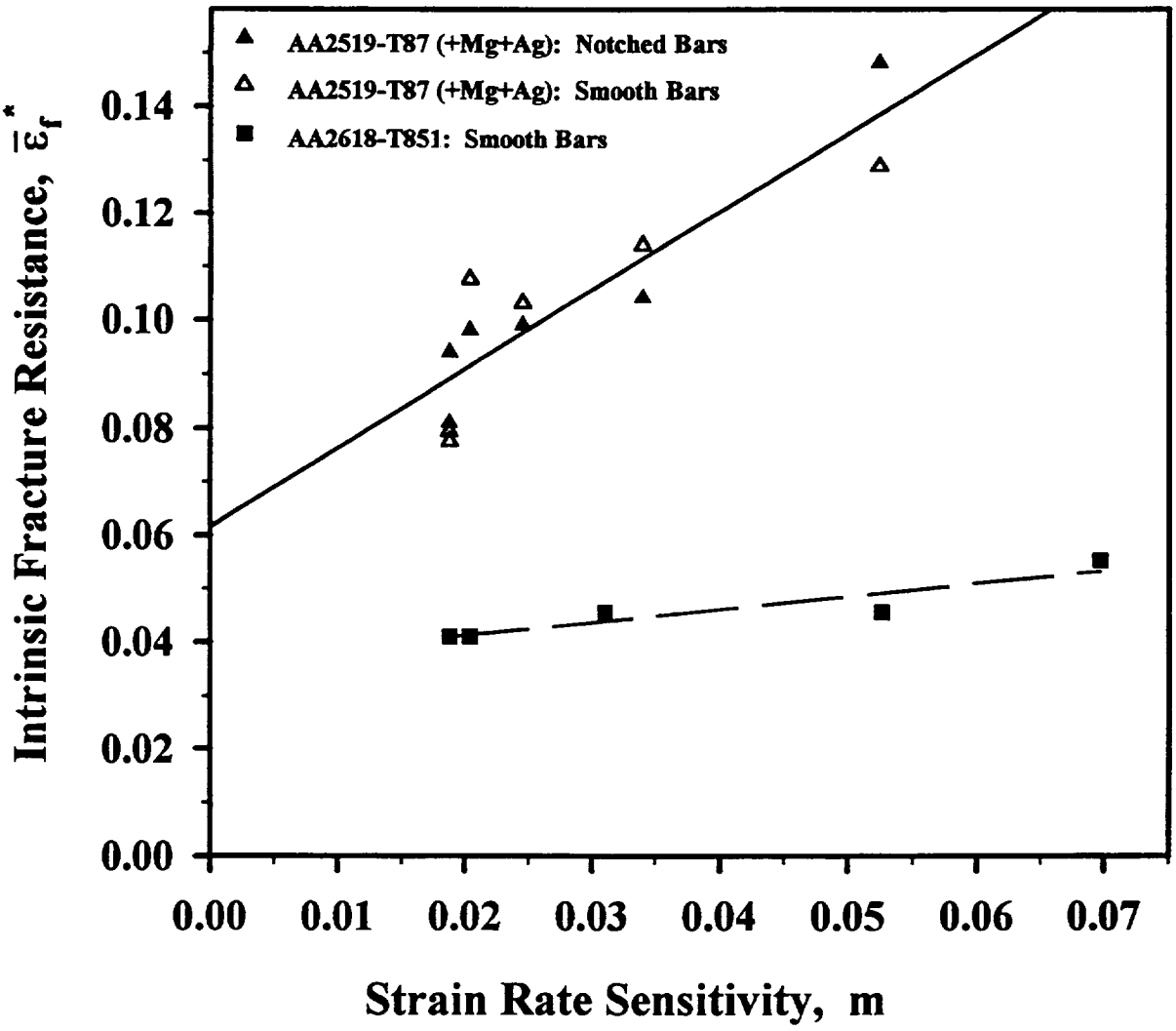

Figure 61: Correlations between strain rate sensitivity, m, and $\bar{\epsilon}_f^*$ for AA2519+Mg+Ag and AA2618-T851 [39].

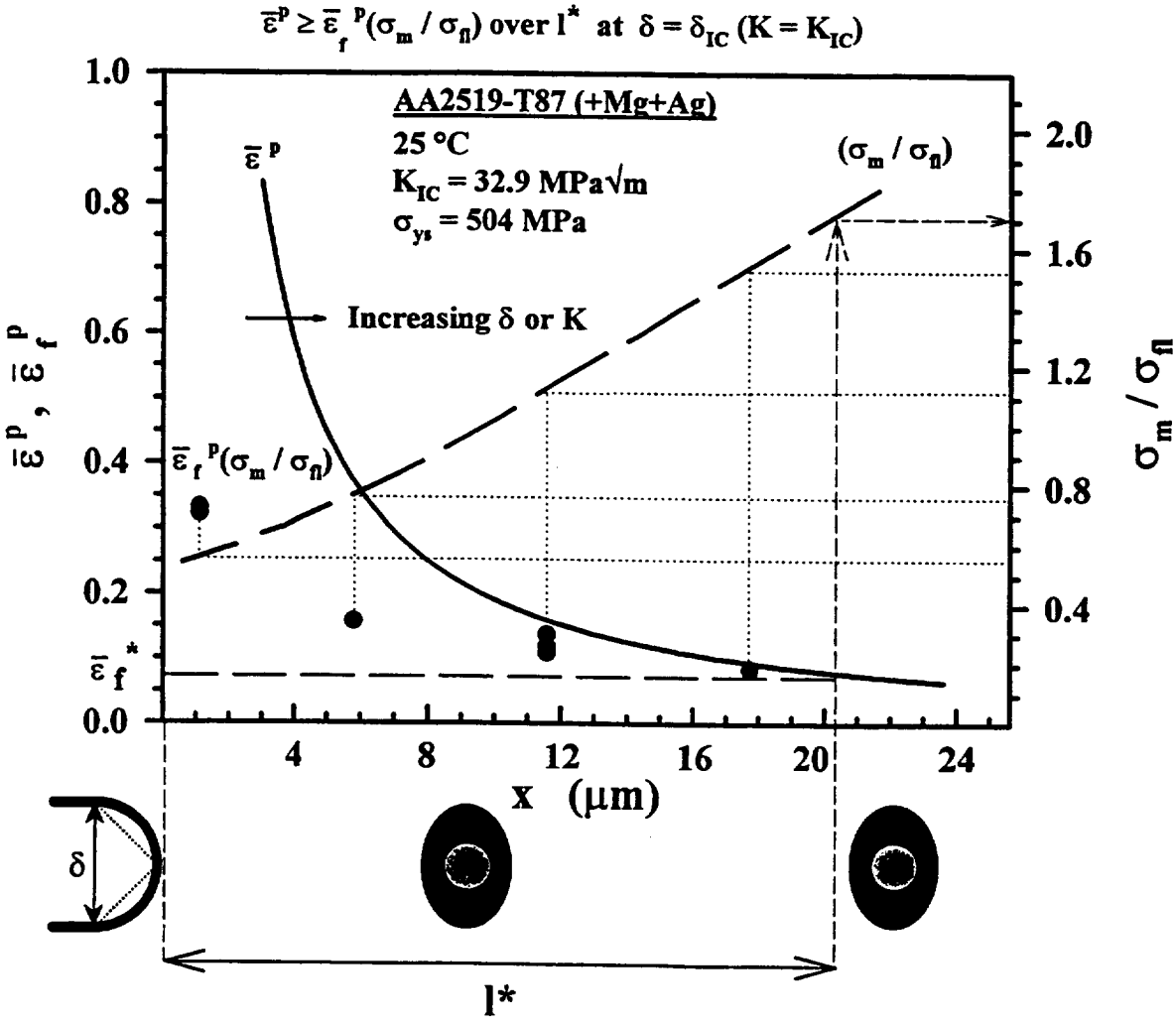

Figure 62: Illustration of the Critical Plastic Strain-Controlled Model. The crack tip effective plastic strain field ($\bar{\varepsilon}^p$) [143] and stress-state-triaxiality field (σ_m/σ_{fl}) [163] are plotted with heavy solid and heavy dashed lines, respectively. The filled circles represent an experimental determination of a failure strain locus ($\bar{\varepsilon}_f^{\,p}(\sigma_m/\sigma_{fl})$). For fracture initiation, $\bar{\varepsilon}^p$ must exceed $\bar{\varepsilon}_f^{\,p}(\sigma_m/\sigma_{fl})$ over a critical distance (l^*).

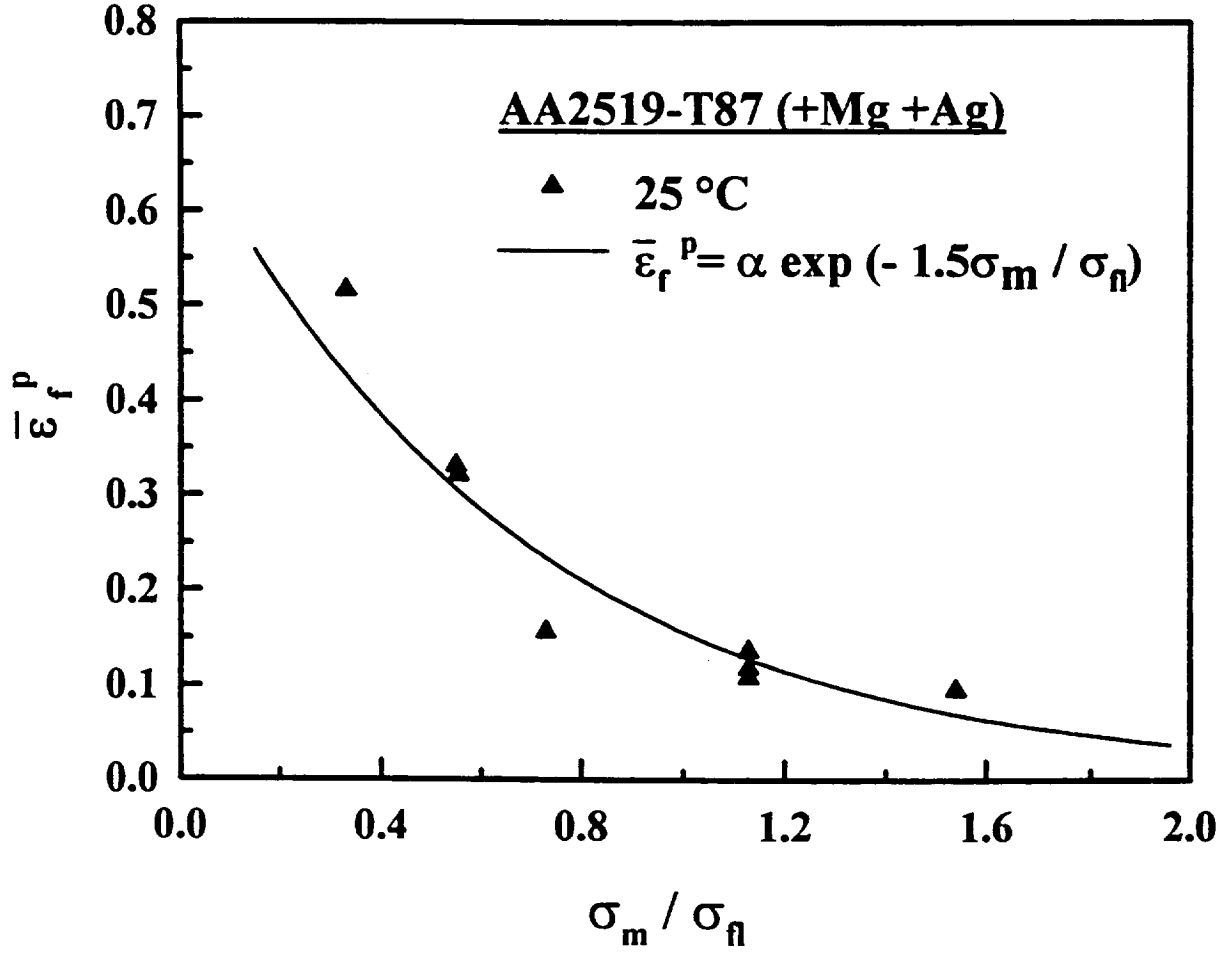

Figure 63: Stress-state dependent failure strain for AA2519-T87(+Mg+Ag) at 25°C [19]. A theoretical prediction from integration of Rice and Tracey's void growth law is indicated by the solid line [103,125].

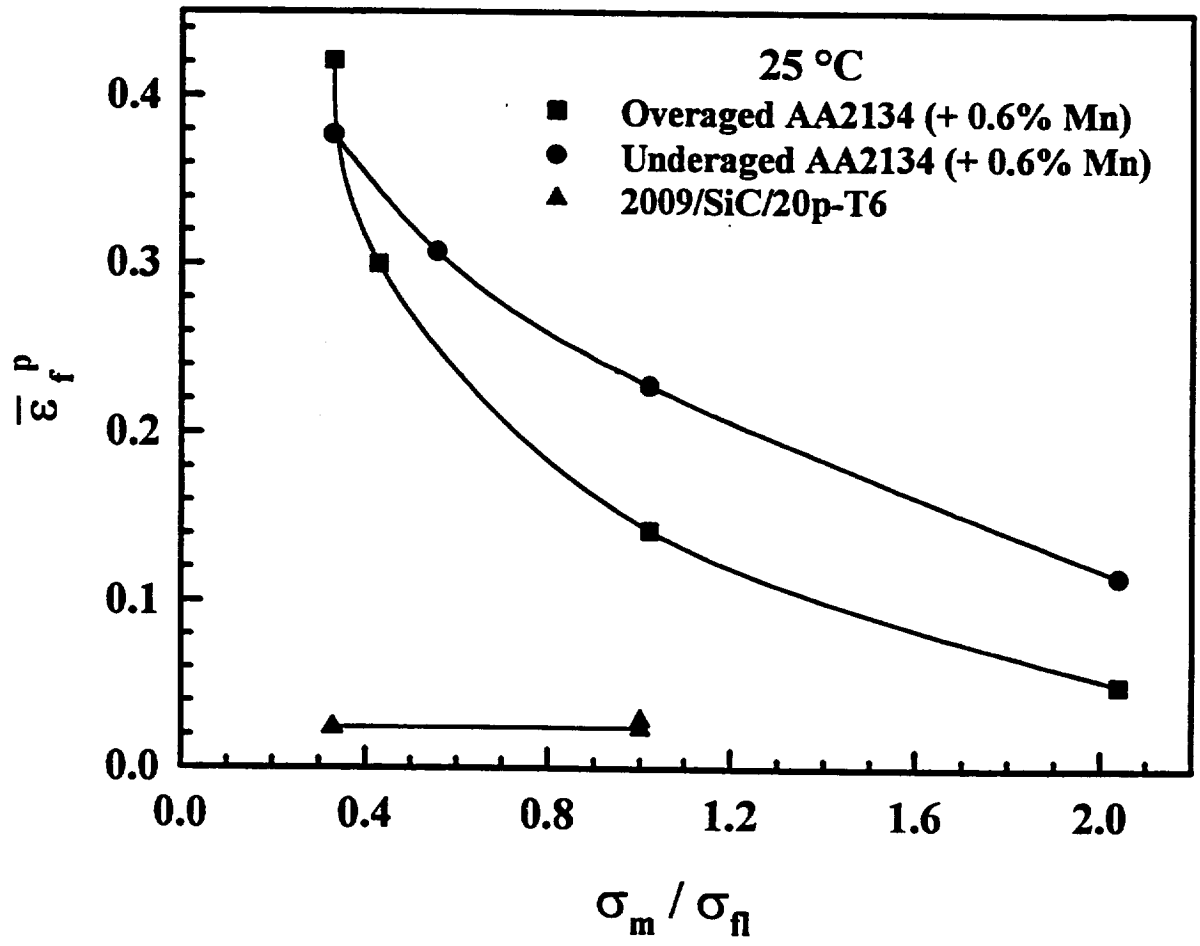

Figure 64: Ambient temperature, stress-state dependent failure loci for AA2009/SiC/20p-T6 [63] and AA2134 in the underaged and overaged tempers [119].

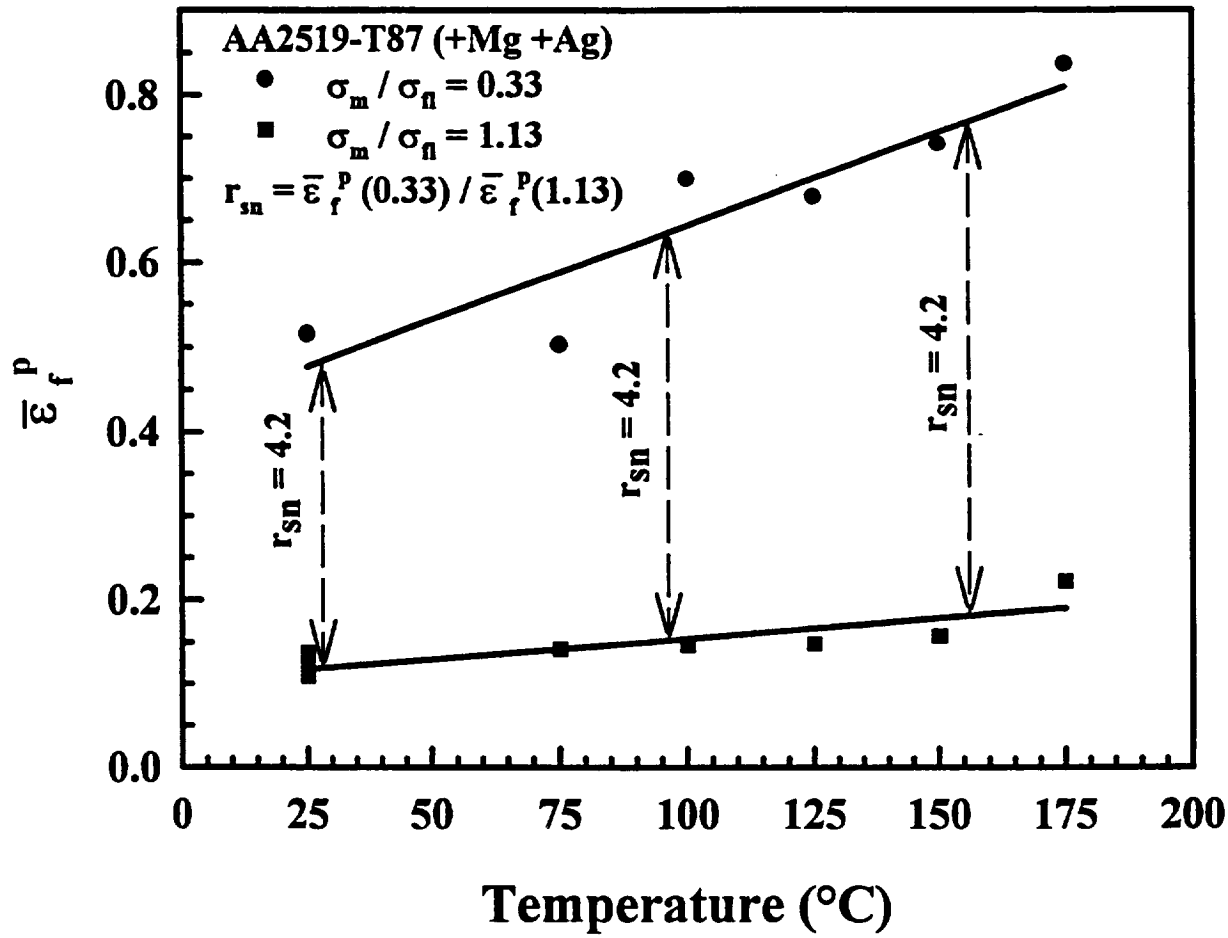

Figure 65: Effective plastic strain to failure of smooth and notched bars of AA2519+Mg+Ag, demonstrating the temperature independence of the constraint ratio, r_{sn} [19].

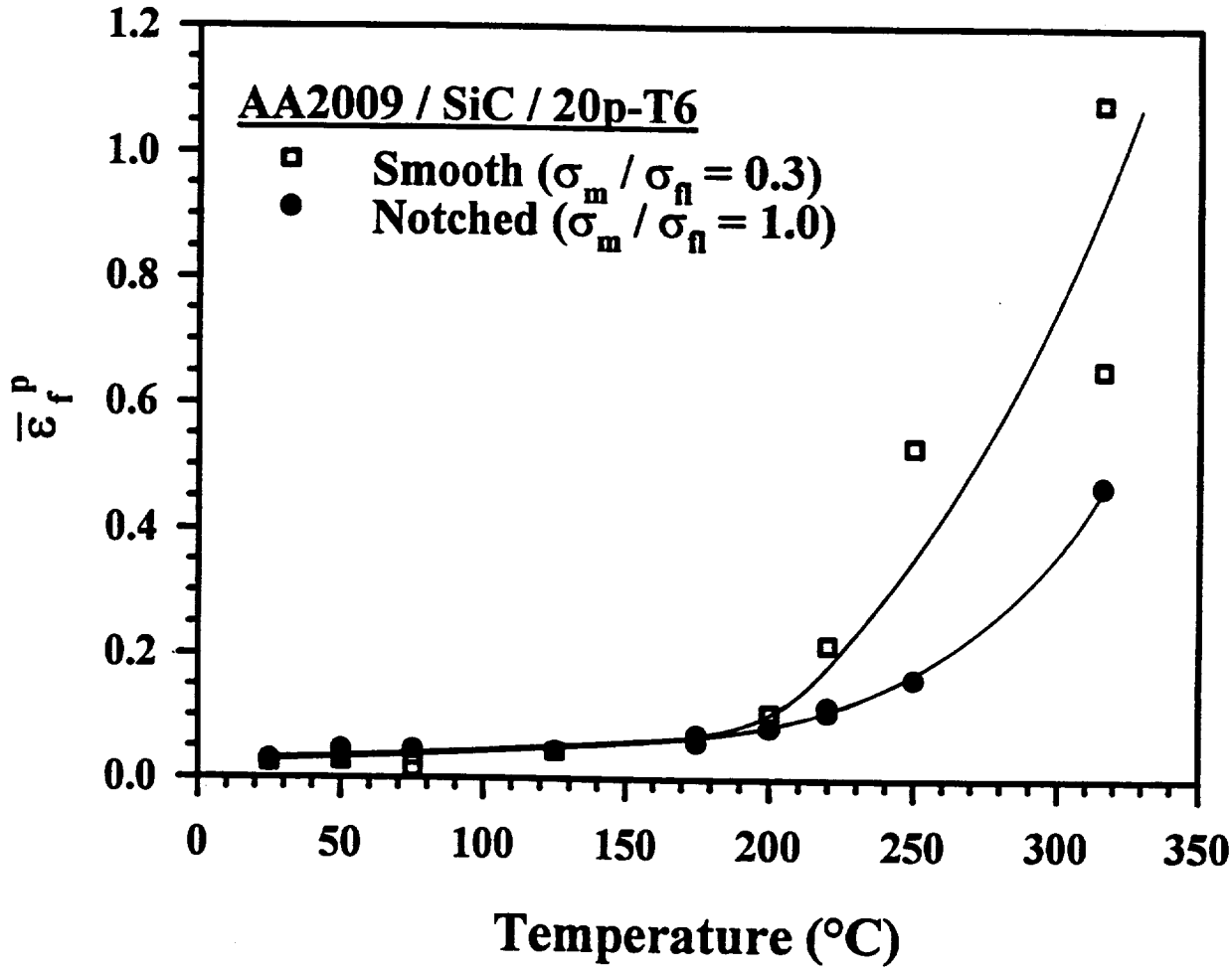

Figure 66: Effective plastic strain to failure of smooth and notched bars of AA2009/SiC/20p-T6 plotted as a function of temperature, demonstrating the insensitivity of $\bar{\varepsilon}_f^p$ to global stress-state-triaxiality at temperatures up to 175°C [63].

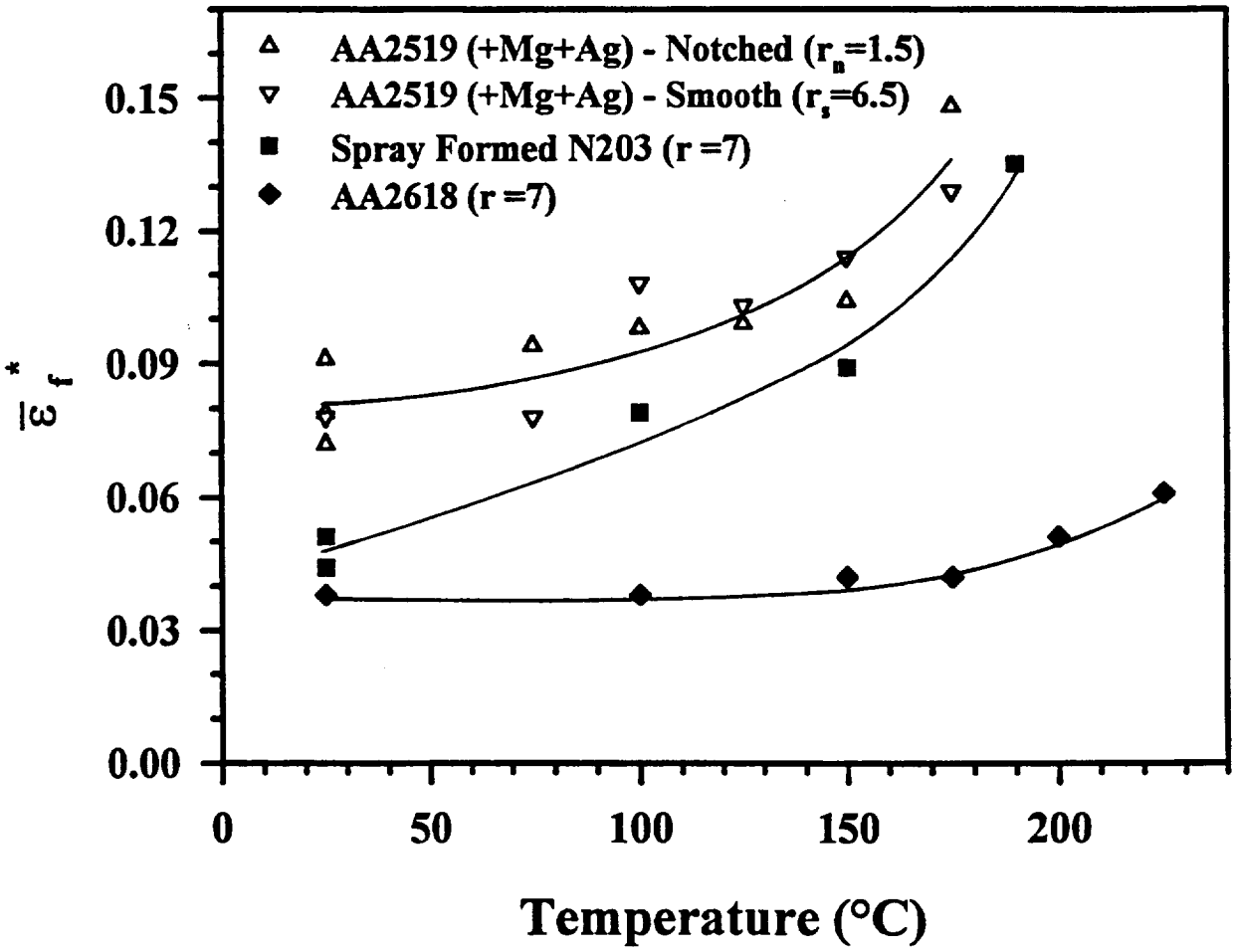

Figure 67: The critical fracture strain for spray formed N203-T6, AA2618-T851 [24], and AA2519-T87(+Mg+Ag) [19] as a function of temperature.

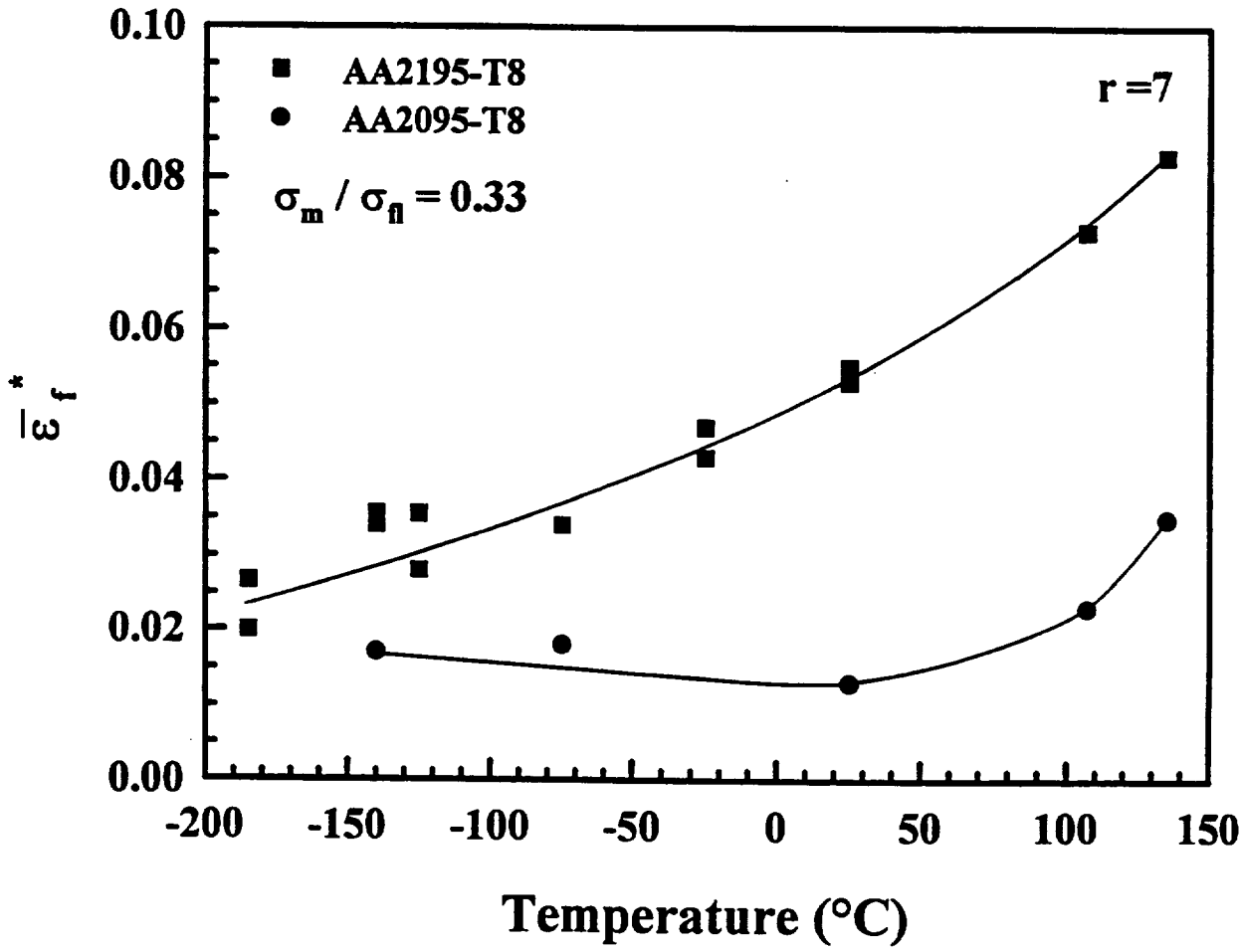

Figure 68: The critical fracture strain for AA2095-T8 and AA2195-T8 from cryogenic to slightly elevated temperatures [169].

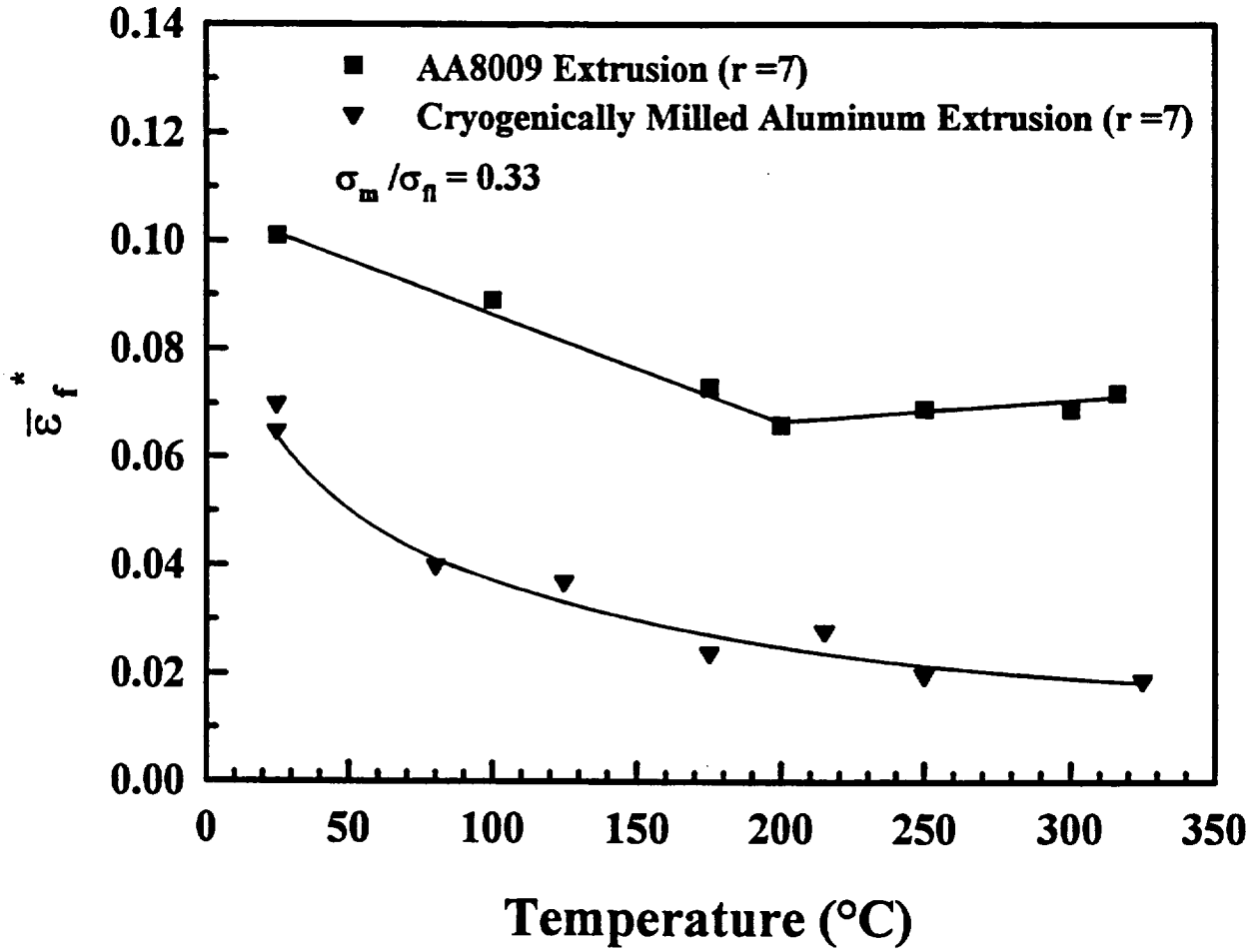

Figure 69: Critical fracture strain vs. temperature for submicron grain-size AA8009 [24] and cryogenically milled aluminum [144].

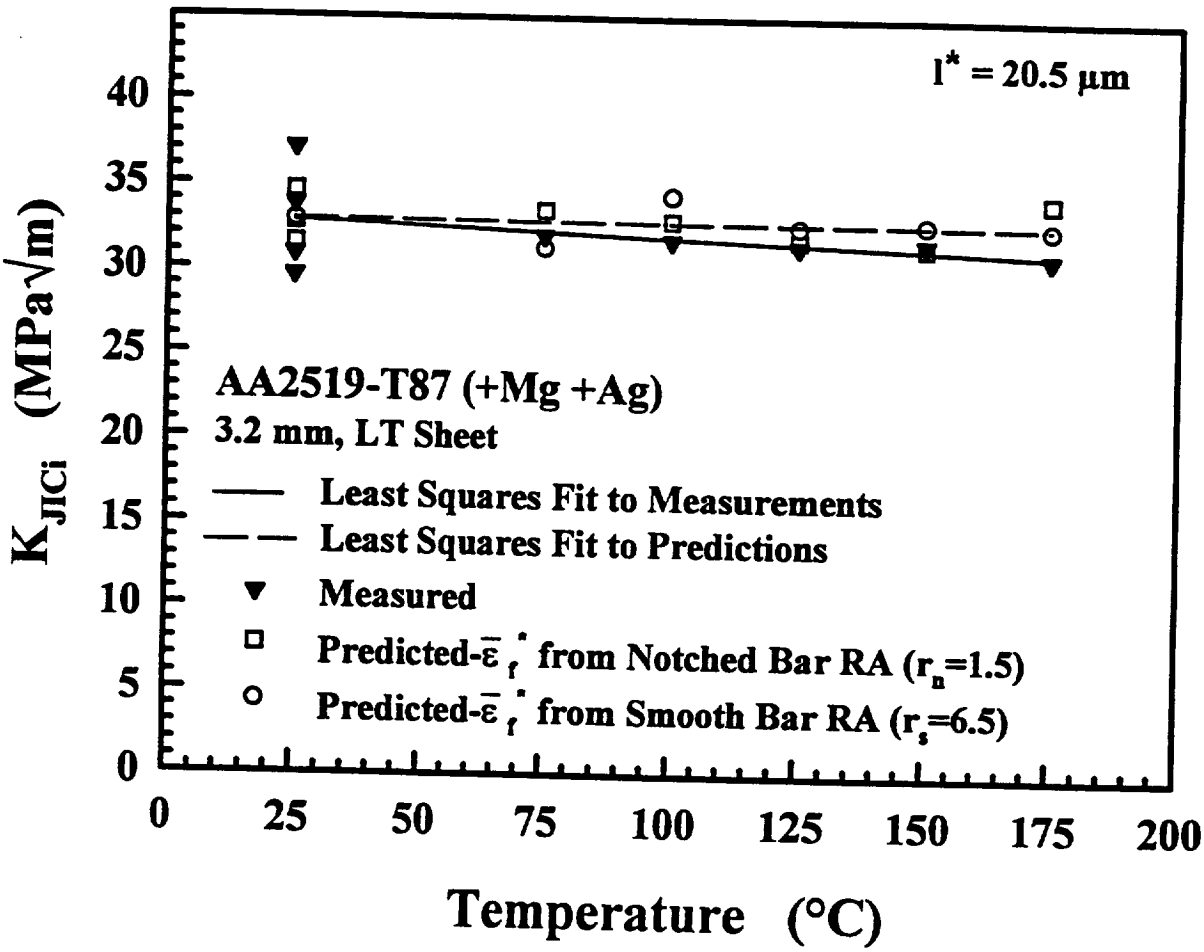

Figure 70: Critical plastic strain-controlled model predictions and experimentally measured values of the initiation toughness (K_{JICi}) as a function of temperature for AA2519-T87(+Mg+Ag) [19].

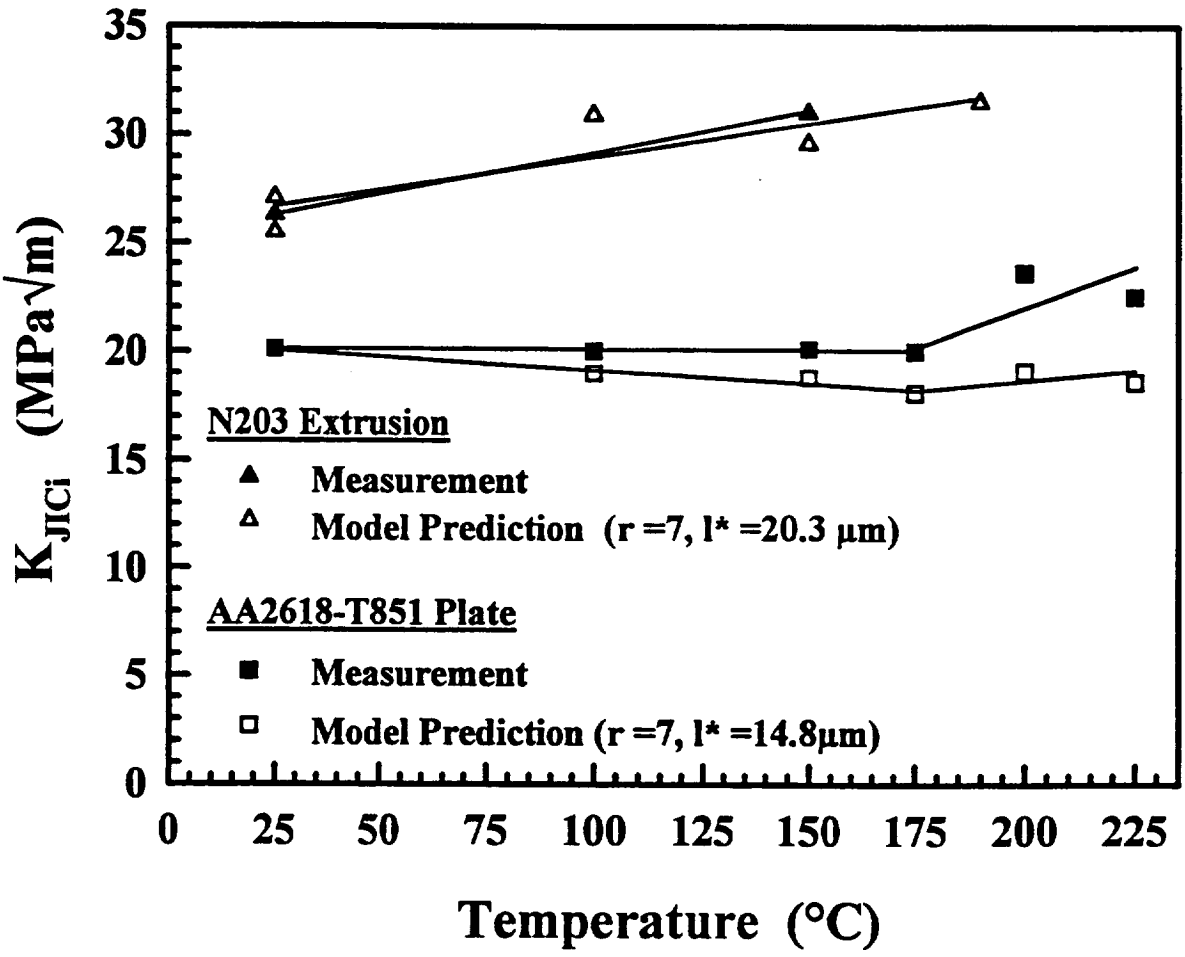

Figure 71: Critical plastic strain-controlled model predictions and experimentally measured values of K_{JICi} as a function of temperature for AA2618-T851 and spray formed N203-T6.

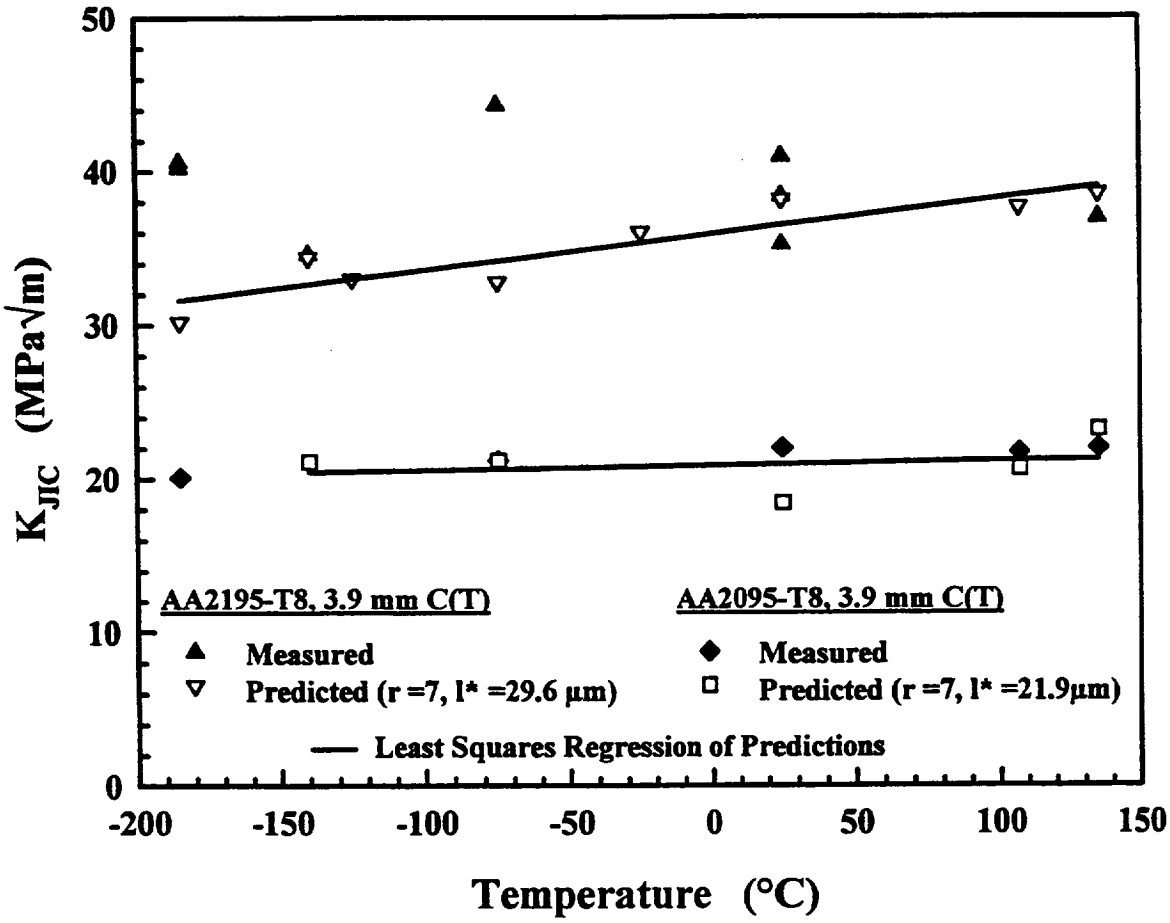

Figure 72: Critical plastic strain-controlled model predictions and experimentally measured values of K_{JIC} as a function of temperature for AA2095-T8 and AA2195-T8.

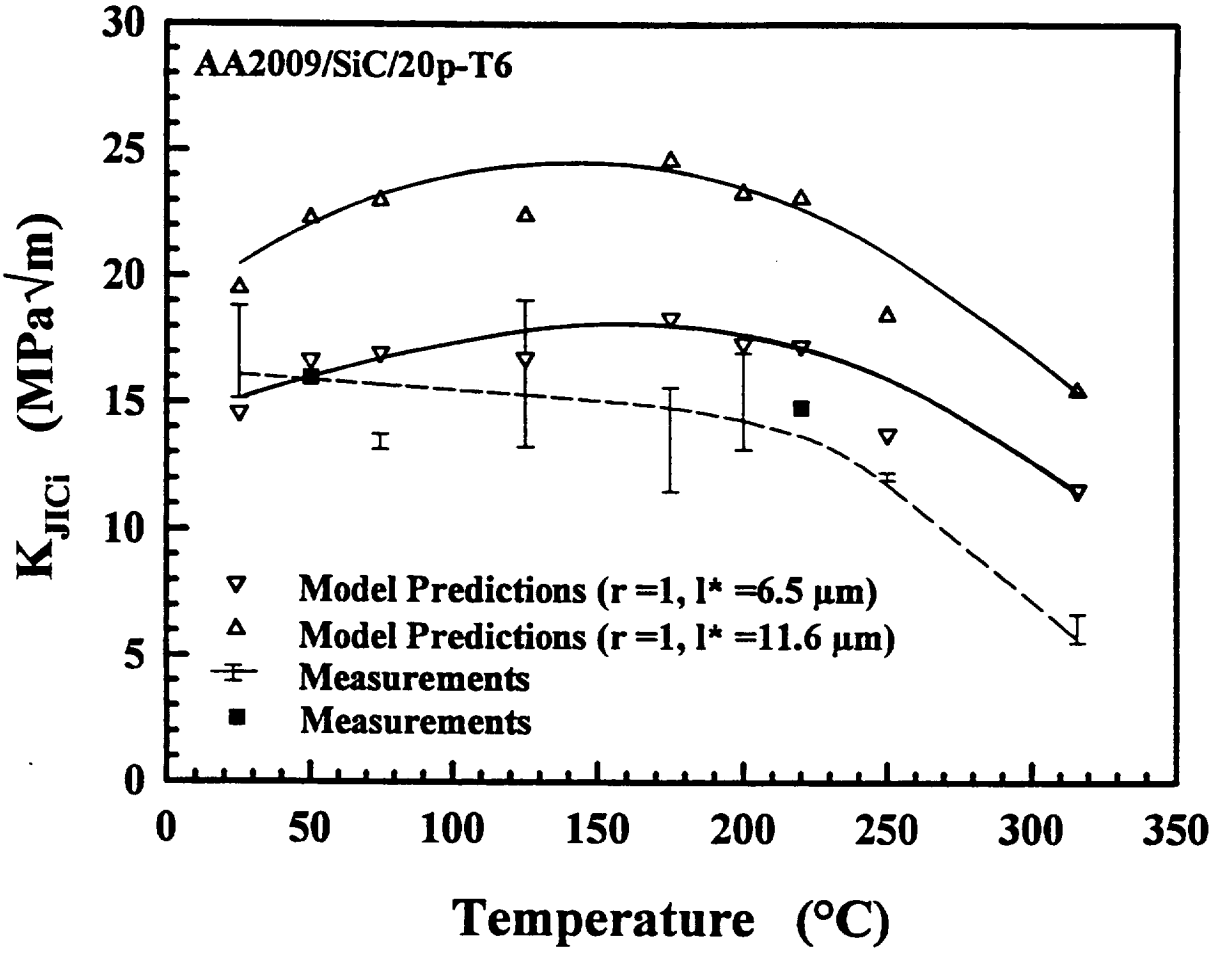

Figure 73: Critical plastic strain-controlled model predictions and experimentally measured values of K_{JICi} as a function of temperature for AA2009/SiC/20p-T6 [61].

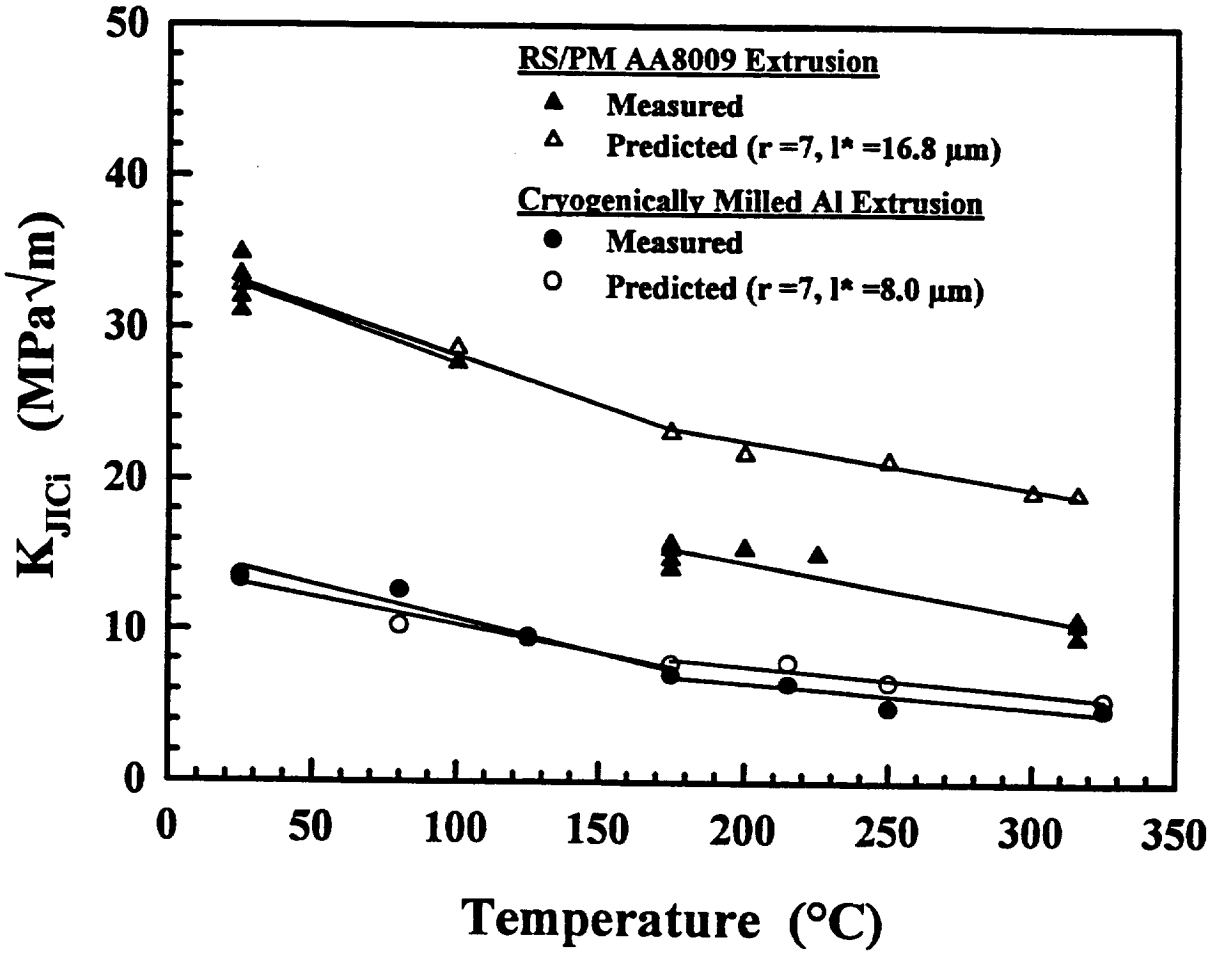

Figure 74: Critical plastic strain-controlled model predictions and experimentally measured values of K_{JICi} as a function of temperature for AA8009 [24] and CM Al [144].

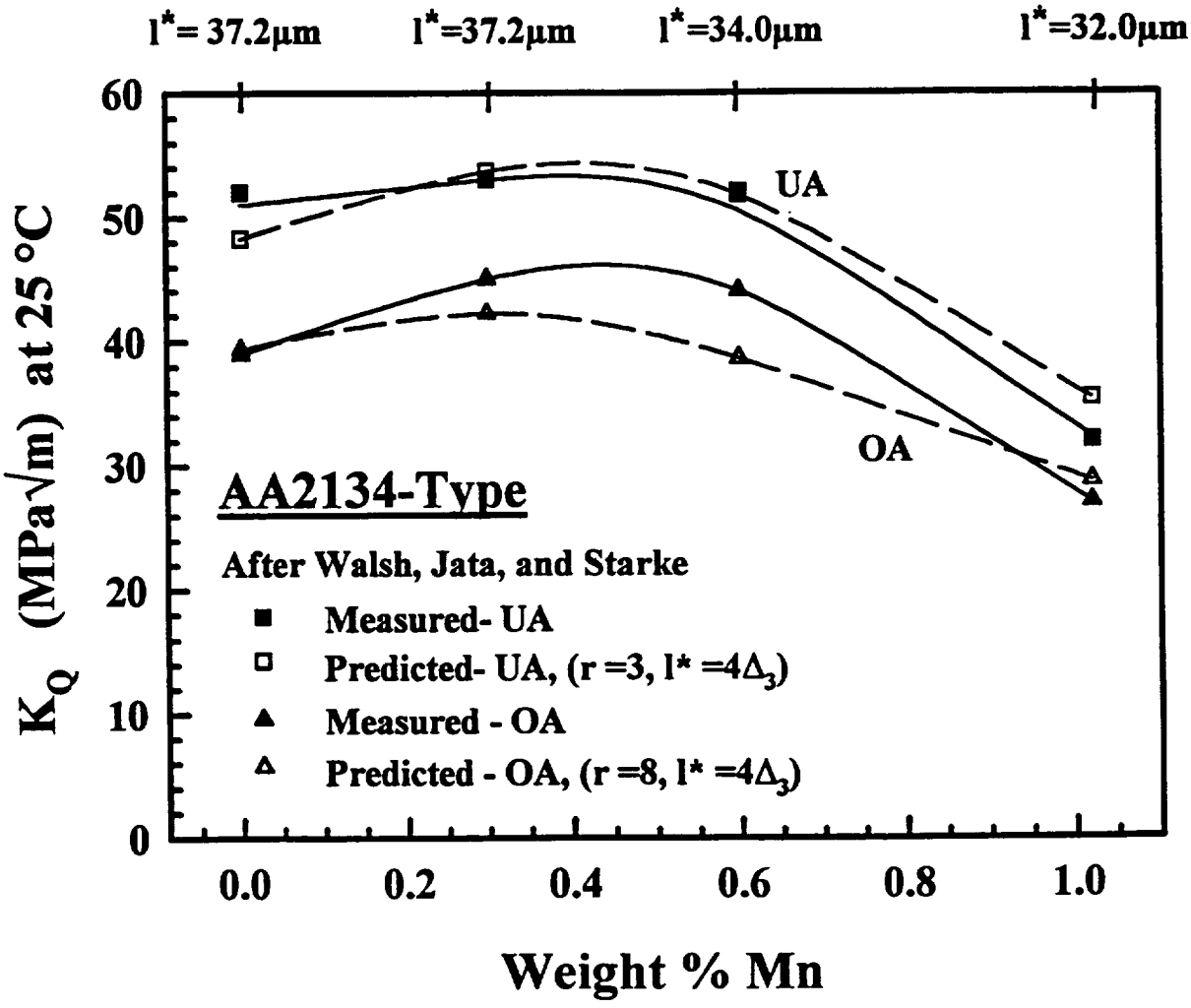

Figure 75: Critical plastic strain-controlled model predictions and experimentally measured values of K_Q as a function of Mn content for underaged and overaged AA2134 [119].

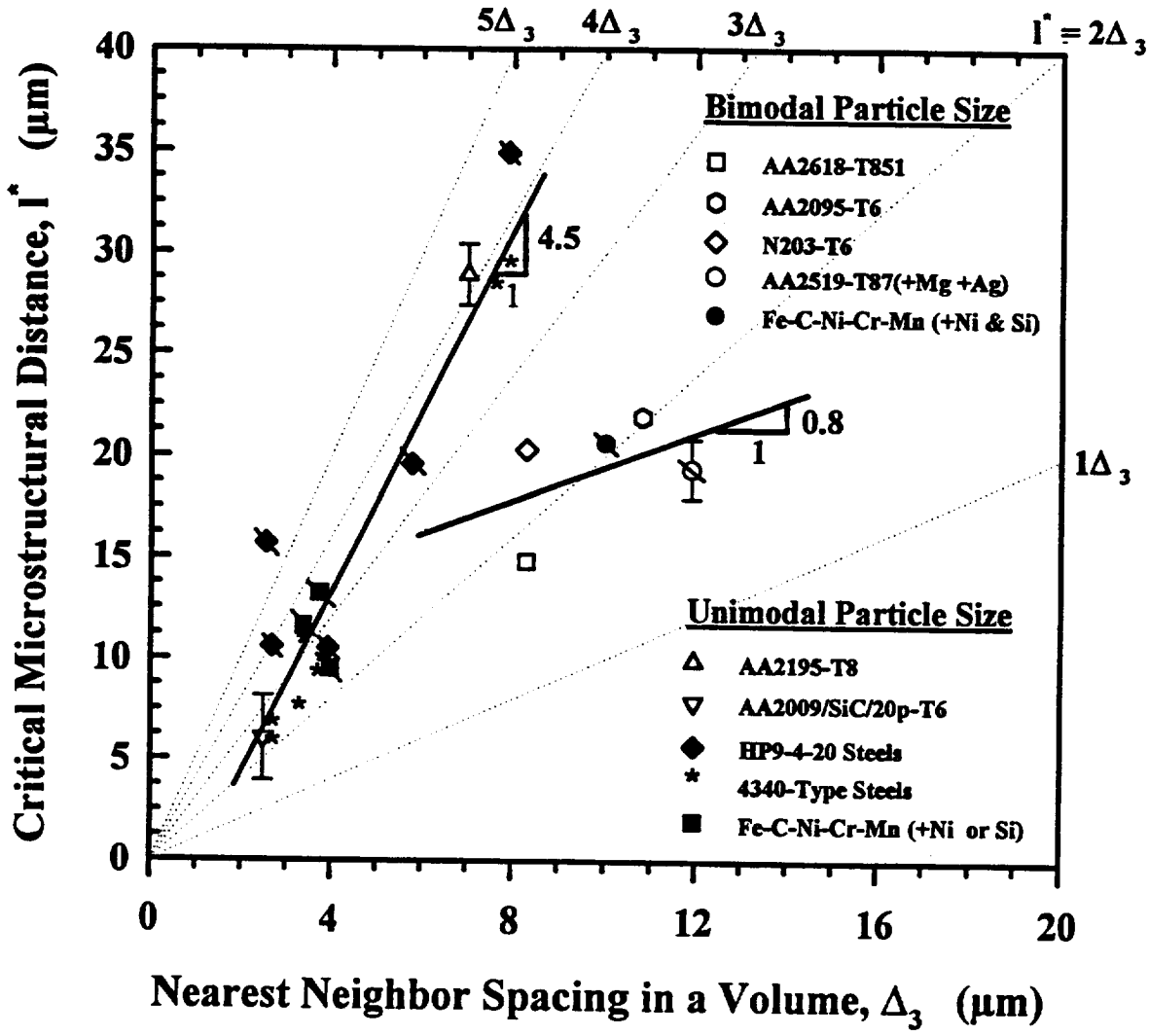

Figure 76: Correlations between nearest neighbor particle spacing in a volume (Δ_3) and the calculated critical distance (l^*) in steels [174-176] and aluminum alloys, for single and bimodal distributions of void-nucleating particles.

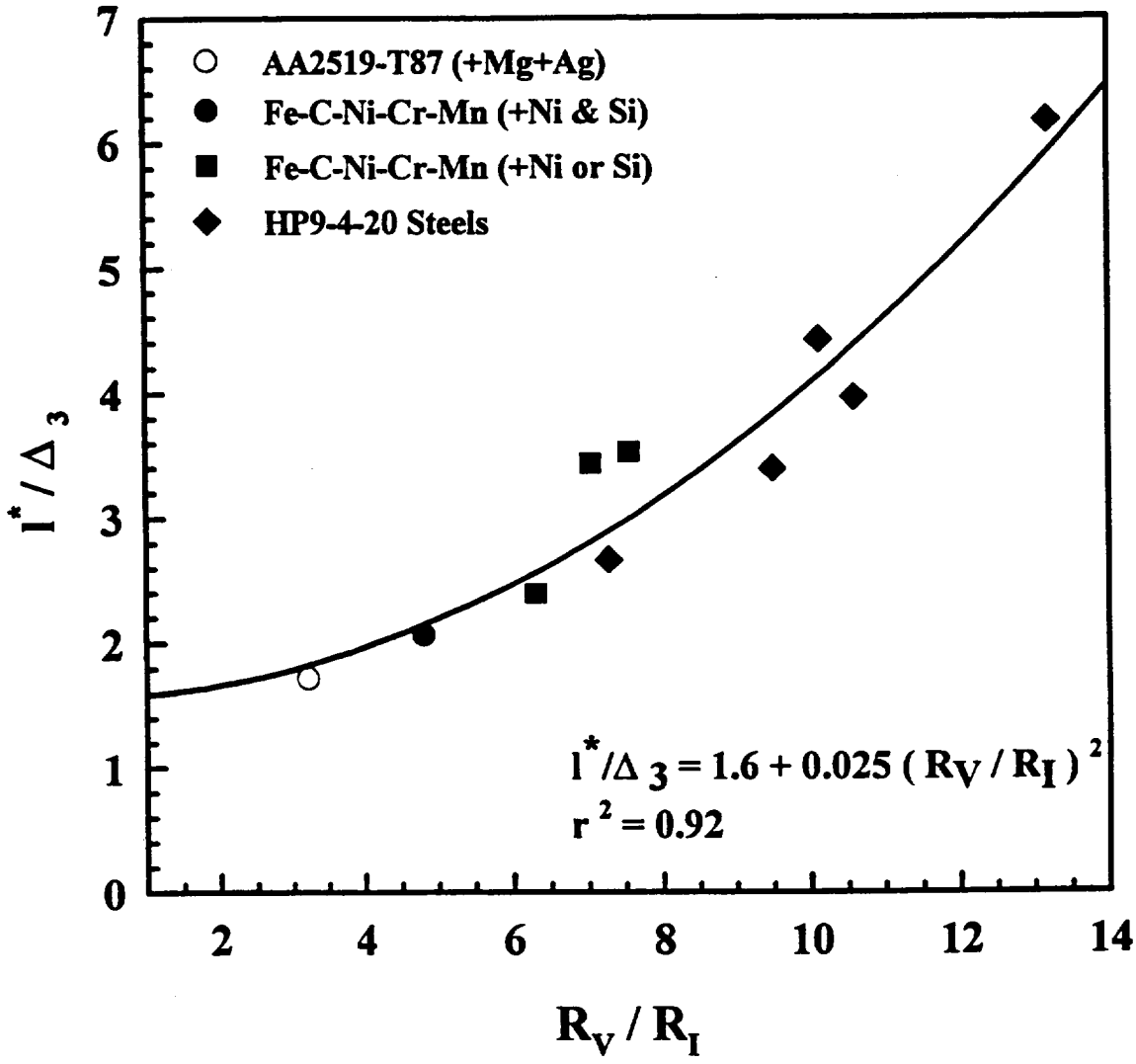

Figure 77: Relationship between the extent of primary void growth, quantified by the ratio of final void radius to initial void-nucleating particle radius, and l^* normalized by particle spacing in a volume. Data are for steels [174,175] (solid symbols) and a single aluminum alloy (open symbol).

UNIVERSITY OF VIRGINIA

A Study of the Microstructure/Property Evolution Characteristics of the Al-Cu-Mg-Li-Ag System with RX818 Alloy

Principal Investigator: Dr. J. M. Howe
Research Associate: Dr. Y. Mou

Abstract

The purpose of this research was to understand and quantify microstructural evolution in RX818 alloy as a function of time, temperature, alloy composition and initial microstructure in order to explain and predict the mechanical behavior of RX818 base alloys after elevated temperature exposure. Significant progress was made in five different areas in this research. First, the effect of alloy composition (Ag and Mg) and high-temperature thermal exposure such as 250°C (482°F) on the microstructure of RX818-T8 alloy were determined by TEM. Secondly, evolution of the T_1 particle size distribution in RX818-T8 alloy was quantified for exposures of up to 7016 hrs at temperatures of 106-163°C (225-325°F) by TEM for comparison with the mechanical property behavior. Thirdly, the behavior of grain boundary precipitates in RX818 alloy was studied as a function of time and temperature and correlated with the grain boundary fracture behavior. Fourthly, kinetic models were developed to calculate the diffusion fields around spheroidal particles which undergo both size and shape coarsening with time. Lastly, microstructures of DSC samples of RX818 were examined by TEM in order to understand the DSC thermograms.

Introduction

Work at Reynolds Metals Company demonstrated that an Al-Cu-Mg-Li-Ag alloy designated RX818 could potentially meet the strength and fracture toughness properties after substantial elevated temperature exposure required for high a speed civil transport (HSCT) airframe. This alloy is mainly strengthened by a fine distribution of equilibrium plate-shaped T_1 (Al_2CuLi) precipitates with some additional lath-shaped S' (Al_2CuMg) precipitates.

Objectives

The purpose of this research was to understand and quantify microstructural evolution in RX818 alloy as a function of time, temperature and alloy composition. Five tasks were

undertaken to accomplish this objective and some of the more important results from each task are summarized below.

Results

Task 1 - Composition and High-Temperature Exposure

Four different compositions of RX818-T8 alloy were examined by TEM. All of the coarsening experiments were performed on the RX818 alloy identified as Lot No. 64667 below. The microstructure of the alloy in the -T8 condition viewed along three low-index zone axes is shown in Fig. 1.

Lot No.	Cu	Mg	Li	Ag	Zr	Si	Fe
64667**	3.5	0.4	0.8	0.4	0.13	-	-
64653	3.6	0.4	0.8	0.4	0.14	0.05	0.07
64627	3.8	0.7	0.9	0.4	0.13	0.06	0.06
64667	3.6	0.8	0.8	0.8	0.14	0.06	0.07

**This was the base alloy used for the coarsening studies.

The TEM studies revealed that increasing the Mg content in RX818-T8 alloy produces a higher volume fraction of S' phase and less T_1 while increasing both the Mg and Ag contents causes relatively coarse S' plates to form in the matrix. TEM also revealed that aging the alloy for relatively short time thermal exposure at a temperature of 250°C (482°F) produces a dramatic change in the microstructure of RX818 alloy, as seen by comparing Fig. 2 with Fig. 1.

Task 2 - Coarsening Behavior of T_1 Plates

The results from this task were discussed in detail in a previous NASA semi-annual report for this grant. Briefly, quantitative precipitate size distribution measurements by TEM show that the average thickness and diameter of the matrix T_1 plates increase with time for a given temperature or with temperature for constant time (Figs. 3a and b). The T_1 plates are about twice as thick and 1.5 times wider after aging at 163°C (325°F) than at 107°C (225°F). The number density of T_1 plates was found to decrease with increasing time and temperature,

as shown in Fig. 3d. The difference is small for 107°C (225°F) but substantial for 163°C (325°F). The volume fraction of matrix T_1 plates increases with time and temperature and approaches a value of about 0.025 after long times (7016 hrs) at 107°C (225°F) and 163°C (325°F), as shown in Fig. 3e. In addition, the aspect ratio of the T_1 plates approaches 17:1 for long aging times indicating that this may be an equilibrium value (Fig. 3c). It was also found that extended thermal exposures at low temperatures such as 107°C (225°F) result in precipitation of additional metastable δ' and S' phases in the alloy, as shown in Fig. 4.

Task 3 - Behavior of Grain Boundary Precipitates

The results from this task were published [1], and the following is a summary of those results. Briefly, TEM examination showed that the sizes of the grain boundary T_1 and S phases generally increase with aging time and temperature in RX818-T8 alloy for exposures of up to 7016 hrs at temperatures of 106-163°C (225-325°F). The proportion of S phase also appears to increase in comparison to T_1 phase as aging progresses and a precipitate free zone develops with increasing aging time and temperature. Additionally, T_1 plates and S precipitates are usually thicker at the grain boundaries than in the matrix. These features are shown in Fig. 5.

TEM examination also showed that the lengths of the grain boundary precipitates depends on the angle between their habit plane and the grain boundary plane. In general, the plates/laths increase in length as the angle decreases. Further comparison between the TEM microsctructures and SEM examination of fracture surfaces indicates that grain boundary T_1 and S precipitates, particularly blocky S particles, very long S laths and long, thick T_1 plates, are responsible for the formation of voids at the grain boundaries, which leads to early fracture and a reduction in the fracture toughness of the alloy. This is shown in Fig. 6, where the transition from smooth intergranular fracture in Figs. 6a and b contrasts with the dimpled fracture surface due to void formation at grain boundary particles in Fig. 6c.

Task 4 - Kinetic Models of Shape Coarsening

The experimentally determined coarsening data in Task 2 indicated that T_1 plates in RX818-T8 alloy undergo both size and shape coarsening during prolonged thermal exposure at temperatures of 107-163°C (225-325°F). In the present task, kinetic models were developed to include the effect of shape evolution during coarsening of precipitate plates and rods. The full

treatments were published [2, 3] and follow the summary below.

The diffusion fields or solute concentrations distributed around prolate (rod-shaped) and oblate (disc-shaped) spheroidal particles were solved for various particle aspect ratios and varying concentrations along the precipitate surface due to the curvature effect. These geometries are indicated schematically in Fig. 7. It was also found that the tangent component of the concentration gradients due to particle curvature may cause complicated mass transfer which is responsible for shape coarsening. The concentration distributions around both prolate and oblate spheroidal particles reduce to the concentration around a spherical precipitate when the aspect rarios of the spheroids approaches unity.

Task 5 - Analysis of DSC Samples

Briefly, TEM analysis of DSC samples of RX818 alloy quenched from various temperatures (Fig. 8) show that most of the endo/exothermic reactions can be attributed to precipitation and dissolution of the T_1 and θ (or θ') phases. A variant of θ phase often called Ω phase was also found in DSC samples quenched from above 360°C, as shown in Fig. 9. Results from the DSC study that were published [4] follow.

Summary

1) In this research, progress was made in understanding and quantifying the behavior of matrix and grain boundary precipitates in RX818-T8 alloy as a function of time and temperature in ranges appropriate to a HSCT airframe.

2) The effect of microstructural evolution in RX818 alloy was qualitatively correlated with the mechanical behavior of the alloy, particularly with the reduction in fracture toughness associated with long-term thermal exposure.

3) Kinetic models which are capable of describing the shape evolution of T_1 plates (oblate spheroids) during the coarsening process were developed.

Publications

1. Y. Mou, J. M. Howe and E. A. Starke, Jr., "Grain-Boundary Precipitation and Fracture Behavior of an Al-Cu-Li-Mg-Ag Alloy", *Metall. Mater. Trans.*, vol. 26A, 1591 (1995).

2. Y. Mou and J. M. Howe, "Diffusion Fields Associated with Prolate Spheroids in Size and Shape Coarsening", *Acta Mater.*, vol. 45, 823 (1997).

3. Y. Mou and J. M. Howe, "Diffusion Fields Associated with Size and Shape Coarsening of Oblate Spheroids", *Metall. Mater.Trans.*, vol. 28A, 39 (1997).

4. R. N. Shenoy and J. M. Howe, "A Differential Scanning Calorimetric Study of a Weldalite™ Alloy" *Scripta Metall. Mater.*, vol. 33, 651 (1995).

Two additional manuscripts are in preparation.

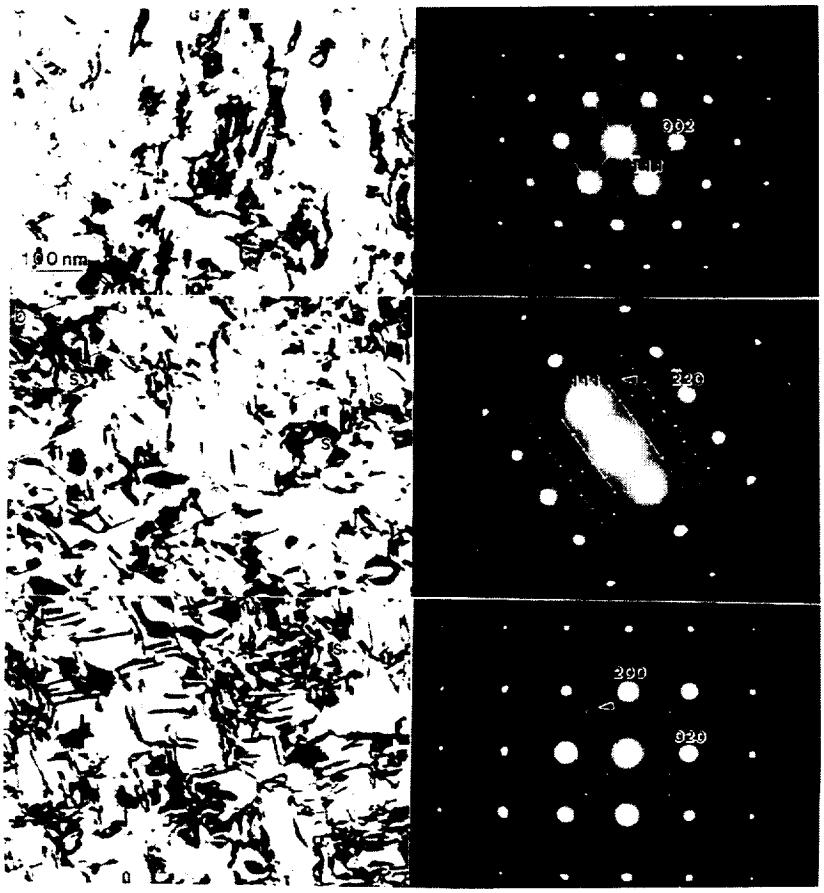

Figure 1. Bright-field TEM images and diffraction patterns of RX818-T8 alloy in: a) <110>, b) <112, and c) <100> matrix operations.

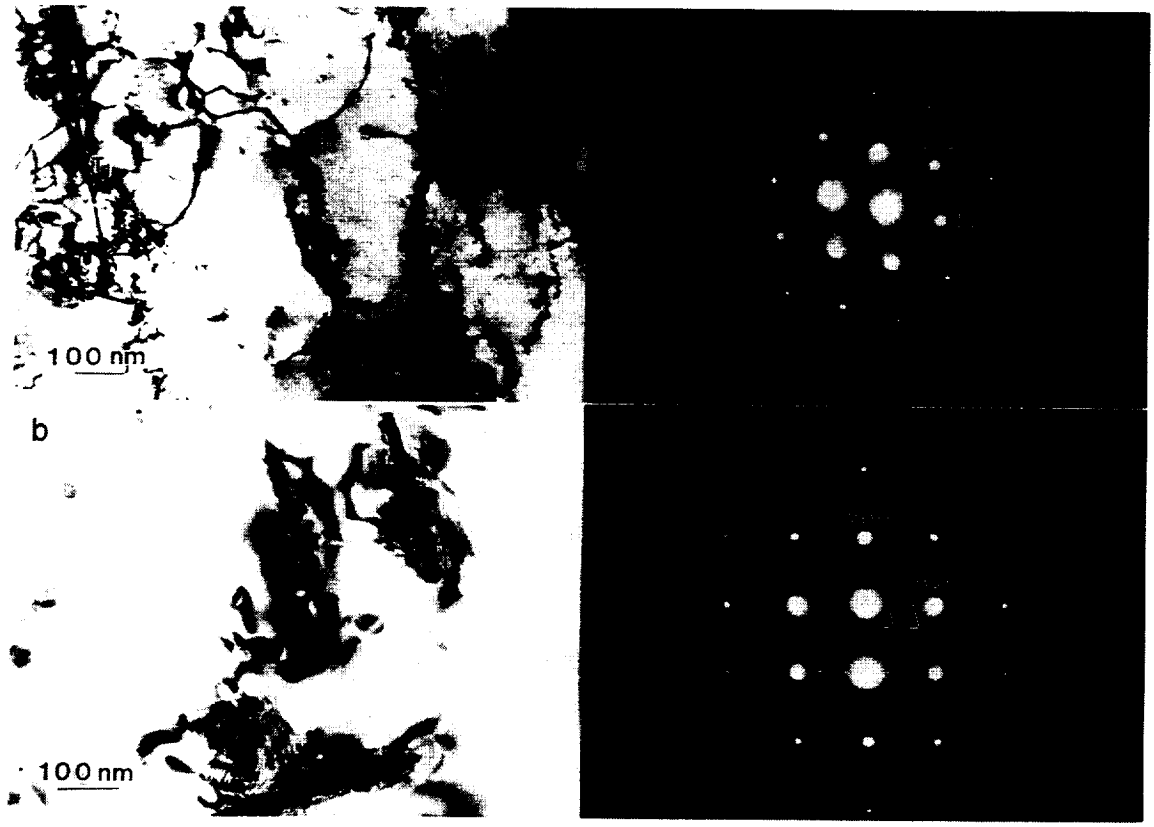

Figure 2. Bright-field TEM images and diffraction patterns of RX818-T8 alloy in after additional aging for 168 hrs at 250°C (428°F) in: a) <110> and b) <100> matrix operations. Arrows in b) indicate reflections due to θ'phase.

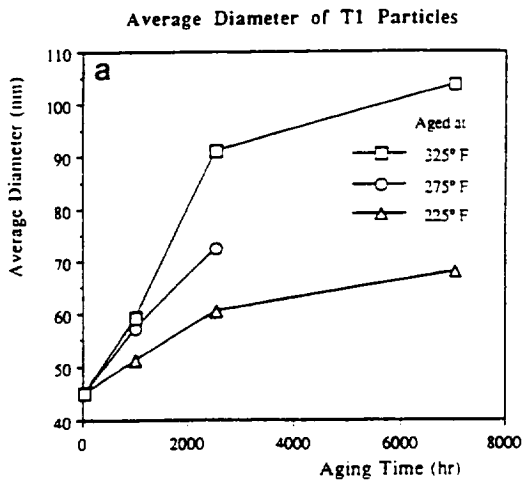

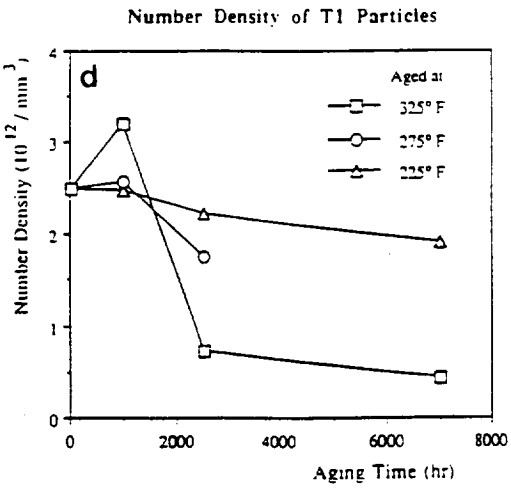

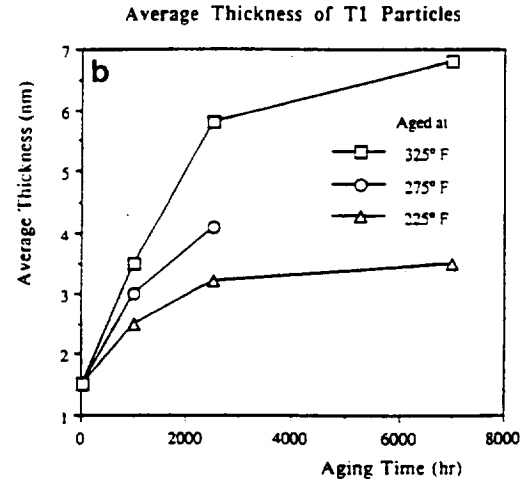

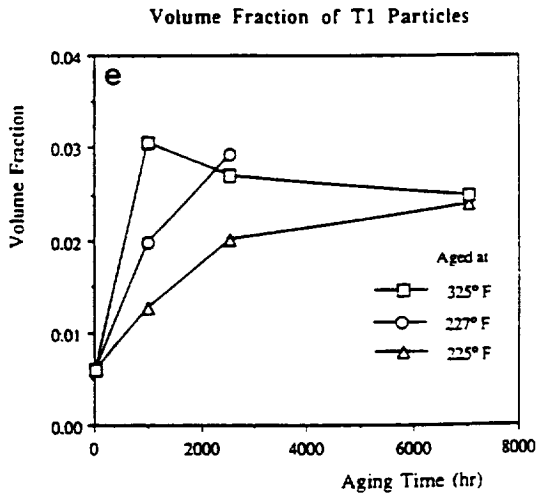

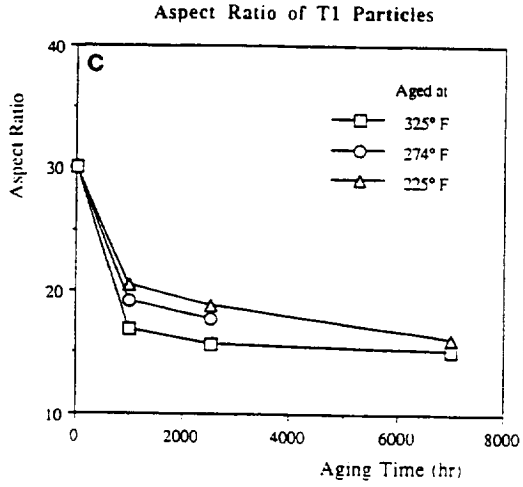

Figure 3. (a) Average diameter, (b) thickness, (c) aspect ratio, (d) number density and (e) volume fraction of matrix T_1 plates in RX818-T8 alloy as a function of aging time and temperature.

Figure 4. Dark-field TEM image showing S' laths (arrows) and δ' spheres in RX818-T8 alloy aged for 2518 hrs at 107°C (225°F).

Figure 5. Grain-boundary T_1 precipitates in RX818-T8 alloy aged at 163°C (325°F) for an additional 7016 hrs: a) T_1 precipitates at subgrain boundaries, b) long T_1 and S' particles along a low-angle boundary, c) very thick T_1 particles and their corresponding diffraction pattern.

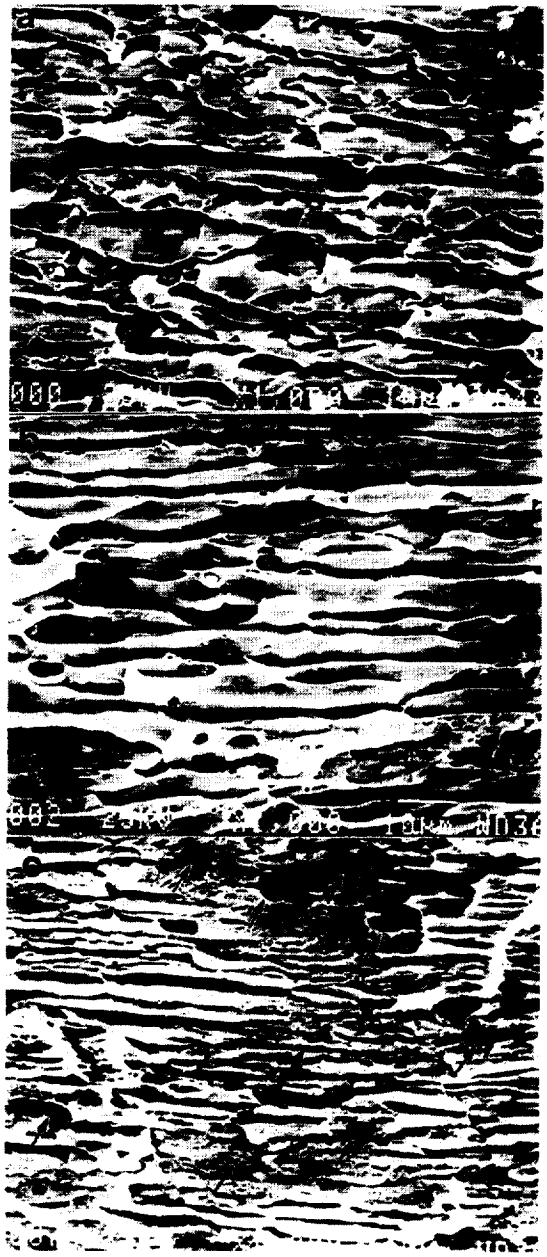

Figure 6. SEM micrographs of the tensile fracture surfaces of RX818-T8 alloy with different heat treatments: a) the initial -T8 temper, and after additional aging at b) 107°C (225°F) and c) 163°C (325°F) for 7016 hrs.

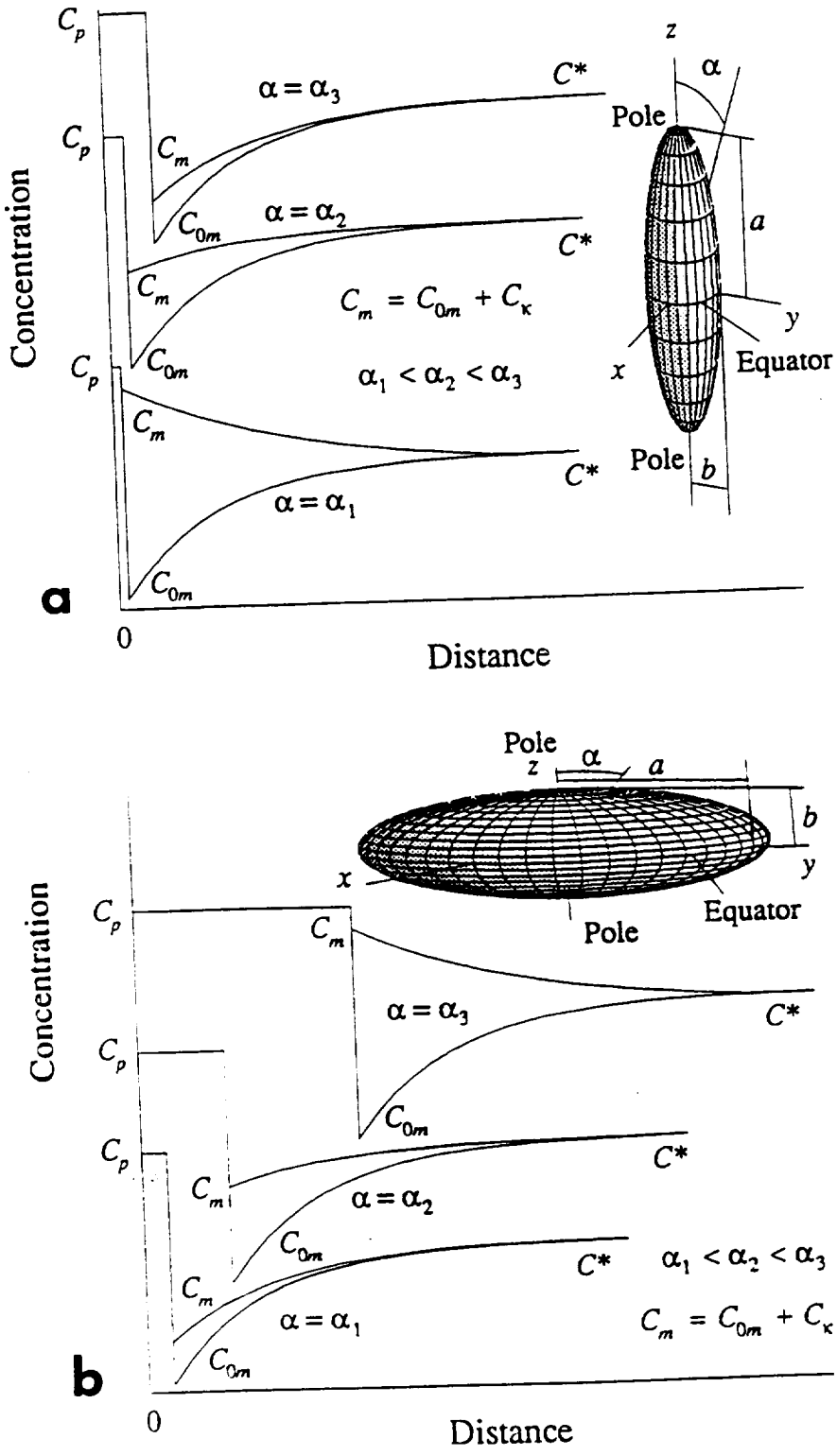

Figure 7. Schematic concentration profiles versus distance for (a) prolate and (b) oblate spheroidal particles. C_p is the precipitate composition, C^* is the matrix composition, C_{0m} is the interface composition without curvature, C_K is the increase in composition due to curvature, and α is the angle from the z-axis.

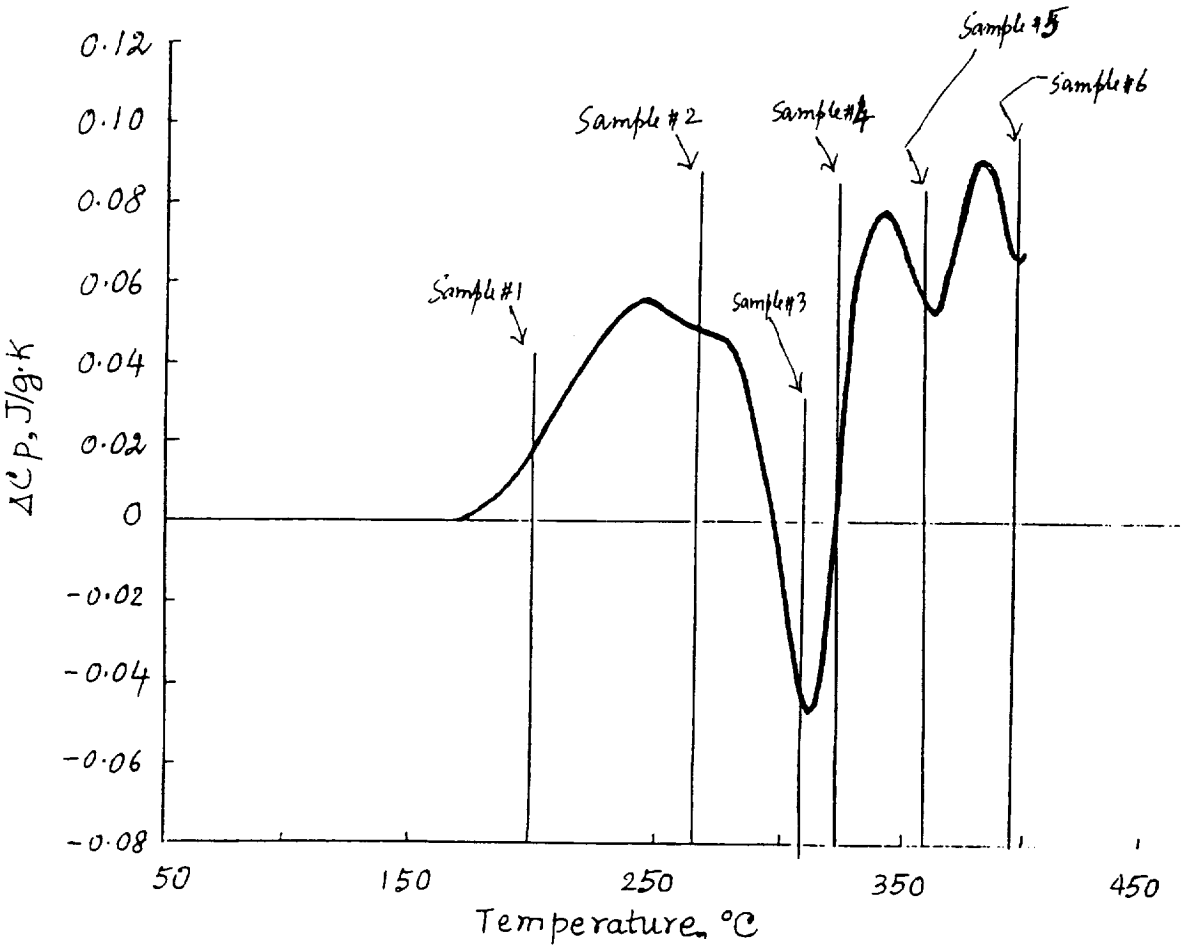

Figure 8. DSC thermogram of RX818-T8 alloy with positions of TEM samples indicated (from R. Shenoy).

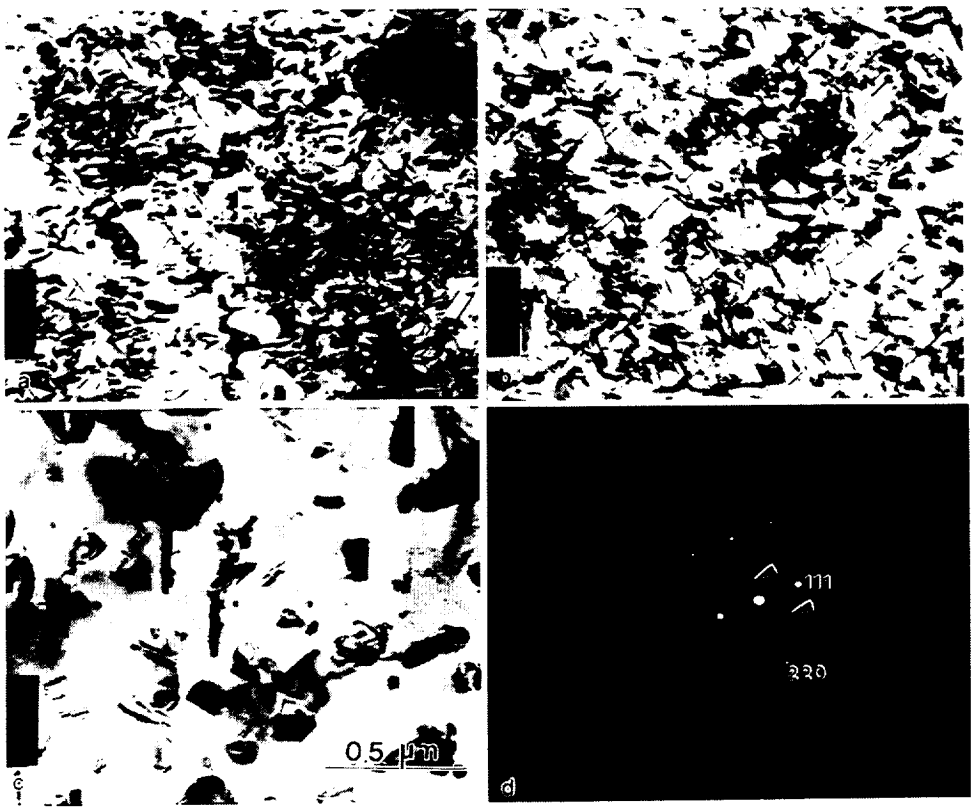

Figure 9. Bright-field TEM images of DSC samples quenched from: a) 200°C, b) 310°C and c) 360°C. T_1 plates are present in a) and b). The <112> diffraction pattern in d) was obtained from the vertical plate near the center of the image in c) and the arrows indicate reflections corresponding to {111} θ (or Ω) phase.

UNIVERSITY OF VIRGINIA

On the Effect of Stress on Nucleation and Growth of Precipitates in an Al-Cu-Mg-Ag Alloy

Principal Investigator: E. A. Starke, Jr.
Co-Principal Investigator: G. J. Shiflet
Post Doctoral Fellow: Birgit Skrotzki

Abstract

A study has been made of the effect of an externally applied tensile stress on Ω and Θ′ precipitate nucleation and growth in an Al-Cu-Mg-Ag alloy and a binary Al-Cu alloy which was used as a model system. Both solutionized and solutionized and aged conditions were studied. The mechanical properties have been measured and the microstructures have been characterized by transmission electron microscopy (TEM). The volume fraction and number density as well as the precipitate size have been experimentally determined. It was found that for as-solutionized samples aged under stress, precipitation occurs preferentially parallel to the stress axis. A threshold stress has to be exceeded before this effect can be observed. The critical stress for influencing the precipitate habit plane is between 120 and 140 MPa for Ω and between 16 and 19 MPa for Θ′ for the aging temperature of 160°C. The major affect of the applied stress is on the nucleation process. The results are discussed in terms of the role of the lattice misfit between the matrix and the precipitate nucleus.

Introduction

Al-Cu-Mg-Ag alloys with high Cu:Mg ratios show high strength after artificial aging. This can be attributed to the precipitation of very thin, hexagonal shaped Ω plates on {111} Al matrix planes which is stimulated by trace additions of Ag. Alloys based on the Al-Cu-Mg-Ag system have attractive room and high temperature strength and creep resistance for temperatures up to120°C and are superior to 2618 and 2219 (1,2). The behavior under creep conditions is primarily controlled by the thermal stability of the precipitates, i.e., how the precipitate structure is affected by temperature, time and stress exposure.

In the Al-Cu-Mg-Ag alloy, Ω partially or completely replaces the well known {001}-type precipitate sequence in Al-Cu-based systems, i.e., G.P. zones, Θ″ and Θ′, as

transition phases before the equilibrium Θ (Al_2Cu). As Ω was recently discovered, the structure of this precipitate is still under discussion. Proposed structures include monoclinic (3,4), hexagonal (5), oththorhomibic (6,7) and tetragonal (8) symmetries. Various chemical analyses of Ω have also been carried out (7,9,10,11,12) revealing compostion close to Θ-Al_2Cu. Results indicate that the role of Ag and Mg and the requirement of a high Cu:Mg ratio in promoting Ω is still unclear. Recent atom probe field ion microscopy (APFIM) studies by Hono et al. (13) showed that in the as-quenched condition independent clusters of Cu, Mg and Ag were present. After 15 s at 180°C, co-clustering of Ag and Mg was observed. After aging for 30 s at 180°C, they detected extremely small precipitates containing Ag, Mg and Cu atoms. They assume that this is a precursor phase for the formation of Ω.

In general, nucleation of precipitates in an age hardenable aluminum alloy can be described by:

$$\Delta G = -V \cdot \Delta G_V + A \cdot \gamma + V \cdot \Delta G_s \qquad (1)$$

where ΔG is the Gibbs free energy change for the transformation to a more stable phase, ΔG_V is the volume free energy change for the formation of the precipitate nucleus, V is the volume of the new phase, A is the area of the interface between the matrix and the precipitate, γ is the energy of the new surface formed, and ΔG_s is the increase in elastic strain energy per unit volume of precipitate. The elastic strain energy depends on the misfit, δ, between both phases and the elastic constants of the matrix phase. It is this term the present investigation addresses.

Under normal aging conditions, i.e., when no applied or residual stresses are present, an even distribution of precipitates should form on all habit planes. If precipitation occurs preferentially on certain habit planes, an anisotropy of strength properties may result. It is well known that plastic anisotropy of a textured single phase material is usually changed when it is strengthened by second phase particles. The effect depends on both shape and habit planes of the precipitates and may reduce or increase anisotropy (14-16).

Coherency strains are usually considered to stabilize a single-phase field, i.e., they shift the solvus line into the equilibrium two-phase field. Externally imposed strains may change the stability of a phase and may move the solvus line either into the single-phase or two-phase region. Consequently, externally applied stresses and internal stresses associated with second

phase particles can affect both nucleation and growth of precipitates and subsequently their coarsening behavior (17,18).

In several alloy systems it has been found that an externally applied stress may result in preferential orientation of precipitates. The reported results are contradictory. This is due to the fact that different alloy systems were investigated with precipitates having different morphologies and different amounts of positive or negative misfit. Even when similar alloy systems were studied they were aged at different temperatures and stresses. In some alloys the nucleation and growth of the precipitation process was studied, while in others the coarsening behavior was examined. A brief review is given in the following.

Nucleation and growth was investigated for the following systems and it was found that aging under an externally applied *tensile stress* results in orienting of Ti-hydride in Ti-H (19), Zr-hydride in Zircaloy-2 (20), $Fe_{16}N_2$ in Fe-N (21), Ni_3Nb in a Ni-base superalloy (22) and Au-rich plates in Fe-Mo-Au (23) *perpendicular* to the stress axis. Contradictory results are reported for Θ' in the Al-Cu system and for Ni_3Al-γ' precipitates in Ni-base superalloys.

Hosford and Agrawal (24) found most of the Θ' precipitates oriented *perpendicular* to the tensile stress axis whereas Eto et al. (25), observed precipitation *parallel* to the stress axis. It has to be noted that different aging temperatures were used. In the Ni-base alloy the coarsening of an already aged microstructure was investigated. Tien and Copley (26) found that tensile annealing enhances γ' coarsening on cube planes *perpendicular* to the stress axis but Miyazaki et al. (27), observed that the precipitates tend to be *parallel* to the stress direction. However, the chemical composition was different and this has a sensitive effect on the misfit between precipitate and matrix.

The objective of the present study was to determine the effect of an externally applied stress on the nucleation and growth of the Ω and Θ' precipitates in a modified 2519 alloy containing additions of Mg and Ag to produce the Ω phase. An Al-Cu binary alloy was also studied as a model system.

Procedure

The composition of the investigated sheet material is given in Table I. Alloy 1 (Al-Cu) was cast at Reynolds Metals Co. and rolled to 6.3 mm sheet. Alloy 2 (Al-Cu-Mg-Ag) was cast at the Alcoa Technical Center as 152 mm x 406 mm x > 1524 mm ingot, preheated and rolled to 3.2 mm sheet. At appropriate temperatures the binary Al-Cu system has the precipitate

sequence G.P. zones, Θ″ (GP2) and Θ′ as transition phases before the equilibrium Θ (Al_2Cu) (28). The microstructure of alloy 2 is more complicated. In addition to the former mentioned precipitates, the phases Ω and S′ (Al_2CuMg) are formed. Ω has a hexagonal plate morphology and because its habit plane is $\{111\}_{Al}$, it can be easily distinguished from Θ′ and S′ whose habit planes are $\{100\}_{Al}$ and $\{210\}_{Al}$, respectively.

Texture measurements were carried out at half sheet thickness after solution heat treatment of the as received material. A Siemens texture goniometer was used in combination with the Schultz reflection method and a Cu-K_α x-ray tube ($\gamma_{Cu\text{-}K\alpha}$ = 0.154178 nm). The software package "popLA" (29) was used to calculate the orientation distribution function (ODF) from {111}, {200} and {220} pole figures and the fully constrained Taylor factor as a function of orientation. Differential scanning calorimetry (DSC) was performed on solutionized and water quenched samples in a PERKIN-ELMER DSC-7 instrument. Different heating rates of 2°C/min, 20°C/min and 50°C/min were used to heat samples from room temperature to 500°C.

The age hardening response was determined for alloy 2 for aging at T = 160°C using Vickers hardness measurements. For the peak-aged T6 temper, samples were solution-heat-treated at 520°C for one hour, cold water quenched and aged for 20 hours at 160° C. For the peak-aged T8 temper, samples were solution-heat-treated at 520 ° C for one hour, cold water quenched, stretched 2% and aged for 16 hours at 160° C. The mechanical properties at room temperature and T = 160°C were measured for both alloys using a MTS tensile test machine. The strain rate was 10^{-3} 1/s. For the high temperature tensile tests, a laser extensometer was used to measure the strain. Rectangular subsize tension test specimens were used in accordance with ASTM B 557-84 (30).

Samples of constant area (Fig. 1a) were aged at 160°C under a tensile stress in a creep machine for different times (10, 100, 1000 h) and under various constant loads in the as-solution heat treated and the peak aged (T6) conditions. As the deformation is very low the stress σ is considered as constant. The as-solution heat treated samples were transferred to the creep machine immediately after the cold water quench in order to avoid aging at room temperature. The stress was applied to the sample prior to encasement by the furnace. Tapered samples (Fig. 1b) were used to give various stresses and strains in a single sample.

The microstructure was characterized by conventional TEM using a 120 and 200 keV and high-resolution TEM (HRTEM) with a top-entry 400keV microscope. Samples were prepared by twin jet polishing at ~15 V using a solution of 1/3 HNO_3 and 2/3 Methanol cooled to -30°C. The stress direction was marked before samples were punched out from creep samples. The approach of Underwood (31) for projected images was applied to determine the volume fraction and number density of precipitates. Under the assumption that the precipitates are disc shaped, the volume fraction of precipitates V_V can be calculated by:

$$V_v = -2 \cdot \ln(1 - A_A) \cdot \left(\frac{\bar{c}}{c + t} \right) \qquad (2)$$

A_A' is the area fraction for projected images, ε the average thickness of the precipitate and τ the foil thickness. The number of precipitates per volume (number density) N_V is given by:

$$N_V = \frac{4 \cdot V_V}{\pi \cdot \bar{c} \cdot \bar{D}^2} \qquad (3)$$

c and D are the average precipitate thickness and diameter, respectively. Convergent beam electron diffraction (CBED) was employed to determine the foil thickness (32).

Results

Texture and Mechanical Properties

Fig. 2 shows that the microstructures were completely recrystallized after solution heat treatment. The mean grain size was 307 μm for alloy 1 and 38 μm for alloy 2. A typical TEM micrograph of alloy 2 after solutionizing and aging for 20 h at 160°C, peak strength, is shown in Fig. 3.

Fig. 3a was taken under a [110] zone axis and two variants of Θ and one variant of Θ′ are visible. Fig. 3b shows two variants of Θ′. The zone axis is [001].

The texture measurements of alloy 2 showed a completely random crystal distribution (Fig. 4). This is not the normal recrystallization texture of aluminum alloys. The reason for the observed texture may be associated with the high volume fraction of constituent phases (size ≈

9 μm) which produced deformation zones during rolling. These deformation zones can serve as recrystallization sites during subsequent heat treatment and result in a random texture (33). The texture components are low, between 1.3 and 1.9 times random except for the brass component which is 3.1 times random. Due to the large grain size of the Al-Cu alloy, texture analysis was somewhat difficult. The orientation distribution functions show that there is no texture component present other than rotated cube, which is strong.

Fig. 5 shows the age hardening response after aging at 160°C for alloy 2. The maximum hardness is reached after about 20 h aging and it remains constant after further aging due to the high thermal stability of the Ω phase. The mechanical properties at room and high temperature are shown in Table II. Alloy 2 is very isotropic in uniaxial tensile tests, with only an 8.3% increase in the yield strength between the rolling direction and 45° to the RD for the as-solution heat treated condition and a 1.9% decrease in yield strength between the RD and 45° to the RD for the T6 condition. The fairly isotropic behavior was expected for the solution heat treated condition because the texture measurements showed a random texture. The swing of 10.2% that occured during aging must be associated with the precipitation of the Ω and Θ′ phases. It has been found that the precipitates on {111} planes usually increase and those on {100} planes usually decrease anisotropy (15,16). Further analysis of the effect of precipitation on anisotropy is being conducted under a separate study. Calculations of the Taylor factor, M, associated with the texture affect, predict an isotropic mechanical behavior. M was found to be close to 3.06 which is the theoretical value for random crystal structures.

Tensile strength for the peak aged (T6) condition is increased considerably over that for the solution heat treated condition. As expected, the yield strength is lower at 160°C for the T6 samples. For the solution heat treated samples, higher strength values were measured at higher temperature. This is due to the very fast precipitation during heating the samples to the test temperature. The heating was done as fast as possible but it took about 20 min. before the test could be carried out. This is obviously enough time for age hardening to take place.

Aging under Tensile Stress

A TEM micrograph of an Al-Cu sample (alloy 1) solutionized and then heated to 180°C in a DSC (heatup rate: 50 deg./min) with no external stresses, and then immediately quenched, is shown in Fig. 6a. The Θ″ precipitates are equally distributed, which can be seen by close examination of the micrograph and diffraction pattern. The SAD associated with Fig. 6a

reveals streaking that is uniform in both directions. When alloy 1 is heated to 160°C under an applied load, σ=69.5 MPa, and then immediately cooled, the Θ'' precipitates align with the stress axis (Fig. 6b). The associated SAD confirms the preferred orientation of the plates by the appearance of streaks in only one direction. More precipitates are formed parallel to the stress axis than perpendicular to it. This is supported by the diffraction pattern which shows streaks with a higher intensity for those precipitates parallel to the stress axis (Fig. 6b). Fig. 6c show the case where the stress axis in approximately 40 degrees from a cube direction. Here the sample was heated to 160°C with σ = 59.7 MPa and then isothermally aged for 2 h while maintaining the stress of 59.7 MPa followed by a cold water quench. Careful analysis of the micrograph and the streaking in the associated SAD indicates that there are more precipitate plates whose axis is nearer the stress direction. In the quaternary alloy the Θ'' precipitates are even smaller than in the binary alloy and the orientation effect was also observed. Neither the bright field, nor the diffraction pattern show any indication of Ω (Fig. 6d).

DSC results were obtained for both alloys using different heating rates (2, 20, and 50 deg/min). In the binary alloy the precipitation of Θ'' was not detected and even Θ' was difficult to observe. For slow heating rates only a straight line was obtained. Presumably, the reaction is taking place over a wide temperature range and, therefore, cannot be resolved. Even for the faster heating rate (50 deg/min) the exothermic peak is very wide. For the quaternary alloy the precipitation of Θ' was not observed in the DSC measurements although it was observed in TEM. The exothermic peaks at 210°C and 225°C, respectively, are attributed to the precipitation of the Ω phase. The reaction temperatures are in agreement with TEM results which did not show any Ω at 160°C.

Samples of alloy 2 with constant area were aged under a tensile stress which was 40% of the room temperature yield stress, i.e., 69 MPa for solution heat treated samples and 191 MPa for peak aged (T6, 160°C/20 hrs) samples. The stress applied to the solutionized tapered samples was up to 175 MPa which is equivalent to the yield stress at room temperature.

For a quantitative characterization of the stress aged microstructures, the volume fraction of precipitates, the number of particles per volume, the particle diameter and thickness have all been experimentally determined. Data from samples aged under stress were compared to those aged without stress (T6) and 2% prestrained and peak aged (T8). Figs. 7a - d show the results of the quantitative microstructural analysis. Although comparisons can be made

between the different testing conditions they will generally be made with respect to the T6 condition. Quantitative metallography was conducted following several types of experiments combining thermal treatment and applied stress. Each of the four plots can be divided into three sections. The first two data points on the four plots in Fig. 7 are for the peak aged (T6) and prestraining followed by aging to peak strength (T8) conditions. No applied stress was involved during aging. The next set of data are for solution heat treating (SHT) the samples under an applied stress for 10, 100, and 1000 hours at 40% of the yield strength. The fourth data point in this particular set is identical to the previous 100 hr aging treatment except that now the applied stress is equal to the yield strength (marked by an *). The last three data points are for applying a stress *after* peak strength was obtained (T6).

The results show that the 2% prestraining (which greatly increases the dislocation interactions (34) followed by heat treating to peak strength increases the volume fraction of both precipitates (Fig. 7a) but does not increase the number density of Ω precipitates (Fig. 7b). The number density of Θ′ precipitates is increased by a factor of two. The plate lengths (Fig. 7c) and thicknesses (Fig. 7d) of both types increase slightly from T6 to T8.

Aging under stress, i.e., nucleation and growth, (SHT+creep, Fig. 7) reveals that when the applied stress is 40% of the yield stress the volume fraction of Ω increases dramatically (from 0.7 after 10 hrs to 1.4% after 1000 hrs) and Θ' remains relatively constant, while the particle density of Ω drops at a much higher rate (0.04 particles/hr) than Θ′ (0.008 particles/hr) on aging from 10 to 1000 hrs. Note, however, the greatly increased Ω particle density at SHT+10 hrs compared with the T6 or T8 condition. Figs. 7c & d support these changes of aging under an applied stress by demonstrating that the plates increase in diameter and thickness at about the same rate. This means that coarsening and growth occur simultaneously. The effect of increasing the applied stress to equal the yield stress (marked "SHT*" in Fig. 7) results in little change in Ω after 100 h except for slightly larger particles, but for Θ′ the number of particles per unit volume is larger, as is the volume fraction. This may be due to the resultant plasticity and concomitant increase in dislocation density.

The third general section of the four plots in Fig. 7 is for material first peak aged (T6) prior to applying the stress. This experiment is designed to examine precipitate growth and coarsening under an external load. After 10 hrs in this condition both the volume fraction and

density of Ω is greater than for the T6 condition. The plate diameter and thickness are about the same. In contrast, Θ′ is about the same after 10 hours compared to the T6 treatment.

As time under stress increases the volume fraction of Ω grows while its number density decreases significantly, by about 1/3 at 1000 h compared to 10 h (Fig. 7b). The initial increased volume fraction is due to the increased number density compared to T6. Apparently, there is further nucleation of particles. The Ω particle diameter and thickness also increase with increasing aging time under stress. For times greater than 10 hr,the volume fraction of Θ′ is fairly constant and the slight increase is due to the increased thickness (Fig. 7d) of the particles.

The number density remains nearly unchanged. After extensive aging times Ω shows a higher thermal stability than Θ′ . The Θ′ precipitates start to grow and coarsen very early. Considerable growth of Ω does not occur before 100 h aging.

Further analysis was conducted to investigate whether preferential nucleation or growth on certain habit planes occur. Therefore, the volume fraction was determined separately for every precipitate variant and the angle between the precipitate and the direction of the applied load was measured. The results are illustrated in Figs. 8 and 9.

The value of the measured angle, α, between precipitate and the stress direction is subtracted from 90°. This means that precipitates with |90° - α| = 0° are perpendicular and those with |90° - α| = 90° are parallel to the stress direction. The experiment was done twice. Once for SHT+creep under an applied load (Fig. 8) and repeated for samples that were aged to peak strength with no applied load (T6), followed by further aging under an external stress (Fig. 9). The former examines nucleation and growth while the latter focuses on growth and coarsening. For solution heat treated samples of alloy 2, it was found that the higher volume fractions of Θ′ are parallel and the lower volume fractions are perpendicular to the stress direction (Fig. 8a). For Ω the values are randomly scattered over the whole spectrum of angles (Fig. 8b). No comparable effect was found for samples aged under stress in the T6 condition (Figs. 9a-b) neither for the volume fractions, nor for the number density or the size of the precipitates. In order to investigate the possibility of a threshold stress that must be exceeded before a similar effect could be observed for (, samples were aged under a higher stress. Fig. 10 shows that after aging under the higher stress, which is equivalent to the room temperature yield stress, the

higher volume fractions are observed parallel to the stress axis for both type of precipitates. The threshold stress for Ω in this alloy is estimated to be between 119 and 142 MPa for solution heat treated samples.

Tapered samples of the solutionized binary Al-Cu material (alloy 1) were also aged under stress to study the observed effect in greater detail. Fig. 11 shows that the results are consistent with those obtained on the quaternary alloy (Fig. 10). The Θ′ phase precipitates preferentially parallel to the stress axis. The threshold stress for Θ′ was estimated to be between 16 and 19 MPa. Fig. 12 is a micrograph of an aged sample. The direction of the applied stress is indicated by arrows. The micrograph shows very clearly that almost all precipitates are aligned parallel to the stress axis. Figs. 13 and 14 show the volume fraction and the number density as a function of the externally applied stress for the binary and the quaternary alloy. In the quaternary alloy (alloy 2) (Fig. 13) it was found that the number density of Ω precipitates decreased with increasing stress whereas the number density of Θ′ increased with rising stress. For the binary alloy (Fig. 14) both volume fraction and precipitate density correlates with 19 MPa as the threshold stress whereby greater stresses align Θ′ parallel to the stress axis. After an initial increase, the number density of Θ′ decreases with increasing stress.

Discussion

Initially the discussion will focus on Θ′ rather than on Ω because of the simpler binary system. However, even here the precipitate sequence that inevitably results due to our experimental design make interpretation complicated. Specifically, the material is first solutionized and quenched before heating up to 160°C (with and without an external stress). This means that precipitation begins with GP zones and because Θ′ is present at peak strength, the sequence likely passes through the Θ″ phase (Fig. 6). As Θ″ (sometimes referred to as GP2) generally follows GP zones by forming a second layer of Cu atoms parallel to the GP zone on the (001) plane, ideally with two Al planes between the two Cu planes, the effect of an external stress on the arrangement is not known. Even without an external stress the layering of Al planes is sometimes two or four planes instead of three. Calculations by deFontaine (35) show that three planes minimizes the strain. There are two models concerning the Θ″ -> Θ′

transition. The first is based on the classical interpretation of Θ′ heterogeneous nucleation at the Θ″ /Al matrix interface or nearby at a defect and dissolving the Θ″ precipitate by utilizing the Cu. The second is that there are rearrangements of atoms within the Θ″ lattice that lead to the correct stoichiometry and crystal structure of Θ′ (36). This occurs by a gradual evolution of the new crystal structure rather than by nucleating a new phase by forming an embryo.

The present results clearly show that for binary Al-Cu both Θ″ (Fig. 6b) and Θ′ (Fig. 12) preferentially align with the applied stress (Fig. 15), provided the stress is above a critical value. Likewise Ω shows exactly the same behavior at a higher critical stress value. Again, focusing on the Al-Cu binary alloy and assuming that the precipitation of Θ′ is by classical nucleation and growth, the question of whether the preferred orientation of the plates parallel to the stress axis is due to nucleation or growth can be examined by quantitatively examining the data when the alloy is brought to the annealing temperature, all the while under an external stress, and comparing these results with samples that were first aged to peak strength and then further aged under an applied stress (Figs. 8 and 9). In the former case the Θ′ plates align with the applied stress and in the latter they remain randomly distributed. Further, the data in Fig. 11 and the TEM image in Fig. 12 clearly demonstrate that Θ′ preferentially aligns with the applied stress direction. These data were obtained from a tapered sample where the cross sectional area gave a stress value of about 50% of the yield stress for this alloy, or 59 MPa. Examination of other cross sectional areas where the effective stress is greater and less revealed that there is a critical stress of approximately 19 MPa below which no effect of the applied stress is detected in the binary alloy. This result is additionally strengthened by Fig. 14a,b where at 20 MPa and above the density and volume fraction data fall into two clear groups, *viz.*, {001} planes that contain a high density of Θ′ plates and {001} that have nearly zero density of plates. Again, TEM reveals that the high density of plates are parallel to the stress axis. The data from Fig. 11 agree with the conclusion of Eto et al (25) that the phenomenon of Θ′ plate alignment is due to nucleation and not subsequent growth. Also, Eto et al have reported that there is a critical temperature where this effect applies, which when coupled with our observations of a critical stress at a particular temperture, i.e, 160°C, suggests that it is the nucleation of these plates that leads to alignment with the stress axis. Because of the different expansion coefficients between

the precipitate plates and the aluminum matrix, the critical stress, σ_c, dividing the regimes between plate alignment and randomness is most likely to be temperature dependent. The applied stress reported by Eto et al is 73.5 MPa which produced alignment of θ' with the stress axis. However, they did not vary the stress to obtain the minimum, or critical value, dividing the two regimes. Note also, from Fig. 14, that the volume fraction data seem to be constant as the applied stress is increased up to the yield point and only the relative population densities on the cube planes change.

Turning to the quaternary alloy, the trend for the number density (Fig. 13a,b) of Ω precipitates with increasing external stress is downwards. The density on the {111} aluminum matrix planes parallel to the stress axis (Ω(h)) initially decreases and then after about 120 MPa remains constant, whereas those on the matrix planes approximately perpendicular to the stress axis (Ω(l)) continuously decrease in numbers as the stress rises. This finding correlates with the results of Ringer et al (37) who noted that Ω densities are dramatically decreased with a T8 treatment. Data from Ringer et al. (37) are plotted on Figs. 7a,b along with our data. Although their alloy has a different composition than the alloy used in this study, they did observe the same relative decrease in Ω density with prior deformation. They attribute this to the possibility of dislocations disrupting precursor clusters that lead to Ω nucleation. Perhaps elastic strain has a similar effect on these clusters if they do exist. Regardless, it suggests a nucleation effect.

The number density of Θ' increases with rising stress on {001} planes parallel to the stress axis (higher precipitate density) and those perpendicular to the stress axis (lower density). This result is similar to the binary alloy, but not as dramatic, and wide separation does not occur until a much higher applied stresses. This could be due to an effective screening effect of the Ω plates.

As Θ' precipitates preferentially nucleate at dislocations and Θ'' interfaces, it was expected that the number density might increase with a prior plastic strain. The amount of prestraining (2%) was probably too low to provide a considerable higher number of nucleation sites. Ringer, et al. (37) recently showed that cold work (6%) before aging refines the mean size and thickness of Ω but the number density is considerably reduced compared to

undeformed material. On the other hand, Θ' was observed in a more uniform dispersion. They attribute this to the interference of cold work with the nucleation of Ω because the passage of dislocations through the matrix disrupts the clustering processes and also alters the vacancy content that may be a precurser to Ω nucleation. In contrast to this, dislocations provide sites to facilitate heterogeneous nucleation of Θ'.

The present effort indicates nucleation is responsible for the observed effect of an applied stress. Cassada et al. (34) and Wang and Shiflet (38) have demonstrated that the influence of a stress field can not only determine the nucleation site but also that classical nucleation theory, modified to account for the stress surrounding a lattice defect, can be successfully applied to explain the experimental observation. In their studies, the stress field surrounding an edge dislocation was shown to dominate in the nucleation of δ' precipitates in Al-Li alloys at the aging temperature employed (210-260°C). The present situation is to account for the alignment of Θ'' and Θ' precipitates with the stress axis once the critical stress for the specific aging temperature has been applied. Like the δ' precipitation on dislocations, the Θ' plates will form as to minimize the strain energy associated with nucleation. Because δ' has a negative volume misfit with respect to the aluminum matrix, the embryos nucleate only on the compressive side of an edge dislocation. Likewise it is not surprising that because Θ' plates have a negative misfit with the aluminum matrix they will nucleate to cancel this misfit, i.e., along the cube planes associated with a compressive area, or parallel to the applied stress, and thereby reduce the energy barrier associated with nucleation. As only the earliest stages of formation should then be considered, a crystallographic representation of the critical embryo is required. A model developed by Dahmen and Westmacott (36) suggest that the smallest Θ' precipitate (critical nucleus) is 2 unit cells which would have a vacancy misfit (negative). Stobbs and Purdy (39) have experimentally shown that 2 unit cells or smaller indeed have a vacancy-type misfit (Fig. 16). Fig. 17 shows a crystallographic model of a Θ' precipitate in an Al-matrix properly oriented in the cube/cube relationship. A two unit cell Θ' precipitate fits into 3 unit cells of the Al-matrix with a misfit of - 4.5% (calculated from the lattice parameters, Table III). The current results suggest that in the presence of an applied stress the lattice strain

is such as to reduce this vacancy misfit when the Θ′ plates nucleate parallel to the stress axis.

This contradicts the results of Hosford and Agrawal (24) but is in agreement with Eto et al. (25). Hosford and Agrawal found a higher density of Θ′ precipitates perpendicular to the tensile stress axis. Nevertheless, their single published micrograph (in a [310] orientation) is not conclusive and they did not carry out any quantitative analysis. Eto et al.(25), tried to reproduce Hosford and Agrawal's results by aging some samples at 210°C but they could not produce oriented precipitates at this temperature. They found a strong effect on nucleation after aging at 170°C. Oriented Θ′ precipitates were observed after aging under stress followed by stress free aging. No orienting effect was observed for stress free aging followed by stress aging. Eto et al observed the same effect for GP1 and GP2 (Θ″) zones after aging at 80°C. This led to the conclusion that an applied tensile stress produces, preferentially, variants of GP1 zones parallel to the tensile stress axis which act as nuclei for GP2 (Θ″) and these will grow further to Θ′ . They suggest that there is a critical temperature ($180°C < T_c < 190°C$). If the alloy is aged at $T > T_c$, Θ′ is formed directly and the precipitation is not affected by an applied stress. This is the reason they give for not reproducing Hosford and Agrawal's results. Eto *et al* explain their results through the interaction energy between the GP zones and an applied stress. The interaction energy can be expressed by the modulus effect due to the difference of the elastic moduli and the misfit effect due to the presence of misfit strain between the matrix and the zone. Calculations show that a reverse of the stress direction does not affect the modulus effect and, therefore, the modulus effect cannot be the reason for the preferential precipitation. The suggestion is made by Eto et al that there is a larger effect due to the misfit strain of GP1 zones which is larger parallel to the disc plane than in the perpendicular direction. The present results indicate that there is a critical stress, σ_c, coupled with a possible critical temperature, T_c, proposed by Eto et al.

In contrast to this, Sauthoff (23) found that stress orienting occurs primarily by selective coarsening, but he found a smaller, but observable effect on nucleation, too. He showed that there is an energy difference between particles which are oriented differently to the external stress axis (40). He discussed theoretically, how nucleation, growth and coarsening are affected by the orienting energy and found that particle orienting is feasible primarily by

coarsening (41). We do not agree with Sauthoff because of the strict application of classical nucleation theory at such a large undercooling.

The threshold stress for an orienting effect was found to be very different for Ω and Θ′. This may have different reasons. There is not as much information available for Ω as for Θ′ which makes the discussion about the observed results more difficult. However, similar explanations for the effect on Θ′ should be valid for Ω, as well. First of all, the habit plane is different for Ω and Θ′. This means the elastic modulus of the Al-matrix is 20% higher in the [111] direction for Ω than in the [100] direction for Θ′. Even so, there must be another reason because this difference in the modulus is not high enough to explain the large difference in the threshold stresses. A second important variable should be the amount of misfit between the precipitate and the matrix. The calculated misfit of Ω is twice as high as that of Θ′ at very early stages of development and would require a higher stress to accommodate it. Experiments have determined that (has a large negative misfit of -9.3% (42) or -8.3% (12) for 1 unit cell thick nuclei (Table IV) . In addition, the crystal structure of the precipitates is probably not the same.

Concerning growth, prestraining (T8) increases the volume fraction of Ω and Θ′ precipitates but there is only a little change in the number density, compared to the peak aged condition (T6). This means that growth kinetics were accelerated. For plate growth and latter stages of development, including coarsening, it is generally accepted now that plate shaped particles grow by a ledge mechanism (43). Fig. 18 shows a high resolution TEM micrograph with a growth ledge on a Ω precipitate. During growth the growth ledge height should have the requisite number of Ω subunits (half unit cells) to minimize the elastic accommodation strain. The mechanism for Ω growth ledges by Fonda et al (42), based on HRTEM observations, involved both positve and negative misfit associated with the growth ledge. Their model indicates that multiples of Ω planes can give the requisite misfit that accomodates the applied stress. Under the present conditions with the plates aligned with the applied stress the ledges should yield a negative misfit. The micrograph in Fig. 18, when compared to Figs. 6 and 9 in ref. (42) confirm this conclusion. However, because the growth ledges can accomodate both positve and negative misfit by merely adjusting the height of the growth riser, growth rates should not be very different in different directions relative to the applied stress. In coarsening

studies under an applied stress following a normal temper T8, coarsening rates were not much different on habit plane variants parallel or perpendicular to the applied stress axis (44). This, again, gives support that the primary affect of an applied stress manifests itself during nucleation and not growth. Further HRTEM work has to be done to analyze the growth ledge height. Due to the fact that T6 samples did not show preferential orientation after further stress aging, we assume that in our experiments the nucleation of precipitates is primarily affected.

Conclusion

It was found that Ω and Θ' precipitates are preferentially oriented parallel to an externally applied tensile stress in the solution heat treated condition. The nucleation of the precipitates is strongly affected by the applied stress and there is a critical value of stress that must be exceeded that leads to preverential nucleation on habit plane varients. Both Θ' and Ω plates have a negative misfit with the matrix when very thin which leads to plate nucleation on variants under compression. For Θ' the critical stress is between 16 and 19 MPa and for Ω it is between 120 and 140 MPa at a temperture of 160°C. When combined with the results of Eto et al (25) this critical stress is temperature dependent.

References

1. I. J. Polmear, M. J. Couper, "Design and Development of an Experimental Wrought Aluminum Alloy for Use at Elevated Temperatures", in *Metall. Trans. A*, 1988, vol. 19A, pp. 1027 - 1035
2. E. A. Starke, Jr., Editor, NASA Contractor Report 4645, "NASA-UVa Light Aerospace Alloy and Structure Technology Program Supplement: Aluminum-Based Materials for High Speed Arcraft, Grant NAG-1-745, Feb. 1995.
3. J. H Auld, *Acta Cryst.*, 1972, vol. A28, p. 98S.
4. J. H. Auld, "Structure of Metastable Precipitate in Some Al-Cu-Mg-Ag Alloys", in *Mat. Sci. Tech.*, 1986, vol. 2, pp. 784 - 787.
5. S. Kerry, V. D. Scott, "Structure and Orientation Relationship of Precipitates Formed in Al-Cu-Mg-Ag Alloys", in *Met. Sci.*: 1984, vol. 18, pp. 289 - 294.
6. K. M. Knowles, W. M. Stobbs, *Acta Cryst.*, 1988, vol. B44, pp. 207 - 227.
7. B. C. Muddle, I. J. Polmear, "The Precipitate Ω Phase in Al-Cu-Mg-Ag Alloys," *Acta Metall.*, 1989, vol. 37, pp. 777 - 789.
8. A. Garg, J. M. Howe, "Nucleation and Growth of Omega Phase in Al-4.0 Cu-0.5 Mg-0.5 Ag Alloy - An Insitu Hot-Stage TEM Study", in *Acta Metall. Mater.*, 1991, vol. 39, pp. 1939 - 1946.
9. Y. C. Chang, J. M. Howe, "Composition and Stability of Omega Phase in an Al-Cu-Mg-Ag Alloy", in *Metall. Trans. A*, 1993, vol. 24A, pp. 1461 - 1470.
10. K. Hono, N.Sano, S. S. Babu, R. Okano, T. Sakurai, "Atom Probe Study ofthe Precipitation Process in Al-Cu-Mg-Ag Alloys", *Acta Metall. Mater.*, 1993, vol. 41, pp. 829 - 838.
11. B. A. Shollock, C. R. M. Grovenor, K. M. Knowles, "Compositional Studies of Omega-Precipitates and O'-Precipitates in an Al-Cu-Mg-Ag Alloy", *Scripta Metall. Mater.*, 1990, vol. 24, pp. 1239 - 1244.
12. J. M. Howe, "Analytical Transmission Electron Microscopy Analysis of Ag and Mg Segregation to θ Precipitate Plates in an Al-Cu-Mg-Ag Alloy," *Phil. Mag. Letters*, 1994, vol. 70, pp. 111 - 120.
13. K. Hono, T. Sakurai, I. J. Polmear, "Pre-Precipitate Clustering in an Al-Cu-Mg-Ag Alloy", *Scripta Metall. Mater.*, 1994, vol. 30, pp. 659 -700.

14. W. F. Hosford, R. H. Zeisloft, "The Anisotropy of Age-Hardened Al-4% Cu Single Crystals During Plane-Strain Compression," in *Metall. Trans.*, 1972, vol. 3, pp. 113 - 121.

15. P. Bate, W. T. Roberts, D. V. Wilson, "Plastic Anisotropy of Two-Phase Aluminum Alloys - I. Anisotropy in Unidirectional Deformation", in *Acta Met.*, 1981, vol. 29, pp. 1797 - 1814.

16. P. Bate, W. T. Roberts, D. V. Wilson, "The Plastic Anisotropy of Two-Phase Aluminum Alloys - II. Anisotropic Behavior in Load-Reversal Tests", in *Acta Met.*, 1982, vol. 30, pp. 725 - 738.

17. W. C. Johnson, C. S. Chiang, "Phase Equilibrium and Stability of Elastically Stressed Heteroepitaxial Thin Films", in *J. Appl. Phys.*, 1988, vol. 64, pp. 1155 - 1165.

18. C. S. Chiang, W. C. Johnson, "Coherent Phase Equilibria in Systems Possessing a Consolute Critical Point," *J. Mater. Res.*, 1989, vol. 4, pp. 678 - 687.

19. M. R. Louthan, Jr., "Stress Orientation of Titanium Hydride in Titanium," *Trans. AIME*, 1963, vol. 227, pp. 1166 - 1170.

20. M. R. Louthan, Jr., C. L. Angerman, "The Influence of Stress on the Hydride Habit Plane in Zircalloy-2," *Trans. AIME*, 1966, vol. 236, pp. 221 - 222.

21. Y. Nakada, W. C. Leslie, T. P. Churay, "Stress-Orienting of $Fe_{16}N_2$ Precipitates in an Fe-N Alloy," *Trans. ASM*, 1967, vol. 60, pp. 223 - 227.

22. J. M. Oblak, D. F. Paulonis, D. S. Duvall, "Coherency Strengthening in Ni Base Alloys Hardened by DO_{22} γ'' Precipitates," *Metall. Trans.*, 1974, vol. 5, pp. 143 - 153.

23. G. Sauthoff, "Orienting of Precipitating Au Particles in a Fe-Mo-Au Alloy by External Elastic Stress," *Z. Metallk.*, 1977, vol. 68, pp. 500 - 505.

24. W. F. Hosford, S. P. Agrawal, "Effect of Stress During Aging on the Precipitation of θ' in Al-4 Wt Pct Cu," *Metall. Trans. A*, 1975, vol. 6A, pp. 487 - 491.

25. T. Eto, A. Sato, T. Mori, "Stress-Oriented Precipitation of G.P. Zones and θ' in an Al-Cu Alloy," *Acta Metall.*, 1978, vol. 26, pp. 499 - 508.

26. J. K. Tien, S. M. Copley, "The Effect of Uniaxial Stress on the Periodic Morphology of Coherent Gamma Prime Precipitates in Nickel-Based Superalloy Crystals," *Metall. Trans.*, 1971, vol. 2, pp. 215 - 219.

27. T. Miyazaki, K. Nakamura, H. Mori, "Experimental and Theoretical Investigations on Morphological Changes of γ' Precipitates in Ni-Al-Single Crystals During Uniaxial Stress-Annealing," *J. Mat. Sci.*, 1979, vol. 14, pp. 1827 - 1837.

28. G. Lorimer: *Precipitation Processes in Solids*, K. C. Russel, I. Aaronson (Eds.), The Metallurgical Society of AIME, 1978, pp. 87 - 160.

29. U. F. Kocks, J. S. Kallend, H.-R. Wenk, A. D. Rollett, S. I. Wright: "popLA - Preferred Orientation Package - Los Alamos", July 1994, Los Alamos National Laboratory.

30. Annual Book of ASTM Standards, Section3, Metals Test Methods and Analytical Procedures, Volume 03.01, Metals-Mechanical Testing; Elevated and Low-Temperature Tests; Metallography, Philadelphia, PA, 1992.

31. E. E. Underwood, *Quantitative Stereology*, (Reading, MA: Addisone-Wesley Publishing Company, 1970), p. 178.

32. D. B. Williams, *Practical Analytical Electron Microscopy in Materials Science*, Verlag Chemie International, 1984, p. 78.

33. J. C. Williams, E. A. Starke, Jr., "The Role of Thermomechanical Processing in Tailoring the Properties of Aluminum and Titanium Alloys," in *Deformation, Processing and Structure*, ed. George Krauss, ASM, Metals Park, OH, 1984, pp. 279 - 354.

34. W. A. Cassada, G. J. Shiflet, W. A. Jesser, "Heterogeneous Nucleation and Growth of Delta' in Al-8 at Precent-Li", in *Acta Metall. Mater.*, 1992, vol. 40, pp. 2101 - 2111.

35. E. Seitz and D. DeFontaine, "Elastic Interaction Energy Calculations for Guinier-Preston Zones in Al-Cu and Cu-Be," *Acta Metall.*, 1978, vol. 26, pp.1671 - 1679.

36. U. Dahmen, K. H. Westmacott, "Ledge Structure and the Mechanism of θ' Precipitate Growth in Al-Cu," *Phys. Stat. Sol., (a)* , 1983, vol. 80, pp. 249 - 262.

37. S. P. Ringer, B. C. Muddle, I. J. Polmear, "Effects of Cold Work on Precpitation in Al-Cu-Mg-(Ag) and Al-Cu-Li-(mg-Ag) Alloys", in *Metall. Trans. A*, 1995, vol. 26A, pp. 1659 - 1671.

38. Z.M. Wang and G.J. Shiflet, "Heterogeneous Nucleation of δ' on Dislocations in a Dilute Aluminum-Lithium Alloy," *Metall. Trans. A*, in press, 1996.

39. W. M. Stobbs, G. R. Purdy, "The Elastic Accommodation of Semicoherent θ' in Al-4 wt.%Cu Alloy," *Acta Metall.*, 1978, vol. 26, pp. 1069 - 1081.

40. G. Sauthoff: *Z. Metallk.*, "Orienting of Precipitating Gold Particles in an Iron-Molybdenum-Gold Alloy by Exernal Elastic Stress," 1975, vol. 66, pp. 106 - 109.

41. G. Sauthoff: *Z. Metallk.*, "Orienting of Precipitating Au Particles in an Fe-Mo-Au Alloy by External Elastic Stress," 1976, vol. 67, pp. 25 - 29.
42. R. W. Fonda, W. A. Cassada, G. J. Shiflet, "Accommodation of the Misfit Strain Surrounding (III) Precipitates (Omega) in Al-Cu-Mg-(Ag)", in *Acta Metall. Mater.*, 1992, vol. 40, pp 2539 - 2546.
43. H. I. Aaronson, C. Laird, K. R. Kinsman, *Phase Transformations*, Am. Soc. Metals, Metals Park, Ohio, 1970, pp. 313
44. B. Strotzki, H. Hargarter and E.A. Starke, Jr., in Proceedings of the 5th Intern. Conf. on Aluminum Alloys, Their Physical and Mech. Prop., Grenoble, France, July 1996, in press.

Table I: Chemical Composition in wt.%.

Alloy	Cu	Mg	Mn	Ag	Zr	V	Fe	Si	Al
1*	5.00								Bal.
2	5.75	0.52	0.30	0.49	0.16	0.09	0.06	0.05	Bal.

* high purity

Table II: Mechanical Properties at Ambient and Elevated Temperature

Alloy	Condition	Orientation	T [°C]	σ_y [MPa]	UTS [MPa]	ε_f [%]
1	SHT	RD	RT	120.1	274.5	30.8
1	SHT	RD	163	168.8	-	-
2	SHT	RD	RT	167.0	408.8	24.3
2	SHT	45°	RT	181.2	405.2	24.2
2	SHT	TD	RT	169.5	402.8	24.2
2	SHT	RD	163	244.4	-	-
2	T6	RD	RT	480.0	535.4	12.1
2	T6	45°	RT	471.1	520.5	13.3
2	T6	TD	RT	481.4	526.7	12.0
2	T6	RD	163	366.7	-	-

Table III: Misfit, δ, calculated from lattice parameters for Θ″ and Θ′ in aluminum matrix (a_{Al} = 0.4049 nm, $a_{\Theta''}$ = 0.404 nm, $c_{\Theta''}$ = 0.768 nm, $a_{\Theta'}$ = 0.404 nm, $c_{\Theta'}$ = 0.580 nm).

Number of Θ″ unit cells	Number of Al unit cells	Misfit δ [%]	Number of Θ″ unit cells	Number of Al unit cells	Misfit δ [%]
1	2	- 5.2	1	2	- 28
1.5	3	- 5.2	1.5	2	+ 7.4
2	4	- 5.2	2*	3	- 4.5
2.5	5	- 5.2	2.5	4	- 10.5
3	6	- 5.2	3	4	+ 7.4
3.5	7	- 5.2	3.5	5	+ 0.3
4	8	- 5.2	4	6	- 4.5
4.5	9	- 5.2	4.5	6	+ 7.4
5	10	- 5.2	5	7	+ 2.3
			5.5	8	- 1.5
			6	9	- 4.5
			6.5	9	+ 2.1
			7	10	+ 0.3

* Smallest observed Θ′ nucleus

Table IV: Misfit, δ, calculated from lattice parameters for Ω (orthorhombic and tetragonal) in aluminum matrix (a_{Al} = 0.4049 nm, $a_{\Omega, orthorh.}$ = 0.496 nm, $b_{\Omega, orthorh.}$ = 0.895 nm, $c_{\Omega, orthorh.}$ = 0.848 nm, $a_{\Omega, tetra.}$ = 0.6066 nm, $c_{\Omega, tetra.}$ = 0.496 nm).

Number of Ω unit cells (orthorhomb.)	Number of Al unit cells	Misfit δ [%]	Number of Ω unit cells (tetragonal)	Number of Al unit cells	Misfit δ [%]
1	4	- 9.3	1	2	- 8.3
1.5	5	+8.8	1.5	3	- 8.3
2	7	+ 3.6	2	4	- 8.3
2.5	9	+ 0.8	2.5	5	- 8.3
3	11	- 1.1	3	6	- 8.3
3.5	13	- 2.3	3.5	6	+ 7.0
4	15	- 3.3	4	7	+ 4.8
4.5	16	+ 2.0	4.5	8	+ 3.2
5	18	+ 0.8	5	9	+ 1.9
5.5	20	- 0.3	5.5	10	+ 0.8
6	22	- 1.1	6	11	+ 0.1
6.5	24	- 1.8	6.5	12	- 0.1
7	25	+ 1.6	7	13	- 1.2
7.5	28	- 2.8	7.5	14	- 1.7
8	29	+ 0.1	8	15	- 2.2
8.5	31	- 0.5			

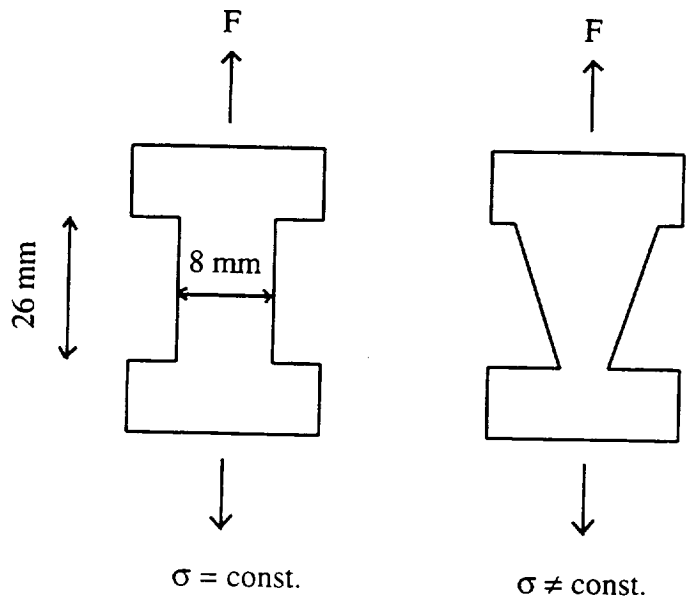

t = sheet thickness

Fig. 1: Creep sample geometry. a) sample with constant cross section b) tapered sample.

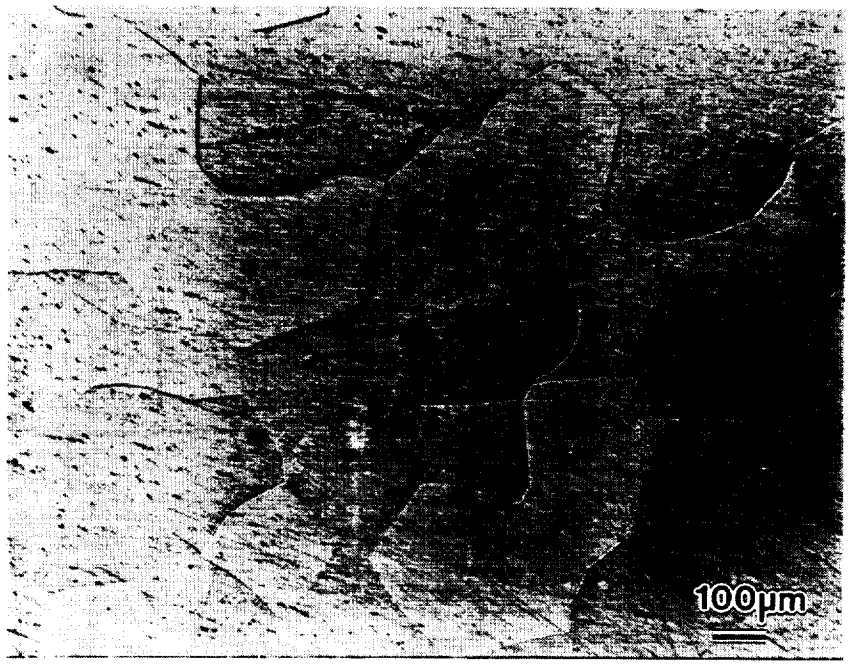

a)

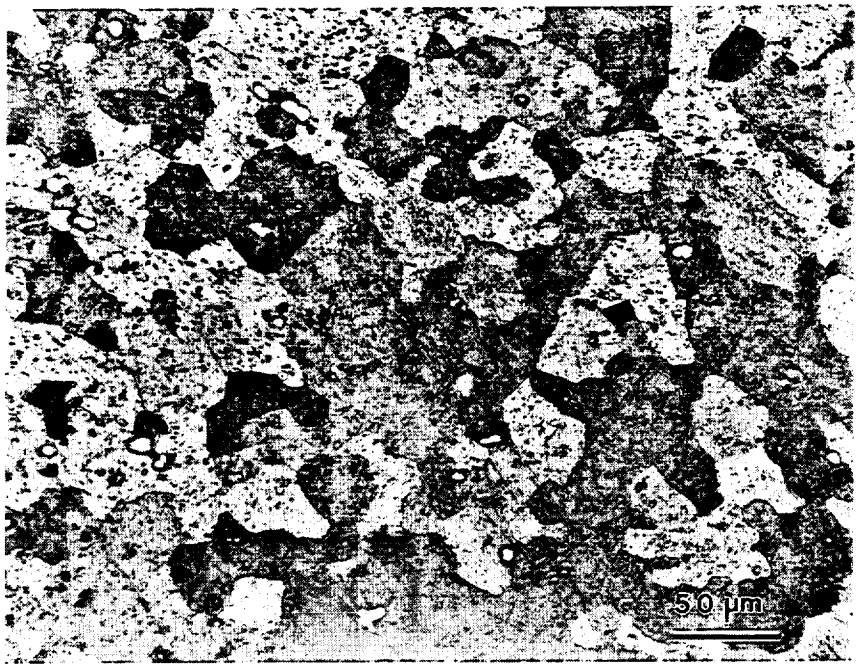

b)

Fig. 2: Completely recrystallized microstructure after solution heat treatment. a) Al-Cu (alloy 1) b) Al-Cu-Mg-Ag (alloy 2). (LM)

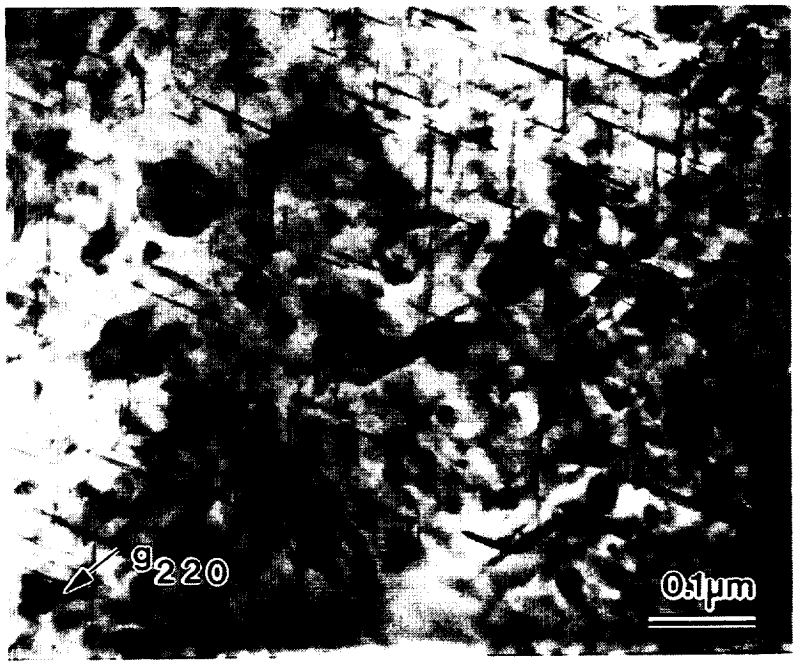

a)

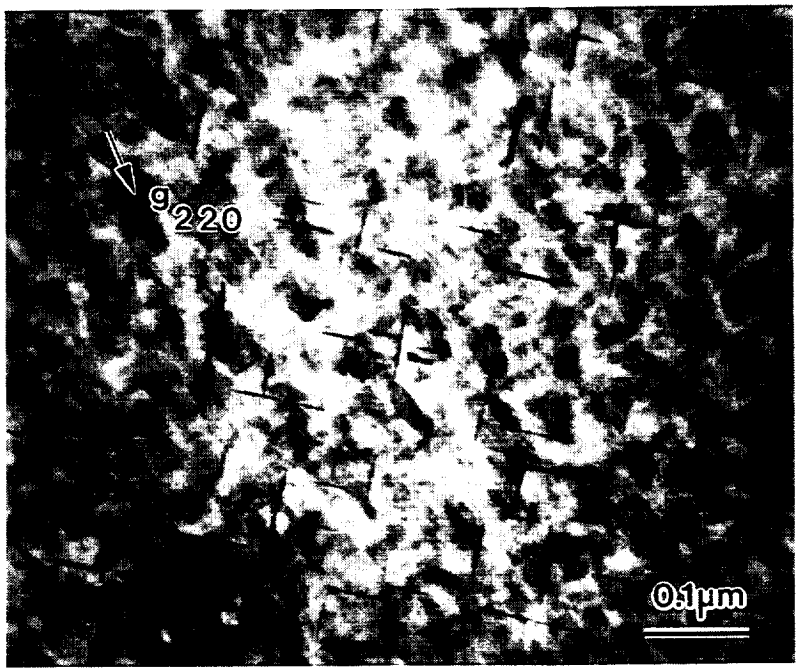

b)

Fig. 3: Microstructure of alloy 2 solution heat treated and aged 20h/160°C/cold water quenched. a) Two Ω and one Θ′ variant: [110] zone axis. b) Two Θ′ variants; [001] zone axis.

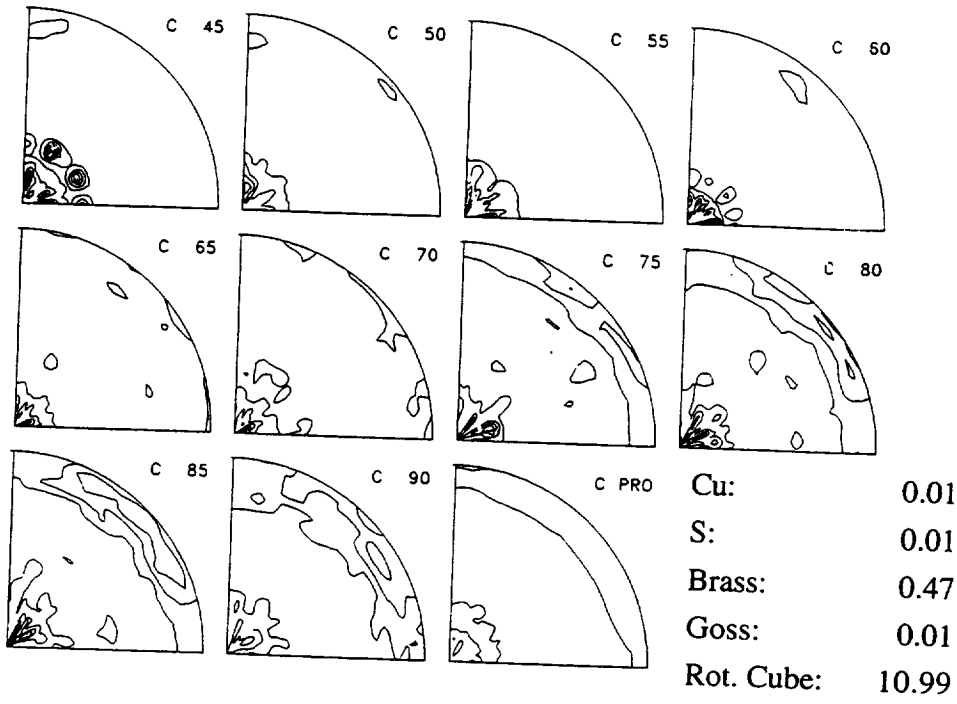

a)

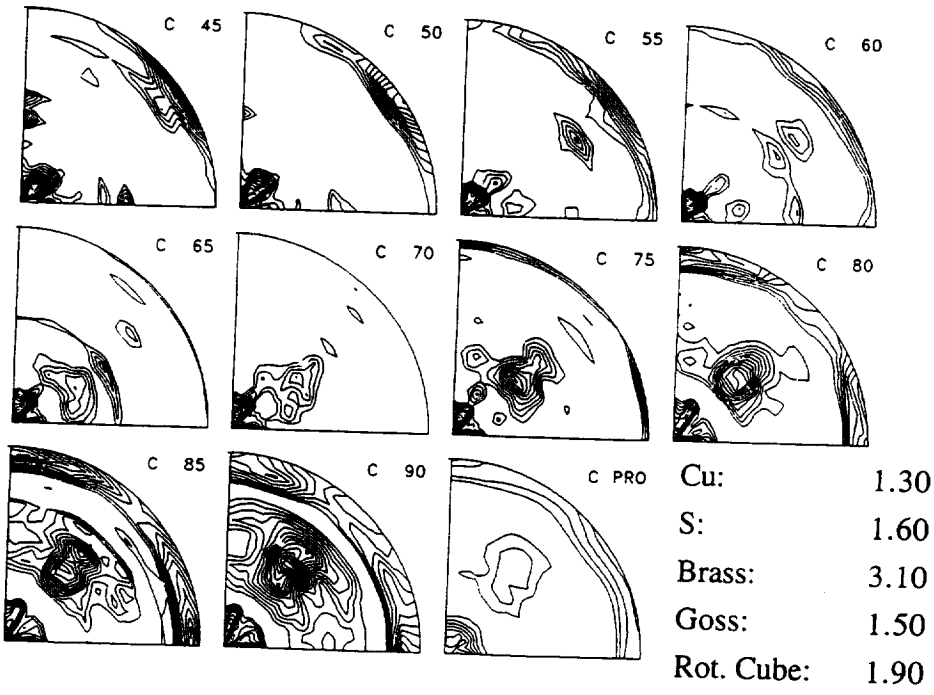

b)

Fig. 4: Orientation distribution functions (ODF) and texture components (in times rando calculated from {111}, {200} and {220} pole figures. Kock's notation, rolling direction w horizontal. a) Al-Cu b) Al-Cu-Mg-Ag.

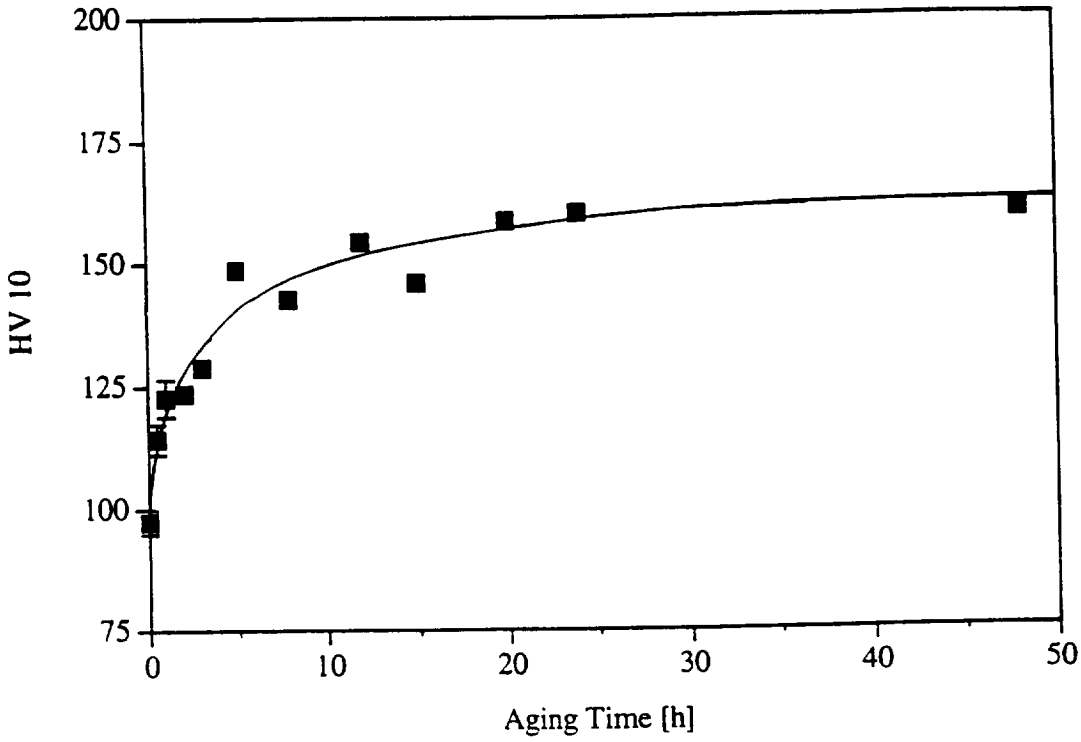

Fig. 5: Age hardening response of alloy 2 after aging at 160°C.

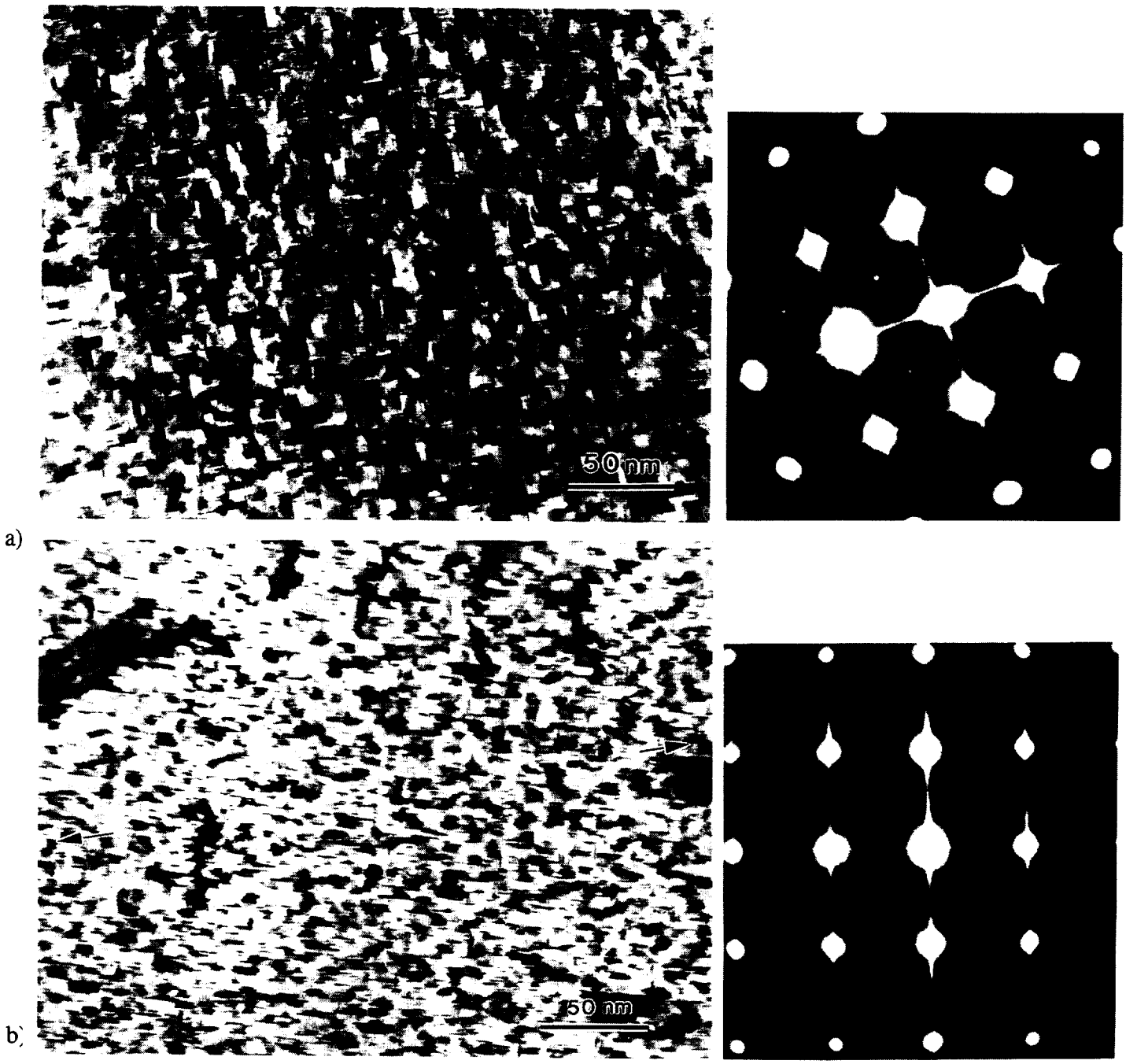

Fig. 6: Initial microstructure of the solutionized material. a) Al-Cu: DSC sample heated to 180°C, no stress applied. Θ″ is randomly distributed and streak intensity is the same for both orientations. [001] zone axis b) Al-Cu: creep sample heated to 160°C with σ = 69.5 MPa applied and cold water quenched. Θ″ precipitates preferentially parallel to the stress axis. The streak intensity is higher for this orientation. [001] zone axis c) Al-Cu: creep sample heated to 160°C with σ = 59.7 MPa + 2h/59.7MPa/160°C/cold water quenched. Θ″ is preferentially oriented parallel to the stress axis. The streaks begin to break up. Their intensity is higher for parallel oriented precipitates. [001] zone axis d) Al-Cu-Mg-Ag: creep sample heated to 160°C with σ = 140.9 MPa and cold water quenched. Θ″ precipitates preferentially parallel to the stress axis No indication for Ω. [110] zone axis.

c)

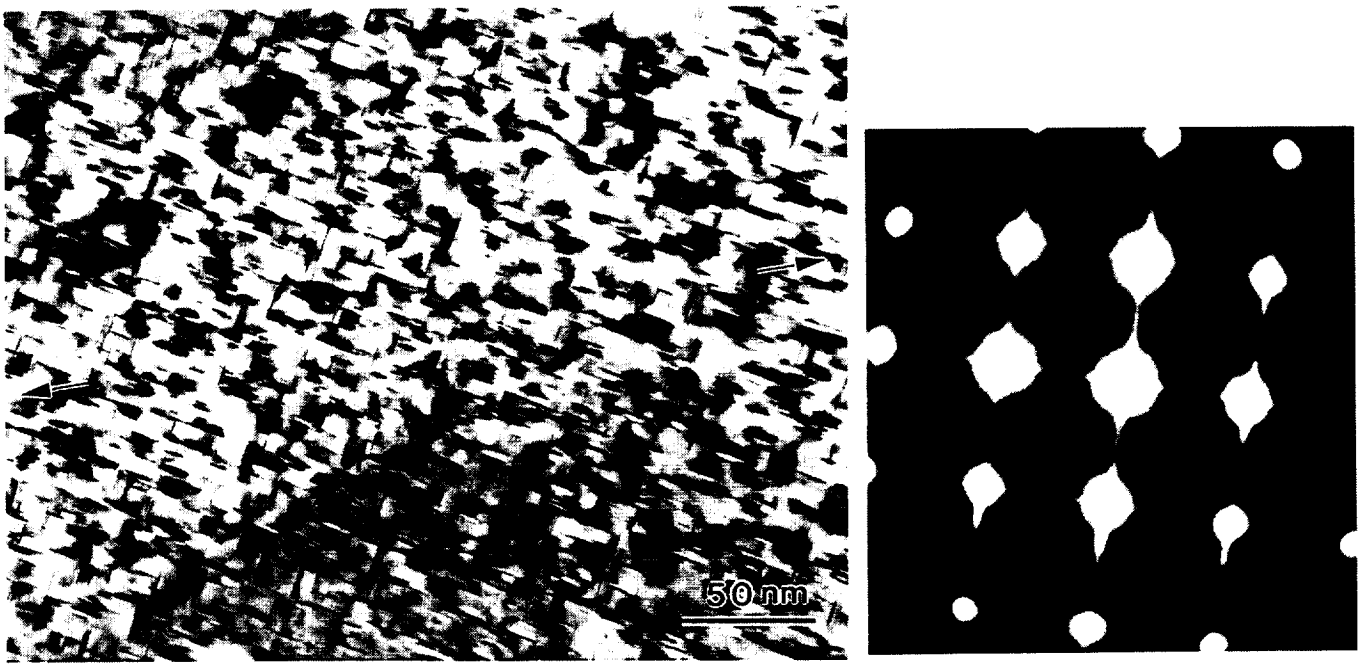

d)

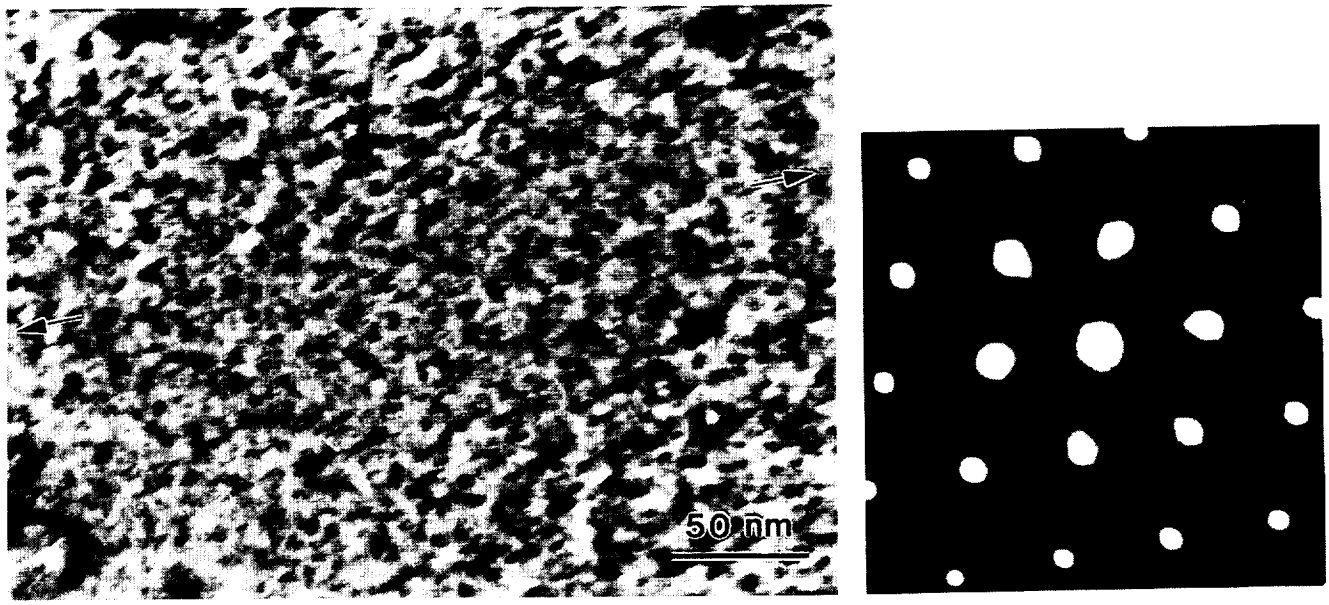

Fig. 6 continued

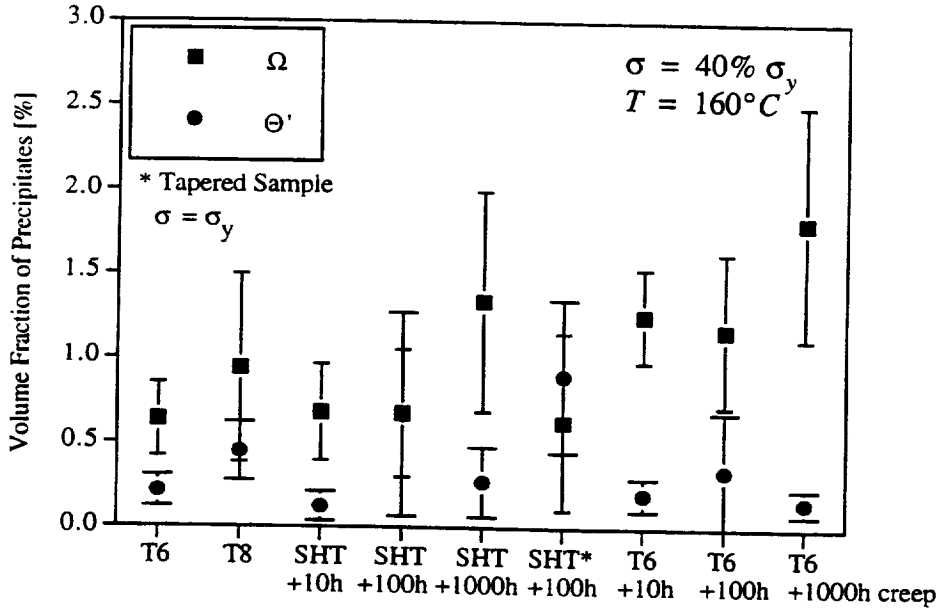

a)

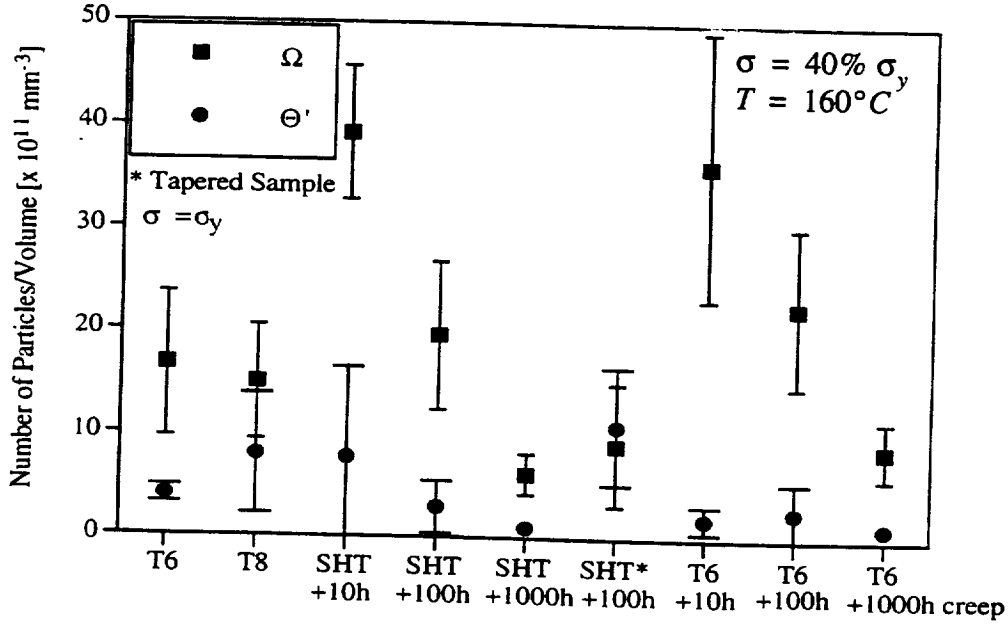

b)

Fig. 7: Quantitative characterization of the microstructure of Al-Cu-Mg-Ag. a) Volume fraction and b) number density of Ω and Θ′ precipitates after conventional aging (T6 and T8) and aging under tensile stress at 160°C in a creep machine. Applied stress was 40 % of the room temperature yield stress in samples with constant cross section and 175 MPa in the tapered sample. c) Average diameter and d) thickness of Ω and Θ′ precipitates. Data from Ringer et al (37) "O" included in c and d.

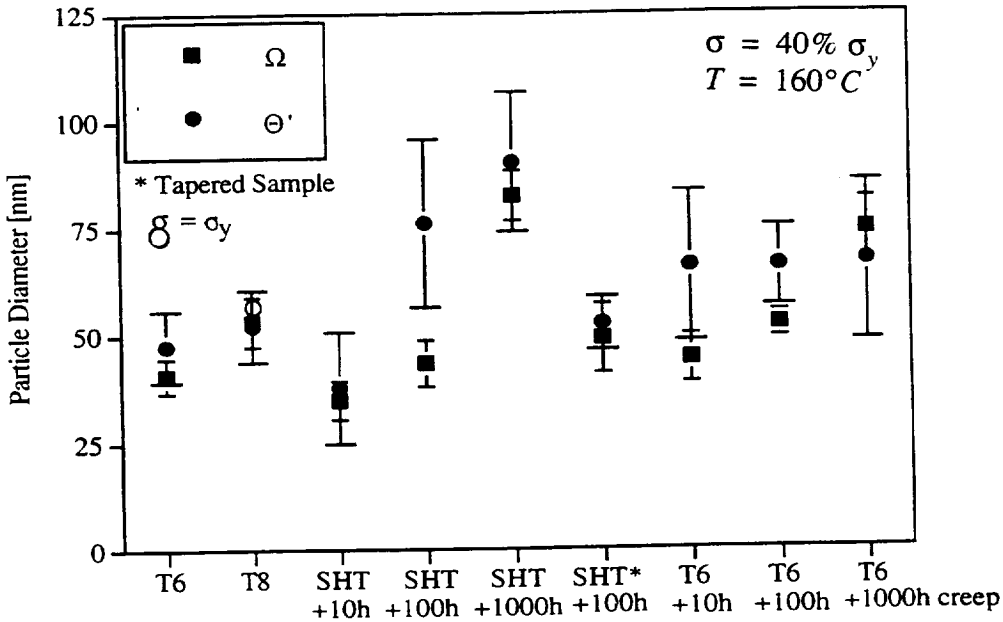

c)

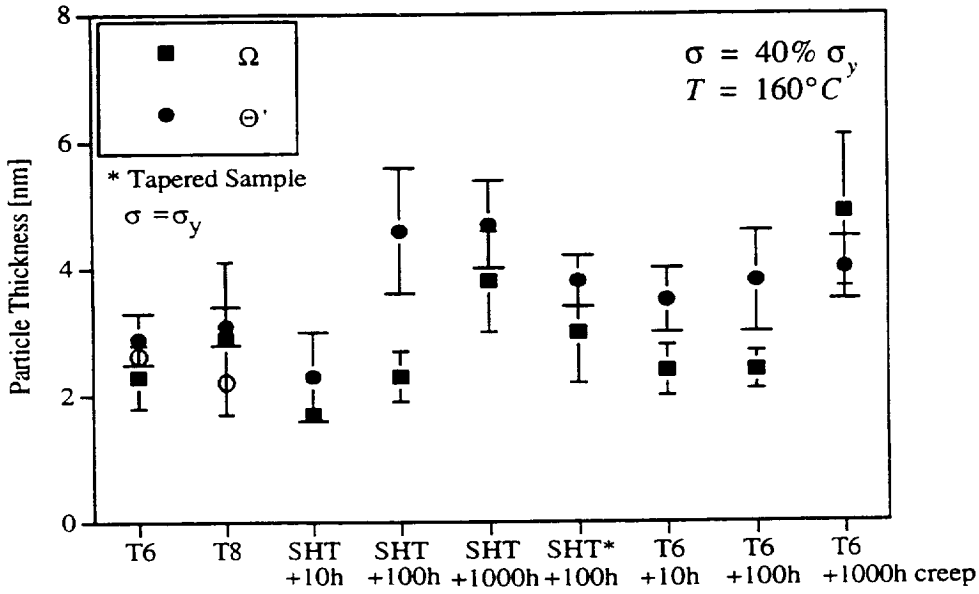

d)

Fig. 7 continued

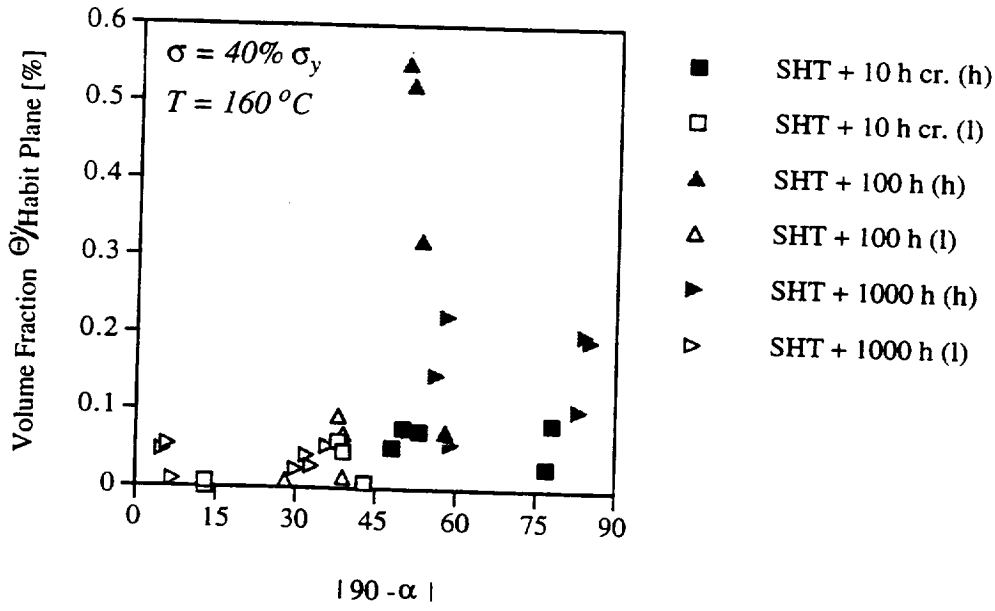

a)

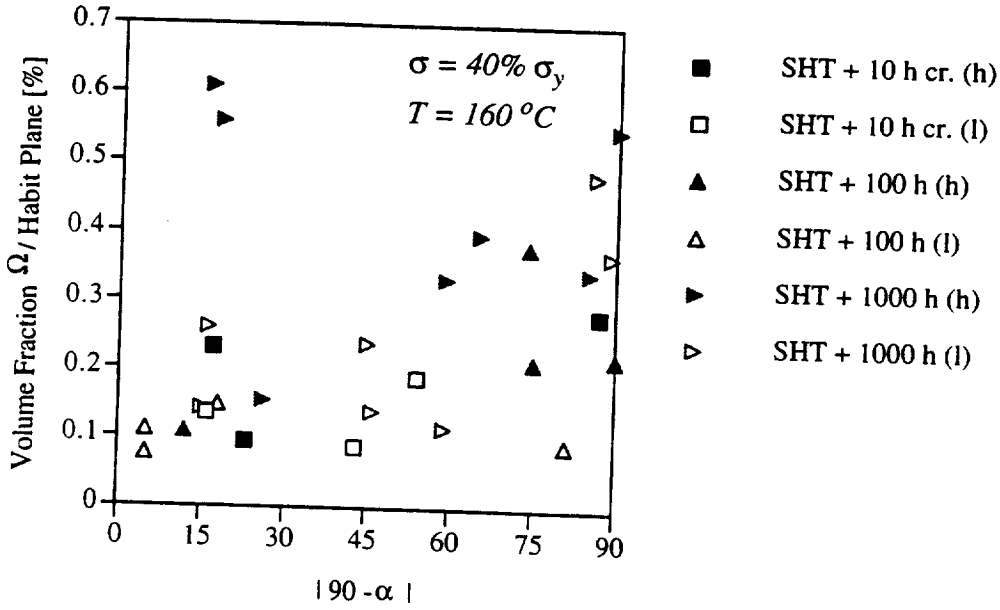

b)

Fig. 8: Volume fraction of precipitates with respect to the angle between precipitate and applied stress axis for alloy 2 after solutionizing. a) Θ′ and b) Ω phase. Full symbols for higher (h), open symbols for lower (l) volume fractions.

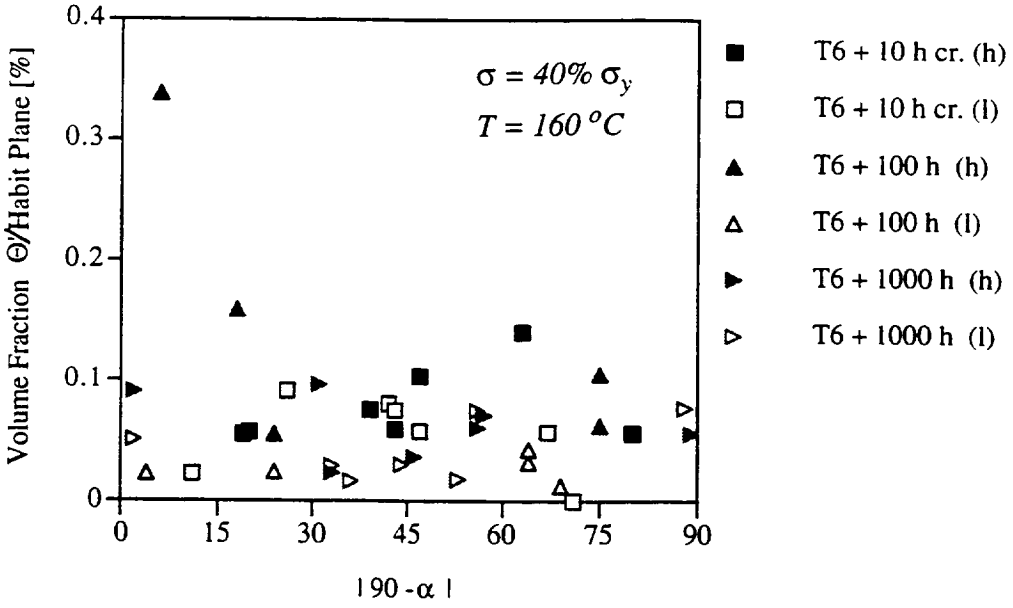

a)

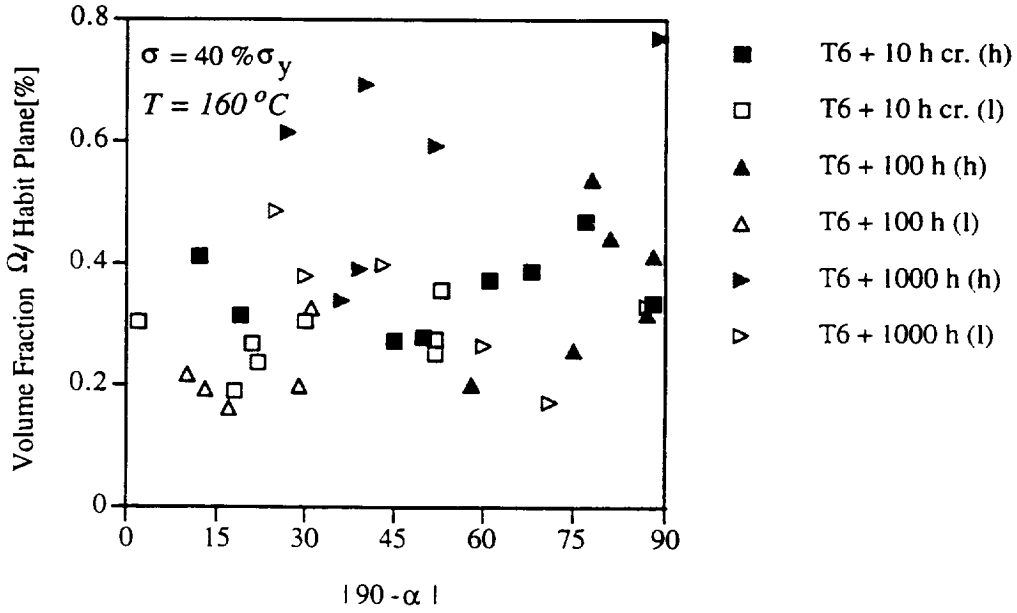

b)

Fig. 9: Volume fraction of precipitates with respect to the angle between precipitate and applied stress axis for alloy 2 in T6 condition. a) Θ′ and b) Ω phase. Full symbols for higher (h), open symbols for lower (l) volume fractions.

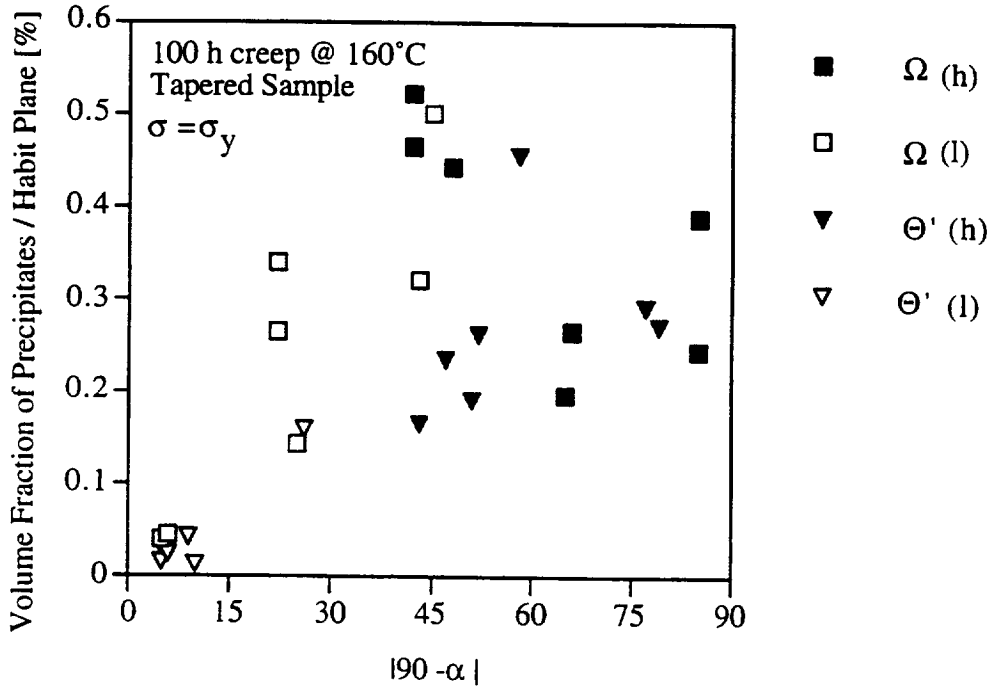

Fig. 10: Preferential precipitation of Ω and Θ′ in solutionized Al-Cu-Mg-Ag. Higher volume fractions (full symbols) are found parallel to the stress axis. The threshold stress has to be exceeded before this effect can be observed.

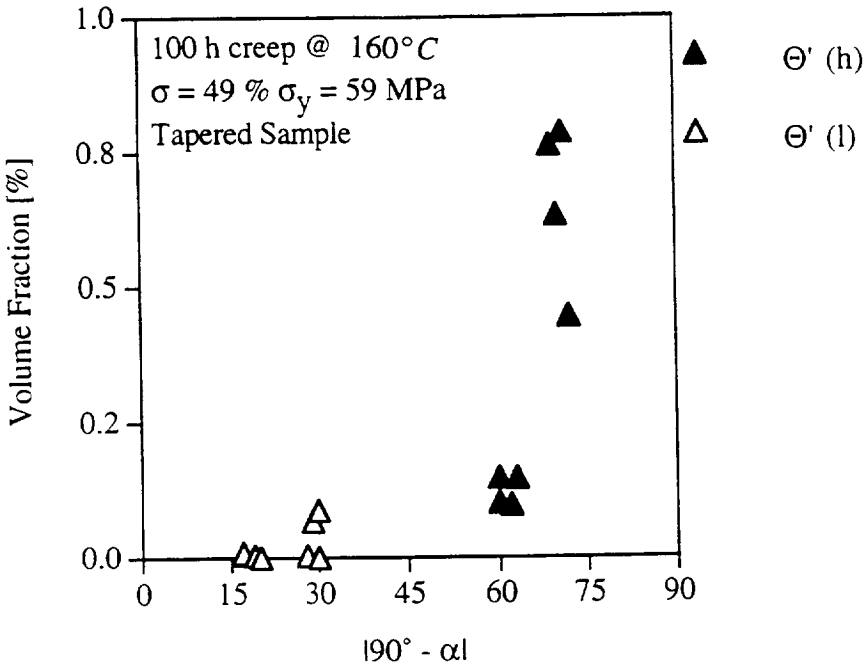

Fig. 11: Θ′ particles precipitate preferentially in Al-Cu. Higher volume fractions (full symbols) are observed parallel to the stress axis.

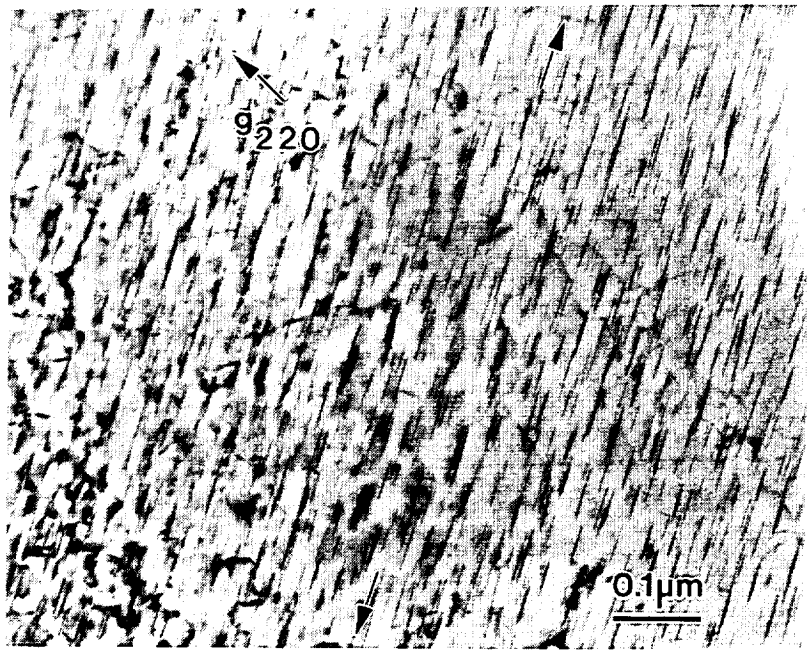

Fig. 12: Microstructure of Al-Cu, solutionized, quenched and aged under a stress of 33.4 MPa for 100 h at 160°C. The stress direction is indicated by arrows. Θ′ precipitates are preferentially oriented parallel to the stress axis.

a)

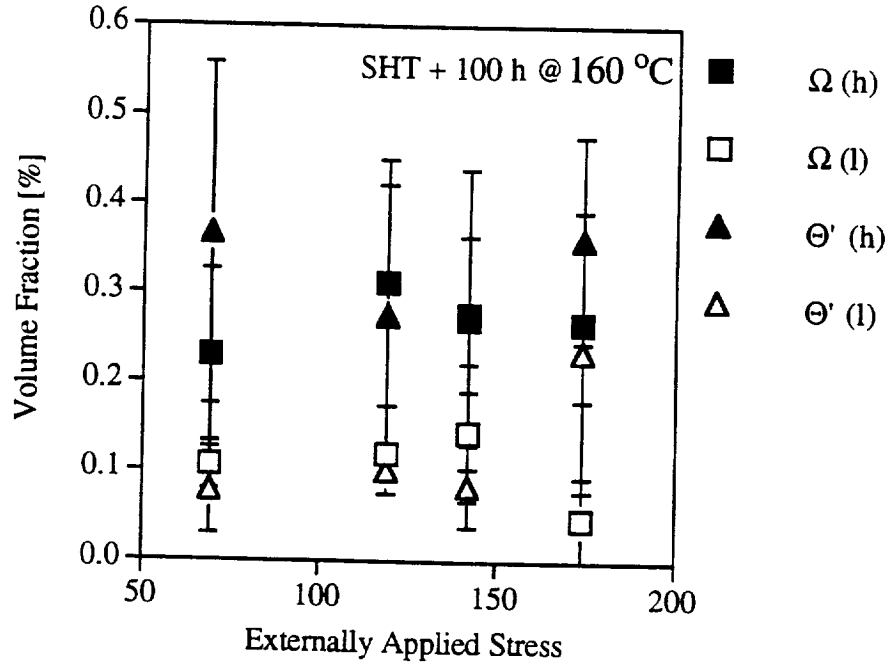

b)

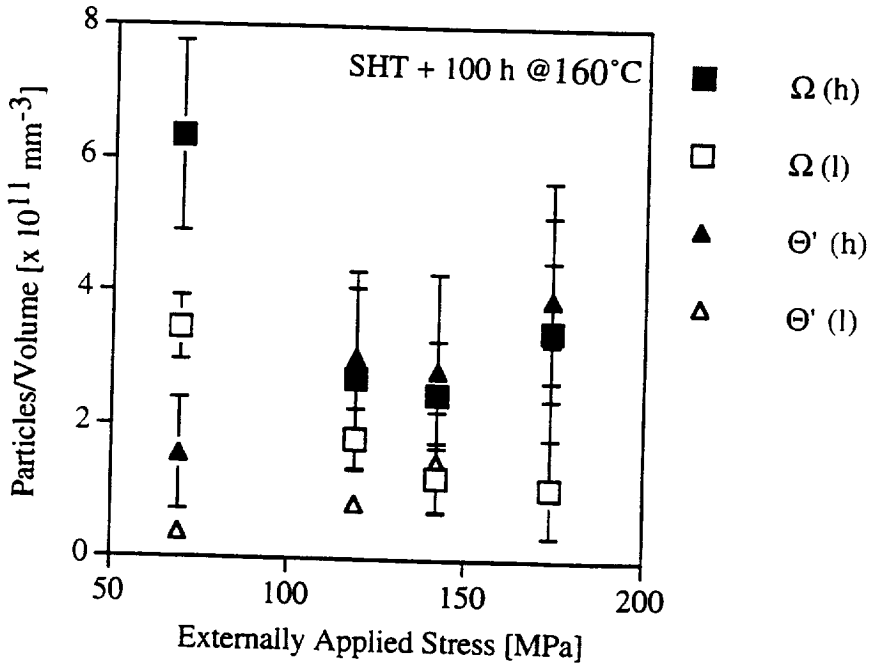

Fig. 13: a) Volume fraction and b) number density of precipitates in Al-Cu-Mg-Ag as a function of the externally applied stress.

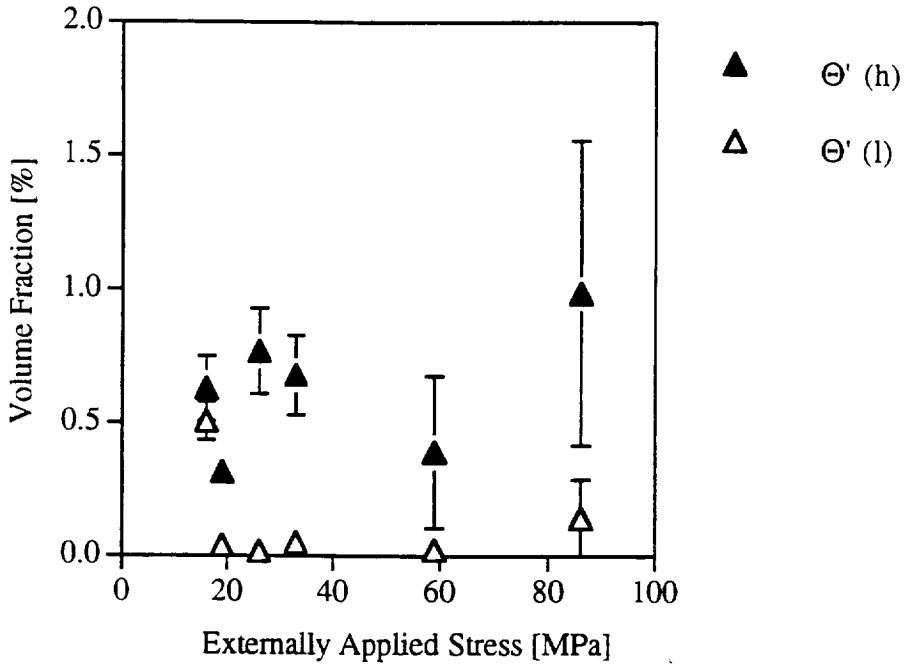

a)

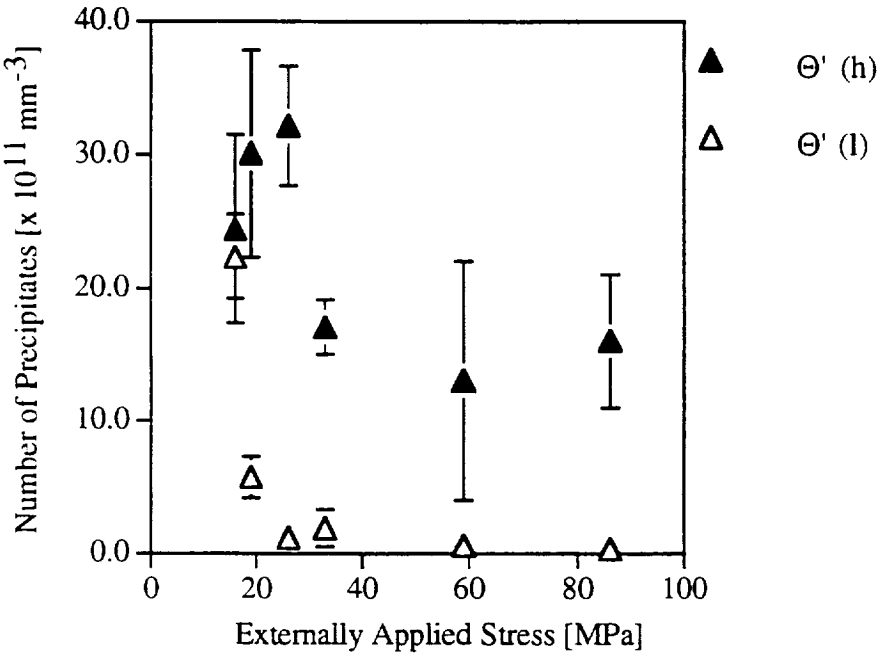

b)

Fig. 14: a) Volume fraction and b) number density of Θ′ precipitates in Al-Cu as a function of the externally applied stress.

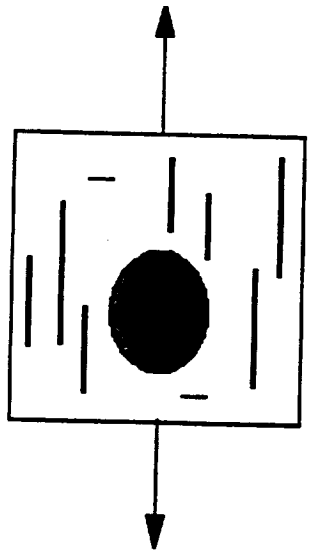

Fig. 15: Precipitates are preferentially aligned parallel to the external stress direction (schematic drawing).

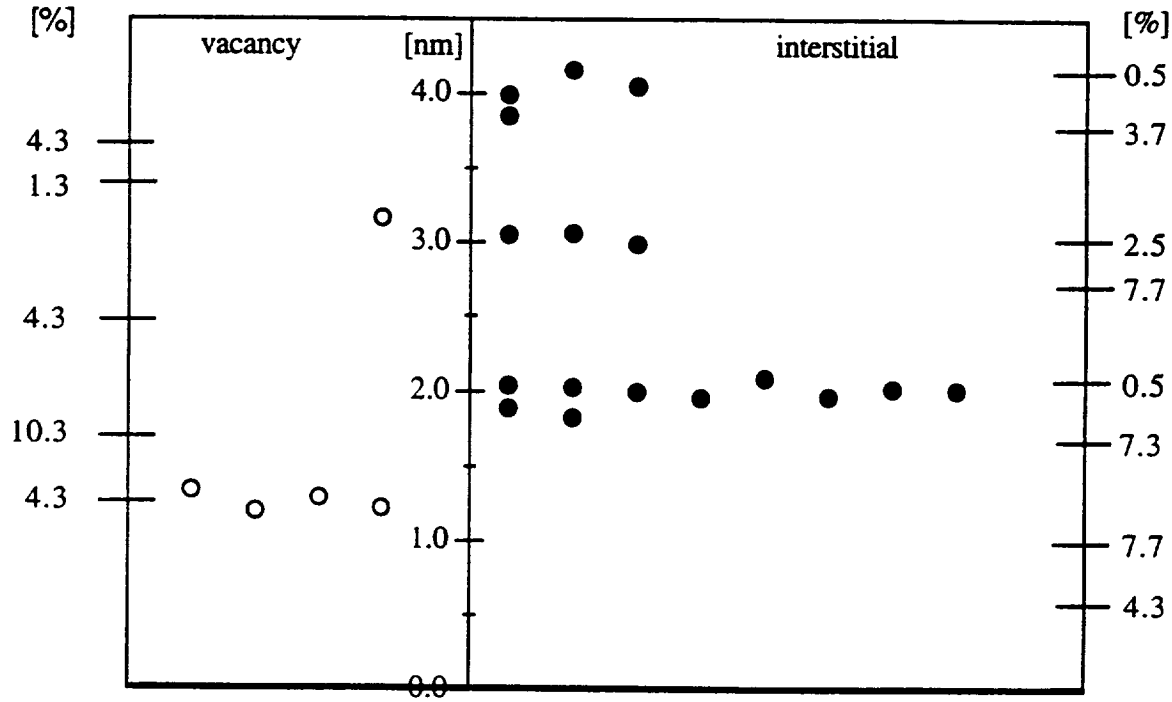

Fig. 16: Correlation of the sense of misfit with plate thickness for thinner plates (< 4 nm). For comparison the thicknesses of successive full and half Θ′ unit cells are marked. Those on the left have a negative misfit and those on the right a positive. (W. M. Stobbs, G. R. Purdy[39])

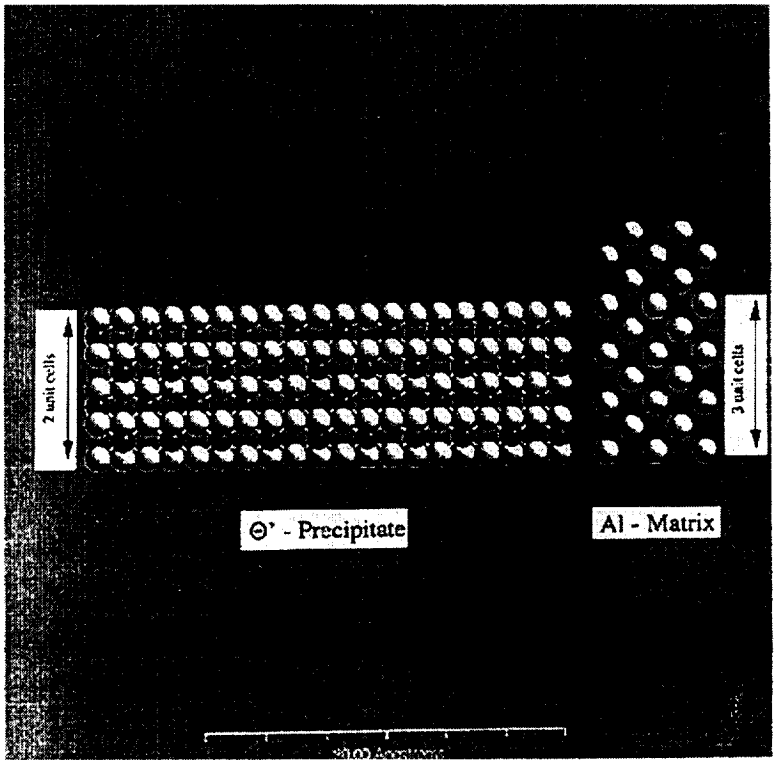

Fig. 17: Crystallographic model of a 2 unit cell Θ′ nucleus which fits into 3 unit cells of the Aluminum matrix. Cube/cube relationship.

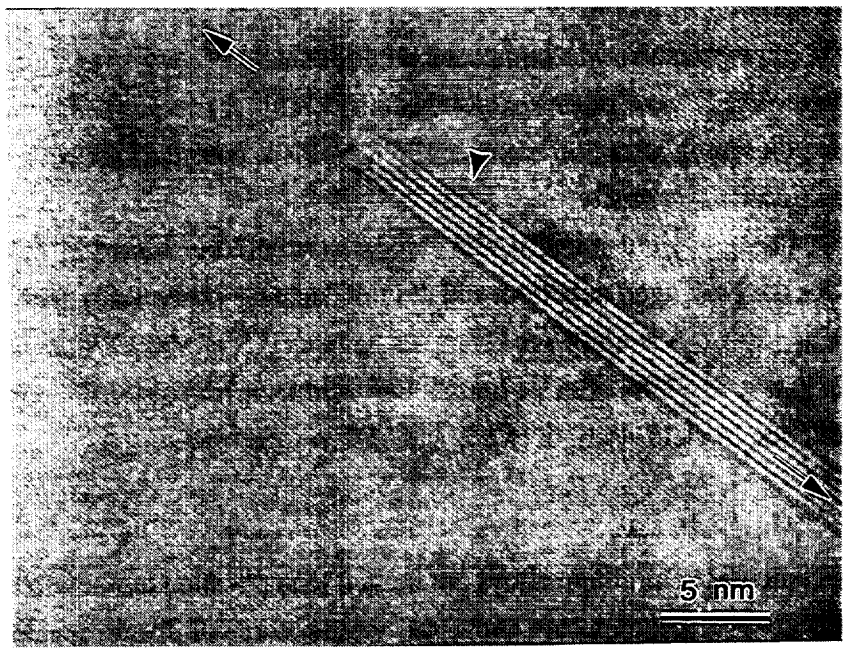

Fig. 18: HRTEM micrograph of Al-Cu-Mg-Ag, solutionized and aged 1000 h at 160°C with a tensile stress of 69 MPa. Ω precipitate with a growth ledge. The stress axis is indicated by arrows. [110] zone axis.

UNIVERSITY OF VIRGINIA

Investigation of the Formation of the Ω Phase In Modified 2009 (Al-Cu-Mg/SiCp) And Characterization of the Modified Alloys' Thermomechanical Properties

Principal Investigator: Professor Frank Wawner
Consultant: Professor E.A. Starke
Graduate Student: Mr. Qiong Li

Foreword

This report is a summary of the PhD dissertation of Dr. Qiong Li. The complete dissertation was submitted in the form of a final project report to NASA, to the attention of Dennis Dicus and William Brewer, project monitors.

Abstract

The objective of this investigation was to modify 2009 (a Al/SiC particulate material produced by Advanced Composite Materials Corporation) by adding silver to promote the formation of the Ω phase in the material in order to increase the composite's elevated temperature stability.

The anticipated Ω phase was not obtained in the matrix of the 2009M/SiC composite. It is felt that this is due to the low Cu/Mg ratio in the material produced by ACMC and an unexpected large amount of Si in the matrix due to aluminum reaction with the SiC particles from exceeding the solidus temperature during composite fabrication. Silicon in an Al-Cu-Mg-Ag alloy has been shown to inhibit Ω phase formation.

The matrix microstructure was composed predominately of very small, uniformly distributed S' phase. The S' precipitates exhibited considerable thermal stability in that they showed very little coarsening after 500 hours at 150°C. This is considerably better than literature data on similar composite systems.

The tensile strength, yield strength, and elongation to failture were 521 MPa, 424 MPa and 5% respectively for the peak aged condition and did not decrease appreciably with prolonged thermal exposure at 150°C. Naturally aged samples gave a UTS of 500 MPa, a yield strength of 305 MPa and elongation of >10% after 24 hours. Elevated temperature tensile tests at 150°C and 177°C gave a reduction in yield strength of 8% and 15% respectively.

Introduction

Most age hardenable aluminum alloys are limited to application temperatures below approximately 100°C. Thermal exposure above this temperature will result in a degradation of

mechanical properties due to coarsening of the precipitates on which the alloys depend for their strength. Discontinuous reinforced composites composed of Al-Cu-Mg/SiC_p, because of their higher modulus than conventional Al alloys, are being considered for elevated temperature applications such as the High Speed Civil Transport (HSCT) program.

Al-Cu-Mg alloys containing a small amount of Ag have been shown to possess superior mechanical properties and thermal stability above 100°C. This is mainly due to formation of the semi-coherent Ω phase in the alloy, which is more thermally stable than the normal θ′ percipitate. It was felt that using an alloy strengthened by the Ω phase as a matrix alloy could generate a high modulus composite material with greater elevated temperature stablity in HSCT applications.

The objective of this study was to modify 2009 (an Al-Cu-Mg/SiC_p material produced by Advanced Composite Materials Corporation) with Ag additions and optimum Cu/Mg ratio in an attempt to achieve the formation of the Ω phase in the composite. This modified material was then characterized with respect to microstructure, aging response, thermal stability, and mechanical properties.

Summary of Results

Matrix Alloy Development: The results from the Al-Cu-Mg-Ag alloy (to be used for the composite matrix) studies indicate that variations as small as 0.1 (wt%) Ag addition can change the thermal stability and hardness of the alloy. The study shows that higher Cu/Mg ratio gives higher strength. Lower Cu/Mg ratio gives more thermal stability.

All of the experimental Ag containing alloys were more thermally stable than similar alloys without the Ag addition. Hardness and shear strength data indicated that the alloy Al-3.2Cu-0.45Mg-O.5Ag (wt%) and designated A11MM possesses the best thermal stability among the experimental alloys. The shear strength dropped only 15% for the A11MM alloy after aging at 150°C for 3023 hours.

Four precipitate phases were found in the Al-Cu-Mg-Ag experimental alloys. The Ω phase was the primary phase while θ′ and S′ were present in minor amounts. A cubic phase, σ ($Al_5Cu_6Mg_2$), was also found in the alloy. This phase was scattered throughout the alloy, however it was not determined how to routinely obtain it in high volume percent.

The σ phase has a cube-on-cube relationship and is semicoherent with the Al matrix. The point group of this phase was determined as 23 (one of the cubic point groups) by using Convergent Beam Electron Diffraction (CBED) techniques. The Young's modulus, shear modulus

and Poisson's ratio of the intermetallic σ phase were determined to be: E=159.3 Gpa; G=60.89 Gpa; and Poisson's ratio = 0.308. The σ phase possesses a high hardness value at room temperature (H=546 Kg/mm^2), which translates to a high value for yield strength (1784 MPa). At 350°C, the hardness of the intermetallic σ phase retained 70% of its room temperature value. A very low coarsening behavior for this phase was found after aging at 200°C, which implies that Al alloys strengthened by the σ precipitate could have superior thermal stability.

Coarsening studies show that the θ′ phase in an Al-Cu alloy has a larger size and a longer growth period than the Ω and σ phases in Al-Cu-Mg-Ag alloys at 200°C. The Ω phase has a larger size and a longer growth period than the σ phase at 200°C. The morphologies of growth ledges vary in different precipitates. Straight and facet ledges (which were observed in Ω and σ) correspond to a small size and low growth rate in precipitates. Rounded ledges (as were seen in θ′) correspond to a large size and high growth rate. Results from the present study indicate that the growth of Ω and σ do not follow Lifshitz-Slyozov-Wagner (LSW) predictions. The experimental data suggests that the Ω phase may not be a stable phase for extended elevated temperature exposure. After exposure at 150°C for 3023 hours, TEM results show that the density of θ′ and S′ precipitates increases, some large size θ develops, and the density of the Ω phase decreases.

Estimates for the interfacial energies of the Ω and σ phases were determined. Based on the van de Merwe model and broken bond model, calculations for the interfacial energy of the σ phase was estimated as 0.014 J/m^2. Using the Zener-Hillert equation, the interfacial energy for the Ω phase was estimated to be 0.0118 J/m^2 for the coherent face and 0.354 J/m^2 for the edge.

A strengthening mechanism resulting from dislocation shearing was proposed for alloys containing semicoherent precipitates. TEM and HRTEM observations showed that multiple cutting and small steps with the same height occurred in the Ω phase. The cutting caused antiphase boundaries and disorder in the Ω phase which could be resolved in the TEM. Because of the difference in crystal structure and slip systems between the precipitates and the matrix, the moving direction of a dislocation changes as it impinges on the semicoherent precipitate. After cutting, a high energy interface with a mismatched bond is created at the semicoherent precipitate/matrix interface because of the different crystal structure and Burgers vector in each phase. The larger the

Burgers vectors are, the higher the interfacial energy of the newly created interface. Multiple small cutting of a semicoherent phase, such as Ω, is energetically more favorable than a large cutting in one location, therefore, as the Burgers vector increases, the interfacial energy of the new interface could increase nonlinearly. As a result, dislocation shearing weakens alloys with coherent precipitates but those with semicoherent precipitates are strengthened.

Investigation of the effect of dislocation density on Ω phase formation indicates that preaging deformation of the Al-Cu-Mg-Ag alloy can promote S′ and θ′ formation and reduce the amount of Ω phase. In order to obtain maximum Ω phase in the alloys preaging deformation must be minimized.

Modified Composite Development: The alloy with the composition Al-3.2Cu-0.45Mg-0.5Ag (designated A11MM) was selected as the matrix alloy for forming the composites since it was determined that this alloy precipitated a high density of the Ω phase with optimum heat treatment and exhibited the best thermal stability. The composites (2009M/SiC_p) produced from this alloy did not contain appreciable amounts of the Ω phase. The S′ phase was seen to be the predominant precipitate in the 2009M/SiC_p material. The reasons for the Ω phase suppression can be summarized as follows:

i) high Si content in the matrix of the composite which dissolved from the SiC particles during composite fabrication (as a result of exceeding the solidus) inhibits the Ω phase formation

ii) high dislocation density caused by the Coefficient of Thermal Expansion (CTE) difference of the reinforcement and matrix promotes S′ and θ′ precipitate formation in lieu of Ω in the matrix

iii) a low vacancy concentration may be present in the matrix of the composites due to the high density of vacancy sinks such as sub-grain and grain boundaries (the material has very small grain size), the Al/SiC_p interfaces, and the large number of dislocations

iv) composition segregation which occurred at grain boundaries, triple points, and Al/SiC interfaces may also alter the matrix composition.

Although the Ω phase was not achieved in the 2009M/SiC_p material, Ag addition gave a matrix microstructure that was composed predominately of very small, uniformly distributed S′ phase. The S′ precipitates exhibited unusual thermal stability in that they showed very little coarsening after 1600 hours at 150°C. This is considerably better than literature data on similar composite systems. The study shows that kinetics data (KT value) for coarsening of the S′ precipitate in 2009M/SiC_p is lower than for the Ω phase in most Al- Cu-Mg-Ag alloys and S′ in the standard 2009/SiC composite. The thermal stability of the modified composite was comparable to the A11MM alloy (Ω phase strengthened).

The room temperature tensile strength, yield strength, and elongation to failure for the 2009M/SiC_p composites were 521 MPa, 424 MPa, and >5% respectively for the 190°C peak aged condition and did not decrease apprecibly with prolonged thermal exposure at 150°C (8% after 1600 hours). Exposure at 177°C showed a 12% and 19% reduction in UTS after 125 and 500 hours respectively. Peak aging at 160°C gave the highest strengths and elongation (542 MPa, 440 MPa, 6.1%). Elevated temperature tensile tests at 150 and 177°C gave a reduction in yield strength of 8% and 15% respectively. Thermal cycling over the range of 32-150°C for 500 cycles did not degrade tensile properties. Fracture toughness for the composite is similar to the standard material with an unmodified matrix, 22.7 $MPam^{1/2}$, does not decrease when determined at 150°C.

Based on the experimental results and theoretical analysis, it is suggested that residual stress in the particulate reinforced composite reduces the nucleation barrier and increases the driving force for precipitation in the composite. This may result in a shift of the T-T-T curve and a uniform distribution of the S′ precipitation in the composite. This can also contribute to the aging acceleration for the composites. As a result of the analysis, the aging acceleration of the composites can be considered as a combination of several factors:

i) high dislocation density promotes a higher number of nucleation sites, and a lower nucleation barrier for precipitation

ii) residual stress increases driving force of the precipitation and decreases the nucleation barrier

iii) relaxation of the residual stresses may contribute to the sharp increase of the aging curve.

A comparison of some characteristics for the matrix alloy (A11MM), 2009M/SiC_p are summarized in the following table.

Summary of the characteristics of the alloy and composite

	A11MM	2009M/SiC_p 15 v/o	2009/SiC_p 19 v/o
precipitate (major)	Ω	S'	S'
hardness (HRB)	69	80	-
E (GPa)	70	91	96
UTS (MPa)	440	550	550
YS (MPa)	344	410	410
elongation (%)	>10	5≈6	3
n (R-O) 25°C	13.8	11.1	7.5
n (R-O) 150°C	32.5	13.8	-
k^{1c} MPa√M	>30	21.2	20.3
Q (kJ/mol)	132 (Ω)	69 (S')	55.3 (S') (15 v/o)
KT (knm^3s^{-1}) 190°C	321 (Ω)	50 (S')	149 (S') (15 v/o)

REPORT DOCUMENTATION PAGE

Form Approved
OMB No. 0704-0188

1. AGENCY USE ONLY (Leave blank)	2. REPORT DATE	3. REPORT TYPE AND DATES COVERED
	December 1997	Contractor Report 1/1/92 to 10/31/95

4. TITLE AND SUBTITLE
NASA-UVa Light Aerospace Alloy and Structure Technology Program
Supplement: Aluminum-Based Materials for High Speed Aircraft
Final Report

5. FUNDING NUMBERS
G NAG1-745
WU 537-06-31-20

6. AUTHOR(S)
E.A. Starke, Jr.

7. PERFORMING ORGANIZATION NAME(S) AND ADDRESS(ES)
School of Engineering and Applied Science
University of Virginia
Thornton Hall
Charlottesville, VA 22903

8. PERFORMING ORGANIZATION REPORT NUMBER
UVA/528266/MSE96/120

9. SPONSORING/MONITORING AGENCY NAME(S) AND ADDRESS(ES)
National Aeronautics and Space Administration
Langley Research Center
Hampton, VA 23681-2199

10. SPONSORING/MONITORING AGENCY REPORT NUMBER
NASA/CR-97-206248

11. SUPPLEMENTARY NOTES
Langley Technical Monitor: Dennis L. Dicus

12a. DISTRIBUTION/AVAILABILITY STATEMENT
Unclassified - Unlimited
Subject Category 26
Distribution: Standard
Availability: NASA CASI (301) 621-0390

12b. DISTRIBUTION CODE

13. ABSTRACT *(Maximum 200 words)*

This is the final report of the study "Aluminum-Based Materials for High Speed Aircraft" which had the objectives (1) to identify the most promising aluminum-based materials with respect to major structural use on the HSCT and to further develop those materials and (2) to assess the materials through detailed trade and evaluation studies with respect to their structural efficiency on the HSCT. The research team consisted of ALCOA, Allied-Signal, Boeing, McDonnell Douglas, Reynolds Metals and the University of Virginia. Four classes of aluminum alloys were investigated: (1) I/M 2XXX containing Li and I/M 2XXX without Li, (2) I/M 6XXX, (3) two P/M 2XXX alloys, and (4) two different aluminum-based metal matrix composites (MMC). The I/M alloys were targeted for a Mach 2.0 aircraft and the P/M and MMC alloys were targeted for a Mach 2.4 aircraft. Design studies were conducted using several different concepts including skin/stiffener (baseline), honeycomb sandwich, integrally stiffened and hybrid adaptations (conventionally stiffened thin-sandwich skins). Alloy development included fundamental studies of coarsening behavior, the effect of stress on nucleation and growth of precipitates, and fracture toughness as a function of temperature were an integral part of this program. The details of all phases of the research are described in this final report.

14. SUBJECT TERMS
alloys, composites

15. NUMBER OF PAGES
574

16. PRICE CODE
A24

17. SECURITY CLASSIFICATION OF REPORT	18. SECURITY CLASSIFICATION OF THIS PAGE	19. SECURITY CLASSIFICATION OF ABSTRACT	20. LIMITATION OF ABSTRACT
Unclassified	Unclassified	Unclassified	UL